UAB
Universitat Autònoma de Barcelona

Development of functional inks and printed devices for transient and eco-friendly electronics

Tammy Leung

Universitat Autònoma de Barcelona

Tesi doctoral

Development of functional inks and printed devices for transient and eco-friendly electronics

Tammy Leung

Directors:

Dr. Eloi Ramon Garcia

Dra. Carme Martínez Domingo

Tutor:

Dr. Lluís Terés Terés

Universitat Autònoma de Barcelona

Departament d'Enginyeria Electrònica

Programa de Doctorat en Enginyeria Electrònica i de Telecomunicació

Bellaterra (Barcelona), Setembre 2023

I certify that I have read the dissertation "*Development of functional inks and printed devices for transient and eco-friendly electronics*" and agree that it adequately fulfills all requirements as a dissertation for the degree of Doctor of Philosophy.

Universitat Autònoma de Barcelona
Departament d'Enginyeria Electrònica
Programa de Doctorat en Enginyeria Electrònica i de Telecomunicació

This work was mainly carried out at Institut de Microelectrònica de Barcelona - Centre Nacional de Microelectrònica, IMB-CNM (CSIC).

The universe is not required to be in perfect harmony with human ambition

Carl Sagan

Abstract

Humans are at a critical point in history where our decisions now will have dramatic impact in the future, one of which is our effort in reducing the amount of electronic waste generated every year. For this reason, implementation of biodegradable materials and eco-friendly manufacturing methods into the development of electronics is paramount. This is achievable using low impact and low waste techniques such as inkjet printing that can deposit any ink material onto any chosen substrate. This coupled with a host of low temperature sintering techniques such as plasma, chemical, and photonic sintering can generate conductive thin metal films thus facilitating the development of a wide range of electronic components.

Therefore, the focus of this thesis is on the development of transient electronics through replacement of different layers with known biodegradable materials and adapting them to processing techniques. Starting at its core, a materials selection process was conducted to choose an appropriate substrate based on their respective material properties achieving surface roughness < 10 nm with good thermal stability. From this, silk fibroin and CNF were deemed compatible while PVA was utilized as the primary substrate throughout the thesis. Simultaneously, two different types of inks were formulated, and inkjet printed onto these respective substrates to verify their suitability. Here, the formulation of biodegradable Zn and Mo metal inks were established based on their reactivity towards a large range of solvents and stabilizers until good stability was achieved. Due to their respective nanoparticle melting point depression, photonic curing was pursued as the primary sintering method achieving films with conductivities as high as 1×10^3 $S \cdot m^{-1}$ for Zn and resistances in the range of hundreds of ohm for Mo as oxidation remained a problem for these materials.

Alternatively, metal salt decomposition (MSD) inks concentrated mainly on the development of noble metal thin films by oxygen plasma sintering, namely Au and Pt, producing films with good conductivity as high as 3×10^5 and 4×10^4 $S \cdot m^{-1}$ respectively. Film conductivity was maximized by adjusting both printing and sintering parameters accordingly showing that sintering temperatures never exceeded 37°C. Here, Au films were formed on wide range of non-conventional substrates such as polymers, papers, and textiles demonstrating that such films showed excellent conformity, durability, and flexibility. These characteristics are particularly advantageous in the development of wearable electronics which saw excellent tensile strain resistance beyond 10% never exhibiting a complete failure. Additionally, Au nanoparticle (NP) films were used as both the working and counter electrode in the development of a fully inkjet printed glucose biosensor. Here, the non-enzymatic detection of glucose was achieved through electrooxidation showing detection in the mM range.

Additionally, an innovative approach to the development of room temperature Au NP film formation was discovered when combining the Au MSD ink with PVA as the reducing substrate.

Here the reduction mechanism was identified to be a pairing between chemical sintering responsible for Au NP synthesis and light sintering where Au NPs aggregated forming a conductive film. Each film was then subjected to thin film analysis validating the formation of a polycrystalline Au film via XRD and EDS and morphology via SEM and confocal microscopy confirming a uniform and continuous film explaining its excellent electrical conductivity up to 1.09×10^6 $S \cdot m^{-1}$. This then allowed for the development of conductive tracks, strain sensors, and antennas. The very same reducing mechanism was then further exploited in the development of PVA-based ion gel combining PVA-PEMA as the polymer matrix and a choline-malate ionic liquid to ensure biodegradability. The versatile gel itself was found to maintain its reducing ability to form Au films while exhibiting ionic conductivity and capacitance of 0.28 $\mu S \cdot cm^{-1}$ and 0.16 $\mu F \cdot cm^{-2}$ respectively.

Lastly, an in-plane EGOFET was demonstrated combining all previously discussed and characterized layers where PVA was used as the substrate/dielectric layer, Au NP film as the gate/source/drain electrodes, and TMTES pentacene as the semiconductor layer. These results support that low temperature processed transistor based on biodegradable materials is feasible thus contributing to the realization of fully printed and biodegradable devices rarely reported in literature.

Resum

Els humans estem en un moment crític de la història on les nostres decisions actuals tindran un gran impacte en el futur. Una d´elles és el nostre esforç per reduir la quantitat de residus electrònics que es generen cada any. Per aquest motiu, la implementació de materials biodegradables i l'ús de mètodes de fabricació sostenibles en el desenvolupament de l'electrònica és primordial. Aquest objectiu es pot aconseguir mitjançant tècniques de baix impacte ambiental i baix residu, com ara la impressió d'injecció de tinta, que pot dipositar qualsevol tinta sobre un substrat seleccionat. Juntament amb una sèrie de tècniques de sinterització a baixa temperatura com ara la sinterització de plasma, química i fotònica, es poden generar pel·lícules fines metàl·liques i conductores facilitant així el desenvolupament d'una àmplia gamma de components electrònics.

Aquesta tesi planteja el desenvolupament de l'electrònica transitòria mitjançant la substitució de diferents capes per materials biodegradables coneguts i l'adaptació a les tècniques de processament. En una primera fase es va dur a terme un procés de selecció de materials per triar un substrat adequat en funció de les respectives propietats aconseguint una rugositat superficial inferior a 10 nm amb una bona estabilitat tèrmica. En base a això, la fibroïna de seda i el CNF es van considerar compatibles tot i que finalment va ser el PVA el que es va utilitzar com a substrat principal durant tota la tesi. Simultàniament, es van formular dos tipus diferents de tintes i es van imprimir amb injecció de tinta sobre aquests substrats per verificar-ne la idoneïtat. La formulació de tintes metàl·liques biodegradables de Zn i Mo es va establir en funció de la seva reactivitat enfront a una àmplia gamma de dissolvents i estabilitzadors fins a aconseguir una bona estabilitat. A causa de la respectiva depressió del punt de fusió de nanopartícules, es va emprar el curat fotònic com a mètode de sinterització principal per aconseguir pel·lícules amb conductivitats elevades com 1×10^3 $S \cdot m^{-1}$ per a Zn i resistències baixes en el rang de centenars d'ohms per a Mo, ja que l'oxidació continuava sent un problema per a aquests materials.

Alternativament, es van emprar tintes de descomposició de sal metàl·lica (MSD) per al desenvolupament de pel·lícules primes de metalls nobles per sinterització de plasma d'oxigen, és a dir, Au i Pt, produint pel·lícules amb una bona conductivitat de fins a 3×10^5 i 4×10^4 $S \cdot m^{-1}$ respectivament. La conductivitat de la pel·lícula es va maximitzar ajustant tant els paràmetres d'impressió com de sinteritzat i demostrant que les temperatures de sinterització mai van superar els 37 °C. Les pel·lícules d'Au es van formar sobre una àmplia gamma de substrats no convencionals, com ara polímers, papers i tèxtils, demostrant que aquestes pel·lícules mostraven una excel·lent conformitat, durabilitat i flexibilitat. Aquestes característiques són particularment avantatjoses en el desenvolupament d'electrònica portàtil amb una excel·lent resistència a la tensió per sobre del 10% i sense arribar a presentar una fallada completa. A més, les pel·lícules

d'Au NP es van utilitzar com a elèctrode de treball i com a contra-elèctrode en el desenvolupament d'un biosensor de glucosa totalment imprès per injecció de tinta. La detecció no enzimàtica de glucosa es va aconseguir mitjançant electrooxidació amb un rang de detecció de mM.

En paral·lel es va descobrir un enfocament innovador per al desenvolupament de la formació de pel·lícules Au NP a temperatura ambient en combinar la tinta Au MSD amb PVA com a substrat reductor. Es va identificar que el mecanisme de reducció era un aparellament entre la sinterització química responsable de la síntesi d'Au NP i la sinterització lleugera on les nanopartícules d'Au s'agregaven formant una pel·lícula conductora. Cada pel·lícula es va sotmetre a una anàlisi de pel·lícula fina validant la formació d'una pel·lícula Au policristal·lina mitjançant XRD i EDS, la morfologia mitjançant SEM i microscòpia confocal i demostrant una pel·lícula uniforme i contínua que explica la seva excel·lent conductivitat elèctrica fins a 1,09 x 10^6 $S \cdot m^{-1}$. Això va permetre el desenvolupament de pistes conductores, sensors de tensió i antenes. El mateix mecanisme de reducció es va aprofitar encara més en el desenvolupament de gel iònic basat en PVA que combina PVA-PEMA com a matriu de polímer i un líquid iònic de choline-malate per garantir la biodegradabilitat. Es va trobar que el gel mantenia la seva capacitat reductora de formar pel·lícules Au mentre presentava una conductivitat iònica i una capacitat de 0,28 $\mu S \cdot cm^{-1}$ i 0,16 $\mu F \cdot cm^{-2}$, respectivament.

Finalment, es va demostrar un EGOFET combinant totes les capes esmentades i caracteritzades anteriorment on es va utilitzar PVA com a capa de substrat i dielèctric, la pel·lícula de nanopartíclues d'Au com a elèctrodes de porta, font i drenatge, i el TMTES-pentacene com a capa semiconductora. Aquests resultats confirmen que el transistor processat a baixa temperatura basat en materials biodegradables és factible, contribuint així a la realització de dispositius totalment impresos i biodegradables, poc presents a la literatura.

Acknowledgements

I would like to especially thank Carme who was not only my thesis director but also provided me as much help as she possibly could even with her crazy busy schedule. I really would have been completely lost without her direction. Her patience and kindness to me throughout the years is unmatched and I will be eternally grateful to her and wish only the best for her exciting future to come. Additionally, I would like to thank Eloi for providing me the opportunity to pursue a PhD under his guidance. The experience has been eye opening and I enjoy our chats about life outside of academia helping me to appreciate and understand life to its fullest. And of course, I cannot forget my colleagues Sandra and Miquel for offering both their scientific knowledge and contributions to my thesis, without them for sure my thesis would not have been possible. I very much enjoyed working with them throughout the years as we shared our insights on different topics in and outside of academia which provided much needed relief from time to time during these challenging years.

DV has been a constant means of support to me both mentally and physically during these stressful years. The old saying here that “company loves misery” really rings true here. Your methodical and rational thinking gave me the encouragement I needed to continue through the hard times making you truly the best partner I have ever been lucky to have. Thank you so much for just being you as I look forward to what life will throw at us next.

My scientific curiosity is a result of my father’s influence ever since I was born. Our talks together have always impressed me how smart you are even in your advanced age. I am grateful that you passed your genes onto me as I hope that I will be able to achieve that which you believe you were unable to.

Last but not least, I wanted to dedicate this thesis to RE who always provided emotional support and advice whenever I was having a bad day. His smile was infectious, making working a much more enjoyable task. I was always comforted knowing that he would be in the office so in your absence it was much harder to keep focused. You are by far the nicest and kindest human being I know that treated everyone fairly and always with a positive attitude which always made you a delight to be around. Because of this, I dedicate my thesis to you whom I cannot even begin to explain how thankful I am to have gotten to know and work with you.

Tammy Leung

Table of contents

1

Dissertation overview

Since the invention of the transistor in 1947, there have been significant technological advances in electronics and computing. This all maybe thanks to Moore's Law which states that the number of transistors on an integrated circuit predictably doubles every two years. However, to achieve such immense growth requires heavy reliance on semiconductor device fabrication techniques performed in a cleanroom setting. However traditional fabrication processes are established around inorganic and rigid materials. This then severely restricts the development of novel electronics to conventional silicon substrates as other non-conventional substrates are incompatible with these techniques.

As a response, flexible electronics bridges this technological gap where the same electrical components can be directly fabricated onto a flexible polymer substrate. Thus, new manufacturing processes such as inkjet, screen, and gravure printing were introduced as a result. This then allowed for the facile development of low cost, disposable equivalents as they no longer relied on costly semiconductor fabrication techniques. Additionally, the incorporation of a flexible form factor introduced additional properties such as bending, folding, twisting, and stretchability impossible with standard electronics.[1] The growing interest in flexible electronics provides an opportunity to develop new applications such as wearable electronics and sensors, robotics, display technologies, and flexible lighting for the consumer.[2] In fact, the flexible organic and printed electronics market is predicted to grow to US $300 billion by 2028 thus iterating its place in the electronics market.[3]

More recently, next generation electronics known as transient electronics was first pioneered by John Rogers in 2012 with the discovery of dissolvable silicon thin films.[4] This further evolved

into the development of biodegradable and bioresorable electronics both of which are meant to dissolve after usage. Such applications for this include environmental sensors and food monitoring, medical implants, and bioelectronics. Since its inception, transient electronics highlights the move towards green or eco-friendly electronics.

1.1 | MOTIVATION AND OBJECTIVES

Our heavy and increasing reliance on disposable electronics has brought us to the precipice where electronic waste generates approximately 40 million tons per year.[5] The ever-growing pollution produced from electronic waste is driving factor for how electronics will be made in the future which requires an fundamental study of viable materials and their respective processing methods. For this reason, transient electronics has grown remarkably, mostly targeting the electronics and biomedical field. Unfortunately, zero-impact standards have not yet been realized for this new generation due to the reliance on conventional fabrication techniques. Because of this, there is a very limited number of papers found in literature that address this issue showing great potential for the development of biodegradable printed electronics.

Therefore, the main goal of this thesis was to build electronic components and ultimately transistors using completely biodegradable and transient materials. Inkjet printing will be used as the principal device to deposit thin films while low temperature sintering techniques were explored due to temperature restrictions dependent on the chosen substrate below. Here, a layer-by-layer approach was followed where each layer was thoroughly characterized and optimized before implementation into the target application.

Phase I: Substrate Investigation

The materials selection process first considered a wide range of biodegradable materials from inorganic to natural and synthetic polymers. Once reliably synthesized and fabricated, if necessary, each material was tested for its inherent materials properties including its respective glass transition, melting temperature, roughness, surface tension, and dissolvability. Only those materials which obtained the highest glass transition temperature with low surface roughness would be considered for the next phase of testing.

Phase II: Conductive metal films

Multiple novel inks were prepared and investigated for their ability to produce conductive and biodegradable films. To achieve this, low temperature sintering methods such as plasma and photonic sintering must be considered on account of the glass transition temperature of the

substrate. Here, deposition of Metal Salt Decomposition (MSD) inks is preferred over nanoparticle inks as they are known to be notoriously difficult to deposit via inkjet printing.

- **Metal Salt Decomposition (MSD) inks**

Both noble and biodegradable metals were considered for their potential reducibility via plasma sintering. The development of metal films is fully dependent on the reduction potential of each metal salt where a highly positively value is more prone to reduce to its elemental state. If successfully formed, materials characterization of the surface morphology as well as the chemical composition should be defined. However out of all these factors, optimization of both printing and sintering parameters is the most important as it must be adjusted to maximize its film conductivity.

- **Biodegradation nanoparticle inks**

Both Zn and Mo nanoparticle inks were targeted for their high theoretical conductivity compared to other biodegradable metals. Additionally, the proclivity of biodegradable metals to oxidize is a problem that must be addressed either in solution or during the post treatment process which in this case is photonic curing. An in-depth study should be performed on nanoparticle compatibility and stability in different solvents and stabilizers to formulate an ink. If achieved, ink printability will be tested to determine which combination creates a reliable and uniform layer. Simultaneously, thin film analysis will be performed on each treated film to determine if the oxide layer was removed during the photonic curing process effectively increasing film conductivity.

Phase III: Dielectric Development

PVA itself is considered a dielectric however must be utilized as a thick film in order to ensure low leakage and display low capacitance value.[6,7] Thus different thickness should be deposited to determine the optimal thickness using the previously mentioned properties. However, this can be proven difficult to work with when fabricating a transistor, thus a second strategy was adopted with the development of a PVA-based ion gel. To maintain its biodegradability, a biodegradable ionic liquid will be synthesized and incorporated into the gel. To be deemed successful, it is essential that this ion gel fulfill two requirements, that is 1) produce conductive Au thin films while 2) exhibiting high capacitance and ionic conductivity. Achieving both characteristics at the same time will be challenging as the development of the ion gel is reliant on the elimination of hydroxyl groups, the exact same mechanism used to develop the conductive films.

Phase IV: Applications

Different electronic components were considered utilizing the previously developed layers developed from Metal Salt Decomposition (MSD) and biodegradable nanoparticle inks as either interconnects or electrodes. As flexible substrates will be used for the entirety of this thesis, deformation resistance should be conducted to verify its durability. These results will then influence which applications can be achieved and/or adapted for the development of each component. Afterwards, they must each be characterized accordingly to their respective function. In the case of transistors, multiple architectures were considered to achieve the best results with such inks. It is expected that electrolyte gated transistors (EGT) and electrolyte-gated organic field-effect transistors (EGOFETs) would see a significantly lower operational voltage than the bottom gate bottom contact (BGBC) thin film transistors (TFT) however a functional transistor would be enough as a proof-of-concept.

1.2 | MAIN CONTRIBUTION

As previously stated, the main goals of this thesis were to determine the feasibility of incorporating biodegradable materials into everyday electrical components. Therefore, the main emphasis was placed on materials development and thin film characterization of every layer, especially those that play an active role in the functionality of any electronic component, namely the conductive metal layers.

The first technological development in this dissertation is the in-depth characterization of novel metal salt decomposition (MSD) inks. This is the first instance where oxygen plasma was used as the primary sintering device which provided a clear limitation on its reducing ability. Although previously reported in literature, the results were lacking in a detailed morphological study of the reduced thin films and were limited to conventional, planar polymers substrates. Our study further expands on this base of knowledge by demonstrating its compatibility with non-conventional, non-planar, and temperature sensitive substrates providing a full investigation in the different types of developed films and their respective electrical characteristics. This was achieved at ultra-low sintering temperatures never reaching above 37°C, one of the lowest ever reported to date especially for Pt NP films. Specifically, the direct printing and sintering onto a porous substrate (i.e. paper and textile) without an intermediary coating has not been previously reported, giving an opportunity to facilitate the development of wearable electronics. Lastly, this study yielded an alternative Au ink at 1/3rd the cost of commercially available Au NP inks thereby significantly reducing the manufacturing costs to produce biosensors and other components.

Secondly, the most important contribution reported relates to the discovery of room temperature sintered Au NP films by chemical-light sintering. As previous studies with MSD inks are limited, their reactivity to reducing substrates is an unexplored and new topic to printed electronics in general. This thesis identifies concrete examples where multiple green polysaccharide substrates were tested for their reaction to the Au MSD inks resulting in different films and resistances. Although reactive inkjet printing provides a relatively similar reaction, its reliance on light in response to nanoparticle formation sets this apart. This reduction mechanism of the ink and film formation is well documented achieving excellent conductivity beyond those found in commercially available inks up to 10^6 $S \cdot m^{-1}$. The advantage here is that nanoparticles are grown in situ where the conductive layer resembles a CVD grown film where the nanoparticles are tightly packed minimizing any gaps instead of displaying a stacked a porous structure as typically seen with nanoparticle inks. This provides an avenue for the development of low or room temperature sintered devices at low cost and impact including but not limited to conductive tracks, strain sensors, antennas, and transistors. Specifically, the fabrication of a low temperature processed EGOFET was demonstrated, however must be further refined in terms of electrical performance.

Additionally, these very same PVA reduction mechanisms were further tested with the development of a PVA-PEMA ion gel. Although there have been previous reports developing a fully biodegradable ion gel, this is the first demonstration combining PVA-based gel with a biodegradable ionic liquid both of which have been documented separately. However, the versatility of PVA was explored highlighting its reducing abilities while enhancing its dielectric properties simultaneously. The results discussed in this thesis are promising, especially in the development of electrolyte gated transistors (EGTs).

Lastly, please note that the pandemic took place for the entire duration of the thesis meaning that previously available equipment and institutes were no longer accessible to external users severely slowing the research process. In the end this added extra complexity that delayed progress with certain experiments up to 1 year unfortunately limiting the scope of this thesis. However, it is believed that the contributions presented here provide enough evidence for its quality.

1.3 | OUTLINE

This thesis follows the organization of a total of 8 chapters where:

Chapter 2, titled *Printing and Sintering Techniques*, gives a summary of different additive thin film deposition methods including solution processing and printing techniques. Particular emphasis will be placed onto inkjet printing, reviewing the droplet formation during the jetting

process and film formation on the substrate surface. However, in order to form a functional layer, the deposited film must be sintered. Here, as temperature sensitive substrates will be implemented, alternative sintering techniques will be compared and discussed.

Chapter 3, titled *Introduction to inks and formulation*, focuses on inkjet printed inks, that is those mainly composed of nanoparticles and metal organic decomposition (MOD) inks. Ink properties and behavior can be adjusted using different components to meet the strict printing and stability requirements. A comparison between the different types of inks is made highlighting the advantages and disadvantages of each ink with respect to their ink properties, film development, and conductivity.

Chapter 4, titled *Substrate Investigation*, investigates known biodegradable substrates and classified them according to their respective material properties. First, several materials were chosen based on their temperature stability and synthesized accordingly if necessary. Second, a material selection process was reported where each fabricated substrate was subjected to testing for their respective properties including surface roughness, surface tension, dissolvability, and glass transition and melting temperatures.

Chapter 5, titled *Ink formulation and development*, introduces biodegradable metals and a state-of-the-art discussion about biodegradable inks and pastes already demonstrated in literature. Specifically novel Zn and Mo nanoparticle (NP) inks were explored in terms of their respective formulation, stability, and printability. The resulting thin films were then tested for their electrical properties in response to different sintering methods on both conventional and biodegradable, flexible substrates.

Chapter 6, titled *Inkjet printed plasma reduced metal films*, delves into the development of Au, Pt, and Ag metal salt decomposition (MSD) inks and formation of metal thin films by oxygen plasma sintering on a variety of substrates from conventional polymers, papers, and textile. Optimal printing and sintering parameters were defined for each ink. Next, each of the resulting films were subjected to materials and electrical characterization including morphology, chemical composition, surface roughness, durability, and conductivity measurements. From this, different applications such as printed conductive tracks on textile and fully printed biosensor on polymer substrates were explored for their implementation into wearable and biomedical applications.

Chapter 7, titled *Self sintered Au nanoparticle films,* introduces a new sintering technique combining the reducing ability of green polysaccharide substrates with the MSD inks. Specifically, the Au MSD ink coupled with PVA showed the most consistent results producing films with high conductivity achieved at room temperature. Here the possible reduction process

is defined as well as microstructural analysis of the films. These same films were then used to explore applications such as electrodes, strain sensors, antennas, and transistors, each with their own requirements.

Finally, Chapter 8 concludes with a summary of all work performed during the PhD as well as a discussion about future work to be explored.

1.4 | FRAMEWORK

Much of this thesis was performed at the Institut de Microelectrònica de Barcelona (IMB-CNM) associated with the Consejo Superior de Investigaciones Científicas (CSIC). Specifically, research was carried out under the Integrated Circuits and Systems (ICAS) group led by Dr. Lluis Terés with a concentration in printed electronics at the Printe-eLab run by Dr. Eloi Ramon.

All PhD work was supported under the following projects:

- ECOTRONIC: "Disposable Paper Electronic Devices for Sustainable Eco-friendly Platforms", MCIU/AEI/FEDER Funding agency (RTI2018-102070-B-C21). Partners: IMB-CNM and Universitat de Girona. Funding dates: 01/03/2019-31/12/2021.

- SensiFlexTag: "Advanced platform for IoT applications with printed electronics for traceability solutions, monitoring and locating people or products in risk environment", Ministry of Science, Innovation and Universities (RTC-2017-6679-7). Funding dates: 01/03/2019-31/12/2020.

- AUTEN-TIC: "Authentication and identification system based on chipless RFID tags
- recyclable and biodegradable", Ministry of Science and Innovation (RTC2019-007226-7). Funding dates: 01/04/2020-31/12/2022.

Additionally, a 3-month research stay at Karlsruhe Institute of Technology (KIT) in Karlsruhe, Germany at the Institute of Nanotechnology (INT) under the direction of Dr. Ben Breitung to obtain an International Doctoral Research mention.

1.5 | REFERENCES

1. Cheng I-C, Wagner S. Overview of Flexible Electronics Technology. In: Wong WS, Salleo A, eds. *Flexible Electronics: Materials and Applications*. Springer US; 2009:1-28. https://doi.org/10.1007/978-0-387-74363-9_1. Accessed October 18, 2021.

2. Baran D, Corzo D, Blazquez GT. Flexible Electronics: Status, Challenges and Opportunities. *Front Electron*. 2020;1:594003. doi:10.3389/FELEC.2020.594003

3. Raut NC, Al-Shamery K. Inkjet printing metals on flexible materials for plastic and paper electronics. *J Mater Chem C*. 2018;6(7):1618-1641. doi:10.1039/c7tc04804a

4. Hwang SW, Tao H, Kim DH, et al. A physically transient form of silicon electronics. *Science (80-)*. 2012;337(6102):1640-1644. doi:10.1126/science.1226325

5. Zhang K, Schnoor JL, Zeng EY. E-waste recycling: Where does it go from here? *Environ Sci Technol*. 2012;46(20):10861-10867. doi:10.1021/es303166s

6. Wang B, Huang W, Chi L, Al-Hashimi M, Marks TJ, Facchetti A. High- k Gate Dielectrics for Emerging Flexible and Stretchable Electronics. *Chem Rev*. 2018;118(11):5690-5754. doi:10.1021/acs.chemrev.8b00045

7. Liu X, Guo Y, Ma Y, et al. Flexible, low-voltage and high-performance polymer thin-film transistors and their application in photo/thermal detectors. *Adv Mater*. 2014;26(22):3631-3636. doi:10.1002/adma.201306084

2

Introduction to Inks and Formulation

This chapter serves as a review of different types of inks: nanoparticle and metal organic decomposition inks with respect to their formulation along with concrete examples found in literature. In addition, direct comparison of both inks will highlight their respective advantages and disadvantages thus affecting their overall film conductivity.

2.1 | OVERVIEW OF INKS

Figure 2.1 below compares standard microfabrication vacuum processing such as chemical vapor deposition (CVD) and physical vapor deposition (PVD) techniques against printable metal inks and their respective achievable conductivites. A wider range of conductivites can be achieved with the introduction of conductive polymers such as PEDOT and silver nanowires therefore providing more materials to choose from to produce transparent conductors.[1] Additionally, relatively new materials such carbon derivates and metal oxides can be easily incorporated into inks and deposited using deposition techniques described in Chapter 3. Even thin metal film conductivites achievable by evaporation match those found in metal NP inks displaying the superiority of printable conductors which are still in development compared to well established vaccuum processing methods. This shows the great potential of printable conductive inks as new materials which continue to be developed and explored.

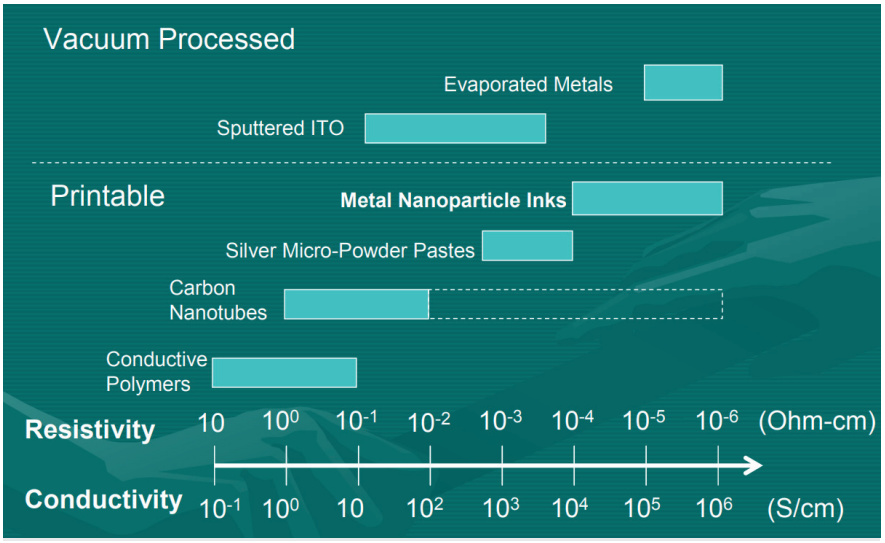

Figure 2.1. Comparison between vacuum processed and printed conductive thin films[2]

Ink formulation requires a good understanding of both chemistry as well as material properties which ultimately dictate the respective electric and mechanical properties of the deposited and processed films. Such films may never surpass its bulk equivalent in terms of conductivity nor achieve lower melting temperature dues to a wide range of factors such as particle size, metal and solvent content, nanoparticle dependent morphology, and post treatment options. However, some factors are controllable more than others such as the particle size, and metal and solvent content which distinguishes the two principal classes of inks in existence: those containing nanoparticles (colloidal inks) and particle free or metalorganic decomposition (MOD) inks.

2.2 | NANOPARTICLE/COLLODIAL INKS

2.2.1 | MELTING POINT DEPRESSION

The disproportionate amount of Ag metals inks currently on the market and reported in research has to do with the lower melting point of the nanoparticles with respect to their bulk equivalents called melting point depression. This is due to the increased surface area that lowers the melting point making these inks usable under reasonable conditions. The temperature changes depending on both the shape and size of the nanoparticle. That is, as the nanoparticle size increases, so does the melting temperature eventually reach the same temperature as its bulk equivalent as is the case for Au NPs as shown in Figure 2.2. This specifically occurs in smaller crystals whereby taking the surface area to volume ratio into account in which the bonds between

the atoms are significantly starved and manifests itself in a decrease in energy needed to melt the material lowering the overall melting point.[3] Additionally, pre-melting of the outer skin layer of the nanoparticle has been shown to occur due to the loss of solid ordering of surface atoms also lowering its melting temperature [4]. Once reaching this point, neck formation then occurs between particles generating percolation paths allowing for conduction.[5] However, depending on the sintering process used, partial melting occurs dependent on the temperature thus resulting in a porous structured film with lower conductivity compared to its bulk. Essentially voids are developed reducing the overall conductivity of the film. Therefore, appropriate and effective sintering techniques must be chosen to achieve optimal results.

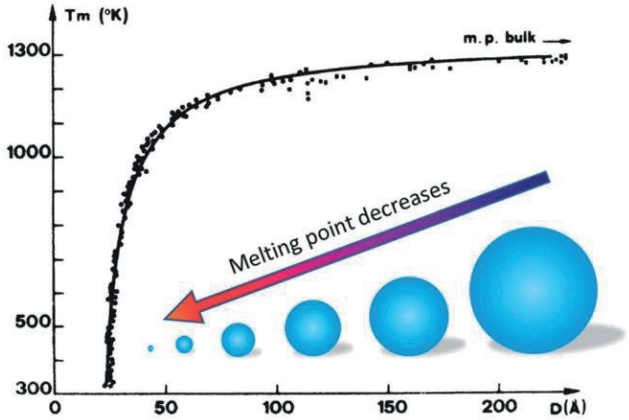

Figure 2.2. Size dependent melting point depression of a Au NPs nanoparticle as reproduced from Yang et al.[6]

2.2.2 | INK FORMULATION AND COMPONENTS

Colloidal inks are complicated to develop as they often consist of not only nanomaterial fillers but also other components in order to provide stable and functional inks. There are three very important characteristics for any suspension to ensure stability: low particle size, low density, and have uniform distribution.[7] Ink loading levels should never exceed 30% in order to ensure that a non-Newtonian liquid is developed and can be printable which also means lower conductivity of the film in the case of conductive inks. Nanoparticles synthesized by liquid-phase techniques are composed of a metallic core and encapsulant material surrounding the particle which may include capping agents or surfactants. The encapsulant helps to prevent both aggregation and precipitation but also prevents a continuous film from forming. Additionally, a large amount of surfactants are needed to monodisperse the nanoparticles in a stable suspension to avoid formation of aggregates or sediments and improve the solubility in the chosen solvent.[8] Such examples are sodium dodecylbenzene sulfonate (SDS) and sodium polymethacrylate (NaPMA) as they were shown to be effective in the reduction of oxidation of Si NPs in solution.[9]

However, it maybe through the use of surfactants that nanoparticles begin to cluster leading to nozzle clogging.[10]

Figure 2.3 shows that ink formulation consists of many different components include fillers, binders, additives, and solvents all of which have their own separate purpose. The main active component is the filler which can be organic, metallic, or ceramic in various nanomaterial forms.[11] This then must be combined with a binder to create a homogenous dispersion. As the name itself suggests, the binder is used to hold ink components together following solvent evaporation, uniformly disperses the fillers in the ink, and improves adhesion of the ink to the substrate. Typically, polymeric materials chosen such as PVP, acrylic, silicone, styrene, epoxy, vinyl, fluoroelastomers, and urethane serve as the binder.[11] Finding a suitable binder is dependent on the surface chemistry of the filler particles as well as the overall application. For example, acrylic, silicone, and vinyl have been used to develop CNT/graphene inks as they have shown to prevent strong van der Waals interactions between the particles while additives allow inks to achieve rheological, wetting, stretching, or even healing properties.[11] Both binders and additives play an important role in the overall flexibility of the inks. In the case of the binder, a uniform distribution is essential as it allows for uniform strain when flexed therefore having little effect on the filler material. However, if this is not effective enough, adhesion promoters can be applied to reduce the shear stress generated between the substrate and ink when bent, one of which is triazine thiol which has been shown to improve adhesion of both conductive and semiconductor particles to the substrate.[11] Although the addition of these components serve to prevent interparticle agglomeration, they simultaneously impede electron flow between particles making non-conductive films.[1] Lastly, the overall ink properties of the ink is defined by the solvent. The solvent affects the flow of the ink itself, defining the viscosity, surface tension, homogeneity, and sintering behavior depending on its boiling point. Typical solvents such as water and ethylene glycol (EG) are used for inkjet printed inks as this helps to lower and increase the viscosity respectively. This is especially important when considering the use of low temperature polymeric substrates that cannot withstand temperatures greater than 200ºC.

All these components were important in determining the overall stability of the ink where if not properly formulated leads to sedimentation. The stabilization of inks ultimately determines the shelf life as the Brownian motion of nanoparticles in solvent tends to exhibit two behaviors: attraction due to van der Waals forces and an electrostatic repulsion.[12] Nanoparticle ink stability can be determined by the surface charge of NPs in a solution, known as its zeta potential. A zeta potential value of $> \pm 25$mV is defined as the electrostatic stabilization of colloids.[13] Lower values indicate that NPs exhibit van der Waal interactions thus resulting in agglomeration, flocculation, or coagulation.[14] Commercially available inks exhibit chemical stability and significantly higher loading as compared to others.[15] This is the case for Ag and Au inks which

are well studied, well developed, and are commercial available in comparison to other inks due to their aversion to oxidation meaning the development of such inks is relatively easy.

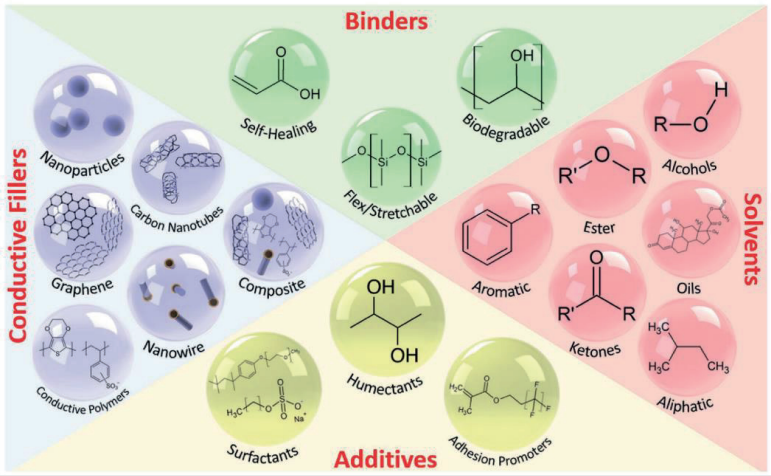

Figure 2.3. Various ink components used to develop conductive inks[11]

The development of nanoparticles inks is a complex process that may begin with the chemical synthesis of nanoparticles that must be further stabilized with organic capping agents, additives, and other co-solvents as shown in Figure 2.4 below. Nanoparticle inks are prone to agglomeration due to their higher particle densities and surface energy of the nanoparticles.[16] This in turn further increases the sintering temperature in order to reach reasonable conductivities thus limiting the use of thermosensitive substrates. This treatment results in stacked and porous films where only slight necking of the nanoparticles appears while overall, crack formation can also occur. One effective way to reduce crack formation is by performing a two-step gradual curing process at a lower temperature followed by the target sintering temperature depending on the ink.[17]

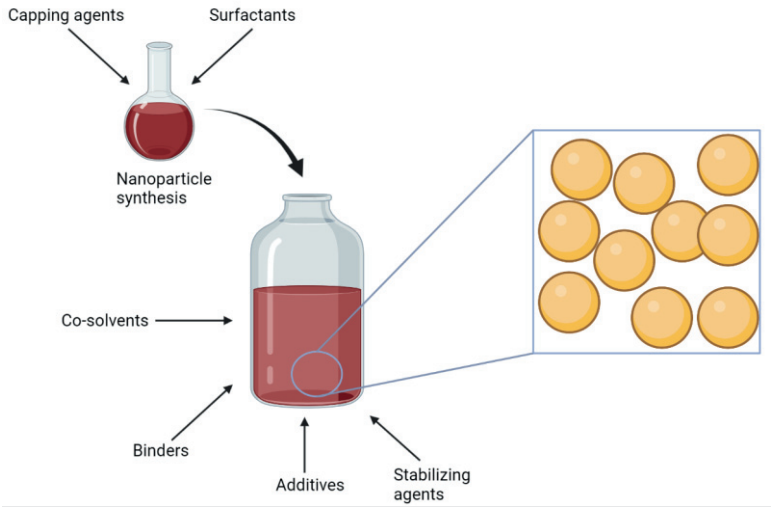

Figure 2.4. Different components needed to formulate NP inks

When developing NP inks, the material composition, particle size and shape as well as concentration must be considered. Inkjet printable inks are composed of NP sizes ranging from 1 – 100 nm suspended in liquid mediums.[1] However with the addition of stabilizing agents, the NP size can grow beyond 100 nm in size potentially causing nozzle blockage. Due to the stringent restrictions of inkjet printing, customized and optimized inks are necessary for the successful printing of targeted structures. This includes the adaption of its rheological properties to the standards stated below in Table 2.1. Additionally, the material properties of the conductive filler such as oxidation stability ultimately defines the conductivity of the deposited film. Although there are a large number of metals in existences, ink development has centered around Au and Ag NPs for their oxidation stability as well as their high conductivity. One exception here is Cu NPs ink development which is considerably cheaper with respect to Au and Ag NPs however forms oxide quickly and therefore exhibits significantly low conductivity. Ag NP inks have the widest commercial availability of all metal inks that require sintering from 100 to 300°C with reported resistivities between 3 – 50 μΩ·cm.[1] Limited commercially availability of Au NP inks ranged from sintering temperatures as little as 120°C to 200°C with varying sintering times and exhibited excellent resistivity from 10^{-4} Ω·cm to 10^{-5} Ω·cm range.[18] However, the development of low temperature Au NP inks is still lagging behind Ag NP ink research due to its higher melting point depression temperature (~1000K for ~1 nm Au NP vs. (~700K for ~1 nm Ag NP)[19], high ink instability due to its affinity for agglomeration, and its prohibitive material costs.

Table 2.1. Ink formulation Recommendations[20]

Parameter	Standard
Viscosity	10 – 12 cPs
Surface Tension	32 – 42 dynes
Volatility (Boiling point)	> 100°C
Specific gravity	> 1
pH	4 - 9

Once the NP ink film was successfully deposited onto the target substrate, it then must be subjected to a multistep process which includes both drying and sintering steps to produce conductive films as shown in Figure 2.5 below. This sintering step is necessary to remove any organic stabilizers and/or additives surrounding the NPs to begin necking and eventual full coalescence if possible. The decomposition temperature of most solvents are typically > 100°C meaning that the overall sintering temperature is greater than 150°C limiting the use of even some polymer substrates and any temperature sensitive substrates. Often, organic compounds decompose at temperatures between 150 – 200ºC.[21] In this case, both the stabilizing ligand adsorption energy as well as its decomposition temperature should be considered.[21] This combination would ideally lessen any effects of ligand desorption which drives the development of Ostwald ripening agglomeration.[21] Therefore, a ligand must be chosen based on its strong interaction with the metal NP core preventing agglomeration while simultaneously desorbing and/or decomposing below its respective sintering temperature.[21] A good example of this was implemented by Grouchko et al. whom utilized a chloride based destabilizer --- polyacrylic acid sodium salt (PAANa), that triggers polymer desorption of the stabilizer from the Ag NP when exposed to HCl vapor or NaCl. This resulted in sintered patterns that exhibited 41% conductivity as compared to bulk silver. In comparison, similar conductivities were found only after heating the dispersion to 320°C for 30 minutes.[22] Additionally, it was discovered that gas trapping further complicates NP ink printing on flexible substrates according to Jung et al.[23] This can lead to crack formation which is known to reduce conductivity by lengthening and impeding established percolation pathways.[24,25]

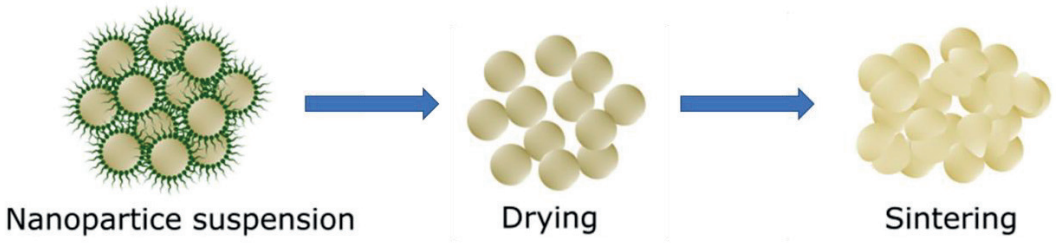

Figure 2.5. NP sintering process

A comprehensive study was performed by Wolf et al. whom utilized the commercial available Agfa-Gevaert N. V. Ag NP ink containing 14–17 wt% metal content gave more insight on the sintering behavior of Ag NPs at different sintering temperatures as shown in Figure 2.6 below. At 100°C the NP appeared to be densified with a higher number of grain boundaries and separate NPs as shown in Figure 2.6a. Necking formation was observed at 150°C (Figure 2.6b) while at 200°C showed porous structures reaching the final conductivity 40% of bulk Ag.[26] Although the number of grain boundaries reduced, exposure to higher temperatures also resulted in larger pores (Figure 2.6c and 2.6d). This shows the limitations plaguing even commercially available inks that may never match characteristics found using typical thin film deposition techniques.

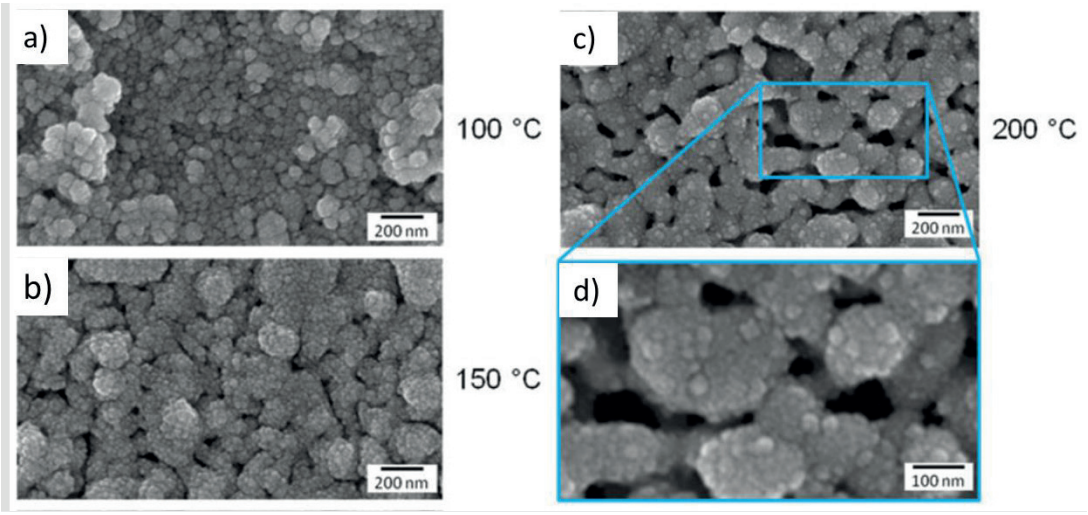

Figure 2.6. Ag NP ink under various sintering conditions a) 100°C, b) 150°C, c) 200°C, and d) enhanced view of agglomerated NPs

2.3 | METAL ORGANIC DECOMPOSITION (MOD) INKS

Metal Organic decomposition (MOD) inks are particle-free inks based on metal precursors, complexes, or metal salts. In terms of microfabrication processing, the use of such inks resembles Metal-Organic Chemical Vapor Deposition (MOCVD) processing which employs the same precursors to develop thin films.[27] Instead of a gas phase reaction which requires transportation and adsorption of the precursor to the substrate surface, the direct deposition of the ink concentrates only on the surface reactions which lead to nucleation and thin film growth. Keeping this in mind, this opens a wide large range of types of thin films which can be developed not typically possible with NP inks such as bimetallic thin films.

Unlike NP inks, the metal precursors are readily dissolved in solvents or organic complexing agents such as water, ethanol, ethylene glycol, butanol, xylene, or toluene.[8,21] The introduction of solvents are often used to either disperse or dissolve the precursor in order to adjust rheological properties such as ink viscosity and surface tension. In fact the use of low molecular weight alcohols are highly valued as they contain hydroxyl groups that may contribute to its reducing ability, are less toxic compared to other solvents, and evaporate easily.[28] The application of glycol ether solvents into such inks facilitates in the development of inkjet printable inks[29] therefore the inks can be catered to whichever printed technique through the addition of organic solvents. It is the simplicity of such inks that removes any difficulties pertaining to condensation, agglomeration, and clogging typically associated with printing NP inks. Additionally, as these metal precursor inks exist in a ionic form in the absence of stabilizing agents, neither aggregation nor sedimentation is found after long term storage (> 6 months).[18,28]

Figure 2.7 below highlights the most common metal precursors used for MOD ink development where the appropriate precursor must first be chosen as it dictates the overall thermal and electrical properties of the resulting metal film. For example, it is known that metal aliphatic carboxylates degrade via decarboxylation reaction[30] at decomposition temperatures lower than 200 ºC, the lowest of the silver precursors.[28] Depending on the type of precursor (metal vs semiconductor), annealing temperatures can vary widely from 150°C to 580°C[27] where for metal precursors normally sees lower sintering temperatures from 90°C to 200°C.[28] Because these inks are known for their chemical and thermal stability for temperatures over 150°C, it is necessary to force a decomposition reaction of the printed precursor to develop conductive structures. Heating is used to initiate decomposition leading to the release of organic groups which then allows for nucleation and growth.[31] As a result of the process, side or unreacted products produced at the surface must be removed by a post-treatment washing step in order to achieve conductive patterns. Ideally, precursors containing at least 10 – 40 wt% metal is a good balance between ink printability and overall film conductivity.[28,32]

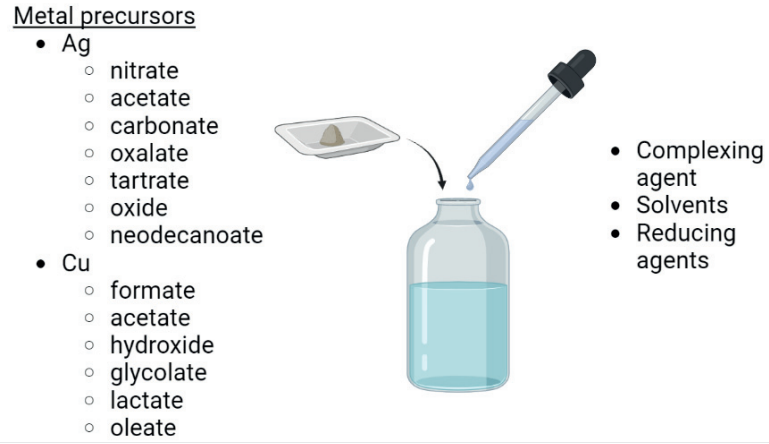

Figure 2.7 MOD ink formulation listing the most common metal precursors

However, the simplified ink formulation comes with some disadvantages leading to overall lower conductivity compared to thin films deposited with NP inks. First, the solubility of the organometallic compound in any solvent automatically limits the amount of solid metallic content which is further compounded by the fact that is there is only a molecular fraction of the metal within the compound itself thereby affecting the overall loading.[8,21] This means that because they tend to have lower metal loading, they exhibit low viscosities resulting in higher contact resistances and mechanically unstable films.[8,21] Second, the resulting film maybe chemically impure leaving contaminants such as salt on the surface which can cause deterioration of adjacent materials.[21] This behavior maybe partially due to solvent evaporation from the use of low temperature solvents which can causes salt precipitation instead of decomposition. Lastly, films from such inks see an 80% volume loss that often appears as voids or disconnected patterns resulting in poor conductivity.[8] However, this can be mitigated by printing the layer using multiple passes thereby increasing the thickness and conductivity.

Similarly to NP inks, research has mainly focused on the development of metal conductive inks such as Ag and Cu inks both due to their relative cost and excellent conductivity. The first known MOD ink was introduced in 1988 by Teng and West whom combined silver neodecanoate with xylene to produce a silver metal grid thermally reduced at 300°C.[33] Almost 2 decades later, Walker and Lewis achieved significantly lower sintering temperature at 90°C from a silver acetate, ammonia, and formic acid composed ink.[34] Cu MOD inks are also heavily studied concentrating mostly on the use of copper formate (CuF) which is known to self-reduce reporting decomposition temperatures near 200°C.[28,35] Farraj et al. took advantage of this property by combining CuF with 2-amino-2-methyl-1-propanol (AMP) demonstrating that metallic Cu reduces under nitrogen at 140°C.[29] A similar study was conducted by Mrig et al. whom tailored coordinate Cu complexes to achieve Cu interconnects with resistivity between

4.7–5.3 × 10^{-7} Ω·m on PI and 3.83 × 10^{-6} Ω·m on paper.[36] If combined with plasma and intense pulsed light (IPL) sintering methods, even lower sintering temperatures could be achieved as they both provide the ability to remove organic compounds and sinter any deposited patterns at the same time. However, both Ag and Cu films are prone to oxidation paving the way for the development of metal oxide layers as a promising line of research which is still very much in development. For example, Singaraju et al. demonstrated inkjet printable In_2O_3 precursor to develop densely packed semiconductor layer when heated to 350°C.[37] Research pertaining to metal oxides are still in an infancy however MOD inks provides the vehicle to produce stoichiometrically controlled thin films.

2.4 | METALLIC NP INKS VS MOD INKS

Table 2.2 below reviews the main differences between NP and MOD inks showing an overall evolution in inks where both the complexity of the formulation and sintering temperature is being reduced as the introduction of thermosensitive substrates becomes more important for the development of flexible electronics. However, the majority of sintering temperatures is still beyond 100°C once again limiting the use of biodegradable substrates with even lower glass transition temperatures. In terms of film morphology, two films deposited by a commercially Au NP ink and Au MOD ink are displayed below in Figure 2.8. The NP sintered ink exhibited a stacked and porous film with a surface roughness of 43.1 nm as shown in Figure 2.8a. This increased roughness is most certainly due to the use of NPs and their inability to coalesce even when exposed to high temperatures. On the other hand, the film deposited by MOD inks indicates a much smoother film seen in Figure 2.8b with a more continuous layer, almost devoid of any voids. However, contamination from the Au metal salt precursor is found across the entire film surface. However, the film morphology does not always dictate the overall conductivity as this is driven by the metal content, in this case, where NP ink is significantly greater. Therefore, conductivity of NP ink on average tends to be higher than those found with MOD inks. Simultaneously, the cost of the ink is lowered with every generation as NP inks require a precise combination of NP synthesis and solvents thereby driving the costs of a commercial Au ink to above 100€/mL while MOD inks can be easily formulated and are only limited by the starting costs of the precursor itself. Lastly, another advantage that MOD inks has over NP ink is its ability to deposit a wide range of metallic films. This once again stems from the instability of NP inks limiting the range of materials to Ag and Au NP inks thus far.

Table 2.2. Comparison between nanoparticle and MOD inks

	Nanoparticle (NP) inks	**Metalloorganic decomposition (MOD) inks**
Formulation	Complex	Moderate
Metal content	Moderate to high	Low
Printability	Clogging	None
Post treatment	> 150°C	> 100°C
Thermosensitive substrates	No	Yes
Film morphology	Stacked and porous	Porous
Conductivity	Good to excellent	Good
Costs	Expensive	Low
Others	Limited to Ag NPs	Ag, Cu, Au, Al, Ni, films

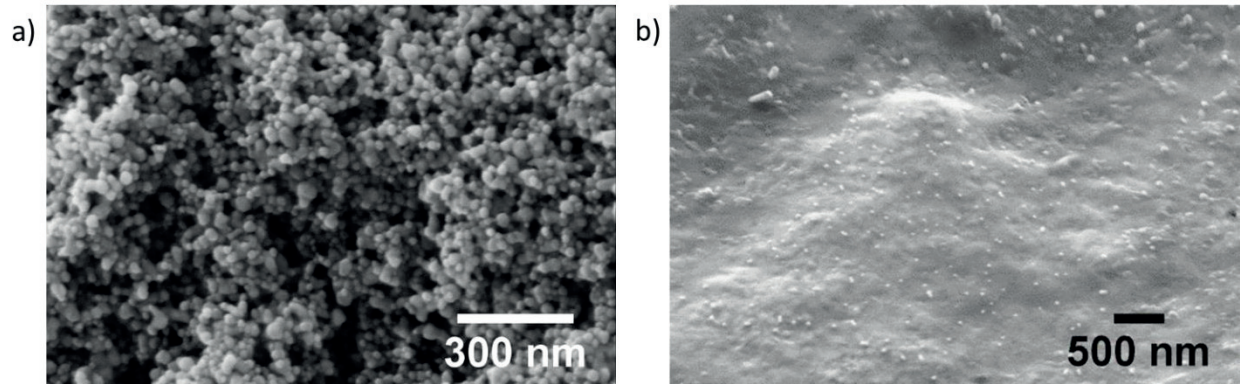

Figure 2.8. SEM micrographs of a) Au NP ink (C-ink's DryCure J1010B) thin film heated treated at 150°C and b) Plasma treated Au MOD ink thin film

2.5 | REFERENCES

1. Tan HW, An J, Chua CK, Tran T. Metallic Nanoparticle Inks for 3D Printing of Electronics. Adv Electron Mater. 2019;5(5). doi:10.1002/aelm.201800831

2. Yang, Zhihao (NanoMas Technologies I. Nanoparticle Inks for Printed Electronics. http://www.nanoparticles.org/pdf/YangZ.pdf. Published 2007.

3. Sadie J. Three-Dimensional Inkjet-Printed Metal Nanoparticles: Ink and Application Development. 2017. http://www2.eecs.berkeley.edu/Pubs/TechRpts/2017/EECS-2017-168.html.

4. Moitra A, Kim S, Houze J, et al. Melting tungsten nanoparticles: A molecular dynamics study. J Phys D Appl Phys. 2008;41(18). doi:10.1088/0022-3727/41/18/185406

5. Cronin HM, Stoeva Z, Brown M, Shkunov M, Silva SRP. Photonic Curing of Low-Cost Aqueous Silver Flake Inks for Printed Conductors with Increased Yield. ACS Appl Mater Interfaces. 2018;10(25):21398-21410. doi:10.1021/acsami.8b04157

6. Yang C, Wong CP, Yuen MMF. Printed electrically conductive composites: Conductive filler designs and surface engineering. J Mater Chem C. 2013;1(26):4052-4069. doi:10.1039/c3tc00572k

7. Varghese J, Surendran KP, Sebastian MT. Room temperature curable silica ink. RSC Adv. 2014;4(88):47701-47707. doi:10.1039/c4ra06479h

8. Choi Y, Seong K dong, Piao Y. Metal−Organic Decomposition Ink for Printed Electronics. Adv Mater Interfaces. 2019;6(20):1-14. doi:10.1002/admi.201901002

9. Drahi E, Blayac S, Borbely A, Benaben P. Impact of ink synthesis on processing of inkjet-printed silicon nanoparticle thin films: A comparison of Rapid Thermal Annealing and photonic sintering. Thin Solid Films. 2015;574:169-176. doi:10.1016/j.tsf.2014.11.079

10. Lohse D. Fundamental Fluid Dynamics Challenges in Inkjet Printing. Annu Rev Fluid Mech. 2021;54:349-382. doi:10.1146/annurev-fluid-022321-114001

11. Kim J, Kumar R, Bandodkar AJ, Wang J. Advanced Materials for Printed Wearable Electrochemical Devices: A Review. Adv Electron Mater. 2017;3(1):1-15. doi:10.1002/aelm.201600260

12. Mulla MA, Yow HN, Zhang H, Cayre OJ, Biggs S. Colloid Particles in Ink Formulations. In: Fundamentals of Inkjet Printing. John Wiley & Sons, Ltd; 2016:141-168. doi:https://doi.org/10.1002/9783527684724.ch6

13. Shnoudeh AJ, Hamad I, Abdo RW, et al. Synthesis, Characterization, and Applications of Metal Nanoparticles. In: Biomaterials and Bionanotechnology. Elsevier; 2019:527-612. doi:10.1016/B978-0-12-814427-5.00015-9

14. Sapsford KE, Tyner KM, Dair BJ, Deschamps JR, Medintz IL. Analyzing nanomaterial bioconjugates: A review of current and emerging purification and characterization techniques. Anal Chem. 2011;83(12):4453-4488. doi:10.1021/ac200853a

15. Perelaer J, Jani R, Grouchko M, Kamyshny A, Magdassi S, Schubert US. Plasma and microwave flash sintering of a tailored silver nanoparticle ink, yielding 60% bulk conductivity on cost-effective polymer foils. Adv Mater. 2012;24(29):3993-3998. doi:10.1002/adma.201200899

16. Baby TT, Garlapati SK, Dehm S, et al. A general route toward complete room temperature processing of printed and high performance oxide electronics. ACS Nano. 2015;9(3):3075-3083. doi:10.1021/nn507326z

17. Moya A, Sowade E, del Campo FJ, et al. All-inkjet-printed dissolved oxygen sensors on flexible plastic substrates. Org Electron. 2016;39:168-176. doi:10.1016/j.orgel.2016.10.002

18. Leung TSW, Ramon E, Martínez-Domingo C. Low-Temperature Plasma Sintering of Inkjet-Printed Metal Salt Decomposition Inks on Flexible Substrates. Adv Eng Mater. 2022;2200834. doi:10.1002/adem.202200834

19. Jiang Q, Zhang S, Zhao M. Size-dependent melting point of noble metals. Mater Chem Phys. 2003;82(1):225-227. doi:https://doi.org/10.1016/S0254-0584(03)00201-3

20. FUJIFILM. FUJIFILM Dimatix Ink Tutorial, waveform. 2008:6. https://www.cnfusers.cornell.edu/sites/default/files/Equipment-Resources/Ink formulation tutorial.pdf.

21. Raut NC, Al-Shamery K. Inkjet printing metals on flexible materials for plastic and paper electronics. J Mater Chem C. 2018;6(7):1618-1641. doi:10.1039/c7tc04804a

22. Grouchko M, Kamyshny A, Mihailescu CF, Anghel DF, Magdassi S. Conductive inks with a “built-in” mechanism that enables sintering at room temperature. ACS Nano. 2011;5(4):3354-3359. doi:10.1021/nn2005848

23. Jung J, Kang S. Compaction as a Critical Factor for Success in the Sintering of Ultra-Fine WC–Co Powders. J Am Ceram Soc. 2005;88(11):3032-3036. doi:https://doi.org/10.1111/j.1551-2916.2005.00595.x

24. Schneider M, Maurath J, Fischer SB, Weiß M, Willenbacher N, Koos E. Suppressing Crack Formation in Particulate Systems by Utilizing Capillary Forces. ACS Appl Mater Interfaces. 2017;9(12):11095-11105. doi:10.1021/ACSAMI.6B13624/ASSET/IMAGES/MEDIUM/AM-2016-13624H_0009.GIF

25. Last BJ, Thouless DJ. Percolation Theory and Electrical Conductivity. Phys Rev Lett. 1971;27(25):1719-1721. doi:10.1103/PhysRevLett.27.1719

26. Wolf FM, Perelaer J, Stumpf S, Bollen D, Kriebel F, Schubert US. Rapid low-pressure plasma sintering of inkjet-printed silver nanoparticles for RFID antennas. J Mater Res. 2013;28(9):1254-1261. doi:10.1557/jmr.2013.73

27. Sui Y, of Graduate Studies. EECS - Electrical Engineering CWRUS, Theses OE, Center D. A Low-Temperature Printing Technology for Fabricating Electrically Conductive Structures and Devices Using Plasma-Activated Stabilizer-Free Inks. Case Western Reserve University School of Graduate Studies; 2019. https://books.google.be/books?id=nh9WzAEACAAJ.

28. Yang W, List-Kratochvil EJW, Wang C. Metal particle-free inks for printed flexible electronics. J Mater Chem C. 2019;7(48):15098-15117. doi:10.1039/c9tc05463d

29. Farraj Y, Grouchko M, Magdassi S. Self-reduction of a copper complex MOD ink for inkjet printing conductive patterns on plastics. Chem Commun. 2015;51(9):1587-1590. doi:10.1039/c4cc08749f

30. Ombaba MM, Hasegawa T, Lu L, et al. Hierarchical silver nanoparticle micro-clustering in poly(methyl methacrylate) matrix in spin-coatable electrically conductive thermoplastics. Sci Adv Mater. 2013;5(11):1546-1555. doi:10.1166/SAM.2013.1672

31. Sui Y, Dai Y, Liu CC, Sankaran RM, Zorman CA. A New Class of Low-Temperature Plasma-Activated, Inorganic Salt-Based Particle-Free Inks for Inkjet Printing Metals. Adv Mater Technol. 2019;4(8):1900119. doi:10.1002/admt.201900119

32. Qin Y, Alam AU, Howlader MMR, Hu N-X, Deen MJ. Inkjet Printing of a Highly Loaded Palladium Ink for Integrated, Low-Cost pH Sensors. Adv Funct Mater. 2016;26(27):4923-4933. doi:https://doi.org/10.1002/adfm.201600657

33. Dearden AL, Smith PJ, Shin D-Y, Reis N, Derby B, O'Brien P. A Low Curing Temperature Silver Ink for Use in Ink-Jet Printing and Subsequent Production of Conductive Tracks. Macromol Rapid Commun. 2005;26(4):315-318. doi:https://doi.org/10.1002/marc.200400445

34. Walker SB, Lewis JA. Reactive silver inks for patterning high-conductivity features at mild temperatures. J Am Chem Soc. 2012;134(3):1419-1421. doi:10.1021/ja209267c

35. Yong Y, Nguyen MT, Tsukamoto H, Matsubara M, Liao Y-C, Yonezawa T. Effect of decomposition and organic residues on resistivity of copper films fabricated via low-temperature sintering of complex particle mixed dispersions. Sci Rep. 2017;7:45150. doi:10.1038/srep45150

36. Mrig S, Bhide MA, Zhou Y, et al. Unraveling the Steric Link to Copper Precursor Decomposition: A Multi-Faceted Study for the Printing of Flexible Electronics. Small Methods. 2023;2300038(I):1-7. doi:10.1002/smtd.202300038

37. Singaraju SA, Marques GC, Gruber P, et al. Fully Printed Inverters using Metal-Oxide Semiconductor and Graphene Passives on Flexible Substrates. Phys Status Solidi - Rapid Res Lett. 2020;14(9):1-6. doi:10.1002/pssr.202000252

3

Introduction to Printed Electronics: Deposition Methods and Sintering Techniques

3.1 | OVERVIEW OF PRINTED ELECTRONICS

Traditionally, everyday electronics are built using semiconductor device fabrication which is a multistep and subtractive process that relies heavily on rigid Si wafer as the substrate. Fabrication typically begins with thermal oxidation to grow a SiO_2 layer which then can be patterned using photolithography or etched removing any unwanted layers during processing. Additional processing steps include thin film deposition that allows for the development of a wide range of films with tailored stoichiometries of which can be further manipulated with doping with the help of ion implantation. Films such as metals, dielectrics/insulators, and semiconductors are the basis of any electronic device from a simple resistor to a more complex transistor. All these processes can occur on the micrometer scale producing large well-defined features with exorbitant costs. Unfortunately, large volumes of chemical waste are produced during this process from toxic contaminants such as acids, arsenic, solvents, nanoparticulates, and organic and inorganic compounds making it an unsustainable process.[1]

Printed electronics is a response to these deficiencies which instead utilizes an additive approach to build electronic circuits and microelectromechanical systems (MEMS) on flexible and temperature sensitive substrates such as natural and synthetic polymers and textile which

was previously incompatible with microfabrication processes. Additionally, the low development costs which are not achievable using standard methods are highly attractive in reaching sustainability goals. These techniques allow any type of film to be directly deposited once formulated into an ink. Once deposited onto the target substrate, it then must be heat treated in order to remove any ink solvents and develop functional layers, the basic building blocks of any electronic device.

Applications

Early adoption of printed electronics saw the incorporation of printed silver conductors to develop RFID tags, sensors, printed circuit boards (PCBs), touch screens, electroluminescent lighting, and flat panel displays eliminating the need for lithography and vacuum processing techniques.[4–6] Entire electrical components and systems such as strain gauge[7], capacitors[8], diode and memristors[9], energy generation and harvesting[10–12], transistors[13], and radio frequency electronics[14–16] were fabricated. These components are the basis of any electrical device, that thanks to a consumer driven society has seen a massive rise in electronic waste. This then drove the development of transient electronics, which can be divided into two major categories: biodegradable and bioresorbable (and biocompatible) electronics spanning agricultural and medical industries. In terms of biosensors alone, this brought about innovations in environmental sensors[8], food monitoring[17,18], and health monitoring[19–22] through seamless wireless communication electronics integration.

Electrical components

More basic structures such as strain gauges, radio circuits, triboelectric generators, and memristors have been demonstrated combining both biodegradable materials and printing techniques while more complex structures such as PCB, transistors, and batteries still heavily rely on the use of evaporation methods and the incorporation of non-biodegradable material. However, the cases described below are rare examples that exemplify the future of electronics. Shou et al. fabricated mechanically stable and biodegradable resistive strain gauges based on Zn NP ink deposited onto a Na-CMC substrate by bar coating and laser sintering (Figure 3.1a and 3.1b). Figure 3.1c showed that it exhibited good strain resistance which only increased by 0.1-0.2% under linear strain of 0.15%.[7] Using a similar ink composition, Li et al. presented screen printed radio circuit comprised of a meander antenna, voltage regulator, and an oscillator connected by Zn conductive tracks as shown in Figure 3.1d. The antenna itself generated radio frequency (RF) signal at 414 MHz frequency with an average amplitude of -35.22 dBm.[15] By replacing the resistor with a thermistor in the circuit, a wireless temperature monitoring system displayed an output signal as a function of the temperature (Figure 3.1e). The entire circuit was shown to dissolve within 30 minutes leaving small traces of Zn NPs behind. Additionally, the

cytotoxicity of the ink was tested with different assays displaying only 1% of cell necrosis and the effect on cell proliferation was found to be that 83.48 and 78.05% of the cells were viable when tested with the Zn/PVA bilayer.[15]

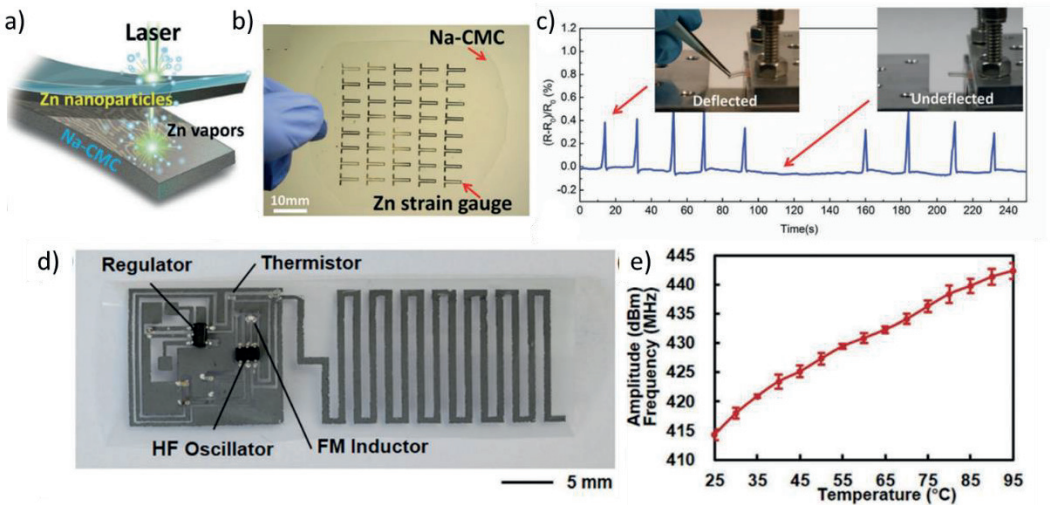

Figure 3.1. Flexible Zn printed components a) laser sintering process of Zn NP ink onto a Na-CMC susbtrate[7], b) strain gauge array[7], and c) strain testing[7], d) screen printed radio circuit and its components[15] and its e) temperature output signal[15]

Even more complex structures were introduced by Yang et al. and Molina-Lopez et al. taking advantage of different printing and sintering techniques. Yang et al.[9] developed functional diodes and memristors combining the use of inkjet printing to deposit MOD inks and the sintering power of femtosecond and green continuous-wave lasers to form Ag, Pt, and ZnO films respectively (Figure 3.2a). This demonstrated the wide range of applications possible when combining techniques together in the development of diodes (Figure 3.2b).

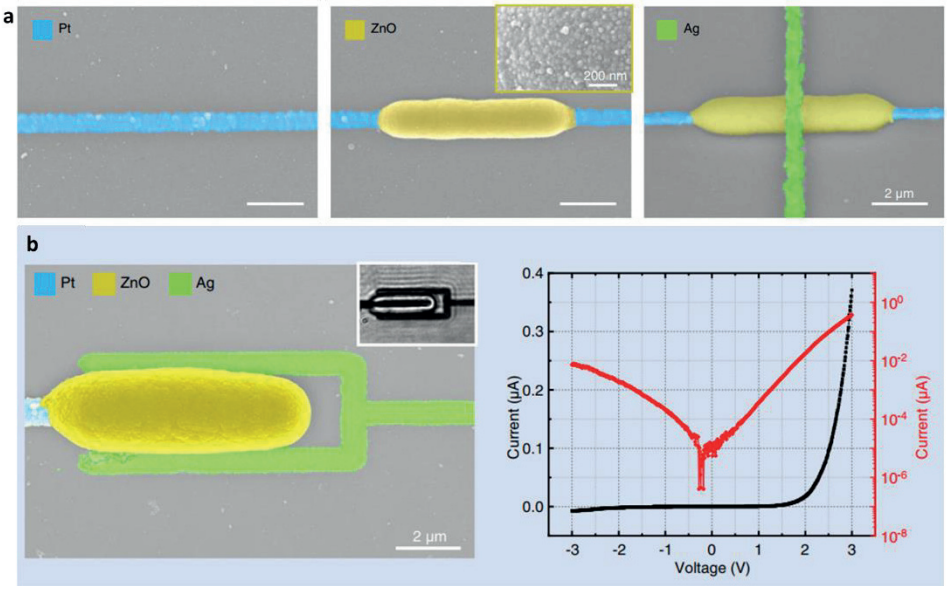

Figure 3.2. Laser printed structures a) Layer-by-layer printing of a memristor and b) single diode and characteristics

Molina-Lopez et al. demonstrated fully inkjet printed flexible, stretchable synaptic FETs array consisting of stacked layers of poly(3,4-ethylenedioxythiophene)-poly(styrenesulfonate) (PEDOT:PSS) as the source/drain/gate electrodes and interconnects, SWCNTs for semiconductor layer, and poly(vinylidene fluorideco-hexafluoropropylene) (PVDF-HFP) as the gate dielectric on an elastomeric styrene-ethylene-butadiene-styrene (SEBS) substrate (Figure 3.3a and 3.3b). Thanks to the PVDF-HFP dielectric, the transistors displayed mobilities as high as 30 $cm^2\ V^{-1}\ s^{-1}$ with operation voltages as low as 1 V, $I_{on}/I_{off} > 10^4$ (Figure 3.3c) with an $I_{on}/I_{off} > 10^4$, maximum transconductance of 47 ± 9 µS (Figure 3.3d), and excellent stretching strain up to 20% (Figure 3.3e).[13] This work displays the versatility of the inkjet printing technique allowing entire components to be fabricated due to its simultaneous deposition, alignment, and patterning abilities.[13]

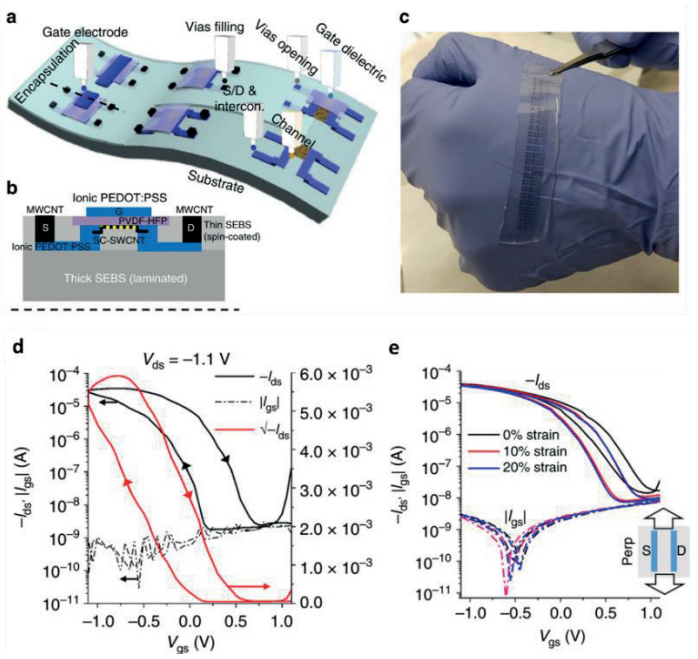

Figure 3.3. Fully inkjet printed synaptic transistor a) multilayer inkjet printing b) profile view of the FET structure, c) actual representation of the printed transistor array, d) transfer output curves of the FET, and e) transistor output when subjected to strain applied in the perpendicular direction[13]

Food monitoring

Edible sensors serve a dual purpose that not only monitors the safety of the food but also is non-intrusive and non-hazardous to the human body if consumed as well-known food products themselves are used to fabricate these sensors. Tao et al. presented edible food sensors that can monitor fruit ripening (Figure 3.4a) and dairy product spoilage (Figure 3.4b – 3.4c) using wireless passive inkjet printed antennas through continuous resonant response. Such sensors can even provide extra protection for the consumer by effectively killing any disease-causing bacteria.[17] This was achieved by Wang et al. whom developed edible supercapacitors that could even power an endoscope camera through a manual layer by layer fabrication process using cheese, gold leaf, activated charcoal, seaweed, Gatorade, and gelatin as shown in Figure 3.4e below.[18]

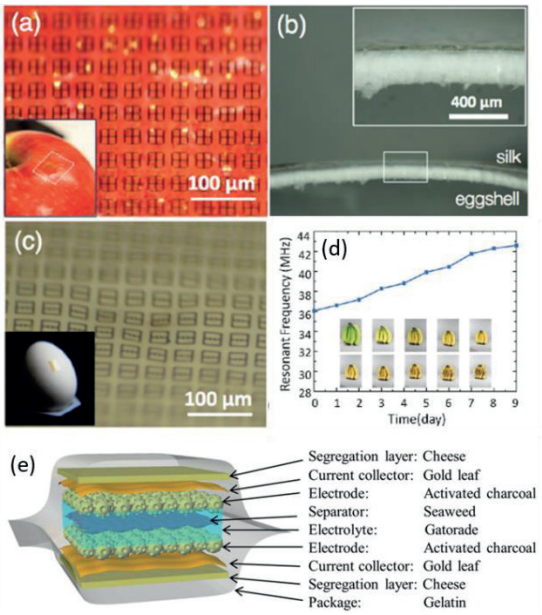

Figure 3.4. Food monitoring sensors a-d) edible silk-based sensor[17] and e) edible supercapacitors[18]

Environmental monitoring

Compared to other sensors, environmental sensors require stability and reliability over an extended period. In this case, incorporation of biodegradable materials can be detrimental to its functionality however can still be made onto flexible substrates. Molina-Lopez et al. fabricated interdigitated capacitors on polymeric foil PET (Figure 3.5a) comprised of inkjet printed Ag conductive tracks coated with electrodeposited Ni followed by an inkjet printed cellulose acetate butyrate (CAB) to act as a temperature and humidity sensor (Figure 3.5b). In comparison, to a commercially available sensor, higher differential values in relative humidity and greater variation in capacitance were reported suggesting that the sensor lacked stability as shown in Figure 3.5c.[8]

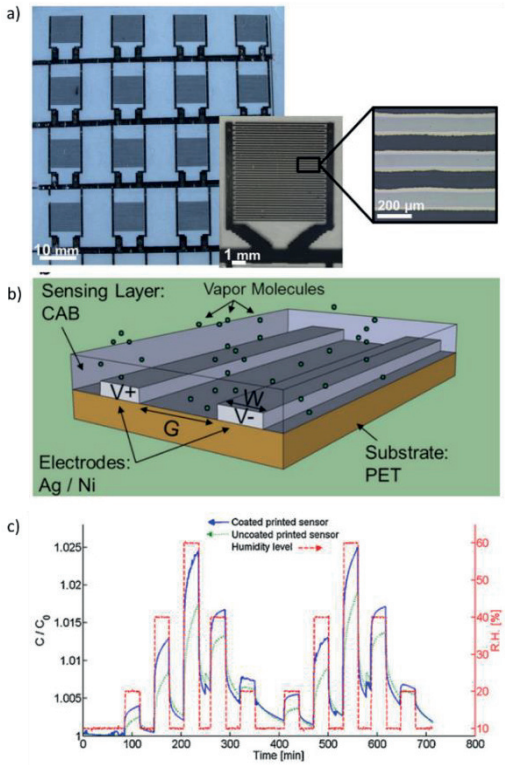

Figure 3.5. Humidity sensor a) photo of the interdigitated capacitive sensors b) schematic representation of the sensor and working principle, and c) comparison between the Ni coated and non-coated sensor in terms of humidity[8]

Health monitoring

The introduction of a flexible substrate saw an explosion in individual patient health monitoring devices for wireless blood flow monitoring[19], electrocardiographic recording[20], orthopedic[21], and neuroregenerative therapy.[22] However each of these required some microfabrication reliant processing steps such as evaporation of electrodes, conductive tracks, or patterning of 3D structures therefore such devices have not yet been fully printed requiring more innovation on behalf of printed technologies.

This chapter seeks to identify and provide the reader with a general background of the most commonly used deposition methods including both solution processing and printing techniques as well as alternative sintering techniques needed to achieve the same or similar results typically found with microfabrication processing.

3.2 | DEPOSITION TECHNIQUES

There is a myriad of deposition techniques that can be used to deposit a film from the simple solution processing techniques to the more complex printing techniques. All techniques discussed in this section below can be found in Figure 3.6 where all solution processing techniques were ordered in terms of increasing complexity. Drop casting and spin coating require a holder or planar and rigid substrates respectively to correctly form the film which limits the available substrates that can be used. In contrast, meniscus-guided coating techniques such as dip coating, doctor blading, bar coating, and slot die coating do not have these restrictions. However, none of these techniques mentioned above permitted patterning until the introduction of printing technologies such as screen and inkjet printing. Printing techniques will be discussed in the starting from screen printing, aerosol jet printing, gravure printing, and ending with an in-depth discussion of inkjet printing.

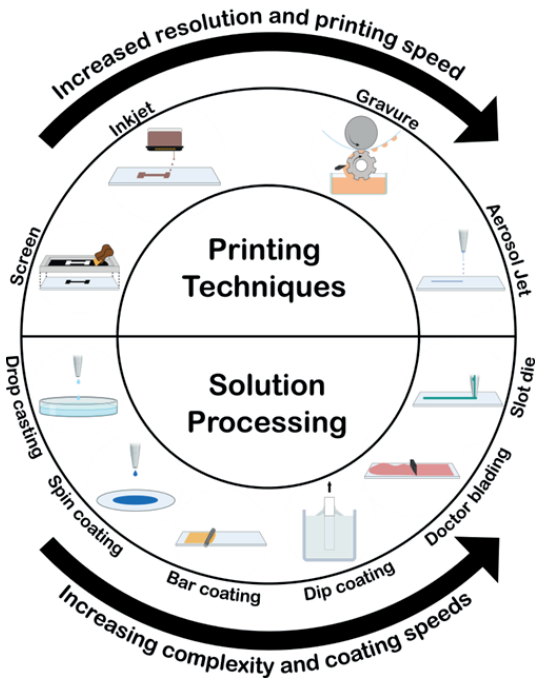

Figure 3.6. Schematic representation of solution processing and printing techniques

3.2.1 | SOLUTION PROCESSING TECHNIQUES

3.2.1.1 | *DROP CASTING*

Drop casting is considered the easiest out of all the solution processing techniques for thin film deposition where the target solution is simply casted into a mold using a pipette. As long as

the solution is viscous enough, a specified amount can be placed into a receptacle and spread by itself coating the bottom of the container (Figure 3.7a). Here the thickness is dependent on the volume of the receptacle and the amount of solution used.[23] Flatness is another variation that may arise simply due to the inclination of where the receptacle was placed during the evaporation phase. Additionally, the roughness of the receptacle also plays a role in the resulting roughness of the film which must be considered with a glass or polystyrene substrate being ideal for planar substrates. This is then left to dry through solvent evaporation at room temperature or can be accelerated using an oven to create the film (Figure 3.2b). Unfortunately, this technique is not repeatable due to varying factors if not controlled precisely. However it does provide a quick insight into the behavior of the solution, however more precise control can be achieved with the next following techniques.

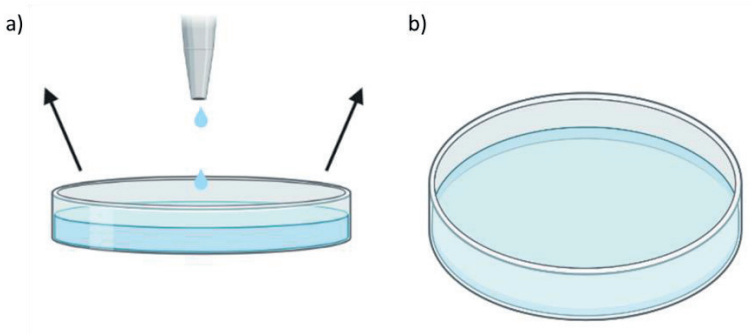

Figure 3.7. Drop casting process a) solution is placed into a petri dish where evaporation begins until b) a dried film is developed

3.2.1.2 | *SPIN COATING*

Spin coating is a 4-step process which is first initiated by depositing a set amount of liquid (Figure 3.8a) onto either a spinning or static substrate using a pipette. Once the substrate reaches the targeted speed, any excess solution is removed from the substrate (Figure 3.8b). The fluid becomes level when both the solution and substrate match in speed. During the spin-off stage, the solution has completely thinned on the substrate and is dominated by viscous forces. This is also the stage at which the film begins to dry due to the rotational speed. Next, evaporation of any solvent in the fluid occurs and can cause non-uniformities in the film simply due to the solvent chosen (Figure 3.8c). With the help of centripetal force, the solution deposited at the center of the substrate is evenly spread and coats the substrate resulting in an ordered structure (Figure 3.8d).[24] Here, the thickness is determined by the speed of the rotation used or the sheer force applied.

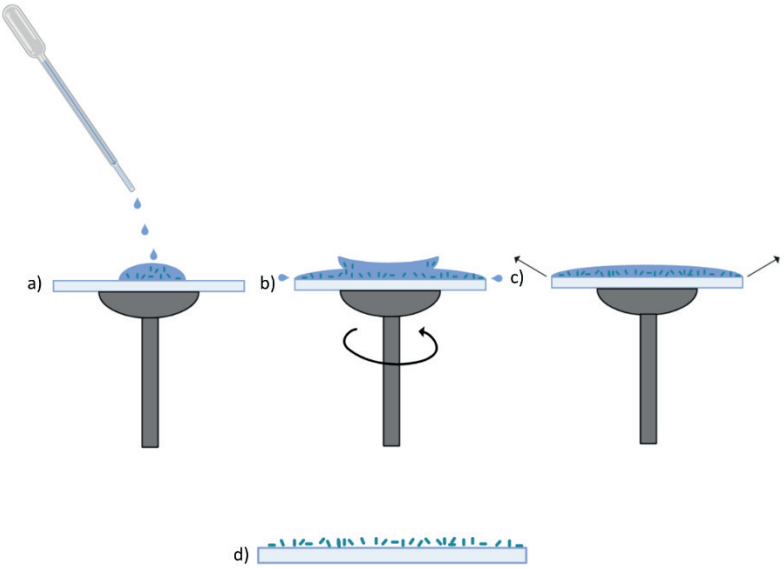

Figure 3.8. Stages of spin coating where a) solution is deposited onto the target substrate, b) the centripetal force evenly spreads across the surface, and c) begins evaporation until d) an ordered structure is developed as adapted from Ossila[24]

This simple technique allows for a wide range of viscosities to be deposited onto any substrate with large area deposition and is normally followed by a drying technique either on a hot plate or in the oven. Specifically, it has been optimized for small, flat circular surfaces with often quick drying times due to rotation achieving films thickness ranging from nm to µm. Generally, film thickness increases with increasing solution concentration, decreasing spin speed, and with the use of high vapor pressure solvents.[25] However, the residual waste from unused material (in excess of > 90%) and uneven coverage occurs if the substrate is not circular in shape nor placed equidistant to the center, uncontrollable thickness, and the inability to pattern the surface, and slow and individual processing times are major disadvantages when using this technique.[25] Additionally, a slow spinning speed is used to give more time for self-assembly often leads to uneven coating of the surface creating a coffee ring effect. Therefore, in order to create reproducible films, deposition must always be performed under the same parameters and in a controlled environment such as a cleanroom.

3.2.1.3 | *DIP COATING*

Dip coating is a facile method that takes advantage of capillary forces to deposit thin films.[23] This is a 4 step process where upon immersion the substrate is fully immersed in the solution (Figure 3.9a) for a determined amount of time called the dwelling time which is proceeded by the withdrawal (Figure 3.9b) where a thin layer of the liquid film is attached to the substrate

surface, and followed by drying where any solvents in the solution begin to evaporate and thus form a dry film (Figure 3.9c). The resulting thickness is dependent on the control of the withdraw and drying stages where multiple passes after drying the film previously result in thicker coatings.

Advantages of using this method include uniform coatings with surface roughness in nm and the ability to create gradient coatings by adjusting the withdrawal speed which is optimized for flat rigid substrates. However, there is also very little control over the amount of coating which often results in deposition along the entire surface of the substrate making localized deposition impossible.[23] Additionally, if the surface is curved or flexible, this will result in uneven coating. The drying phase can also be temperamental to external environmental factors that need to be well controlled. Simply due to the nature of this deposition technique, a large amount of waste is produced as a large volume of solution is needed to achieve a uniform coating.

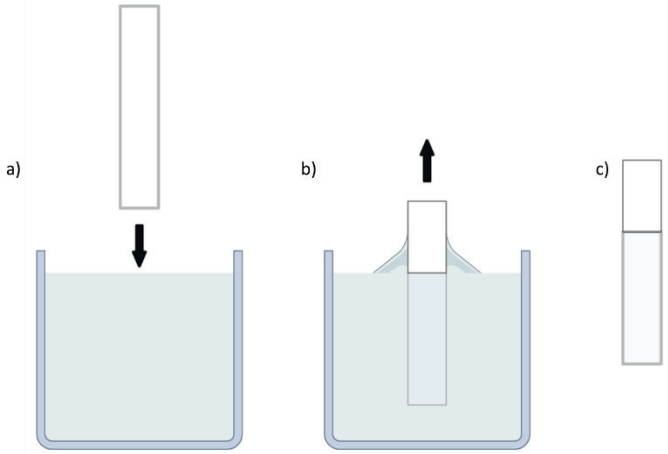

Figure 3.9. Dip coating procedure a) a rigid substrate is immersed in the target solution and then b) removed after a set time period leaving c) a thin film on the substrate surface

3.2.1.4 | *DOCTOR BLADING*

Doctor blading is a technique that either uses a blade held over the substrate which runs along the surface or moves the substrate where the blade is held stationary as shown in Figure 3.10. The small gap between the surfaces determines the overall thickness and controls how much liquid can pass through allowing for spreading of the liquid across the surface.[23] A large range of viscosities can also be used in this case and coat both flexible and rigid substrates. Here, the thickness of the film is determined by the viscoelastic properties of the solution and the coating speed.[23] Good uniformity of the film is achieved with good wetting where the surface tension of the ink is lower than that of the substrate.[25] The solute concentration also influences

the overall uniformity. This technique is best used to create uniform thin films over large surface areas. As compared to dip or spin coating, the deposition of the solution is controlled using a reservoir meaning less waste.[23] However, limitations include the fact that only film thicknesses down to 10s of microns can be produced. Because of the nature of the technique, patterning is not possible along with poor reproducibility. Also, when compared to spin coating, the processing speed is much slower.

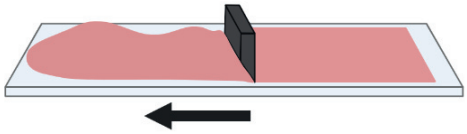

Figure 3.10. Graphical representation of the doctor blading process

3.2.1.5 | *BAR COATING*

This technique is technically very similar to the doctor blading technique mentioned previously where solution is placed on the substrate and flattened with a bar dragged across the surface as shown in Figure 3.11. The bar is essentially a long, flat cylindrical bar with or without an intertwined spiraled wire surrounding the body. Similar to the function of the blade in doctor blading, the amount of liquid is controlled by the gap between the bar and the substrate defining the overall film thickness.[23] This technique is relatively easy and inexpensive form of deposition for developing consistently uniform films. The ability to create a film over large surface areas on both rigid and flexible substrates with a controllable drying time is highly advantageous compared to other coating techniques. However, similarly, the minimum thickness possible is around 10 μm with no option to pattern the films. Due to the slow coating speed dictated by how quickly gaps are filled by capillary force, contamination is another affecting factor that can form streaks creating non-uniform films.[23]

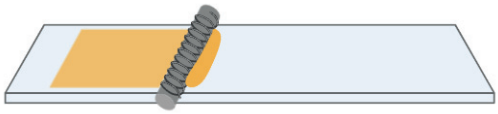

Figure 3.11. Graphical representation of the bar coating technique with spiraled wire

3.2.1.6 | *SLOT DIE COATING*

The most industrialized yet technically more complicated out of all the solution processing techniques discussed is slot die coating. The basic system consists of a solution reservoir and

pump that directly connects to the slot die head which ejects the solution onto the moving substrate by a roller (Figure 3.12). Where the head is positioned with respect to the substrate has a great effect on the film quality. Because the uniformity and thickness of the coating is dependent on the dispense rate of the solution, solution metering is necessary through the means of either peristaltic or rotary pumps.[23] Here, there are only two factors controlling the wet-film thickness: the speed of the substrate in respect to the head and the flow rate of the solution. A range of film thicknesses can be achieved from a few nm to microns. For this reason, this technique is widely adopted as it can produce uniform layers on an industrial scale.[27] This technique offers advantages over spin- and dip-coating techniques as it can be easily scaled and integrated into roll-to-roll coating and sheet-to-sheet deposition systems.[23]

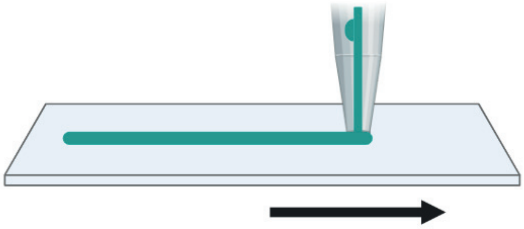

Figure 3.12. Schematic representation of slot die coating

3.2.2 | PRINTING TECHNIQUES

Printing techniques were developed not only as an alternative to the wasteful, expensive, exclusive nature of microfabrication techniques but also encompassed the ease of solution processing techniques with the ability to pattern films. Not only this but flexible and temperature sensitive substrates could be incorporated into the process. One heavily utilized printing or "inking" technique not explored in this thesis is micro transfer printing which utilizes an elastomeric stamp that can essentially "pick and place" microstructures from a donor to a receiver substrate, the latter of which is typically made of a non-conventional material with temperature sensitivity.[28] This technique has mainly been used for the development of biodegradable electronics however will not be address here as it conflicts with the motivation of this thesis and requires the use of microfabrication techniques prior to printing.

3.2.2.1 | *SCREEN PRINTING*

Screen printing is a technique that typically uses paste with a wide range of viscosities (10-300 Pa·s) that when passed through a mesh/screen/stencil defines the desired pattern as shown in Figure 3.13a below.[29] This is done using a metal or rubber squeegee to force a highly viscous fluid through that undergoes sheer thinning.[30] The different phases of printing are shown below

in Figure 3.13b where at Stage I, the ink is gently pushed through the mesh after application with the squeegee, staying in between the openings of the mesh. Stage II displays that when pressure is applied, the mesh and substrate come into contact while the pseudoplastic ink becomes thin.[31] The ink is then attached to both the mesh and substrate (Stage III) whereby as the printing continues downwards the mesh pulling the upper part of the mesh upwards causing the ink to rise at Stage IV.[32] From this, filaments begin to form just underneath the raised mesh wires at Stage V where finally by Stage VI, the deposition thickness is defined following the breaking filaments and print levels.[31] Critical factors in determining the print quality are the distance between the mesh and substrate and the mesh geometry.[33]

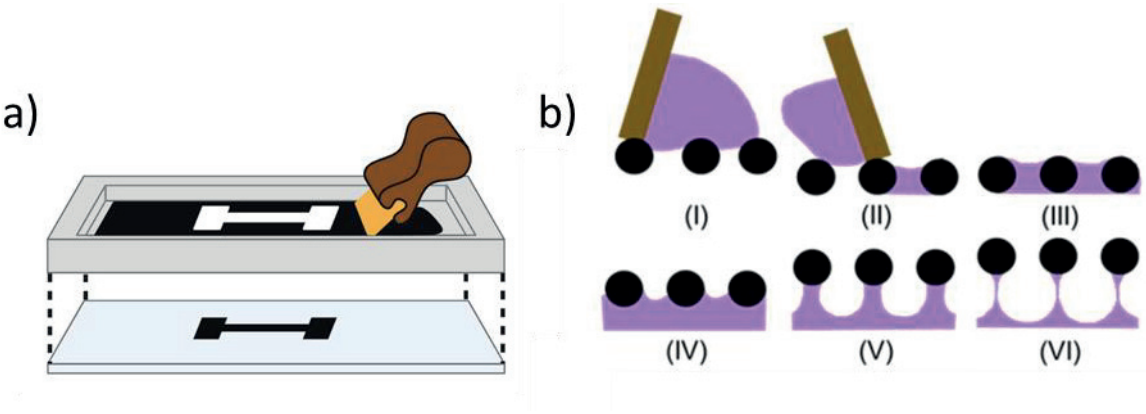

Figure 3.13. a) Schematic representation of the screen printing process and b) the six phase printing reaction[31]

The limiting factor for this technique stems from the mesh quality itself where nanoparticles up to micron sizes can be used with high loading from 50 up to 90% which often advantageous for conductive inks.[31,34] These inks are comprised of slow drying solvents (boiling point > 190°C) which must dried and sintered at temperatures higher than 120°C making them incompatible with temperature sensitive substrates.[34] These inks exhibit higher viscosity (due to the high loading factor) resulting in reproducibly thicker layers with high aspect ratio structures.[30] For this reason, screen printing has been used for the fabrication of larger structures such as electrochemical sensors and photovoltaics where accurate dimensions are not needed. As there are little restrictions in terms of ink properties, there is a wide range of commercially available inks including ink pastes where curing occurs from RT to hundreds of degrees depending on the type of material.[35,36] Minimum printing resolution for this technique is approximately 70 μm when using 140 threads/cm mesh count.[31,37] However with the implementation of fine-scale silicon stencils, silver ink lines as small as 22 μm could be achieved.[37] However this stencil required additional microfabrication processing thereby defeating the purpose of using screen printing as a technique altogether.

However, the simplicity of the technique may not outweigh its numerous disadvantages including ink waste, limited resolution, and excessive cleaning. Due to the nature of screen printing itself, a large amount of ink is first needed to force the ink through the openings while the rest is wasted in the process. A unique screen is needed for every new pattern making the cost associated with this technique is both high and inflexible. Dimension sizes are limited to the patterned mesh where poor resolution (> 75 μm) is apparent when creating large features and large thickness. For example, printing of drain and source contacts can be challenging as the resolution is too low further limiting its potential applications.[38] Additionally, if an ink dries too quickly, openings can be blocked and thereby change the print quality. Due to this, the screen can only be used for a certain period before cleaning needs to be done. On top of this, manual cleaning of the screens is extremely time consuming as they must be properly cleaned without the use of harsh chemicals as they may damage the screen. In terms of manufacturing, metallization by screen printing may cause a bottleneck in production of solar cells as the throughput is limited to 0.9 seconds per solar cell and line questioning its compatibility with large scale processing.[39] However, when compared to inkjet printing and 3D dispensing, its speed is almost 70 times faster.[30]

3.2.2.2 | *AEROSOL JET PRINTING*

Electrohydrodynamic deposition, also known as aerosol jet printing, is a coating technique that is typically used to make large area coatings and films through electrified ink fluid ejected through a nozzle onto a substrate. The substrate is placed onto an electrically grounded metal plate support at a static and defined distance away from the printhead. Movement of the stage is controlled in the x- and y- axis are controlled by servomotors while the z-axis is by a stepper motor. A power supply provides DC voltage applied between the nozzle and the metal plate to generate an electric field. This causes the “mobile ions in the ink to accumulate near the surface of the pendent meniscus at the nozzle”.[40] Due to the intrinsic coulombic repulsion between ions, a deformed meniscus in the form of a conical shape is induced called a Taylor cone.[41] This occurs as a tangential stress is forced onto the liquid surface creating a cone shape. When a sufficiently high electric field is applied, charged fluid droplets eject from the apex of the liquid cone as the electrostatic stress is greater than the capillary tension as seen in Figure 3.14.[41] These droplets can be categorized into different jetting modes that fall under dripping or jet modes. In the dipping mode, only a partial part of the liquid is ejected from the nozzle forming either fine droplets, large regular drops, or elongated spindles that coalesce into spherical droplets when they reach the substrate.[41] Similarly, jetting mode which allows for an elongated and fine jet can be jetted in a regular, rotated, or oscillated way that also disintegrates into droplets.[41] This type of deposition can be utilized for complex chemistry of thin films as in the case of solar cell development however a number of researchers has also shown an alternative application for this technique developing biodegradable polymer nanoparticles for drug delivery applications. Nath

et al. utilized the electrospraying technique to prepare PLGA microspheres[42] while Guarino and Wu et al. developed chitosan nanoparticles dependent on the voltage and flow rate of the technique and PCL microspheres dependent on the concentration used.[43,44]

Out of the techniques discussed; this technique has the widest range of viscosities acceptable allowing for the control of the droplet sizes down to nanometers by adjusting the applied flow rate and voltage.[45] Reproducible resolution for this technique for printing coarse lines is generally 20 – 30 µm which is the direct result from droplets with diameters ranging from 10-20 µm.[40] However, a simple modification of the nozzle to a smaller inner diameter of the capillary leads to smaller resolution. Other advantages include is its deposition efficiency up to 80% and direct transport of droplets by electrical forces thereby reducing any additional processing steps.[40] However, drawbacks of such a technique include the limited jet stability due to capillary break-up and varicose and whipping instabilities.[46] The quality of the film is dependent on many factors including the spray parameters, rheological and material properties of the ink, and physical parameters such as nozzle diameter and distance between the nozzle and grounded substrate, all of which need to be controlled for reproducible films.

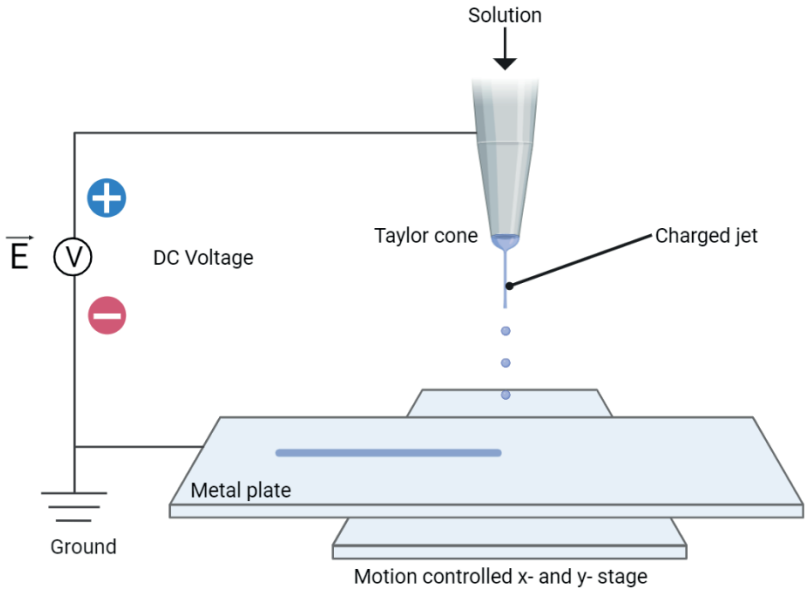

Figure 3.14. Schematic representation of aerosol jet printing

3.2.2.3 | *GRAVURE AND FLEXOGRAPHIC PRINTING*

Gravure and flexographic printing are considered roll-to-roll (R2R) processing techniques implemented in manufacturing due to its high throughput, substrate independent, and tolerance of various inks especially when compared to inkjet printing.[47] Here, printing rolls are fed into an

ink bath wetting the engraved cells on the surface where then a doctor blade removes excess ink from the cells.[47] The remaining ink is then printed onto the target substrate found between the printing and impression roll as shown in Figure 3.15 below. A successful transfer is dependent on the substrate surface energy, ink viscosity, ink surface tension, and evaporation rate of the solvent in the ink. Both the surface energy and wetting behavior of the substrate must be greater than that on printing plate so that the ink is released.[47] Additionally, the printing speed and ink shear behavior must be adjusted so that the ink will be attracted and attached to the substrate.[47] Additionally, the ink viscosity should be well controlled as those with low viscosity (10 cP) result in poor ink transfer leading to film breakup while those with higher viscosities of 100 cP produce optimal films with defined edges lacking any pinholes.[48] This technique has many advantageous over standard printing as it can produce large batches and be scaled up to an industrial level. These well-established techniques can reach resolution sizes down to 10 µm at high printing speeds up to 15 m/s with low ink waste.[49] Even smaller feature sizes can be achieved using advanced femtoliter-scale microgravure printing (µGRavure) that can execute high resolution from several nanometers to 10s of µm at speeds up to 1 m/s.[48] High speed is necessary in order to guarantee well form dots. However, in this case, the entire process must be well standardized before implementation as smaller experimental batches cannot be effectively incorporated into the process.

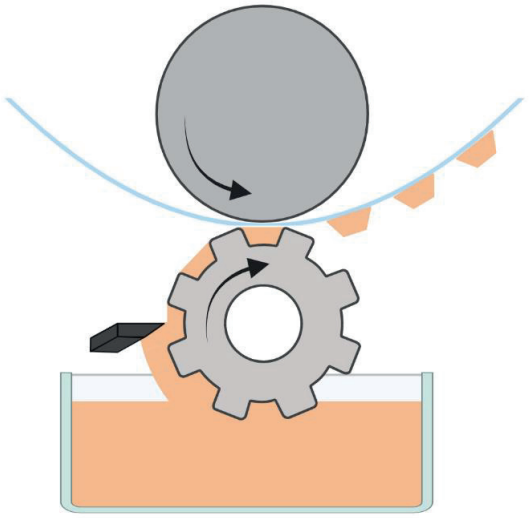

Figure 3.15. Schematic representation of gravure printing

3.2.2.4 | *INKJET PRINTING*

Introduction

Conception of the first known inkjet printer was introduced by Elmqvist in 1951 paving the way for other variations such as the continuous inkjet printing in the 1960s, followed by the invention of the drop-on-demand (DOD) inkjet printing system in the 1970s.[50] This technique operates with the help of liquid phase materials such as inks that vary in the number of components based on their respective functionality.[51] The continuous method ejects ink in the form of a jet whereby surface tension breaks the stream into regular, uniform sized drops. On the other hand, DOD printing is governed by two actuation mechanisms: thermal or piezoelectric actuation to generate drops through a nozzle from a reservoir. With thermal actuation, there is a heating element that is activated when a drop is ejected. Heating causes partially evaporation of the ink and formation of a gas bubble in the reservoir.[52] The pressure generated forces the liquid through the nozzle creating droplets. Then the heating element is then switched off generating a vacuum drawing ink into the reservoir where then the process begins all over again. On the other hand, piezoelectric DOD uses specific crystal materials that convert voltage into mechanical movement. A drop is created when a voltage pulse is sent to the reservoir walls which become contracted creating a pressure increase causing the ejection of the of the ink through the nozzle.[52] Once the droplet hits the substrate, the ink spreads under momentum and dictated by the interfacial behavior between the liquid and solid substrate often characterized as its surface tension either with the help of an external heating source or naturally.[53] Next, the droplet dries under solvent evaporation dependent on the boiling point of the solvent.[54] The ink parameters such as viscosity play an important role on the overall printed shape of the desired pattern.[55]

As shown in Figure 3.16 below, inkjet printing is comprised of different systems beginning with the electrical elements controlled by the input waveform that signals the piezoelectric actuator to mechanically deform building localized pressure in the ink chamber causing it to acoustically generate a wave that forces the ink to be ejected from the nozzles governed by its fluid dynamic behavior. The droplet then lands onto the substrate, where with enough sequential droplets, begins to coalesce together and form a film. The following sections here will review each of these elements of the inkjet printing process in detail below.

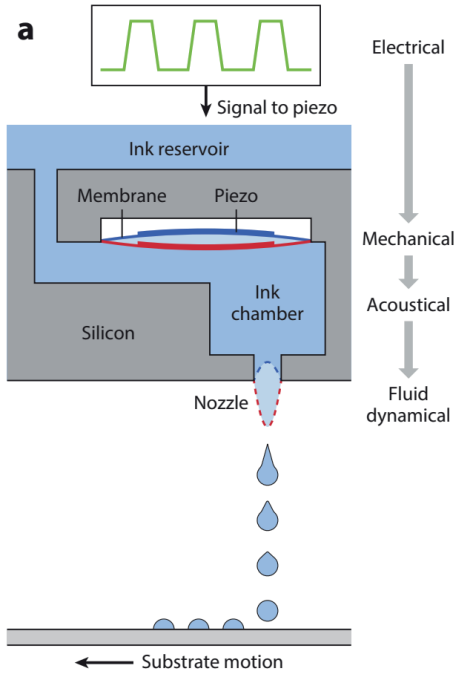

Figure 3.16. General overview of the different components that comprise the inkjet printing process[56]

Printer Components

The inkjet printing mainly used for the majority of this work was a Fujifilm Dimatix DMP-2831 Materials DOD inkjet printer based on piezoelectric technology as shown below in Figure 3.17a. The printer itself consists of many components such as the vacuum platen (heating up to 60°C) with a large print area up to 210 mm x 315 mm. Alignment, precise positioning, and inspection of the printed pattern are adjustable with the use of a fiducial camera which allows for the facile development of multilayer devices. Additional protection from dust during the printing process is provided for by the plastic lid. Once the print cartridge and substrate are loaded into the cartridge holder and set to the right drop spacing (DS), a connected computer pre-installed with the software can be used for pattern development and manual control of the printer. This includes the drop watcher and blotting pad which are used in conjunction when investigating if the desired ink is jettable under set conditions and if not, can be cleaned with the help of the blotting pad. The print carriage gives the printer the freedom to move in the x-, y-, and z-directions while the printing direction is confined in the x-direction, important to consider when depositing a film onto the substrate surface. Lastly, one of the most important components in the printer is the print cartridge (Figure 3.17b). The printhead itself contains a piezoelectric jetting element with a fillable reservoir up to 1.5 mL. Two different printheads may be used with a difference only in volume. DMC-11601 and DMC-11610 printheads eject 1 and 10 pL drop volumes respectively, each containing 16 nozzles with a 254 µm spacing in a single row. The

freedom and ease in using this system allows for facile deposition of any material onto planar substrates, in direct competition to standard microfabrication techniques down to tens of microns.

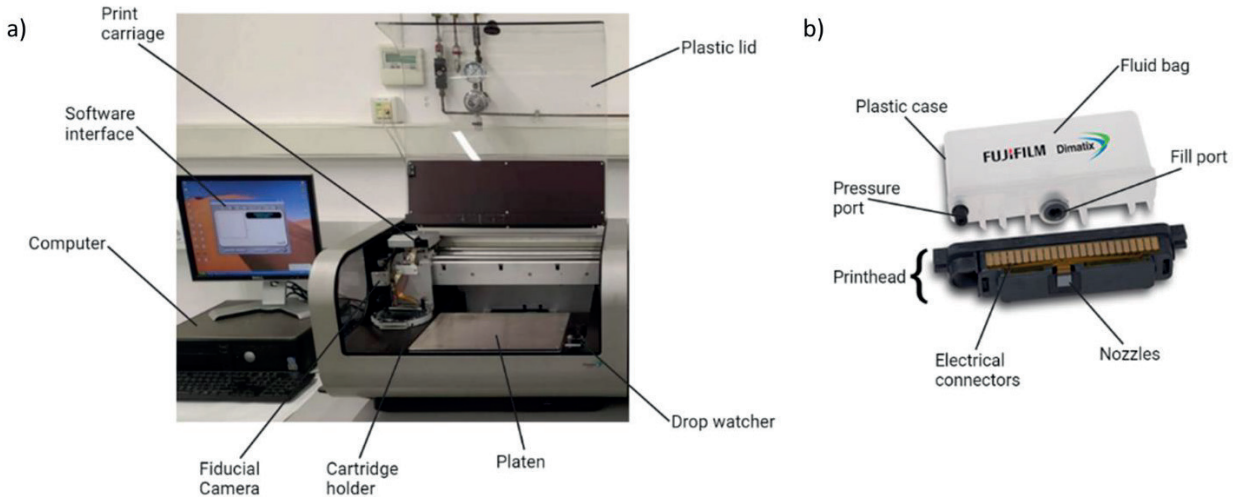

Figure 3.17. Inkjet printing equipment a) FUJIFILM DIMATIX DMP-2831 inkjet printer[57] and b) print cartridge[58]

Waveform control and manipulation

It is through the manipulation of the waveform that controls the ink ejection through the printhead nozzle. This process occurs in 3 phases noted here as fill, ejection, and recovery as shown in Figure 3.18 below. Initially, the pumping chamber containing a refill inlet and exit nozzle is under compression by a bias voltage applied to the piezoacoustic actuators.[56,59] Phase 1 is initiated following the application of a negative voltage placing the piezo component in a neutral state whereby the ink is drawn into the chamber from the inlet creating fluid flow thus further pulling on the meniscus created at the nozzle. Phase 2 provides a firing pulse which depending on the slope, provides energy for the ejection of the droplet. At this stage, the chamber once again is under compression due to the increased voltage forcing fluid flow in opposite directions out of both the inlet and outlet. By this point, the droplet should be full ejected and heading towards the target substrate. Recovery to the initial state begins at Phase 3 where the piezoelectric transducer (PZT) is brough back to its null state to the bias level. The compression occurs partially which prevents any air displacement into the printhead and then fully to introduce fluid flow back into the chamber to start the process over again.

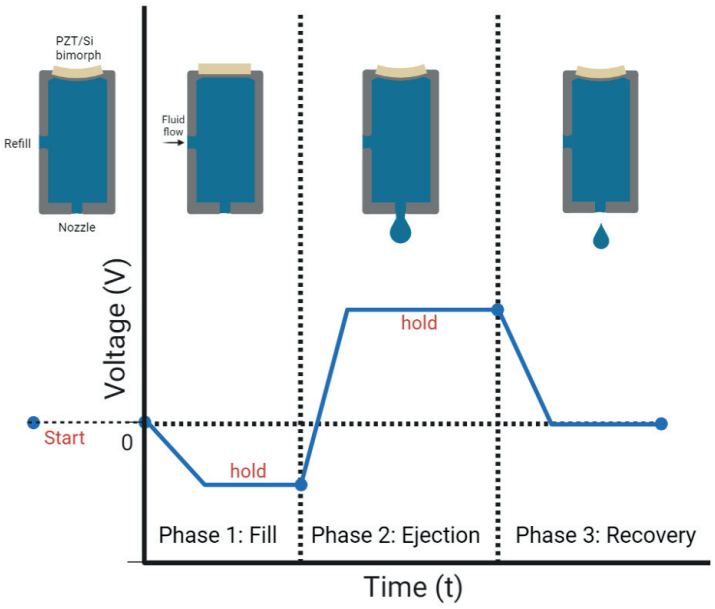

Figure 3.18. Different phases of droplet ejection through waveform control as adapted from[59] and Dimatix tutorial

The ideal droplet ejection and formation is displayed below in Figure 3.19a which exhibits a long tail ejected from the nozzle and culminating into a single droplet before reaching the substrate. However, there are also a wide range of failure mechanisms that can be seen during this process mostly depending on the ink properties such as viscosity from the solvents used to prepare the inks. There are a total of 5 different failure modes: no jetting, production of satellite drops, and ejections of multiple drops, misdirected droplet, and uneven droplet velocities as appears below in Figure 3.19.[60] No jetting is a result of failure to from a droplet due to high viscosity and/or low perturbation energy.[60] Conversely, high viscosity inks combined with high drop velocity are likely to form satellite drops. A combination of both aspects of low viscosity coupled with high drop velocity result in multiple drop formation as reported in Figure 3.19b. If either of these failure mechanisms are observed, its respective waveform, ink viscosity, or heating of the ink should be adjusted accordingly. Figure 3.19c displays nozzle contamination from debris or trapped air in the nozzle descender are the main causes for misdirected nozzles.[61] This failure mechanism may be resolved by introducing a cleaning cycle, replacing a used cleaning pad, or by filtering the ink further.[61] Lastly, uneven velocities between the adjacent drops (Figure 3.19d) may simply be seen however this maybe the result of a misaligned view which can easily be adjust through the Dimatix software.[61]

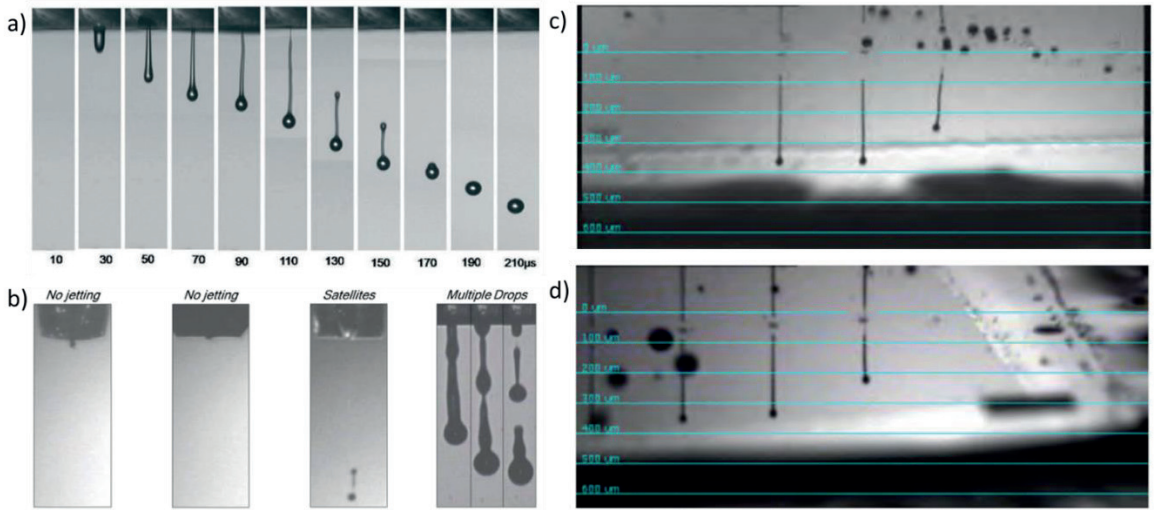

Figure 3.19. Different Jettability modes where a) displays good jettability as captured by Jang[62] and b) shows different failure modes as reproduced and modified from Sadie[60], c) misdirected nozzles[61], and d) uneven velocities[61]

Defining jettability

Although there are a wide variety of factors that can describe fluids, the four most pertinent to inkjet printing are Reynold number (*Re*), Ohnesorge number (*Oh*), capillary number (*Ca*), and Weber number (*We*).

Reynold number (*Re*) is defined in Equation 3.1 below:

$$Re = UR \,/\, \nu \tag{3.1}$$

where U represents the droplet velocity as a result of pressure growth in the ink reservoir, R is the droplet radius, and ν is defined as the kinematic ink viscosity.

Ohnesorge (*Oh*) as seen in Equation 3.2 below

$$Oh = \eta \,/\, \sqrt{\rho\sigma R} = \upsilon\rho \,/\, \sqrt{\rho\sigma R} \tag{3.2}$$

where η represents the dynamic ink viscosity, ρ is the liquid density, and σ is defined as the surface tension.

Physically ink behavior can be predicted as shown in Figure 3.20 below defining the optimal operating mode based on *Oh* and *Re* numbers which represent ink material properties and inkjet velocity respectively. Only a narrow window of intermediate *Re* and intermediate *Oh* values are deemed reliable operating parameters for successful jettability. A smaller *Re* results in weak actuation that does not allow jetting while a larger *Re* indicates splashing because of rapid droplet impact onto the substrate.[56] Similarly a small *Oh* exhibits strong surface tension leading to the formation of random satellite drops while a large *Oh* notes that the ink is too viscous impeding jetting.[56]

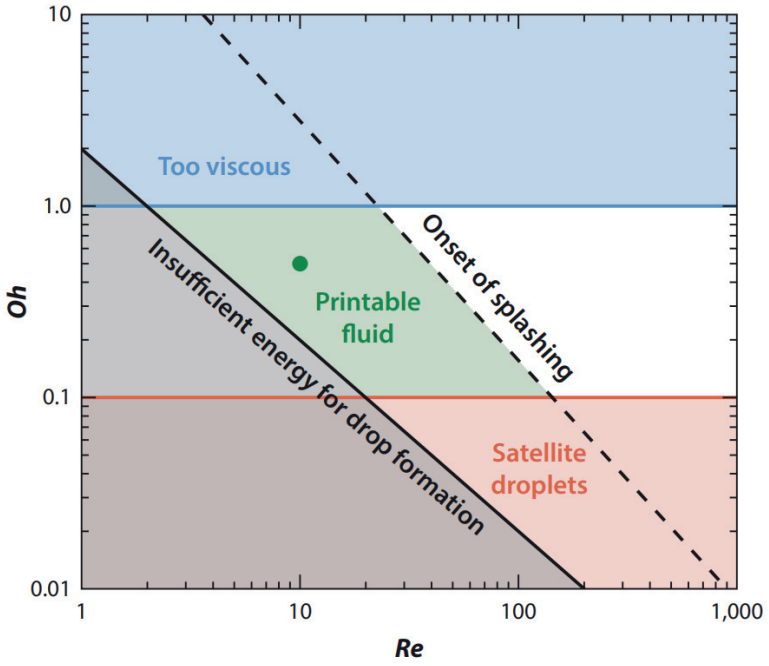

Figure 3.20. Operating regime for DOD inkjet printing in terms of Ohnesorge and Reynolds numbers as reported by Detlef Lohse[56]

This precise window can also be further defined using Capillary number (*Ca*) and Weber number (*We*) as stated below in Equations 3.3 and 3.4.

Capillary number (*Ca*) represents the ratio of viscous to capillary forces where

$$Ca = \eta U \,/\, \sigma = \upsilon \rho U \,/\, \sigma \tag{3.3}$$

showing a dependency on η, the dynamic viscosity.

Weber number (We) is defined as

$$We = (\rho U\text{^}2\ R)\ /\ \sigma \tag{3.4}$$

both of which have a clear reliance on surface tension (σ). Figure 3.21 presents a jettability window that is defined by *Ca-We* numbers that were studied for a wide range of common solvents. Every plotted point represents the specific velocity of the target ink which was achieved by manipulating the pulse voltage. With respect to drop velocity, *Ca* exhibits a linear dependency while *We* displays a quadratic dependence.[60] The functional jettability range was defined by the plotted lines outside of which indicated jetting instability which was shown as the case for both higher and lower drop velocities. In this respect, *Ca* represents both the minimum and maximum limits tolerable for inkjet printing. This graph provides a quantitative insight on why certain jettability failure modes result as shown in Figure 3.13b.

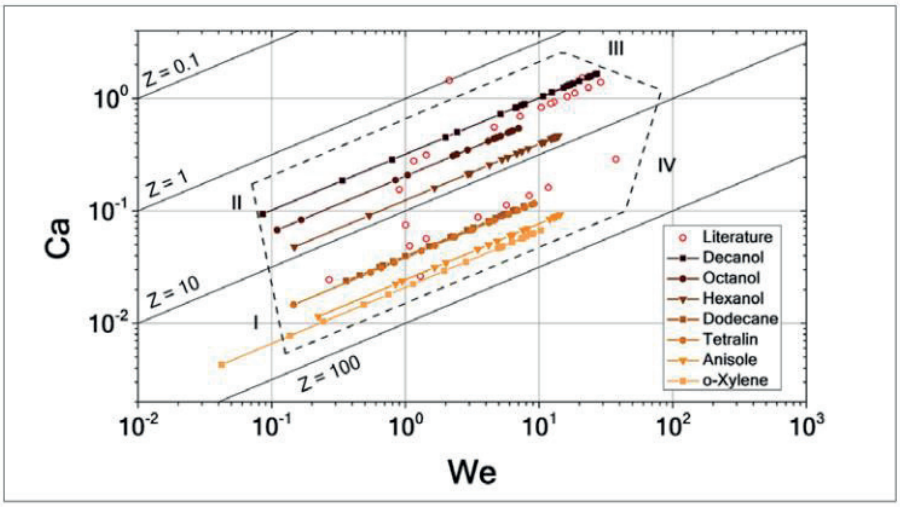

Figure 3.21. Ca-We Jettability window on a log scale as defined by Jake Sadie[60]

Droplet impact fluid dynamics

Just as important is the interaction of the droplets onto the dry target (non-porous) surface which can create various flow patterns.[63] Its behavior can be affect by one of many factors including the liquid properties which vary greatly depending on the density, viscosity, surface tension, and elasticity, and the target substrate surface which can range from being the ideal hydrophilic, planar, and smooth to hydrophobic, rough, and non-planar surfaces.[56] For simplification, mainly an ideal surface will be discussed for the rest of this section. The droplet

before impact (Figure 3.22a) appears with a deformed shape due to the pressure buildup as an air cushion appears just above the receiving substrate.[56] Once the droplet lands on the substrate, it begins to spread radially forming a rim at the edges where then it may recoil or further wet the substrate as shown in Figure 3.22b.

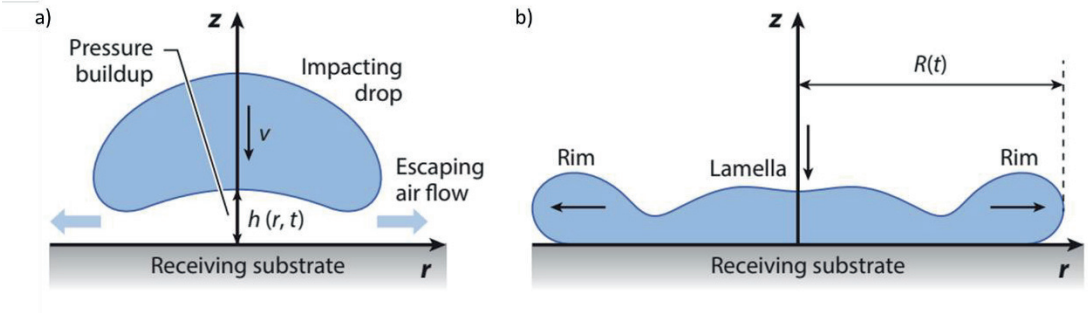

Figure 3.22. Impact dynamics of a droplet a) before and d) after hitting the substrate[56]

Figure 3.23 below shows a wide range of impact modes that can occur where from these 6 cases, the most desired is the one noted as "deposition" creating a perfectly circular shape which is expected for inkjet printing standards, otherwise a film would not be formed. The prompt splash is a result of ink introduction to rough surfaces while impact on liquid films result in a corona splash where additional droplets are formed at the later stage of impact with the substrate. The receding breakup is characterized by a droplet at its maximum spreading radius that begins to retract partially leaving some smaller droplets behind.[64] Lastly both rebound modes can occur because of highly energetic impacts followed by a receding phase where the difference is characterized by the static receding contact angle.[64] All other impact modes will result in an incomplete and inhomogeneous film which can be manipulated by adjusting the ink properties.

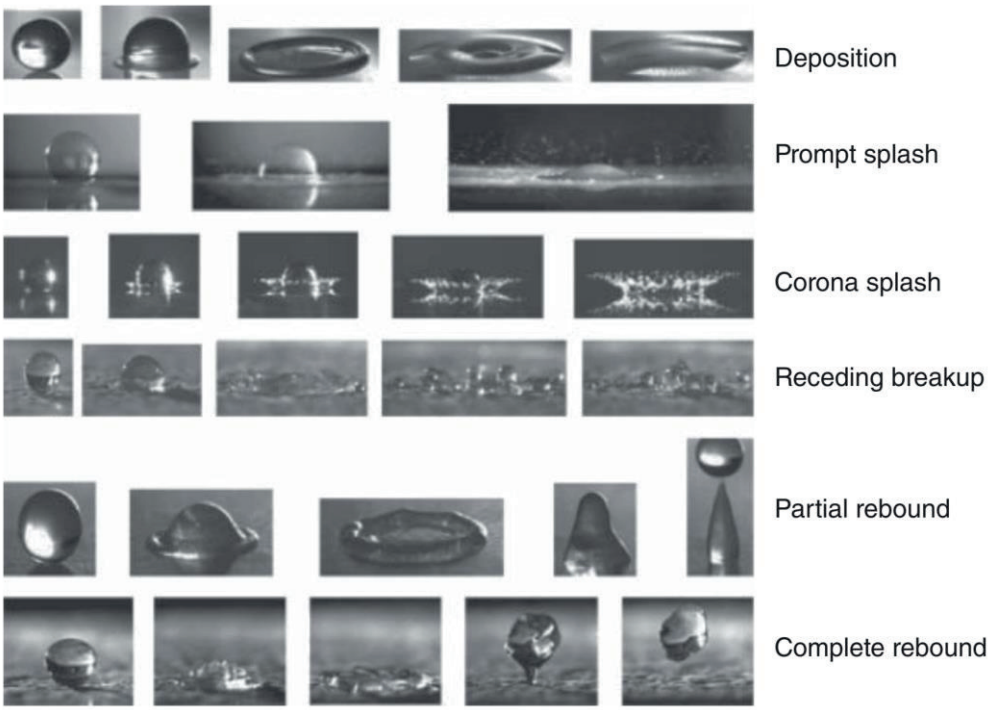

Figure 3.23. Different droplet impact modes on a dry surface[64]

However, often times, the challenges in optimizing the fluid dynamics relies on both the ink behavior when ejected from the printhead as well as the target substrate properties. These include the flow of the ink inside the printhead, jet formation, and meniscus dynamics while on the substrate side includes droplet impact, substrate wetting, and droplet/solvent evaporation amongst others.[56] For non-conventional substrates outside of polymer materials, this can be even more challenging as the requirements maybe conflicting making optimization far more difficult.

Spreading

Ink droplet spreads on account of the Marangoni effect, the principle which explains the movement of a liquid drop on a surface which often creates surface tension driven fluid flow in the direction towards the higher surface energy.[65] Tangential stress at the solid-liquid surface is caused either by temperature or spatial variations (i.e. liquid composition) that causes interfacial fluid motion which is then further transmitted to the bulk fluid.[66] The action of the droplet spreading on the surface can be characterized into 5 phases starting with the kinematic, spreading, relaxation, wetting, and finally equilibrium.[63] The spreading phase sees the radial droplet expansion where the initial kinetic energy of the drop prior to contact is used. Here, the drop behavior is dependent on the drop speed, wettability with the surface, and ink properties. A larger drop size or higher impact speed is characterized by faster spreading while inks with

higher viscosity or surface tension retards expansion. Following this stage, the drop can either exhibit relaxation or shape oscillation through retraction. Droplet rebound or receding is often seen on hydrophobic surfaces while those on a hydrophilic surface can display oscillation followed by more spreading on account of capillary effects until an equilibrium state is reached.[66]

Film formation

Once a larger number of droplets were sequentially printed, they can begin to interact through capillary effects.[56] An important factor that must be defined in this case is the optimal DS, the distance between two centers of the drop as shown in Figure 3.24a. An internal standard for defining this parameter was created by a former PhD student at the Technical University of Chemnitz (TUC), Enrico Sowade, referred to as a line pattern test (Figure 3.24b) which consists of uniformly spaced drops from 5 up to 140 μm. Once printed for a particular ink and substrate, the optimal DS can be defined by seeing which DS develops a well-defined line. In the case provided by Figure 3.24c, the top row with the highest DS showed isolated drops undesirable for film development. The line just below formed a scalloped appearance showing that the drops coalesced but still maintained their shape. This morphology can appear as a result of too large of DS deposited at the appropriate temperature.[67] Following this, a continuous and straight line was seen further verifying that this DS was optimal for printing patterns. Afterwards, as the DS further decreased, the deposited line appeared to be bloated or bulging as the droplets began to overlap and accumulate past the desired pattern. This behavior is deemed unacceptable as using this DS may distort the desired pattern. This is often caused by smaller drop spacing which may or may not be due to slow drying rate.[67]

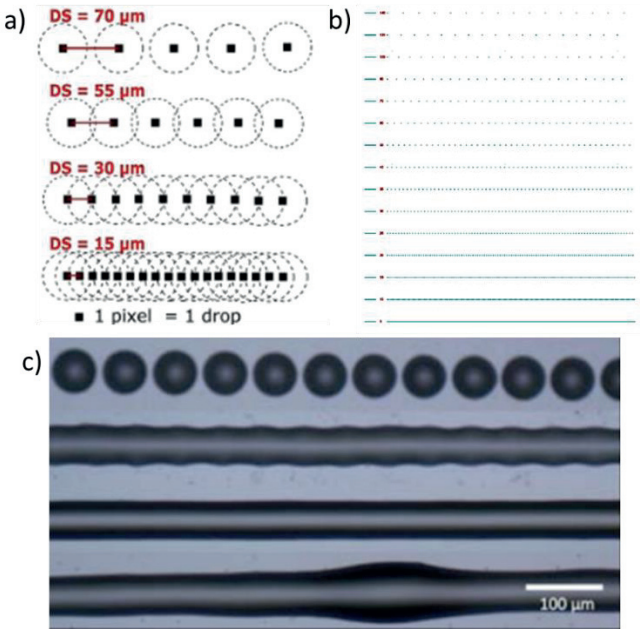

Figure 3.24. Line pattern is defined by a) DS which is the distance between the centers of two successive drops, b) containing DS from 5 - 140 µm, and c) actual printed line pattern showing different behaviors as the DS decreases as adapted from Enrico Sowade[68]

It is then by the series and number of droplets that must be first defined to generate a pattern. This is achieved through measuring the drops per inch (dpi), that is how many drops are printed within 1 inch which also helps define the final resolution. Figure 3.25 below shows the relation between DS and resolution where isolated drops (with high DS) are synonymous with low resolution while those with high resolution tend to have a low DS and thus creating well defined patterns.[69] This behavior is essential in the development of a continuous film and must be predefined when generating in equivalent BMP digital file that can be read and printed by the Dimatix Printer. The digital file containing the pattern to be printed is rendered as pixels representing a single droplet as it hits the substrate surface. The complete pattern is then printed by the movement of the head as it rasters about the substrate.

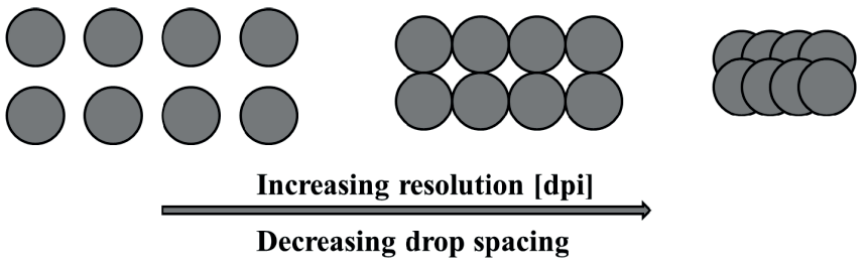

Figure 3.25. Relationship between dpi and DS as acquired from Petr Krčmář[69]

Solvent evaporation effects

Once the desired film surface is printed, solvent evaporation occurs in different modes according to its ink composition. The evaporation rate of colloidal drops displayed below in Figure 3.26 is indicated by the length of the arrow and controlled by the vapor diffusion.[56] Figure 3.26a displays the evaporation mode for a colloidal droplet singular solvent system where the evaporation rate is highest in the rim region. As the rim region becomes more dry, more liquid is constantly replenished from the solvent at the center of the droplet and dried accumulating solutes along the edges of the droplet creating a ring-like deposit as seen in Figure 3.26b.[56,70] This mode was observed during the evaporation of a water droplet in the absence of circulating flow. [37] This effect can be reduced through the optimization of rheological properties thereby controlling liquid drop formation and behavior at the ink-substrate interface. Another effective way in avoiding this effect is through the counteracting ability of what is known as the Marangoni flow which naturally occurs due to surface tension gradients. [53,56,70,71] Figure 3.26c and 26e represent different evaporation modes in a binary solvent system where the volatile liquid in this system either contains higher or lower surface tension respectively. In the case of the regulated Marangoni flow as seen in Figure 3.26c, the flow pulls particles from the free liquid surface towards the top inwards portion of the droplet forcing it further downward where the solute can either settle onto the substrate center or continue to the edge of the droplet and become recirculated back to the free surface at the top of the droplet.[70] This movement is first initiated through evaporative cooling which occurs during the droplet evaporation phase producing nonuniform cooling where the temperature at the top center of the droplet is lower indicating high surface tension in that region creating the inward flow generating a surface tension gradient. [66,70] Majumder et al. reported that nanoparticle dispersion a mixture of ethanol and water created a regulated Marangoni flow that served to homogenize the solute deposition creating an homogenous film reducing the coffee ring effect (Figure 3.26d).[71] Additionally, this reducing effect was also seen with the use of other solvents such as octane and other alkanes.[70] This morphological defect can negatively affect the overall conductivity of the film.[4] Conversely, for binary ink solvents containing a lower surface tension shows an internal flow that goes outwards to the rim of the droplet as dictated again by the surface tension gradient as seen in Figure 3.26e. In this case, the Marangoni flow governs the entire system to the point where solutes tend to concentrate mostly at the center of the of the droplet-substrate interface creating a smaller disk then what initially deposited (Figure 3.26f).

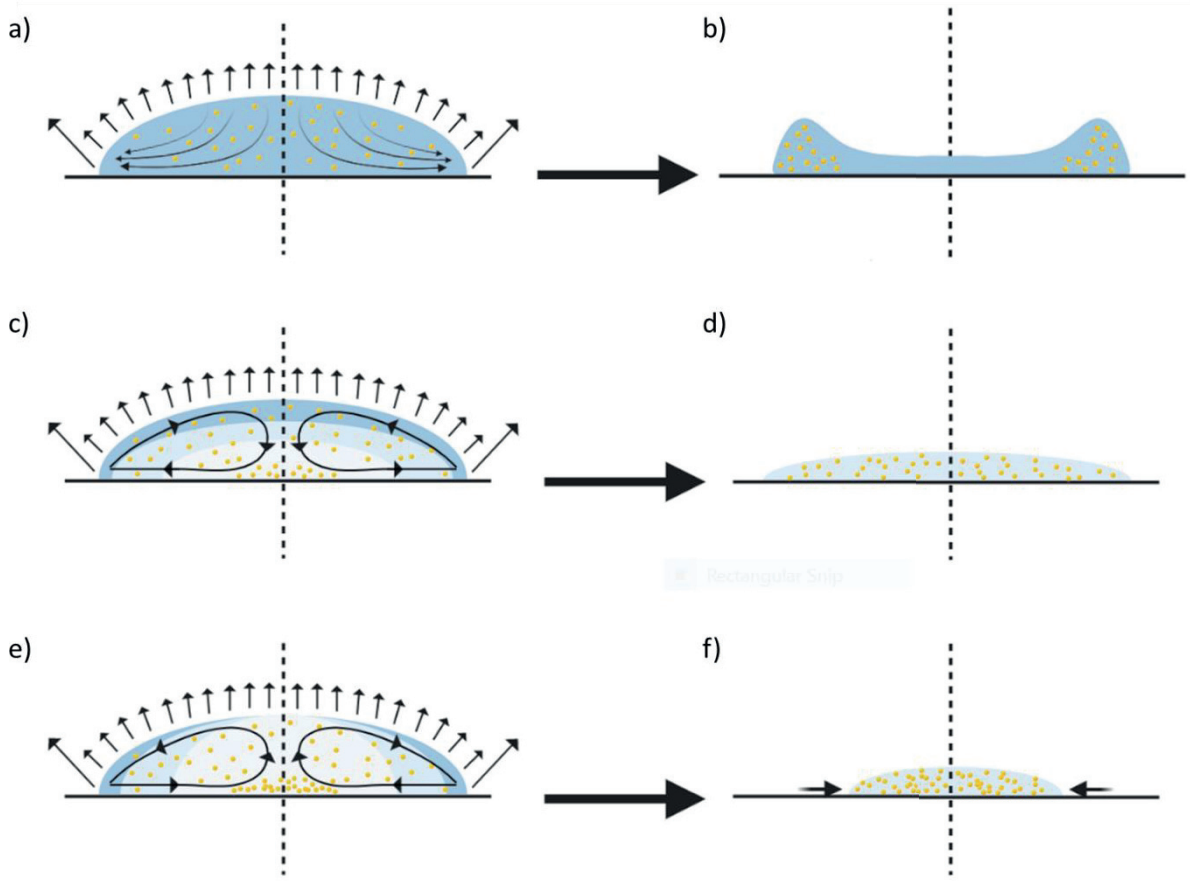

Figure 3.26. Sessile droplet evaporation modes where for a) a singular solvent system with little flow, results in b) the coffee ring effect. For dual solvent systems with c) a higher surface tension volatile solvent with recirculating Marangoni flow results in d) a homogenous film, and e) a lower surface tension volatile solvent dominated by Marangoni flow concluded in f) as adapted from Lohse[56] and Pavlos Giannakou[67]

Advantages and disadvantages

As compared to microfabrication processing, the appeal of inkjet printing is due to its low cost and low material waste all while having the ability to create a wide range of thin films including metals, semiconductors, and dielectrics.[51] This has allowed inkjet printing to become an important industry standard for printed electronics in the development of sensors[25,72], transistors[27,73], LEDs[56,74], and photovoltaics.[41,56] In contrast to the subtractive nature of the microfabrication techniques to create similar films, this additive technique allows for patterns from 10s of microns. This maskless and non-contact approach operates based on a digital file where on-the-fly design allows for easily changeable designs. Once an inkjet printing process is defined, it can be rapidly scaled up for production equally onto both small and large substrates.

However, the success of this technique is dependent on many factors including the optimization of process parameters, ink concentration, and solvent or solute parameters.[25] Here, it is necessary to use low viscosity inks to maintain stable flow through the nozzles and minimize the risk of clogging often associated with this technique.[46] If the ink itself is not fully optimized, variability in both the drop size and the resulting layer during a single print can occur challenge the reliability of this technique. This is often the case when nozzles are blocked causing intermittent printing. Agglomeration or accumulation of nanoparticles ink can easily block the nozzles entirely making it impossible to print. Additionally, some nanomaterial architectures like nanoflakes and nanowires are simply too large to print due to their large surface area and surface-to-volume ratio. Because of this, extremely low viscosity inks containing nanoparticles with sizes up to 100 nm are essential for successful printing. Low viscosity inks (between 2-25 mPa·s) are necessary however, a larger range of viscosities can be printed when heating the printhead. To achieve this, often inks are made with low filler loading < 20% to help prevent issues such as agglomeration but result in an overall low conductivity of the film.[75] This can be overcome with multiple printing passes creating multiple conductive layers. Additionally, both the layer thickness and pattern resolution are dependent on nozzle diameter (typically 10 - 150 μm for commercial piezoelectric inkjet printers) achieving sub-nanoliter volumes.[52,76] The droplet diameter often dictated by the drop volume ejected from the printhead severely restricts the lateral resolution to approx. 30 μm.[52] This means that inkjet printing is unable to compete in the realm of nanofabrication techniques, however with the introduction, super fine inkjet printing, this resolution can be improved down to 1 μm although it is not yet a widely implemented technique.

Unfortunately, printability on curved surfaces is nearly impossible as this requires flat substrates with low surface roughness to print well defined patterns. This again is partially due to the low viscosities inks necessary to print. It is also for this reason why inks are more readily available for both screen and aerosol jet printing as opposed to inkjet printing. When compared to other techniques such as gravure printing, the throughput speed is relatively slow and offers minimal substrate contamination. All such factors discussed here must be taken into consideration when choosing the correct printing method for device fabrication.

3.3 | SINTERING TECHNIQUES

The adaption of temperature sensitive polymeric substrates to biodegradable electronics relies heavily on the post-treatment sintering techniques to treat the deposited ink layers. Standard techniques such as thermal annealing have been implemented due to ease and controllability using rigid substrates such as Si and glass which is well known to withstand temperatures as high as 1700ºC. As the materials discussed here may require up to 3000ºC, this limits the scope of substrates that can be used. Therefore, other strategies that have little to no

effect on the underlying substrate below are necessary to provide localized heat to the printed patterns. Additionally, a common issue facing printable inks is the inability to completely remove these capping and stabilizing agents and organic compounds. Large amounts of organic residuals left can adversely affect the conductivity therefore techniques that can also provide enough energy for solvent evaporation is indispensable. Alternative technologies such as chemical, plasma, intense pulsed light, laser, and microwave sintering can be used to sinter conductive tracks on top of temperature sensitive substrates with minimal effects and have shown increased conductivity. The success of these potential techniques must fulfill two conditions: 1) that the majority of any organic or stabilizer components be removed to initiate sintering while the 2) heating or conduction of the substrate should be minimized.

3.3.1 | THERMAL ANNEALING

The most widely used heat treatment for developing deposited films can be done using an oven, hot plate, or furnace simply due to the convenience and good temperature control allowing uniform sintering. This is especially important for colloidal inks that require elevated sintering temperatures which can be easily and quickly reached using these instruments. Thermal treatment serves to remove the organic stabilizer or components as they reach their boiling points which is found for both MOD and NP inks. However, it must be noted that multiple sintering/curing steps maybe necessary as crack formation can occur in a single sintering step thereby reducing the overall conductivity.[77] Sudden evaporation can also generate defects such as pores or cracks in the film, therefore a pre-annealing is suggested.[78] However, if high enough temperatures are not reached, the deposited nanoparticles do not melt completely but are instead bridged with another in a liquid state. Because of this behavior, these films exhibit high porosity which results in low conductivity. Often times, the surface topography of the film is highly dependent on the evaporation conditions. Although this standard has been typically used for processing, it is incompatible with temperature sensitive substrates which see the same temperatures as the ink thereby limiting substrates to temperature stable substrates. In order to incorporate thermo-sensitive substrates other alternatives must be considered which are discussed below.

3.3.2 | CHEMICAL SINTERING

Regarded as a direct alternative to thermal sintering, chemical sintering is an approach intended for laboratory research as opposed to manufacturing purposes as high throughput is not possible. This technique involves the exposure to or addition of chemicals to deposited ink or direct ink formulation onto the substrate surface which can be achieved at room temperature. Different approaches to chemical sintering are considered in colloidal vs. MOD inks. For colloidal solutions, this chemical reaction causes a destabilization of the metal particles/stabilizer

system by dissolving or detachment to the organic molecules therefore allowing direct access to the particle surface to initiate sintering on the surface. Such examples include the use of reducing agents in a gaseous form such as anhydride, acetic acid, HCl, hydrazine, NaCl, and $MgCl_2$ gases.[15,35,79] Exposure to reducing vapors and agents such as ethylene glycol and ascorbic acid have also been reported to initiate the thermal decomposition of silver MOD inks.[80] Similarly, this effect can be achieved by immersing structures into an alcohol solution such as methanol, ethanol, or isoproponal.[79] For MOD inks, printed metal precursors (metal cations) need to be chemically reduced and converted into a zerovalent metal.[81] This has been carried out in the form of what is called reactive inkjet printing where the reducing chemical reaction occurs directly on the substrate. Abulikemu et al. demonstrated the development of Au NP films using this technique by first printing a mixture of oleylamine and 1,2-dichlorobenzene as the capping and reducing agents respectively followed by a gold(III) chloride trihydrate ($HAuCl_4 \cdot 3H_2O$) precursor onto a substrate.[82] Similarly, Li et al. successfully employed a copper citrate solution and nickel sulfate ($NiSO_4$) as the metal salts and sodium borohydride ($NaBH_4$) as the reducing agent to deposited both Cu and Ni lines onto paper using sequential printing. This quick and effective technique has mostly been demonstrated in the development of metals but can extended to other materials such as polymers to be used as dielectrics. However, it must be noted that etching of the developed film may occur if not precisely controlled.

3.3.3 | LASER SINTERING

Laser sintering allows for direct concentrated energy on small targeted areas at high power densities thus allowing for high spatial resolution.[83] Here, fast localized heating occurs as the wavelength of the irradiation is absorbed directly into the ink. Laser melting occurs when the phonon emission from the light source excites the atoms enough increasing the mobility in the lattice up to or beyond the melting point of the material without increasing its thermal energy.[84] Heating induced by the laser propagates throughout the film allowing the microparticles to form interconnected networks with a good adherence to the substrate making it highly resistant during solvent rinsing as shown in Figure 3.27.To achieve the most efficient energy absorption, the laser wavelength is tuned around the strong absorption peak for metals (400 – 700 nm).[85] To reach this range, a spectrum of lasers can be considered that include gas or solid state lasers such as Ar ion and yttrium aluminium garnet (Nd:YAG) lasers respectively. A high laser power is required in order to promote interparticular grain growth thus resulting in ablation effects. Thus far, laser sintering has mainly been successfully demonstrated with Au or Ag particles as they display high resistance to oxidation. Moreover, it can be used to initiate both the sintering and reduction of nanoparticles, especially in terms of thermally unstable oxides.[86] The particle surface begins to melt as the lattice temperature approaches the melting point. However, to reach this temperature, it may be necessary to expose the particles to multiple pulses as it was reported that melting of Cu nanoparticles did not occur until the third pass as residual thermal energy accumulates with

each pass.[87] In doing so, the temperature of the ink must also be regulated to avoid heat dissipation into the substrate past its glass transition temperature making the use of glass substrates more ubiquitous for this technique. If tailored to the ink properly, processing temperatures can reach as low as 150ºC, which is still somewhat limiting for temperature sensitive polymeric substrates.[79] Unfortunately, temperature sensitive substrates limit the resulting conductivity to 20% that of the bulk equivalent compared to 40% on heat resistive substrates such as Si and glass.[79] Recently, an article demonstrated laser sintering of Pt MOD, Ag MOD and ZnO semiconductor precursor inks achieved a minimum feature size of 1 µm lines onto a glass substrate showing that laser sintering was even effective for stacked layers and compatible with different types of inks.[9]

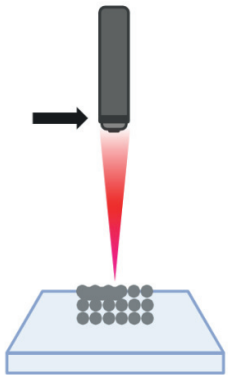

Figure 3.27. Schematic of laser sintering of metal nanoparticles

Sintering such substrates requires the optimization of parameters such as power, wavelength, operation mode, and writing velocity.[79] It is a well-established method for digital fabrication however; resolution is limited to micrometer features due to limitations on heat diffusion and light diffraction.[84] For this reason, an ultrashort pulsed laser is necessary to achieve submicrometer features which can overcome these limitations.[84] The sintering resolution is defined by the laser spot size in the nm to µm range meaning this tool can produce high resolution comparable to inkjet printing and lithography. Writing speeds up to 100 mm/s are possible meaning that this technique is compatible for R2R manufacturing purposes. However, the efficiency of this technique is also a drawback where rastering effects such as increased roughness or an uneven surface can result due to the fast volume reduction and volatilization of the organic matter in the ink. Additionally, high localized temperatures can create effects such as the coffee stain effect. Thus, to avoid these effects, an optimized process which defines in the pulse repetition and writing velocity are necessary.[79] Other parameter such as number of treatment cycles and the overall target material also define the sintering process. High absorbing laser such as green laser showed fast metallization of the ink on its surface leading to the development of a dense skin layer riddled with defects as volatile compounds such as solvents

and stabilizers see fast evaporation thus resulting in poor adhesion to the substrate as the bottom layers were not sintered.[79] However, lasers in the NIR region penetrate through the ink layer down to the substrate/film interface, changing sintering from a bottom to top process resulting in a homogenous and smoother film.

3.3.4 | MICROWAVE SINTERING

Unlike, plasma and laser sintering, microwave sintering is rapid flash technique that provides volumetric heating of structures within seconds to minutes of exposure. This technique is more commonly used for dielectric and conductive materials as well as synthetic chemistry purposes.[79,87] Microwave radiation is only effective in micrometer sized metal particles as absorbance occurs at a greater rate than in its bulk form which is known as the antenna effect.[88] Perelaer et al. studied this effect and found that as the surface area of the electrodes increased, a decrease in resistance was seen due to an improved absorption limited to 30s of microwave exposure. They reported that following microwave flash exposure, most organic material is removed allowing the particles to form large agglomerates. Rapid heating can occur within the first 5 to 40 seconds of initially heating the sample because of rapid interparticle necking and agglomeration as exposed nanoparticles are superheated.[79] This means that the sintering time is 20 times less than conventional heating methods while achieving the same conductivities.[89] Even, selective sintering is possible through microwave radiation of conductive particles which readily absorb these waves while the polymeric substrates below absorb a negligible amount of energy making this technique perfect for temperature sensitive polymer substrates.

However, microwave sintering is complicated and is not a very well understood technique. Its function is believed to be based on Maxwell-Wagner polarization resulting from “the accumulation of charge at the material interface, electric conduction, and eddy currents”.[79] In order for this treatment to be successful, the dimension of the object perpendicular to the plane of incidence of the waves must be on the same order as the penetration depth.[79] Additionally, during the operation, multiple hot spots can appear uncontrollability making the sintering homogeneity difficult to achieve. Uniform heating can be enhanced by increasing the frequency which results in the loss of penetration depth. In order to shorten the sintering time, antenna structures or silicon substrates acting as a susceptor should be introduced.[88] Thus far, this technique has only been demonstrated in a laboratory setting which means that up-scaling to sinter larger samples is not possible due to issues involving inhomogeneous heating and local overheating.

3.3.5 | PLASMA SINTERING

Plasma, also known as the 4th state of matter, is generated when enough energy is applied to ionized gas species. Figure 3.28a displays the system where plasma is generated when a carrier gas in introduced between to charge plates (stainless steel electrodes) exciting the input gas particles by high frequency. The particles collide knocking out electrons from the outer electron shells surrounding the atoms that creates free electron and positively charged ions (Figure 3.28b).[90] The dielectric layer prevents arc transition and facilitates plasma generation at non-equilibrium conditions.[91] Depending on the gas used, the plasma can have an inert (noble gases or N_2), oxidizing (O_2), or reducing effect (H_2).[79] A wide range of films spanning from organic to inorganic films with a few nm to 10s of µm thickness can be achieved.[91]

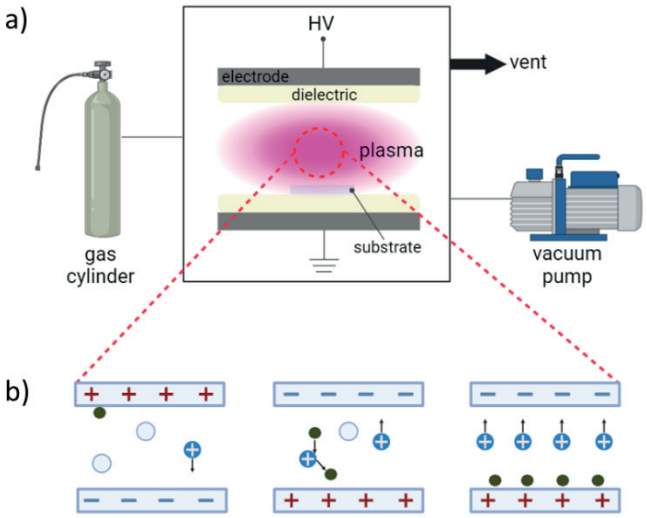

Figure 3.28. Parallel plate plasma system a) schematic overview of the equipment setup and components and b) how plasma is generated. This figure was adapted and combined from references[90,91].

In particular, this tool is indispensable for thin film development from the dry synthesis of metal nanoparticles for inks, surface modification of substrates (cleaning and/or improving adhesion), and sintering of deposited layers to developing conductive structures, all while observing little to no heating of the substrate.[80,91,92] Plasma generates excited species such as ions, radical, and UV irradiation, all of which play a role in the decomposition of stabilizing agents in inks, allowing direct contact between metal particles that form a dense network of conducting material by densification and grain boundary diffusion.[93] Depending on the type of ink, plasma sintering is utilized in two different ways: as a vehicle to decompose and remove any organic stabilizers in the case of NP inks or as a technique to reduce of ionic metals to its metallic form in the case of MOD inks. In the former, low pressure plasma treatment allows for

the use of temperature sensitive substrates to be processed at low operating temperatures. Here, both Ar and O_2 gases have been shown to increase the conductivity of printed structures.[80,81] For the latter case, both inert and reductive plasmas have been shown to convert metal salt ink precursors to their conductive zerovalent form.[81]

However, it must be noted that this technique is a top-down approach where only the top layers are exposed while the bottom layers require significantly more time. This phenomenon is known as the skin effect and means that only a few 100 nm layers can be processed at a time. Here, the outcome is highly dependent on the power and flow rate of gas applied. Increasing the plasma power increases incident ion energy and flux which translates into deeper ion penetration and enhanced volatility of the non-metallic species.[80] This effectively leads to thicker and denser layers that in turn reduces the ion penetration depth and hinders the release of volatile species from the bulk.[79] Due to this, it was shown that processing times of 30 minutes or more are necessary to fully sinter printed patterns.[81] Therefore, this technique can suffer from long processing times which is highly dependent on the stability of the precursor ink.[94] Detrimental effects of prolonged exposure can lead to oxidation thus reducing the conductivity or overall etching of the material. For commonly used polymeric substrates such as PI, PET, and PMMA, etching rates of 0.087, 0.32, 0.26 μm/hr respectively must be taken into account.[95] Extended use can also lead to substrate heating where a maximum temperature of 77 and 138ºC was found for plasma powers of 150 and 300W respectively, the latter of which can exceed the glass transition temperature of many polymeric substrates.[81] Additionally, plasma sintering is only effective under targeted ink formulation taking both the particle size and stabilizer used into account as well as the dimensions of the pattern. For this reason, this technique cannot be used in scaled-up manufacturing processes due to the lack of compatible equipment for R2R applications and long processing times.

3.3.6 | INTENSE PULSED LIGHT SINTERING (PHOTONIC CURING)

Intense pulsed light sintering (IPL) also commercially known as photonic curing is a rapid sintering technique capable of sintering any target material within a few μs to several ms. This is achieved using a Xenon stroboscope lamp that can generate radiation in a range from 200 – 1200 nm.[79] As the light hits the surface, a fair amount of radiation is reflected from the surface of the sample while the rest is absorbed and dissipated as heat as shown in Figure 3.29 below. The chosen wavelength is often completely transparent to the substrate materials causing localized heating of the deposited ink making this technique ideal for temperature sensitive substrates. In terms of colloidal inks, non-conductive nanoparticles are locally heated which help to eliminate the any organics or additives surround the particles and initiate sintering between the particles forming a conductive film. This then allows for neck formation and grain growth of the adjacent

particles. In general, this technique is highly dependent on the spectral absorption and reflection of the materials for example metals respond to the UV visible and IR regions as well as light sensitive polymers.[79] As opposed to laser sintering, IPL sintering is an energy efficient technology where 30% of the input electrical power is converted to radiation, a magnitude greater than that of a laser.[79] This technique provides high-throughput processing for large area fabrication even for materials with sensitives to oxidation. Additionally, processing speeds of up to 10 m/min have been reported meaning this technique can be applicable for R2R equipment.[79,96]

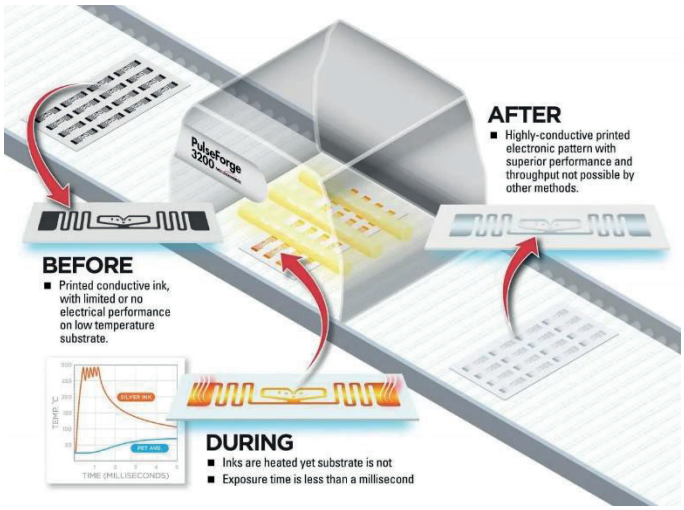

Figure 3.29. Schematic representation of PulseForge photonic curing system acquired from Novacentrix[97]

Optimization of this process relies on many factors such as operational parameters and material properties of the substate and ink. The former includes parameters such as energy (intensity of the lamp), number of pulses, and pulse length in order to find the correct recipe.[85] Homogenous sintering throughout the layer must be optimized where the entire ink volume sees high peak temperatures.[79] Essentially this can be done by making sure that the pulse length is greater than the time the ink/substrate reaches thermal equilibrium.[79] This requires temperature distribution control which can be calculated using parameters such as pulse duration, pulse shape, intensity, and frequency. As the pulse energy increases, larger grains (and thus higher roughness) and higher conductivities result due to faster sintering.[79] Smoother morphologies can be achieved if using a greater number of shorter pulses reducing the chances for excessive vaporization or interruptions in the conductive network formed.[98] However, at the same time, the deposited layer tends to shrink due to solvent evaporation and stabilizer removal meaning heat conduction can occur faster. If both high energy density and high flashing frequency is applied, the sample will experience overheating and damage. High intensities may cause the formation of explosive decomposition gases resulting in highly porous layers.[79] Therefore, in order to avoid

this effect, increasing the number of pulses prevented the sample from damage and allowed the sample to reach its final conductivity. If it is radiated multiple times, it is best to cool the substrate to room temperature.[99] As reported by Schroder et al., the optimal irradiation period is 20 μs – 10 ms as sintering would not be successful if shorter than 5 μs but if longer than 1 second would result in photo degradation and heat deterioration. For multiple passes, the optimal irradiation interval is 2000 μs – 2 s with a wavelength between 200 – 300 nm is preferable.[100]

In terms of ink and substrate material properties, optimization is dependent on evaporation enthalpies of the solvents and thermal stability of organic components in the ink, temperature sensitivity of the substrate, and the sintering properties of the materials used to formulate the ink. Requirements for the success of this technique includes that the film thickness must be considerably thinner than the substrate thickness.[99] Although the substrate itself will not be affected as much as the film above, heat will still accumulate on top meaning that a substantial enough substrate should be used to in order to compensate for this. If too much energy is applied, it can result in shattering the substrate below. Other such failure modes such as clean film ablation, delamination, and substrate warpage can result. [85,99] Such a wide range of adjustable factors means that with every ink/substrate combination requires individualized optimization which may be time consuming and tedious as compared to the previously mentioned sintering techniques.

A wide range of films can be developed using this method from metal and semiconductor nanoparticles ink to dielectric nanoparticles.[101] For the purposes of this thesis, photonic curing of metal nanoparticles will be discussed. The most widely studied material are Ag nanoparticle inks on temperature sensitive substrates[102] including Cronin et al. whom reported that microsized Ag flake ink deposited onto a PET substrate reportedly saw interparticle necking between the flakes achieving an average conductivity of 60 μΩ·cm, 40% less than those treated with thermal sintering.[103] Garlapati et al. demonstrated the use of UV-photonic curing to achieve curing of indium oxide (In_2O_3) semiconductor nanoparticle ink through ligand removal.[104] Even 2D material synthesis of a transition metal dichalcogenides (TMDCs) was reported by Kim et al. where localized heating of the film induced crystallization from amorphous MoS_2 to polycrytalline 2H-MoS_2 films.[105] Additionally, this technique has not only been shown to help sinter nanoparticles but can also assist in the reduction of metal oxides to its elemental form.[27] Kang et al. showed the potential in this technique to reduce inkjet printed or spray coated CuO to conductive Cu.[27,85] They successfully achieved a low resistivity of 55.4 nΩm (or 30% of bulk Cu). It was proposed that the reduction of the CuO shell to Cu occurs due to reactive sintering where the photoactive polymers in the ink act like reductants or alcohol due to the IPL process.[85] Under SEM analysis, grain size increases proportionally with increasing irradiation energy, showing more agglomerated NPs and better conductive network through neck formation with small pore sizes.

3.3.7 | COMPARING AND COMBINING SINTERING METHODS

The resulting film may vary wildly depending on the chosen sintering technique affecting not only the film morphology but also its electrical properties. Figure 3.30 below displays both Ag and Cu MOD inks treated by thermal, microwave, and plasma sintering techniques. Here, thermal sintering serves to decompose MOD inks into stacked Ag NPs leaving a highly porous film with high roughness as result (Figure 3.30a). The NPs appear to be isolated from another seeing at most point contacts between NPs. In contrast, application of more advanced sintering techniques such as microwave and plasma (Figure 3.30b and 3.30c) sintering both exhibit necking to complete coalescence between nanoparticles. Because of this, the resulting film has reduced surface roughness albeit accompanied by voids in the film. Ultimately this discontinuity in the film affects the conductivity of the film which can be further enhanced when combining sintering techniques together.

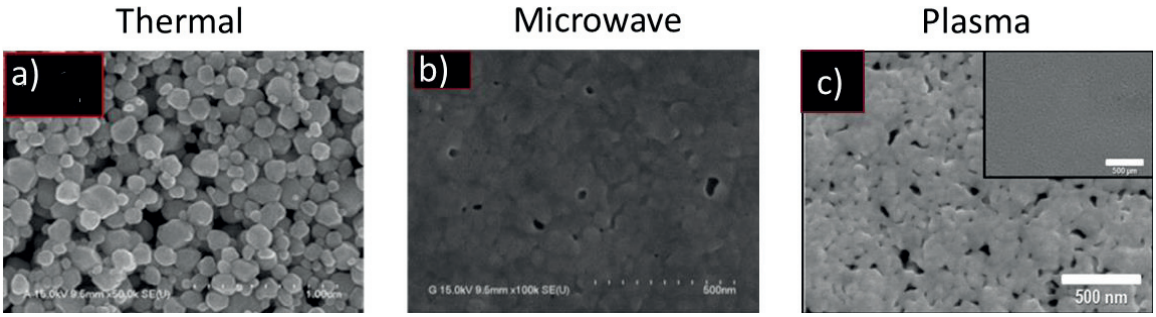

Figure 3.30. The resulting NP film heated annealed by a) thermal[106], b) microwave[106] of Ag MOD ink, and c) plasma sintering[107] of Cu precursor ink

If certain techniques are not effective on their own, different techniques can be combined together fulfilling different roles in the sintering process therefore that effectively reduce the overall sintering time. Perelaer et al. demonstrated the use of plasma and microwave sintering together in order to improve the conductivity.[108] The use of plasma gave the printed features low conductivity which plateaued in effectiveness and presented the film as a continuous but porous layer while microwave sintering allowed for better conductivities reaching up to 60% that of bulk Ag. Additionally, microwave sintering can be combined with IPL in order to shorten the sintering time necessary where both drying and sintering occur at the same time.[109] The skin depth, defined as the distance where the incident power is reduced to half of its initial value. In terms of microwaves with a frequency of 2.45 GHz can penetrate metals with a skin depth of 2 μm which for Ag and Cu is 1.3 and 1.6 μm respectively.[79,87] This small penetration depth is due to the high conductivity of metals. Here they used photonic curing as the thermal heating step to significantly reduce the sintering time for the following step and microwave for the sintering.

This combination resulted in highly conductive silver films where they achieved a conductivity up to 40% of bulk silver which was sintered within 15 seconds. Other combinations such as low-pressure Ar plasma treatment combined with microwave sintering has also been reported achieving conductivities up to 60% for bulk silver.[108] Additionally, Cronin et al. compared the separate and combined abilities of both thermal and photonic curing together where just thermal treatment saw 1000 μΩ·cm, just photonic saw 150 μΩ·cm, and together saw 100 μΩ·cm for conductive silver flake films albeit with superior yield of 100% for the latter combination. Lastly, although not formally communicated in this thesis, experimental work with a commercial Au nanoparticle ink for inkjet printing was subjected to both thermal and plasma sintering thereby reducing the initial resistance value by at least 90% for all deposited films. This is believed to occur as the thermal sintering serves to remove the organic solvents while plasma sintering helps to develop percolating network of nanoparticles.

3.4 | REFERENCES

1. Shen C, Tran PP, Minh Ly PT. Chemical Waste Management in the U.S. Semiconductor Industry. *Sustainability*. 2018;10(5). doi:10.3390/su10051545

2. Gerard M. Pollution prevention opportunity. Assessment for microfab and sifab facilities at Sandia National Laboratories. 2011;(December):1-37.

3. Tan HW, An J, Chua CK, Tran T. Metallic Nanoparticle Inks for 3D Printing of Electronics. *Adv Electron Mater*. 2019;5(5). doi:10.1002/aelm.201800831

4. Nayak L, Mohanty S, Nayak SK, Ramadoss A. A review on inkjet printing of nanoparticle inks for flexible electronics. *J Mater Chem C*. 2019;7(29):8771-8795. doi:10.1039/c9tc01630a

5. Yang, Zhihao (NanoMas Technologies I. Nanoparticle Inks for Printed Electronics. http://www.nanoparticles.org/pdf/YangZ.pdf. Published 2007.

6. Kim J, Imani S, De WR, et al. Wearable salivary uric acid mouthguard biosensor with integrated wireless electronics. *Biosens Bioelectron*. 2015. doi:10.1016/j.bios.2015.07.039

7. Shou W, Mahajan BK, Ludwig B, et al. Low-Cost Manufacturing of Bioresorbable Conductors by Evaporation–Condensation-Mediated Laser Printing and Sintering of Zn Nanoparticles. *Adv Mater*. 2017;29(26):1-7. doi:10.1002/adma.201700172

8. Molina-Lopez F, Briand D, de Rooij NF. All additive inkjet printed humidity sensors on plastic substrate. *Sensors Actuators B Chem*. 2012;166-167:212-222. doi:https://doi.org/10.1016/j.snb.2012.02.042

9. Yang L, Hu H, Scholz A, et al. Laser printed microelectronics. *Nat Commun*. 2023;14(1):1103. doi:10.1038/s41467-023-36722-7

10. Zhao C, Zhang J, Wang ZL, Ren K. A Poly(l -Lactic Acid) Polymer-Based Thermally Stable Cantilever for Vibration Energy Harvesting Applications . *Adv Sustain Syst*. 2017;1(9):1700068. doi:10.1002/adsu.201700068

11. Wan H, Cao Y, Lo L-W, Xu Z, Sepúlveda N, Wang C. Screen-printed soft triboelectric nanogenerator with porous PDMS and stretchable PEDOT:PSS electrode. *J Semicond*. 2019;40(11):112601. doi:10.1088/1674-4926/40/11/112601

12. Zhang C, Zhang L, Bao B, et al. Customizing Triboelectric Nanogenerator on Everyday Clothes by Screen-Printing Technology for Biomechanical Energy Harvesting and Human-Interactive Applications. *Adv Mater Technol*. 2023;8(4):2201138. doi:https://doi.org/10.1002/admt.202201138

13. Molina-Lopez F, Gao TZ, Kraft U, et al. Inkjet-printed stretchable and low voltage synaptic transistor array. *Nat Commun*. 2019;10(1):1-10. doi:10.1038/s41467-019-10569-3

14. Feng S, Cao S, Tian Z, Zhu H, Kong D. Maskless Patterning of Biodegradable Conductors by Selective Laser Sintering of Microparticle Inks and Its Application in Flexible Transient Electronics. *ACS Appl Mater Interfaces*. 2019;11(49):45844-45852. doi:10.1021/acsami.9b14431

15. Li J, Xu H, Zhang Z, Hao Y, Wang H, Huang X. Anhydride-Assisted Spontaneous Room Temperature Sintering of Printed Bioresorbable Electronics. *Adv Funct Mater*. 2019;1905024:1905024. doi:10.1002/adfm.201905024

16. Huang X, Liu Y, Hwang SW, et al. Biodegradable materials for multilayer transient printed circuit boards. *Adv Mater*. 2014;26(43):7371-7377. doi:10.1002/adma.201403164

17. Tao H, Brenckle MA, Yang M, et al. Silk-Based Conformal, Adhesive, Edible Food Sensors. *Adv Mater*. 2012;24(8):1067-1072. doi:10.1002/adma.201103814

18. Wang X, Xu W, Chatterjee P, et al. Food-Materials-Based Edible Supercapacitors. *Adv Mater Technol*. 2016;1(3):1-7. doi:10.1002/admt.201600059

19. Boutry CM, Beker L, Kaizawa Y, et al. Biodegradable and flexible arterial-pulse sensor for the wireless monitoring of blood flow. *Nat Biomed Eng*. 2019;3(1):47-57. doi:10.1038/s41551-018-0336-5

20. Campana A, Cramer T, Simon DT, Berggren M, Biscarini F. Electrocardiographic Recording with Conformable Organic Electrochemical Transistor Fabricated on Resorbable Bioscaffold. *Adv Mater*. 2014;26(23):3874-3878. doi:10.1002/adma.201400263

21. Boutry CM, Kaizawa Y, Schroeder BC, et al. A stretchable and biodegradable strain and pressure sensor for orthopaedic application. *Nat Electron*. 2018;1(5):314-321. doi:10.1038/s41928-018-0071-7

22. Koo J, MacEwan MR, Kang SK, et al. Wireless bioresorbable electronic system enables sustained nonpharmacological neuroregenerative therapy. *Nat Med*. 2018;24(12):1830-1836. doi:10.1038/s41591-018-0196-2

23. Solution Coating Methods | Comparison of Techniques | Ossila. https://www.ossila.com/en-eu/pages/solution-processing-techniques-comparison. Accessed June 17, 2023.

24. Spin Coating: Complete Guide to Theory and Techniques | Ossila. https://www.ossila.com/en-eu/pages/spin-coating. Accessed June 17, 2023.

25. Teichler A, Perelaer J, Schubert US. Inkjet printing of organic electronics-comparison of deposition techniques and state-of-the-art developments. *J Mater Chem C*. 2013;1(10):1910-1925. doi:10.1039/c2tc00255h

26. Norrman K, Ghanbari-Siahkali A, Larsen NB. 6 Studies of spin-coated polymer films. *Annu Rep Prog Chem{,} Sect C Phys Chem*. 2005;101(0):174-201. doi:10.1039/B408857N

27. Paglia F, Vak D, Van Embden J, et al. Photonic Sintering of Copper through the Controlled Reduction of Printed CuO Nanocrystals. *ACS Appl Mater Interfaces*. 2015;7(45):25473-25478. doi:10.1021/acsami.5b08430

28. Meitl MA, Zhu ZT, Kumar V, et al. Transfer printing by kinetic control of adhesion to an elastomeric stamp. *Nat Mater*. 2006;5(1):33-38. doi:10.1038/nmat1532

29. Lee S, Koo J, Kang SK, et al. Metal microparticle – Polymer composites as printable, bio/ecoresorbable conductive inks. *Mater Today*. 2018;21(3):207-215. doi:10.1016/j.mattod.2017.12.005

30. Kim J, Kumar R, Bandodkar AJ, Wang J. Advanced Materials for Printed Wearable Electrochemical Devices: A Review. *Adv Electron Mater*. 2017;3(1):1-15. doi:10.1002/aelm.201600260

31. Zavanelli N, Kim J, Yeo WH. Recent advances in high-throughput nanomaterial manufacturing for hybrid flexible bioelectronics. *Materials (Basel)*. 2021;14(11):1-35. doi:10.3390/ma14112973

32. Potts S-J, Phillips C, Jewell E, Clifford B, Lau YC, Claypole T. High-speed imaging the effect of snap-off distance and squeegee speed on the ink transfer mechanism of screen-printed carbon pastes. *J Coatings Technol Res*. 2020;17(2):447-459. doi:10.1007/s11998-019-00291-6

33. Philip B, Jewell E, Greenwood P, Weirman C. Material and process optimization screen printing carbon graphite pastes for mass production of heating elements. *J Manuf Process*. 2016;22:185-191. doi:10.1016/J.JMAPRO.2016.03.001

34. Gordon SE, Dorfman JR, Kirk D, Adams K. Advances in Conductive Inks across Multiple Applications and Deposition Platforms.

35. Lee YK, Kim J, Kim Y, Kwak JW, Yoon Y, Rogers JA. Room Temperature Electrochemical Sintering of Zn Microparticles and Its Use in Printable Conducting Inks for Bioresorbable Electronics. *Adv Mater*. 2017;29(38):1-8. doi:10.1002/adma.201702665

36. Varghese J, Surendran KP, Sebastian MT. Room temperature curable silica ink. *RSC Adv*. 2014;4(88):47701-47707. doi:10.1039/c4ra06479h

37. Hyun WJ, Lim S, Ahn BY, Lewis JA, Frisbie CD, Francis LF. Screen Printing of Highly Loaded Silver Inks on Plastic Substrates Using Silicon Stencils. *ACS Appl Mater Interfaces*. 2015;7(23):12619-12624. doi:10.1021/ACSAMI.5B02487/SUPPL_FILE/AM5B02487_SI_001.PDF

38. Parashkov R, Becker E, Riedl T, Johannes HH, Kowalsky W. Large area electronics using printing methods. *Proc IEEE*. 2005;93(7):1321-1329. doi:10.1109/JPROC.2005.850304

39. Demonstrator machine for high-throughput solar cell metallization – pv magazine International. https://www.pv-magazine.com/2022/03/18/demonstrator-machine-for-high-throughput-solar-cell-metallization/. Accessed June 17, 2023.

40. Park JU, Hardy M, Kang SJ, et al. High-resolution electrohydrodynamic jet printing. *Nat Mater*. 2007;6(10):782-789. doi:10.1038/nmat1974

41. Disintegration of water drops in an electric field. *Proc R Soc London Ser A Math Phys Sci*. 1964;280(1382):383-397. doi:10.1098/rspa.1964.0151

42. Nath SD, Son S, Sadiasa A, Min YK, Lee BT. Preparation and characterization of PLGA microspheres by the electrospraying method for delivering simvastatin for bone regeneration. *Int J Pharm*. 2013;443(1-2):87-94. doi:10.1016/j.ijpharm.2012.12.037

43. Guarino V, Khodir WKWA, Ambrosio L. Biodegradable microparticles and nanoparticles by electrospraying techniques. *J Appl Biomater Funct Mater*. 2012;10(3):191-196. doi:10.5301/JABFM.2012.10369

44. Wu Y, Kennedy SJ, Clark RL. Polymeric particle formation through electrospraying at low atmospheric pressure. *J Biomed Mater Res Part B Appl Biomater*. 2008;90B(1):381-387. doi:10.1002/jbm.b.31296

45. Jaworek A, Sobczyk AT. Electrospraying route to nanotechnology: An overview. *J Electrostat*. 2008;66(3-4):197-219. doi:10.1016/j.elstat.2007.10.001

46. Hashimdeen SH, Miodownik M, Edirisinghe MJ. Print head design and control for electrohydrodynamic printing of silk fibroin. *Mater Sci Eng C*. 2013;33(6):3309-3318. doi:10.1016/j.msec.2013.04.020

47. Voigt MM, Cuite A, Chung DY, et al. Polymer field-effect transistors fabricated by the sequential gravure printing of polythiophene, two insulator layers, and a metal ink gate. *Adv Funct Mater*. 2010;20(2):239-246. doi:10.1002/adfm.200901597

48. Kang H, Kitsomboonloha R, Jang J, Subramanian V. High-performance printed transistors realized using femtoliter gravure-printed sub-10 μm metallic nanoparticle patterns and highly uniform polymer dielectric and semiconductor layers. *Adv Mater*. 2012;24(22):3065-3069. doi:10.1002/adma.201200924

49. Hübler A, Trnovec B, Zillger T, et al. Printed paper photovoltaic cells. *Adv Energy Mater*. 2011;1(6):1018-1022. doi:10.1002/aenm.201100394

50. Ozbolat IT. Droplet-Based Bioprinting ∗ ∗With contributions by Hemanth Gudupati and Madhuri Dey, The Pennsylvania State University. In: *3D Bioprinting*. Elsevier; 2017:125-163. doi:10.1016/b978-0-12-803010-3.00005-6

51. Singh M, Haverinen HM, Dhagat P, Jabbour GE. Inkjet printing-process and its applications. *Adv Mater*. 2010;22(6):673-685. doi:10.1002/adma.200901141

52. Mattana G, Loi A, Woytasik M, Barbaro M, Noël V, Piro B. Inkjet-Printing: A New Fabrication Technology for Organic Transistors. *Adv Mater Technol*. 2017;2(10):1-27. doi:10.1002/admt.201700063

53. Pesach D, Marmur A. Marangoni effects in the spreading of liquid mixtures on a solid. *Langmuir*. 1987;3(4):519-524. doi:10.1021/la00076a013

54. Lim JA, Lee WH, Lee HS, Lee JH, Park YD, Cho K. Self-Organization of Ink-jet-Printed Triisopropylsilylethynyl Pentacene via Evaporation-Induced Flows in a Drying Droplet. *Adv Funct Mater*. 2008;18(2):229-234. doi:https://doi.org/10.1002/adfm.200700859

55. Perelaer J, Smith PJ, van den Bosch E, van Grootel SSC, Ketelaars PHJM, Schubert US. The Spreading of Inkjet-Printed Droplets with Varying Polymer Molar Mass on a Dry Solid Substrate. *Macromol Chem Phys*. 2009;210(6):495-502. doi:https://doi.org/10.1002/macp.200800569

56. Lohse D. Fundamental Fluid Dynamics Challenges in Inkjet Printing. *Annu Rev Fluid Mech*. 2021;54:349-382. doi:10.1146/annurev-fluid-022321-114001

57. Printed Electronics Laboratory | IMB CNM. https://www.imb-cnm.csic.es/en/laboratories/printed-electronics-laboratory. Accessed June 6, 2023.

58. Fujifilm. Dimatix Materials Cartridge. Fujifilm Products. http://www.fujifilmusa.com/products/industrial_inkjet_printheads/deposition-products/materials-cartridge/index.html. Published 2017.

59. FUJIFILM. FUJIFILM Dimatix Ink Tutorial, waveform. 2008:6. https://www.cnfusers.cornell.edu/sites/default/files/Equipment-Resources/Ink formulation tutorial.pdf.

60. Sadie J. Three-Dimensional Inkjet-Printed Metal Nanoparticles: Ink and Application Development. 2017. http://www2.eecs.berkeley.edu/Pubs/TechRpts/2017/EECS-2017-168.html.

61. Fujifilm. FUJIFILM Dimatix Materials Printer User Manual. 2010.

62. Jang D, Kim D, Moon J. Influence of Fluid Physical Properties on Ink-Jet Printability. *Langmuir*. 2009;25(5):2629-2635. doi:10.1021/la900059m

63. Jung S, Hoath SD, Martin GD, Hutchings IM. Inkjet Printing Process for Large Area Electronics. In: *Large Area and Flexible Electronics*. ; 2015:315-344. doi:https://doi.org/10.1002/9783527679973.ch11

64. Rioboo R, Tropea C. OUTCOMES FROM A DROP IMPACT ON SOLID SURFACES. *At Sprays*. 2001;11(2):155-165. doi:10.1615/AtomizSpr.v11.i2.40

65. Wasan DT, Nikolov AD, Brenner H. Droplets Speeding on Surfaces. *Science (80-)*. 2001;291(5504):605-606. doi:10.1126/science.1058466

66. Edwards DA, Brenner H, Wasan DT. CHAPTER 5 - Interfacial Transport of Species. In: Edwards DA, Brenner H, Wasan DT, eds. *Interfacial Transport Processes and Rheology*. Boston: Butterworth-Heinemann; 1991:160-190. doi:https://doi.org/10.1016/B978-0-7506-9185-7.50009-X

67. Giannakou P. Printed Transition Metal Oxide Electrochemical Capacitors for Energy Harvesting Applications. 2021. doi:10.15126/thesis.900042

68. Moya, A., Sowade, E., del Campo, F. J., Mitra, K. Y., Ramon, E., Villa, R., ... & Gabriel, G. (2016). All-inkjet-printed dissolved oxygen sensors on flexible plastic substrates. Organic Electronics, 39, 168-176.

69. Krčmář P. Fully inkjet printed gas and humidity CuO sensor on flexible polymer substrate. 2019.

70. Hu H, Larson RG. Marangoni effect reverses coffee-ring depositions. *J Phys Chem B*. 2006;110(14):7090-7094. doi:10.1021/JP0609232/SUPPL_FILE/JP0609232SI20060213_090622.AVI

71. Majumder M, Rendall CS, Eukel JA, et al. Overcoming the “coffee-stain” effect by compositional marangoni-flow-assisted drop-drying. *J Phys Chem B*. 2012;116(22):6536-6542. doi:10.1021/jp3009628

72. Eslamian M. Inorganic and Organic Solution-Processed Thin Film Devices. *Nano-Micro Lett*. 2017;9(1):1-23. doi:10.1007/s40820-016-0106-4

73. Taylor SL, Jakus AE, Shah RN, Dunand DC. Iron and Nickel Cellular Structures by Sintering of 3D-Printed Oxide or Metallic Particle Inks. *Adv Eng Mater*. 2017;19(11):1-8. doi:10.1002/adem.201600365

74. Kim J, Kumar R, Bandodkar AJ, Wang J. Advanced Materials for Printed Wearable Electrochemical Devices: A Review. *Adv Electron Mater*. 2017;3(1):1-15. doi:10.1002/aelm.201600260

75. Shen A, Caldwell D, Ma AWK, Dardona S. Direct write fabrication of high-density parallel silver interconnects. *Addit Manuf*. 2018;22:343-350. doi:10.1016/J.ADDMA.2018.05.010

76. Kuscer D, Shen JZ. Advanced Direct Forming Processes for the Future. In: *Advanced Ceramics for Dentistry*. Elsevier Inc.; 2014:375-390. doi:10.1016/B978-0-12-394619-5.00023-7

77. Moya A, Sowade E, del Campo FJ, et al. All-inkjet-printed dissolved oxygen sensors on flexible plastic substrates. *Org Electron physics, Mater Appl*. 2016. doi:10.1016/j.orgel.2016.10.002

78. Jeong Y, Pearson C, Kim HG, et al. Optimization of a Solution-Processed SiO2 Gate Insulator by Plasma Treatment for Zinc Oxide Thin Film Transistors. *ACS Appl Mater Interfaces*. 2016;8(3):2061-2070. doi:10.1021/acsami.5b10520

79. Wünscher S, Abbel R, Perelaer J, Schubert US. Progress of alternative sintering approaches of inkjet-printed metal inks and their application for manufacturing of flexible electronic devices. *J Mater Chem C*. 2014;2(48):10232-10261. doi:10.1039/c4tc01820f

80. Bromberg V, Ma S, Egitto FD, Singler TJ. Highly conductive lines by plasma-induced conversion of inkjet-printed silver nitrate traces. *J Mater Chem C*. 2013;1(41):6842-6849. doi:10.1039/c3tc31361a

81. Sui Y, Dai Y, Liu CC, Sankaran RM, Zorman CA. A New Class of Low-Temperature Plasma-Activated, Inorganic Salt-Based Particle-Free Inks for Inkjet Printing Metals. *Adv Mater Technol*. 2019;4(8):1900119. doi:10.1002/admt.201900119

82. Abulikemu M, Da’as EH, Haverinen H, Cha D, Malik MA, Jabbour GE. In Situ Synthesis of Self-Assembled Gold Nanoparticles on Glass or Silicon Substrates through Reactive Inkjet Printing. *Angew Chemie Int Ed*. 2014;53(2):420-423. doi:10.1002/anie.201308429

83. Theodorakos I, Zacharatos F, Geremia R, Karnakis D, Zergioti I. Selective laser sintering of Ag nanoparticles ink for applications in flexible electronics. *Appl Surf Sci*. 2015;336:157-162. doi:10.1016/J.APSUSC.2014.10.120

84. Son Y, Yeo J, Moon H, et al. Nanoscale Electronics: Digital Fabrication by Direct Femtosecond Laser Processing of Metal Nanoparticles. *Adv Mater*. 2011;23(28):3176-3181. doi:10.1002/adma.201100717

85. Kang H, Sowade E, Baumann RR. Direct Intense Pulsed Light Sintering of Inkjet-Printed Copper Oxide Layers within Six Milliseconds. *ACS Appl Mater Interfaces*. 2014;6(3):1682-1687. doi:10.1021/am404581b

86. Petritz A, Wolfberger A, Fian A, et al. Cellulose as biodegradable high-k dielectric layer in organic complementary inverters. *Appl Phys Lett*. 2013;103(15). doi:10.1063/1.4824701

87. Perelaer J, De Gans BJ, Schubert US. Ink-jet printing and microwave sintering of conductive silver tracks. *Adv Mater*. 2006;18(16):2101-2104. doi:10.1002/adma.200502422

88. Perelaer J, Klokkenburg M, Hendriks CE, Schubert US. Microwave flash sintering of inkjet-printed silver tracks on polymer substrates. *Adv Mater*. 2009;21(47):4830-4834. doi:10.1002/adma.200901081

89. Choi Y, Seong K dong, Piao Y. Metal−Organic Decomposition Ink for Printed Electronics. *Adv Mater Interfaces*. 2019;6(20):1-14. doi:10.1002/admi.201901002

90. Halbleiter.org. Plasma, the fourth aggregation state of a material - Deposition - Semiconductor Technology from A to Z. https://www.halbleiter.org/en/deposition/plasma/. Accessed June 15, 2023.

91. Uricchio A, Fanelli F. Low-temperature atmospheric pressure plasma processes for the deposition of nanocomposite coatings. *Processes*. 2021;9(11). doi:10.3390/pr9112069

92. Mangolini L, Kortshagen U. Plasma-assisted synthesis of silicon nanocrystal inks. *Adv Mater*. 2007;19(18):2513-2519. doi:10.1002/adma.200700595

93. Raut NC, Al-Shamery K. Inkjet printing metals on flexible materials for plastic and paper electronics. *J Mater Chem C*. 2018;6(7):1618-1641. doi:10.1039/c7tc04804a

94. Wolf FM, Perelaer J, Stumpf S, Bollen D, Kriebel F, Schubert US. Rapid low-pressure plasma sintering of inkjet-printed silver nanoparticles for RFID antennas. *J Mater Res*. 2013;28(9):1254-1261. doi:10.1557/jmr.2013.73

95. Wünscher S, Stumpf S, Teichler A, et al. Localized atmospheric plasma sintering of inkjet printed silver nanoparticles. *J Mater Chem*. 2012;22(47):24569-24576. doi:10.1039/c2jm35586h

96. Daunis TB, Schroder KA, Hsu JWP. Photonic curing of solution-deposited ZrO2 dielectric on PEN: a path towards high-throughput processing of oxide electronics. *npj Flex Electron 2020 41*. 2020;4(1):1-7. doi:10.1038/s41528-020-0070-4

97. PulseForge – NTV USA, LLC – Innovative Technology Solutions. https://ntvusa.biz/pulseforge/. Accessed June 18, 2023.

98. Han WS, Hong JM, Kim HS, Song YW. Multi-pulsed white light sintering of printed Cu nanoinks. *Nanotechnology*. 2011;22(39):395705. doi:10.1088/0957-4484/22/39/395705

99. Schroder KA. Mechanisms of photonic curing???: Processing high temperature films on low temperature substrates. *Tech Proc 2011 NSTI Nanotechnol Conf Expo, NSTI-Nanotech 2011*. 2011;2:220-223.

100. US9631283B2 - Substrate for printed electronics and photonic curing process - Google Patents. https://patents.google.com/patent/US9631283B2/en?oq=9%2C631.283. Accessed November 28, 2019.

101. West J, Carter M, Smith S, Sears J. Photonic Curing of silver nanoparticle based inks. *Nanotechnol 2010 Electron Devices, Fabr MEMS, Fluid Comput - Tech Proc 2010 NSTI Nanotechnol Conf Expo, NSTI-Nanotech 2010*. 2010;2(October 2015):210-213.

102. Mattana G, Briand D, Marette A, Vásquez Quintero A, De Rooij NF. Polylactic acid as a biodegradable material for all-solution-processed organic electronic devices. *Org Electron physics, Mater Appl*. 2015;17:77-86. doi:10.1016/j.orgel.2014.11.010

103. Cronin HM, Stoeva Z, Brown M, Shkunov M, Silva SRP. Photonic Curing of Low-Cost Aqueous Silver Flake Inks for Printed Conductors with Increased Yield. *ACS Appl Mater Interfaces*. 2018;10(25):21398-21410. doi:10.1021/acsami.8b04157

104. Garlapati SK, Gebauer JS, Dehm S, et al. Room-Temperature Processing of Printed Oxide FETs Using Ultraviolet Photonic Curing. *Adv Electron Mater*. 2017;3(9):1-6. doi:10.1002/aelm.201600476

105. Kim RH, Leem J, Muratore C, et al. Photonic crystallization of two-dimensional MoS 2 for stretchable photodetectors . *Nanoscale*. 2019;11(28):13260-13268. doi:10.1039/c9nr02173f

106. Vaseem M, Lee SK, Kim JG, Hahn YB. Silver-ethanolamine-formate complex based transparent and stable ink: Electrical assessment with microwave plasma vs thermal sintering. *Chem Eng J*. 2016;306:796-805. doi:10.1016/j.cej.2016.08.003

107. Kwon YT, Lee YI, Kim S, Lee KJ, Choa YH. Full densification of inkjet-printed copper conductive tracks on a flexible substrate utilizing a hydrogen plasma sintering. *Appl Surf Sci*. 2017;396:1239-1244. doi:10.1016/j.apsusc.2016.11.122

108. Perelaer J, Jani R, Grouchko M, Kamyshny A, Magdassi S, Schubert US. Plasma and microwave flash sintering of a tailored silver nanoparticle ink, yielding 60% bulk conductivity on cost-effective polymer foils. *Adv Mater*. 2012;24(29):3993-3998. doi:10.1002/adma.201200899

109. Perelaer J, Abbel R, Wünscher S, Jani R, Van Lammeren T, Schubert US. Roll-to-roll compatible sintering of inkjet printed features by photonic and microwave exposure: From non-conductive ink to 40% bulk silver conductivity in less than 15 seconds. *Adv Mater*. 2012;24(19):2620-2625. doi:10.1002/adma.201104417

4

Substrate Investigation

As the substrate accounts for 90% of any electronic component, one of the easiest ways to improve sustainability is by replacing the substrate with a biodegradable alternative. However, unlike conventional polymer substrates, biodegradable substrates are known to have low glass transition temperatures making them notoriously difficult to integrate with printed electronics and sintering techniques. For this reason, substrate selection must be carefully considered with respect to each of these limitations as it will affect the overall electrical properties of the thin film deposited above.

4.1 | SUBSTRATE REQUIREMENTS AND SELECTION PROCESS

A wide range of biodegradable materials were considered for the substrate selection including a large variety of natural and synthetic polymers, cellulose-based papers amongst others. Each substrate and their respective glass transition temperature (T_g) was tabulated below in Table 4.1 below. One by one, substrates were eliminated based on strict criteria related to the post treatment of typically deposited inks which require high curing temperatures above 130ºC as indicated in the Legend.

Table 4.1. Select biodegradable substrates and their respective theoretical glass transition temperatures

Type of Material	Substrate	Tg (°C)
Synthetic Polymers	Poly(lactic-co-glycolic acid) (PLGA)	40 - 55
	Polyvinyl alcohol (PVA)	83
	Polylactic acid (PLA)	45 – 65
	Polycaprolactone (PCL)	-65 to -60
	Poly(glycolic acid) (PGA)	40
	Poly(L-lactide) (PLLA)	55 – 65
	Polyhydroxyalkanoates (PHA/PHB/PHV)	Ambient temperature
	Poly(4-hydroxybutyrate) (P4HB)	< 60
	Poly Octanediol-Co-Citrate (POC)	0.29 – 9.96
	Biodegradable hydrogels	< 90
	Poly(trimethylene carbonate) (PTMC)	< 25
	Poly(glycerol sebacate) (PGS)	< 10
Papers	Cellophane (regenerated cellulose)	130
	Biocellulose	57
	Cellulose acetate (CA)	105
	Cellulose nanofibril (CNF)	N/A
	Sodium carboxymethyl cellulose (Na-CMC)	185.65
Natural	Shellac	42.2
	Ecoflex (potato startch)	91
	Chitosan	80 - 120
	Collagen	35
	Silk fibrolin	178
Others	Thin metal foils (Fe, Mo, W, Zn)	N/A
	PDMS	N/A

Legend
< 70°C
< 70 - 130°C
acceptable

Any materials highlighted in red exhibit glass transition temperatures below 70°C are deemed unacceptable for use as this is at least 2 times less than typical sintering temperatures for nanoparticle inks. Those highlighted in yellow indicate slightly greater glass transition temperatures that could be considered however still may cause problems during the sintering process as such substrates tend to soften, loose their shape, shrink, or decompose as a result of long periods of exposure. Next, those substrates in green were deemed acceptable as their respective glass transition temperatures were high. Although SiO_2 is considered to be biodegradable, its viability as a substrate is tenuous as it cannot handled without a carrier and must be grown using microfabrication techniques therefore, this substrate was eliminated. In the end, the majority of the substrates shown here were eliminated except for some cellulose derivates, silk fibroin, PDMS, and metal foils. Additionally, polyvinyl alcohol or PVA was chosen as it showed the highest glass transition temperature of all synthetic polymers and could be utilized in situations where the glass transition temperature was not reached by using UV or room temperature curable inks. Out of all materials considered here, silk fibroin is an excellent contender as it offers the best combination in terms of both processing temperature and biodegradability.

4.2 | FABRICATION

As a planar substrate was necessary for inkjet printing, different coating techniques such as solution casting and spin coating were explored as shown below in Figure 4.1. If the substrate itself was not provided, it was chemically synthesized or extracted in the case of natural materials such as silk. Due to their availability, a total of 4 substrates were fabricated while the 3 remaining were either purchased or acquired from a collaboration with an external university as noted.

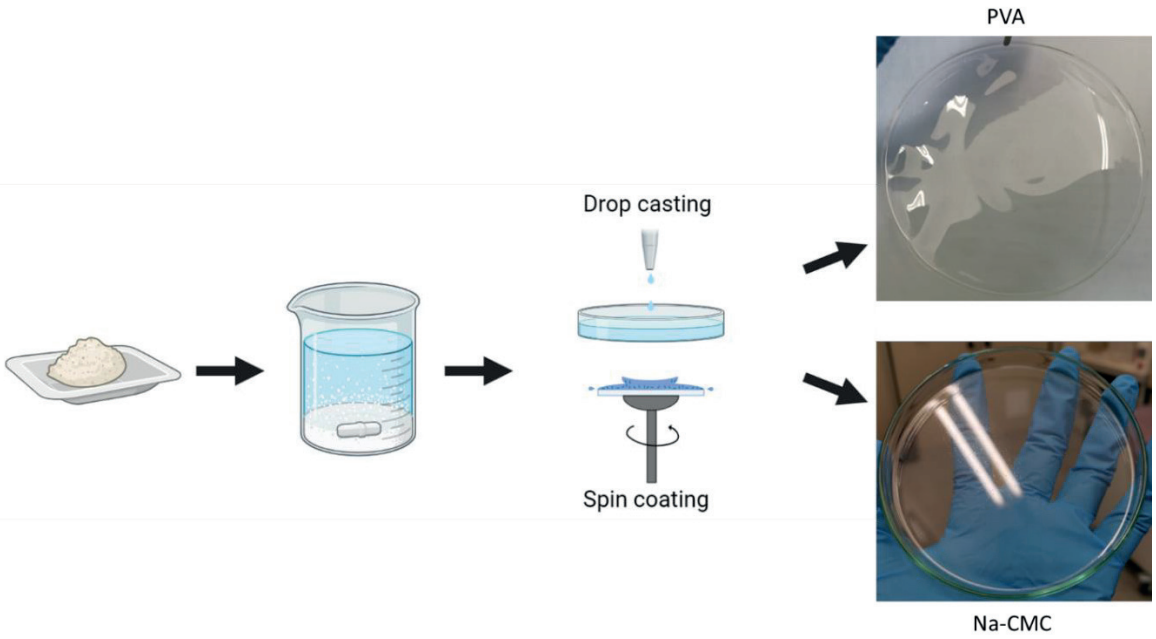

Figure 4.1 Schematic of experimental procedure and fabrication methods such as drop casting and spin coating used to develop PVA and Na-CMC films

The PDMS substrate was prepared using Sylgard® 184 Silicone Elastomer Base and Elastomer Curing Agent purchased from Farnell Components SL which was combined at a 10:1 by weight ratio and mixed. Degassing was performed by placing the bubble ridden PDMS solution into a 50 mL falcon tube and centrifuged for 2 minutes at 3200 rpm eliminating all bubbles. Once prepared, it was transferred into a plastic petri dish and left to cure overnight on a leveled table or at 80ºC for 1 hr in an oven. Alternatively, the solution itself could also be spin coated onto a glass slide at 1000 rpm for 60 seconds and placed into a 100ºC oven for 15 minutes for rapid curing.

A 4 wt% PVA solution was synthesized using 1g of PVA (MW 31,000–50,000) powder acquired from Sigma-Aldrich that was heated on a hot plate with temperatures > 100°C, stirred

at 300 rpm, and combined with 10 mL of deionized (DI) water and 15 mL of ethanol and scaled up or increased/decreased in concentration whenever necessary. The solution itself was transparent and did not need any filtering. The use of ethanol here is essential as this solvent is optimal for creating spin coated films. Depending on the characterization technique, the solution could be drop casted into a petri dish and left overnight to dry on a flat surface in air or spin coated onto glass slides at 500 or 1000 rpm for 30s or 60s depending on the substrate size and film thickness desired. Following the coating, it was dried at 60°C for 15 minutes on a hot plate. For 1 layer, the thickness was found to be approximately 1.5 μm.

Na-CMC powder (MW 90,000) obtained from Sigma-Aldrich was used to synthesize a 2% wt solution containing 20 mg/mL dissolved in DI water at 50°C at 600 rpm for at least 2 hrs or until clear. As some powder remained undissolved, the solution was passed through a 0.45 μm PTFE filter. The solution was then either drop casted into a petri dish and air dried for 6 days or dried on a hot plate for 2.5 hrs at 50°C to create a usable substrate.

The silk fibroin extraction process is an extensive process that takes place over multiple days which was well documented by Rockwood et al.[1] but for this thesis will be summarized as shown in Figure 4.2a. A 0.02M solution of sodium carbonate (Na_2CO_3) powder (Purity ≥99.5%, ACS reagent) purchased from Sigma Aldrich was dissolved in 2 liters of Milli-Q water (ρ = 18.2 MΩ·cm @ 25 °C) until boiling point. At the same time, silk cocoons purchased from a farm in La Adrada, Spain were divided into small pieces weighing approximately 5 g and added to the boiling solution for exactly 30 minutes to maintain reproducibility as the fibroin will start to degrade under longer times. This particular step is used to remove the sericin or degum the silk as seen in Figure 4.2b.[1] Next, the silk fibroin was placed in 1 L of Milli-Q water to be gently rinsed and stirred at 300 rpm which was repeated for a total of 3 times. After the final washing step, all water excess was removed from the fibroin and placed overnight to dry as shown in Figure 4.2b. A 9.3 M lithium bromide (LiBr) solution was calculated based on the weight of the dried silk multiplied by 4 in order to account for the 20% (wt/v) desired solution. The dried silk fibroin was dissolved in the prepared LiBr solution in an oven at 60°C for 4h which should result in a highly viscous and transparent amber colored solution. Next, the solution was subjected to purification using SLIDE-A_LYZER 3.5KD dialysis cassettes purchased from Fischer Scientific -Thermofischer that could hold between 3 – 12 mL of liquid. Every disc was placed into 1 L of Mili-Q water which was stirred at 450 rpm and replaced at least 6 times in 48 hrs. The dialysis was extended if there was incomplete removal of the LiBr which occurred within 10 filtering steps. The silk was then carefully removed from the disks and placed into 50 mL falcon tube in centrifuged at 6000 rpm for 30 minutes at 4°C to remove any remaining impurities which were evacuated after separating and transferring to another falcon. This step was repeated a minimum of 3 times in order to remove any white flocculent or brown matter left behind as displayed in Figure 4.2c.[1] The resulting silk fibroin solution (Figure 4.2d) was highly viscous with a milky

whitish amber transparent color indicating its purity. Depending on the amount of silk extracted, the concentration can vary between 8 – 12% m/v but was always calculated by placing 0.5 mL to dry in a petri dish at 60°C. The solution itself could be stored at 4°C for approximately 1 month before complete gelation occurred. To create silk films, the solution can be placed directly into a glass petri dish and dried overnight. However, to achieve planar films, the highly viscous nature of the silk solution must first be diluted to a 6% concentration to be spin coated onto a glass wafer. Approximately 6 – 7 mL of the silk solution was needed to cover the 4-inch quartz wafers and spin coated at 1000 rpm for 60 seconds for good coverage. The film itself was then fully dried on a hot plate at 60ºC for 20 minutes followed by an oven bake at 65ºC for 4 hrs. Lastly, the silk film was subjected to water annealing, that is placed into a desiccator with water under vacuum for 1 day. Water annealing utilizes controlled water vapor to increase the crystallization of amorphous silk by inducing β-sheets showing crystallinity up to 30.3% thus preventing quick dissolution in water.[2]

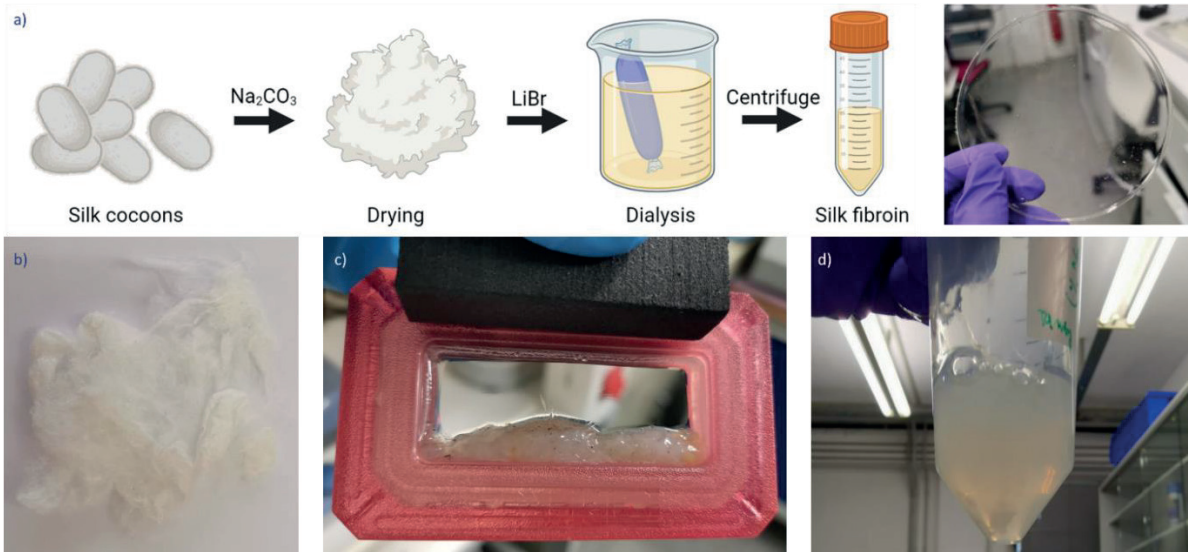

Figure 4.2. Silk fibroin extraction procedure at different stages where a) is a schematic representation of the entire procedure beginning cleaning the raw silk cocoons with sodium carbonate to a usable material that when combined with lithium bromide breaks down into silk fibroin. Multiple dialysis steps were needed to separate and purify the silk fibroin from the lithium bromide solution that following multiple centrifuging steps resulted in 8 wt% silk solution. Actual photos taken during the process where b) is the dry and degummed silk fibroin, c) is a dialysis cassette with remaining white flocculent and brown matter following the last purification step and removal, and d) is the resulting silk solution

CNF was provided by the University of Girona (UdG) where previous iterations resulted in an optimized flat surface with excellent printing properties. Cellulose pulp (wood-derived fiber) provided by Domsjō (Sweden) was used as the starting cellulose raw material and processed into CNF papers following the procedure described by Conti et al. and Lay et al.[3,4] but will be briefly

summarized here. 2,2,6,6-tetramethylpiperidine-1-oxyl radical (TEMPO)-mediated oxidation preparation of all materials were performed using 5/10/15 mM of NaClO until constant pH of 10 was reached. The resulting cellulose suspension went through 5 filtering and distilled water washing steps to remove free ions and any remaining unreacted reagents. Once a 1 wt% concentration was achieved, the suspension was subjected to a high-pressure homogenizer sequentially at pressures of 300, 600, and 900 bars. Lastly, the nanopapers were dried using a Rapid Köthen sheet dryer at a pressure of 0.5 – 0.6 bar for 20 minutes at 85ºC. Individual sheets with varying sizes were made dependent on the diameter used. One of the as received substrates is shown below which many vary in composition as noted by the white patches seen in Figure 4.3.

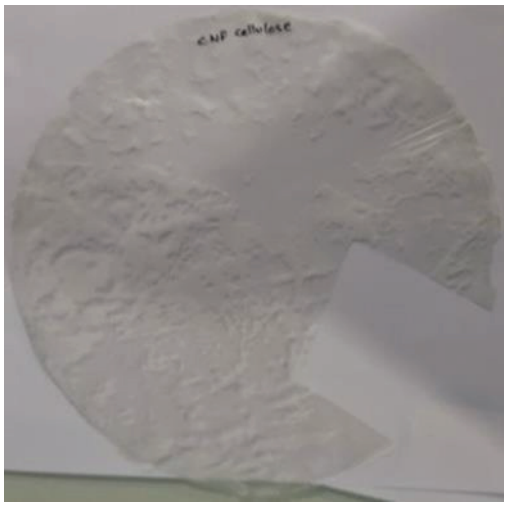

Figure 4.3. Image of CNF nanocellulose paper as delivered

The Zn metal foil was purchased from Cymit Quimica under the Puratronic® brand with a 0.25 mm thickness and a 50 x 50 mm area. Mg foil was also purchased at the same time however due to its volatility to air exposure, proper testing could not be done without complications.

Bacterial cellulose (Biocellulose) was provided for in collaboration with Professor Henrique L. Gomes at Universidade do Algarve, Faculdade de Ciências e Tecnologia.[5] The experimental procedure was reported by Inácio et al. but will be summarized here. Gluconacetobacter sacchari bacteria was cultivated in Hestrin and Schramm (HS) medium with glucose as the nutrient source under static conditions at 30 °C for 96 h producing cellulose membranes. Afterwards, the membranes were treated with 0.5M sodium hydroxide NaOH at 90 °C for 30 min 3 times, followed by purification using distilled water. Next, the membranes were dried at 40 °C.

4.3 | MATERIALS CHARACTERIZATION

Different materials properties were taken into consideration and tested for in terms of their printability, temperature sensitivity, and their degradability. Each of these characteristics were defined using a range of techniques such as an Atomic Force Microscope (AFM), optical tensiometer, and Differential scanning calorimetry (DSC). Substrate requirements for each technique is as follows:

- Minimize surface roughness as much as possible but at least must be < 1 μm (AFM)
- High surface tension value (Tensiometer)
- Glass transition temperature must be below at least 120°C (DSC)
- Degradation must occur within a reasonable period (Dissolvability)

Two different factors were determined in measuring their respective potential printability of the ink: the overall surface roughness of the substrate and how it interacts with the ink during the printing process. It is imperative that the roughness be as low as possible as inkjet printing as a technique requires planar surfaces to define a pattern. Topographical imaging for a large 5 x 5 μm area was measured by Keysight 5500 AFM and Leica DCM 3D Confocal Microscope with various sample areas such as biocellulose, CNF paper, Zn foil, PVA, PDMS, silk fibroin, and Na-CMC can be seen in Figure 4.4 below. As expected, all polymer substrates exhibited the lowest root mean square (R_{sq}) roughness (< 5 nm) while all papers showed the highest (> 20 nm). The Zn foil was determined to be directly in between at 9.77 nm which is expected for a metal substrate. Not only did AFM analysis provide information relating to the roughness but also information regarding their respective microstructures. In terms of both the biocellulose and CNF, the higher roughness can be explained in terms of the material itself which is composed of nanometer sized fibers which gives the substrates both some roughness as well as porosity. The Zn foil appeared to have elongated grains either as a result from the cold working process to make thinner sheets or foils or could simply be due to the rough grinding and/or polishing process. Both PVA and PDMS were comprised of small grains as previously reported by Xi et al.[6] and Chen et al.[7] which explains the low roughness which is ideal for inkjet printing. Lastly, both silk and Na-CMC substrates were measured by confocal microscopy as AFM was no longer available for external use. For this, an even larger sample area (250 x 200 μm) was taken with a 50x objective which indicated an RMS roughness of 0.21 nm, the lowest value obtained for all substrates. As silk is known as a natural polymer, this result is not a surprise as its roughness will mimic whatever surface it adheres to. Na-CMC, on the other hand, was measured with a 10x objective with a large sample size of 1300 x 1000 μm showing a significantly greater surface roughness at 2.45 μm. Based on surface roughness alone, all substrates remained viable candidates for further testing although it is noted that due to the higher roughness of both

cellulose derivatives indicates that any conductive structures deposited on top may have greater resistances than desired.

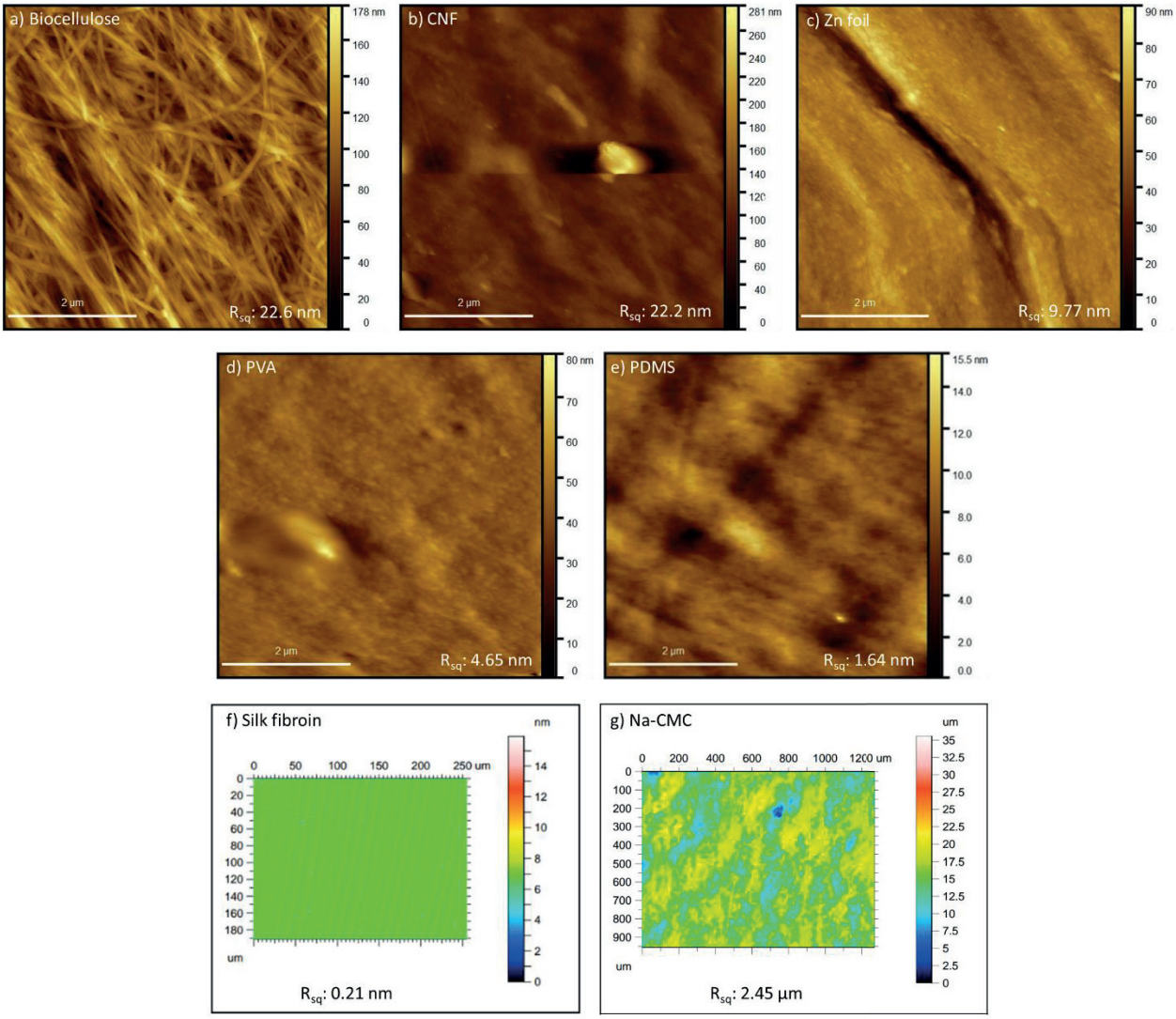

Figure 4.4. AFM and confocal microscopy images of each substrate and their respective roughness values a) biocellulose, b) CNF, c) Zn foil, d) PVA, e) PDMS, f) silk fibroin, and g) Na-CMC

Sessile drop method conducted using the Sigma 701 force tensiometer (Biolin Scientific) was used to determine interfacial tension between the solid substrate and liquid ink and their wettability. This test is used as a first indicator of the interfacial behavior between the ink and the target substrate to determine its overall success for printability. In this case, as mostly water-based inks were utilized, contact angle testing was performed with a 5 µL drop of DI water. The contact angle between the substrate and the ink was measured and used to estimate the substrate

surface energy (γ_s) using Equations 4.1 and 4.2 below as there is no direct measurement possible for solid polymers.

$$\gamma_s = \gamma_l \left(\frac{(1 + cos\theta^2)}{4\Phi^2} \right) \tag{4.1}$$

$$\Phi = \frac{4(V_s V_l)^{1/3}}{\left(V_s^{1/3} + V_l^{1/3}\right)^2} \tag{4.2}$$

Where γ_l is the surface tension of the liquid which in this case is 72.8 mJ/m^2 for H_2O, θ is the measured contact angle, V_s is the calculated volume of the solid polymer, and V_l is the volume of water which is 18 cm^3/mol.

All results are presented below in Figure 4.5 which showed a variety of behaviors based on their respective angles. The 3 highest (Zn foil, PDMS, and CNF) were at 90° or greater indicating poor wettability and low surface tension, and thus, poor printability. It must be noted that this angle can be manipulated if the substrate is treated with solvents such as acetone, isopropanol, or oxygen plasma treatments however for simplification, each substrate was used as is. PVA, biocellulose, and silk showed good to excellent results as their contact angle is low making their respective surface tension higher. Overall this means excellent printability however if the contact angle is too low, the droplet is prone to spreading leading to separation or retreating the desired shape.[8] Both PVA and silk are known to be hydrophilic films meaning that a droplet of water will initiate the dissolution process making the contact angle lower. This process did not occur rapidly therefore changes in the contact angle were not seen during testing. However, Na-CMC did exhibited this behavior to the extreme as a single droplet of water instantaneously initiated dissolution preventing any accurate measurement from occurring. TEMPO-oxidized celluloses not only serves to disperse individual nanofibrils but also introduces carboxyl groups typically producing hydrophilic substrates.[9] The result seen in Figure 4.5c indicates that the TEMPO treatment performed on these substrates were insufficient for inkjet printing which were later on mitigated. Due to these results, both Zn foil and PDMS were excluded from further testing. It must be noted that substrate roughness has an influence on the resulting contact angle however this parameter was not accounted for as the roughness for most of the substrates was under 1 micron with the exception of Na-CMC. Additionally, silk fibroin was tested, however due to the inconsistent molecular weight measurements depending on the batch, the surface

tension reported by Zhang et al.[10] was predicted to be between 43 – 52 mJ/m^2 which is consistent when taking into account the previous calculations of all other substrates seen here.

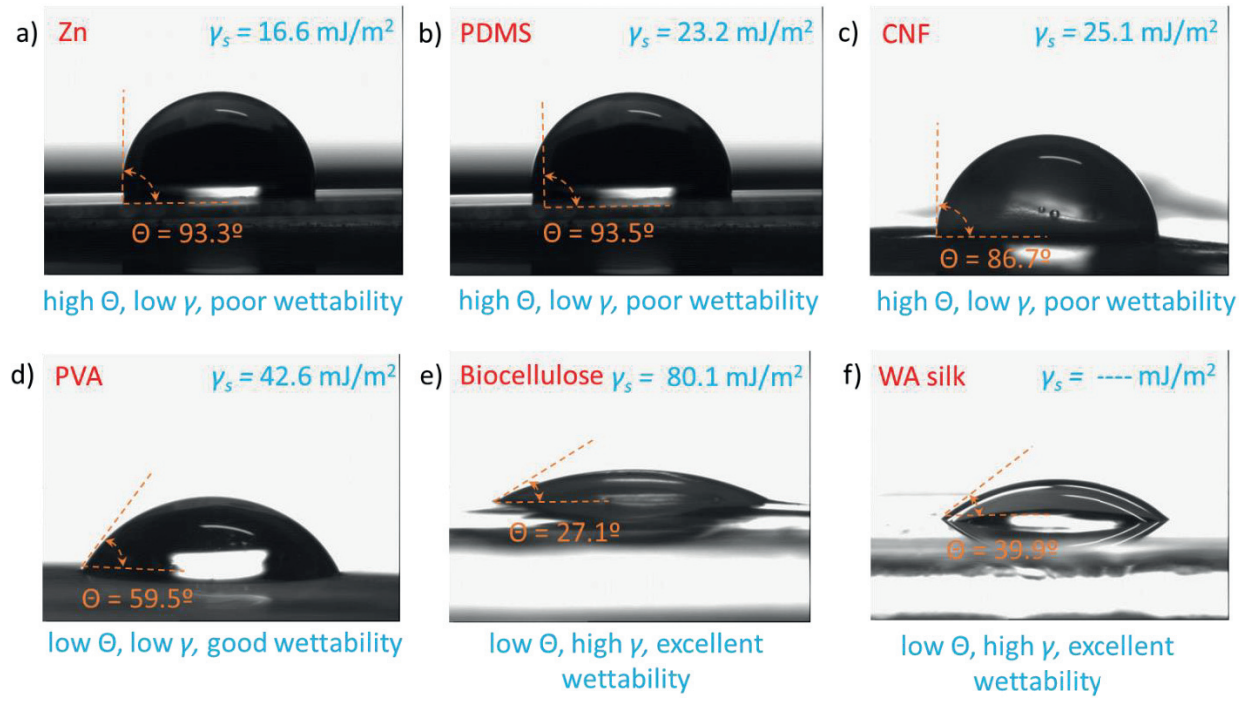

Figure 4.5. Contact angle measurement for all substrates except Na-CMC

DSC analysis of the remaining substrates (PVA, Silk/WA, Na-CMC, biocellulose, and CNF) as stated by Figure 4.6 were performed using the Perkin Elmer DSC8500 LAB SYS. For every substrate, 3 samples were tested to account for variability for 1 cycle where the heating cycle was done at 25 -200°C at a rate of 5°C/min and cooled with the same protocol from 200 – 25°C at a rate of 5°C/min. Each of the biodegradable substrates exhibited different thermal properties than their theoretical values. This, for example, was the case for PVA where the glass transition temperature was expected to be 83°C but tested to be at approximately 59°C with a melting temperature at 225°C as seen in Figure 4.6a. This difference in value can be explained by the concentration and molecular weight of PVA used during testing. This makes PVA a bit more difficult to be used as a substrate however one effective way to increase this temperature is by crosslinking its hydroxyl groups it with glutaraldehyde, poly(ethylene-alt-maleic anhydride) (PEMA), suberic, and terephthalic acid to make a highly resistant hydrogel.[11–13]

Beyond the fusion or melting temperature is considered decomposition of the material which is typically seen as an exponential decrease. The thermal behavior of both the silk and water annealed silk were extremely different in that the silk fibroin alone had a high glass transition

temperature at 179.6°C while the water annealed did not have any identifiable glass transition temperature as indicated in Figure 4.6b and 4.6c. This verified that the water annealing process dramatically enhanced the thermal behavior of the silk fibroin making it more resistant to heat and an excellent candidate to be used. The same could not be said of the silk fibroin although it did exhibit a high melting temperature at 280°C. Both types of silk are acceptable as they meet the substrate requirements however water annealed silk was preferred due to its superior heat resistance. The Na-CMC substrate displayed the next highest glass transition temperature at 102°C as displayed in Figure 4.6d however, in contrast, CNF showed the lowest glass transition at 58.8°C with no visible melting point after multiple tests. Papers are general characterized using a range of decomposition temperatures with no glass transition temperature due to its high degree of crystallinity.[14] This exact behavior is well noted in biocellulose sample as no indication of glass, melting, nor decomposition temperature was found (Figure 4.6e). However due to the reactivity of Na-CMC, decomposition initiated around 317°C as found in Figure 4.6f. In general, this means that all cellulose substrates could reliably be used for further testing. It must be indicated that although these results indicate that temperature has no effect on paper substrates, experimentally it was found that each of these types of substrates tend to undergo warping beyond 100°C which is not ideal for the sintering process.

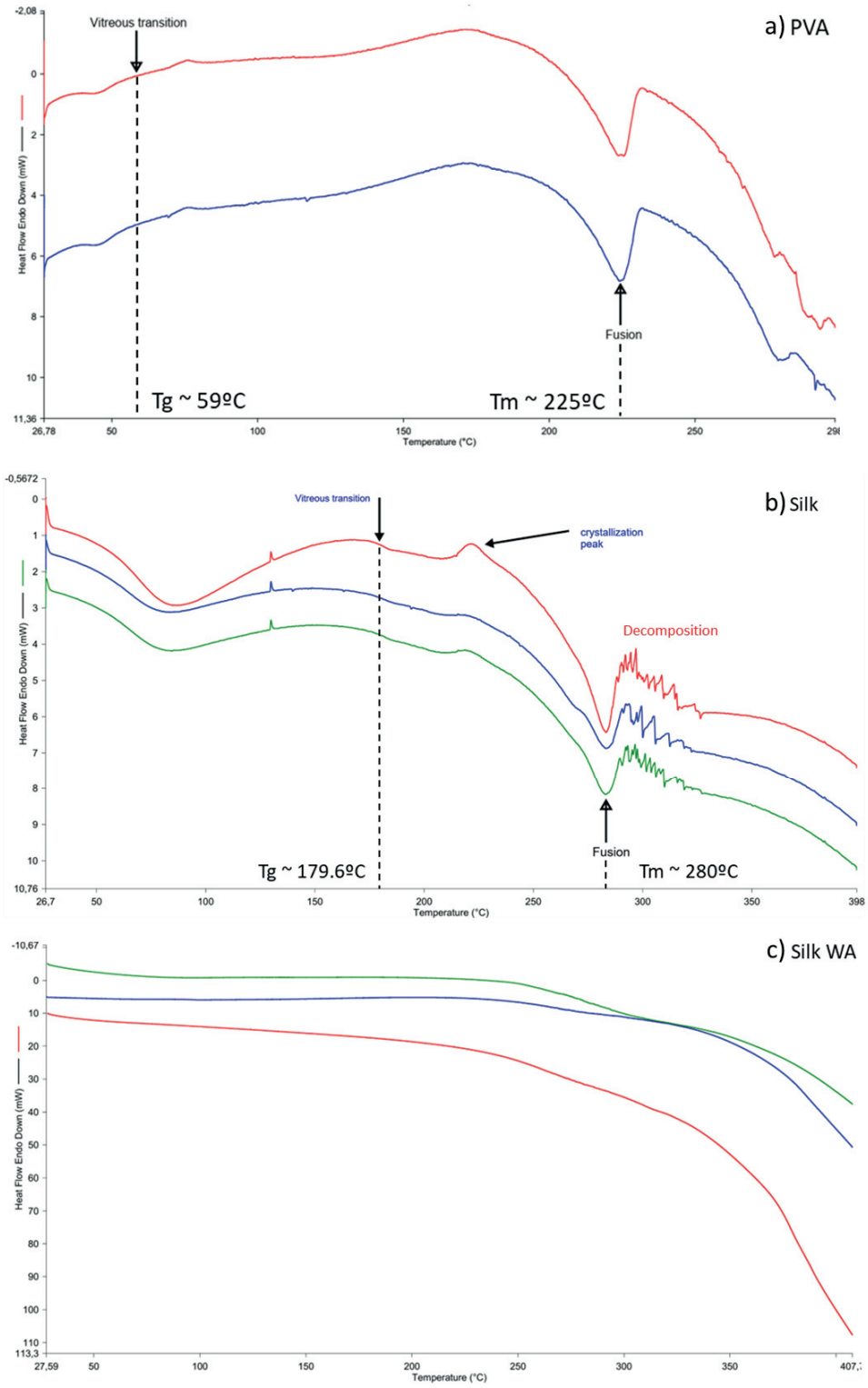
a) PVA
Vitreous transition
Fusion
Tg ~ 59ºC
Tm ~ 225ºC
Heat Flow Endo Down (mW)
Temperature (°C)
b) Silk
Vitreous transition
crystallization peak
Decomposition
Fusion
Tg ~ 179.6ºC
Tm ~ 280ºC
Heat Flow Endo Down (mW)
Temperature (°C)
c) Silk WA
Heat Flow Endo Down (mW)
Temperature (°C)

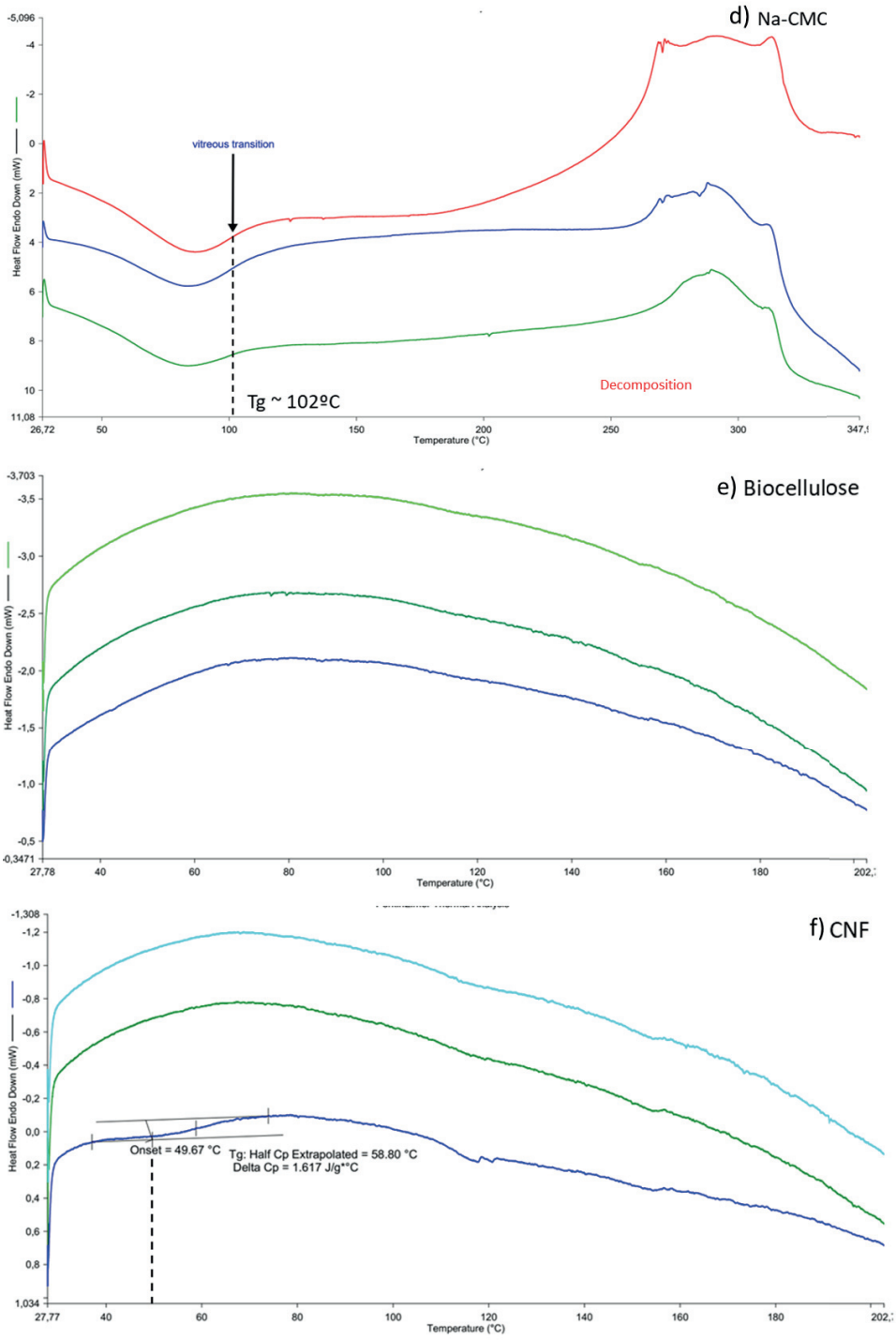

Figure 4.6. DSC Thermographs of a) PVA, b) silk, c) water-annealed silk, d) Na-CMC, e) biocellulose, and f) CNF identifying their respective thermal properties

Finally, dissolution of each of the substrates was tested in order to verify their degradability. Three of the 7 substrates had sensitivity to water, namely PVA, Na-CMC, and silk as reported. Both Na-CMC and PVA showed little resistance when exposed to water, that is, they both began to dissolve immediately. This process occurred more rapidly for Na-CMC than for PVA as the dissolution is dependent on the overall film thickness. When silk began reacting within 5 minutes where the film began to lose its shape and began to curl in onto itself. Even under multiple days of observation and replenishing water, the silk remained in its rolled shape never completely dissolving. The remaining cellulose derivatives such as biocellulose and CNF were known to be compostable using fungi after 60 days or degradable using soil within 5 days respectively as previously reported.[15,16] Lastly, although not explored here due to the elimination of the Zn foil during testing, Kang et al. previously reported that degradation in PBS occurred at a rate of 3.5 μm/day[17]. In terms of dissolution testing, the only unusable substrate is Na-CMC with a rapid reaction when exposed to water. This makes this substrate incompatible with water-based inks however may not be the case with different solvent-based inks.

4.4 | CONCLUSIONS

A summary of all tested biodegradable substrates and their tested properties can be seen below in Table 4.2. From AFM testing no single substrate could be eliminated as the surface roughness of every substrate was acceptable at this point. From contact angle measurement, PDMS, Na-CMC, Zn, and biocellulose substrates were excluded either due to their excessively high (low surface tension) or low contact angle /high surface tension). Na-CMC faired the worse among all candidates as its quick dissolvability made it difficult to measure the contact angle making it incompatible with any ink. On top of this, the surface roughness was found to be the highest among the substrates as whole making it the worst candidate and ultimately removed. The only metal substrate in the selection was acceptable in terms of roughness, dissolvability, and thermal behavior, however its respective contact angle was similar to PDMS making it unusable. Biocellulose had the exact opposite problem where although it showed good potential, the resulting contact angle was far below the acceptable range. Lastly, both CNF and PVA were initially acceptable for their respective surface roughness, high surface tension, low contact angle, and degradability however its overall thermal sensitivity to temperature was inadequate. However, it is possible to still consider both as potential substrates if the sintering step remains below the glass transition temperature using advanced sintering techniques which was verified with further testing as described in Chapter 2. Thus the only remaining substrate was discovered to be silk fibroin which passed all materials characterization and testing requirements.

Table 4.2. Summary of substrates and their respective materials properties

Substrate	RMS Roughness	Surface Tension (mJ/m^2)	T_g (°C)	T_m (°C)	Dissolvability
PDMS	1.6 nm	23.2	----	----	Does not apply
Sodium Carboxymethyl cellulose (Na-CMC)	2.5 µm	Dissolved during testing	~102	N/A	Complete in 5 minutes
Zn	9.8 nm	16.6	----	----	3.5 µm/day in PBS
Biocellulose	22.6 nm	80.1	----	----	Biodegradable by soil
Polyvinyl alcohol (PVA)	4.7 nm	42.6	~59	~225°C	With 5 minutes for 40 µm film
Cellulose nanofibril (CNF)	22.2 nm	25.1	58.8	N/A	Compostable by fungi
Silk fibroin (WA)	0.2 nm	43 – 52	179.6	~280	Softens when immersed
	AFM R_{sq} < 100 nm	Optical Tensiometer	DSC T_g > 120°C		

4.5 | REFERENCES

1. Rockwood DN, Preda RC, Yücel T, Wang X, Lovett ML, Kaplan DL. Materials fabrication from Bombyx mori silk fibroin. *Nat Protoc*. 2011;6(10):1612-1631. doi:10.1038/nprot.2011.379

2. Hu X, Shmelev K, Sun L, et al. Regulation of Silk Material Structure by Temperature-Controlled Water Vapor Annealing. *Biomacromolecules*. 2011;12(5):1686-1696. doi:10.1021/bm200062a

3. Conti S, Martínez-Domingo C, Lay M, Terés L, Vilaseca F, Ramon E. Nanopaper-Based Organic Inkjet-Printed Diodes. *Adv Mater Technol*. 2020;5(6):1900773. doi:10.1002/admt.201900773

4. Lay M, Méndez JA, Delgado-Aguilar M, Bun KN, Vilaseca F. Strong and electrically conductive nanopaper from cellulose nanofibers and polypyrrole. *Carbohydr Polym*. 2016;152:361-369. doi:10.1016/j.carbpol.2016.06.102

5. Inácio PMC, Medeiros MCR, Carvalho T, et al. Ultra-low noise PEDOT:PSS electrodes on bacterial cellulose: A sensor to access bioelectrical signals in non-electrogenic cells. *Org Electron*. 2020;85:105882. doi:https://doi.org/10.1016/j.orgel.2020.105882

6. Xi H, Chen D, Lv L, et al. High performance transient organic solar cells on biodegradable polyvinyl alcohol composite substrates. *RSC Adv*. 2017;7(83):52930-52937. doi:10.1039/c7ra11191f

7. Chen H, Brook MA, Sheardown H. Silicone elastomers for reduced protein adsorption. *Biomaterials*. 2004;25(12):2273-2282. doi:10.1016/J.BIOMATERIALS.2003.09.023

8. Soltman D, Smith B, Morris SJS, Subramanian V. Inkjet printing of precisely defined features using contact-angle hysteresis. *J Colloid Interface Sci*. 2013;400:135-139. doi:10.1016/J.JCIS.2013.03.006

9. Kaffashsaie E, Yousefi H, Nishino T, et al. Direct conversion of raw wood to TEMPO-oxidized cellulose nanofibers. *Carbohydr Polym*. 2021;262:117938. doi:10.1016/J.CARBPOL.2021.117938

10. Zhang J, Du S, Kafi A, et al. Surface energy of silk fibroin and mechanical properties of silk cocoon composites. *RSC Adv*. 2015;5(2):1640-1647. doi:10.1039/c4ra09482d

11. Ben Halima N. Poly(vinyl alcohol): Review of its promising applications and insights into biodegradation. *RSC Adv*. 2016;6(46):39823-39832. doi:10.1039/c6ra05742j

12. Jeong J, Marques GC, Feng X, et al. Ink-Jet Printable, Self-Assembled, and Chemically Crosslinked Ion-Gel as Electrolyte for Thin Film, Printable Transistors. *Adv Mater Interfaces*. 2019;6(21). doi:10.1002/admi.201901074

13. Sonker AK, Rathore K, Nagarale RK, Verma V. Crosslinking of Polyvinyl Alcohol (PVA) and Effect of Crosslinker Shape (Aliphatic and Aromatic) Thereof. *J Polym Environ 2017 265*. 2017;26(5):1782-1794. doi:10.1007/S10924-017-1077-3

14. Lay M, Méndez JA, Delgado-Aguilar M, Bun KN, Vilaseca F. Strong and electrically conductive nanopaper from cellulose nanofibers and polypyrrole. *Carbohydr Polym*. 2016;152:361-369. doi:10.1016/j.carbpol.2016.06.102

15. Jung YH, Chang TH, Zhang H, et al. High-performance green flexible electronics based on biodegradable cellulose nanofibril paper. *Nat Commun*. 2015;6(May):1-11. doi:10.1038/ncomms8170

16. Huang W-Y, Chang Y-C, Sie Y-F, Yu C-R, Wu C-Y, Hsu Y-L. Bio-Cellulose Substrate for Fabricating Fully Biodegradable Resistive Random Access Devices. *ACS Appl Polym Mater*. 2021;3(9):4478-4484. doi:10.1021/acsapm.1c00485

17. Kang SK, Hwang SW, Yu S, et al. Biodegradable thin metal foils and spin-on glass materials for transient electronics. *Adv Funct Mater*. 2015;25(12):1789-1797. doi:10.1002/adfm.201403469

5

Biodegradable Nanoparticle Ink Formulation and Development

Advances in printing techniques have not only helped to facilitate the development of flexible electronics but also provides a means to create transient electronics with minimal waste. Because biodegradable materials typically exhibit lower glass transition temperatures (<100°C) as compared to more conventional polymer materials, low temperature sintering techniques must also be employed for the development of conductive and biodegradable metal thin films. However, in order to create biodegradable inks, a good understanding of the basic material properties of biodegradable metals is needed. Therefore, this chapter begins with some background about biodegradable metals and the current state of art of such inks and pastes before delving into Zn and Mo ink development and thin film characterization.

5.1 | INTRODUCTION TO BIODEGRADABLE METALS

Biodegradable metals (BMs) have been shown to be viable replacements as conductors for electronic devices in terms of both biodegradability and bioresorbability in the body. These metals exhibit biodegradability due to their respective electrode potentials and thermodynamic factors such as Gibbs free energy.[1] The defining factor here is the change in Gibbs free energy (ΔG) which is apparent in hydrolysis or enzymatic reaction when placed in a biological environment. In general, it is believed that the greater negative value of ΔG signifies its ability to corrode. The potential degradation of any metal can be initiated through hydrogen evolution reaction if its standard electrode potential is lower than hydrogen ($E_0 < 0$ V) under standard

conditions in an aqueous environment. It has been shown that a metal degrades more readily in an aqueous solution as the standard electrode potential is more negative.[2] Pure elements such as zinc (Zn), magnesium (Mg), calcium (Ca), and strontium (Sr) have a negative electrode potential meaning that their reaction with water will be both irreversible and spontaneous.[3] Tungsten (W) is a particular case because the standard electrode potential is slightly positive at +0.05V. In this case, W undergoes corrosion based on oxygen absorption (E_0 < +0.4V) in an aqueous environment. BMs such as W, iron (Fe), and molybdenum (Mo) tend to dissolve by hydrolysis into a form of an oxide.[4] Figure 5.1 below lists the full range of BMs, their respective reduction reactions and standard electrode potentials, as well as their biodegradability mechanism.

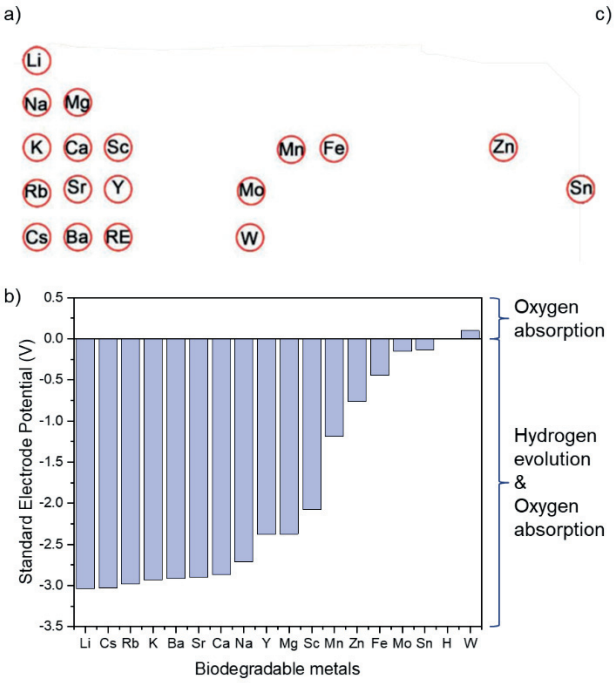

c)

Metals	Half reactions	Standard Electrode Potential (V)
W	$WO_4^{2-} + 8H^+ \rightleftharpoons W_{(s)} + 4H_2O$	0.049
H	$2H^+ + 2e^- \rightleftharpoons H_{2(g)}$	0
Sn	$Sn^{2+} + 2e^- \rightleftharpoons Sn_{(s)}$	-0.13
Mo	$MoO_{2(s)} + 4H^+ + 4e^- \rightleftharpoons Mo_{(s)} + 2H_2O$	-0.15
Fe	$Fe^{2+} + 2e^- \rightleftharpoons Fe_{(s)}$	-0.44
Zn	$Zn^{2+} + 2e^- \rightleftharpoons Zn_{(s)}$	-0.7618
Mn	$Mn^{2+} + 2e^- \rightleftharpoons Mn_{(s)}$	-1.185
Sc	$Sc^{3+} + 3e^- \rightleftharpoons Sc_{(s)}$	-2.077
Mg	$Mg^{2+} + 2e^- \rightleftharpoons Mg_{(s)}$	-2.372
Y	$Y^{3+} + 3e^- \rightleftharpoons Y_{(s)}$	-2.372
Na	$Na^+ + e^- \rightleftharpoons Na_{(s)}$	-2.71
Ca	$Ca^{2+} + 2e^- \rightleftharpoons Ca_{(s)}$	-2.868
Sr	$Sr^{2+} + 2e^- \rightleftharpoons Sr_{(s)}$	-2.899
Ba	$Ba^{2+} + 2e^- \rightleftharpoons Ba_{(s)}$	-2.912
K	$K^+ + e^- \rightleftharpoons K_{(s)}$	-2.931
Rb	$Rb^+ + e^- \rightleftharpoons Rb_{(s)}$	-2.98
Cs	$Cs^+ + e^- \rightleftharpoons Cs_{(s)}$	-3.026
Li	$Li^+ + e^- \rightleftharpoons Li_{(s)}$	-3.0401

Figure 5.1. Biodegradable metals organized based on a) the periodic table reproduced from Liu et al.[3] and b) their respective standard electrode potentials and biodegradability mechanisms as taken and adapted from Liu et al.[3], and c) their respective reduction reactions.

For the continuation of this chapter, two specific biodegradable metals, namely Mo and and Zn were focused on as they presented the next highest conductivities following Mg at 2.3×10^7 $S\cdot m^{-1}$ and Zn at 1.7 x 10^7 $S\cdot m^{-1}$ respectively.[5] Mg itself was not chosen due to its quick and violent reaction when exposed to water which in general would cause experimental issues when developing an ink.

Unlike Mg, Mo has a mild reaction to water and therefore is a more ideal metal in terms of stability. This is due to the fact that Mo has an overall lower solubility in water as compared to

oxygen rich environment.[6] The dissolution chemistry of Mo occurs through hydrolysis as shown in Equation 5.1 where[6–9]:

$$2Mo + 3O_2 + 2H_2O \rightarrow 2H_2MoO_4 \quad (5.1)$$

In terms of bioresorbability, Huang et al. reported the dissolution in biofluids such as PBS and Hanks solution were 0.02 μm/day in pH 7.4 @ 37ºC and 0.005 μm/day respectively.[10,11] Kang et al. reported similar results where Mo foil placed into PBS (pH 7.4 @ 37ºC) saw complete dissolution at 25 days. However, a daily intake between 0.1 - 0.5 mg must not be exceeded when placed into the body.[10]

Zn is also known as one of the essential elements for biological function in the body and found in daily food sources. However, there is a daily allowance of 15 mg where if absorbed in excess concentrations can cause neurotoxicity and hinder bone development.[11] Zn is a unique elemental metal in that the dissolution does not occur via hydrolysis with direct exposure to water. Instead, its reaction to water forms an insoluble zinc hydroxide as shown in Equation 5.2 below[12]:

$$Zn + 2H_2O \rightarrow Zn(OH)_2 + H_2 \quad (5.2)$$

Kang et al. reported the dissolution of Zn foil with dissolution rates of 3.5 μm/day in PBS (pH 7.4) at 37ºC while in Hanks solution increases to 7.2 μm/day.[10] Bowen et al. demonstrated the corrosion behavior of elemental Zn as stents placed into the abdominal aorta of Sprague-Dawley rats. After 1.5 – 3 months, there were signs of relatively uniform corrosion while after 4.5 – 6 months showed more serve localized corrosion where the penetration depth increases exponentially over time.[13] Studied in vivo, it showed degradation rate of ≈ 5 × 10−3 μm/h.[13] After this time period, rapid degradation continued where it was found that compact corrosion occurred which resulted in zinc oxide (ZnO) and zinc carbonate formation.[13]

5.2 | STATE-OF-THE-ART BIODEGRADABLE METAL NANOPARTICLE PASTES AND INKS

Biodegradable metals such as Zn, Fe, Mo, Mg, etc. are inherently unstable due to their tendency to form oxides. This means that it is unlikely to obtain stable dispersions using typical solvents. During the ink formation process, metals exposed to air form spontaneous and

sometimes irreversible surface that hinders charge transport.[14–16] Their affinity for oxygen is reflected in their respective electronegativities where Fe and Zn (χ<2) form thicker native oxides than Mo and W (χ>2).[9] However, there are multiple ways to combat this behavior which include forming a protective coating around the NPs to reduce oxidation up to 3 months.[17] For example, reagents such as ethylene glycol are sufficient in the prevention of oxidation which subsequently must be removed in order to create conductive structures. Other strategies include the use of alternative sintering techniques such as chemical, photonic, and laser sintering. However, the conductivities of deposited inks will be significantly lower than its bulk counterpart not only due to the oxidation but also because of the use of ligands, inadequate sintering temperatures, and lower concentration content resulting in porous films. This morphology is the result of using microparticle (MP) pastes that often dominate biodegradable metal inks due to elevated melting temperatures as compared to its Ag/Au NP ink counterparts. Current advances regarding Zn and Mo inks and pastes are reviewed in the section below, comparing the effect of low temperature sintering techniques on overall film development.

5.2.1 | ZN PARTICLE INKS

Of all the biodegradable metal inks, Zn is the most studied, developed, and utilized due to its availability, relatively low melting temperature (420ºC), and bulk conductivity (1.66 x 10^7 $S \cdot m^{-1}$).[14,16] Compared to other metals, this means that alternative sintering methods are able to meet and incorporate these inks onto temperature sensitive substrates. For these reasons, a broad range of printing and sintering technique has been investigated to fabricate Zn films.

A first basic demonstration was forged by Huang et al. whom produced a Zn microparticle transient paste (< 10 μm) mixed with methanol and PEO particles to be used as interconnects. After solvent evaporation, the paste showed a conductivity of 2.4 x 10^{-2} $S \cdot m^{-1}$ which is much lower than expected due to surface oxidation and point contacts between spherical particles.[18] This result shows the importance in both eliminating the oxide formed and the sintering technique used in an effort to increase the conductivity. Lee et al. was able to address this issue by exposing the deposited patterns to acetic acid (CH_3COOH) and H_2O to dissolve the zinc oxide passivation layer surrounding particles thereby promoting a self-exchange between Zn and Zn^{2+} and fusing adjacent particles together.[19] The screen printable ink composed of Zn, PVP, and IPA produced highly conductive patterns at room temperature using electrochemical sintering resulting in a dramatic increase in conductivity to 3 x 10^5 $S \cdot m^{-1}$. Taking inspiration from this chemical sintering process, Sui et al. modified the screen printed ink formulation by replacing the solvent with N-Methyl-2-pyrrolidone (NMP) due to its solvation with PVP as well as its low vapor pressure.[20] Conductive structures were first screen printed and then treated by an inkjet printed acid-based oxide etching agent (dilute acetic acid) for precise drop amount control over the screen printed patterns in order to reduce any damage caused by excessive acid usage.[20] As

this process was achievable at room temperature, biodegradable or temperature sensitive substrates were compatible such as PHBV films displaying conductivities up to 4 x 10^4 $S \cdot m^{-1}$. Majee et al. presented a fully inkjet printed process where first a highly concentrated Zn NP ink (40 wt% content) was printed followed by curing ink to instigate low temperature in situ chemical sintering. The principal ink formulation consisted of polydimethylsiloxane (PDMS) as the surfactant and polyvinyl butyral (PVB) as the binder with dispersed Zn NPs with 40 – 60 nm size while the curing ink consisted of aqueous CH_3COOH, ethylene glycol butyl ether co-solvent, Triton x-100 surfactant, and Xanthan gum rheological modifier.[21] The ink printability remained stable up to 20 days but after 40 days, showed signs of sedimentation or agglomeration which could no longer be jetted. Reactive inkjet printing or sequential printing of these ink resulted in highly conductive tracks of approximately 10^5 $S \cdot m^{-1}$ with excellent stability up to 8 months. However rapid degradation due to humidity occurred between 40 and 60 days seeing a sheet resistance increase of 200%. It was suggested that a ZnO_x passivation layer developed over this time affecting conductivity.

An alternative chemical sintering approach was reported by Li et al. who used anhydride and water solution that produced a localized weak propionic acid to remove the oxide surrounding Zn NPs.[14] Unlike the external drop casted approach taken by Lee et al., the ink itself contained propionic anhydride that triggered sintering between Zn NPs. This room temperature sintered screen and inkjet printable ink contained Zn NPs (170 nm diameter) dispersed in dichloromethane, propionic anhydride, and polyethylene glycol (PEO). The as-printed patterns showed loosely stacked Zn NPs with 70 nm spacing between NPs where sintering occurred under an atmospheric environment in 90% humidity within 300 minutes. When the Zn NPs are exposed to both acidic and static hydrodynamic conditions, excessive Zn^{2+} ions were released and recombined with the electrons on the Zn NP surface essential being redeposited between the particles allowing for the formation of an electrically and mechanically conductive network (Figure 5.2a).[14] Additionally, long term stability of the particles (reduction in further oxidation) occurs during this reaction with the formation of a zinc carboxylate passivation layer. They reported highly conductive patterns of 7.2 x 10^4 $S \cdot m^{-1}$ however, if the films were sintered for a longer period of time, conductivity was shown to degrade. The same concept was tested using larger Zn MPs with a 5 µm diameter however resulted in a lower conductivity of 4.5 x 10^4 $S \cdot m^{-1}$.

Mahajan et al. reported the development of a Zn thin film by comparing different sintering methods to further increase the conductivity. A basic Zn ink was prepared by mixing 1 wt% PVP, 90 wt% methanol, 0.1 wt% Zn NPs (50 nm), and 10% butyl acetate which was then placed onto a Na-CMC substrate with the help of aerosol printing.[22] When subjecting the film to photonic sintering with a single flash, they reported a maximum conductivity of 2.2 x 10^4 $S\ m^{-1}$ which can further be improved when treated with laser sintering to a conductivity as high as 3.5 x 10^4 $S\ m^{-1}$.[22] A previous attempt by Mahajan et al. utilized the aforementioned ink formulation

for screen or spray printing that when combined with photonic curing resulted in a conductivity of 4.5 x 10^4 $S \cdot m^{-1}$.[23] Here, Zn MPs with an average size of ≤ 10 μm were subjected to ball milling which reduced the particles to an average size ≈135 nm.[23] The following results suggest the fact that either larger particle sizes or non-spherical particles translates into higher conductivities as they require less sintering energy to initiate necking between particles. However, one issue with the development of these Zn films that inevitable restricts the conductivity is the void formation from using particles. Li et al. addressed this issue by implementing a multi-process approach including hot rolling and photonic sintering. The reported Zn ink composed of Zn, PVP, glycerol, and methanol that was screen printed onto PVA substrates and subjected to a curing process at 100ºC to remove the solvent that resulted in void formation which was then minimized using the hot rolling process. Both curing and sintering was done under an Ar environment to avoid any further oxidation of the NPs. Additionally, a high loading ratio to 70 wt% of 50 nm diameter Zn NPs was used to increase density with little porosity thereby achieving a conductivity of 6.0 x 10^4 $S \cdot m^{-1}$.[24] Additionally, the electrode biodegradability was tested and placed into DI water showing complete dissolution within 25 minutes.[24]

Out of all alternative sintering techniques, laser sintering provided the best conductivity reaching 10^6 $S \cdot m^{-1}$ as reported by both Shou et al. and Feng et al. Shou et al. presented an evaporation–condensation-mediated laser printing technique achieving maximum conductivity of 1.1 x 10^6 $S \cdot m^{-1}$ or 6.7% of Zn bulk conductivity.[16] The suspension contained 2% loading of 65-75 nm Zn NPs (obtained by an explosion method) combined with methanol, butyl acetate, and 2% loading of Zn NPs deposited using a bar-coating method. Conductive Zn structures with high crystallinity were generated on both glass and Na-CMC substrate using laser tracing sintering with a continuous-wave (CW) laser (Figure 5.2b). The laser provided multiple advantages including a 75% reduction in oxidation of the Zn NPs at 400mW power, generating least 850K or above to initiate melting between particles, which subsequently provided strong adhesion between Zn and the Na-CMC substrate.[16] They also showed that this process could be done under an Ar or air environment without affecting the resulting conductivity. In terms of biodegradability, they reported that both the Na-CMC substrate and the printed structures dissolved within 80-95 minutes in distilled water.

Lastly, two studies performed by Feng et al. defined the importance in the choice of binder when using laser sintering leading to 2x increase reporting the highest reported conductivity for any deposited Zn thin film. The first reported the development of a slurry prepared using Zn MPs with an average size of 1.5 μm and PVP as the binder dissolved in ethyl alcohol. The slurry was deposited using stencil printing which saw highly conductive traces with a conductivity of ≈ 10^6 $S \cdot m^{-1}$ on different biodegradable substrates such as Na-CMC, cellulose acetate (CA), poly(lactic-co-glycolic acid) (PLGA), and PVA (Figure 5.2c). Energetic photons from the laser

provided rapid energy transfer to fuse neighboring particles converting oxides MPs into conductive interconnections as well as partially decompose PVP.[15] However this technique was unable to fully densify the deposited layer due to the skin effect producing a bilayer microstructure where the top layer shows melted microparticles forming a conductive film and the bottom layer is a porous composite film. This effect is a result of a temperature gradient displaying a penetration depth up to 20 µm, thus limiting the overall layer thickness. In an effort to further improve on the conductivity, the ink composition was reevaluated where both the binder and solvent were replaced by polyvinyl acetate (PVAc) and ethyl acetate respectively creating both a spin coated solution or printable slurry depending on the ratio of each component. From this, they reported the highest conductivity to date of 2.1×10^6 $S \cdot m^{-1}$.[14] Unfortunately, it must be noted that the skin effect remained where the unreacted bottom layers need to be dissolved using ethyl acetate and is limited to water resistant substrates ultimately restricting its potential applications and thus is incompatible with some biodegradable substrates.[14] Although impressive achievements in Zn film development has been demonstrated, its compatibility with biodegradable substrates is not possible without the implementation of specialized alternative sintering techniques which still requires further study.

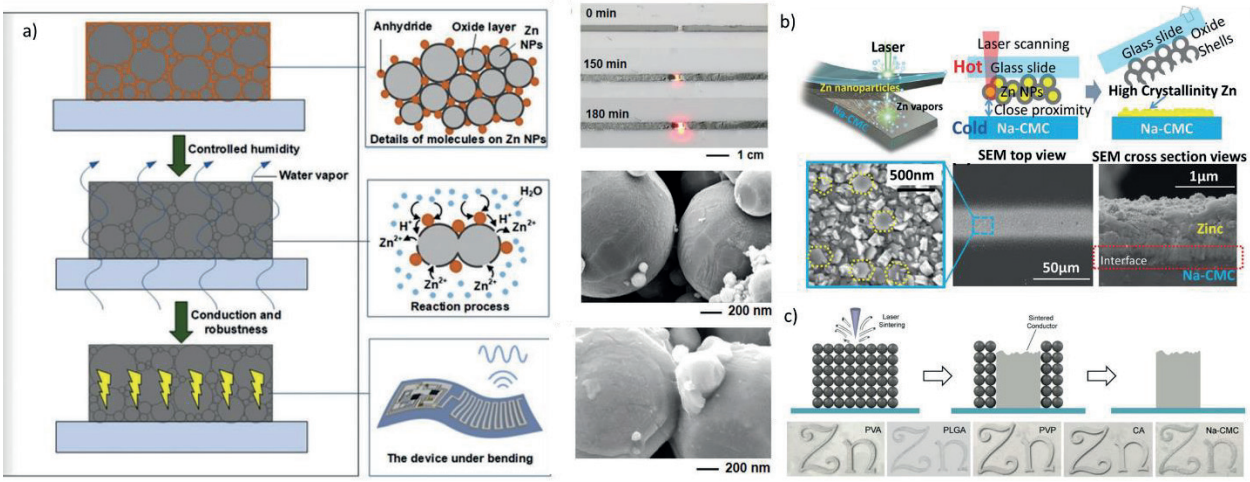

Figure 5.2. Different sintering mechanisms to produce Zn films a) Chemically sintered Zn MP films reproduced with permission from Li et al.[25] Copyright 2017, John Wiley and Sons b) Laser sintered film onto Na-CMC substrate reproduced with permission from Shou et al.[16] Copyright 2019, John Wiley and Sons. c) Laser sintered Zn films deposited onto different substrates reprinted (adapted) with permission from Feng et al.[14] Copyright (2019) American Chemical Society.

5.2.2 | MO PARTICLE INKS

The use of Mo particles presents both advantages and disadvantages over Zn particle inks. Compared to Zn, Mo exhibits stability in air as weak oxidation at room temperature occurs.

However its respective melting point and conductivity are 2622°C and 1.87×10^{7} $S\cdot m^{-1}$, more than 2000°C greater in temperature with only a 12.7% increase in conductivity as compared to Zn. [14,26] Additionally, cytotoxic studies revealed that Mo NPs are non-toxic to human cells at concentrations up to 800 μg/ml proving its biocompatibility and therefore its potential use for biomedical applications.[27] Thus far, only Mo MP pastes have been developed with the inclusion of biodegradable binders to maintain its biodegradability. This is due to the inherent properties of the material where the use of MPs allows for increased conductivity due to both the decreased surface area and high melting temperature making it a prime candidate for conductive pastes over printable inks. Yin et al. was among the first to demonstrate the viability in developing a Mo paste which was composed of Na-CMC and Mo powder (10 μm MPs) to function as electrical contacts.[28] Huang et al. instead combined Mo powder and PLGA as the binder in acetone to develop a Mo paste.[29] However, in both cases, an in-depth study into the development and optimization of the tracks was lacking and under reported.

A study conducted by Lee et al. presented UV curable transient screen printed Mo MP (1-5um were optimal) composite paste that combines Mo MPs and poly butanedithiol 1,3,5-triallyl-1,3,5-triazine-2,4,6 (1H,3H,5H)-trione pentenoic anhydride (PBTPA) together. The hydrophobicity of the PBTPA polymer was found to have good interfacial adhesion with the hydrophobic native oxide layer formed on Mo MPs which proportionally increases with the conductivity while also helping to prevent water penetration thus reducing the dissolution rate while in solution.[9] A loading volume of 35 vol% of Mo is maintained in order to realize a low electrical resistivity at 53.4 nΩ·m. However, in order to achieve high conductivity, the use of advanced sintering techniques such as lasers is necessary to achieve elevated temperatures reaching bulk melting temperatures. Feng et al. utilized selective laser sintering to convert oxidized Mo MPs into conductive interconnections. For this, they developed a spin coated solution mixing Mo MPs and polyvinyl acetate (PVAc) as the binder dissolved in select solvents with a 75:1 weight ratio. They reported insufficient heating up to the melting point of bulk Mo, neck formation between the MPs was found however it was riddled with defects.[14] Although very little change in conductivity was found between the pristine and the laser sintered films, they reported the highest film conductivity to date at 7.0×10^{4} $S\cdot m^{-1}$ for Mo films.[14]

There is an overall lack of development of Mo pastes and inks, mostly due to its melting temperature restrictions that alternative sintering techniques may not be able to address. Additionally, the use of Mo NPs has been left unexplored although the behavior seen with Zn inks is expected to present similarly with Mo inks. For this reason and the advantages listed above, Mo NP ink was developed with the expertise of Dra. Sandra Pérez Rafael at IMB-CNM and is further explored in Section 5.4 below.

5.3 | ZN NP FILM DEVELOPMENT

It must be noted for the entirety of this section, all work is fully attributed to both Enric Casas Aguilera and Dr. Sandra Pérez Rafael who directed and performed all research concerning the development of both Zn and Mo biodegradable nanoparticle inks respectively. However, the work was first conceptualized with experimental procedures in mind by me who was unable to physically conduct experiments at the time. All work conducted by Enric was under Sandra's direction and supervision and was first reported in his bachelor's thesis named "Development of organic electronic devices employing InkJet printing technology" as fulfillment to his obtain his Bachelors degree. All results will be presented and cited accordingly. My contribution instead is more related to the next following sections about the printing and photonic curing of Zn inks onto biodegradable substrates.

5.3.1 | INK DEVELOPMENT

The ink development process requires several factors that mostly take into the account the overall stability of the ink over a period of time and its respective rheological properties such as viscosity and surface tension of the ink which will help in predicting the successful printability of the ink. As inkjet printing was targeted as the main deposition technique, ink requirements established in Chapter 2 were adhered to as much as possible. The following section below goes through the exact processing and characterization steps that concluded in a printable ink.

5.3.1.1 | *ZN NANOPOWDER ANALYSIS*

Although manufacturing standards for the purchased Zn NPs stated a high purity of 99.9%, its reactivity when exposed to air rapidly produces zinc oxide (ZnO). Therefore, it was imperative to understand the actual state of the NPs before ink formulation to understand how the NPs must be treated. Powder X-ray Diffraction (XRD) testing was performed at Karlsruhe Institute of Technology Institute of Nanotechnology (KIT-INT) *(BRUKER D8 Advance)* which revealed that the powder was indeed oxidized before any manipulation despite being stored under vacuum thus heavily influencing the developed Zn film. Figure 5.3 is a composite graph displaying XRD spectra for the Zn powder and matching references for synthetic Zn (JCPDS card 00-004-0831) and ZnO (JCPDS card 01-075-0576). Peaks identified at 31.9°, 34.5°, 47.6°, 56.7°, 63.1°, 66.4°, 68.1°, 69.2°, and 77.1° corresponded to zinc oxide reference peaks at (100), (002), (102), (110), (103), (200), (112), (201), and (202) reflections respectively. The remaining peaks matched synthetic Zn reference found at 36.5°, 39.2°, 43.3°, 54.6°, 70.2°, 71.0°, 82.2°, 83.8°, and 86.6° corresponded to (002), (100), (101), (102), (103), (110), (112), (200), and (201) respectively. The powder saw a good mixture of Zn and ZnO phases thus already limiting the potential conductivity if the oxide cannot be removed during thin film processing.

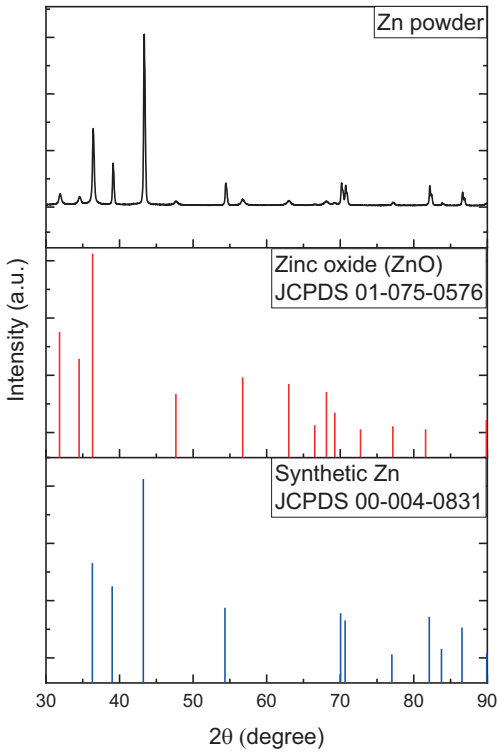

Figure 5.3. XRD spectra of as received Zn nanopowder

5.3.1.2 | *COLLOID STABILITY & RHEOLOGICAL CHARACTERIZATION*

Ink formulation was performed in a step-by-step process beginning with NP stability in various solvents followed by their respective compatibility with a select few stabilizers. A large number of organic dissolvents were considered however are not completely covered here as the reader can refer to Casas Aguilera's work.[30] A 0.3% wt suspension of Zn NPs in 4 mL of dissolvent was prepared by ultrasonication for a minimum of 30 minutes. Although its overall stability could be visually seen, a quantifiable difference was measured by using UV-Vis Spectroscopy (Beckman Coulter DU730) to measure its absorbance after 5 minutes and 48 hrs (Figure 5.4). As the NPs themselves have a dark grey color (Figure 5.4a), a well dispersed ink should exhibit higher absorbance while lower dispersion stability is noted with low absorbance as the NPs are unavailable to interact with the light. Here, the absorbance was taken at 390 nm that indicated the maximum difference for every chosen dissolvent. Although not presented here, the other dissolvents tested showed a greater decrease in absorption beyond 87% except for DMSO, butanol, anisole, 1,2-propanediol, and ethylene glycol (EG) (Figures 5.4b-f). The latter two solvents proved to be too highly viscous (55 and 19 cps) for inkjet printing and were

ultimately discarded. Therefore, the remaining dissolvents were combined with two stabilizing agents with varying concentrations: 1 mg/mL or 5 mg/mL of PEG or PVP. It was discovered that DMSO interacted better with PEG and butanol better with PVP. Unfortunately, anisole was incompatible with either agent and therefore eliminated as a candidate due to variability in absorbance values found during testing.

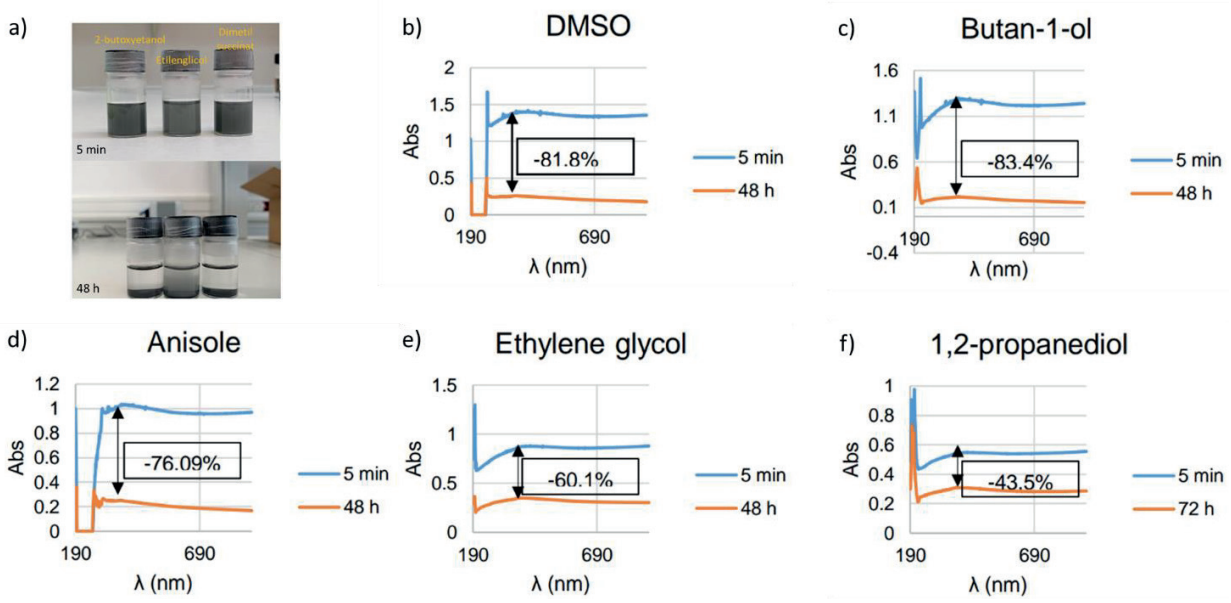

Figure 5.4. Stability testing of Zn NP dispersion over 5 minutes and 48 hrs and their respective absorbance spectra based on a) visual interpretation and quantifiable measurements for b) DMSO, c) butanol, d) anisole, e) EG, and f) 1,2-propanediol. This figure was adapted from results reported by Casas Aguilera[30]

Similarly to the preliminary testing with solvents, each of the printable inks were subjected to Dynamic Light Scattering (DLS) analysis following its synthesis at 0 h and at 72 h. This testing provided information regarding the overall size of the NPs once exposed to the stabilizing agents and solvents, aggregates formation, and general information about the state of the NPs as tabulated in Table 5.1. The low polarization dependence (Pdl) indicates NP size variability where, as the value approaches 1 means greater size variance implying NP aggregation while 0 indicates little variability. Although all inks initially saw near zero values, inks containing DMSO and DMSO/PEG saw a 47.6% and 185.8% increase respectively while DMSO/butanol saw a slight decrease of 7.9% after 72h. The derivative count rate is another quantitative measurement of ink stability based on light intensity where a decrease in the initial value indicates sedimentation of aggregates in solution while and an increases signals new aggregate formation. Of course, results here were in agreement with the Pdl showing sedimentation for the DMSO/butanol ink while DMSO and DMSO/PEG showed large increases in aggregation ultimately making them harder to print after 72hrs. Here, aggregates grew to more than 5 µm in

size which could be removed through filtering. In general, this did not affect the average particle size with all inks presenting sizes below 215 nm.

Taking all these results into consideration, none of the remaining inks presented good stability even with the addition of stabilizers such as PEG. However, the DMSO/butanol combination exhibited the best results under a limited life span of 2 days as extended analysis conducted a week after formulation ultimately revealed agglomeration eventually leading to sedimentation and thus unusable ink.

Table 5.1. Ink stability results for Zn inks after 3 days as reported by Casas Aguilera[30]

	PdI		Derivative Count Rate		Diàmetre (nm)	
	0h	72h	0h	72h	0h	72h
DMSO	0.143	0.211	72967.2	76751.4	150	150
DMSO:Butan-1-ol (1:1)	0.19	0.175	638560.3	593442.7	180	180
DMSO amb PEG (5 mg/mL)	0.106	0.303	71378.2	73289.4	150	150

Although it was noted that the Zn nanopowder obtained from Nanografi had a narrow range of nanoparticle sizes from 60 - 70 nm, both oxidation and NP ink development with the addition of solvents and surfactants, can significantly increase the NP diameter. NPs were dispersed in DMSO and analyzed using DLS and Transmission Electron Microscopy (TEM) techniques to determine the effect of solvent dispersion on NP size. DLS (Malvern Zetasizer Nano ZS, UK) verified that there was a much wider distribution of NP sizes than expected, the majority of which was determined to be between 100 – 240 nm which is not ideal when making inkjet inks as they are much more prone to clogging the printheads (Figure 5.5a). TEM analysis performed at UAB *(High resolution TEM JEOL 2011 with EDX (200kV))* revealed that although individual spherical particles were seen, in general they tended to aggregate together displaying little to no necking behavior between NPs (Figure 5.5b).

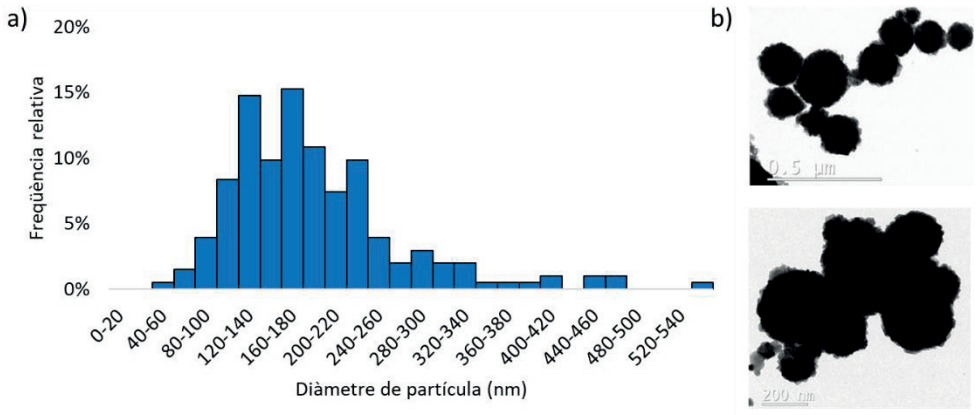

Figure 5.5. Distribution of Zn NP sizes verified by a) TEM and b) DLS as reported by Casas Aguilera[30]

The respective rheological properties of the remaining inks were also verified in terms of ideal printing properties in Table 5.2 below. Because DMSO was the common solvent across all inks, it was then used as the reference. The addition of butanol helped to reduce the viscosity and surface tension. However, PEG showed the opposite effect where the introduction of the stabilizer increased both the viscosity and surface tension. According to the ink formulation guide developed by Cornell University[31] which can also be found in Table 3.1 from Chapter 3, the surface tension should be in between 32 – 42 mN/m. All respective inks were found to be around these values and could be modified with the addition of surfactants, toluene, and/or ethanol if necessary however were acceptable.[31] Unfortunately, in terms of viscosity, all inks were found to be far outside the acceptable range (10 – 12 cPs) and resembled viscosity akin to water at 1 cPs. However, this property can easily be modified by either applying heat to the ink or adding humectants such as EG or glycerol.[31]

Table 5.2. Rheological properties of each respective Zn ink as reported by Casas Aguilera[30]

	DMSO	DMSO:Butan-1-ol (1:1)	DMSO amb PEG (5 mg/mL)
Tensió superficial (mN/m)	43.1	29.0	44.4
Viscositat (cps)	2.43	2.10	2.50

5.3.1.3 | *MATERIALS AND INK FORMULATION*

Commercially available nanoparticles of Zinc (Zn) Nanopowder (High Purity: 99.995+%, Size: 60-70 nm) were purchased from Nanografi Nanotechnology Co. Ltd. and used as is. Ethylene glycol 99% (EG, $C_2H_6O_2$) was purchased from Alfa Aesar while dimethyl sulfoxide (DMSO), anhydrous ≥99.9%, polyvinylpyrrolidone (PVP, average mol wt 10,000),

poly(ethylene glycol) (PEG, average mol wt 200), and 1-Butanol (anhydrous, 99.8%) were obtained from Sigma Aldrich. Poly(acrylic acid, sodium salt) solution (avg Mw 15,000, 35 wt% in H_2O) PAANa stabilizer (10%) and Inframat ® Advanced Materials Yttria Stabilized Zirconia (YSZ) Grinding Media, 0.2 – 0.3 mm beads was provided by KIT- INT facilities from Sigma Aldrich. Polymer substrates such as 125 μm polyethylene naphthalene (PEN) Teonex Q65HA sheets was provided by Dupont Teijin while PVA was synthesized and deposited as stated in Chapter 4 Section 4.2. These were specifically deposited onto ultra-flat quartz coated glass substrates purchased from Ossila Ltd.

Different types of Zn inks were explored and chosen based on their respective reaction to both PEN and PVA substrates as not all solvents are compatible of which were first characterized by Enric Casas Aguilera and Sandra Perez Rafael. All formulations are stated below of which the concentrations were reduced accordingly to 50 mg/mL if too much agglomeration was seen:

Zn/DMSO ink: A 70 mg/mL concentration was prepared where 140 mg of Zn was dispersed in 2 mL of DMSO.

Zn/DMSO/butanol ink: This dispersion contained a 70 mg/mL concentration of Zn dispersed into a 1:1 ratio of DMSO and butanol. That is 140 mg of Zn was combined together with 1 mL of DMSO and 1 mL of butanol.

Zn/DMSO/PEG/butanol ink: A 70 mg/mL concentration of Zn with 5 mg/mL of PEG was combined in 1:1 ratio of DMSO and butanol. That is 140 mg of Zn and 10 mg of PVP were dispersed in 1 mL of DMSO and 1 mL of butanol.

Once each of the components of each of the respective inks were combined, the prepared dispersions were mixed with the vortex for 10s followed by ultra sonication (Elma Ultrasonic LC 20H) for 1 hr. Tip sonicator (BANDELIN Sonoplus HD 3100 Homogenizer, Berlin, Germany) was set at an amplitude of 30% for 5 minutes to facilitate separation between the nanoparticles. Before printing, the supernatant liquid sat for 2 minutes before placing into the ink cartridge.

Additionally, a pearl milled (PM) Zn ink developed at KIT during a 3-month research stay was formulated and tested. Although it was initially desired to use standard solvents such a butanol to reduce any further oxidation of the NPs to prepare the ink, this was not used in the end due to ignition concerns thus DI H_2O was used instead. Therefore the formulation was developed following a recipe first reported by Baby et al.[32] and adapted accordingly to the Zn inks:

0.7398 g of Zn powder

110.97 µL of PAANa stabilizer

7.398 mL of DI H_2O

7.398 mL of 0.2 – 0.3 mm diameter zirconia pearls

A previous work conducted by Mahajan et al.[23] utilized ball milling as a means to reduce the size of Zn MPs however pearl milling has not yet been explored or reported for the development of Zn NP inks. Pearl milling was primarily used in order to break any large agglomerates that may form as a result of ink preparation. Here a laboratory made dispersing unit equip with a Dispermat mixer facilitated the milling process to create the nanoink. The mixture was milled at a rotational speed of 5500 rpm for approximately 2.5 hrs. Next, the zirconia pearls were then separated from the resulting ink through various filtration steps beginning with a 2.7 µm GF-D filter, down to 0.7 µm GF-F filter, and finally passed through a 0.45 µm PVDF filter. Before printing, 20 mM of NaCl solution was added to the ink which should see a change in the ink color. This steps eliminates the the PAANa stabilizer surrounding the Zn NPs. All inks were then placed into a 1.5 ml DMC-11610 cartridge with a 10 pL printhead and placed into FUJIFILM DIMATIX inkjet printer DMP-2831 for testing.

5.3.1.4 | *INKJET PRINTING*

Different iterations combining the acceptable solvents with and without its compatible stabilizer were separately prepared and inkjet printed for inks containing only DMSO, only 1,2-propanediol, butanol/ PVP (5 mg/mL), DMSO/PEG (1 mg/mL), DMSO/PEG (5 mg/mL), DMSO/butanol (1:1), DMSO/butanol (1:2), and DMSO/butanol (1:1)/PVP (5 mg/mL). Different ratios of the DMSO/butanol ink were made in an effort to reduce the sintering temperature by reducing the amount of solvent placed in the ink. It was supposed that quick solvent evaporation would serve to reduce the accumulation of NP in one region thereby improving the overall film homogeneity. As the stability of the ink was limited to 2 days, often the ink was prepared on the same day as printing in order to optimize the printing process and reduce any potential clogging that may result due to NP agglomeration. Inkjet printing tests were performed on PEN substrates for its thermal stability up to 220ºC without deformation. The 4 mm x 4 mm pattern squares were printed for every ink and visually inspected using the Dimatix printer's own camera as shown in Figure 5.6 below.

Figure 5.6a displayed poor printability of the butanol/PEG ink in terms of unpredictable droplet jettability thus forming separate lines most likely due to quick solvent evaporation. This unpredictable behavior ultimately made printing difficult although the film uniformity was acceptable. In contrast, Figure 5.6b – 5.6d showed various poor printability modes in the

development of an overall film. As previously stated, the high viscosity of the Zn ink developed with 1,2- propanediol not only made this ink more difficult to print but also resulted in inhomogeneous distribution of ink resulting in a coffee ring effect as seen in Figure 5.6b. Inks displayed in Figure 5.6c and 5.6d exhibited particle agglomeration during printing creating a non-uniform layer with randomly distributed NPs. DMSO/butanol (1:2) combination contained low viscosity which resulted in undefined patterns where the NPs tended to agglomerate at the edges and was unsuitable for printing as whole. Figure 5.6e – 5.6h showed the most promise in terms of printability however varied greatly in terms of the type of films developed which will be discussed later. Although Figure 5.6e shows a decently distributed Zn film, agglomerations in one area over the other were apparent showing non-uniformity. However in terms of fidelity, DMSO ink is unmatched compared to the rest reported here. Figure 5.6f - 5.6h all showed satellite droplets during printing for each respective ink meaning that the viscosity was lower and surface tension was higher than desired however, their respective printing parameters can be further optimized by manipulating the waveform. Their respective deposited films were acceptable, therefore all formulations presented in Figure 5.6e – 5.6h were maintained for further testing in terms of ink stability and their respective rheological properties.

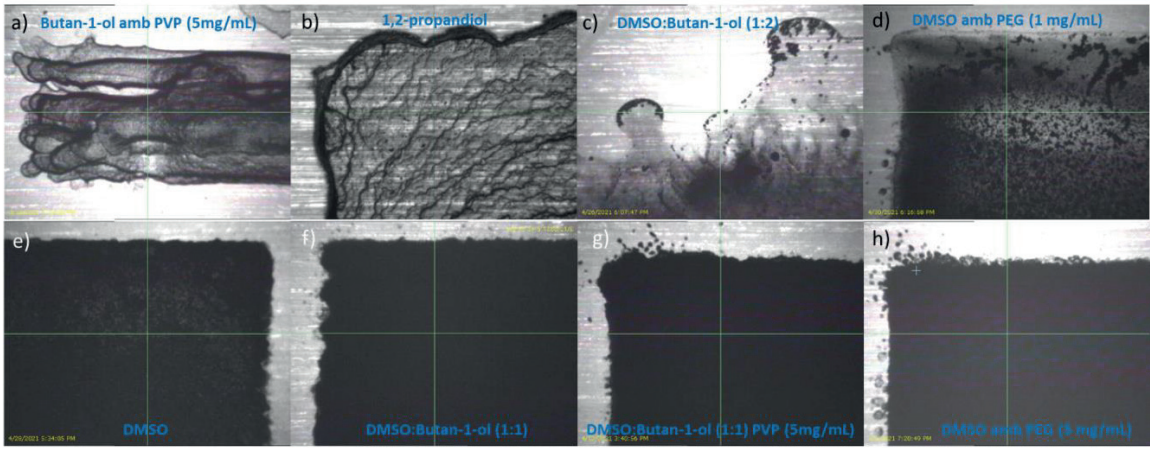

Figure 5.6. Printability of various Zn inks onto PEN substrate as seen through the Dimatix camera where a) butanol/PVP (5 mg/mL), b) 1,2- propanediol, c) DMSO/butanol (1:2), d) DMSO/PEG (1 mg/mL), e) DMSO, f) DMSO/butanol (1:1), g) DMSO/butanol (1:1)/PVP (5 mg/mL), and h) DMSO/PEG (5mg/mL). This figure is taken and adapted from Casas Aguilera [30]

Based on previous results as acquired by Casas Aguilera, 3 different Zn inks were prepared including Zn/DMSO, Zn/DMSO/butanol, and Zn/DMSO/PEG to determine their compatibility with the PVA substrate. All final results are seen in Figure 5.7 below which vary greatly due to their respective response to inkjet printing as well as interaction with the PVA substrate as a whole. Both Zn/DMSO and Zn/DMSO/PEG inks displayed poor printability as shown in Figure 5.7a and 5.7b. Their respective line patterns were an early indication of poor NP dispersion and

quick agglomeration in such inks as the patterns mostly consisted of solvent rather than NPs. This behavior can be remedied with the addition of layers however due to inconsistent printing due to blocked nozzles, an iterative nor comparative study could not be performed between inks as within 2 hrs, the respective inks were non-functional. Although overall, the Zn/DMSO ink performed better than its equivalent treated with PEG, there was no film uniformity across the surface as NP agglomerations appeared in target areas which then proceeded to grow with further printing layers. This behavior is most likely due to chemical compatibility issues with DMSO which is a known dissolvent of PVA where the longer and more the substrate is exposed DMSO will eventually result in the complete erosion of the substrate. On the other hand, the Zn/DMSO/PEG combination showed even poorer performance as the ink displayed sedimentation within 15 – 30 minutes of printing making the print highly unpredictable and unusable. Therefore, these two Zn ink formulations were eliminated from further testing for the PVA substrate. Similarly, the line pattern printed by the Zn/DMSO/butanol ink (Figure 5.7c) indicated poor compatibility with PVA through a bleeding like behavior however printing additional layers seemed to compensate for this lack showing good uniformity with increasing roughness with every printed layer. What happens is that the deposited nanoparticles tend to agglomerate together causing this undesired roughness to occur. By 9 layers, the deposited layer appears to be more uniformly distributed however this is built on the previous roughness as seen at 6 layers. Therefore, the minimum number of layers that must be deposited is 9 layers and beyond. Unfortunately, this ink still lacked stable printability as jetting needed to be verified before and after each layer making the procedure time consuming.

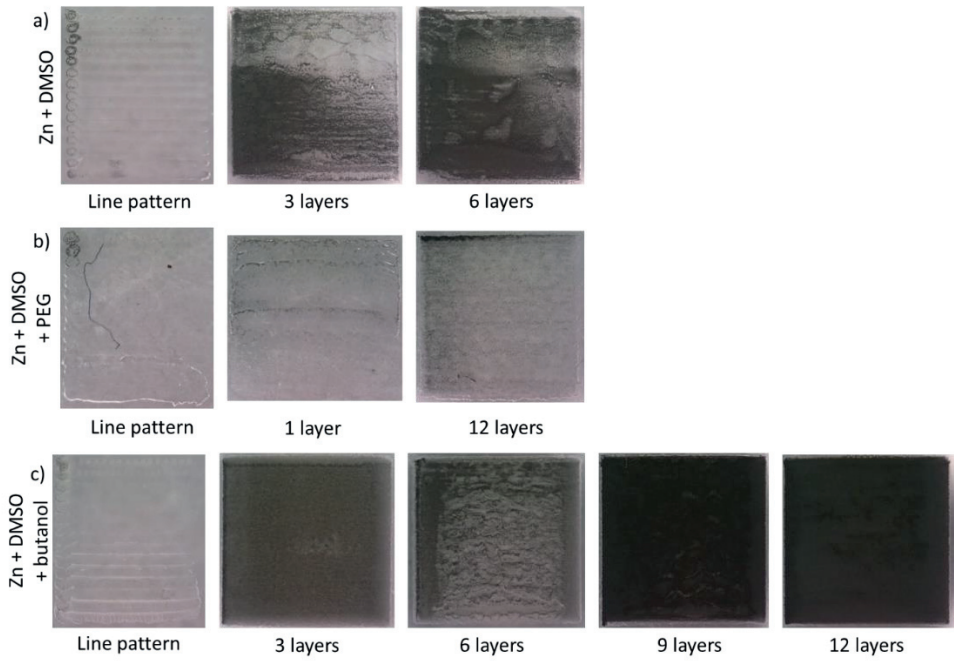

Figure 5.7. Zn square patterns printed onto PVA characterized by deposited line pattern and layers from formulated Zn inks such as a) Zn/DMSO, b) Zn/DMSO/PEG, c) Zn/DMSO/butanol thermally sintered at 80°C

Further optimization of the Zn/DMSO/butanol ink was performed by first defining the optimal drop spacing needed to print a pattern. As shown in Figure 5.8 below, different drop spacing was printed from 35 to 60 µm which saw little difference between the printed patterns as all patterns remained transparent. This once again indicated chemical incompatibility of DMSO in the ink with the PVA substrate.

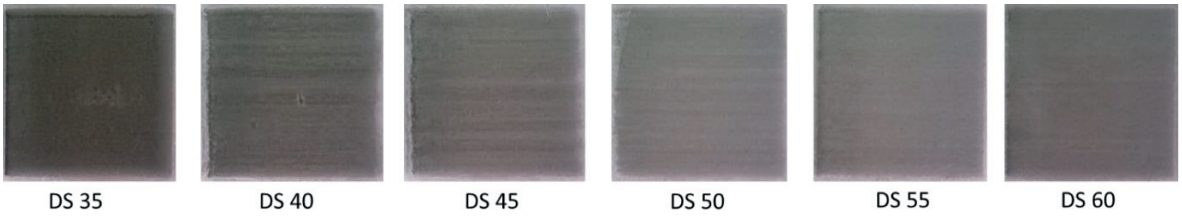

Figure 5.8. Drop spacing (DS) study where 3 layers for each square was printed of the Zn/DMSO/butanol ink

Pearl milling is a wet milling process that produces inks using a high velocity mixing process. This technique serves as a means to break agglomeration between the Zn nanoparticles due to their large surface area and provide ink stability. The resulting ink was found to be extremely hydrophobic compared to previous ones mentioned here likely due to the used of the PAANa stabilizer (Figure 5.9a). Additionally, the ink stability was excellent as compared to the

previous inks stated here remaining printable for over 2 weeks. The reason for this maybe because the nanoparticles became oxidized as a result of processing. Unfortunately, no other solvents could be used for ink processing as the heat produced by the centripetal force of the milling is a fire hazard and thus a limiting factor for easily oxidized materials. Inkjet printing of this ink was facile due to its incredible ink stability creating opaque and homogenous patterns with just 6 printed layers (Figure 5.9b). Unlike the formerly discussed inks, good fidelity was exhibited in the printed pattern. Unfortunately, due to insufficient time, the optimal DS could not be explored and instead multiple printed layers were printed in multiples of 6 up until 24 layers with a chosen DS of 35 μm.

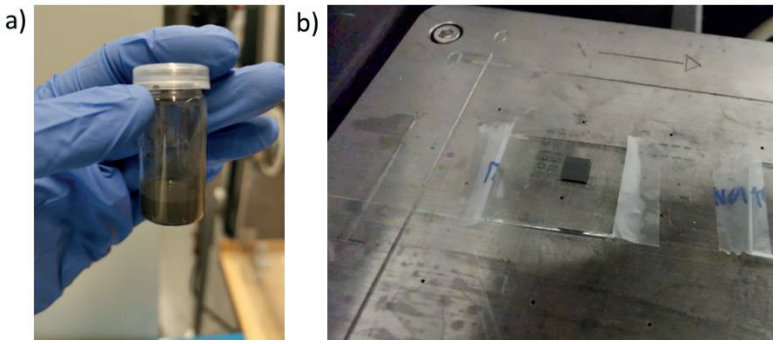

Figure 5.9. a) Pearl milled Zn ink and b) inkjet printed square with 3 layers

5.3.2 | THIN FILM DEVELOPMENT AND CHARACTERIZATION

As previously stated, a good indicator of the potential melting temperature of an ink may be is based on the respective melting point of the NPs (melting point depression). Previous studies indicated that the melting temperature of Zn nanoparticles were not significantly lower than its bulk melting temperature (419.5°C) meaning that this temperature should be used as a target. In this case, two types of sintering techniques were used, conventional thermal sintering in a convection oven and photonic curing, both which maintained low curing temperatures due to the glass transition temperature of the PVA film. For this, both a drying convection oven (Oven FD-53, Binder, Germany) provided for by IMB-CNM and Novacentrix Pulseforge® 1200 photonic curing system was utilized at Karlsruhe Institute of Technology (KIT) at Lichttechnisches Institut (LTI).

5.3.2.1 | *THERMALLY SINTERED FILMS*

Each film was characterized in terms of surface morphology to define both their respective homogeneity as well as their surface roughness. Following this, the electrical properties such as film conductivity was measured and calculated using the Van der Pauw method.

Surface Morphology

Homogeneity across the film surface was explored using scanning electron microscopy (SEM) and profilometry. Heat treated Zn/DMSO films was characterized using SEM displaying large aggregate formation across the surface of the film. The large distribution of NP sizes was further confirmed as previously discussed in Section 5.3.1.2 which showed isolated and poorly packed NPs creating a highly porous film as shown in Figure 5.10 below. This is due to both the poor ink stability of Zn NPs in DMSO as well as the insufficient sintering temperature used to develop such films. DMSO exhibits a high boiling point of 189°C, well below the actual sintering temperature used. However this analysis provided only a microscopic view of the film in a narrow window where homogeneity could not be determined.

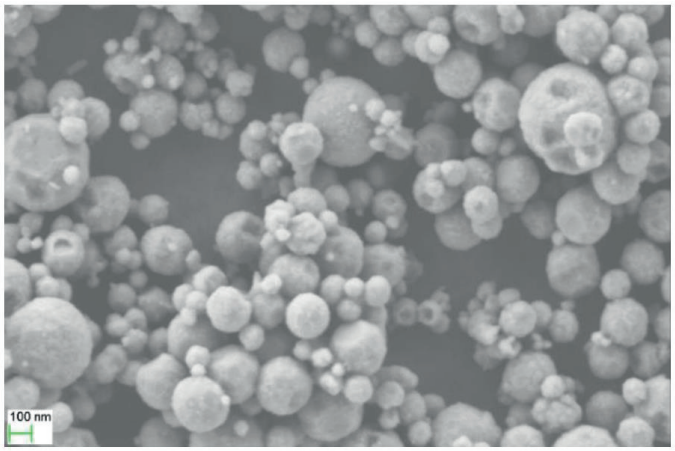

Figure 5.10. SEM micrograph of Zn/DMSO ink deposited film on PEN substrate as reported by Casas Aguilera[30]

Homogeneity or uniformity across the patterned square surface was measured via mechanical profilometry (Tencor P7 Stylus Profiler) as shown in Figure 5.11 below. It showed that both inks displayed opposing behaviors, that is patterns developed with DMSO/butanol exhibited the coffee ring effect (Figure 5.11a) while DMSO/PEG ink saw the Marangoni effect (Figure 5.11b) as described in Chapter 2. The coffee ring effect is typically exhibited in NP inks however in the case of the DMSO/PEG ink, the addition of PEG as the surfactant serves to reduce the surface tension gradient preventing NP accumulation at the edges.[33] The DMSO/butanol deposited film showed high surface roughness as the film thickness varied widely from less than 5 μm up to 20 μm as seen on the edges (Figure 5.11a) while DMSO/PEG sample only saw gradual increase in thickness varying at most 4 μm (Figure 5.11b) between measured points. Unfortunately, due to the limitations of the measurement technique, the surface roughness of the sample could not be accurately extracted and only gives a restricted view of how the sample appears overall.

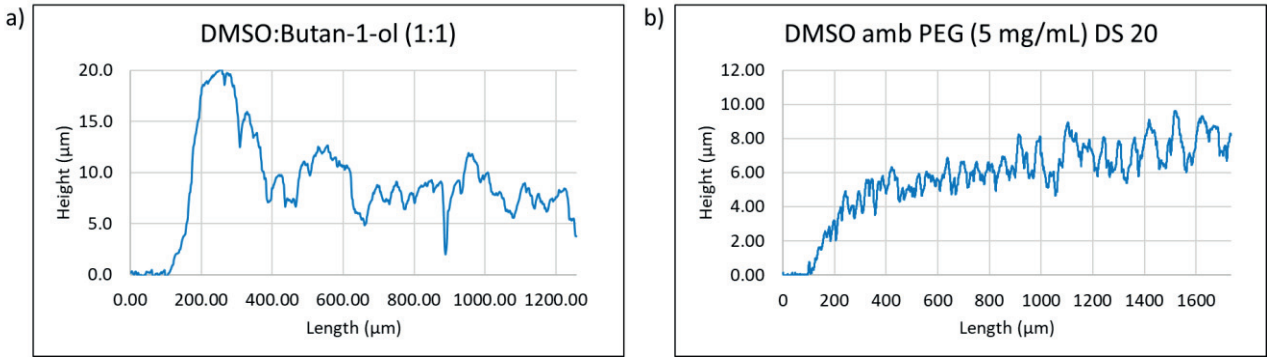

Figure 5.11. Profile measurements of a) DMSO/butanol and b) DMSO/PEG ink films on PET as reported by Casas Aguilera [30]

This same tool could not be used to characterize Zn films deposited onto PVA substrates due to incompatibility with polymer substrates and were thus not directly comparable. Instead, a non-contact method known as optical profilometry (Confocal Microscope Sensofar PLu2300) was used to measure surface roughness based on light intensity reflected from the target surface. Figure 5.12 displays surface roughness for Zn/DMSO and Zn/DMSO/butanol inks which saw 11.70 µm for 6 layers and 5.37 µm for only 3 layers of deposition respectively. As the PVA substrate surface roughness was previously characterized in the nm range, the measured roughness here is 100% due to either the etching of the PVA layer by DMSO and/or those presented from the use of NP ink as a whole. Measurements taken of all other printed layers (6 layers and more) were not reported here as a low number of data points were gathered from incident light from the microscope providing highly inaccurate models. The working principle of confocal microscopy is highly dependent on the reflection of light from film surfaces which in this case were highly opaque and dark structures which instead absorbed light making it notoriously difficult to measure. The reported samples here were successful during measurement as they were somewhat transparent in nature.

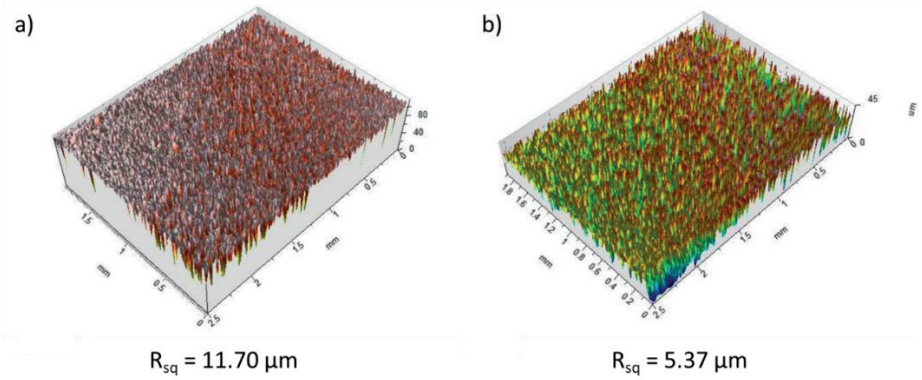

Figure 5.12. Surface roughness measurements obtained from confocal microscopy for a) Zn/DMSO and b) Zn/DMSO/butanol films deposited on PVA substrates

As the use of a confocal microscope was unreliable for the majority of the Zn samples, the HIROX Digital microscope as provided by KIT-INT was used to obtain missing data including the surface roughness and film thickness of opaque samples. An overview of the sample printed (Figure 5.13a) here includes multiple squares increasing by number layers from 1 – 40 layers. Note that a transparent film here is seen as a light grey or white color as depicted in Square no. 4 where the Zn ink was not successfully printed. Thus the appearance of the structures may be deceiving, taking into account how this microscope functions. Figure 5.13b here shows an enhanced view of square no. 1 where 1 layer was printed with a DS of 35 µm. From this photo, the layer appears to be uniform with the appearance of some cracks. Each individually printed square was further investigated by determining their respective surface roughness (Figure 5.13c - 5.13e) and film thickness as reported in Table 5.3 below. Both values obtained for Square no. 1 were inaccurate as the average thickness of the Zn film could not be greater than those deposited with 30x more passes and instead reflects the thickness of the PVA film on the glass substrate. Another reason for this failure in measurement also pertains to the amount of solvent (DMSO) as compared to the NP content (70 mg/mL) that most likely is reacting with and degrading the PVA substrate during the printing process. Towards the bottom of the pattern, the film can be seen as transparent and therefore any values obtained for this layer cannot be used for comparison and cannot be taken at face value. Square no. 2 was printed with 20 layers displaying a surface roughness of 1.130 µm and average film thickness of 1.91 µm which is in agreement with previous printed squares although the extracted roughness is much greater than desired. For 30 layers, the average thickness and surface roughness were found to be 2.27 µm and 1.402 µm respectively. For an increase in the number of layers, a much greater thickness and roughness were expected but not seen.

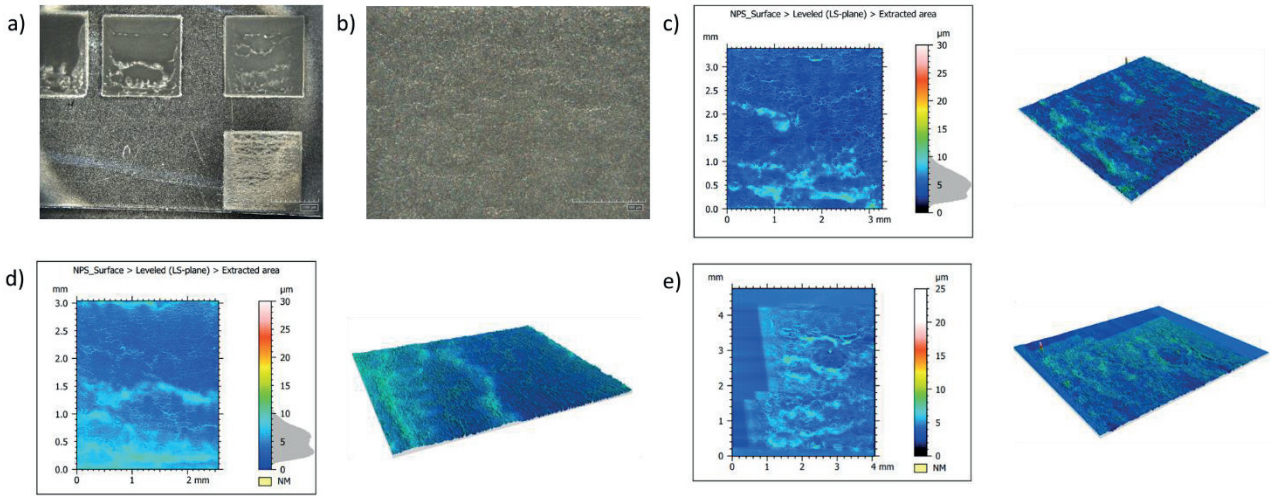

Figure 5.13. Microscopy and profile extraction using HIROX Digital Microscope on Zn/DMSO/butanol inkjet printed films where a) displays all films printed onto a PVA spin coated glass substrate at 20x magnification, b) Printed Square no. 1 viewed at 80x magnification, c) Printed Square no. 1 profile measurements for 1 layer, d) Printed Square no. 2 profile measurements for 20 layers, and e) Printed Square no. 3 profile measurements for 30 layers. Square 4 is not listed nor measured here as it is an unsuccessful printing of a Zn NP film

Table 5.3. Respective film thickness and surface roughness values for each printed square

Square no.	No. of layers	Average thickness (µm)	Surface roughness (µm)
1	1	4.41	1.775
2	20	1.91	1.130
3	30	2.27	1.402

5.3.2.2 | *PEARL MILLED (PM) ZN FILMS*

It must be noted here that PM films were to subject to thermal treatment as it is widely known that heat treatment leads to further oxidation of the NPs therefore the ink was drop casted and dried in air for basic characterization using the SEM. Surprisingly multiple thin film morphologies were seen for the PM Zn films which can be easily distinguished look at Figure 5.14a. Figure 5.14b displays a film composed of NPs that were found to be non-conductive signaling that this planar layer is mostly composed of ZnO. However, Figure 5.14c displays mixture containing both agglomerated NPs and flakes creating this interconnected and stacked network that eventually sees a dominant flake-like behavior as shown in Figure 5.14d. Unfortunately, due to the non-conductive nature of the sample, more in depth view of these films could not be done. It was discovered that the structures seen in Figure 5.14c match the appearance of ZnO crystals (NM-110) that were investigated through TEM showing different

polyhedral morphologies that compose these films giving them a sponge like appearance.[34] These different morphologies display different effects that oxidation may have on a single films, be it due to either water or air exposure. Although it was already previously discovered that the Zn NPs themselves had already shown partial oxidation, it was clear that this behavior was exacerbated during the pearl milling process. Balanand et al. reported the development Zn flakes through a wet milling process using only distilled water. Although their experiment reported here was performed at a larger scale including the use of MP and larger Zr balls, the process is similar and can be equated in this case. The flake-like ZnO layer was a result of the mechanically induced hydrolysis of the Zn MPs. The very use of milling promotes localized hot spots of high temperature and pressure that trigger the Zn/ZnO redox reaction when combining the Zn dust and H_2O.[35] This reaction is known to be exothermic causing thermolysis or water splitting to H^+ and O^{2-} ions that contribute to Zn hydrolysis. Zinc oxide formation occurs following Equation 5.3 below:

$$Zn_{(s)} + H_2O_{(l)} \rightarrow ZnO_{(s)} + H_{2\,(g)} \tag{5.3}$$

The initial ZnO growth is seen at the surface of the Zn particle that accumulates and forms aggregates in a flaky transitional phase that eventually develops only flakes. The results found with pearl milling align precisely with the results reported by Balanand et al. that occurs at a concentrated scale. This provides insight on whether sintering treatment may be effective in further reducing the oxidation of the NPs. In this case, pearl milling was shown to further oxidize the Zn NP during ink development.

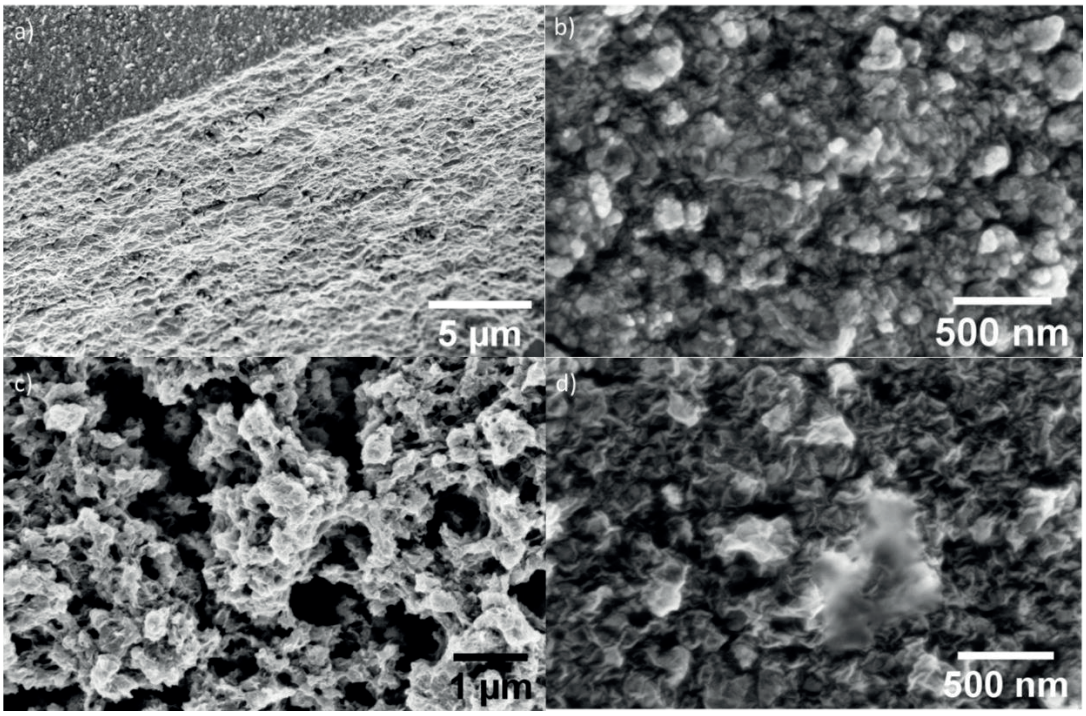

Figure 5.14. Different Zn thin film growth modes acquired through SEM analysis a) contrasting view different film types at a 10,000x magnification, b) non-conductive ZnO NPs structures, c) intermediate mix of nanoparticles and flakes morphology seen at 40,000x magnification, and d) flake-like morphology at 100,000x magnification

Electrical Characterization

A 4 x 4 mm square was printed and used as the standard to measure sheet resistance and calculate resistivity for thin films using the van der Pauw method. Although there are different contact configurations (Figure 5.15), due to restrictions in the use of inkjet printing, a square pattern is used instead to facilitate measurement. When 4 probes are placed at the corners of the printed square, DC current is injected from point 1 to 2 where the output is in amperes (I_{12}) while simultaneously, DC voltage (V_{34}) is measured between points 3 and 4. From this, resistance (R) can be calculated via Ohm´s law as reviewed in Equations 5.4 – 5.6 below

$$R_{12,34} = \frac{V_{34}}{I_{12}} \tag{5.4}$$

$$R_s = \frac{\pi R}{ln\ 2} \tag{5.5}$$

$$\rho = R_s \cdot t \tag{5.6}$$

where t is film thickness and R_s is the sheet resistance.

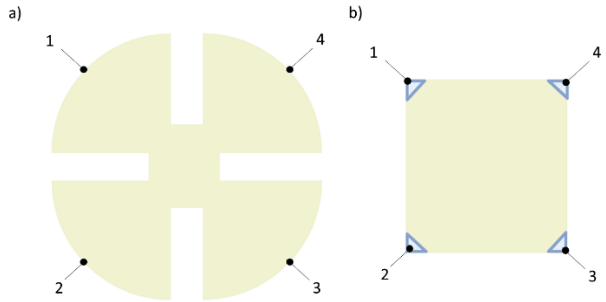

Figure 5.15. Van der Pauw contact placements shown for shapes such as a) cloverleaf and b) square

Sheet resistance measurements were conducted according to this method using the 4-point probe connected to the Agilent B1500 Semiconductor Analyzer.

In terms of sheet resistance as seen in Figure 5.16 (based on samples deposited and shown in Figure 5.8), it was found that due to the higher concentration of Zn NPs, the resistance was the lowest at a DS of 35 µm at a sheet resistance of 68 Ω/□ while the greatest was found at a DS of 55 µm at a value of 773.5 Ω/□. In this case, a DS of 35 µm was chosen as less layers would be needed in order to develop a fully continuous film and saw the lowest sheet resistance.

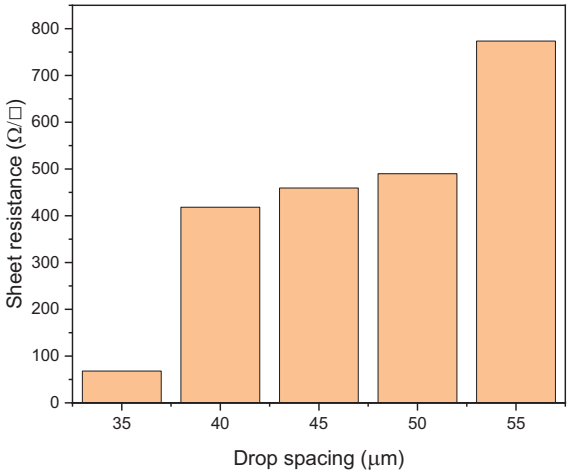

Figure 5.16. Drop spacing and their respective sheet resistances for Zn/DMSO/butanol samples printed on PVA heat treated at 80°C

Different number of layers of Zn/DMSO/PEG ink squares and their respective resistivity values with respect to different heat treatment temperatures (80°C, 120°C, 160°C, and 200°C) is shown below in Figure 5.17. As expected, a greater number of layers sees lower resistivity at increased temperatures (<120°C) mostly likely due to an increased amount of Zn NPs on the surface. For samples treated at 200°C, almost 1 magnitude of difference in resistivity is reported between 10 and 30 layers. This can be explained as samples developed at higher temperatures saw crack formation thus resulting in higher resistivity breaking any electrical percolation pathways between NPs. Although PEN substrates have glass transition temperatures ranging from 112 - 120°C, good thermal stability was found until 140°C, however reaches its operational temperature at temperatures ≥ 170°C in terms of both dielectric strength and mechanical stability.[36] This means that exposing this substrate to 200°C not only displays softening of the material but also deformation therefore affecting the film deposited above explaining the increase in resistivity at this temperature for all layers. In this case, the optimal sintering temperature considering both the temperature limitations of the substrate and the resistivity for both 10 and 30 layers of Zn/DMSO/PEG ink is 160°C.

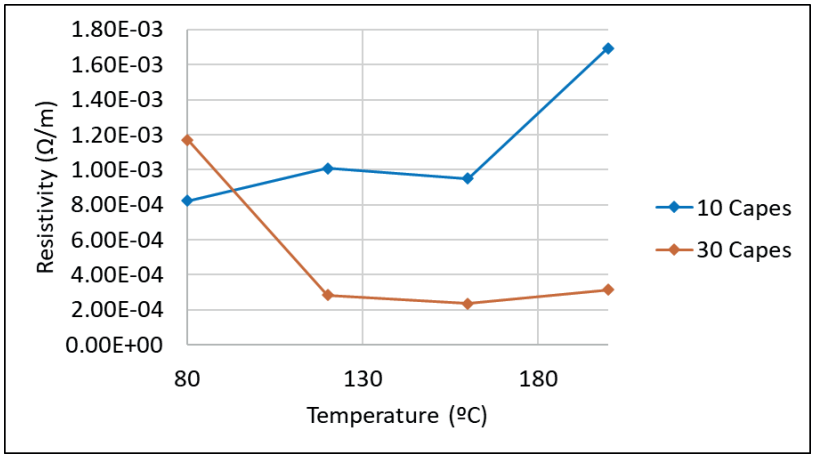

Figure 5.17. Resistivity values for Zn/DMSO/PEG (5 mg/mL) ink printed with a DS of 20 µm on PEN substrate with respect to sintering temperature as reported by and adapted from Casas Aguilera [30]

Table 5.4 below summarizes all Zn inks that were printed, sintering, and characterized below at various sintering temperatures displaying decent conductivities ~10^3 S/m across all inks. The Zn/DMSO ink exhibited the lowest resistivity and thus the highest conductivity of all inks at 8.1 x 10^3 S/m, 0.05% of that of bulk Zn conductivity. In contrast, those with stabilizers such as PEG and PVP saw significantly lower conductivities almost 8 times less. This is because the function of a stabilizer is to isolate the NPs for one another thereby also restricting electrical conduction between NPs as is shown here. This indicates that the stabilizer nor solvent were not fully removed at 160°C. Wide differences in conductivity of square patterns printed with DS of 15 to 20 µm can be accounted for by crack formation in films developed with DS of 15 µm, seeing and almost 4 times difference signifying the importance in optimizing both printing and sinter parameters to achieve highly conductive films.

Table 5.4. Respective Sintering temperature and Electrical Properties of corresponding Zn inks on PEN as reported by Casas Aguilera [30]

	Temperature (ºC)	Resistivity (Ω·m)	Conductivity (S/m)
DMSO	80	$1.24 \cdot 10^{-4}$	$8.05 \cdot 10^{3}$
DMSO:Butan-1-ol (1:1)	160	$5.16 \cdot 10^{-4}$	$1.94 \cdot 10^{3}$
DMSO with PEG (5 mg/mL) i DS 20	160	$2.35 \cdot 10^{-4}$	$4.26 \cdot 10^{3}$
DMSO with PEG (5 mg/mL) i DS 15	160	$7.48 \cdot 10^{-4}$ 10 layers	$1.34 \cdot 10^{3}$ 10 layers
DMSO:Butan-1-ol with PVP (5 mg/mL)	160	$6.35 \cdot 10^{-4}$	$1.57 \cdot 10^{3}$

As previously shown, the same Zn NP ink deposited onto 2 different substrates can result in drastically different properties that is not only limited to printability and appearance but also to its electrical properties. All thin films deposited by Zn/DMSO and Zn/DMSO/butanol inks onto PVA were thermally sintered at low temperatures at 80°C for 1 hr due to the temperature sensitivity of the substrate. As the films were shown to have high roughness, this ultimately had an impact on its respective sheet resistances for individual squares which saw values ranging from 160 to 2000 Ω/□ as seen on Figure 5.18 below. Unfortunately, sheet resistance values determined by 4-point probe measurements were found to be highly inconsistent across all layers due to lack of film uniformity. An increasing number of layers saw significantly reduced resistance seeing an 84.4% decrease from 1.94kΩ/□ to 302.6 Ω/□. Although the two inks could not be directly compared due to the varying number of layers, the Zn/DMSO/butanol ink combination saw overall lower sheet resistances whereby the increase with 9 deposited layers can be explained by nozzle clogging during the printing process making it difficult to determine if the ink was ejecting correctly for an entire layer. This exponential drop in resistance values was also reported by Casas Aguilera on PEN substrates meaning that PVA did not have such a significant impact in terms of film formation.

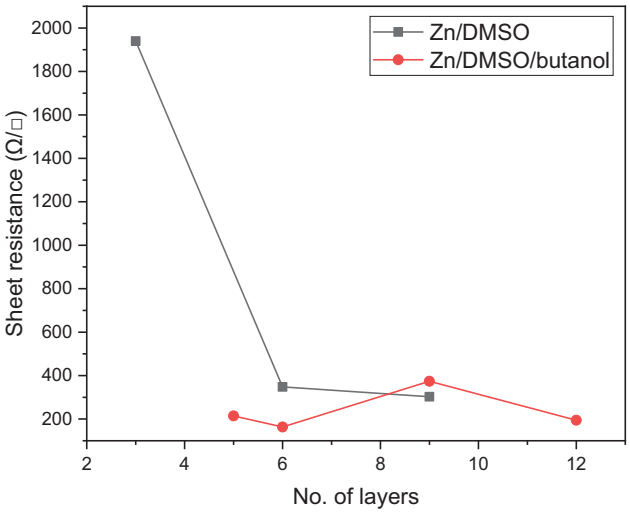

Figure 5.18. Measured sheet resistance values with respect to number of layers for Zn/DMSO and Zn/DMSO/butanol heat treated films on PVA

Although 4 x 4 mm squares are the standard in measuring conductivity, different line lengths and thickness were also explored in terms of their effect on the resulting resistance value. Following the optimal printing results in the last section, different number of layers were explored including 4, 6, and 9 layers, the amount of which was mostly restricted by the stability of the ink. Line widths of 300 – 1000 µm with line lengths ranging from 1 – 10 mm were printed and sintered for 2 hrs at 80°C (Figure 5.19a). As the printed structures were a bit simpler in this case, the standard van der Pauw measurements could not be used therefore two terminal resistance measurements were done instead. Here only line lengths between 1 - 3 mm saw conductivity, varying wildly between 270 MΩ and 135 GΩ. Samples printed with 4 and 9 layers are compared below in Figure 5.19b. Unfortunately, the sample printed with 6 layers was inconclusive as the majority of the lines were non-conductive but showed a huge range of resistance values between 471.3 Ω and 938.1GΩ questioning the overall reliability of the measurement as a whole and therefore is not reported here. For 4 layers, lines 1 mm in length with thicknesses between 300 and 1000 µm generally showed a decrease in resistance. Similar results for lines 2 mm in length also decreased in resistance however lines longer than 3 mm and 300 µm in thickness were found to be completely non-conductive. As expected, as the length of the line decrease, so does the resistance, for example the decrease in resistance from 3 mm to 1 mm for a line thickness of 300 µm is 83% displaying a great dependency on the line length. However, the resistances were determined to be in the GΩ range which is unsuitable for any application including electrodes. Printed lines with 9 layers saw significantly lower resistances ranging from 277.6 MΩ up to 4.95 GΩ. Similarly with this sample, increasing the line length and line thickness leads to higher resistances. Therefore, thermal sintering at 80°C is severely

insufficient for film development meaning that an alternative sintering method is necessary in order to achieve conductive films on PVA substrate which has thermal restrictions.

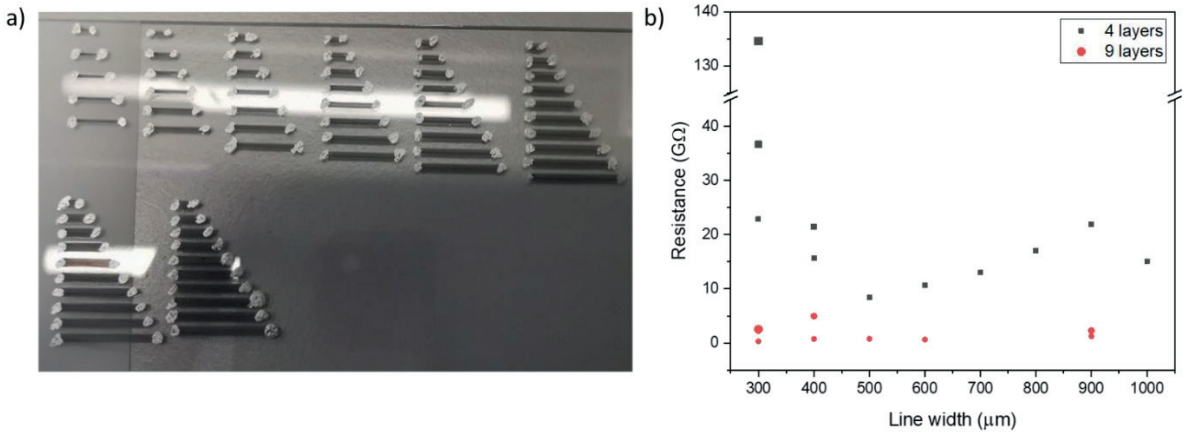

Figure 5.19. a) Various printed line width and line length for Zn ink structures printed with 6 layers of Zn/DSMO/butanol ink and their respective b) resistance values where dot magnitude symbolizes the length of the line from the smallest at 1 mm, 2mm, and 3 mm

5.3.2.3 | *PHOTONICALLY CURED FILMS*

It must be noted that the entirety of this section was performed at KIT-LTI using the equipment provided in the cleanroom facilities including the use of both the photonic curing (Novacentrix Pulseforge® 120) and 4-point manual prober (KeithLink LRS4-TG). Further analysis of the films was also conducted at KIT-INT during my 3-month research stay including the use of the SEM (SEM-FIB Dual Beam Zeiss Auriga 60) and XRD (BRUKER D8 DISCOVER with LynxEye Detector (Cu Kα) and BRUKER D8 advance) for thin film characterization.

Sintering parameters were based on previous experiments related to references such as Li et al. whom maintained an intensity of 4.9 J/cm^2 or 10.88-25.88 J/cm^2, light pulse of 540 µs or 2 ms, and varying number of pulses between 1 – 20.[24] These only provided the initial starting parameters such as voltage and time which depending on the effect of the film was adjusted accordingly. It was also previously found that multiple pulses provide higher sintering temperatures than 1 single pulse which also helped in preventing burning of the substrate.

Table 5.5 below provides a detailed look at each experiment performed and their respective testing parameters and results. On average, the amount of energy that the substrates were subjected to was below < 1.41 kW/cm^2 for preliminary testing which was clearly ineffective at

sintering the film as no color change nor conductivity was found. Therefore, a higher voltage was used resulting in a higher energy applied (< 4.89 kW/cm^2) which was still ineffective in sintering the films. Thus, the following tests mimicked those reported by Li et al. and focused more on manipulating the pulse length. The exact recipe did not result in conductive structures however when increasing the pulse length from 500 to 2280 μs, the film became conductive. However, if the pulse length was increased all the way to 4380 us, the substrate was burnt as a result however the structures remained conductive. Therefore, any recipes with energy near < 10.8 kW/cm^2 were discarded. Therefore, the majority of the testing centered in targeting the radiant power between 6 – 8 kW/cm^2 were ideal to achieve conductive structures across all samples.

Table 5.5. Photonic Sintering parameters for all substrates

Voltage (V)	Pulse length (uS)	uPulses	Height (mm)	Radiant power (kw/cm²)	Repeat count	Result	Sample ID
350	550	1	12	< 1.41	3 -60	No change	Test substrate
500	500	1	12	< 4.89	5	Non-conductive	Test substrate
500	2280	2	12	< 4.87	3	Conductive	Substrate 1
500	4380	3	12	< 10.8	3	Conductive - burnt film	Substrate 2
500	2280	2	12	< 6,48	3	Conductive	Substrate 3
500	2280	3	15	< 7.61	3	Conductive	Substrate 4
500	3080	4	12	< 8.87	3	Burnt substrate	6-15-2022 Zn + DMSO + butanol
500	2280	2	12	< 6.74	3	Non-conductive (hole through the substrate)	Only PVA substrate
500	2880	3	12	< 8.07	3	Change in color – non-conductive	PVA/PDMS/ glass
500	3050	3	12	< 7.79	3	Non-conductive Burnt sample	4 layer pyramid
500	2800	3	15	< 7.14	3	Conductive and uniform across all samples	Zn + DMSO + butanol
500	2280	2	11	< 6.61	3	Non-conductive	PM1
500	1380	4	11	< 5.38	3	Non-conductive (no change in color)	6 layer pyramid
400	1580	3	11	< 3.77	5	Non-conductive (no change in color)	6 layer pyramid
500	2280	3	11	< 7.32	3	Non-conductive	PM2
500	2280	3	11	< 8.18	3	Conductive	9 layer pyramid

New samples made with 1-butanol (non-anhydrous)

Surface Morphology

A notable change in color appeared as the deposited film first appeared as a dark grey color, almost black, where after brief exposure turned into a light grey-milky colored film as seen in Figure 5.20a/5.20c to 5.20b respectively. Photonic curing of the film appears to be uneven where

the microstructure of one area can be completely different than another as seen in Figure 5.20d where there are areas with lighter regions towards the top vs. the darker seen at the bottom with appearance of metallic Zn interspersed between.

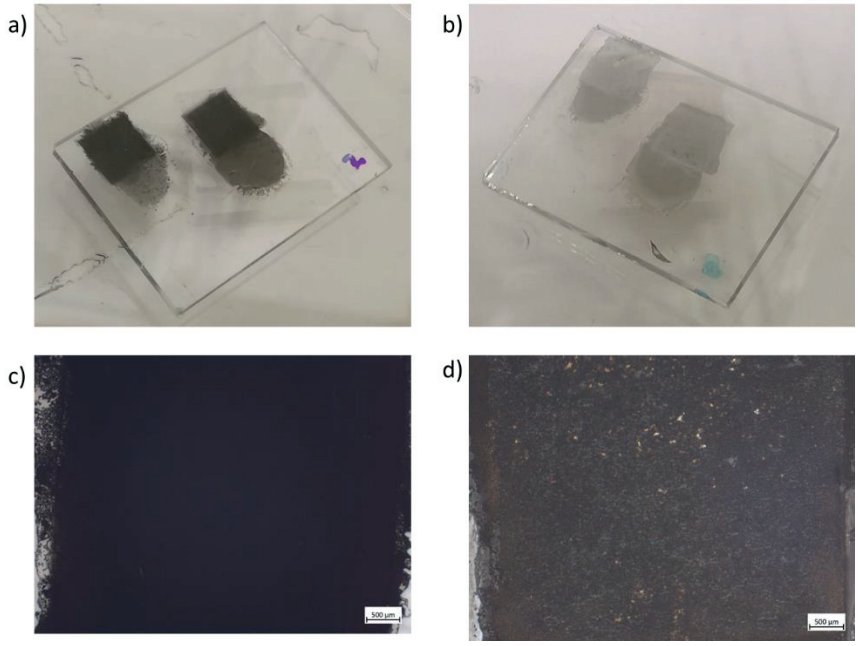

Figure 5.20. Developed Zn/DMSO/butanol films (printed at KIT) a) before and b) after photonic curing

This behavior was even more apparent when looking at Figure 5.21a where grey colored flakes seemed to have covered or created Zn metallic cracks. Under SEM observation (Figure 5.21b-d), these flakes were composed of oxidized Zn NPs that agglomerated together. Behind these areas or the cracks themselves were clusters of individual and closely packed Zn NPs showing the removal of the solvent in these particular areas. Enough of the Zn NPs were exposed that this created a percolation pathway for electrical current to flow resulting in conductivity.

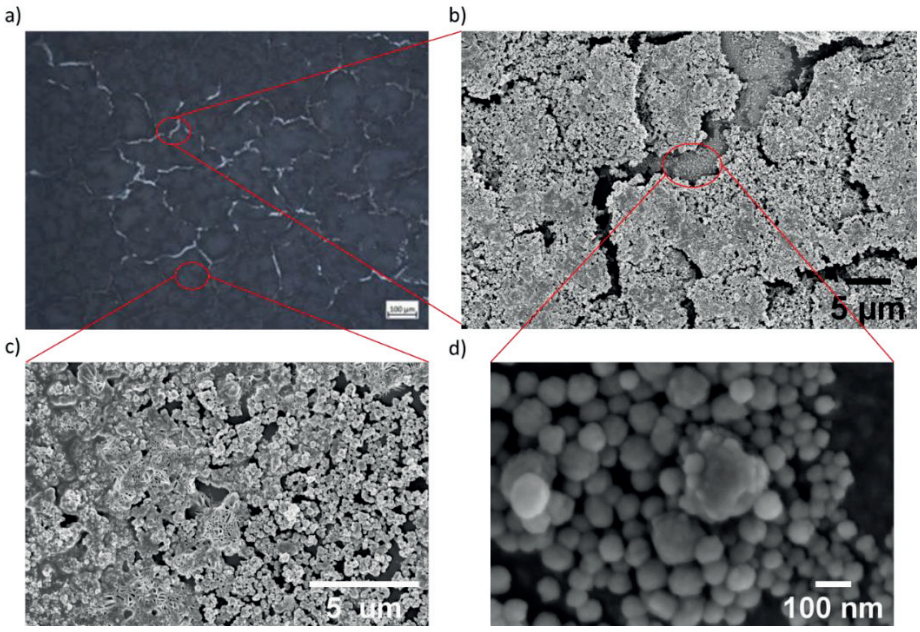

Figure 5.21. Photonic cured Zn film viewed with a) an optical microscope, b) SEM micrograph focused on the crack formation, c) SEM imaging of the oxidized Zn film, while d) represents the stacked Zn NP found beneath the ZnO flakes taken with the help of Ben Breitung at KIT-INT.

As different sintering methods were used in the development of conductive Zn films, Figure 5.22 below compares different spectra based on the starting material, Zn powder against the effect of thermal heat treatment at 80ºC for 1 hr and photonically cured Zn film. The Zn powder itself was found to be partially oxidized which is expected after repeated exposure to air when handling outside a glove box environment. Therefore, even before sintering, the Zn powder itself was already oxidized which must be removed in processing. Whenever a thin film was deposited on a PVA substrate, a broad peak at 19.4º appears which cannot be fully be removed even with the use of Grazing Incidence X-Ray Diffraction (GIXRD). Generally, both sintering treatments saw all peaks shifted to the left when compared to the Zn powder signaling a shift in the lattice parameters. Standard heat treatment at 80ºC in air seemed to result in an amorphous film where additional peaks at 33.1º, 34.5º, 38.1º, and 44.3º are attributed to the remaining solvent as temperatures greater than 80ºC could not be use with PVA. These additional peaks were fully removed (and thus all solvents) when exposed to photonic curing however the same peaks related to ZnO remained as first seen in the Zn powder showing that further oxidation was not induced by photonic curing. In this case, the impertinent factor here is the initial state of the NPs. Although it was theoretically assumed that photonic curing could remove the oxide layer surrounding nanoparticles as reported by Dharmadasa et al., this was not the case.

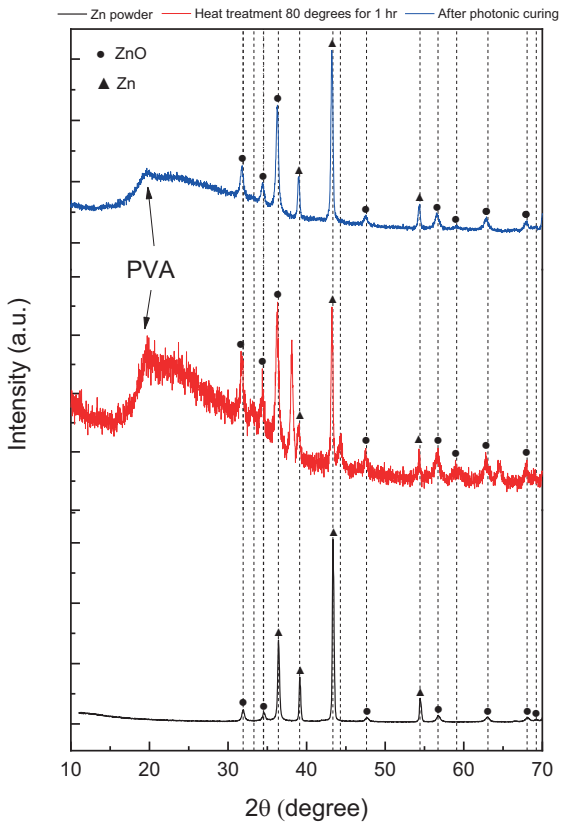

Figure 5.22. Effect of different heat treatment on the Zn films comparing Zn powder, oven thermal treatment at 80°C, and photonic curing

Another effect that was further investigated is whether or not the skin effect from photonic curing has any effect on the overall thin film development. For this, thermally heated treated films were compared against those that were photonically cured as thermal heat treatment tends to be more uniform in terms of penetration depth as compared to plasma and laser sintering. Figure 5.23 showed that not many differences appear in terms of peaks corresponding to Zn and ZnO respectively. However, the prominence or peak height increased with a greater number of layers. Zn related peaks at 43.2º and 54.2º appeared only with a greater number of layers (> 6 layers) meaning that the penetration depth of photonic curing is beyond 6 layers causing the film to lean more towards a ZnO structure. Unmarked peaks at 33.1º, 38.1º and 44.3º again are likely the result of inadequate removal of either butanol or DMSO both of which remained in the 6 layer sample once again reiterating that 6 layers is an insufficient number of layers for photonic curing. ZnO peaks at 59.0º and 64.5º found solely in the heat-treated film were eliminated after photonic sintering perhaps indicating that the process helped to reduce some oxidation first caused by thermal sintering.

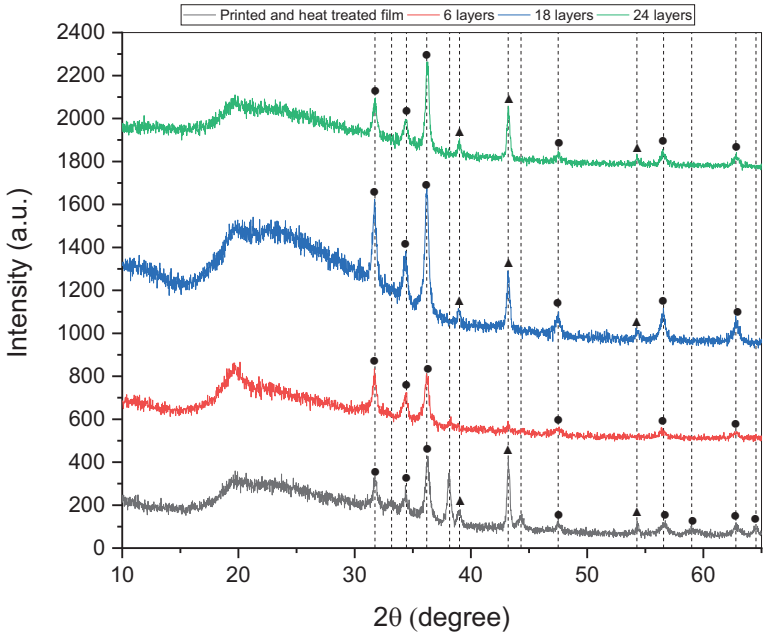

Figure 5.23. Effect of the number of printed Zn layers in response to photonic curing on a PVA/glass substrate

Figure 5.24 below displays different microstructures of photonically cured Zn films that vary depending on the ink used as well as the substrate. It was confirmed from Figure 5.7a that the number of NPs was sparse not only due to the clogging of the nozzles but also the fact that the NPs proceeded to agglomerate. This not only resulted in a discontinuous film but also a highly porous film with high roughness as shown in Figure 5.24a for the Zn/DMSO ink. In contrast, the Zn film developed from the Zn + DMSO + butanol ink (Figure 5.24b) resulted in a densely populated and uniform film where individual Zn nanoparticles can be seen further verifying that this ink formulation was optimal. However crack formation prevailed across the film unlike others. The same exact ink deposited and sintered on a PVA/PDMS substrate saw a mixture of film growth modes where a networking behavior between the NPs was seen however at the same time were aggregated and stacked displaying a non-uniform film that could be seen to the naked eye as shown in Figure 5.24c. In terms of uniformity, the pearl milled Zn ink (Figure 5.24d) was consistent in terms of both printability as well as film structure showing the very same structure as Figure 5.24a. Similarly, there are various white colored NPs that overall made it difficult to image the resulting film. This showed that the film was non-conductive and contained a majority of ZnO NPs as expected due to the milling process.

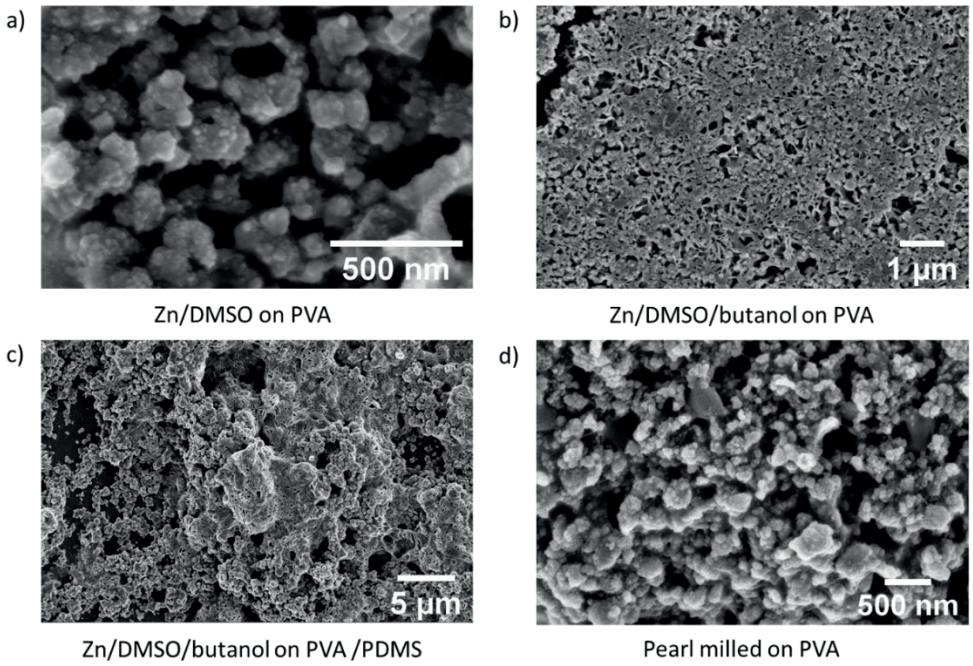

Figure 5.24. Response of photonic cured films on inks and different substrates where a) Zn/DMSO ink on PVA substrate, b) Pearl milled Zn ink on PVA substrate, Zn/DMSO/butanol ink on c) PVA substrate and d) PVA-PDMS substrate taken with the help of Ben Breitung at KIT-INT.

Another aspect to consider during the photonic curing process is the effect that the substrate has on the overall conductivity of the film. For example, initially all glass substrates were spin coated with PVA and initially used as a carrier for mechanical stability. However, once the film was removed or if another layer such as PDMS was added in between, the film was ultimately found to be non-conductive. Once the PVA/PDMS film was removed from the substrate, this dramatically lowered the thickness of the sample within the same order of magnitude (in 10s of microns for both), therefore the substrate saw the full intensity of radiant power applied eventually damaging it as a hole appeared in the middle of the sample. Photonic sintering directly onto PVA/PDMS layer proved difficult as the fragile substrate was more susceptible to delamination, warpage, and burning because the thin film above could not be sufficiently cooled via conduction through the thermal mass of the substrate.[37] This behavior was also seen in Zn films cured on PVA/PDMS/glass substrates where PDMS itself seems to contribute to ineffectiveness of photonic curing when combined together. However further studies must be conducted in order to verify these claims as only 1 sample for each type of substrate was tested. As a whole, as the inks only contained a maximum of 70 mg/mL with no more than 30 layers, the overall NP concentration is significantly less than similarly developed screen printing pastes and therefore should be taken into account.

Further analysis of the effect that the substrate may have on the resulting Zn film was conducted by XRD analysis as shown in Figure 5.25 for Zn films on substrates containing spin coated PVA/glass, spin coated PVA/PDMS/glass, and PVA/PDMS. One of the most prominent differences is the appearance of a broad peak with multiple shoulders spanning from 10 - 25º corresponding to the PDMS substrate below. Although it could not be correctly identified, the appearance of a new and broad peak at 40.6º most likely correlates with PDMS as it did not appear in the Zn/PVA/glass sample. And because of this, the respective XRD spectra for those containing PDMS were amorphous in nature thus preventing the appearance of sharp distinguished peaks. Those that could be identified across all samples were found at 31.7º, 36.2º, and 43.3º, the first of which is related to ZnO while the latter two correspond to Zn. Other peaks found at 38.9º and 54.4º corresponding to Zn and ZnO respectively were only found in the Zn/PVA/glass and Zn/PVA/PDMS/glass noting that the glass substrate not only provided mechanical stability for the films but also facilitated in conductive Zn film development which unfortunately was not the case for the Zn/PVA/PDMS film alone.

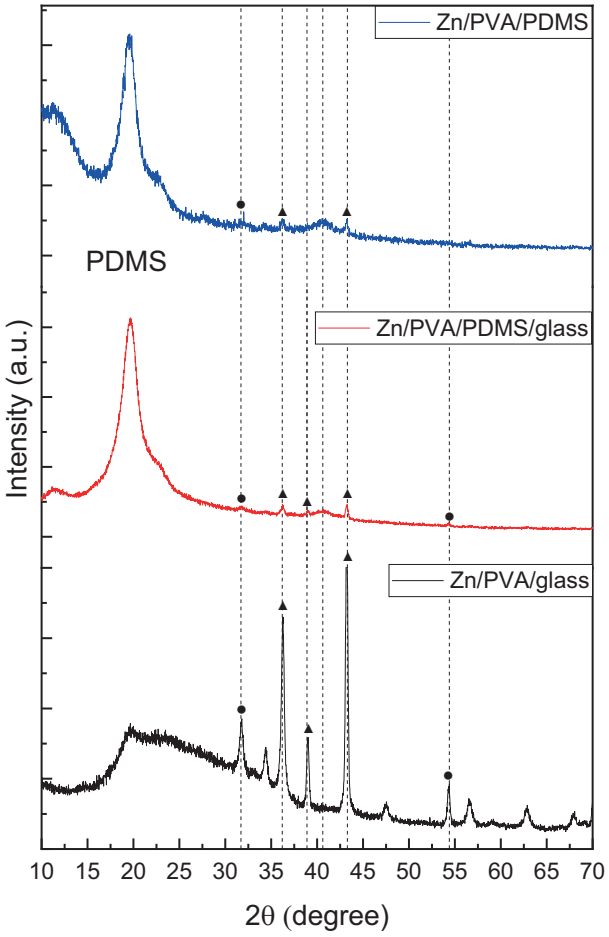

Figure 5.25. Effect of different substrates for Zn film development

Interestingly, when smaller structures such as line patterns were subjected to photonic curing, the appearance of the resulting film was drastically different than those seen with the standard square pattern perhaps showing a dependency of this technique on surface area. However, it is more likely that a smaller printed area equated to less variation in film morphology, meaning these films were more uniform as a result. Thus, completely different surface morphologies were a result signaling both successful and unsuccessful sintering runs are shown below in Figures 5.26 and 5.27 respectively. Figure 5.26 here displays different states of conversion for various line patterns as pictured from the least to the most converted (from Figure 5.26a – 5.26d). Conversion seems to occur specifically at the interior of the sample in clusters composed of either bare Zn NPs or ZnO flakes. This behavior occurs across the entire line surface and at different rates depending on the uniformity and material composition of the sample itself. As shown in Figure 5.26a, only small patches appear which may eventually grow larger if exposed to higher radiant power as shown in Figure 5.26b. However, if too much energy is applied, the film itself could mainly consist of ZnO flakes which is the case in Figure 5.26c.

Amongst all the partially converted films, the only one with the highest success was found for line patterns printed with 4 layers as shown in Figure 5.26d. Like the previously discussed square patterns, the majority of the film contained a mixture of metallic zinc and ZnO flakes with some remaining Zn NP ink interspersed between. In fact these two phases were seen almost contrary to one another as metallic Zn appeared more on the left side of the sample, while the ZnO dominated the right side. On the other hand, unsuccessful films, that is non-conductive structures, showed two modes of failure: film delamination or no change at all as shown in Figure 5.27a and 5.27b respectively. The commonality in these failure modes seems to be dependent on the energy used, that is too much applied energy caused delamination by using only 1 concentrated energy pulse during the single exposure or too little energy where no change in the film color nor to the structure was seen. The image taken in Figure 5.27b is indistinguishable from a non-sintered film still exhibiting a pure black color before and after treatment. Unfortunately, there was no consensus nor relation with the number of deposit layers as treatment with the same sintering parameters resulted in many different films, even on a singular substrate. An interesting commonality between all samples here was the fact that the edges appeared to be less converted than its interior. It is believed that because this ink exhibits the coffee ring effect, the edges were expected to be one of the least converted areas simply due to the height difference which can be as extreme as 12 μm as seen in Figure 5.11a.

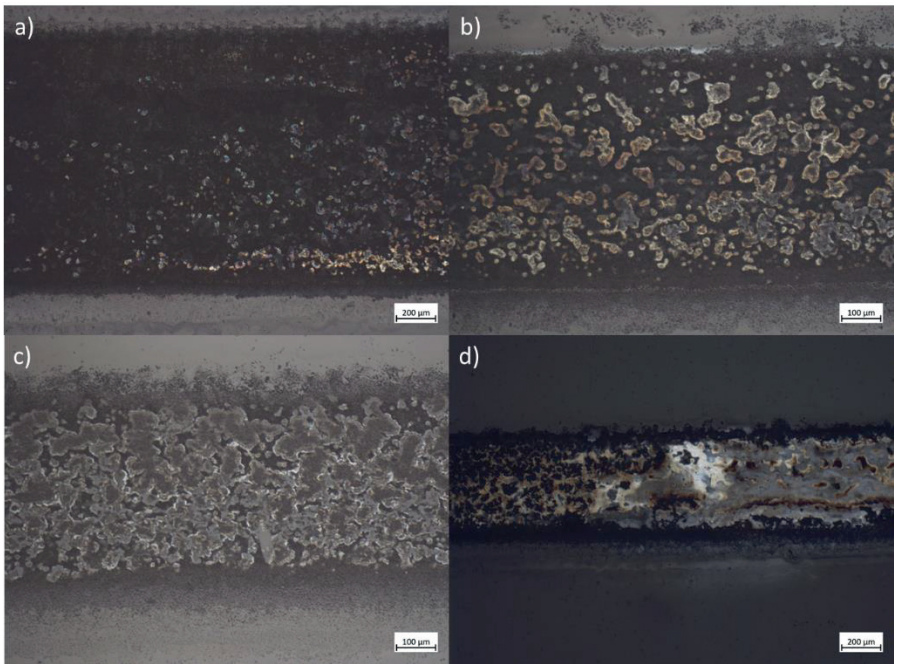

Figure 5.26. Different surface morhologies of photonically cured Zn thin films on spin coated PVA/ glass slides with 4 deposited layers a) 5x magnification, b) 10x magnification, c) 10x magnification, and d) 5x magnification

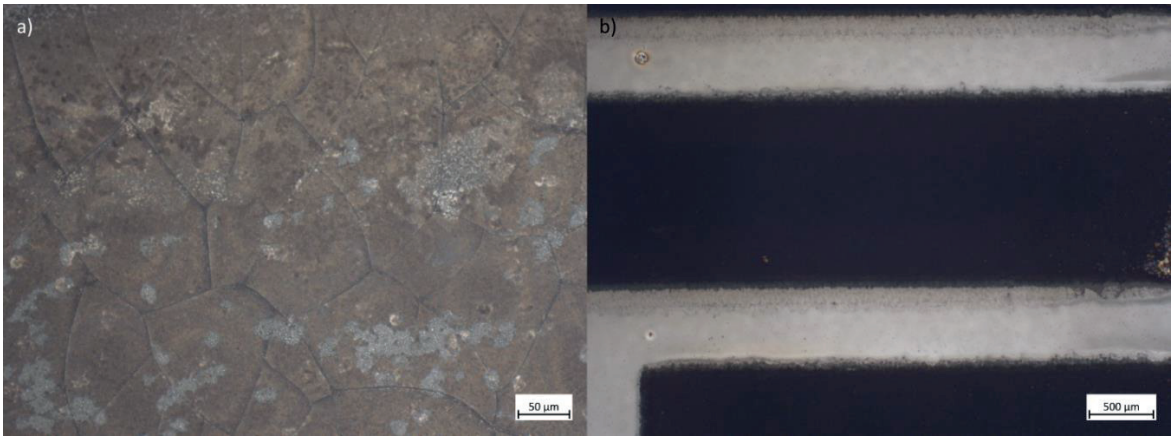

Figure 5.27. Failure modes as seen with photonically cured line pattern films in terms of a) delamination b) no change in color or structure

As testing was not standardized due to the limited testing period and number of samples, only limited conclusions can be drawn at this point without further testing. Although according to XRD analysis, photonic curing was effective in the removal of both DMSO and butanol solvents which helped to expose Zn NPs to make the film conductive. However, both the radiant power applied and film uniformity must be precisely controlled to guarantee the success of this sintering technique.

Pearl Milling Zn films

Although the pearl milled drop casted film already showed different morphologies as reviewed in Figure 5.10, photonic curing served to homogenize the films displaying mostly uniform composition of stacked and clustered NPs for both samples PM1 and PM2 as shown in Figure 5.28a, 5.28c, and 5.28d. However, other crystalline morphologies such as the appearance of a ZnO flower shape were found in sample PM1 as shown in Figure 5.28b. Such growth is typically a result of exposure to alkaline solution that at higher concentrations show an urchin-like appearance.[38,39] Here, Zn^{2+} ions are exposed to OH- groups that result in an $Zn(OH)_4^{2-}$ complex forming a large number of ZnO nuclei.[40,41] These nuclei then create aggregates as a result of high surface energy and electrostatic forces that form ZnO cyrystallites providing active sites that sees preferential growth in the [0001] orientation along the *c-axis* developing nanorods.[40,41] This is what gives the structures a flower-like shape. The existence of such a structure only provides further proof that the sample contained additional ZnO not previously exhibited before its sintering treatment. Sample PM2 showed a consistent NP size with a small distribution signaling that the PAANa stabilizer implemented remained and continued to separate NPs from one another, so much so that no sintering was seen between NPs as shown in Figure 5.28d. Although not exactly something quantifiable, Sample PM1 appeared to be less conductive

than Sample PM2 meaning that a higher applied radiant power equated to a more conductive sample even with pre-oxidized samples such as the PM Zn ink.

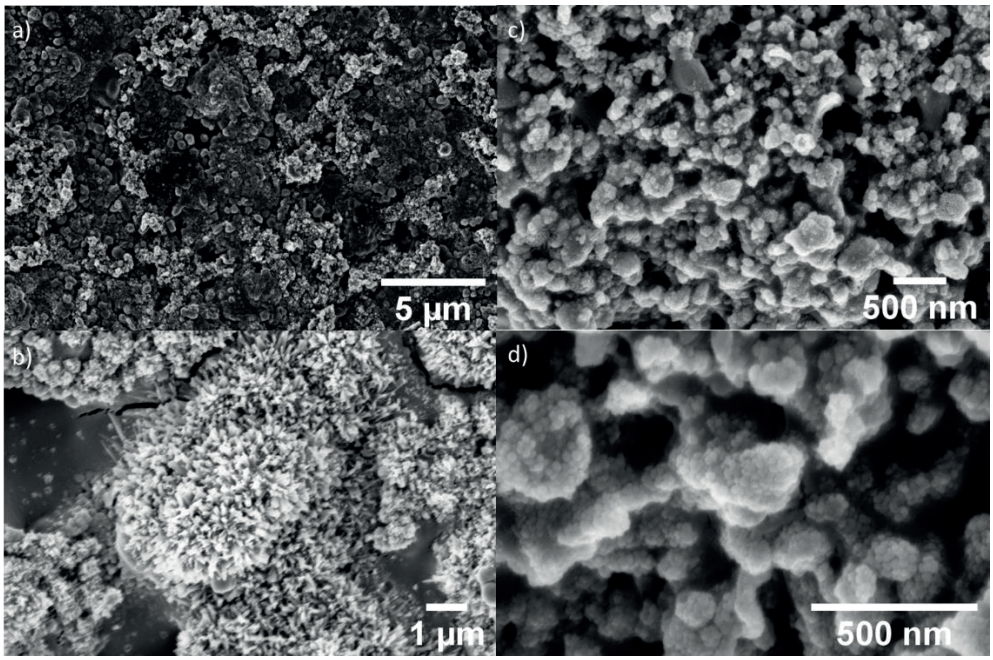

Figure 5.28. SEM analysis of pearl milled (PM) samples a) PM1 at 9000x magnification, b) PM1 at 5000x magnification, c) PM2 at 24,000x magnification, and d) PM2 at 75,000x magnification taken with the help of Ben Breitung at KIT-INT.

Further thin film analysis of the PM samples was done using XRD analysis as displayed in Figure 5.29 below. When compared to the initial Zn powder, both the sintered samples presented amorphous films containing a large amount of background noise making it difficult to identify all peaks. However the identifiable peaks corresponded to both synthetic Zn and ZnO phases in agreement with JCPDS cards no. 01-078-1124 and 01-074-0534 respectively after photonic curing treatment at radiant power of <6.61 kw/cm^2 for sample PM1. Peaks found at 36.2°, 38.9°, and 43.3° corresponded to (002), (100), and (101) crystal planes for hexagonal synthetic Zn while the remaining peaks at 31.7°, 34.4°, 47.5°, 56.6°, 62.9°, and 68.0° corresponded to (100), (002), (102), (110), (103), and (112) crystal planes for cubic ZnO. As sample PM2 was exposed to higher radiant power (<7.32 kw/cm^2), the film was identified to contain 3 phases: Zn, ZnO, and zinc peroxide (ZnO_2) corresponding to JCPDS cards no. 01-078-1124, 01-074-0534, and 00-004-0831 respectively. The appearance of the ZnO_2 cubic structure was identified with the peak at 45.5° that solely appeared in Sample PM2 as the film presented a bright yellow color following the sintering process. According to the XRD spectra, photonic curing of PM Zn ink only served to further oxidize the Zn NPs which was apparent with the disappearance of the Zn peak found at 54.4° for both PM samples as well as the additional disappearance of the

corresponding peak at 39.1° for the PM2 sample. In fact, with higher energy exposure, any remaining peaks relating to synthetic Zn (36.4°, 39.1°, 43.4°, and 54.4°) either reduced drastically in size or were eliminated as a result. By comparison, the identifiable peaks of PM1 and PM2 mostly corresponded to the Zn powder but saw a slight shift to the left. These result shows the limitation of photonic curing that although was found to be successful for CuO, did not have the same effect for oxidized Zn NPs

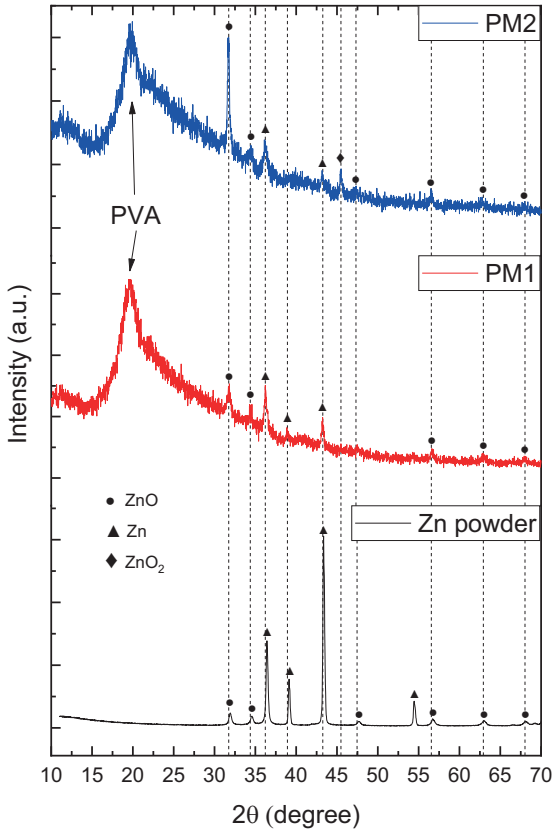

Figure 5.29. XRD analysis of pearl mill Zn inks in comparison with the Zn powder

Electrical Measurements

Those samples investigating line width and line length were also exposed to photonic curing and tested directly before and after sintering using the 4-point probe method as provided by KIT-LTI. This inline type of measurement is highly dependent on the distance between the 4 probes which was determined to be 3 mm (Figure 5.30). Therefore any measurements of shorter line lengths was not possible using this technique and are therefore not reported here. Prior to curing, each of the structures were tested for conductivity of which all appeared to be completely non-conductive or presented a sheet resistance in 100s of MΩ. However after photonic curing was

applied, sheet resistance values varied from as low as 1.97 kΩ to as high as 27.5 MΩ if found to be conductive at all.

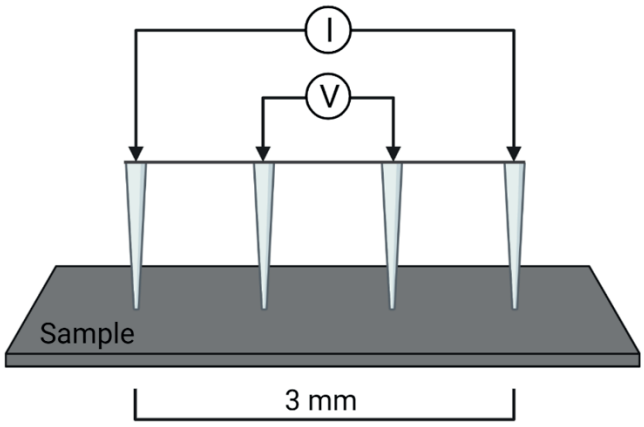

Figure 5.30. Four-point probe measurement

Generally, larger areas presented more conductive structures due to the greater amount of Zn NPs being deposited. Unfortunately, results pertaining to the 4 deposited layer sample were in the end inconclusive mostly due to the variability in uniformity across the sample. In comparison, this sample was highly transparent as 9 layers was previously deemed to be the optimal number of layers showing a huge disparity between samples. In fact, after photonic sintering, the sample was burnt meaning the sintering temperature produced was beyond the boiling point of the solvent leaving residue on the PVA surface after testing resulting in both a cracked and delaminated/ablation film from the PVA surface. Uneven conversion was seen across the surface where lines with greater thickness saw less conversion than thinner lines. This is most likely due to the higher uniformity and quick removal of the solvent from a smaller area. At best, 4 mm x 4 mm squares presented a resistance as low as 1.97 kΩ.

Figure 5.31 displays the printed and photonically cured square with the highest conductivity of the exposed samples. The film sees a mostly light grey color which appears to be a ZnO layer that comprises the majority of the film as shown in Figure 5.31a. Taking a closer look at the film, a silver colored appears in scattered areas around the surface of the film where Zn NPs are exposed making the film conductive, like the behavior shown in Figure 5.21 where percolation pathways are established beneath the ZnO layer. The profile measurement in Figure 5.31c revealed a surface roughness of 2.2 μm and an average film thickness of 0.6 μm. Electrical measurements taken directly after sintering were found to be an average of 6467 Ω, whereby through calculation correlated to a conductivity of 2.7×10^2 $S \cdot m^{-1}$.

Figure 5.31. HIROX Digital microscope measurements for Zn film printed with Zn/DMSO/butanol with 12 layers at a DS of 35 µm a) 40x magnification, b) 130x magnification, and c) extract profile measurement

As stated previously, a minimum of 9 layers must be deposited for the Zn + DMSO + butanol ink as similar samples printed with 4 or 6 layers resulted in highly resistive structures (85MΩ minimum) or no conductivity at all particularly for square samples. Therefore, in order to determine the dependency on minimum line length and width to develop conductive structures, different line lengths ranging from 1 – 10 mm with thicknesses from 300 – 1000 µm were explored as seen in Figure 5.32 below. Due to the probe distance, a line with a minimum length of 3 mm could be measured directly following sintering. All results were tabulated in Figure 5.32a showing that generally the line thickness or width is inversely proportional to its sheet resistance, that is that the sheet resistance decreases with greater line thickness. This is similarly true in terms of line length as well where all sheet resistance values were minimized at line lengths 8 mm or above. In fact, the most consistent values were seen using 900 µm thickness which saw similar resistances across all line lengths as shown in Figure 5.32b. A similar behavior was seen with 600 µm thick lines however on the average tended to be twice the resistance. Therefore, any future structures made with the Zn ink must have at least 9 layers, 900 µm thickness, and contain a line length of at least 4 mm in order to achieve maximum conductivity which in this case was found to be 0.165 MΩ. The exact structures developed for test can be seen in Figure 5.32c below.

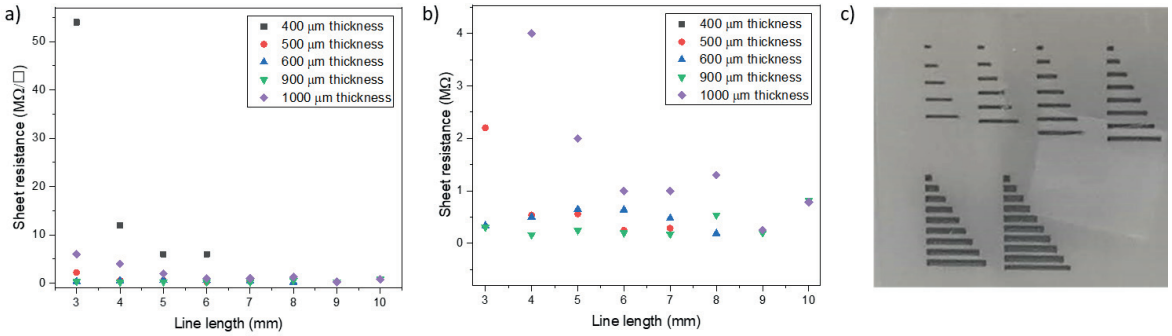

Figure 5.32. Pyramid samples printed with 9 layers a) Effect of line length and thickness on sheet resistance of the Zn films as deposited by a Zn/DMSO/butanol ink for 9 layers and b) photograph of the successful sample

It was proposed that due to the uneven coverage of the Zn film as a result of the inkjet printing process may render photonic curing ineffective. Zn is known to oxidize when exposed to air and because testing could only be conducted in this mode, oxidation was an issue that impeded the optimal sintering for these inks. Although some success was found, the overall conductivity was significantly lower than reported in literature. Additionally, due to a limited time period (approximately 2 weeks) spent with using this technique, this process could not be optimized as desired. It was suggested that perhaps carbon black could be used to help further increase the conductivity without compromising the biodegradability. This amongst others are included in future work.

5.4 | MO NP FILM DEVELOPMENT

All work concerning the development of Mo ink and characterization were performed by Dra. Sandra Pérez Rafael. Her results were reported in several internal presentations as well as a poster as a part of the IMB-CNM Young Researchers Day titled “Development and characterization of biodegradable inks based on molybdenum and zinc nanoparticles”. My contribution to this part is in regards to the integration and viability of Mo NP inks onto biodegradable substrates such as PVA.

5.4.1 | INK DEVELOPMENT

The same exact ink development procedure as stated in Section 5.3.1 was utilized here in order to develop Mo NP inks starting with ink stabilization/compatibility when Mo NPs were dispersed to a large number solvents via ultra sonication for 1.5 hrs which were first visually inspected for stability after 72 hrs as seen in Figure 5.33 below. Tetralin exhibited the worst stability displayed showing immiscibility with Mo NPs, followed by mesitylene and

cyclohexylbenzene where the majority of Mo NPs sedimented while a small amount remained dispersed in the solution. Stability improved slightly using N,N-Dimethylacetamide (DMA), dimethyl sulfoxide (DMSO), and N-Methyl-2-Pyrrolidone (NMP) however their separation is unacceptable for stable ink formulation. Among them, ansiole, cholorobenzene (CB), 1,2-dichlorobenzene (DCB), isopropanol (IPA), and butanol visually exhibit good stability. Although anisole was acceptable, it must be noted that both separation and sedimentation appeared to be occurring at a slower rate than the previously mentioned solvents however still showed good stability compared to others. Here, both butanol and IPA exhibited high stability prompting further testing combining different solvents together to determine if stability could be further improved.

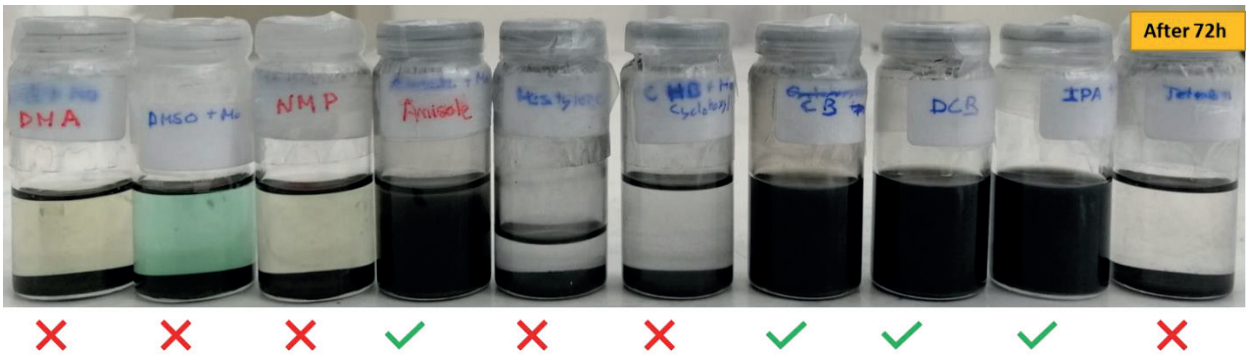

Figure 5.33. Ink stability testing following Mo NP dispersion in (left to right) N,N-Dimethylacetamide (DMA), dimethyl sulfoxide (DMSO), N-Methyl-2-Pyrrolidone (NMP), anisole, mesitylene, cyclohexylbenzene, chlorobenzene (CB), 1,2-dichlorobenzene (DCB), isopropanol (IPA), and tetralin. Results were first reported in unpublished results by the lead scientist for these experiments, Dra. Sandra Perez.

Here, different iterations of butanol and IPA were infused with anisole, CB, DCB, IPA, and ethylene glycol (EG) and tested for 1 week as shown in Figure 5.34 below. It was discovered that if butanol and IPA were combined with other solvents, ink stability decreased. This was especially apparent for those solvents combined with IPA which showed the best result overall followed by the butanol alone. This experiment determined that the addition of an additional solvent did not help to improve the ink stability and therefore was discarded in terms of ink formulation. Following this, different capping agents were also tested such as polyethylene glycol (PEG), polyvinylpyrrolidone (PVP), and ethylenediamine in combination with butanol as shown in Figure 5.35. Ethylenediamine presented the worst results where complete separation of NPs from the solution was seen while others such as PEG and PVP saw decent dispersion stability however each saw sedimentation of NPs at the bottom of the vials. Although not listed here, a dispersion containing 5 mg/mL PVP in butanol saw significantly better stability, therefore the concentration of all capping agents was increased to 5 mg/mL and tested using DLS to determine the exact distribution in NP size after being exposed to different solvents and agents.

Figure 5.36 displays that the average size for each of the inks containing butanol (20 mg/mL), butanol/PEG 200 (5mg/mL), butanol/PEG 10k (5 mg/mL), and butanol/PVP 10k (5mg/mL) are 47.5, 44.6, 85.6, and 118.8 nm respectively. The initial size of the NPs as stated by the manufacturer was stated to be between 30 – 40 nm in size, therefore an increase in size is expected when a stabilizer is used. Butanol/PEG 10k (5 mg/mL) ink exhibited both the narrowest distribution with an average NP size of 44.6 nm. It is believed that PEG was extremely effective at encompassing the NPs and maintaining their initial sizes, which is especially beneficial for inkjet printing. Pure butanol was the next best result however any oxidation issues cannot be resolved using this combination and in the end was discarded. PEG with a larger molecular weight of 10k saw a much wider NP distribution between 30 – 220 nm signaling that this ink maybe incompatible with inkjet printing as NP with sizes above 100 nm have a higher probability for agglomeration and blocking nozzles. A similar result was seen with PVP (10k) which saw two different populations, a smaller one between 15 – 50 nm and another between 50 – 400 nm, widely varying and maybe highly difficult to print as a result with an average that is already higher than recommended for inkjet printing.

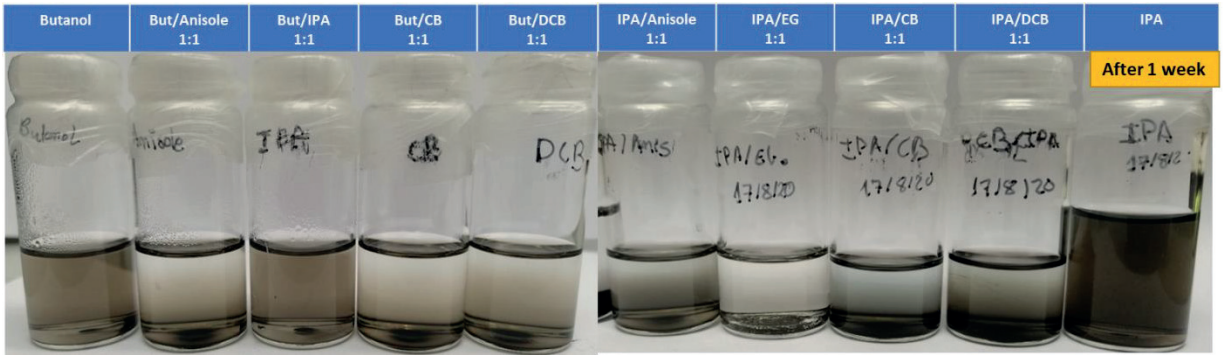

Figure 5.34. Solvent stability testing among (listed from left to right) butanol, butanol/anisole (1:1), butanol/IPA (1:1), butanol/CB (1:1), butanol/DCB (1:1), IPA/anisole, IPA/EG (1:1), IPA/CB (1:1), and IPA/CB (1:1), and IPA. Results were first reported in unpublished results by the lead scientist for these experiments, Dra. Sandra Perez.

Figure 5.35. Capping agent compatibility with butanol as the solvent (as listed from left to right) in PEG 200, PEG 10k, PVP, and ethylenediamine each with a 1 mg/mL. Results were first reported in an unpublished powerpoint presentation by the lead scientist for these experiments, Dra. Sandra Perez.

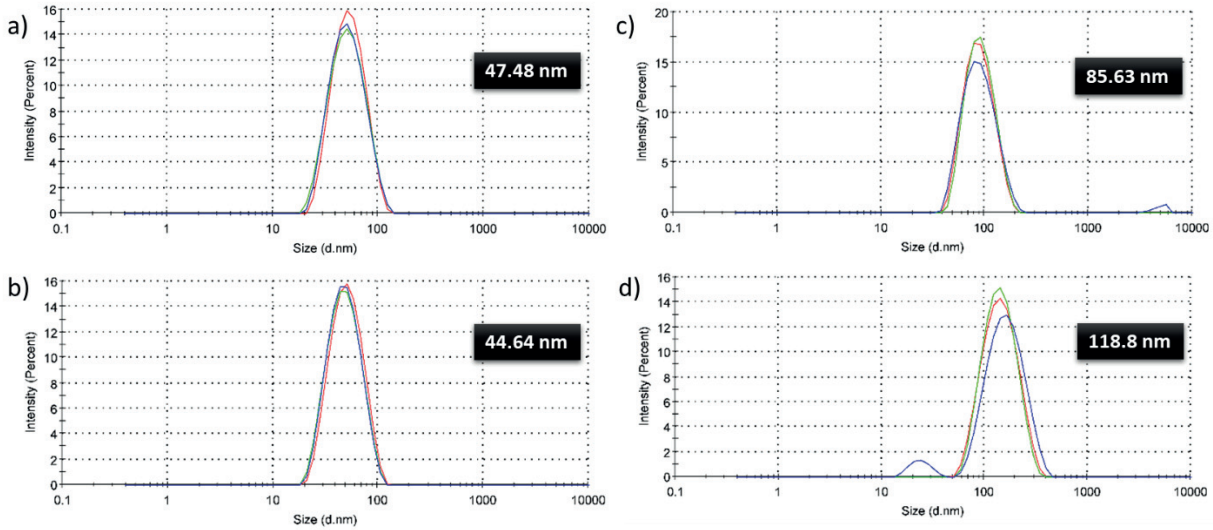

Figure 5.36. DLS measurement results for a) butanol (20 mg/mL), b) butanol/PEG 200 (5mg/mL), c) butanol/PEG 10k (5 mg/mL), and d) butanol/PVP 10k (5mg/mL). Results were first reported in unpublished results by the lead scientist for these experiments, Dra. Sandra Perez.

5.4.2 | INK FORMULATION

Pre-synthesized nanoparticles of Molybdenum (Mo) Nanopowder/Nanoparticles (Purity: 99.95%, Size: 30-40 nm) were purchased from Nanografi Nanotechnology Co. Ltd. and used as is. Ethylene glycol 99% (EG, $C_2H_6O_2$) was purchased from Alfa Aesar while dimethyl sulfoxide (DMSO), anhydrous ≥99.9%, polyvinylpyrrolidone (PVP, average mol wt 10,000),

poly(ethylene glycol) (PEG, average mol wt 200), and 1-Butanol (anhydrous, 99.8%) obtained from Sigma Aldrich was used instead of butanol as this prevented further oxidation to the ink.

As a result, different types of Mo inks were explored and chosen based on their respective reaction to both PEN and PVA substrates as not all solvents were compatible as compared to more conventional polymer substrates which were first characterized by Sandra Perez. All formulations are stated below of which the concentrations were manipulated if too much agglomeration was seen:

Mo/PVP/butanol ink: 100 mg of Mo NPs and 10 mg of PVP were weighed and combined. Next 2 mL of butanol was added resulting in a 50 mg/mL Mo dispersion respectively.

Mo/PVP/butanol/EG ink: 140 mg of Mo NPs and 4 mg of PVP were weighed and placed together. Next, a 9:1 ratio of butanol to EG was added to create a 70 mg/mL dispersion.

Once each of the components for each of the respective inks were combined, the dispersion was then mixed with the vortex for 10s followed by ultra sonication for 1 hr. additionally, tip sonicator was set at an amplitude of 30% for 5 minutes to facilitate separation between the nanoparticles and improve dispersibility. Before printing, the supernatant liquid sat for 2 minutes before placing into the ink cartridge.

5.4.3 | INKJET PRINTING

Different substrates were investigated which varied in terms of maximum processing temperatures. PVA was the lowest at 80°C, followed by PEN at 220°C, and finally glass at 400°C which helped to show a wide range of behaviors in terms of interaction with substrates and the effect of different sintering temperatures.

Inks containing 50 mg/mL in butanol and combined with 5 mg/mL of PVP and butanol were inkjet printed onto PEN substrates. Figure 5.37 below displays line patterns printed for each respective ink at RT and 60°C. Although the Mo/butanol ink was previously noted as one of the most stable inks, its respective printability with PEN using multiple platen temperatures was incompatible with PEN as displayed in Figure 5.37a and 5.37b. This may be due to multiple causes, that is the pre-treatment of PEN was insufficient and/or the surface tension of the ink with respect to the substrate was low displaying poor wettability. In complete contrast, Mo NPs (50 mg/mL)/PVP (5 mg/mL)/butanol ink showed decent printability however bleeding/spreading of the printed patterns was seen in Figure 5.37c. This behavior could be remedied when setting the platen at higher temperatures however the severe coffee ring effect continues to be exhibited regardless of the printing parameters.

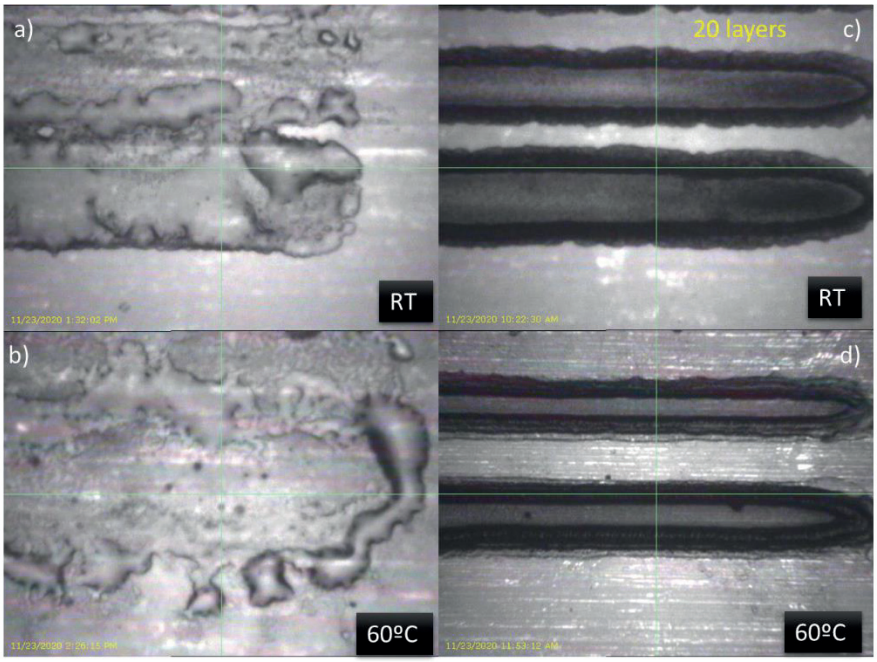

Figure 5.37. Printed line patterns by Mo NPs (50 mg/mL)/butanol ink for 20 layers at a) RT and b) 60°C and Mo NPs (50 mg/mL)/PVP (5 mg/mL)/butanol ink at c) RT and d) 60°C as deposited onto PEN substrates. Results were first reported and adapted from unpublished results by the lead scientist for these experiments, Dra. Sandra Perez.

As PEN substrates can only withstand up to 170°C, less temperature sensitive substrates such as glass was also considered. For this test, two inks were investigated including Mo NP (50 mg/mL)/PVP (5 mg/mL) ink dispersed in butanol and Mo (70 mg/mL)/PVP (2mg/mL) ink dispersed in a 9:1 butanol:ethylene glycol. The optimal DS for each respective ink was 30 µm and 25 µm, smaller than those found on PEN substrate as inks tend to exhibit hydrophobic behavior with glass substrates. The Mo/PVP/butanol ink was printed up to 50 layers at RT (Figure 5.38a) which exhibited severe line roughness behavior previously seen on PEN which only became more exaggerated with more printing layers thus affecting the pattern definition. However, a very thick, almost paste like film was formed as a result displaying similar non-uniformities as previous reported however to a lesser effect. The other ink, Mo (70 mg/mL)/PVP (2mg/mL) dispersed in a 9:1 butanol : ethylene glycol, displayed no line pattern roughness which may be attributed to three factors: the addition of EG, the use of a lower DS, and increased platen temperature to 45°C. Figure 5.38b displays the appearance of the film just after 40 printed layers for a square which saw a wide distribution of holes around all parts of the film. The larger impurities at the center of the film appeared to be due to NP agglomeration whereas the holes more towards the edge of the film appeared as smaller structures.

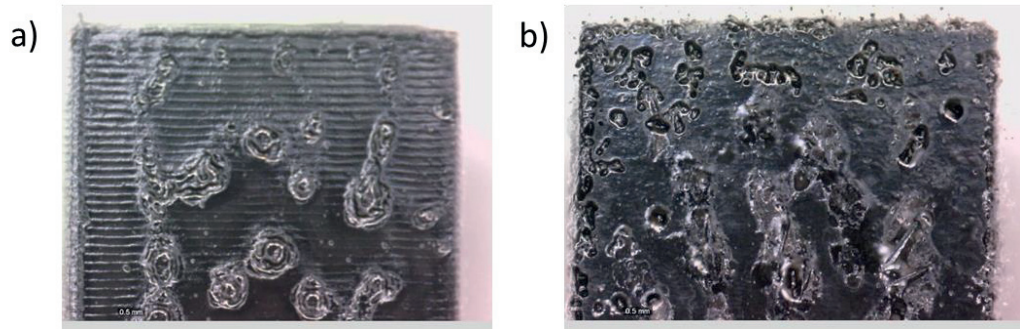

Figure 5.38. Printed Mo ink squares a) 50 layers printed of Mo NP (50 mg/mL)/PVP (5 mg/mL) dispersed in butanol with a DS of 30 μm at RT on glass. b) Mo (70 mg/mL)/PVP (2mg/mL) dispersed in a 9:1 butanol: ethylene glycol deposited ink for 40 layers printed squares with a DS of 25 μm at 45°C on glass substrate. Results were first reported and adapted from unpublished results by the lead scientist for these experiments, Dra. Sandra Perez.

When such inks were printed onto PVA substrates, its overall behavior matched what was seen on both PEN and glass substrates. As the line pattern can be used as an indicator of printability, the lightly packed lines indicated that multiple layers will need to be deposited in order to create a continuous film. There was excellent NP distribution in a single printed line already exhibiting the coffee ring effect for just 1 printed layer (Figure 5.39a). However because NP concentration was lowered to reduce any NP agglomeration, a large number of layers must be deposited in order to develop a continuous film, taking the line pattern as a good indication. Figure c39b - 5.39j documents the layers as they were sequentially printed every 3 layers. Already within 3 layers, non-uniform layer was seen particularly at the center of the deposited film as well as the appearance of line edge roughness from every printed line (Figure 5.39b). This defined the overall roughness of the film which increased with every layer. Specific areas towards the center as well as the edges sees localized NP agglomerations adding more roughness and non-uniformity in the film by 9 layers (Figure 5.39d). Also, the definition of the printed shape became poorer resulting in wavy edges. This behavior continued until 21 printed layers (Figure 5.39g) where then by 24 layers (Figure 5.39h) finally becomes saturated with the ink creating and opaque and extremely rough layer. In comparison, the same ink printed with a DS of 40 μm sees a similar behavior however the square pattern was severely less defined showing poorly defined pattern edges (Figure 5.40a). This perhaps was the result of satellite drops ejected from the ink. Severe NP agglomeration was seen throughout the printed layers beginning at 9 layers until 30 layers (Figure 5.40c – 5.40j). However the larger DS exhibited significantly greater amount of agglomeration and thus higher roughness. The Mo ink containing a concentration of 50 mg/mL required at least 30 layers to have a continuous and opaque film while the Mo ink with 70 mg/mL needed at least 12 layers mostly due to the increased NP concentration.

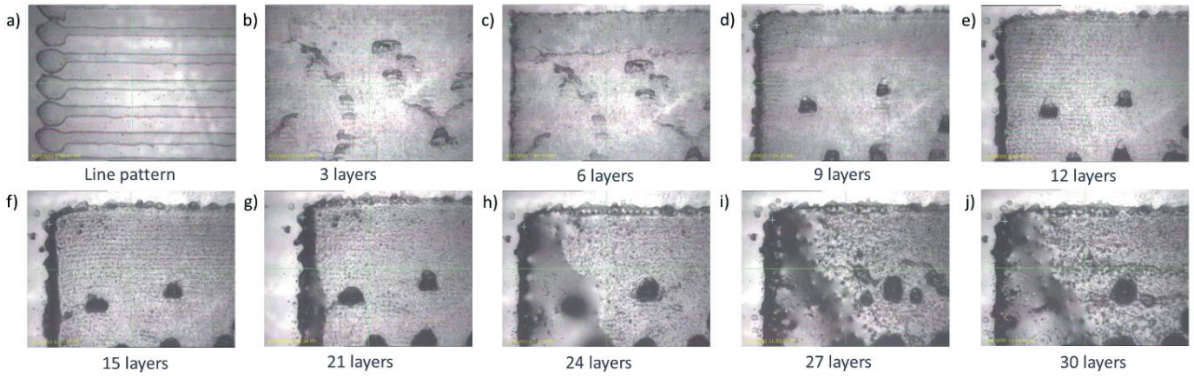

Figure 5.39. Printed patterns of Mo NPs (50 mg/mL) + PVP (5 mg/mL) + butanol ink a) line pattern and b) – j) are sequentially printed layers from 3 – 30 layers for DS of 35 μm on PVA

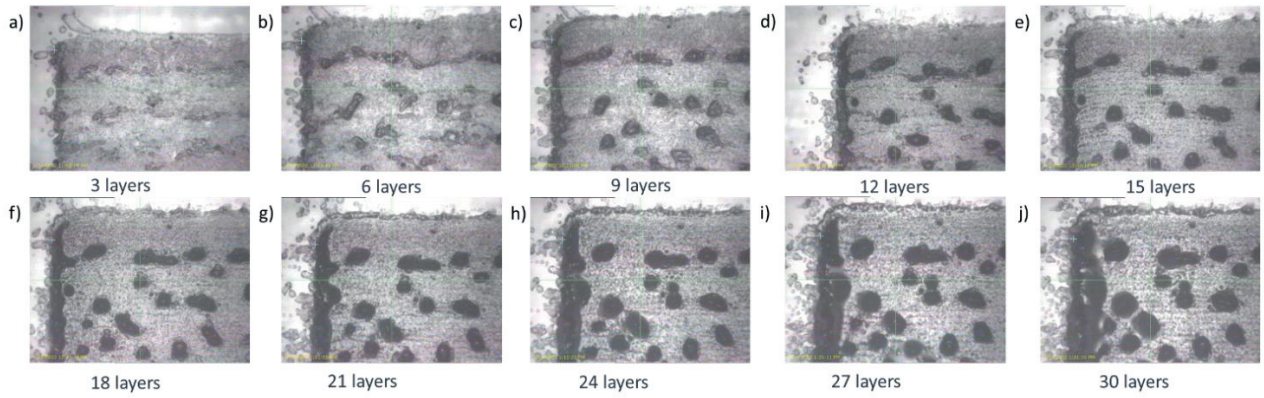

Figure 5.40. Printed patterns of Mo NPs (50 mg/mL) + PVP (5 mg/mL) + butanol ink a) line pattern and b) – j) are sequentially printed layers from 3 – 30 layers for DS of 40 μm on PVA

As a result, large islands of agglomerated NPs were present throughout the printing process which significantly became worse with the growing number of layers as seen in Figure 5.41 below. This effect appears to be slightly more severe as the DS increased creating more gaps and pits throughout the film. Additionally, the color of these films exhibited more of a grey color than the black as shown on PEN and glass substrates meaning that they are more transparent indicating that perhaps a greater number of layers is needed. Unfortunately, the effect of increasing the number of layers is that more NP agglomerations appeared as seen with those films deposited with 42 layers displaying once again the non-uniformity of the film.

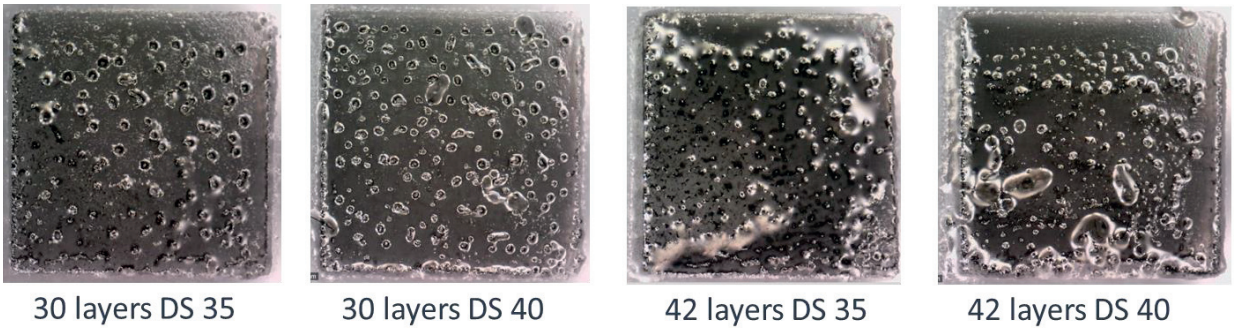

Figure 5.41. Printed and heat treated squares of 30 and 42 printed layers of Mo NPs (50 mg/mL) + PVP (5 mg/mL) + butanol ink on PVA

5.4.4 | THERMALLY TREATED FILMS

Different surface morphology techniques were used to characterize the Mo films including SEM , profilometry, and standard optical microscopy. SEM analysis was conducted on 20 layer printed line patterns printed by the Mo NPs (50 mg/mL)/PVP (5 mg/mL)/butanol ink which revealed good uniformity towards the middle of the pattern while the edges appeared to be non-uniform even exhibiting an entirely different elemental composition either containing more solvent or oxidized NPs as noted by the color difference (Figure 5.42a). When investigating more deeply into the center of the film, Figure 5.42b noted that there was good distribution and uniformity across the film surface displaying NPs of varying sizes as expected. Figure 5.42c provided an even closer view showing that the NPs appeared to be isolated from one another mostly likely due to the insufficient sintering temperatures (220°C) preventing the removal of PVP and thus hindering NP coalescence. These thin films exhibited a film thickness of ≈ 1 μm which contributed to the low conductivity. From this, it is apparent that higher temperatures are needed in order to initiate melting between NPs, therefore, this ink was also deposited onto a glass substrate to determine whether or not increased temperatures would help to facilitate sintering between particles on less temperature sensitive substrates.

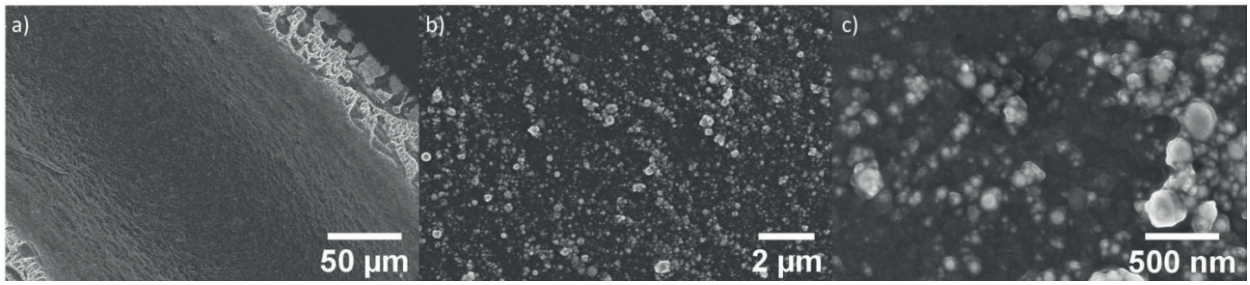

Figure 5.42. SEM micrographs of Mo/PVP/butanol ink deposited and heat treated film at a magnitude of a) 1000x, b) 20,000x, and c) 100,000x. Results were first reported and adapted from unpublished results by the lead scientist for these experiments, Dra. Sandra Perez.

As sintering temperature on PEN was restricted to 220°C, a glass substrate was then used to sinter the ink at higher temperatures (400°C) for 4 hrs in order to enhance the conductivity. For this test, two inks were investigated including Mo NP (50 mg/mL)/PVP (5 mg/mL) ink dispersed in butanol and Mo (70 mg/mL)/PVP (2mg/mL) ink dispersed in a 9:1 butanol/ethylene glycol. The Mo/PVP/butanol ink printed up to 50 layers at RT saw the previously printed irregularities reduced in size most likely due to the complete removal of both the stabilizer and solvent by this point. Here, the film turned from the initial black color of the freshly deposited film to a light grey color as seen in Figure 5.43a. Thermal sintering of the Mo NP (70 mg/mL)/PVP (2mg/mL) dispersed in a 9:1 butanol : ethylene glycol deposited ink squares (Figure 5.43b) saw light and large grey colored impurities and holes scattered across the surface of the film which increased in size compared to its freshly printed state in Figure 5.38b. In fact the edges of these impurities appeared to be less sintered as they showed a cracked and black appearance in contrast to the rest of the film. The larger impurities at the center of the film appeared to be NP agglomerations whereas the holes more towards the edge of the film appeared as smaller structures. Based off of appearance, both films displayed high roughness both before and after sintering treatment for opposing reasons however what is apparent is that Mo NP agglomeration remains the main issue for these inks.

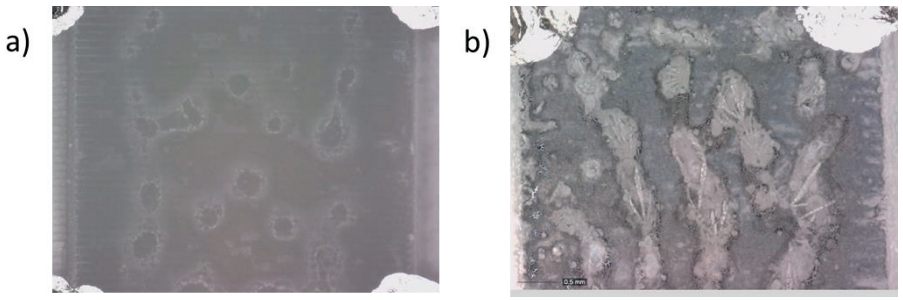

Figure 5.43. Sintered Mo ink squares containing a) 50 layers printed of Mo NP (50 mg/mL)/PVP (5 mg/mL) dispersed in butanol with a DS of 30 µm at RT on glass. b) 40 layers of printed Mo NP (70 mg/mL)/PVP (2mg/mL) dispersed in a 9:1 butanol: ethylene glycol deposited ink with a DS of 25 µm at 45°C on glass substrate. Results were first reported and adapted from unpublished results by the lead scientist for these experiments, Dra. Sandra Perez.

All samples printed on PVA were heat treated in a convection oven at 80ºC for 2 hrs being careful not to reach its glass transition temperature. This resulted in completely non-conductive structures as temperatures achieved here were not great enough to remove PVP from the films. Additionally, the chosen sintering temperature is far below the actual reported melting temperature of Mo making thermal treatment on PVA and other polymer substrates insufficient to create conductive structures thus making photonic curing the only option.

5.4.5 | PHOTONIC CURING

Photonic curing was applied to a variety of squares printed with 40 layers using the 70 mg/ml Mo in Butanol/IPA 2:1 ink in the hopes of improving the conductivity. Figure 5.44a shows a Mo film before undertaking treatment which resulted in a wide range of film modes (Figures 5.44b - 5.44i) depending on the sintering parameters applied. Film peeling appeared first initiating at the edges which with sequential exposure leads to clean film ablation as shown in Figure 5.44b. This is a result of too high radiant energy or power exposure to the film reaching maximum temperatures higher than the substrate gasification temperature.[42] As the Mo ink requires extremely high sintering temperatures, this effect cannot be avoided on flexible polymer substrate unless using a substrate with much greater temperature resistance such as Si. In fact, no color change was seen on treated films when compared to the printed sample typically symbolizing non-conductive samples. However, films with resistances as low as 300Ω were achieved depending on the sintering parameters.

Successful runs, as reported by Sandra Perez Rafael, typically used a voltage of 380V and pulse length of 550 µS with a variety of pulses maintaining a distance of 12 mm. Typically, a single sample here would be exposed to multiple steps until optimal conductivity was achieved. The first among these is Figure 5.44b (Sample 1) displays a wide variety of pulses, voltages, and

pulse lengths applied until the square showed some conductivity. At least 4 pulses at a voltage of 350V at a pulse length of 550 μs was needed to achieve some conductivity found to be 23kΩ. From there, the voltage was increased to 400V seeing a decrease in the resistance down to 5kΩ and finally a last change in voltage back to 350V and an increase in the pulse length to 1150 μs saw the reduction of resistance all the way to 800 Ω. However further treatment with the same exact parameters resulted in a burnt sample, especially in areas where no film was seen and instead only heated the film as shown in Figure 5.44b. Mostly the film at the middle and the top edge of the sample remained mostly showing an overall cohesive failure of the ink with the PEN substrate. An enhanced view seen in Figure 5.45a showed that cracks in the sintered film appeared as weak points where then the film tended to peel while crack formation is in agreement with the line pattern roughness produced from the initial printing. It is known that just a single pulse is not recommended as it often leads quickly to overheating of the sample and a burnt film as shown here.[37] From these trials, at least 350V must be applied with at least 4 pulses is needed to make these films conductive.

Figure 5.44c (Sample 2) is the result of a study of the same type of printed film based on the effect of the number of pulse lengths as the voltage and pulse length were maintained at the same values of 350V and 550 μs respectively. It was confirmed that with Figure 5.45b that a similar behavior was seen here but minimized as much as possible as a step-by-step process in just increasing the number of pules was implemented. Figure 5.46 depicts the reduction in resistance with an increasing number of pulses where the first trial directly applied 4 pulses as confirmed through the last experiment. The direct application of these parameters instead resulted in quick decrease down to 3.3kΩ compared to the 23 kΩ reported in the first sample. It was discovered that if 2 pulses were applied, an average decrease of 37.2% in resistance was exhibited, however after 10 pulses, the resistance value increased to 2.6 kΩ, twice the previously reported values. This increase indicates a limiting reduction value where the ablation of the film begins to occur. Further application of these sintering parameters did not improve on the resistance however only when a higher voltage was applied (380V), did the resistance reduce to 900 Ω at the detriment of ablation of the film at the edges. It must be noted that reduction in resistance value may be a result of the removal of poorly sintered film facilitating electrical conduction.

This same approach was used here in Sample 3 was directly applied with a voltage of 380V at a pulse length of 550 μs using two pulses which immediately saw film ablation with a minimum resistance at 5 kΩ as shown in Figure 5.44d. This verified that a slow and lower starting voltage value must be used in order to prevent immediate film ablation. Interestingly, the film itself did not show any crack formation (Figure 5.45c) as typically seen on all other samples indicating that no gas formed during testing as the temperature of the film did not exceed substrate temperature. Photonically cured films as seen in Figures 5.45b and 5.45d appeared similar in development which began with sintering parameters of voltage at 350V and pulse

length of 550 μs which has repeated shown to make any structure conductive, achieving 7 kΩ after 8 pulses. Further application of these parameters did not resulted in a major improvement of the resistance as it maintained at 6.7 kΩ, therefore a stronger voltage of 360V was applied lowering the resistance by 1 kΩ with every application from 2 – 4 pulses. As these results began to stabilize, a higher voltage of 400V was applied to determine whether this increase could further reduce the resistance. This resulted in a wide range of values as little as 500 Ω to 7 kΩ, the highest resistance seen in the film thus far as reported in Figure 5.47. It was apparent here that generally increasing the voltage greatly reduces the resistance however, it must be noted here that resistance measurements were highly dependent on where the leads of the multimeter tester were placed therefore an accurate and consistent measurement was not achieved here. Any further testing led to degradation of the Sample 4 as seen in Figure 5.44e.

Therefore, Sample 5 as shown in Figure 5.44f was treated at higher voltage as a voltage of 350-360V can only reduce the resistance in the kΩ region, therefore a voltage of 400V was applied with multiple pulses and pulse lengths. Here, a lower pulse length was applied at 250 μs resulting in non-conductive structures, however once the pulse length was changed back to 550 μs, the lowest reported and quickest treated sample here saw a resistance of only 300 Ω with little film ablation as compared to all other samples (Figure 5.45e). The success found in this trial was applied to Sample 6 shown in Figure 5.44g seeing resistance in the 12 – 13 kΩ range, greater than those reported at 350V. The pulse length was lowered to 250 μs for the fear of burning the sample which only saw minuscule improvement even after 16 pulses from 7 – 12 kΩ. For this reason, the pulse length was increased again to 350 μs which saw excellent improvement in the resistance to 2.5 kΩ and finally down to 600 – 3 kΩ after a total of 8 pulses.

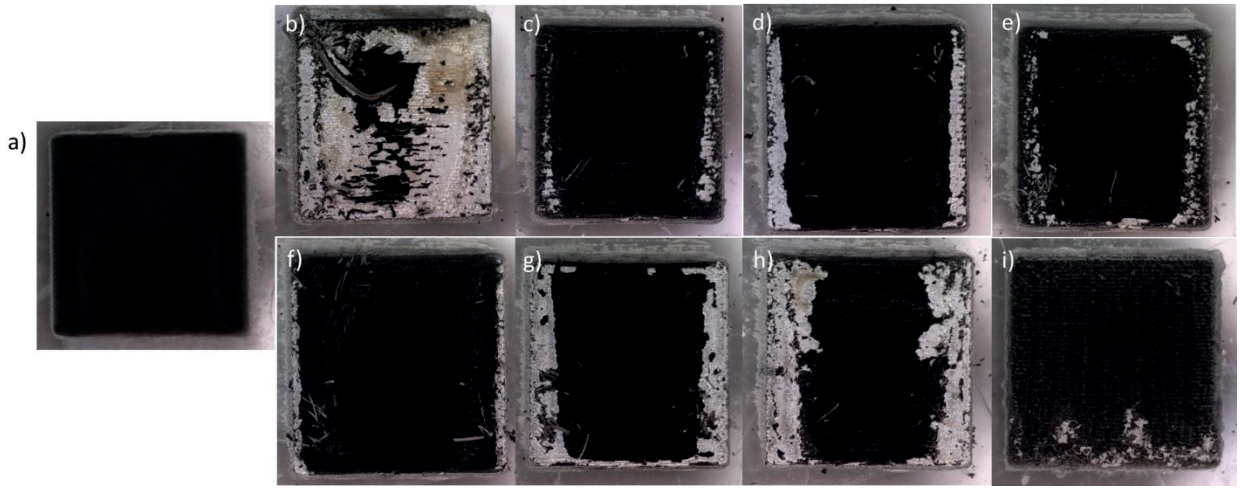

Figure 5.44. 70 mg/ml Mo in Butanol/IPA 2:1 printed squares with 40 layers at a DS of 20 μm at a platen temperature of 50°C a) as printed square while b) Sample 1, c) Sample 2, d) Sample 3, e) Sample 4, f) Sample 5, g) Sample 6, h) Sample 7, and i) Sample 8 are squares treated with various photonic curing conditions. Results were first reported and adapted from unpublished results by the lead scientist for these experiments, Dra. Sandra Perez.

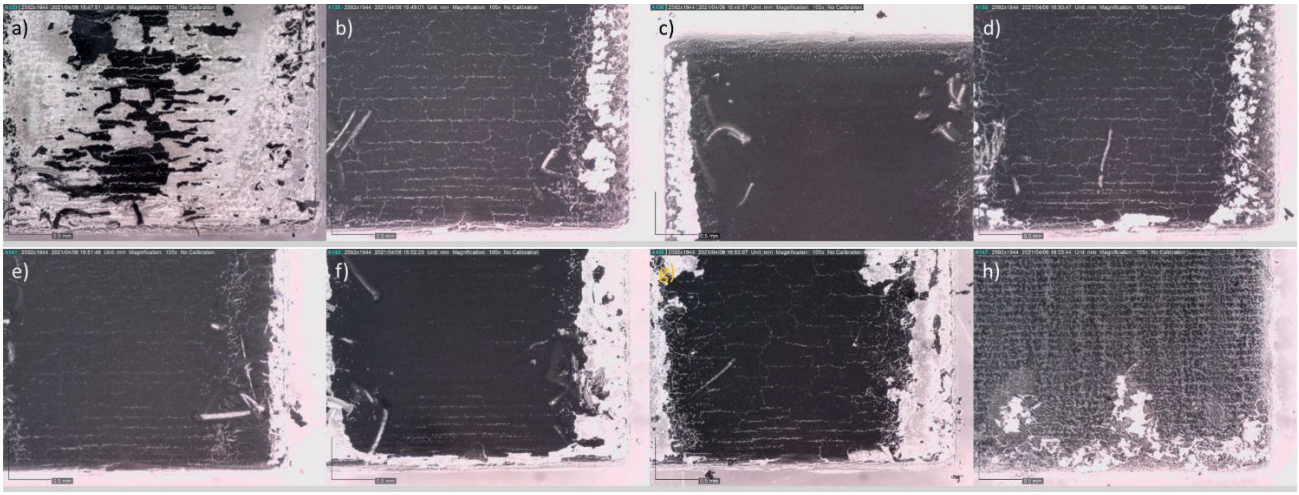

Figure 5.45. Close up view of photonically cured samples as shown in Figure 5.44 for a) Sample 1, b) Sample 2, c) Sample 3, d) Sample 4, e) Sample 5, f) Sample 6, g) Sample 7, and h) Sample 8. Results were first reported and adapted from unpublished results by the lead scientist for these experiments, Dra. Sandra Perez.

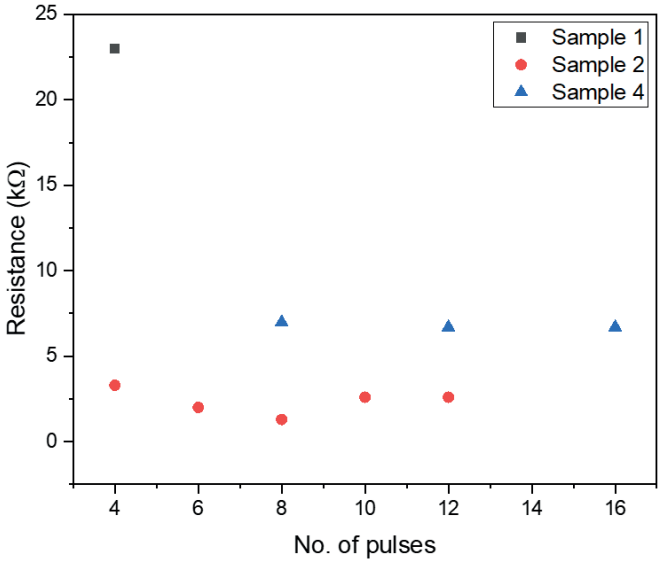

Figure 5.46. Effect of increasing pulse number on the resistance of the deposited Mo film for 10 applied pulses keeping sintering parameters such as voltage 350V and 550 µs pulse length consistent for Samples 1, 2, and 4. Results were first reported and adapted from unpublished results by the lead scientist for these experiments, Dra. Sandra Perez.

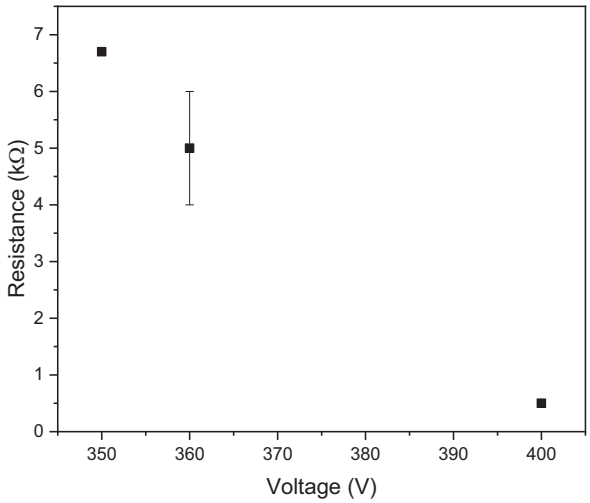

Figure 5.47. Effect of increasing voltage on resistance for Sample 4 Mo film with pulse lengths at 550 µs for 350V and 360V and 500 µs for 400V. Results were first reported and adapted from unpublished results by the lead scientist for these experiments, Dra. Sandra Perez.

When taking Samples 1, 2, and 4 into comparison, the large range of resistance values applied for the same number of pulses calls into question the repeatability of this sintering technique with these films, that being the combination of inkjet printing and photonic curing. This variability is most likely due to the irregularities in the film that reduce the effectiveness of

the sintering technique. This is typically not an issue with thermal sintering as the entire film sees the same temperature however because photonic curing occurs from the top down, the uniformity of the surface as well as the sample thickness plays a role in the conductive film development. After multiple tests, it is clear that the lowest possible resistance achieved for inkjet printed and photonic cured Mo ink on a PEN substrate is ~100s of Ω for a 4 x 4 mm square. A 4x4 mm square was used as a reference for the measurement of relative resistance values with respect to the applied energy via photonic curing.

5.5 | CONCLUSIONS

The development of biodegradable Zn and Mo thin films was presented here for their viability and compatibility with low impact technologies such as inkjet printing and photonic curing. Standard thermal sintering was insufficient to achieve high conductivities as these inks required sintering temperatures of at least 400°C, directly incompatible with temperature sensitive substrates including typical polymer substrates. This was apparent in both thermally treated Zn and Mo films as neither saw conductivities greater than 10^3 $S \cdot m^{-1}$ nor any conductivity at all respectively. It was for this reason that alternative sintering techniques such as photonic curing were considered as they have been previously shown to achieve high conductivities for even oxygen sensitive Cu thin films. It was found that photonic curing was effective in the removal of both DMSO and butanol solvents thereby exposing bare Zn NPs contributing to the film conductivity. However, this was not without side effects as the surface layer was converted to ZnO flakes which displayed a light grey color. This layer acted as a protective layer where the deposited Zn NPs beneath were exposed and saw conductivity up to 8.1 x 10^3 $S \cdot m^{-1}$ for PEN substrates and 2.7 x 10^2 $S \cdot m^{-1}$ on PVA which has room for improvement. All tests performed with photonic curing were limited in terms of accessibility and rushed as a result meaning further optimization is still needed. This was also the case with Mo thin films conducted by Sandra Perez Rafael. As melting temperatures exceeding 2000°C is needed, thermal sintering was ineffective and only resulted in non-conductive structures. With the implementation of photonic curing, printed squares saw resistances as low as 300 Ω but its lack of consistency due to non-uniformities in the printed layer must be addressed. Solely based on these results, the development of Mo NP ink for inkjet printing does not provide any advantages over screen printed inks utilizing MPs as its respective melting temperature is unreasonably high for temperature sensitive substrates even with the help of alternative sintering techniques such as laser and photonic sintering. Research on both Zn and Mo inks is currently ongoing at IMB-CNM by Sandra Perez Rafael where full results will be reported in the future.

5.6 | REFERENCES

(1) Kang, S. K.; Park, G.; Kim, K.; Hwang, S. W.; Cheng, H.; Shin, J.; Chung, S.; Kim, M.; Yin, L.; Lee, J. C.; Lee, K. M.; Rogers, J. A. Dissolution Chemistry and Biocompatibility of Silicon- and Germanium-Based

Semiconductors for Transient Electronics. *ACS Appl. Mater. Interfaces* **2015**, *7* (17), 9297–9305. https://doi.org/10.1021/acsami.5b02526.

(2) Zheng, Y. F.; Gu, X. N.; Witte, F. Biodegradable Metals. *Materials Science and Engineering R: Reports*. Elsevier Ltd March 1, 2014, pp 1–34. https://doi.org/10.1016/j.mser.2014.01.001.

(3) Liu, Y.; Zheng, Y.; Chen, X.; Yang, J.; Pan, H.; Chen, D.; Wang, L.; Zhang, J.; Zhu, D.; Wu, S.; Yeung, K. W. K.; Zeng, R.; Han, Y.; Guan, S. Fundamental Theory of Biodegradable Metals—Definition, Criteria, and Design. *Adv. Funct. Mater.* **2019**, *29* (18), 1805402. https://doi.org/10.1002/adfm.201805402.

(4) Stefánsson, A. Iron(III) Hydrolysis and Solubility at 25°C. *Environ. Sci. Technol.* **2007**, *41* (17), 6117–6123. https://doi.org/10.1021/es070174h.

(5) Electrical Conductivity for all the elements in the Periodic Table https://periodictable.com/Properties/A/ElectricalConductivity.an.html (accessed 2023 -09 -05).

(6) Hwang, S. W.; Tao, H.; Kim, D. H.; Cheng, H.; Song, J. K.; Rill, E.; Brenckle, M. A.; Panilaitis, B.; Won, S. M.; Kim, Y. S.; Song, Y. M.; Yu, K. J.; Ameen, A. A.; Li, R.; Su, Y.; Yang, M.; Kaplan, D. L.; Zakin, M. R.; Slepian, M. J.; Huang, Y.; Omenetto, F. G.; Rogers, J. A. A Physically Transient Form of Silicon Electronics. *Science (80-.).* **2012**, *337* (6102), 1640–1644. https://doi.org/10.1126/science.1226325.

(7) Kang, S. K.; Murphy, R. K. J.; Hwang, S. W.; Lee, S. M.; Harburg, D. V.; Krueger, N. A.; Shin, J.; Gamble, P.; Cheng, H.; Yu, S.; Liu, Z.; McCall, J. G.; Stephen, M.; Ying, H.; Kim, J.; Park, G.; Webb, R. C.; Lee, C. H.; Chung, S.; Wie, D. S.; Gujar, A. D.; Vemulapalli, B.; Kim, A. H.; Lee, K. M.; Cheng, J.; Huang, Y.; Lee, S. H.; Braun, P. V.; Ray, W. Z.; Rogers, J. A. Bioresorbable Silicon Electronic Sensors for the Brain. *Nature* **2016**, *530* (7588), 71–76. https://doi.org/10.1038/nature16492.

(8) Chatterjee, S.; Saxena, M.; Padmanabhan, D.; Jayachandra, M.; Pandya, H. J. Futuristic Medical Implants Using Bioresorbable Materials and Devices. *Biosens. Bioelectron.* **2019**, *142* (June), 111489. https://doi.org/10.1016/j.bios.2019.111489.

(9) Lee, S.; Koo, J.; Kang, S. K.; Park, G.; Lee, Y. J.; Chen, Y. Y.; Lim, S. A.; Lee, K. M.; Rogers, J. A. Metal Microparticle – Polymer Composites as Printable, Bio/Ecoresorbable Conductive Inks. *Mater. Today* **2018**, *21* (3), 207–215. https://doi.org/10.1016/j.mattod.2017.12.005.

(10) Kang, S. K.; Hwang, S. W.; Yu, S.; Seo, J. H.; Corbin, E. A.; Shin, J.; Wie, D. S.; Bashir, R.; Ma, Z.; Rogers, J. A. Biodegradable Thin Metal Foils and Spin-on Glass Materials for Transient Electronics. *Adv. Funct. Mater.* **2015**, *25* (12), 1789–1797. https://doi.org/10.1002/adfm.201403469.

(11) Huang, X. Materials and Applications of Bioresorbable Electronics. *J. Semicond.* **2018**, *39* (1). https://doi.org/10.1088/1674-4926/39/1/011003.

(12) Kang, S. K.; Koo, J.; Lee, Y. K.; Rogers, J. A. Advanced Materials and Devices for Bioresorbable Electronics. *Acc. Chem. Res.* **2018**, *51* (5), 988–998. https://doi.org/10.1021/acs.accounts.7b00548.

(13) Yin, L.; Cheng, H.; Mao, S.; Haasch, R.; Liu, Y.; Xie, X.; Hwang, S. W.; Jain, H.; Kang, S. K.; Su, Y.; Li, R.; Huang, Y.; Rogers, J. A. Dissolvable Metals for Transient Electronics. *Adv. Funct. Mater.* **2014**, *24* (5), 645–658. https://doi.org/10.1002/adfm.201301847.

(14) Feng, S.; Cao, S.; Tian, Z.; Zhu, H.; Kong, D. Maskless Patterning of Biodegradable Conductors by Selective Laser Sintering of Microparticle Inks and Its Application in Flexible Transient Electronics. *ACS Appl. Mater. Interfaces* **2019**, *11* (49), 45844–45852. https://doi.org/10.1021/acsami.9b14431.

(15) Feng, S.; Tian, Z.; Wang, J.; Cao, S.; Kong, D. Laser Sintering of Zn Microparticles and Its Application in Printable Biodegradable Electronics. *Adv. Electron. Mater.* **2019**, *5* (3), 1–7. https://doi.org/10.1002/aelm.201800693.

(16) Shou, W.; Mahajan, B. K.; Ludwig, B.; Yu, X.; Staggs, J.; Huang, X.; Pan, H. Low-Cost Manufacturing of Bioresorbable Conductors by Evaporation–Condensation-Mediated Laser Printing and Sintering of Zn Nanoparticles. *Adv. Mater.* **2017**, *29* (26), 1–7. https://doi.org/10.1002/adma.201700172.

(17) Liao, Y.; Zhang, R.; Qian, J. Printed Electronics Based on Inorganic Conductive Nanomaterials and Their Applications in Intelligent Food Packaging. *RSC Adv.* **2019**, *9* (50), 29154–29172. https://doi.org/10.1039/c9ra05954g.

(18) Huang, X.; Liu, Y.; Hwang, S. W.; Kang, S. K.; Patnaik, D.; Cortes, J. F.; Rogers, J. A. Biodegradable Materials for Multilayer Transient Printed Circuit Boards. *Adv. Mater.* **2014**, *26* (43), 7371–7377. https://doi.org/10.1002/adma.201403164.

(19) Lee, Y. K.; Kim, J.; Kim, Y.; Kwak, J. W.; Yoon, Y.; Rogers, J. A. Room Temperature Electrochemical Sintering of Zn Microparticles and Its Use in Printable Conducting Inks for Bioresorbable Electronics. *Adv. Mater.* **2017**, *29* (38), 1–8. https://doi.org/10.1002/adma.201702665.

(20) Sui, Y.; Radwan, A. N.; Gopalakrishnan, A.; Dikshit, K.; Bruns, C. J.; Zorman, C. A.; Whiting, G. L. A Reactive Inkjet Printing Process for Fabricating Biodegradable Conductive Zinc Structures. *Adv. Eng. Mater.* **2023**, *25* (1), 1–9. https://doi.org/10.1002/adem.202200529.

(21) Majee, S.; Karlsson, M. C. F.; Sawatdee, A.; Mulla, M. Y.; Alvi, N. ul H.; Beni, V.; Nilsson, D. Low Temperature Chemical Sintering of Inkjet-Printed Zn Nanoparticles for Highly Conductive Flexible Electronic Components. *npj Flex. Electron.* **2021**, *5* (1), 1–8. https://doi.org/10.1038/s41528-021-00111-1.

(22) Mahajan, B. K.; Ludwig, B.; Shou, W.; Yu, X.; Fregene, E.; Xu, H.; Pan, H.; Huang, X. Aerosol Printing and Photonic Sintering of Bioresorbable Zinc Nanoparticle Ink for Transient Electronics Manufacturing. *Sci. China Inf. Sci.* **2018**, *61* (6), 1–10. https://doi.org/10.1007/s11432-018-9366-5.

(23) Mahajan, B. K.; Yu, X.; Shou, W.; Pan, H.; Huang, X. Mechanically Milled Irregular Zinc Nanoparticles for Printable Bioresorbable Electronics. *Small* **2017**, *13* (17), 1–8. https://doi.org/10.1002/smll.201700065.

(24) Li, J.; Luo, S.; Liu, J.; Xu, H.; Huang, X. Processing Techniques for Bioresorbable Nanoparticles in Fabricating Flexible Conductive Interconnects. *Materials (Basel).* **2018**, *11* (7). https://doi.org/10.3390/ma11071102.

(25) Li, J.; Xu, H.; Zhang, Z.; Hao, Y.; Wang, H.; Huang, X. Anhydride-Assisted Spontaneous Room Temperature Sintering of Printed Bioresorbable Electronics. *Adv. Funct. Mater.* **2019**, *1905024*, 1905024. https://doi.org/10.1002/adfm.201905024.

(26) Hrubiak, R.; Meng, Y.; Shen, G. Microstructures Define Melting of Molybdenum at High Pressures. *Nat. Commun.* **2017**, *8* (1), 14562. https://doi.org/10.1038/ncomms14562.

(27) Akhtar, M. J.; Ahamed, M.; Alhadlaq, H. A.; Alshamsan, A.; Majeed Khan, M. A.; Alrokayan, S. A. Antioxidative and Cytoprotective Response Elicited by Molybdenum Nanoparticles in Human Cells. *J. Colloid Interface Sci.* **2015**, *457*, 370–377. https://doi.org/10.1016/j.jcis.2015.07.034.

(28) Yin, L.; Huang, X.; Xu, H.; Zhang, Y.; Lam, J.; Cheng, J.; Rogers, J. A. Materials, Designs, and Operational Characteristics for Fully Biodegradable Primary Batteries. *Adv. Mater.* **2014**, *26* (23), 3879–3884. https://doi.org/10.1002/adma.201306304.

(29) Huang, X.; Wang, D.; Yuan, Z.; Xie, W.; Wu, Y.; Li, R.; Zhao, Y.; Luo, D.; Cen, L.; Chen, B.; Wu, H.; Xu, H.; Sheng, X.; Zhang, M.; Zhao, L.; Yin, L. A Fully Biodegradable Battery for Self-Powered Transient Implants. *Small* **2018**, *14* (28), 1–8. https://doi.org/10.1002/smll.201800994.

(30) Aguilera, E. C. *Development of Organic Electronic Devices Employing InkJet Printing Technology*; 2021.

(31) FUJIFILM. FUJIFILM Dimatix Ink Tutorial, Waveform. **2008**, 6.

(32) Baby, T. T.; Garlapati, S. K.; Dehm, S.; Häming, M.; Kruk, R.; Hahn, H.; Dasgupta, S. A General Route toward Complete Room Temperature Processing of Printed and High Performance Oxide Electronics. *ACS Nano* **2015**, *9* (3), 3075–3083. https://doi.org/10.1021/nn507326z.

(33) Seo, C.; Jang, D.; Chae, J.; Shin, S. Altering the Coffee-Ring Effect by Adding a Surfactant-like Viscous Polymer Solution. *Sci. Rep.* **2017**, *7* (1), 500. https://doi.org/10.1038/s41598-017-00497-x.

(34) Singh, C.; Friedrichs, S.; Levin, M.; Birkedal, R.; Jensen, K. A.; Pojana, G.; Wohlleben, W.; Schulte, S.; Wiench, K.; Turney, T.; Koulaeva, O.; Marshall, D.; Hund-Rinke, K.; Kördel, W.; Doren, E. Van; De Temmerman, P.-J.; Abi, M.; Francisco, D.; Mast, J.; Gibson, N.; Koeber, R.; Linsinger, T.; Klein, C. L. *NM-Series of Representative Manufactured Nanomaterials Zinc Oxide NM-110, NM-111, NM-112, NM-113 Characterisation and Test Item Preparation*; 2011. https://doi.org/10.2787/55008.

(35) Balanand, S.; Babitha, K. B.; Jeen Maria, M.; Mohamed, A. A. P.; Ananthakumar, S. Aqueous Mechanical Oxidation of Zn Dust: An Inventive Technique for Bulk Production of ZnO Nanorods. *ACS Sustain. Chem. Eng.* **2018**, *6* (1), 143–154. https://doi.org/10.1021/acssuschemeng.7b01966.

(36) Mebarki, F.; David, E. Dielectric Characterization of Thermally Aged Recycled Polyethylene Terephthalate and Polyethylene Naphthalate Reinforced with Inorganic Fillers. *Polym. Eng. \& Sci.* **2018**, *58* (5), 701–712. https://doi.org/https://doi.org/10.1002/pen.24602.

(37) Schroder, K. A. Mechanisms of Photonic Curing???: Processing High Temperature Films on Low Temperature Substrates. *Tech. Proc. 2011 NSTI Nanotechnol. Conf. Expo, NSTI-Nanotech 2011* **2011**, *2*, 220–223.

(38) Jeon, J.-Y.; Park, S.-J.; Ha, T.-J. Functionalization of Zinc Oxide Nanoflowers with Palladium Nanoparticles via Microwave Absorption for Room Temperature-Operating Hydrogen Gas Sensors in the Ppb Level. *ACS Appl. Mater. Interfaces* **2021**, *13* (21), 25082–25091. https://doi.org/10.1021/acsami.1c03283.

(39) Shi, R.; Yang, P.; Wang, J.; Zhang, A.; Zhu, Y.; Cao, Y.; Ma, Q. Growth of Flower-like ZnO via Surfactant -Free Hydrothermal Synthesis on ITO Substrate at Low Temperature. *CrystEngComm* **2012**, *14* (18), 5996–6003. https://doi.org/10.1039/C2CE25606A.

(40) Tang, J.-F.; Su, H.-H.; Lu, Y.-M.; Chu, S.-Y. Controlled Growth of ZnO Nanoflowers on Nanowall and Nanorod Networks via a Hydrothermal Method. *CrystEngComm* **2015**, *17* (3), 592–597. https://doi.org/10.1039/C4CE01940G.

(41) Pung, S.-Y.; Lee, W.-P.; Aziz, A. Kinetic Study of Organic Dye Degradation Using ZnO Particles with Different Morphologies as a Photocatalyst. *Int. J. Inorg. Chem.* **2012**, *2012*, 1–9. https://doi.org/10.1155/2012/608183.

(42) Schroder, K. A. Photonic Curing Explanation and Application to Printing Copper Traces on Low Temperature Substrates www.novacentrix.com (accessed 2023 -07 -04).

6

Inkjet printed plasma reduced metal films

This chapter serves to provide a new perspective on metal thin film formation by plasma sintering by adapting the use of metal salt-based inks onto a wide variety of substrates previously not seen before. Such inks have only been recently introduced to the scientific community and are still being understood. My contribution here adds to this base of knowledge by utilizing atmospheric oxygen plasma to develop extremely low temperature sintered metal films onto a wide variety of substrates which was published in an article titled for "Low-Temperature Plasma Sintering of Inkjet-Printed Metal Salt Decomposition Inks on Flexible Substrates".[1*] Section by section will provide the thought process behind each experiment and provide an in-depth analysis on the results which were not reported in the paper.

6.1 | INTRODUCTION TO METAL SALT DECOMPOSITION INKS

Metal salt decomposition (MSD) inks are a subset of MOD inks which are primarily salt precursors dissolved in a combination of solvents. Such inks require the ability to be reduced via thermal[1], laser[2], chemical[3], or plasma sintering[4–6] to stimulate NP growth implying that a separate chemical synthesis step is no longer necessary. All such sintering methods were conducted at low temperature meaning that excessive sintering temperatures are not needed with such inks allowing for the implementation of temperature sensitive substrates. Often, Ag and Cu

[1*] Leung TSW, Ramon E, Martínez-Domingo C. Low-Temperature Plasma Sintering of Inkjet-Printed Metal Salt Decomposition Inks on Flexible Substrates. *Adv Eng Mater*. 2022;2200834. doi:10.1002/adem.202200834

are the two most investigated inks mostly due to their low cost for high conductivity elements. There is also a need for other noble metals such as Au and Pt as their excellent corrosion resistance and oxidation stability provide good biocompatibility for sensor and OFET applications. Additionally, unlike typical nanoparticle inks with short shelf life due to the interaction between the NPs and the stabilizer, MSD inks display both excellent chemical and thermal stability due to its simple formulation providing an additional advantage.[4]

Recently Yang et al.[2] demonstrated the reduction of a Pt and Ag salt precursor inks using a femtosecond laser at 780 nm wavelength. The Pt ink was composed of Pt(II) salt, ammonium tetrachloroplatinate ($(NH_4)_2[PtCl_4]$), and an iron(III) oxalate photosensitizer, ammonium iron oxalate trihydrate ($(NH_4)_3[Fe(C_2O_4)_3]$ which resulted in printed Pt micron sized lines with a conductivity of 2.4×10^5 $S \cdot m^{-1}$ as a result of the concentration of photon absorption as provided for by iron oxalate.[2] The Ag ink containing $AgNO_3$ salt combined with trisodium citrate (a reducing agent) saw conductivity up to 5.9×10^6 $S \cdot m^{-1}$ for micron sized printed lines.[2]

Chemical sintering of different metal inks was explored by Wang et al., Li et al., and Abulikemu et al. whom used room temperature techniques to create metal thin films. Wang et al. presented the successful fabrication of Cu films on paper through a multilayer process where the substrate must first be treated with $SnCl_2$ followed by the inkjet printing of a silver based catalyst ink (composed of $AgNO_3$, water, ethyl alcohol, ethylene glycol (EG), n-propanol, and glycerol following a 14:8:7:8:16 ratio by volume), and finally placed into an electroless plating solution made of $CuSO_4 \cdot 5H_2O$, $C_4H_4KNaO_6 \cdot 4H_2O$, $C_{10}H_{16}N_2Na_2O_8$, and NaOH to develop copper thin films. The deposition itself required 30 minutes to achieve 1.1 μm layer displaying high conductivity of 4.0×10^7 $S \cdot m^{-1}$.[7] However this exhaustive process could be simplified with the introduction of reactive inkjet printing. Li et al. also demonstrated Cu and Ni films on a paper substrate solely using a sequential printing process (printing of the metal precursor followed by the reducing agent) requiring hundreds of printing cycles. The salt-based inks were composed of copper citrate and nickel sulfate ($NiSO_4$) both of which required sodium borohydride ($NaBH_4$) as the reducing agent. Conductive Cu lines were achieved after 350 successive printing cycles to obtain a connected "cauliflower" network of aggregated growth with a conductivity of 1.8×10^6 $S \cdot m^{-1}$.[8] On the other hand, a Ni film could be achieved with 250 printing cycles which created a deposited layer of 5 – 10 μm film thickness displaying a conductivity of 2.2×10^4 $S \cdot m^{-1}$.[8] This process could also be extended to the development of other metal films such as Au as demonstrated by Abulikemu et al. Here, reactive inkjet printing of the $HAuCl_4$ salt precursor followed by the oleylamine + 1,2-dichlorobenzene (acting as the capping reducing agent respectively) ink succeeded in developing self-assembled 8 nm Au NPs films after thermal treatment at 120°C for 3h.

Another technique was the implementation of plasma as a sintering technique. The known first occurrence of reduced plasma Au films was reported by Crowther et al.[5] whom used hydrogen plasma to produce Au films from $HAuCl_4$ and Nylon66 ink. This early adoption of reducing metal salt-based inks gave rise a new class of inks as reported by Sui et al. who published a comprehensive paper displaying a large range of metals (Au, Pd, Ag, Pt, Cu, Bi, Pb, Sn) that could be reduced using Ar plasma sintering onto a selection of polymer substrates such as PET, cellophane, PVA, and polyethylene (PE). The reducing power of the plasma could be tuned by the amount of power applied to the substrates up to 300 W for 30 minutes reaching moderate sintering temperatures (<138°C).[4]

6.2 | METAL SALT DECOMPOSITION INK FORMULATION

The most common reagents for substrate preparation and ink formulation were obtained from Sigma-Aldrich (Merck) including ethylene glycol (EG, ReagentPlus®, ≥99%), (3-mercaptopropyl)trimethoxysilane (MPTMS¸95%), hydrochloric acid (HCl, ACS reagent, 37%). Ethanol absolute (99.5% for synthesis) and Acetone (Reag. USP, Ph. Eur.) for analysis, ACS, ISO was purchased from AppliChem GmbH.

MSD ink formulation simply requires a metal salt precursor combined with a solvent and H_2O to dissolve the salt. A wide range of metal salts were obtained from Sigma-Aldrich (Merck) including gold (III) chloride trihydrate ($HAuCl_4 \cdot 3H_2O$, ≥99.9% trace metals basis, with Au content 48.5–50.25%), chloroplatinic acid hydrate ($H_2PtCl_6 \cdot xH_2O$, ≥99.9% trace metals basis, with Pt content 37–40%), tin(II) chloride ($SnCl_2$, Reagent grade 98%), Palladium(II) chloride ($PdCl_2$, ≥99.9%), silver nitrate ($AgNO_3$, ACS reagent, ≥99.0%), Copper(II) sulfate pentahydrate ($CuSO_4 \cdot 5H_2O$, ACS reagent, ≥98.0%), and iron(III) chloride hexahydrate ($FeCl_3 \cdot 6H_2O$, ACS reagent, 97%). Ethylene Glycol (EG) ($C_2H_6O_2$, 99%) was purchased from Alfa Aesar (Thermo Fisher Scientific). Both the Au and Pt inks were produced from a 1.0M metal salt solutions combined with 50% EG and 50% DI water. To create the Pd ink, a 0.5 M salt precursor solution was developed with a 2:1 ratio (v/v) of H_2O to EG, that is 1.5mL of 1.0M $AgNO_3$ + 1 mL (33% EG + 76% DI water). Similarly, a 1.5M solution was prepared with the Ag precursor and mixed with the same 2:1 H_2O:EG ratio as previously stated. A 1.0M solution containing the Cu salt precursor was added to a 1.9:1 ratio (v/v) of H_2O to EG. Lastly, due to their quick oxidation with H_2O, the Sn and Fe inks were mixed together with 50% ethanol and 50% EG to create a 1.0 M solution. Each of the inks are as pictured below in Figure 6.1.

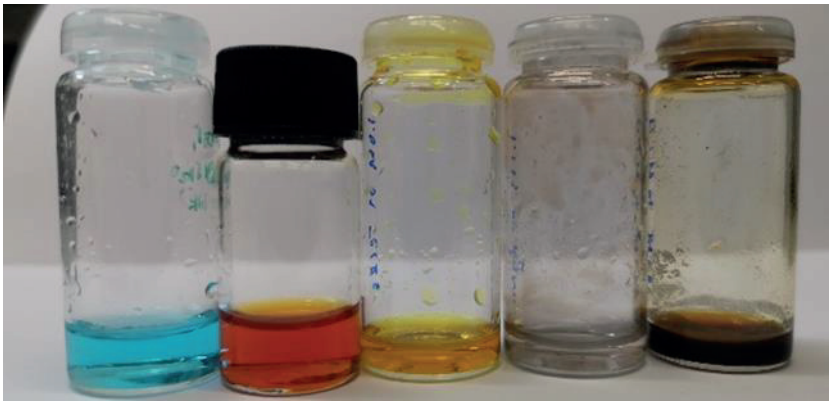

Figure 6.1. All developed MSD inks as pictured from the left to right: $CuSO_4$, H_2PtCl_6, $HAuCl_4$, $SnCl_2$, and $PdCl_2$ inks.

A large variety of substrates including polymers, papers, and fabrics were used for testing, some of which were purchased while others were fabricated as previously discussed in Chapter 4 regarding the Substrate Investigation. All fabricated substrates previously discussed and therefore will not be reviewed here in this section. Polymer substrates used for these experiments included A4 sheets of polyethylene terephthalate (PET) Melinex and polyethylene naphthalate (PEN) 125 μm thick films purchased from DuPont Teijin Films that were pre-treated on one side to adapt for inkjet printing. Dupont Kapton® Polyimide films. All paper substrate included TESLIN® BIO SUBSTRATE (254 μm, Ohio, USA), obtained from PPG Industries, as well as PowerCoat HD paper sheets (size A4, 230 μm) from Arjowiggins France. Fabrics included 100% polyester textile purchased from Decathlon and umbrella fabric (80 μm thickness) purchased from a local store.

Plasma treatment was performed with PlasmaTechnology´s GmbH SmartPlasma2 that could be adjust to any power from 10 – 100% (up to 80W) for different time periods. Unfortunately, accurate control of the O_2 flow nor pressure was possible and may be varied with each test. If a higher voltage was needed with accurate O_2 gas control, Tepla Gigabatch 360M O_2 plasma asher in the CNM cleanroom was used. With this machine, the same recipe was used where the power was set to 200W, with an O_2 flow of 600 standard cubic centimeters per minute (sccm) for 1 or 20 minutes at a time. Additionally, March PX-1000 Plasma Reactive Ion Etching (RIE) System equip with argon gas (Ar) was utilized to investigate the same film development under two conditions:

1) P = 150W, 600 mTorr Ar for 20 minutes

2) P = 66W, 50 sccm Ar, for 20 minutes

Good performance of the ink was seen up to 6 months of storage but was dependent on the metal precursor stability itself. No precipitates formed even after long term storage (83 days).

6.3 | REDUCTION MECHANISM

The reduction mechanism for metals is based on their respective ion reduction potential as stated in Figure 6.2 where the greater the reduction potential denotes the ease of conversion to its elemental form. In contrast, the more neutral or negative the value signifies the resistance or aversion from conversion which is the case for Cu, Sn, and Mg ions including their respective disposition for oxidation. For example, Sui et al. reported that metals exhibiting higher reduction potentials such as Ag, Pd, Au, and Pt were converted using low plasma power of 150W while those with lower reduction potentials required twice the power at 300W at extended exposure times.[4] Additionally, conversion may occur in multiple steps as indicated by the asterisk (*) for both Fe and Pt metals.

Reduction reactions	potential
$Au^{3+} + 3e^- \rightleftharpoons Au_{(s)}$	+1.52 V
$Pd^{2+} + 2e^- \rightleftharpoons Pd_{(s)}$	+0.92 V
$Ag^{+} + e^- \rightleftharpoons Ag_{(s)}$	+0.80 V
$*\, Fe^{3+} + e^- \rightleftharpoons Fe^{2+}$	+0.77 V
$*\, Fe^{2+} + 2e^- \rightleftharpoons Fe_{(s)}$	-0.44 V
$*\, PtCl_6^{2-} + 2e^- \rightleftharpoons PtCl_4^{2-} + 2Cl^-$	+0.68 V
$*\, PtCl_4^{2-} + 2e^- \rightleftharpoons Pt_{(s)} + 4Cl^-$	+0.73 V
$Cu^{2+} + 2e^- \rightleftharpoons Cu_{(s)}$	+0.34 V
$Sn^{2+} + 2e^- \rightleftharpoons Sn_{(s)}$	-0.14 V
$Mg^{2+} + 2e^- \rightleftharpoons Mg_{(s)}$	-2.36 V

Figure 6.2. Respective electrode potentials and their half reduction reactions for common metals organized on decreasing reduction potential. This figure noted here was adapted from Liu et al.[9]

As noted by Figure 6.2, the reduction of an ionic metal is dependent on the ability of the respective technique to form solvated electrons that serve as reducing species.[10] In terms of plasma sintering, the proposed conversion occurs as shown in Figure 6.3 below in a 2 step process. Ion bombardment from Ar^+ ions causes the metal salt to dissociate to metal cations and anions.[4] These cations are then further reduced via electrons provided from the plasma. This then allows for the nucleation and growth of the metal thin film on the substrate surface. The remaining anions are then removed by a dehalogenative coupling reaction.[11]

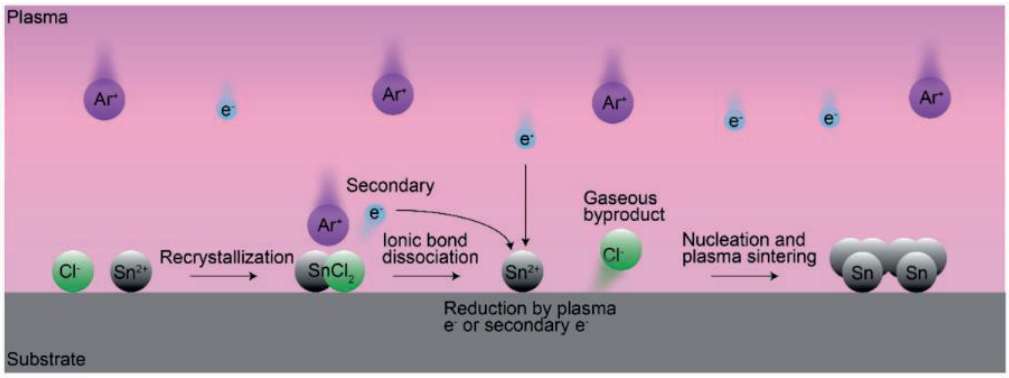

Figure 6.3. Schematic representation of the Ar plasma reduction process of Sn metal salt ink. This figure was adapted from Sui et al.[4]

The reaction above is reported specifically for low pressure and high power Ar plasma which must be adapted in our case which was expanded upon as shown in Figure 6.4 for the development of an Au film on a PET substrate. It is believed that this same process occurs on other substrates and other inks which will be demonstrated later. Inkjet printing with Au ($HAuCl_4$) MSD ink was used to deposit patterned structures onto any desired substrate which for example here is PET (Figure 6.4a). Similarly to the reduction mechanism processed in Figure 6.3, exposure to O_2 plasma (Figure 6.4b) initiates ionic bond dissociation of the metal salt in the MSD ink in the first 5 minutes (Figure 6.4bi). Solvent evaporation occurred rapidly at the edges as these printed structures exhibit the Marangoni effect where the edges contain less solvent as well as a lower thickness. Therefore, conversion of the ink is first initiated at the edges that move to the interior of the sample as seen in Figure 6.4bii. Chlorine ions are released as gaseous byproducts that can be removed in vacuum. This leaves an elemental and conductive Au film on the substrate surface (Figure 6.4biii) after approximately 20 minutes of exposure. A notable difference in film color is seen from the transparent yellow color of the Au MSD ink to an opaque metallic gold appearance as depicted in Figure 6.4c. Exposure and conversion times were individual for each ink and based on overall thickness of the deposited which will be discussed in the following sections.

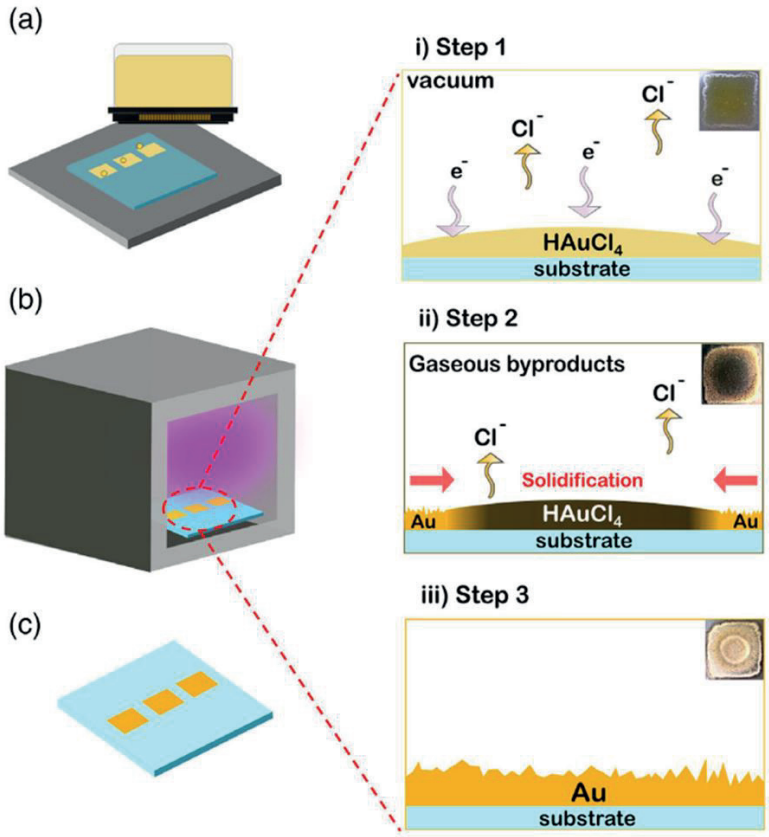

Figure 6.4. Plasma reduction mechanism for Au film development on PET substrate a) $HAuCl_4$ ink is inkjet printed onto the substrate and b) converted using O_2 plasma which provides i) electron reducing species causing bond dissociation of the metal salt to its ionic metal and gaseous Cl- anion forms which initiates solvent evaporation at the ii) edges continuing to the center until ii) a conductive Au colored film is seen within 20 minutes of exposure that evenly occurs c) across all samples on the surface. Any gaseous Cl^- by products are then removed in vacuum. This figure was first published in Advanced Engineering Materials by Leung et al.[6]

6.3.1 | ADVANTAGES AND LIMITATIONS

Atmospheric O_2 plasma is a widely available laboratory equipment often used for surface treatment or removal of organic matter. Such tasks do not require high power, therefore this device normally exhibits low power compared to reactive ion etching (RIE) machines. As a result, both the temperature and energy consumption are maintained at a minimum making this technique ideal for temperature sensitive substrates without the need for high vacuum. Additionally, with the limited functionality, the cost of such a machine is effectively lower and an affordable option for any laboratory. Therefore, this technique provides many advantages including low processing costs and compatible with numerous substrates. However, the use of O_2 in the system prompts oxide formation in oxygen sensitive metals that could be prevented using inert gases such as H_2 and Ar. Therefore, the reduction range of atmospheric O_2 plasma with

other metal salt based was explored. Keeping in mind Figure 6.2, it was discovered that neutral to negative ion reduction potential was incompatible with oxygen plasma. In fact, the plasmonic ions and electrons generated via plasma sintering only served to recrystallize the inks. Such cases can be seen below for Sn and Cu inks respectively.

The concocted $SnCl_2$ MSD ink saw an overall transparent color with a higher viscosity than both Au and Ag inks. Figure 6.5 below shows these results beginning with the line pattern (an explanation as well as the original pattern can be found in Chapter 2 under the Inkjet printing section) in Figure 6.5a where the optimal DS was found at 25 μm. Each of the printed squares ranging from 1 – 3 layers were exposed to oxygen plasma in 1 minute burst and subsequently photographed. Within 1 minute of exposure, all squares appeared to be partially converted mostly at the edges as seen in Figure 6.5c. However with further treatment and drying of the respective films, crystal formation appeared as shown in Figure 6.5b which was especially prominent for 2 and 3 layers. This became more severe over a longer exposure time as the previously converted areas reduced in size and eventually became recrystallized after 9 minutes of exposure for multiple layers. This high roughness due to recrystallization becomes more severe as the number of layers increases. As previously seen, the middle portion of each sample tends to show a different behavior than the exterior as the ink tends to agglomerate in that area thus needing a longer exposure time to be converted. However, this was not to case for these film as no uniform film nor fully converted film could be achieved neither for short nor long times. This is due to the -0.14V reduction potential where plasma exposure serves to further recrystallize the film rather than provide any reducing ability. However its mild success does prove that metal salt precursors of a wide range of reduction potentials can be compatible with oxygen plasma.

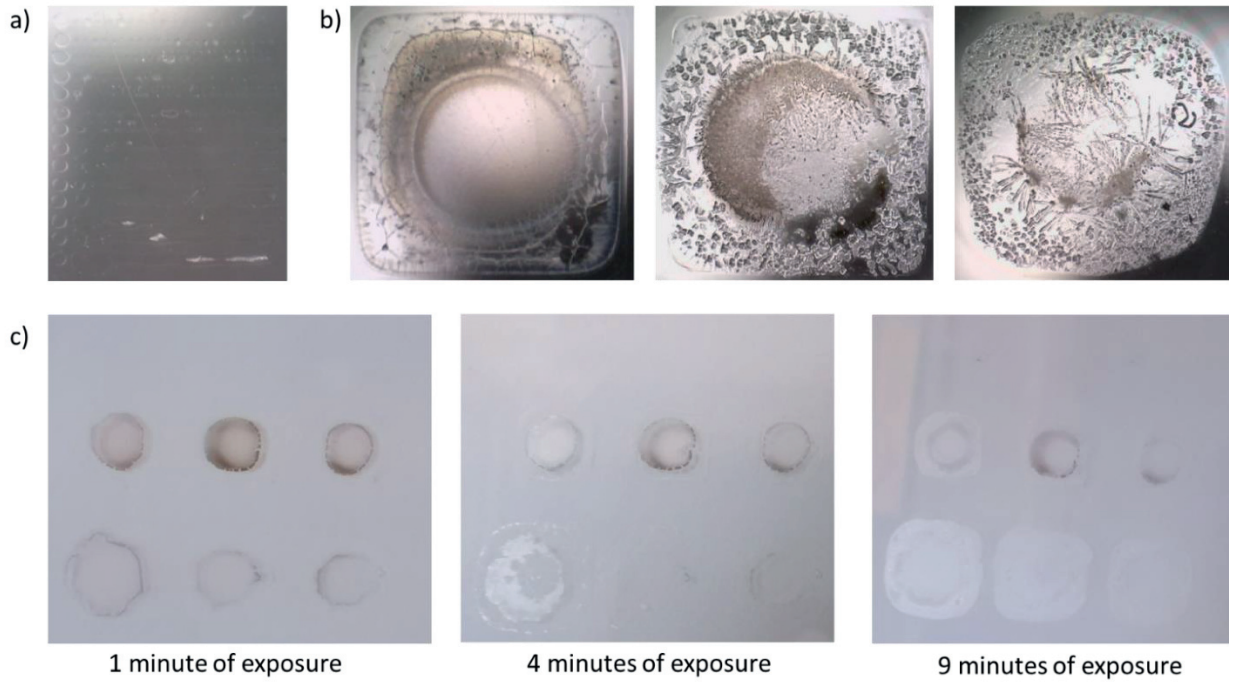

Figure 6.5. Plasma exposed $SnCl_2$ ink on PET substrate a) line pattern, b) printed squares with 1 - 3 layers, and c) time dependent plasma exposure on all layers

Cu MSD ink observed a blue color and also observed higher viscosity than compared to the Au MSD ink. Printing was conducted onto PET substrates beginning with a line pattern (Figure 6.6a) that verified that the ink was generally compatible with the surface. From this, it was determined that a DS of 10 µm would be the most optimal to print future patterns as those above showed scalloped, poorly defined lines while a DS of 5 µm was found to be overly bloated with ink. Oxygen plasma treatment was conducted twice at 40% for 200s and then at 80% for 1 minute. Unfortunately, the only change that was seen in the film was crystal formation as a result of drying as seen in all printed layers in Figure 6.6. It is believed that the salt in the ink only recrystallize with plasma exposure. This result was to be expected as Cu is well known to oxidized rapidly and its respective ion reduction potential is +0.34 eV.

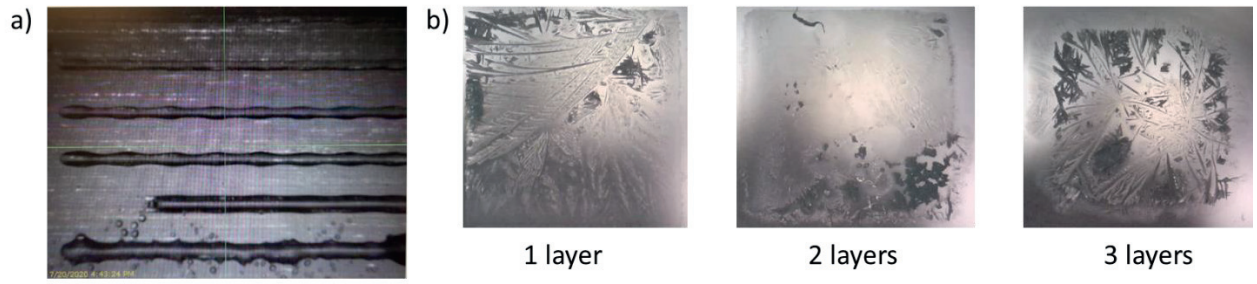

Figure 6.6. Cu MSD ink on PET where a) line pattern and b) squares containing 1 - 3 layers

6.4 | THIN FILM DEVELOPMENT – MATERIALS AND ELECTRICAL CHARACTERIZATION

Due to their respective highly positive reduction potentials, 3 metal salts: $AgNO_3$, H_2PtCl_6, and $HAuCl_4$ were targeted for O_2 plasma conversion. Each of the metals were explored in the same manner starting with ink formulation and manipulation and printing and materials characterization on standard polymer substrates. If sintering was successful on non-conventional substrates, these films were then further characterized. This was achieved through a variety of surface characterization and electrical techniques including optical and confocal microscopy, scanning electron microscope (SEM), x-ray diffraction (XRD), atomic force microscopy (AFM), profilometry, and 4-point probe measurements.

6.4.1 | AG MSD INK – MATERIALS CHARACTERIZATION

The resulting $AgNO_3$ ink has a lower viscosity compared to other inks due to lower EG content which directly improves the printability overall. The ink itself is colorless where there was no apparent sign of precipitates. One of the first tests performed to determine the interaction of this ink with the PET substrate surface was by printing the line pattern. It indicated that the PET substrate must be first pre-treated with oxygen plasma (80% for 30 second) in order to form a continuous line. For this reason, the first printed line pattern as shown in Figure 6.7a was found to be discontinuous for all DS and also already converted to Ag following the surface plasma treatment. The second line pattern following plasma treatment indicated that a wide range of DS were printable ranging from DS of 5 - 40 µm. Eventually it was determined that a DS of 25 µm provided continuous square films with optimal sharpness and integrity which were then subjected to two rounds of 100% plasma power for 1 minute directly following its printing as shown in Figure 6.7b below. After the first plasma treatment, a silver color with high roughness appeared with due to salt crystal formation. A second plasma treatment was performed showing that the film became over oxidized meaning that in general, more than 1 minute of plasma exposure leads to oxidation. It was determined that the deposited ink thickness was important not

only for successful film formation, but also for the oxidation meaning that a precise test was needed to determine what the optimal plasma treatment time was needed for each layer.

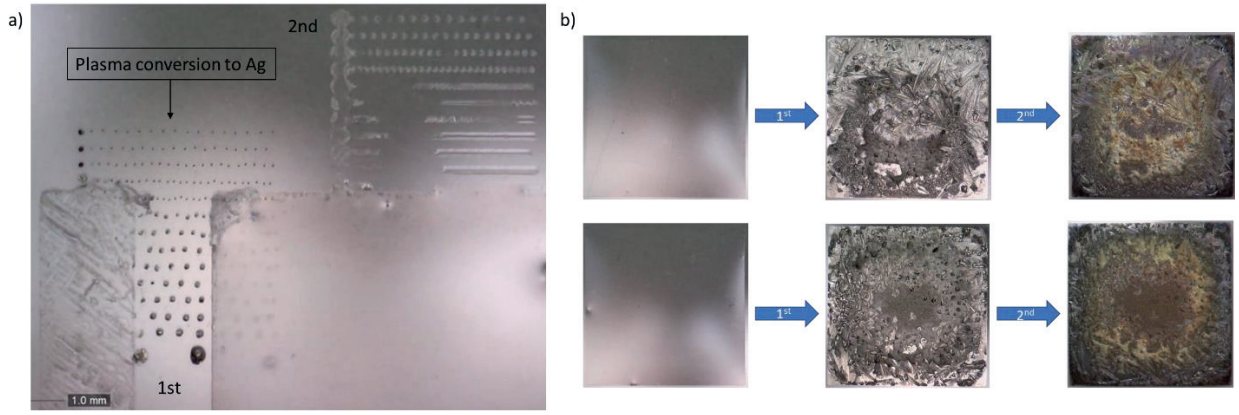

Figure 6.7. Plasma reduced $AgNO_3$ ink on PET a) line pattern before and after conversion and b) stepwise conversion leading to oxidation

Figure 6.8a and 6.8b showed that rapid crystal formation appeared directly following printing for 1 and 2 layers defining the resulting film formation. Conversion of the film for 1 layer required just 45s while 2 layers needed 60s however such layers tended to dry prior to plasma exposure meaning a non-continuous film would be formed as seen with 1 layer in Figure 6.8ai. Those with 3 to 5 layers (Figure 6.8c - 6.8e) also show severe roughness with varying levels of black discoloration seen across the films. This indicates that the both the surface and lower layers may not be fully converted or oxidized as plasma treatment was conducted at 80% power (64W) for 75s. Further plasma exposure was not attempted as previous experience showed that oxidation can occur rapidly. These squares were then tested for their respective sheet resistance values which is not reported here as their values were highly inconsistent which may be due to the varying surface roughness found across similarly printed samples. However, the lowest sheet resistance found was 19.6 Ω/□.

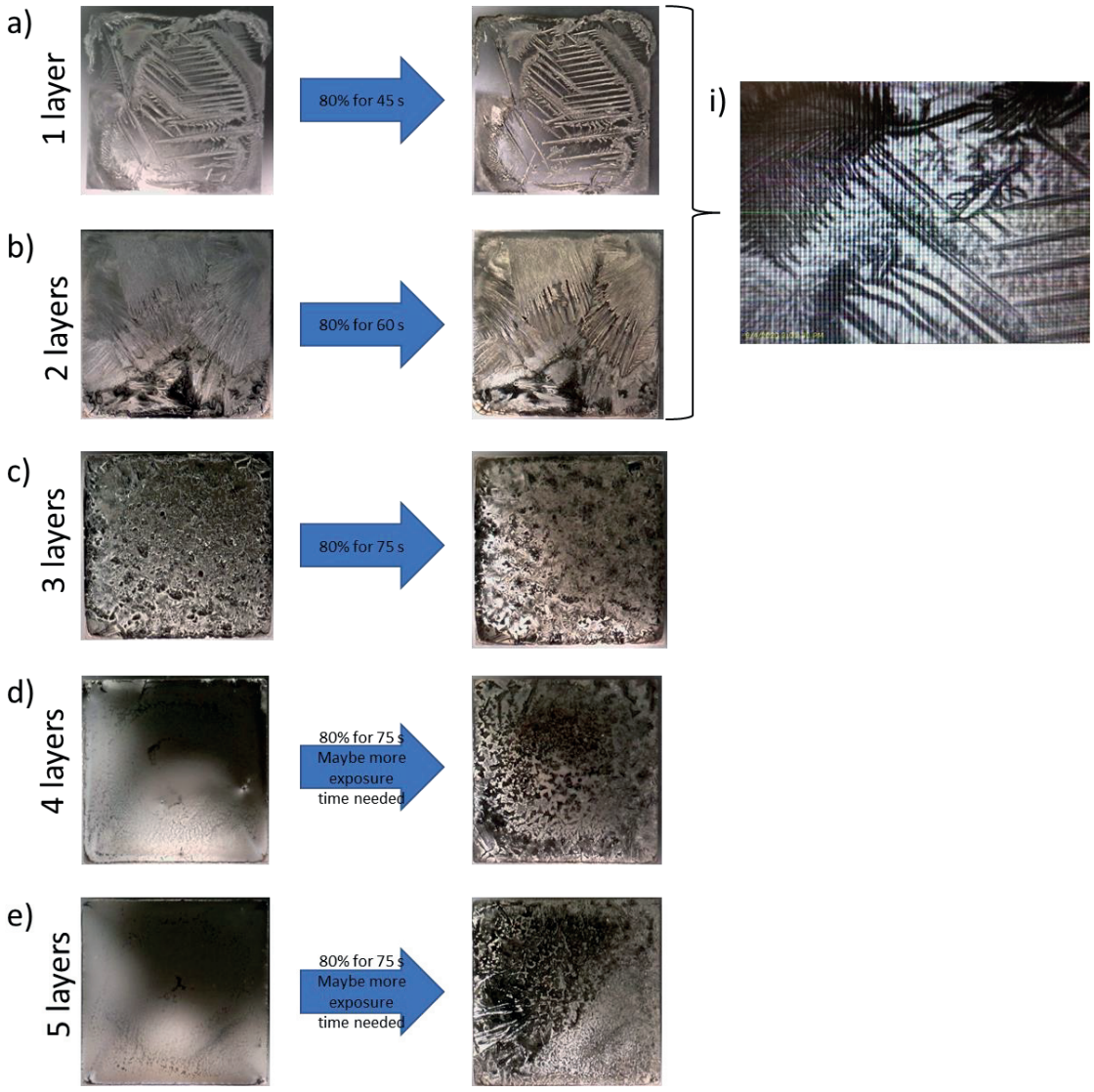

Figure 6.8. Ag film formation before and after plasma treatment showing dependency by layers where a) 1 layer, b) 2 layers, c) 3 layers, d) 4 layers, and e) 5 layers. Figure 6.8ai was taken with the Dimatix fiducial camera showing crystal formation immediately following deposition.

Further characterization of the films explored the surface topography using SEM analysis and its respective chemical composition through energy dispersive X-Ray (EDX) analysis and crystal structure through XRD analysis. As shown in Figure 6.9 below, SEM micrographs revealed that rapid crystallization seen in the films lead to the development of highly porous films (Figure 6.9a). Although this roughness can already be seen by eye, the surface roughness is a result of high porous nature of the reduced Ag films. As sintering was performed at low temperatures, solvent evaporation becomes a major contributing factor where silver salt begins to precipitate before its decomposition thus creating crystals especially prevalent on 1 and 2

layers.[12] Using EDX, the film contained only Ag while C and O contamination are common elements found during analysis as shown in Figure 6.9b. However this result was disputed by Figure 6.9c where XRD analysis showed a variety of unidentifiable peaks which can be attribute to $AgNO_3$ or silver oxide formation. These differences in results are due to the penetration depth of each respective technique meaning XRD analysis penetrated further into the sample revealing the presence of organic contamination that signaled incomplete conversion due to the skin effect.

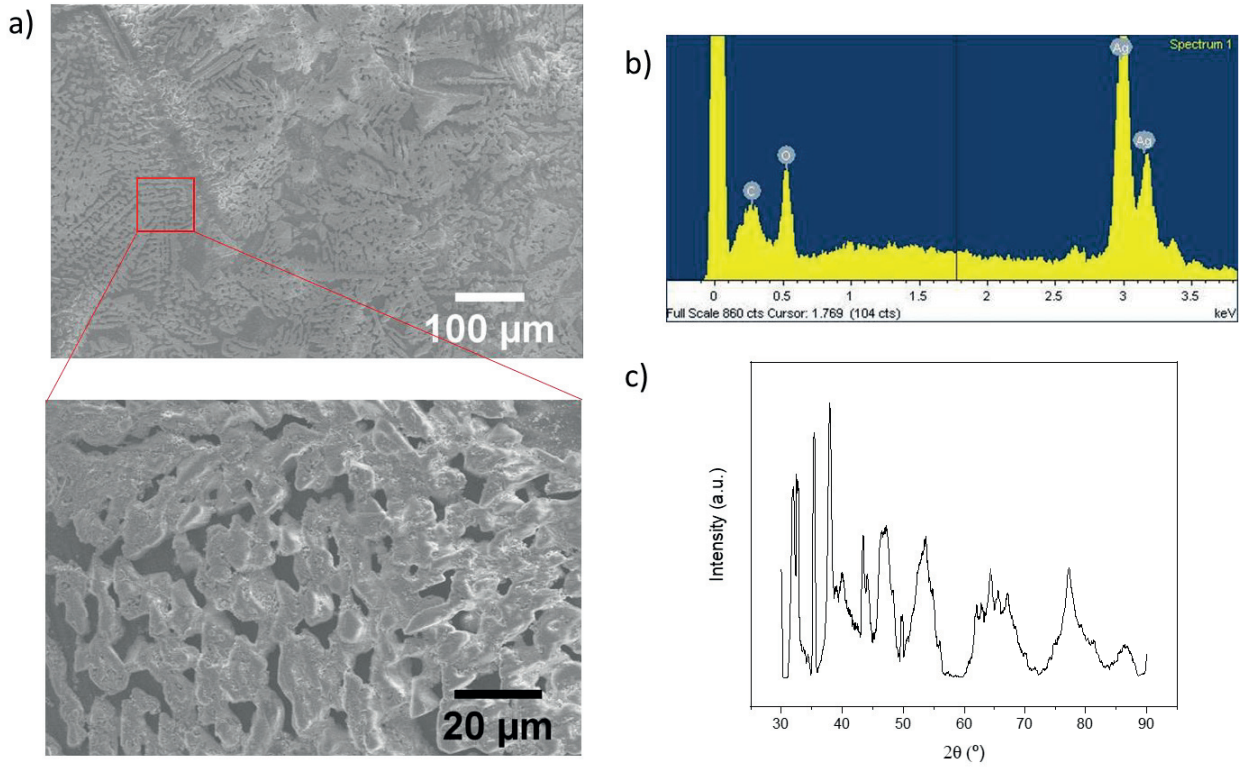

Figure 6.9. Materials characterization of printed Ag films through a) SEM analysis, b) EDX analysis, and c) XRD analysis

Different substrates such as PDMS, paper, and textile were tested to see if plasma processing was compatible with these surfaces. PDMS is a widely used silicone polymer that is known for being extremely hydrophobic as previously discussed and tested in Chapter 4. Therefore, at minimum, the surface must be treated with oxygen plasma and/or with chemical treatments in order to make the surface printable. Figure 6.10 below displays the results of different treatments the PDMS surface was subjected to. It can be seen that without any plasma treatment, droplets with the smallest distance (DS of 5 µm) between them completely merged together and formed larger separate droplets (Figure 6.10a). With increasing DS, the outcome was no better however this result was expected. Figure 6.10b to 6.10d showed that even with

plasma treatment, its development fared no better as the droplets exhibited similar behavior, the only difference being that as the plasma time increased, the droplets became more randomly dispersed and larger in size however never resulting in a continuous film. One last attempt was made to achieve a printable surface which was a multistep chemical and plasma treatment of the PDMS surface as reported by Wu et al.[13] which included 0.5M of (3-Mercaptopropyl)trimethoxy silane (MPTMS) in ethanol + 0.1M HCl followed by exposure to plasma at 37% for 30s. Here, the appearance of the line pattern was massively improved however these printed lines were temporary and eventually rebounded into a bigger droplet. Unfortunately, none of the treatments were found to be sufficient enough to create a bounded square pattern and therefore no further testing was conducted using this substrate.

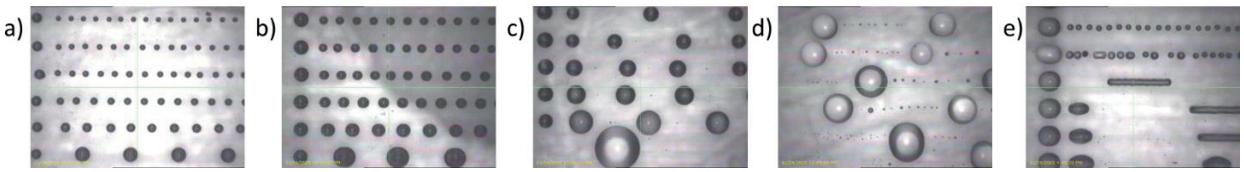

Figure 6.10. Line pattern AgNO3 ink printed on surfaces a) without plasma treatment b) 40% for 20s plasma treatment, c) 40% for 40s plasma treatment, d) 40% for 60s plasma treatment, and e) MPTMS + HCl chemical treatment

Ink behavior and possible reduction was also tested on paper and textile which are known to have higher porosity than polymer substrates meaning there is a high probability for ink absorption further complicating the reduction process. This did in fact play a role as it was not possible to develop conductive Ag structures on either substrate. Figure 6.11 shows results from the multilayer deposition and treatment of the $AgNO_3$ ink on Teslin paper which in fact did see a dramatic change in film color from a pale yellow color until a dark brown color indicating an intermediate Ag film formation occurred that was altogether found to be non-conductive. In the end, all squares had a streaky appearance meaning that a continuous layer was not developed, and the wrong DS was chosen. Within 15 second of plasma treatment at 80% (64W), the squares were visible turning from clear to yellow complexion. After an additional 15 seconds, an even darker yellow appeared however with further plasma sintering, this no further changes were seen. The substrate was monitored for 30 days to see if any changes would occur however the results remained the same. One sign that partial conversion appeared was that the dark brown film observed silver specks where perhaps isolated Ag NPs developed over time. A similar behavior was also found on the Decathlon textile which appeared to be highly porous as the ink was absorbed and spread beyond the original square dimensions. Figure 6.12 displays the overall results where 2 and 3 layers continued to remain brown in color after multiple plasma treatment attempts. However, this brown color appeared immediately for squares with 4 and 5 layers within 30s which continued to remain consistent even following further plasma exposure. The

reason for this rapid change was mostly due to the availability of the $AgNO_3$ ink at the surface for multiple layers as the ink need more time to be absorbed into the fabric. For this reason, a gradient of intermediate brown colored film was seen which grew darker with more layers. Even after a long period of observation, no conductive film was formed and remained in this dark brown color. It is believed that in these cases, that the ink absorption further impeded the Ag film reduction process as plasma sintering could not penetrate past the substrate surface.

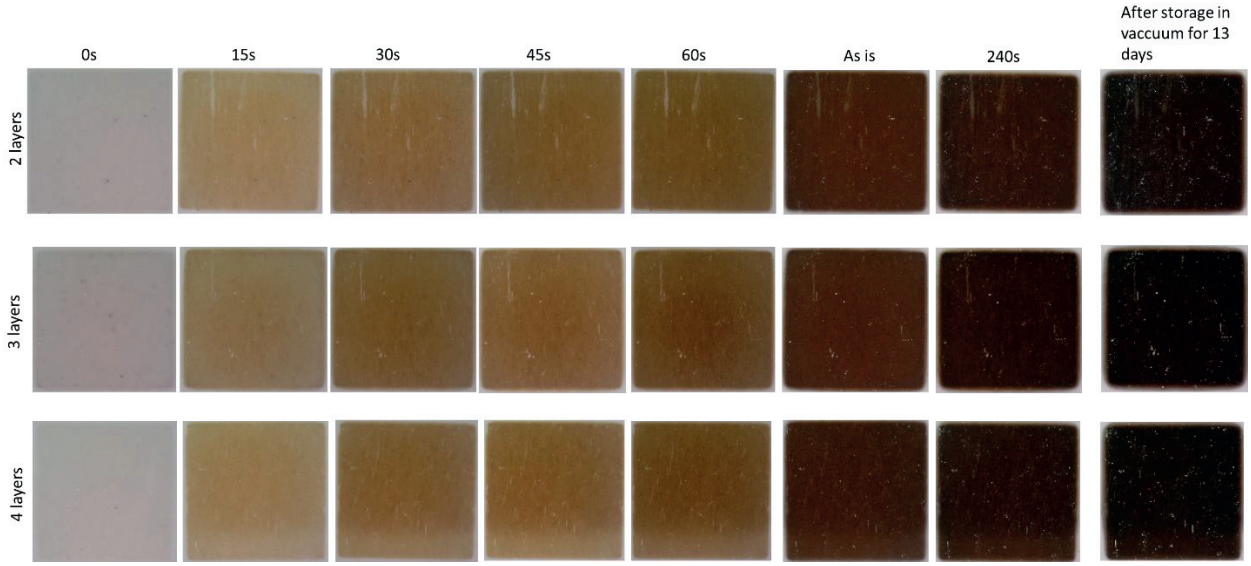

Figure 6.11. Different stages of Ag film growth on Teslin paper for 2, 3, and 4 layers

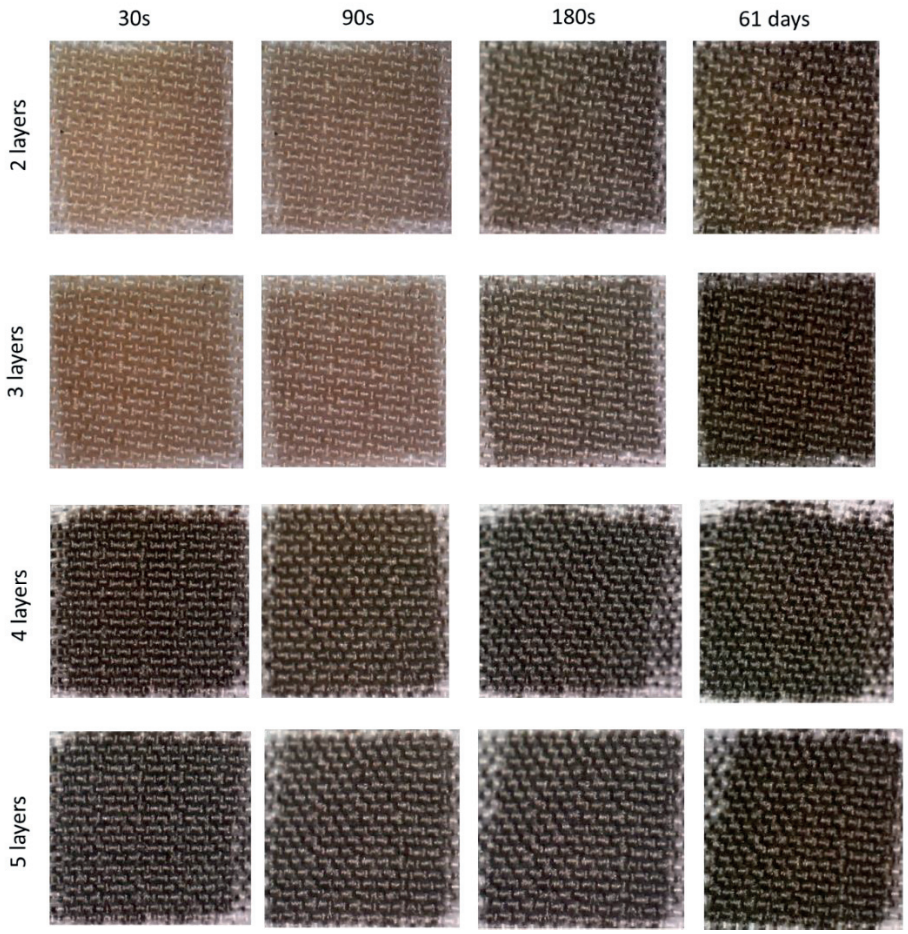

Figure 6.12. Ag film growth by layers on 100% polyester textile

Although an in depth reduction mechanism was not studied here due to the inconsistent growth of the Ag thin films, an updated model was presented by Sui et al. asserting that high surface roughness of such inks is a consequence of solvent evaporation.[14] In this study, they proved that the surface morphology can be adapted by adjusting the $AgNO_3$ ink based on its respective vapor pressure whereby surface roughness, porosity, and thus electrical resistivity all increase with decreasing vapor pressure.[14] Low vapor pressure solvents increase the critical liquid-phase reduction and nucleation time as they remain stable even under vacuum conditions.[14] Initially it was proposed that only $AgNO_3$ is ionized in the solvent however this was revised to include that $AgNO_3$ also recrystallizes due to solvent evaporation. It is the ionic bonds of $AgNO_3$ that are dissociated by the electrostatic attraction from the polar molecules in the solvent.[14] The reduction of the Ag^+ ions to Ag are confined to the surface regions where electron density is the highest and reach a tipping point where nucleation a growth of the thin film occur. Once the solvent completely evaporates, the Ag cations and NO_3 anions increase in concentration and reform back into $AgNO_3$.[14] This account for the crystal structures especially

apparent in smaller thickness films as seen in Figure 6.8a and 6.8b. They show that eventually a bilayer of $Ag/AgNO_3$ film is formed and thus affect the electrical conductivity as was previously suspected. Growth initiated from a liquid will never be able to achieve full densification resulting in porous structures which are seen across all MSD inks. At the same time, these solvents provide a more uniformly reduced Ag film ensuring that the deposited ink in its entirety is converted circumventing the skin effect which is typically seen for plasma sintered films. The findings reported in this paper cannot be fully verified as limited analysis of Ag films was performed due to their quick oxidization using oxygen plasma. However, this does explain the large variety of unidentifiable peaks found during XRD analysis (Figure 6.9c). In contrast, no remaining nitrate or nitrogen was found in the SEM/EDX analysis as the penetration depth only allowed for surface analysis. Instead, this further supports the idea of the skin effect occurring as a result of the sintering technique as mentioned in this paper.

Further testing regarding the printing and plasma optimization or ink formulation improvement could not be performed as there was inconsistent conversion where the deposited films were found to be completely non-conductive across all substrates including PET. Initially, this technique showed promise with Ag but its inconsistency and affinity to oxidize made it incompatible with O_2 plasma but instead has been proven using Ar plasma.[4,14] Additionally, crystallization of the printed ink occurred rapidly due to excessive drying creating isolated islands and disconnected films.[15]

6.4.2 | PT MSD INK – MATERIALS CHARACTERIZATION

Pt MSD ink was composed of 1.0M H_2PtCl_6 (≈0.3928g) combined with 3 mL (50% EG+ 50% DI water) which initially showed an orange color and turned to yellow after 2 weeks storage (Refrigerated at 4°C) perhaps signaling oxidation. Ink exhibited higher viscosity than the Ag MSD ink as expected with the introduction of greater concentration of EG and successfully printed on multiple substrates which will be discussed in detail.

Figure 6.13 shows the typical pre-printing test pattern which was conducted by printing a line pattern onto every new substrate which in this case was first printed onto PET. On plasma treated PET (procedure as stated previously), the line patterns appeared to be bloated which is not 100% ideal for printing as this may cause desired patterns to be larger than expected. This behavior may not be ideal, however a line did appear meaning that printing was acceptable in this state. It was determined from this that the optimal DS appeared to be between 25 – 30 μm. These were the starting printing parameters which were verified in Figure 6.14 showing that ultimately, DS of 20 μm was needed to create a continuous printed layer. However, as the different layers were exposed to O_2 plasma, just 1 printed layer was insufficient to create a square pattern. In this case, at least 2 layers was necessary to create a continuous film, however

its final shape was much more rounded than expected as the deposit ink layer tends to agglomerate at the center. After 3 minutes of sintering, each layer appears to be completely dried and converted while the exterior reduces more rapidly than the middle. This is due to the Marangoni effect which was previously explained in Section 6.3 using Au film formation which directly applies to Pt formation as well. Additionally, a brief optimization of both the printing and plasma sintering parameters was defined as shown in Figure 6.15 below. A limited range of DS were tested mostly due to the DS printing compatibility seen before in Figure 6.13. Here, Figure 6.15a presents 2 DS sizes that varied widely already implying that a DS of 20 µm was the optimal DS which showed a minimal sheet resistance of 64.5 Ω/□ for 1 layer. This parameter was then used later through further testing where up to 3 layers was explored as seen in Figure 6.15b. As previously discussed, 1 layer gave unreliable measurements as the film dried before conversion creating a discontinuous layer. It was discovered that 3 layers reported a sheet resistance of 50.2 Ω/□ whereas 2 layers showed 64.0 Ω/□. Next the sintering parameters were defined where different exposure times from 5 – 11 minutes at 80% (64W) was tested as shown in Figure 6.15c. For 2 layers, the sheet resistance reduced from 65.2 to 57.0 Ω/□, showing only a 12% decrease for an addition 5 minutes of plasma. Therefore, a longer exposure time was not needed showing that already with an exposure time of 7.5 minutes was acceptable. Lastly, Figure 6.15d displayed the layer thickness achieved after printing and plasma sintering where 450 nm and 1.16 µm were found for 2 and 3 layers respectively. This parameter was then used to calculate their respective conductivity values of 3.85 x 10^4 and 2.34 x 10^4 $S \cdot m^{-1}$. From this, it was determined that an optimized Pt film should be printed with a DS of 20 µm with 2 layers and plasma treated with 7.5 min.

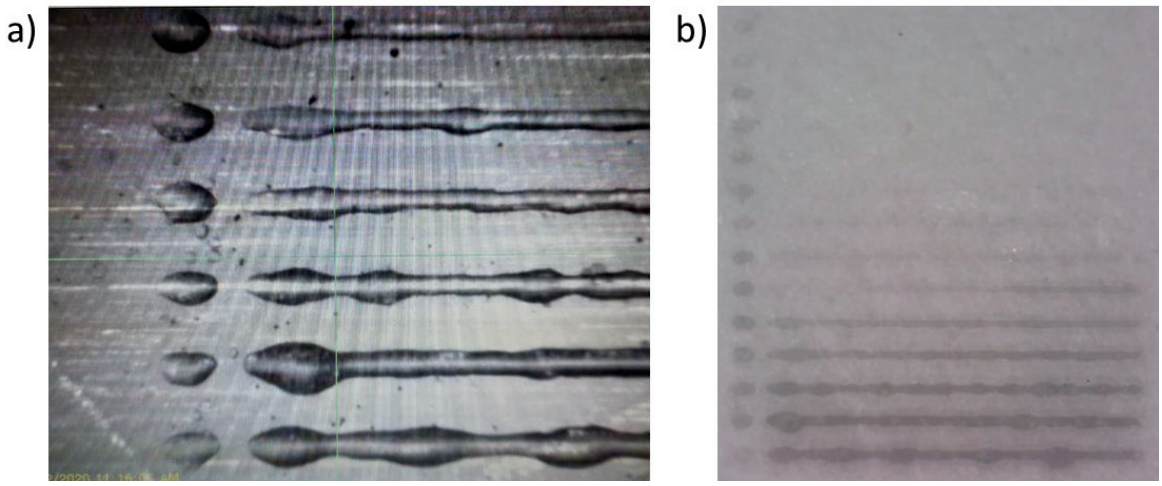

Figure 6.13. Printed line pattern on PET substrate from a) Dimatix fiducial camera view and b) following plasma treatment at 80% (64W) for 30s

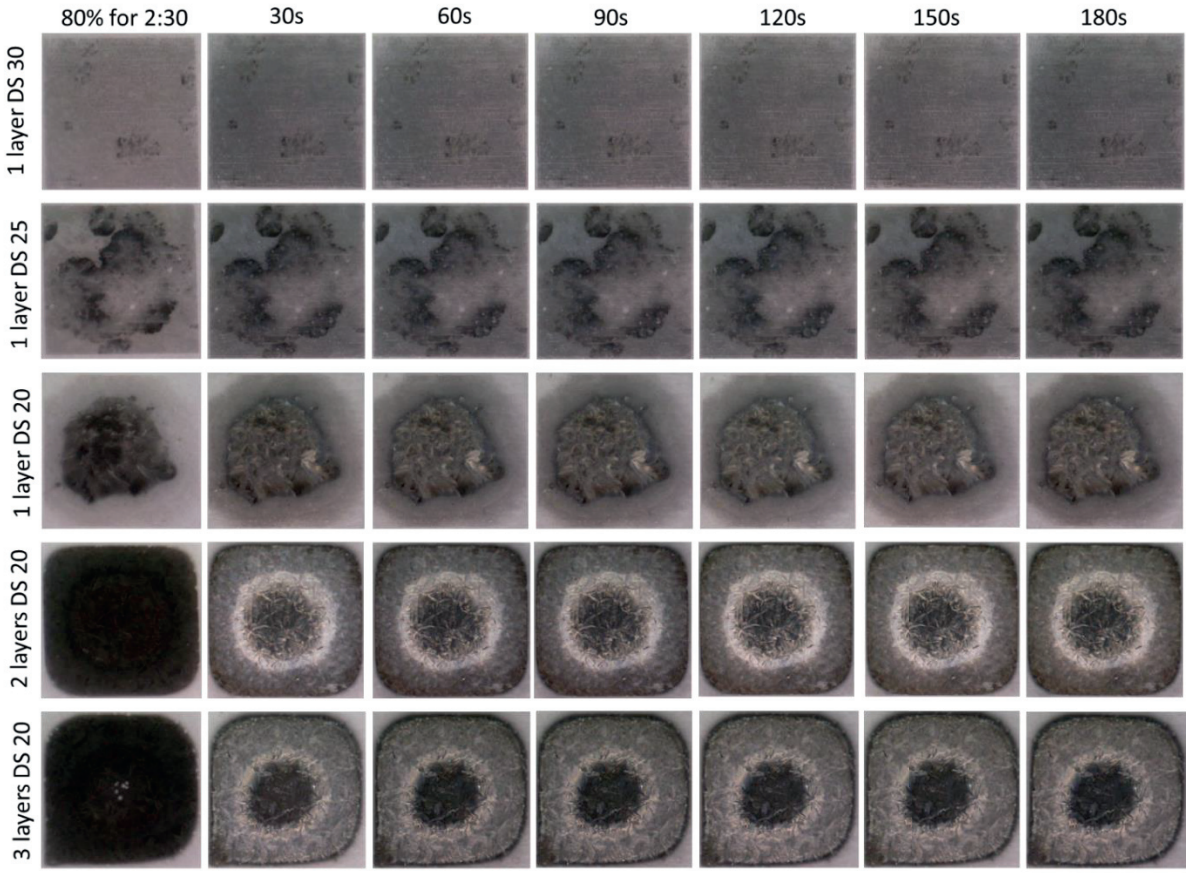

Figure 6.14. Different stages of Pt film growth by plasma sintering at 80% (64W) after 2.5 minutes until 5.5 minutes detailing development every 30 seconds

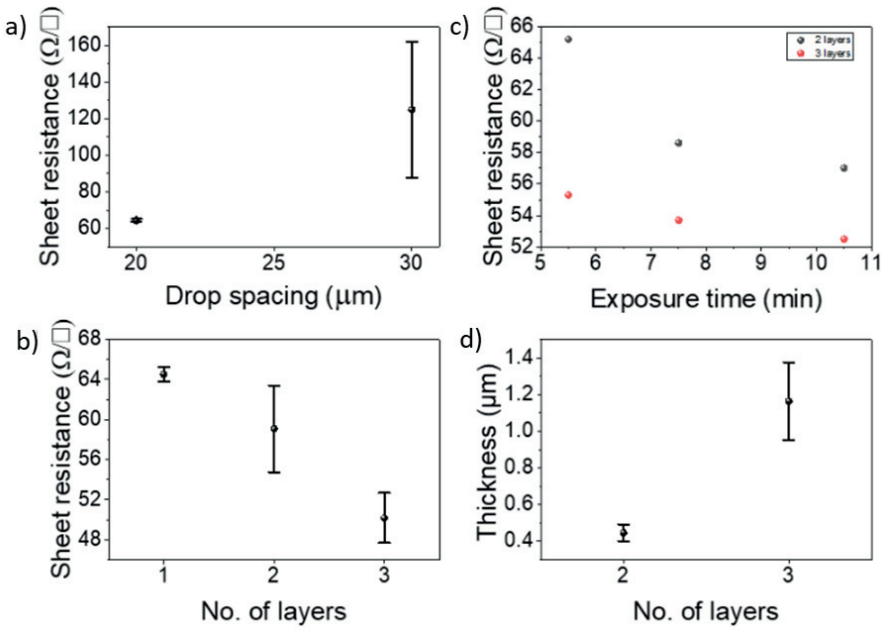

Figure 6.15. Optimization of printed and plasma sintering parameters to develop Pt films

Generally, the Pt film showed large metallic crystal structures that were visible by eye as shown in Figure 6.16a. SEM analysis delved further into the microstructure of the film revealing a lamellar and mesoporous film as shown in Figures 6.16b. This behavior was further verified with Figure 6.16c where a focus ion beam (FIB) cut was used to expose the profile view however did not indicate any visible microstructure. Pore formation is created as a result of the salt byproducts from metal salt precursors where a metal framework forms from the removal of salts that occupy interstitial space between the metal atoms.[6] In fact, the surface itself appeared to be full of complete spherulites or hedrites with a distinct nucleation site at the center that form separate crystals through grain boundary formation.[16] This is considered a type of polycrystalline growth that develops under nonequilibrium conditions.[17] The result is a relatively high surface roughness (Figure 6.16d) at 344.7 nm as compared to evaporated Pt films.

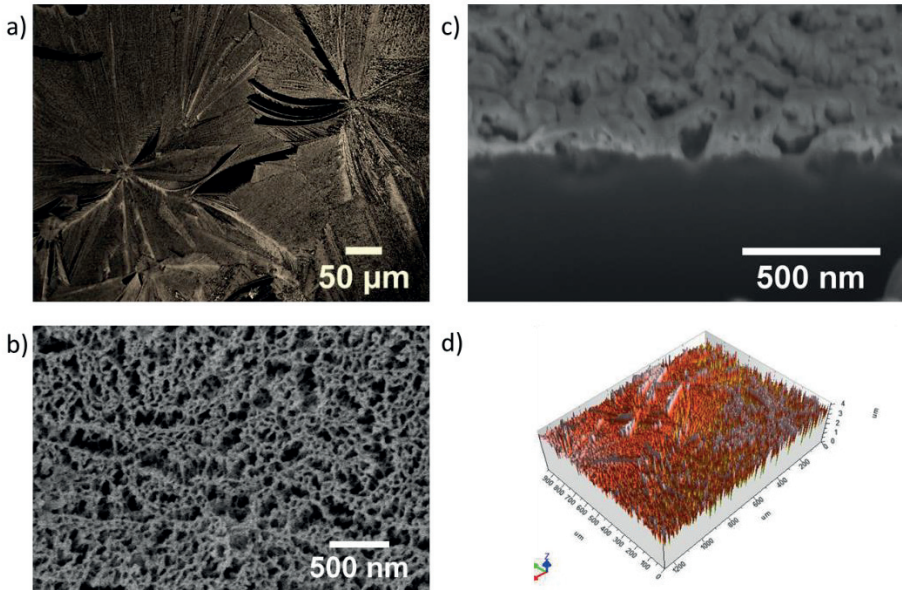

Figure 6.16. Surface topography images of the Pt film taken by a) an optical microscope at 20x magnification, b) SEM analysis at a magnification of 10,000x, c) FIB profile cut at 70,000x magnification and d) surface profile measurement taken by confocal microscopy

Strangely enough, when enough layers were printed and converted, such as the case with 2 and 3 layers with a DS of 20 µm, the inner portion of the sample sees a highly reflective silver color which is then surrounded by a ring. These different growth regions were further investigated with SEM-EDX analysis as shown in Figure 6.17a and 6.17b. Under SEM analysis, the center region (Figure 6.17b) exhibited a more disorganized behavior where the film itself showed more random island growth formation and chlorine which was surrounded by the organized crystalline structure in the outer regions. Figure 6.17a showed that the outer edge regions saw only Pt meaning this region was already fully converted. The difference in these two spectrums signaled that reduction of the ink occurred unevenly as ink accumulated in the middle meaning more exposure time was necessary for complete reduction. However, this behavior was expected as conversion followed the reduction mechanism was proposed in Section 6.3 due to the Marangoni effect of the ink. XRD analysis in Figure 6.17c showed an amorphous film with a wide range of peaks including those identified being related to pure Pt at 39.7°, 46.8°, 67.5°, 81.4°, and 85.6° corresponding to (111), (200), (220), (311), and (222) crystal planes respectively. Those peaks found at 53.4° and 77.1° correspond to interference found from the PET substrate below due to the thin film. All other peaks identified here could not be identified but are attributed most likely due to Cl contaminants from the incomplete reduction. When initially printed, the squares started out from a translucent yellow to dark grey to a silver color with obvious crystal formation. Already this crystal formation was seen at the intermediate grey color stage which may be due to the recrystallization of the metal salt as seen with the $AgNO_3$

ink. However, this behavior is believed to be more severe here when looking at the stepwise chemical reaction at Equations 6.1 and 6.2 below:

$$PtCl_6^{2-} + 2e^- \leftrightarrow PtCl_4^{2-} + 2Cl^- \qquad E_0 = +0.68V \tag{6.1}$$

$$PtCl_4^{2-} + 2e^- \leftrightarrow Pt_{(s)} + 4Cl^- \qquad E_0 = +0.73V \tag{6.2}$$

As the reaction is reversible and more energy is required to fully reduce the Pt ion to its non-zero valent state where the probability that Cl anions contaminate the film quality which appears during XRD analysis.

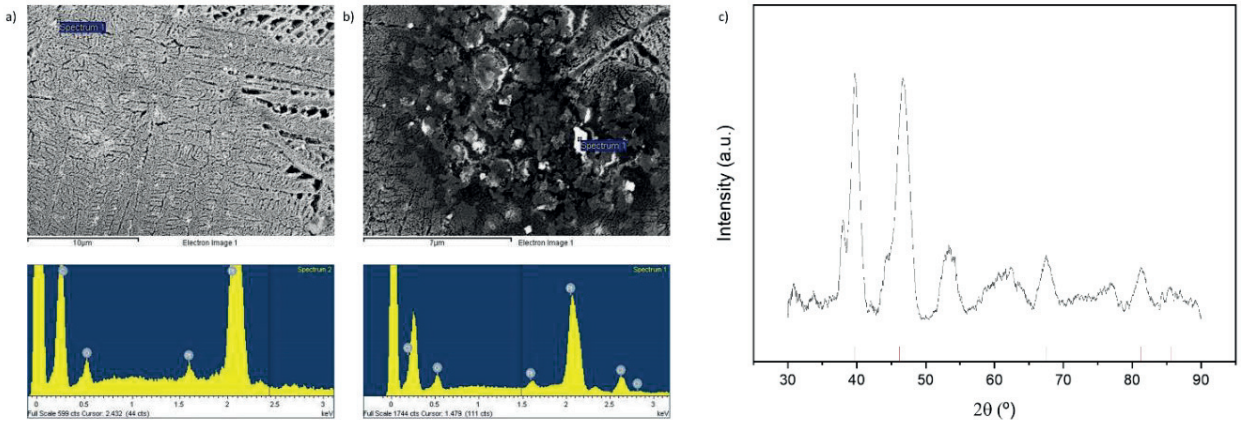

Figure 6.17. Chemical composition analysis through a) SEM-EDX on the outer area of the sample, b) SEM-EDX on the inner area of the sample, and c) XRD analysis

Pt MSD ink presents similar roughness from porous film growth as plasma reduced Ag films which is typically found in the reduction of MSD inks. Table 6.1 below provides an overview of the Pt thin film properties including it metal content which was calculated to be 15.8%, lower than similar NP inks previously characterized at 20.5 wt%.[18] This ultimately affected the final conductivity which was found to be 3.85 x 10^4 S·m^{-1}, significantly lower than its bulk equivalent at only 0.41%. However, this may additionally be in part due to the high reported surface roughness at 344.7 nm for a 400 nm thick film. However, an advantage of this technique was with respect to its low processing temperature that did not reach beyond 32°C which is unachievable if using standard NP inks. All these factors must be taken under consideration as the use of plasma sintering allowed for low temperature production of conductive films which may be viable with thermosensitive substrates.

Table 6.1. Summary of Pt thin film properties on PET

Metallic Content [%]	Processing Temperatures [ºC]	Thickness [µm]	Surface Roughness [nm]	Conductivity [S m^{-1}]	Bulk Conductivity [%]
15.8	31.5	0.401	344.7	3.85x10^{4}	0.41

6.4.2.1 | *PT THIN FILM DEVELOPMENT ON NON-CONVENTIONAL SUBSTRATES*

Due to the success of this film, a myriad of other substrates was investigated including tattoo paper, PVA, Teslin, Powercoat HD, and abaca CNF paper, and decathlon and umbrella fabric. As expected, the most successful conversions were exhibited on other polymer substrates such as tattoo paper and PVA at varying degrees. Tattoo paper is a multilayer substrate composed of ethylcellulose attached to paper via an intermediary layer often made of PVA. As seen in Figure 6.18a, this substrate was composed of dotted PVA layer that made inkjet printing especially difficult as it did not meet printing requirements. Several plasma treatment tests were done in order to manipulate the surface however this proved unsuccessful. Because of this, no defined pattern could be printed, neither a square nor the line pattern which always resulted in amorphous shapes. However, reduction to Pt required at least 8 minutes at 80% (64W) power which displayed a resistance of 0.8kΩ meaning that a poorly conductive film was achieved. With PVA, the ink reacted quite differently either due to the substrate itself or the fact that the ink became oxidized over time. A DS of 5 µm was necessary to create continuous layer where after 19.5 minutes, no complete conversion was found. The results can be seen in Figure 6.18b and 6.18c for 1 and 2 layers of deposition respectively. The edges of the sample with 1 layer appeared to be converted while the center remained in an intermediary stage which did not improve with further plasma exposure. This fared no better with 2 layers as no Pt film growth was apparent leaving only remnants of the dried deposit ink behind ultimately proving this combination to be unsuccessful. Although this could be for a number of reasons, this proved to be unsuccessful mostly due to the ink stability which became easily oxidize once exposed to air meaning that this ink could only be used for a short time period after fabrication. Therefore, this directly affected this and the next following results which in affect should be replicated however this was not possible as the manufacturing standards of the metal salt varied widely where the previous formulation was no longer available.

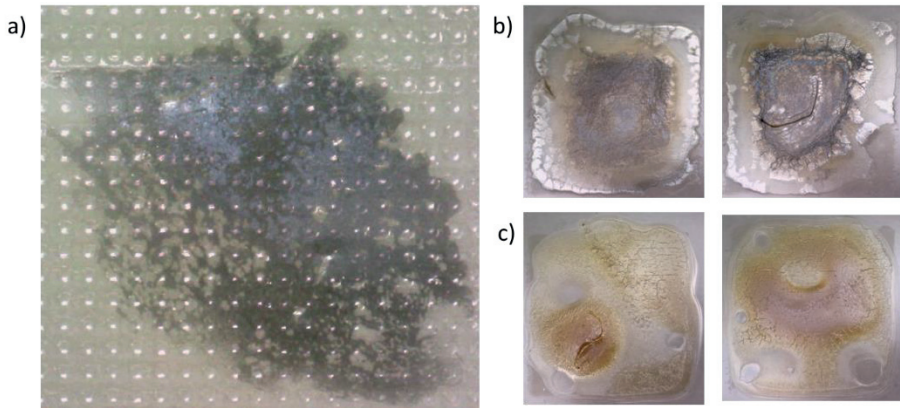

Figure 6.18. Printed and converted Pt films on a) tattoo paper, b) PVA with 1 layer, and c) PVA with 2 layers

In general, Pt ink deposition and reduction was altogether unsuccessful on both paper and fabric substrates most likely due to their respective porous and absorptive natures. On Teslin paper, although enhanced for inkjet printing, tended to absorb such a low viscosity ink that multiple layers were needed to create a uniform film. Thus 3 to 6 printed layers were deposited, sintered, and tracked for a maximum of 94 days to see if any film would possibly develop over this period. After the initial printing of the line pattern test, the ink was readily absorbed into the paper and could not be identified therefore a random DS was chosen at 15 µm taken from previous tests. No changes were identified following plasma treatment leaving a transparent yellow color which only over time started to grow to a darker grey colored film after 28 days as shown in Figure 6.19. By day 94, there were no further changes seen and the substrate was no longer monitored. There were even less impressive results when using the Powercoat HD as uniform layer could not be formed even after multiple surface treatment attempts as shown on Figure 6.20. Initially the printed line pattern had given a good indication that a layer possibly could be printed, however this was not the case in practice. Although not shown, a DS of 5 µm still could not printed as a continuous layer and therefore not subjected to plasma treatment. Results on abaca CNF paper (Figure 6.21) which was engineered for inkjet printing provided poor results as no conductive film could be developed. Following 9 minutes of exposure, the color of the ink darkened from 1 – 3 layers (most likely due to drying) while 5 layers still remained wet. A total of 19.5 minutes of sintering was done seeing no further changes in terms of colors of the film indicating that not even NPs were developed.

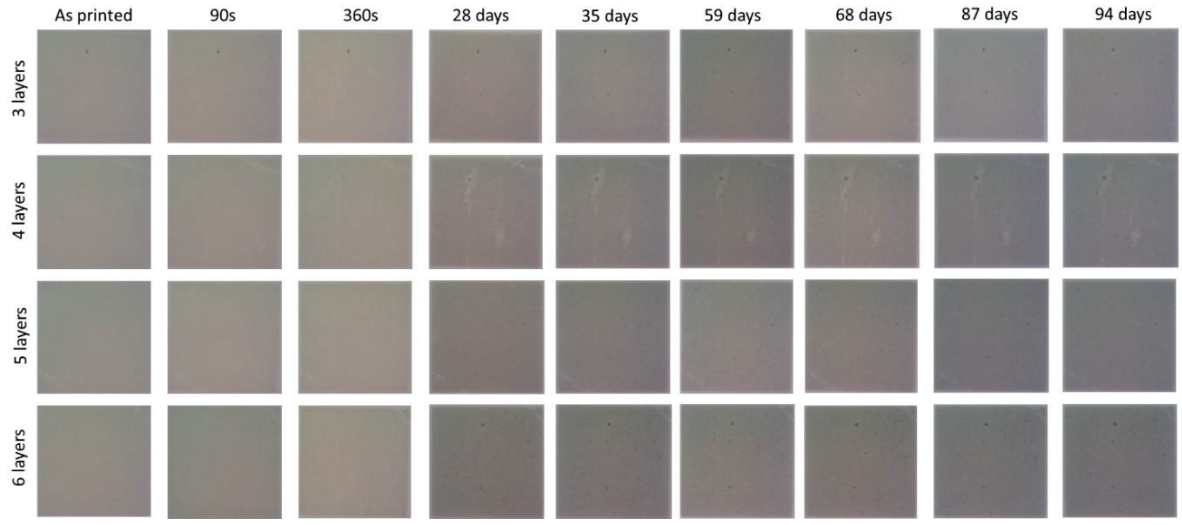

Figure 6.19. Deposited Pt films on Teslin paper from 3 - 6 layers

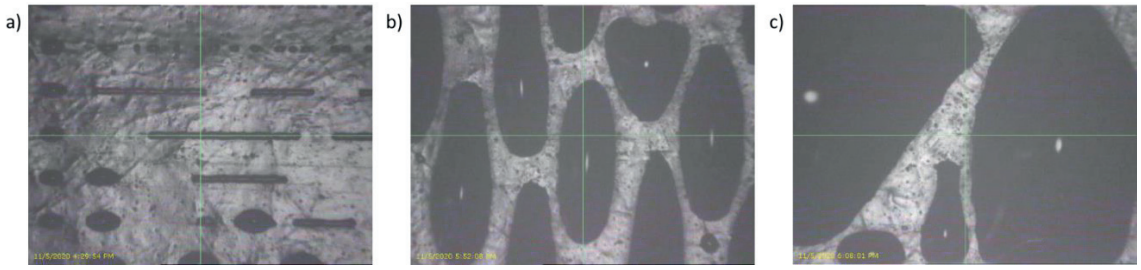

Figure 6.20. Printed Pt ink on Powercoat HD substrate pre-treated with O2 plasma at 40% power and 60s a) line pattern, b) DS of 20 µm, and c) DS of 10 µm

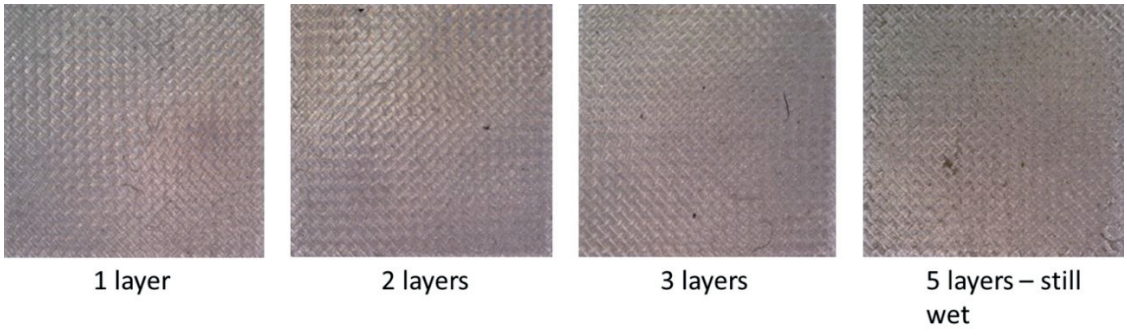

Figure 6.21. Multiple Pt ink layers printed onto abaca CNF paper

Almost identical results were found on fabric substrates such as the Decathlon polyester textile and umbrella fabric. Although it wasn't initially visual, the deposited ink on the Decathlon textile shorts began to bleed into surround areas of the patterns showing that this substrate was

highly porous thus negatively affecting the metal film development as shown on Figure 6.22. Plasma treatment was performed at 80% (64W) for 60s and investigated or imaged directly after. Darkening of the square was seen with every treatment up to 7 minutes. The substrate was then left at RT to track if any film would eventually develop after 90 days. Each respective film did indeed become noticeably darker by day 10 and 17 after deposition however after 91 days, there was not much of a difference was seen. All films remained non-conductive and never showed a metallic silver color making the conversion unsuccessful with this substrate. However by this time, it was clear that the Pt MSD ink was expired and could no longer be used as not even a conductive film could be produced using PET. Therefore a new ink was made which was also discovered to be non-functional as the metal salt precursor by this time was already expired. Regardless, the newly developed ink was printed onto umbrella fabric as shown in Figure 6.23 below. After 20 minutes of plasma, no difference was found in the deposited films before and after treatment. In fact they appeared similar to those films first printed onto the Decathlon textile but saw no improvement even after tracking for a longer period of time in ambient conditions.

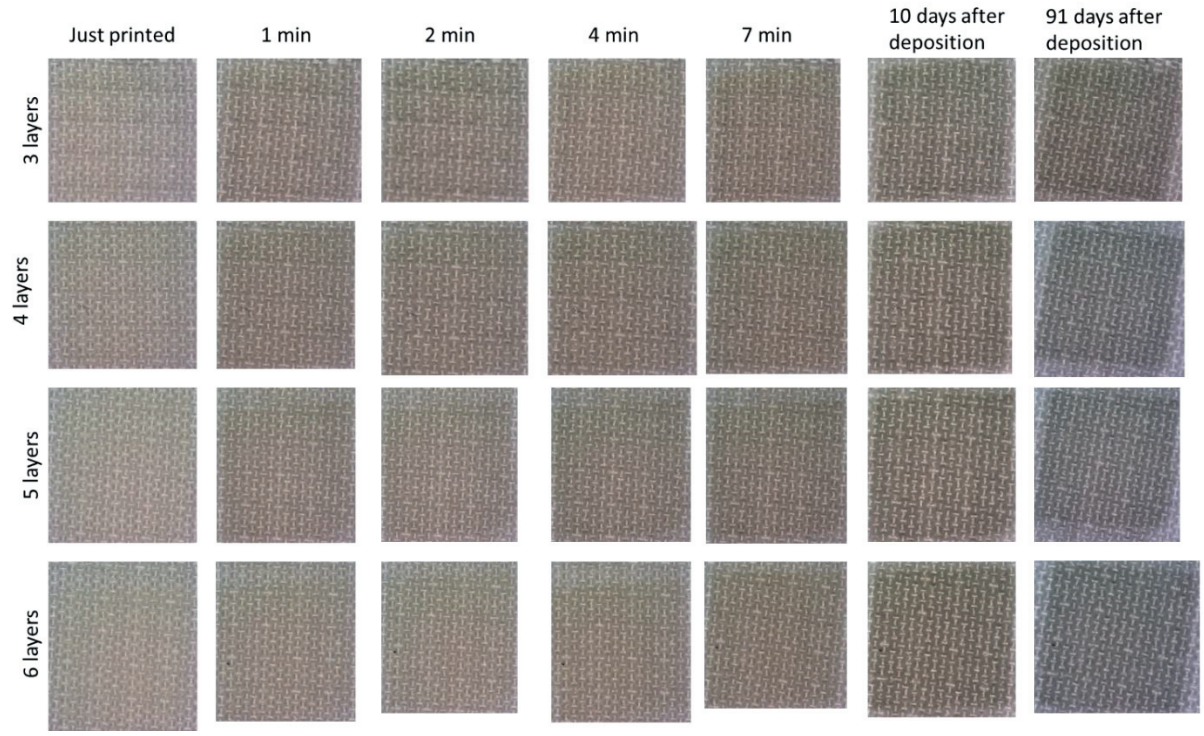

Figure 6.22. Printed square on decathlon textile following plasma treatment

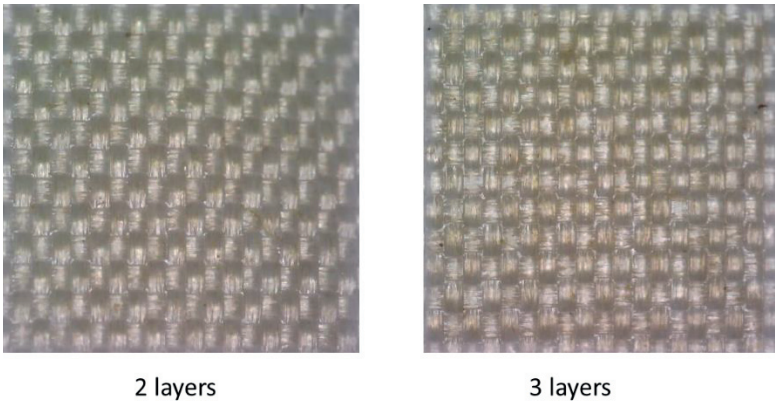

Figure 6.23. Results following plasma treatment of Pt MSD ink on 100% Polyester fabric

This unreliable behavior exhibited with the Pt ink made it difficult to work with it through further optimization or displaying whether it could be deposited and converted onto other substrate surfaces. It was very clear that when the Pt ink was first developed and printed onto PET and the tattoo paper, that the ink was fully functioning at this point but eventually results even on PET substrates became inconsistent and could no longer be replicated. This behavior can be account for by a change in manufacturing standards as the pandemic brought about an undesirable delay that ultimately affect all developed inks. This was an unfortunate coincidence therefore no further definitive testing could be conducted by using this ink.

6.4.3 | AU MSD INK – MATERIALS CHARACTERIZATION

Equation 6.3 displays the chemical decomposition mechanism of Au metal salt that requires a reduction potential of +1.00V to convert to elemental Au in a one-step reaction. Here, plasma sintering supplies high energy electrons enough to initiate the decomposition which occurs exactly as shown in Figure 6.4 as previously explained in Section 6.3.

$$AuCl_4^- + 3e^- \leftrightarrow Au + 4Cl^- \qquad E_0 = +1.00V \tag{6.3}$$

In order to fully optimize the entire process, factors such as inkjet printing and plasma sintering parameters must first be defined in order to obtain Au films with the highest possible conductivity. Afterwards, the films were then subject to materials thin film and electrical characterization techniques and demonstrated on a wide variety of substrates before incorporation into applications such as conductive tracks to build electrical circuits and biosensors.

6.4.3.1 | *OPTIMIZATION OF INKJET PRINTING AND PLASMA SINTERING PARAMETERS*

Both printing and sintering parameters were explored and defined in Figures 6.24 & 6.25 below including DS, number of layers, exposure time, and plasma power respectively. Each parameter was characterized in terms of their respective sheet resistance measurement and calculated conductivity taking the respective film thickness into consideration.

Figure 6.24a and 6.25a defined the effect of exposure time using 80% (64W) plasma power on multiple squares printed with a DS of 25 μm for 1 – 4 layers. It was clear that an exposure time of 20 minutes provided the lowest sheet resistance for 1 layer as seen in Figure 6.24a however for 4 layers, the result was more ambiguous. However, when looking at Figure 6.25a, it was clear that 30 minutes of exposure for 4 layers was necessary showing an increase of 82% in conductivity between 20 and 30 minutes. This behavior indicated the appearance of the skin effect where more time was needed for an increasing number of layers. With prolonged periods of time, over exposure to O_2 plasma resulted in oxidize films displaying almost 3 times higher sheet resistance from 122.7 to 364.7 Ω/□ for 1 layer. A similar result was seen in 4 layers as the sheet resistance increased from 18.8 to 66.3 Ω/□ for 30 to 40 minutes respectively. However, both the respective sheet resistance and conductivity seen here were still unoptimized at this point where further testing was still needed.

The optimal DS was explored in Figures 6.24b and 6.25b ranging from 10 to 40 μm for 1 printed layer that was treated with 80% (64W) of power for 20 minutes of plasma. Any films deposited with either DS of 10 μm or 40 μm were not reported as they displayed extreme bloating or discontinuous films respectively. These behaviors affected their respective sheet resistance values showing variability even for those with DS of 15 and 35 μm. In this case, DS of 20 and 25 μm exhibited similar sheet resistance values of 14.6 and 18.7 Ω/□ respectively as shown in Figure 6.24b. Figure 6.25b helped to further clarify that a DS of 20 μm exhibited an almost 2 times increase in conductivity, therefore 20 μm was deemed the optimal value continued to be used for subsequent testing.

Further printing parameters such as the number of layers was examined from 1 – 4 layers for squares printed with a DS of 20 μm and treated with plasma power of 80% (64W) for 20 minutes. Figures 6.24c and 6.25c came to the same conclusion where 2 layers displayed the lowest sheet resistance coupled with the highest conductivity. Specifically Figure 6.24c saw a 66% decrease in sheet resistance from 18.7 Ω/□ for 1 layer to 6.6 Ω/□ for 2 layers. Conversely, those with 3 or more layers saw bloating and thus loss in resolution, undesirable for developing precise patterns. This then resulted in an almost 1 order of magnitude difference in conductivity

between 2 vs. 3 and 4 layers as shown in Figure 6.25c. Therefore, 2 printed layers was maintained for further testing.

Finally, the last parameter to be tested was concerning the applied plasma power which had a limited range from 20 – 100% or 16 to 80W. All previously optimized parameters were maintained such as plasma exposure time of 20 minutes, DS of 20 μm, and 2 printed layers for each sample square. During preparation, all samples treated with only 20% or 16W of power showed incomplete conversion therefore the values obtained here were unreported. The reported sheet resistances for those treated with 40% or 32W as shown in Figure 6.24d displayed partial conversion thus contributing to high variability. In contrast, a dramatic reduction in sheet resistance values was seen when exposed to 60% or 48W, at 0.69 Ω/□. Similarly, those films exposed at 100% or 80W saw sheet resistance of 0.68 Ω/□, albeit with greater variability. As this was indistinguishable, the respective conductivity values for both was seen in Figure 6.25d as 1.2 x 10^6 S/m and 2.3 x 10^6 S/m for 80% or 64W and 100% or 80W respectively. This clarified that 100% or 80W was indeed the far superior plasma power to use to maximize the Au film conductivity to 10^6 $S \cdot m^{-1}$.

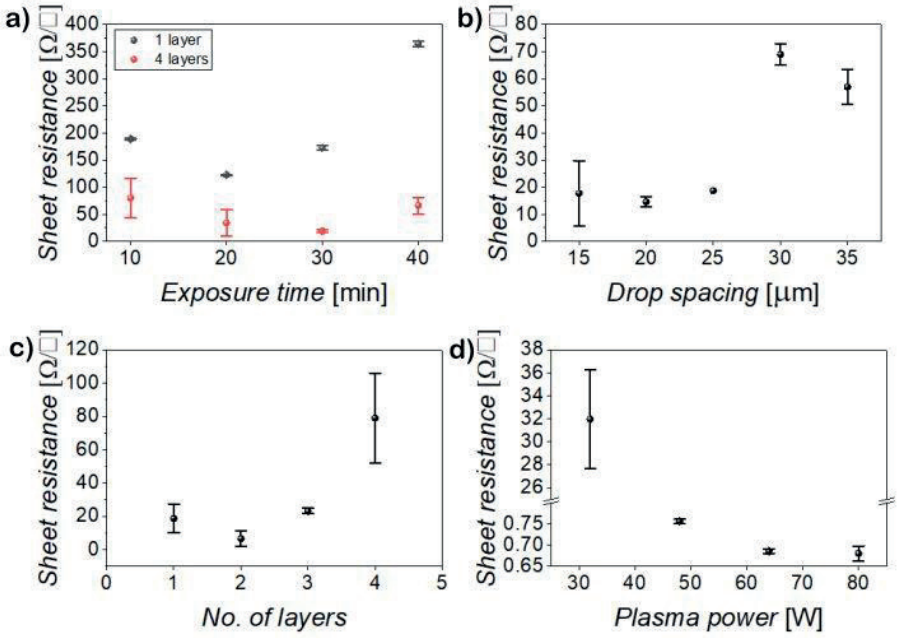

Figure 6.24. Optimized inkjet printing and plasma sintering parameters with respect to sheet resistance measurements a) 20 min plasma exposure time for 1 layer and 30 minute exposure time for 4 layers (test conditions: 1–4 layers, DS 25 μm, 64 W), b) DS of 20 μm (test conditions: 20 min exposure time, 1 layers, 64 W), c) 2 printed layers (test conditions: 20 min exposure, DS 20 μm, 64 W), and d) a plasma power at 80W (test conditions: 1–4 layers, DS 20 μm, 20 min exposure time) achieved optimal results, obtaining a minimal sheet resistance of 0.68 Ω/□. All given test points here were obtained from a minimum of 3 samples from which their respective resistance and

standard error values were calculated as an average. This figure was first published in Advanced Engineering Materials by Leung et al.[6]

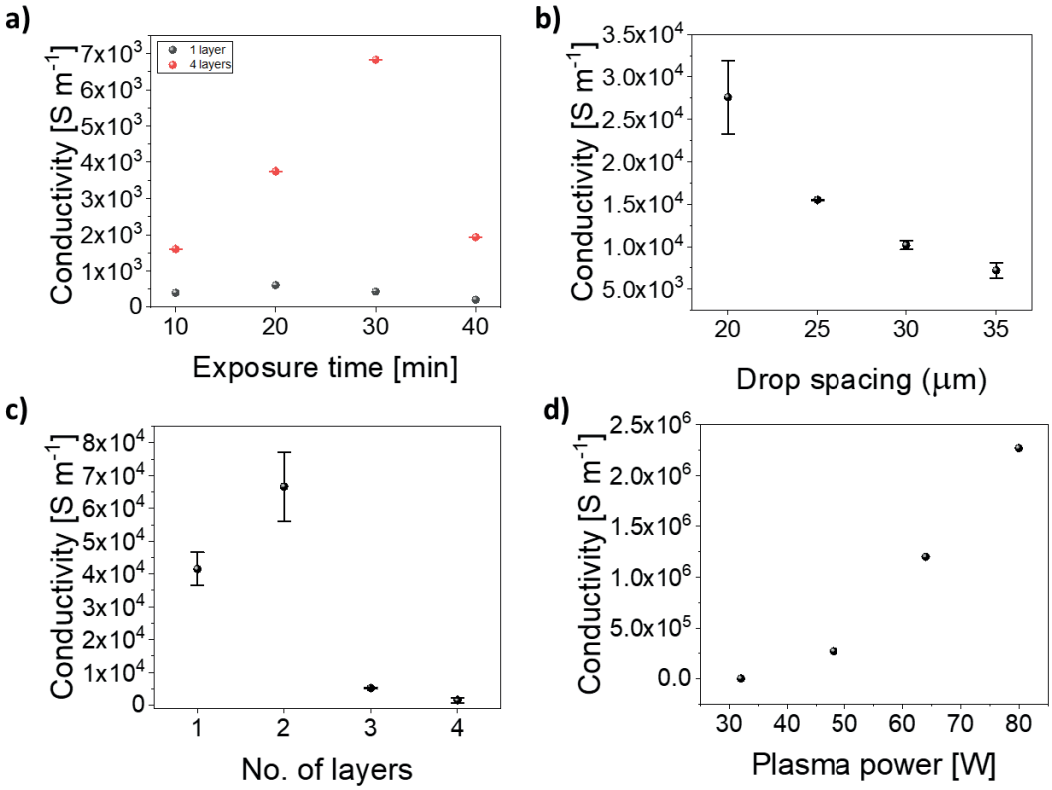

Figure 6.25. Printing and sintering parameters with respect to conductivity where the a) optimal exposure time for 1 and 4 layers is 20 and 30 minutes respectively, b) displays an optimal DS at 20 µm, c) 2 printed layers was determined to be the optimal, and d) conductivity was superior at 80W plasma power. This figure was first published in Advanced Engineering Materials under Supporting Information by Leung et al.[6]

Inkjet Printing limitation

One of the very first printing tests conducted with every new ink on every new substrate is known as the line pattern test as shown in Figure 6.26a to primarily assess the printability of the ink as well as defined the minimum separation distance between drops, a metric of pattern resolution. Here this distance was found to be to be 19.2 ± 2.8 µm for a DS of 60 µm. Additionally, a more standardized approach to define pattern resolution as seen in Figure 6.26b was conducted through the printing and conversion of a large range of squares printed with 1 and 2 layers from 5 µm up to 4 mm in length. Here, the minimum pattern resolution possible was defined at 30 µm where smaller patterns were indistinguishable from the next. This result was as

expected as inkjet printing is known to have a printing limitation at 10s of microns which could further be improved with the implementation of super fine inkjet printing.

All previously discussed results were achieved using 10pL printhead however, films deposited with a 1 pL printhead saw similar results achieving transparent Au films with a green-gray tint as shown in Figure 6.26c below. This converted Au film was sintered within just 5 minutes of plasma exposure at a reduced film thickness of 1.33 µm obtaining a significantly reduced conductivity of 1.5 x 10^4 $S \cdot m^{-1}$, 2 orders of magnitude lower. This can potentially be used as a semi-transparent electrode to replace ITO, PEDOT:PSS, and silver nanowires for biological applications known for its biocompatibility.

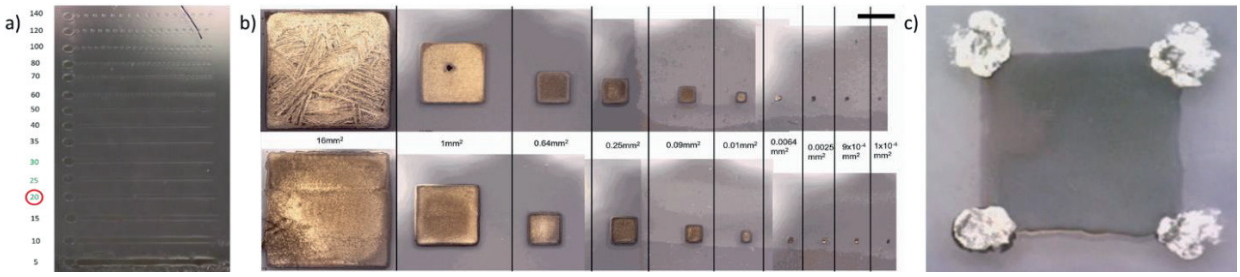

Figure 6.26. Printing extremes and limitations a) printed line pattern onto PVA surface printed with 10pL printhead, and b) printed and converted squares for (top) 1 layer and (bottom) 2 layers based on size restrictions. The scale bar indicated here is 0.5 mm in length for reference. c) Transparent Au film printed with a 1 pL printhead. This figure was first published in Advanced Engineering Materials under Supporting Information by Leung et al.[6]

6.4.3.2 | *MATERIALS CHARACTERIZATION*

Different surface characterization techniques were used to investigate the plasma reduced Au films through optical microscopy, SEM/ focused ion beam (FIB), and optical 3D surface profiler confocal microscopy as shown in Figure 6.27 to define not only the visual surface but also detail its respective microstructure. Optical microscopy revealed that different microstructural zones were developed from a fibrous to recrystallized structure as indicated by grain formation typically seen in a polycrystalline film (Figure 6.27a). Here, intermediate spherulitic (Category 2) or hedrite microstructures were identified in the Au film indicating that polycrystalline growth occurred under non-equilibrium conditions.[17] Under SEM observation, the entire Au film surface appeared to be a uniform and continuous film (Figure 6.27b) where with the help of SEM/FIB showed a thick and conformal Au layer displaying a columnar grain structure (Figure 6.27c). However, a large area FIB cut revealed that the film itself was not continuous and showed some porosity across the entire sample surface (Figure 6.27d).

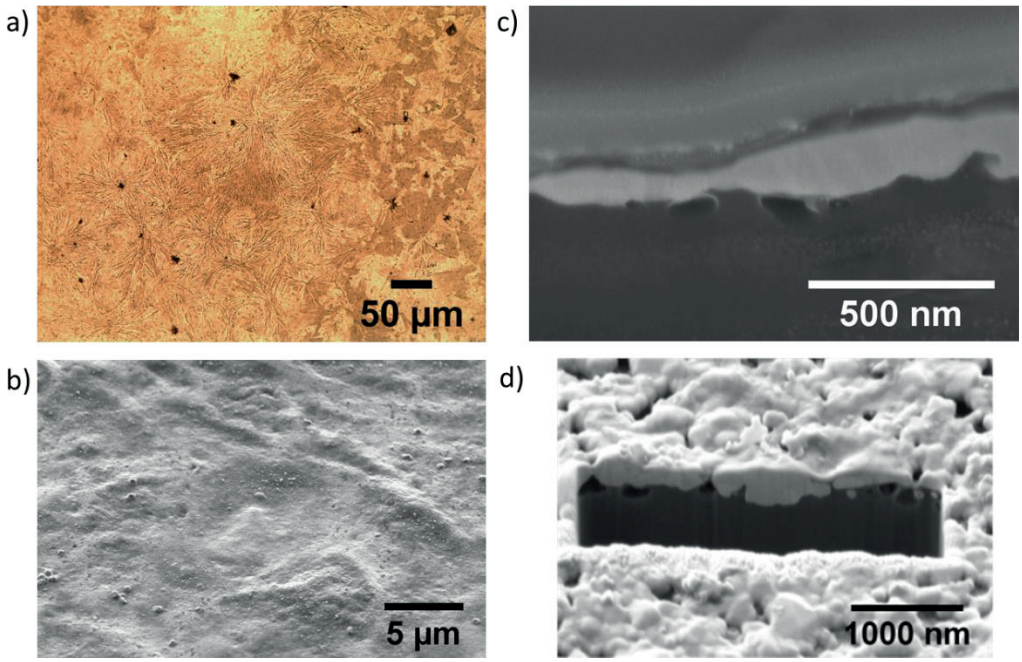

Figure 6.27. Surface topography of the Au film on PET as taken by a) an optical microscope at 20x magnification, b) SEM analysis at a magnification of 10,000x, c) SEM-FIB profile cut at 200,000x magnification, and d) overview of SEM-FIB profile cut at 20,000x. This figure was first published in Advanced Engineering Materials and adapted from Leung et al.[6]

The chemical composition of the Au films were analyzed using SEM-EDX (equip with energy dispersive X-ray spectroscopy) showing a wide range of different results depending on the size of the area as well as the color. As a reference, the metal salt ink itself contained at most 58% Au and 41.7% Cl where it is expected that following plasma sintering should ideally contain 100% Au and no Cl. Large area analysis was conducted as shown in Figure 6.28a contained the highest amount of Au at 88.8% with minimal presence of Cl at 3.5%. Specifically for this sample, sintering was highly successful showing high purity and quality of the reduced Au film. However this was not the case for all films as seen in Figure 6.28b and 6.28c. Here, different regions of the same sample were analyzed noted as darker and lighter areas in the SEM micrograph. Figure 6.28b concentrated on the analysis of a darker area revealing a significantly lower Au composition of 54.2% and Cl composition at 14.2%. The Au value reported here was even lower than what was expected for the Au metal salt meaning that this particular part of the film was severely underdeveloped. Conversely, Figure 6.28c focused on a lighter region where the film was composed of 83.5% and 7.9% Au and Cl respectively. This meant that the film itself was unevenly reduced as color was a clear indication of lack of development. Additionally, the presence of C and O contamination found can be accounted for contact with organics during the handling of the sample and oxidation from the use of plasma sintering respectively.

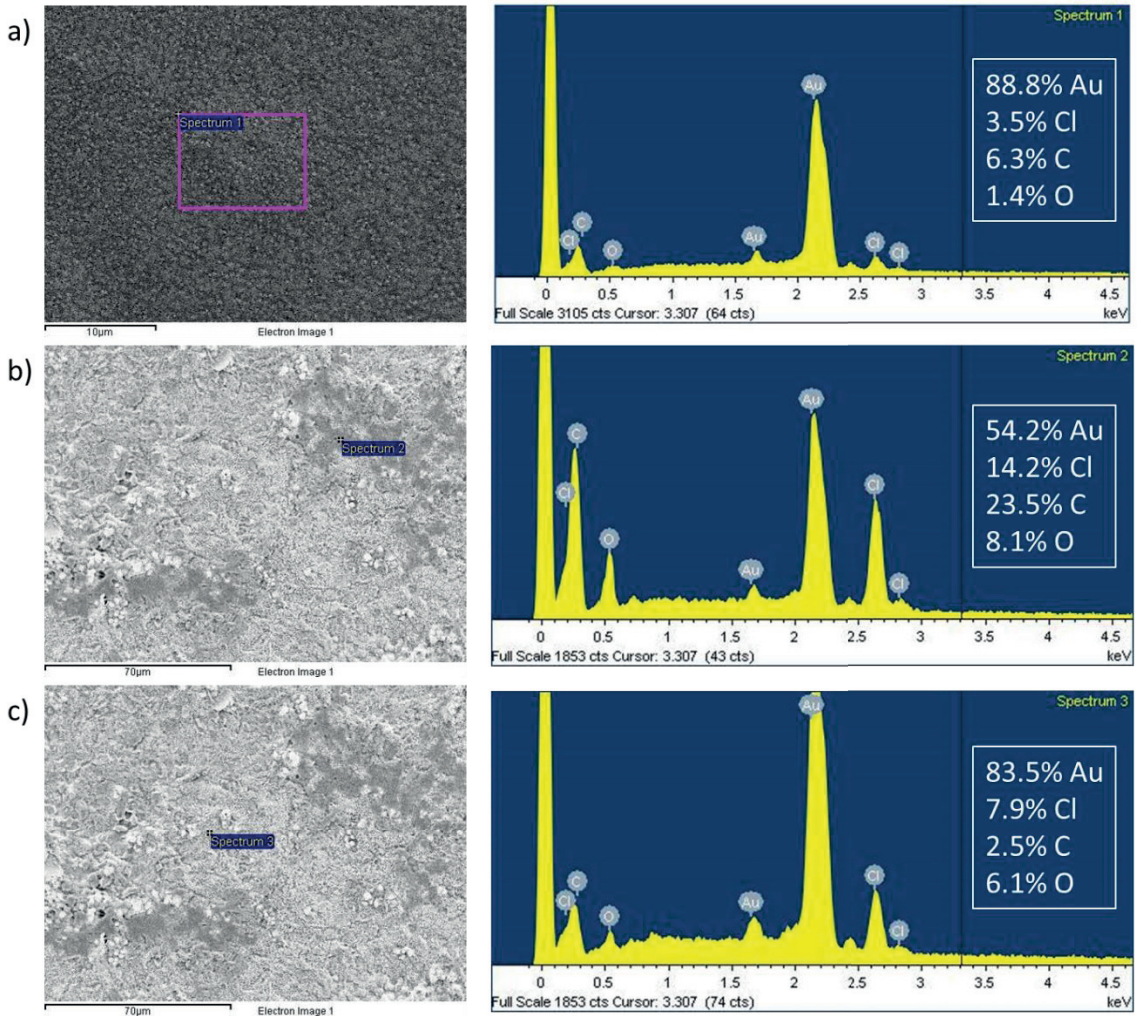

Figure 6.28. SEM-EDX results for Au films across different areas and different samples revealing different chemical compositions a) large area analysis, while different areas on the same sample were taken on b) dark region, and c) the light region

As the surface roughness could not be directly determined from SEM, two different techniques were used in conjunction: confocal microscopy and mechanical profilometry. Confocal microscopy measurements reported an average root mean square (RMS) surface roughness of 116.4 nm over a large 1 x 1.2 mm area (Figure 6.29a). Although unrecognizable in the SEM photos, mechanical profilometry revealed that the thickness varied from one region to another where within a short 2 mm scan which can see the thickness rapidly increase from 1 to 3 µm. This confirmed the Marangoni effect as expected for this type of ink reiterating that a non-flat film was developed with an overall average thickness of 2.631 µm (Figure 6.29b). Additionally, this behavior highlighted that the film displayed a mesoporous crystalline structure explaining the periodic troughs. This porosity thereby increased the surface roughness which

maybe a result of the removal of chlorine ions from the metal salt as reported with similarly reduced Si thin films.[19] It is believed that for these metal salts, the interstitial space is occupied by the salt that once removed creates a metal framework leading to pore formation.

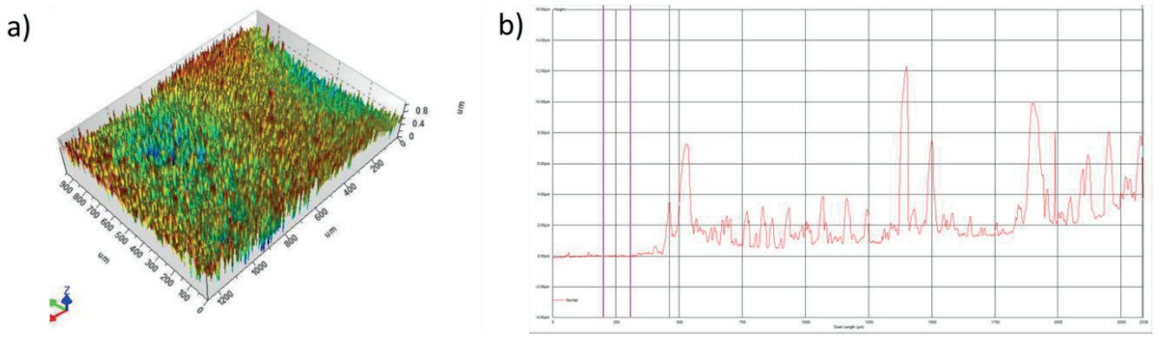

Figure 6.29. Surface morphology measurement of the Au film on PET as taken by a) confocal microcopy at 20x magnification and b) mechanical profilometer measurement for 1 layer. This figure was first published in Advanced Engineering Materials and adapted from Leung et al.[6]

Crystallinity of the films were verified using XRD analysis as displayed in Figure 6.30 below. The polycrystalline nature of the Au film was verified with matching peaks at 38.1°, 44.3°, 64.4°, 77.5°, and 81.6° corresponding to (111), (200), (220), (311), and (222) diffraction planes respectively. The average grain size was calculated to be 15.0 ± 1.5 nm with the Scherrer equation as stated below in Equation 6.4:

$$D = {}^{\kappa\lambda}/_{\beta cos\theta} \tag{6.4}$$

Variable and constants in the equation are defined as D for the grain size, κ as 0.9 (Scherrer constant), λ as the wavelength for an X-Ray source (0.15406 nm), β as the full width at half maximum, and θ notes the peak position. Surprisingly, no residual chlorine was identified using XRD as was seen with SEM-EDX showing the dependency of different analysis volumes each technique has. As GIXRD is the standard used for thin films where the analysis volume is significantly smaller than SEM-EDX which is known to have an analysis volume up to 3 μm.[20] This can account for the difference in results between the two techniques where XRD in this case analyzes only the film surface while SEM-EDX penetrates further into the sample where the film maybe less developed due to the skin effect caused by plasma sintering.

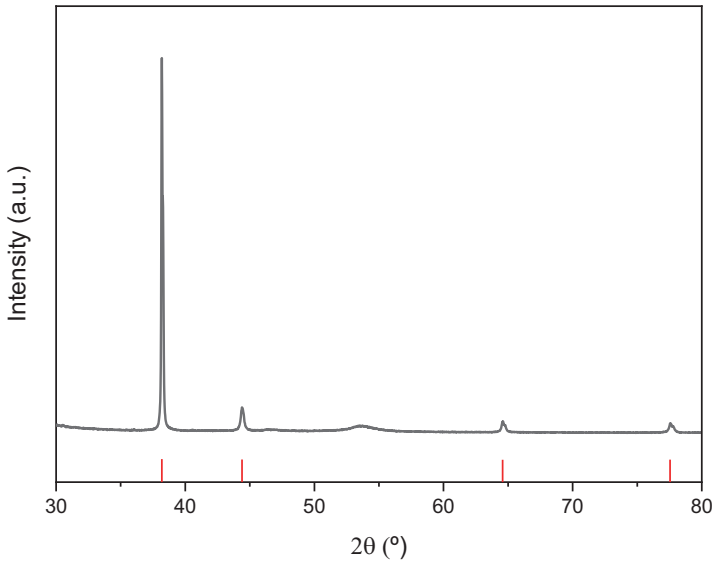

Figure 6.30. XRD analysis of plasma reduced Au thin film

All results obtained from various surface metrology and electrical measurements of the Au thin film is summarized below in Table 6.2. Generally, MSD inks have lower metal content as compared to NP inks often displaying lower conductivity[21] however it was discovered that our inks were on par with manufactured inks which may be due to the lack of a polymer component inside the ink, thus allowing for direct sintering of the ink without the need for high temperatures. For this ink, a metallic content of 19.3% for a conductivity of 3.17 x 10^5 $S \cdot m^{-1}$ was achieved on a PET substrate. Although when compared against the bulk conductivity of Au, the film conductivity only reached a mere 0.77%. This may partially be due to the lack of uniformity across the surface thus increasing the surface roughness to 116.4 nm. Such films were fabricated with processing temperatures below 37°C verifying that this process can be used on temperature sensitive substrates as opposed to NP inks.

Table 6.2. Summary of Au thin film material properties on PET

Metallic Content [%]	Processing Temperature [ºC]	Thickness [µm]	Surface Roughness [nm]	Conductivity [$S \cdot m^{-1}$]	Bulk Conductivity [%]
19.3	36.2	2.631	116.4	3.17×10^5	0.77

6.4.3.3 | *AU THIN FILM DEVELOPMENT ON NON-CONVENTIONAL SUBSTRATES*

The low sintering temperatures achieved with plasma sintering permitted the use of temperature sensitive substrates such as paper, polymers, and even textiles. This included paper substrates composed of cellulose nanofibers (CNF) from abaca and eucalyptus plants, biodegradable polymers such as PVA, and polyester textiles. Traditionally, highly viscous screen printing inks were used on porous substrates like paper and textile for their coating effect which cannot be achieved using low viscosity inkjet printing inks which typically require additional coatings.[7,22,23] Additionally, low viscosity inks require planar and smooth surfaces as they cannot hold their shape which can be problematic for unconventional porous paper and interwoven fabrics. However, this was not the case for the Au MSD ink as good printability was achieved on all substrates without the need for additional surface treatments nor coatings. Results for each substrate were investigated using optical and confocal microscopy as shown in Figure 6.31 below. Here, a wide range of substrate roughness were evaluated and deemed to be compatible with inkjet printing and plasma sintering displaying Au films with a range of different hues which may be dependent on the surface below.

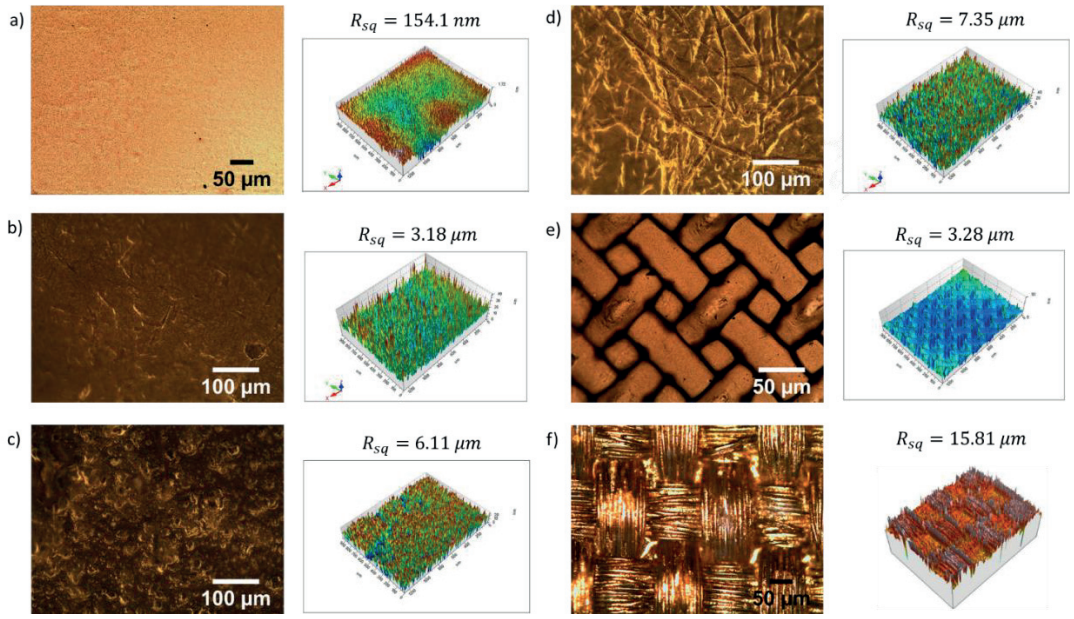

Figure 6.31. Optical microscope images of Au films and their corresponding surface roughness obtained from confocal microscopy as deposited on a) PVA, b) CNF paper, c) Au film on Teslin- 0.5wt%, d) eucalyptus CNF paper, e) abaca CNF, and f) polyester fabric. This figure was first published in Advanced Engineering Materials and adapted the supporting information section from Leung et al.[6]

Au film surface roughness for all substrates was compared against their respective sheet resistances as shown in Figure 6.32 below. A general trend that was seen showed that the sheet resistance increases with respect to the surface roughness of the film. Polymer substrates such as PET and PVA exhibited the lowest roughness and thus the lowest reported sheet resistance of 1.2 and 6.6 Ω/□ respectively. In these cases, both the films appeared to be highly uniform exhibiting a prominent gold sheen. The higher sheet resistance found in Au films deposited onto paper and fabric were 7x and 4x greater than films found on PET likely the cause of increased roughness. This roughness results from increasing porosity as seen between the abaca CNF paper and polyester fabric seeing almost a two-fold increase in sheet resistance from 25.8 to 45.8 Ω/□. Of all substrates, the fabric presented a low sheet resistance of 45.8 Ω/□ with a high surface roughness of 15.81 µm. This is because fabric is composed of an interwoven structure of individual fibers as seen in Figure 6.31f creating this high reported roughness. However, the material is made from extruded PET pellets thus acting similar to planar PET film inhibiting the absorption of the ink with the exception of porosity throughout the substrate. This provides sufficient time for plasma sintering to penetrate the ink before being absorbed completely into the substrate. This same reaction is expected to occur amongst all paper substrates stated here, all with varying absorption times thus affecting the overall sheet resistance.

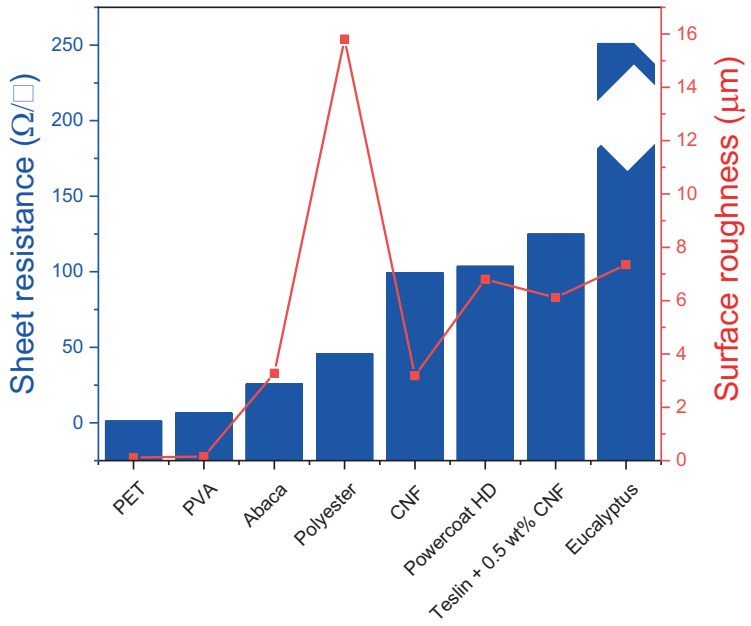

Figure 6.32. All respective sheet resistance measurements on various substrates and their corresponding roughness showed a linear relationship. This figure was first published in Advanced Engineering Materials and adapted from Leung et al.[6]

Figure 6.33 explores select Au films on PVA, abaca CNF paper, and polyester fabric at the microscale level revealing completely different films which were a direct result of the underlying substrate. The conformal nature of such films was seen across all substrates despite the initial roughness or uneven structures found on the substrate surface. In fact, this conformal behavior is similar to that found in chemical vapor deposition of thin films regardless of the rugosity of the substrate. SEM imaging in Figure 6.33a revealed that the Au film on PVA contained chlorine salt residuals however it did not affect the film formation. However, film formation was heavily influenced by the substrate surface as was seen in Figure 6.33b and 6.33c for the abaca CNF paper and polyester fabric respectively. The abaca CNF paper had periodic structures as a result of the drying process with a filter creating surrounding walls across the surface. This and the paper roughness contributed to a Au film with voids that were not visible from the film surface. It is believed that shadowing created by the periodic structures led to the formation of voids thus creating a porous structure.[24] The Au film grown on the polyester fabric exhibited excellent conformal coverage even on single strands in a row of fibers creating the interwoven structures as shown in Figure 6.31f. However, this film was shown to be the most densely porous of the Au films (Figure 6.33c) but remained conductive following 4-point probe testing.

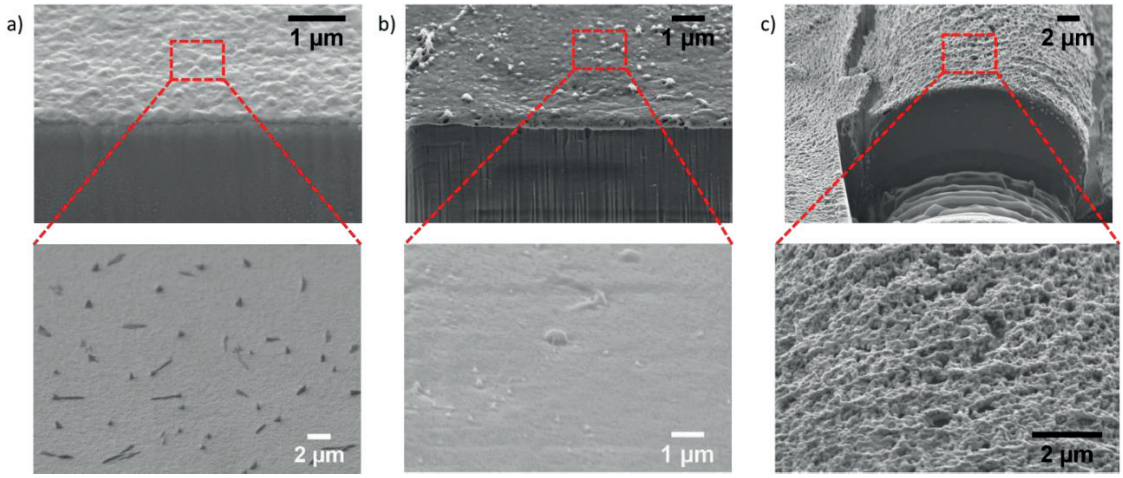

Figure 6.33. SEM micrographs of Au film on various non-conventional substrates using a) an SEM-FIB cut on PVA b) abaca CNF paper, and c) polyester fabric. This figure was first published in Advanced Engineering Materials and adapted from Leung et al.[6]

6.5 | DEVELOPMENT OF APPLICATIONS: LED CIRCUIT AND GLUCOSE BIOSENSOR

As Au films were successfully developed on a wide range of films, different flexible electronic applications were demonstrated such as an LED circuit on polyester fabric and a

glucose biosensor on PET substrate thus displaying a wide range of potential applications spanning both the wearable electronics and biomedical device markets.

6.5.1.1 | *LED CIRCUIT*

Fabrication

A white polyester fabric was purchased from a local shop and cut to a 10 cm x 10 cm square sheet. As the fabric was too flexible to handle on its own, it was adhered to a PET sheet cut to the same size for mechanical stability using scotch tape. Using the Fujifilm Dimatix Inkjet Printer (DMP-2831), a parallel circuit was printed in a cross pattern and using the Au MSD ($HAuCl_4$) ink directly onto the polyester fabric without the need for any surface treatment. A 10 pL printhead was used in conjunction with a custom waveform adapted to the ink where the optimal printing parameters defined on polyester was 2 printed layers at a DS of 15 μm. The printed pattern was then subjected to plasma sintering at 64W of power for 20 minutes which resulted in metallic gold film. To verify its respective conductivity, the tracks were tested for its resistance with a multimeter. Kingbright Super Bright Yellow LEDs (3.2 mm x 1.6 mm x 1.1 mm) purchased from RS Components were attached onto the tracks using a two-component silver epoxy paste (EPO-TEK H20E) obtained from Epoxy Technology and prepared in a 1:1 ratio directly before usage. The paste required at least 30 minutes curing at 80ºC which was minimized to reduce any effects the temperature may have on the substrate. A Hewlett Packard DC Power Supply (E3641A) provided the power source to illuminate the LEDs following manufacturing recommendations of providing a maximum forward voltage of 2V and maximum reverse current at 10 μA.

Results

Au conductive electrodes were successfully and repeatedly printed onto polyester fabric (Figure 6.34a) seeing an average of 2353.8 ± 34.1Ω and 68.6 ± 6.3Ω for 1 and 2 printed and converted layers respectively. The substrate naturally provided flexibility to the electrodes which could be tested under neutral and tensile strains. In particular, the Au thin films with 1 and 2 printed layers were tested under tensile bending strain of 0.10%, 0.50%, 1%, 2%, 10%, and > 10% which correspond to bending radii of 50, 10, 5, 2.5, 0.5, < 0.5 mm (Figure 6.34b). Samples with 1 layer exhibited a 90% failure after being subjected to 0.50% strain showing that the thin film developed here was too fragile for further testing. Bend test results for samples with 2 layers are presented below in Table 6.3 which generally showed that the resistance in the film remained stable until subjected to a 1% strain which saw an increase in resistance of 28.3% from 68.6 to 88.0Ω. It is believed that the increase in resistance is a result of crack formation in the film initiating from 0.5% strain on which sees a steady increase until 2% strain. However, the largest

resistance increase occurred between 10% and >10% at 29.3% from 95.9 Ω to 116.0 Ω indicating severe crack propagation in the film. As bending strains increased past 10%, the resistance increased 69.1% from its original value never displaying a concrete failure point (Figure 6.34c).

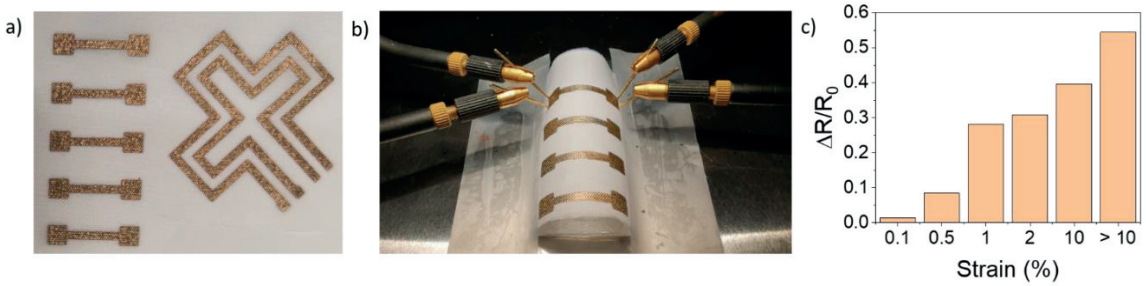

Figure 6.34. Au films printed and converted on a polyester substrate a) electrode and conductive track structures b) electrode tensile strain testing with a bending radius of 5mm, and c) bend testing results for tensile strains from 0–10% for 2 printed layers. This figure was first published and adapted from Leung et al.[6]

Table 6.3. Tensile bend test result for 2 layer electrode samples

Bending strain (%)	0	0.1	0.5	1.0	2.0	10.0	10+
Average resistance values (Ω)	68.6 ± 6.3	69.6 ± 6.1	74.5 ± 7.0	88.0 ± 10.0	89.8 ± 12.7	95.9 ± 1.3	116.0 ± 29.1

Durability of the Au film was explored in Figure 6.35a where cyclical strain testing at 3.33% tensile strain (bending radius of 1.5 mm) was conducted up to 1000 cycles. A 3.33% strain was chosen particularly because evaporated Au films (2 µm thick) are able to withstand strains up to 2%.[25] All samples saw an average resistance of 56.21 ± 0.25 Ω that never saw resistance values past 112.1 Ω showing excellent durability for extended test periods. A notable increase in resistance by 99.4% appeared within the first 90 cycles due to crack and/or fracture development that continued to affect the film on seen on cycles 220, 290, 450, and 480. In fact, as the cycles approached 300, the average resistance was calculated to be 83.58 ± 8.04 µm however from this point on sees a gradual decrease until 700 cycles where the resistance stabilizes at 65.59 ± 2.81 Ω, only a 16.7% increase from its initial value. This behavior signifies that the development of fractures and cracks did not permanently affect the conductivity of the film which can be

attributed to the conformal growth of the thin film that covered both the interwoven fiber walls and grooves as seen in Figure 6.33c. In fact, these films even exhibited a self-healing mechanism as the stretched fibers of the Au film initially deposited on the fiber walls are exposed compensating for the crack formation and returning the film to its original state. Additionally, it was revealed that the initial resistance values obtained before tensile bend testing were retrieved following 11 months of storage reiterating the possible recovery abilities of such films.

Next, Au conductive tracks were successfully and repeatedly printed onto polyester fabric displaying consistent resistance of ≈ 1kΩ range. These served as interconnects for 5 connected yellow LEDs that did not add any significant resistance as shown in its neutral state in Figure 6.35b. Under both compressive and tensile strain conditions, these structures were remained functional and maintained good connectivity showing no effect on the light intensity as the fabric wrinkles displayed in Figure 6.35c. During its lifetime, there was no delamination found between the Au film and polyester fabric as typically seen with evaporated Au films that typically require an adhesion layer. This again is the result of the conformal nature of the Au film where the fibrous structure of the substrate creates serpentine interconnects that are able withstand tensile strains beyond 10%, ideal for stretchable electronics.[26,27] Stretchable circuits are defined as structures that have the ability to maintain elastic and reversible mechanical response under both tensile or compressive strains greater than 1%. In fact, such structures could be considered electronic textiles (e-textiles) for smart or wearable clothing for upper body contours as they must be able to withstand at least 10% strain.[28] This process potentially has great significance in the future for facile development of wearable electronic clothing using commercially available fabric without the need for creating special interwoven or knitted textile.

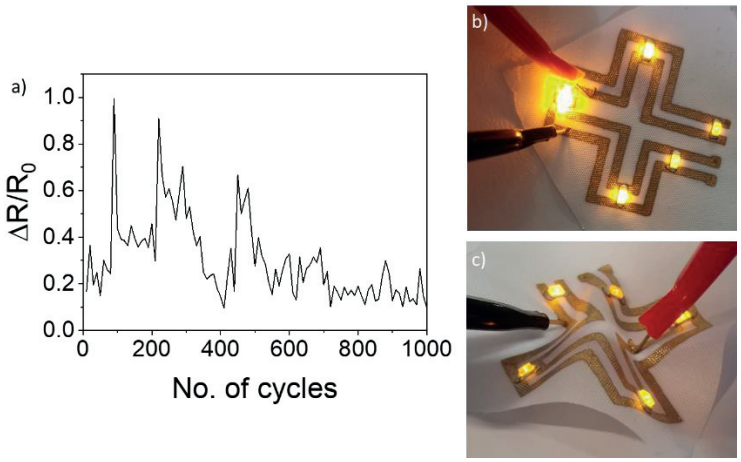

Figure 6.35. Au LED circuit on polyester fabric a) 3.33% cyclical strain testing up to 1000 cycles for 3.33%, illumination of LEDs under b) neutral and c) tensile strains. This figure was first published and adapted from Leung et al.[6]

Although not presented in these results, larger area tracks spanning an approximately 9 cm x 9 cm area was printable with a total track length of ~ 43 cm and fitted with 33 LEDs surrounding the perimeter exhibiting good flexibility (Figure 6.36a). Unfortunately, breaks in the tracks (Figure 6.36b and 6.36c) were found in various areas mostly likely due to variability in the printing process which exceeded 12 hours. Therefore, inkjet printing of larger areas was inconsistent even seeing a wide range of conductivities varying from 8kΩ to 25kΩ for a single line. For this reason, smaller structures as shown in Figure 6.36b and 6.36c were printed instead with greater consistency.

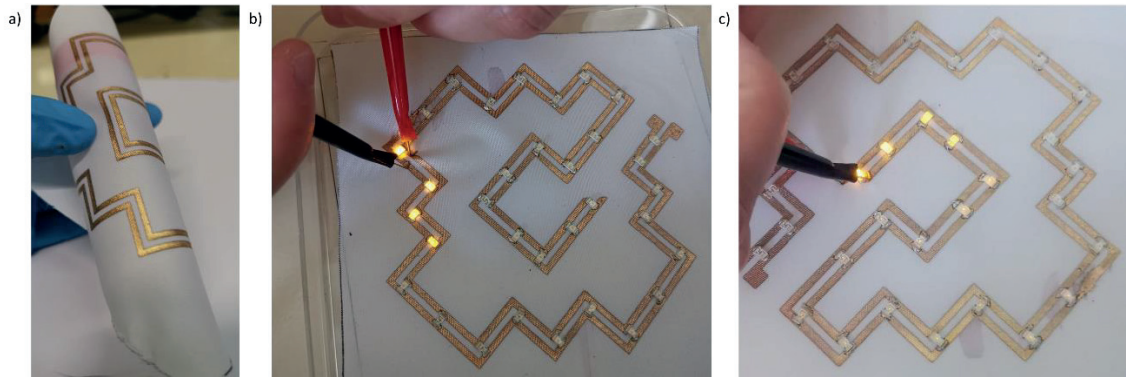

Figure 6.36. Large area (10 cm x 10 cm) printed Au film LED circuit displaying a) good flexibility around a 3 cm diameter sample container however b-c) multiple discontinuities were found showing that all LEDs could not be illuminated at the same time. This figure was first published and adapted from Leung et al.[6]

6.5.2 | GLUCOSE BIOSENSOR FABRICATION AND CHARACTERIZATION

Because Au, Pt, and Ag films were previously demonstrated using these processing techniques, an excellent archetype and application for all such films was the development of biosensors, in particular glucose biosensors as they are the most commonly developed for blood glucose control that may benefit from wearable and thus flexible devices. This section will review both the materials and processing method used to create these devices along with their respective results.

6.5.2.1 | *MATERIALS AND METHODS*

Sodium hydroxide (NaOH, ACS reagent, ≥ 97.0%, pellets), D-(+)-Glucose (ACS Reagent), glucose oxidase from Aspergillus niger (GOD, Type VII, lyophilized powder, ≥100,000 units/g solid (without added oxygen)), Nafion™ 117 solution (~5% in a mixture of lower aliphatic

alcohols and water), and potassium chloride (KCl, ACS reagent, 99.0-100.5%) were all purchased from Sigma Alrich (Merck) and used for the testing of the sensors.

The electrochemical biosensor was directly printed onto PET foil where the surface was first cleaned with an acetone, IPA, and DI water wash which was then dried with nitrogen. This was then followed by oxygen plasma treatment at 80% for 30 seconds. Due to the temporary effect of the plasma, printing of the Au working (WE) and counter electrode (CE) using the Au MSD ink was applied directly afterwards using a Fujifilm Dimatix DMP 2831 inkjet printer. Due to the properties of the ink with this substrate, 2 layers at a DS of 20 μm was used as these were the optimal printing properties. This pattern was then left to dry at 50ºC on a hot plate. To produce the Au films, oxygen plasma exposure for 20 minutes was necessary at 80% power. Due to the remaining presence of Cl on the Au film, an overnight washing step in 30ºC water was needed to fully remove the contamination from the surface. This step was necessary as previous trials with direct printing of the Ag NP ink proved unsuccessful as the Cl contamination rendered the Ag film non-conductive and turned the film black. Next, the Ag NP ink purchased from AGFA was used to deposit both the reference electrode (RE) and conductive tracks for external connection. As the substrate was previously treated with plasma following the Au film development, the optimal DS was increased to 35 μm for 1 layer of printing and dried at 50ºC. However, in order to properly test the biosensor, the Ag conductive tracks with the exception of the pads were encased in Microchem PriElex® (Epoxy SU8) ink. Additionally, a ring surrounding the WE was also printed in order to facilitate functionalization. A total of 4 layers was printed using DS of 40 μm which was deemed sufficient enough to electrically isolate the lines. The printed SU8 pattern was then exposed to UV light treatment for 1 minute to be cured. An image of the current state of sensors can be seen below in Figure 6.37. Before testing, a pseudo-reference electrode (RE) Ag/AgCl electrode was created when the silver pad was exposed to 3M of KCl under a 100mV voltage for 60s until a darkened electrode was seen. Glucose concentrations ranging between 100nM – 100 mM aliquots were prepared tested with cyclical voltammetry (CV) conducted from -0.8 to 0.8V. All electrochemical testing was carried out using a Metrohm μAUTOLABIII potentiostat in a custom glass cell.

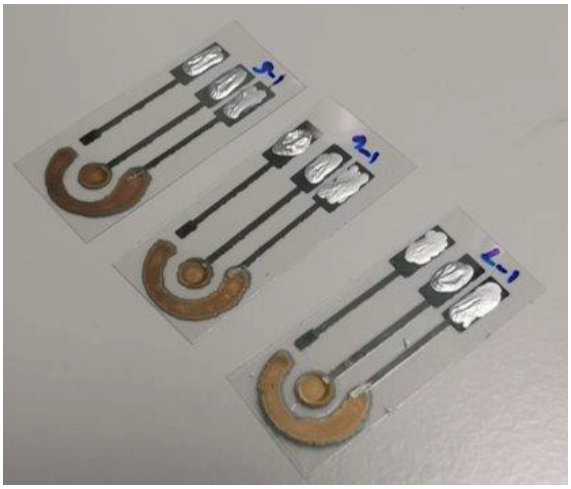

Figure 6.37. Fully inkjet printed biosensors using Au MSD ink and Ag NP ink before the Ag chloronization step

6.5.2.2 | *RESULTS*

The fully inkjet printed biosensor here relies on non-enzymatic detection of glucose as depicted in Figure 6.38 below where the reaction is driven by the release of two electrons and protons that instigate hydrolysis of gluconolactone.[29] Glucose electrooxidation has been studied on various metals and is highly dependent on the electrode material, which in this case for Au occurs in 3 steps: 1) through the absorption of glucose on the electrode surface by dehydrogenation, whereby 2) the direct oxidation occurs where the dehydrogenated molecule transforms to gluconate, and 3) further oxidation of the dehydrogenated glucose leads to the transformation to gluconate by a hydroxide ion.[30] An additional advantage not first considered here is that the roughness of the Au electrode provides increased surface area and thus increased the signal obtained during glucose electro-oxidation.[31] Additionally, the reaction efficiency is determined to be the highest in an alkaline solution which is why NaOH was specifically chosen.[29]

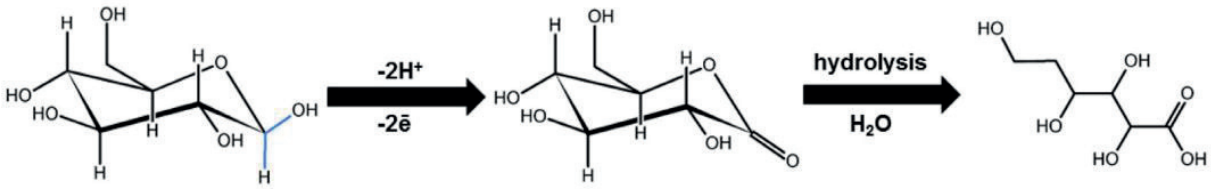

Figure 6.38. Electrooxidation mechanism of glucose as reproduced from Opallo et al.[29]

Figure 6.39 below displays all results obtained from a single sensor in an effort to first characterize the viability and stability of the Au WE in terms of its respective electrochemical

reversibility using cyclical voltammetry (CV). Looking solely at the WE response in the absence of glucose, it was noted that the oxidation and reduction peaks found at 0.26V and -0.14V corresponded to the oxidation of Au and further reduction of gold oxides respectively as shown in Figure 6.39a. When different glucose concentrations were added ranging from 0.05 to 5 mM, two anodic peaks at 0.05V and 0.25V were recorded where the first represents the oxidation of glucose to gluconolactone and the latter represents the consequential oxidation of gluconolactone (Figure 6.39b and 6.39c). Unfortunately, the response shows a shift in the potential to a more oxidative voltage behavior indicating chemical modification of the Au WE. Therefore, glucose detection cannot be correctly extracted due to this movement. Instead, if this shift was eliminated (Figure 6.39d), a clear increase in current as the glucose concentration increased was seen at 0.075V. If this behavior was rectified, the respective sensitivity is calculated as 0.63 μAL/mol or 0.29μAL/mM as shown in Figure 6.35e. A photograph depicting a sensor following testing as seen in Figure 6.35f indicated acceptable Au film adhesion with the PET substrate which historically requires the use of an additional Cr or Ti adhesion layer due to their low chemical reactivity.[32] Considering this, our films showed excellent adhesion which only saw delamination due to prolonged amperometric testing however remained intact during multiple washing steps. This was the result of multiple failure mechanisms, one of which maybe due to the porous nature of the WE where within the wicking mode, bubble nucleation occurred at both the electrode surface and porous film itself and detached periodically.[33] The analysis of these results was completed with the help of Carme Martinez Domingo who helped to clarify the reaction seen here.

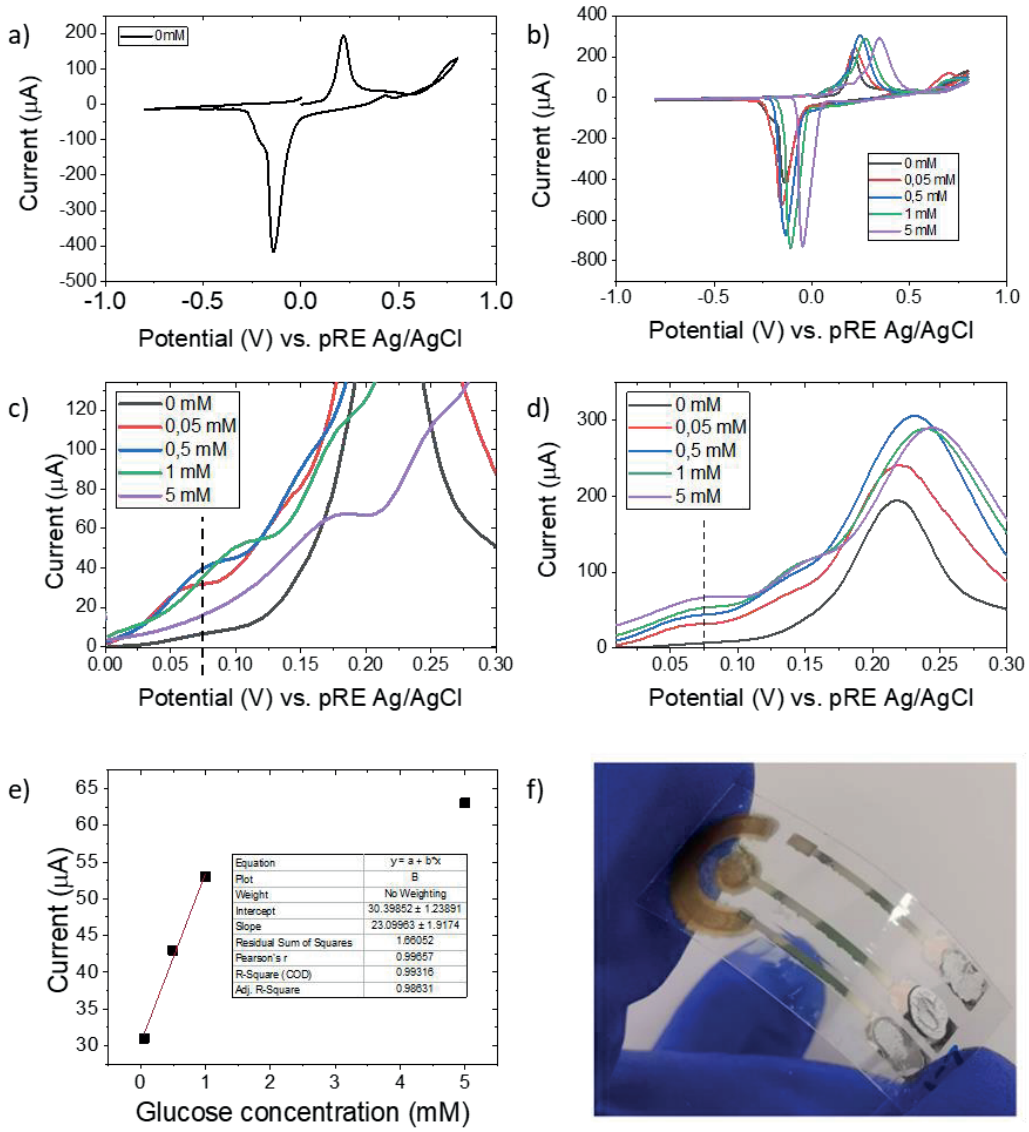

Figure 6.39. Electrochemical characterization of a fully inkjet printed biosensor a) CV was performed in the absence of glucose in 0.01M NaOH solution, b) CV was performed including those test with glucose concentrations of 0, 0.05, 0.5, 1, and 5 mM, c) and d) are enhanced CV graphs with and without the shifts respectively indicating a tendency at 0.075V. Further analysis through e) linear regression showed poor linearity in the mM range, and f) photo of the tested sensor. All graphs seen here were created and analyzed by Carme Martinez Domingo.

The CE was initially planned to be developed via the Pt MSD inks however its short lifetime and extreme sensitivity to air exposure in addition to the manufacturer change in formulation of the H_2PtCl_6 salt meant that the Pt films initially characterized were no longer achievable under the same conditions. Different strategies were implemented including manipulation of ink formulation, ink preparation, as well as a reduction in production timing, all of which did not result in conductive films. In fact, different test runs with the same ink resulted in completely

different results ranging from no color change to an intermediate stage as seen below in Figure 6.40. Conductive Pt films with a silver color were not obtained following the first batch of Pt metal salt obtained from Sigma Aldrich verifying that the differentiation in batch quality led to the unsuccessful conversion of Pt and therefore could not be used for further testing.

Figure 6.40. Failed Pt film conversion after 20 minutes of O2 plasma exposure

6.6 | SUMMARY AND CONCLUSIONS

A subset of MOD inks, named Metal Salt Decomposition (MSD) inks requires a simple formulation containing only a metal salt precursor, and solvent, and H_2O to dissolve the salt making this a particle free ink that can easily print without clogging issues. Based on their respective reduction potentials, highly positive metals such as Ag, Pt, and Au were chosen as targets to determine their compatibility with O_2 plasma as a low sintering temperature method. A general observation found when plasma sintering MSD inks was that the physical appearance of the dried pattern affected the final result and indirectly reflected the quality of the film which in this case presented itself with high surface roughness due to salt removal.[34] However, this comes at the detriment of the metal content which is consistently lower than that of NP inks. Conductivities reported for each film as shown below in Table 6.4 which entails all characteristics reported for each of the developed films including exposure times, sintering temperature, surface roughness, and their respectively electrical properties. This also included information related to technical limitations of other attempted films such as Cu and Sn which is highly dependent the reduction potential. When such inks are combined with alternative sintering methods such as plasma, the sintering temperatures have been shown to reduce to as little as 77ºC[4] however, we demonstrated significantly lower sintering temperatures never exceeding 37ºC. This then allowed for the incorporation of a large variety of temperature sensitive substrates mostly demonstrated with Au films on various biodegradable polymers, papers and fabrics although Pt films initially saw promise on various substrates. The ink itself could be deposited on both conventional and non-conventional substrates without any additional coating

and reduced directly. This permitted the development of conductive tracks on polyester fabric for wearable applications as the tracks saw excellent stability under continuous cyclical strain and durability against tensile and compressive strains. Additionally, a glucose biosensor was attempted however due to its instability as an electrode, has still has yet to be optimized. All work presented here plus extra information was culminated into a peer-reviewed journal article under the title ‘’Low-Temperature Plasma Sintering of Inkjet-Printed Metal Salt Decomposition Inks on Flexible Substrates’’ published in September 2022 in Advanced Engineering Materials in under the direction of Carme Martínez-Domingo.

Table 6.4. Overview of MSD inks and their respective traits

Inks: decreasing ion reduction potential

Ink	Au	Ag	Pt	Cu	Sn
Reducible	✓	✓	✓	✗	✗
Plasma exposure time	5 to 20 min	> 30 s	6 min	-------	--------
Sintering temperature (°C)	33.4	<25	30.5	-------	-------
Reaction notes	N/A	Occurs rapidly but can oxidize quickly	Middle more developed	Dries and oxidizes quickly	Dries and oxidizes quickly
Surface roughness (nm)	116.4	-------	344.7	-------	-------
Film thickness (µm)	2.63	-------	0.40	-------	-------
Sheet resistance (Ω/□)	1.2	19.6	48	-------	-------
Conductivity (S/m)	3.17×10^5	-------	3.85×10^4	-------	-------

6.7 | REFERENCES

(1) Zhou, Y.; Xu, Z.; Bai, H.; Knapp, C. E. Room Temperature Electronic Functionalization of Thermally Sensitive Substrates by Inkjet Printing of a Reactive Silver-Based MOD Ink. *Adv. Mater. Technol.* **2023**, *8* (8), 2201557. https://doi.org/https://doi.org/10.1002/admt.202201557.

(2) Yang, L.; Hu, H.; Scholz, A.; Feist, F.; Cadilha Marques, G.; Kraus, S.; Bojanowski, N. M.; Blasco, E.; Barner-Kowollik, C.; Aghassi-Hagmann, J.; Wegener, M. Laser Printed Microelectronics. *Nat. Commun.* **2023**, *14* (1), 1103. https://doi.org/10.1038/s41467-023-36722-7.

(3) Abulikemu, M.; Da'as, E. H.; Haverinen, H.; Cha, D.; Malik, M. A.; Jabbour, G. E. In Situ Synthesis of Self-Assembled Gold Nanoparticles on Glass or Silicon Substrates through Reactive Inkjet Printing. *Angew. Chemie Int. Ed.* **2014**, *53* (2), 420–423. https://doi.org/10.1002/anie.201308429.

(4) Sui, Y.; Dai, Y.; Liu, C. C.; Sankaran, R. M.; Zorman, C. A. A New Class of Low-Temperature Plasma-Activated, Inorganic Salt-Based Particle-Free Inks for Inkjet Printing Metals. *Adv. Mater. Technol.* **2019**, *4* (8), 1900119. https://doi.org/10.1002/admt.201900119.

(5) Crowther, J. M.; Badyal, J. P. S. Non-Isothermal Plasma Metallization of Polymer-Supported Gold(III) Complexes. *Adv. Mater.* **1998**, *10* (5), 407–411. https://doi.org/10.1002/(SICI)1521-4095(199803)10:5<407::AID-ADMA407>3.0.CO;2-5.

(6) Leung, T. S. W.; Ramon, E.; Martínez-Domingo, C. Low-Temperature Plasma Sintering of Inkjet-Printed Metal Salt Decomposition Inks on Flexible Substrates. *Adv. Eng. Mater.* **2022**, *2200834*. https://doi.org/10.1002/adem.202200834.

(7) Wang, Y.; Guo, H.; Chen, J.; Sowade, E.; Wang, Y.; Liang, K.; Marcus, K.; Baumann, R. R.; Feng, Z. Paper-Based Inkjet-Printed Flexible Electronic Circuits. *ACS Appl. Mater. Interfaces* **2016**, *8* (39), 26112–26118. https://doi.org/10.1021/acsami.6b06704.

(8) Li, D.; Sutton, D.; Burgess, A.; Graham, D.; Calvert, P. D. Conductive Copper and Nickel Lines via Reactive Inkjet Printing. *J. Mater. Chem.* **2009**, *19* (22), 3719–3724. https://doi.org/10.1039/b820459d.

(9) Liu, Y.; Zheng, Y.; Chen, X.; Yang, J.; Pan, H.; Chen, D.; Wang, L.; Zhang, J.; Zhu, D.; Wu, S.; Yeung, K. W. K.; Zeng, R.; Han, Y.; Guan, S. Fundamental Theory of Biodegradable Metals—Definition, Criteria, and Design. *Adv. Funct. Mater.* **2019**, *29* (18), 1805402. https://doi.org/10.1002/adfm.201805402.

(10) Bresin, M.; Chamberlain, A.; Donev, E. U.; Samantaray, C. B.; Schardien, G. S.; Hastings, J. T. Electron-Beam-Induced Deposition of Bimetallic Nanostructures from Bulk Liquids. *Angew. Chemie Int. Ed.* **2013**, *52* (31), 8004–8007. https://doi.org/https://doi.org/10.1002/anie.201303740.

(11) Hartl, H.; Guo, Y.; Ostrikov, K.; Xian, Y.; Zheng, J.; Li, X.; Fairfull-Smith, K. E.; MacLeod, J. Film Formation from Plasma-Enabled Surface-Catalyzed Dehalogenative Coupling of a Small Organic Molecule. *RSC Adv.* **2019**, *9* (5), 2848–2856. https://doi.org/10.1039/C8RA08920E.

(12) Perelaer, J.; Hendriks, C. E.; De Laat, A. W. M.; Schubert, U. S. One-Step Inkjet Printing of Conductive Silver Tracks on Polymer Substrates. *Nanotechnology* **2009**, *20* (16), 165303. https://doi.org/10.1088/0957-4484/20/16/165303.

(13) Wu, J.; Roberts, R. C.; Tien, N. C.; Li, D. Inkjet Printed Silver Patterning on PDMS to Fabricate Microelectrodes for Microfluidic Sensing. In *SENSORS, 2014 IEEE*; 2014; pp 1100–1103. https://doi.org/10.1109/ICSENS.2014.6985197.

(14) Sui, Y.; Hess-Dunning, A.; Radwan, A. N.; Sankaran, R. M.; Zorman, C. A. Engineering the Surface Morphology of Inkjet Printed Ag by Controlling Solvent Evaporation during Plasma Conversion of AgNO3 Inks. *J. Mater. Chem. C* **2022**, *10* (13), 5257–5265. https://doi.org/10.1039/D1TC06174G.

(15) Farraj, Y.; Smooha, A.; Kamyshny, A.; Magdassi, S. Plasma-Induced Decomposition of Copper Complex Ink for the Formation of Highly Conductive Copper Tracks on Heat-Sensitive Substrates. *ACS Appl. Mater. Interfaces* **2017**, *9* (10), 8766–8773. https://doi.org/10.1021/acsami.6b14462.

(16) Sperling, L. H. The Crystalline State. In *Introduction to Physical Polymer Science, 4th ed.*; John Wiley & Sons, Ltd, 2005; pp 239–323. https://doi.org/10.1002/0471757128.CH6.

(17) Gránásy, L.; Pusztai, T.; Tegze, G.; Warren, J. A.; Douglas, J. F. Growth and Form of Spherulites. *Phys. Rev. E* **2005**, *72* (1), 011605. https://doi.org/10.1103/PhysRevE.72.011605.

(18) Zea, M.; Moya, A.; Fritsch, M.; Ramon, E.; Villa, R.; Gabriel, G. Enhanced Performance Stability of Iridium Oxide-Based PH Sensors Fabricated on Rough Inkjet-Printed Platinum. *ACS Appl. Mater. Interfaces* **2019**, *11* (16), 15160–15169. https://doi.org/10.1021/acsami.9b03085.

(19) Dai, F.; Zai, J.; Yi, R.; Gordin, M. L.; Sohn, H.; Chen, S.; Wang, D. Bottom-up Synthesis of High Surface Area Mesoporous Crystalline Silicon and Evaluation of Its Hydrogen Evolution Performance. *Nat. Commun.* **2014**, *5*, 1–11. https://doi.org/10.1038/ncomms4605.

(20) Energy Dispersive X-ray Spectroscopy Services | EAG Laboratories https://www.eag.com/techniques/spectroscopy/energy-dispersive-x-ray-spectroscopy-eds/ (accessed 2023 -07 -24).

(21) Choi, Y.; Seong, K. dong; Piao, Y. Metal−Organic Decomposition Ink for Printed Electronics. *Adv. Mater. Interfaces* **2019**, *6* (20), 1–14. https://doi.org/10.1002/admi.201901002.

(22) Nechyporchuk, O.; Yu, J.; Nierstrasz, V. A.; Bordes, R. Cellulose Nanofibril-Based Coatings of Woven Cotton Fabrics for Improved Inkjet Printing with a Potential in E-Textile Manufacturing. *ACS Sustain. Chem. Eng.* **2017**, *5* (6), 4793–4801. https://doi.org/10.1021/acssuschemeng.7b00200.

(23) Zea, M.; Moya, A.; Abrao-Nemeir, I.; Gallardo-Gonzalez, J.; Zine, N.; Errachid, A.; Villa, R.; Gabriel, G. All Inkjet Printing Sensor Device on Paper: For Immunosensors Applications. In *2019 20th International Conference on Solid-State Sensors, Actuators and Microsystems and Eurosensors XXXIII, TRANSDUCERS 2019 and EUROSENSORS XXXIII*; Institute of Electrical and Electronics Engineers Inc.: Berlin, 2019; pp 2472–2475. https://doi.org/10.1109/TRANSDUCERS.2019.8808473.

(24) Čekada, M. Properties and Characterization of Thin Films. In *Surface Properties And Engineering Of Complex Intermetallics, 3rd ed.*; World Scientific Publishing Co. Pte. Ltd., 2010; pp 1–48. https://doi.org/10.1142/9789814304771_0001.

(25) Emery, R. D.; Povirk, G. L. Tensile Behavior of Free-Standing Gold Films. Part I. Coarse-Grained Films. *Acta Mater.* **2003**, *51* (7), 2067–2078. https://doi.org/10.1016/S1359-6454(03)00006-5.

(26) Kim, D. H.; Kim, Y. S.; Wu, J.; Liu, Z.; Song, J.; Kim, H. S.; Huang, Y. Y.; Hwang, K. C.; Rogers, J. A. Ultrathin Silicon Circuits with Strain-Isolation Layers and Mesh Layouts for High-Performance Electronics on Fabric, Vinyl, Leather, and Paper. *Adv. Mater.* **2009**, *21* (36), 3703–3707. https://doi.org/10.1002/adma.200900405.

(27) Han, M.; Chen, L.; Aras, K.; Liang, C.; Chen, X.; Zhao, H.; Li, K.; Faye, N. R.; Sun, B.; Kim, J. H.; Bai, W.; Yang, Q.; Ma, Y.; Lu, W.; Song, E.; Baek, J. M.; Lee, Y.; Liu, C.; Model, J. B.; Yang, G.; Ghaffari, R.; Huang, Y.; Efimov, I. R.; Rogers, J. A. Catheter-Integrated Soft Multilayer Electronic Arrays for Multiplexed Sensing and Actuation during Cardiac Surgery. *Nat. Biomed. Eng.* **2020**, *4* (10), 997–1009. https://doi.org/10.1038/s41551-020-00604-w.

(28) Wicaksono, I.; Tucker, C. I.; Sun, T.; Guerrero, C. A.; Liu, C.; Woo, W. M.; Pence, E. J.; Dagdeviren, C. A Tailored, Electronic Textile Conformable Suit for Large-Scale Spatiotemporal Physiological Sensing in Vivo. *npj Flex. Electron.* **2020**, *4* (1), 1–13. https://doi.org/10.1038/s41528-020-0068-y.

(29) Opallo, M.; Dolinska, J. *Glucose Electrooxidation*; Elsevier, 2018. https://doi.org/10.1016/B978-0-12-409547-2.13331-1.

(30) Pasta, M.; La Mantia, F.; Cui, Y. Mechanism of Glucose Electrochemical Oxidation on Gold Surface. *Electrochim. Acta* **2010**, *55* (20), 5561–5568. https://doi.org/10.1016/j.electacta.2010.04.069.

(31) Romeo, A.; Moya, A.; Leung, T. S.; Gabriel, G.; Villa, R.; Sánchez, S. Inkjet Printed Flexible Non-Enzymatic Glucose Sensor for Tear Fluid Analysis. *Appl. Mater. Today* **2018**, *10*, 133–141. https://doi.org/10.1016/j.apmt.2017.12.016.

(32) Todeschini, M.; Bastos Da Silva Fanta, A.; Jensen, F.; Wagner, J. B.; Han, A. Influence of Ti and Cr Adhesion Layers on Ultrathin Au Films. *ACS Appl. Mater. Interfaces* **2017**, *9* (42), 37374–37385. https://doi.org/10.1021/ACSAMI.7B10136/SUPPL_FILE/AM7B10136_SI_001.PDF.

(33) Iwata, R.; Zhang, L.; Wilke, K. L.; Gong, S.; He, M.; Gallant, B. M.; Wang, E. N. Bubble Growth and Departure Modes on Wettable/Non-Wettable Porous Foams in Alkaline Water Splitting. *Joule* **2021**, *5* (4), 887–900. https://doi.org/10.1016/J.JOULE.2021.02.015.

(34) Lohse, D. Fundamental Fluid Dynamics Challenges in Inkjet Printing. *Annu. Rev. Fluid Mech.* **2021**, *54*, 349–382. https://doi.org/10.1146/annurev-fluid-022321-114001.

7

Self-sintered Au nanoparticle films

Although metal salt based inks have primarily been reduced using laser or plasma sintering, this chapter reveals a new type of self-sintering process that initiates at room temperature (RT) without the need for an additional reducing agent as seen with reactive inkjet printing nor a chemical sintering agent for the development of conductive Au metal films. This technique removes to need for nanoparticle synthesis and its respective processing steps and instead develops nanoparticles in situ thanks to multifaceted PVA which acts as the substrate, capping agent, and reducing agent. This chapter serves to delve into other potential reducing substrates, the exact reduction mechanism behind the Au film growth on PVA, its material properties defined through materials characterization techniques as well as its limitations and potential applications such as a gauge sensor and transistor through the development of an ionic PVA gel.

7.1 | REDUCING SUBSTRATES

Printed and flexible electronics continues to rely on polyester polymers such as PET and PEN, both of which are not known for their biodegradability therefore contributing to the growing electronics waste problem. One way to reduce this effect is by incorporating environmentally friendly or biodegradable polymers instead that can fulfil the same function, in this case as the substrate which 90% of an electrical component. Instead, abundant natural polymers with excellent biodegradability and biocompatibility containing hydroxyl and carboxylic groups can be a good replacement.[1] These polymers are either plant-based such as cellulose and starch or animal-based in the case of silk, chitosan, and carrageenan amongst others. Natural polymers can also be categorized by their chemical structure including

polysaccharides, proteins, and polyesters.[2] It was reported that polysaccharides were highly effective as green reducing agents in nanoparticle synthesis. The main reason for this behavior is the same reason for its highly soluble nature in water, namely due to the number of hydroxyl groups that give the ability to reduce both metal and semiconductor precursors.[3] This is in contrast to what are referred to here as non-reactive substrates such as glass and PET. The chemical structure of these substrates and their differences are noted below in Figure 7.1. Duan et al. reported that polysaccharide reducing agents such as β-D-glucose and amylose (starch) have been demonstrated in the formation of Au NPs through the reduction of metal ionic precursors.[3] Here, PVA is also deemed as a reducing agent because its large number of OH groups facilitates the formation and reduction of metal ion complexes (i.e. reduced Ag ions to Ag NPs at RT).[4] The advantage here is that polymer structures exist in a chain structure meaning that there could be an infinite potential of available hydroxyl groups advantageous for the reduction of metal salts.

What unknown here is to what degree or what number of hydroxyl groups on the surface is necessary to instigate the reduction process. For this reason, a myriad of substrates were chosen as there is no reduction potential posited in this sense as the idea of reducing substrates did not exist before this investigation. Substrates such as CNF, Na-CMC, carrageenan, silk fibroin, and OSTEMER were explored for their respective potential to convert metal salt inks to metal films. As seen in Figure 7.1, all potential reducing substrates contain OH or thiol groups to varying degrees which will help to give a better idea of how such substrates will react. Thus far, studies have mostly been conducted on this use of these respective materials as stabilizing or capping agents in the development for NPs however their primary use as a reducing substrate has not yet been document.

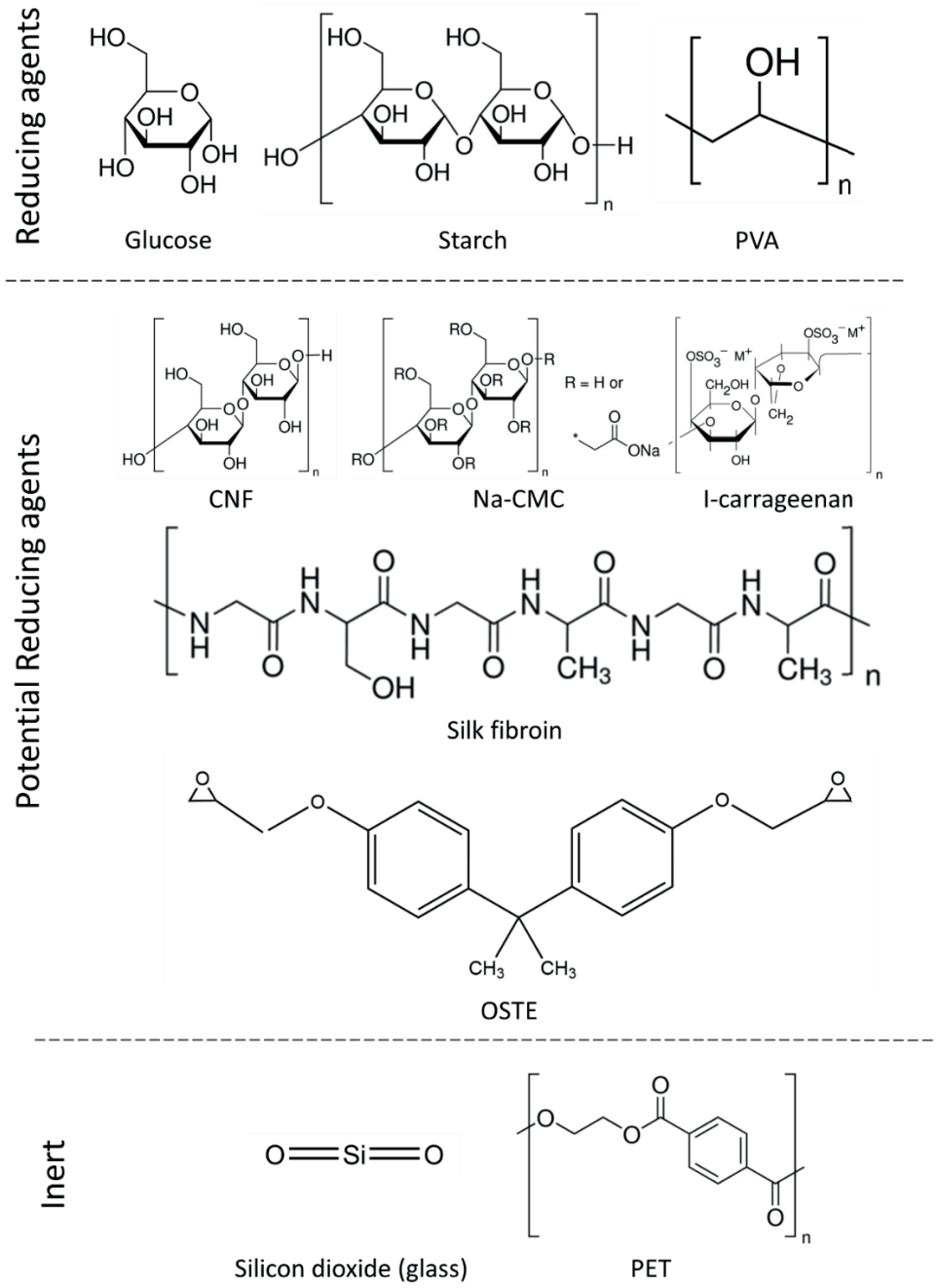

Figure 7.1. List of different substrates categorized and their respective chemical structures. The majority of the structures here were obtained from Sigma-Aldrich (Merck) with the exception of glass and OSTEMER structures which were drawn using ChemDraw.

7.1.1 | SUBSTRATE FABRICATION

Different substrates were explored to determine their respective reducibility potential when in contact with Au MSD ink. This ink was primarily used because of its proven repeatable reduction across a wide range of substrates as compared to other inks due to its high ionization energy compared to other metals. The fabrication regarding substrates such as silk fibroin, PVA, CNF, and Na-CMC were previously addressed in Chapter 4 however for this experimentation, additional substrates were considered based on the number of hydroxyl groups they contained. Therefore, two new substrates were introduced namely carrageenan and OSTEMER, an off-stoichiometry thiol-ene polymer. Carrageenan membranes or substrates were kindly provided by an IMB-CNM member who prepared test substrates with 1 wt% solid of Iota carrageenan (ι-Carrageenan) was purchased from Sigma-Aldrich (Merck) and dissolved in DI water under magnetic stirring for 50h at 40°C. Once completely dissolved, the resulting solution was then casted onto petri dishes and deep freeze dried at -80°C for 24 hrs. This exact procedure was reported by Serra et al. and adapted accordingly which was verified using both optical microscopy and Dimatix fiducial camera as shown below in Figure 7.2.[5] OSTEMER 322 Crystal Clear was obtained from Mercene Labs AB, Sweden is a two-component resin akin to PDMS. As such, the two resins were combined together in a 1.09:1 ratio and poured into a mold to be cured under UV light for 60s to shape and bonded in the oven at 90C for 60 minutes. The film could then be easily released using tweezers just before printing. The samples were provided in collaboration with Dr. Ferran Pujol from IMB-CNM.

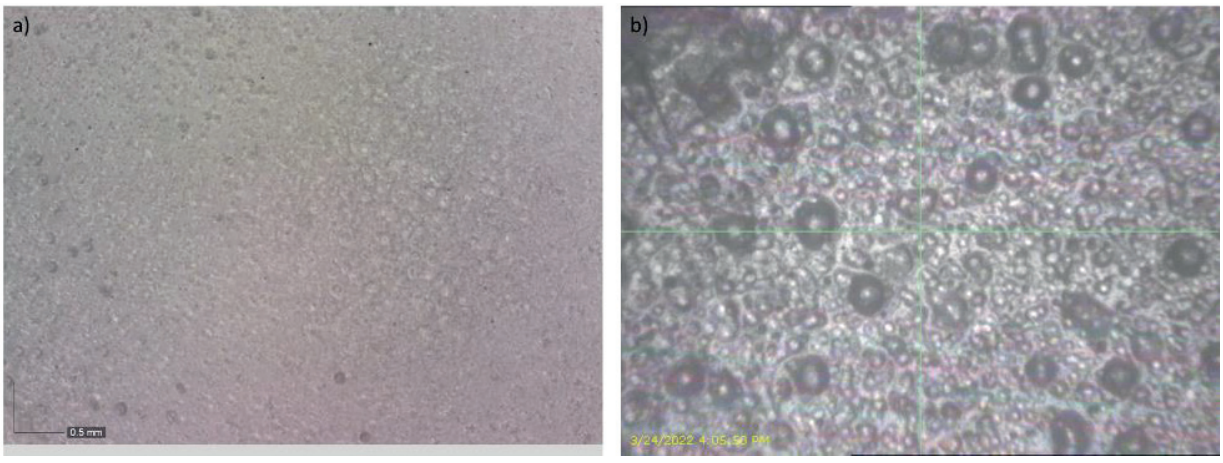

Figure 7.2.Images of Carrageenan membranes at a) 55x (Scale: 0.5mm) and taken with the b) Dimatix camera before printing

PET is considered an unreactive substrate and for this reason is used a reference against all other substrates. Looking purely at its chemical composition as shown in Figure 7.1, there are no

hydroxyl groups available to produce the reduction reaction which was then verified after 1 month observation period at RT of printed Au MSD ink squares as shown in Figure 7.3. As the PET film is a non-porous polymer, 100% of the ink layer printed on top was available for conversion and remained wet until Day 5. The film layer itself dried transparent and maintained its appearance throughout the 30 days with any growth or gold color appearance to the film showing no reaction with the Au MSD ink. Although not documented here, glass or SiO_2 reacted similarly as the lack of hydroxyl groups lead to no reduction of the ink as expected.

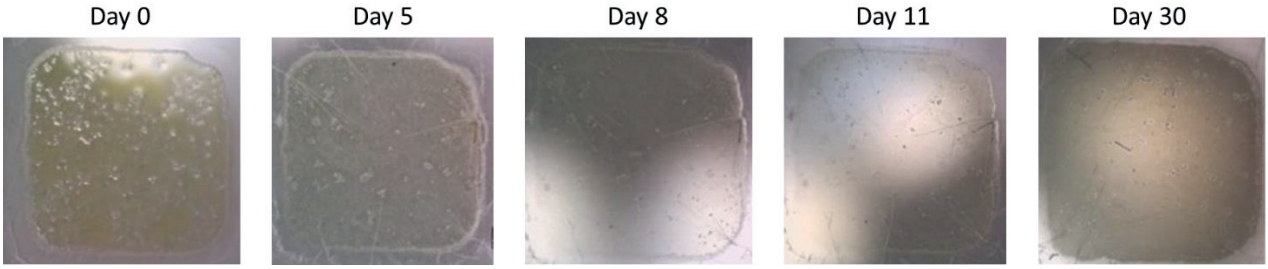

Figure 7.3. Evolution of a Au MSD ink deposited on PET substrate documented for 30 days

7.1.2 | SILK

It was initially predicted that lack of hydroxyl groups in the chemical composition of silk indicated that Au NP growth would not be possible. Regardless of this fact, typical Au MSD ink squares were printed and tracked upwards of 90 days displaying partial but slow growth as shown in Figure 7.4 below. Unfortunately, because silk fibroin is known to be water soluble even with water annealing treatment, its effect was already seen directly after printing as the water-based ink attacked the substrate and began to fuse the square printed patterns together. By Day 4, the ink was absorbed into the substrate creating wrinkles. The black dots indicate that Au NPs were forming by Day 4 but did not show the characteristic gold color. The deposited film finally completely dried by Day 6 which made it much easier to see that different shapes of Au NP appear across the surface of the film. This was also seen by Day 5 but less prominent in terms of concentration which was seen by Day 6 which appeared as triangular, hexagonal, and spherical particulates. By Day 13, not many changes in terms of Au NP growth nor further dark spot growth were detected. In fact, NP growth with different shapes was also seen towards the bottom of the sample however at a much lower concentration. The interior of the sample continued to see growth as differently shaped NPs appeared by Day 19 which did not show further growth nor changes from that point on. In total, there were separate growth mechanisms where the top part of the sample showed slow growth with the dark black spots while the middle and bottom sample exhibited isolated Au NPs as if the growth occurred exclusively of one another. The dark spots on the top part of the sample progressively turn to a white color initiating from the exterior to the

interior of the circle as indicated by Day 29. By Day 30, the previously noted white spots turn to a darker yellow-gold color, indicating another an intermediate growth stage.

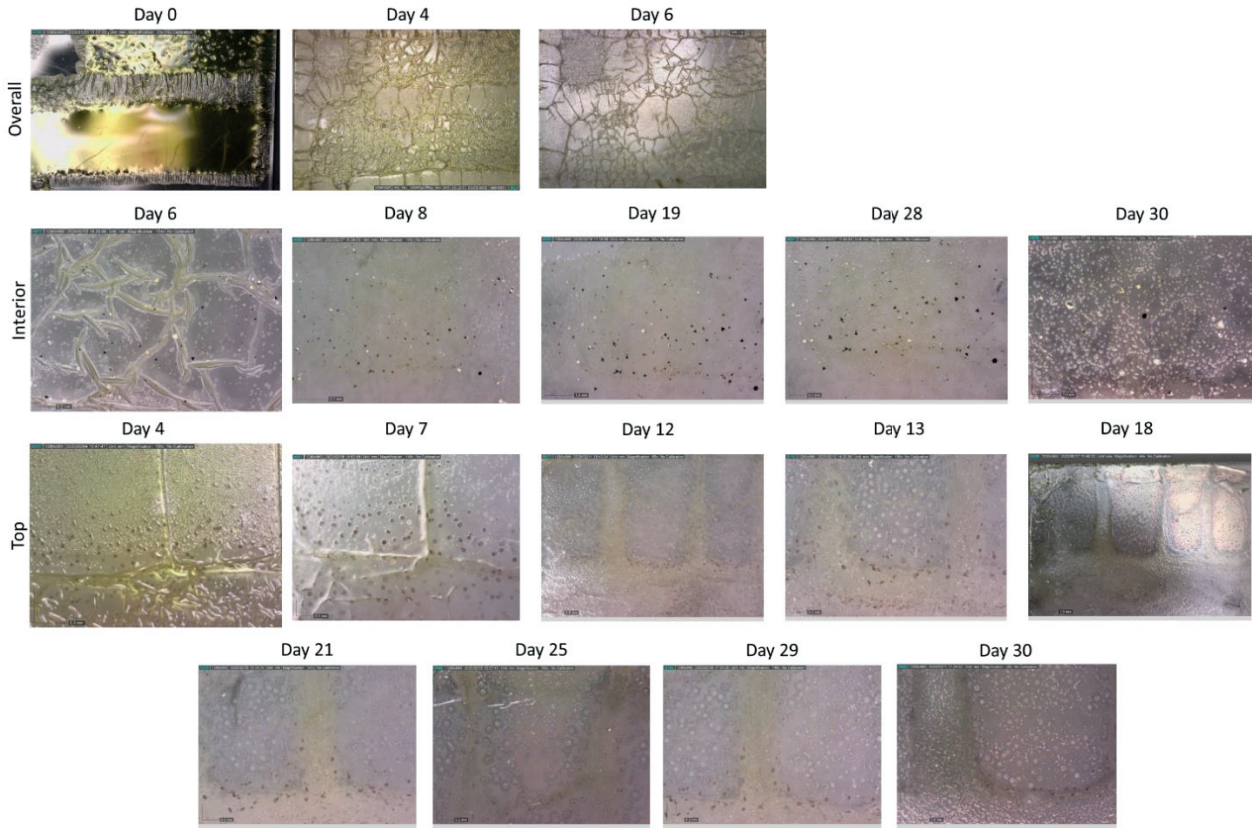

Figure 7.4. Au film development on silk substrate tracked up to 30 days

The sample was eventually placed into the desiccator for long term storage due to COVID restrictions, thus affecting both the growth and appearance of the silk film as bubbles formed and the became partially detached from the glass substrate. In total, these samples were placed into a desiccator for 83 days which once imaged again appeared completely different than expected as different colored films were found on the surface. More of a Au-like appearance was seen towards the edges where a smaller amount ink was deposited while the interior saw a more Cu-like color. The reason for this color difference is simply the difference in Au NP size within that area. The previously noted black dots eventually turned to a Au color however did not increase in size. This behavior was highlighted in Figure 7.5 where uniformly dispersed and isolated nanoparticles and clusters were seen. In contrast, the gold like areas were comprised of large circular NPs with 55.4 ± 5.6 μm diameter surrounded by the nucleation of smaller Au NPs giving the area a more gold like appearance. Unfortunately, neither a continuous nor conductive film was found as the NPs were isolated from one another. There is a possibility that with more

time and greater $HAuCl_4$ concentration (> 1M) that a conductive Au film could be obtained as coalescence between two larger Au NPs was already seen however after observation of over 100 days, this experiment was no longer tracked. Palui et al. reported that a 60 day old aged $HAuCl_4$ solution displayed aggregation between Au NPs due to Ostwald ripening process where a thermodynamically stable state in solution is reached through the minimization of the surface to area ratio whereby smaller particles are subsequently deposited onto larger ones.[6] This behavior explains larger Au NP surrounded by significantly smaller ones, although no change in the size was seen after 100 days perhaps signaling that the reducing reaction with silk fibroin was spent.

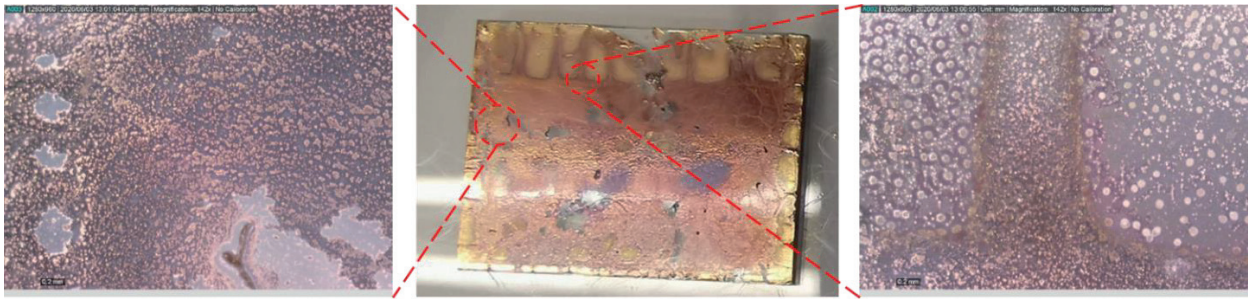

Figure 7.5. Au film development on silk substrate at 31 days (+83 days vacuum sealed)

These results suggested that silk fibroin could indeed be used as a green reducing agent in the development of Au NPs but also acted as a stabilizing agent as the nanoparticles remained isolated from one another therefore a conductive film could not be achieved as desired. However, unlike typically used stabilizing agents, silk fibroin may present difficulty in the removal process which may be released using water but this has not been reported in literature as this is not a standard synthesis process considering the extended synthesis time needed if achieved at RT. Instead, this could perhaps be better used for biomedical applications as previously suggested by Ranjana et al.

7.1.3 | CNF AND NA-CMC

Cellulose derivatives such as cellulose nanocrystals have been reported as a green reducing and stabilizing agent for the synthesis of Au NPs and Ag NPs respectively however these were embedded into the cellulose matrix indicating the growth of individual NPs.[7,8] For this reason, both CNF and Na-CMC substrates were investigated as their respective chemical structures in Figure 7.1 indicate an excellent potential to create conductive films due to the large presence of hydroxyl groups. On CNF, squares with 2 and 3 printed layers at a DS of 25 µm and tracked for 17 days maximum before COVID-19 pandemic restrictions interrupted daily tracking. In general, very minimal growth or changes were seen as the issue here is derived from the porous nature of the paper which tends to absorb the ink instead of allowing the solution to interact directly with

the surface. Figure 7.6 showed slight changes in appearance were seen on the border of the pattern where a grey ring appears signaling conversion on the edges which again tends to have less ink therefore tends to react faster than the interior of the square. By Day 5, this ring is much more pronounced where the outer ring appears as a green color while the interior displays more of a brown color progressing in growth or at least saturation of the substrate. This appeared in different ways as the ink itself seems to have bleed outside of its original dimensions which was to be expected for a porous substrate. Day 7 saw the first appearance of Au specks on the fibers specifically on the bottom left-hand side of the sample while the top left-hand corner did not have any signs of growth (Day 9). This growth is supposed to be the development of isolated Au NPs reacting to the hydroxyl groups in cellulose. Au NP formation continued to appear evenly across the bottom surface by Day 12 while Day 13 saw even more darkening of the ring layer towards the center of the substrate. The ring layer coloration seemed to indicate that NP growth was exhausted in those specific regions as little NP growth appeared. This once again is expected as a smaller amount of ink accumulates in this area therefore having less time to interact with the surface. This NP growth continued to grow almost exponentially from day to day whereby Day 16, the film appeared to have a metallic and almost gold like appearance on the middle part. Unfortunately, this was not the case for the bottom left-hand side of the sample as no further progression in Au growth was made but instead saw the area continue to darken to a brown color. Unfortunately, daily progression of the film could not be achieved due to mandatory COVID-19 restrictions put into place meaning samples were stored under vacuum for approximately 3 months before being imaged. By Day 18, physically 93 days under vacuum, saw a dramatic difference in the appearance of the film where the film exhibited a deep red wine color. Less of a metallic appearance was seen however the entire substrate itself was unified to one color where the same Au specs or Au NPs were seen throughout the surface, isolated from one another. This meant that the film remained non-conductive as a connected network did not appear. Unfortunately, it is believed here that such a low cellulose concentration (1%) was insufficient in the complete conversion of the deposited Au MSD ink into a conductive film. In fact this behavior was already reported previously indicating the successful development of NP but only sparsely on the individual fibers as significantly lower $HAuCl_4/AgNO_3$ and cellulose concentrations were demonstrated.[7,8] Increasing both the concentrations of both the metal salt ink and cellulose did not have a dramatic effect other than produce a greater amount of isolated NP on the surface which perhaps can be utilized for other application such as antimicrobial polymer films.

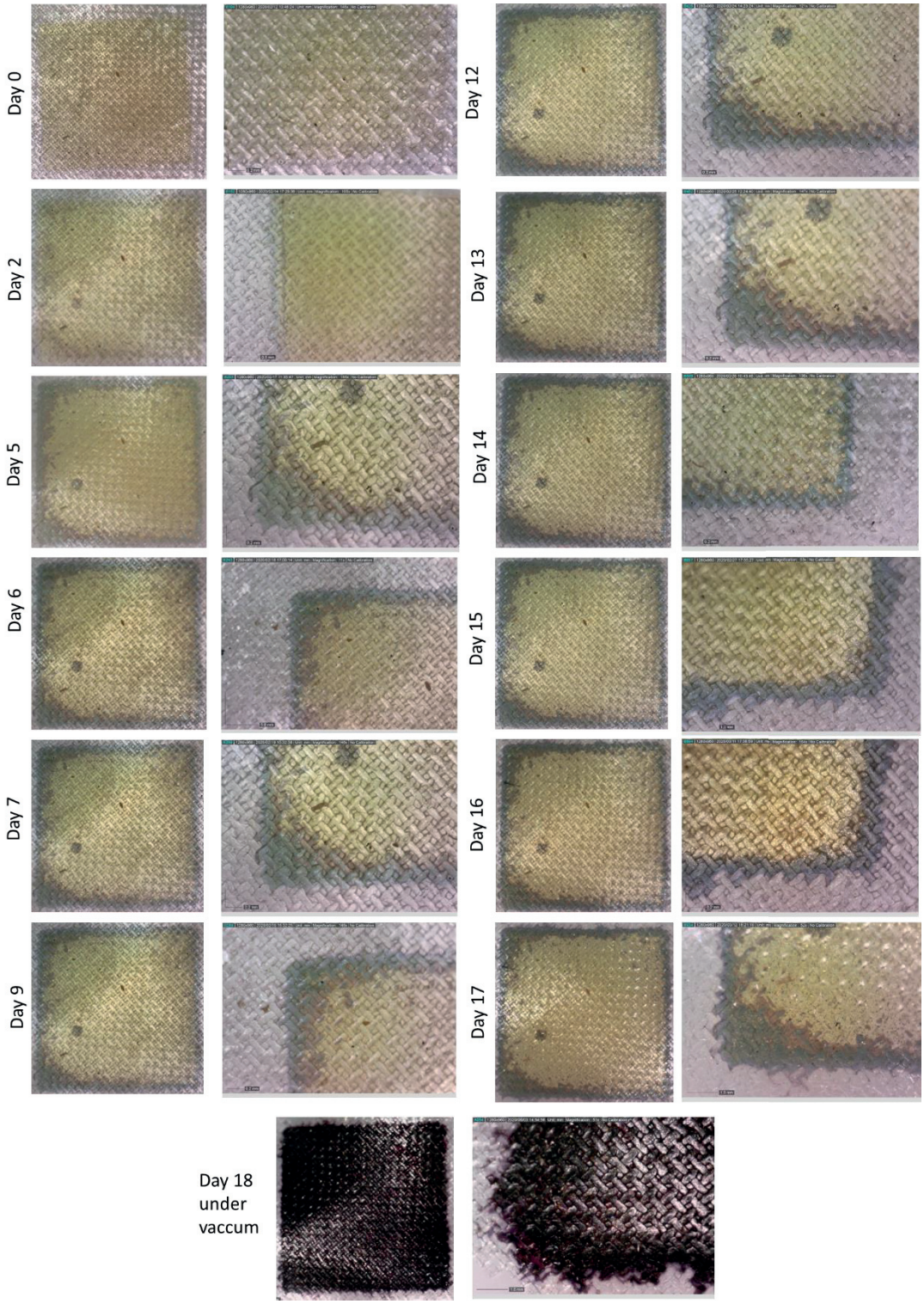

Figure 7.6. Au film formation progress on CNF substrate over 18 day+ period. The first row of photos was taken at 55x magnification while the second at 120x.

Unfortunately, the reactivity of Na-CMC with water made the deposition of this ink impossible without dissolving the substrate below as shown in Figure 7.7. The film itself tends to absorb the film instead of reacting with the solution surface severely limiting it compatibility with any water-based ink such as MSD inks. This means that this reaction will most likely be similar that found with PET. From Day 0, an irregular square shape is deposited and left to dry in ambient temperatures. By the first day, the pattern then proceeds to spread past the printed boundaries deforming the shape further. Although the film is still not dried, Au specs appear prominently at the bottom left-hand side of the square by Day 7 and by Day 8, they continue to grow where even some Au at the edges were formed. Day 16 begins to present a dark border at the outskirts of the pattern and the new appearance of black dots in the interior of the sample. This was not directly related to the reaction between the $HAuCl_4$ ink and the Na-CMC substrate itself but instead was mold from humidity that formed after long incubation times. No changes in terms of growth in the interior of the sample were seen however the edges of the sample show recrystallization of the metal salt by Day 21. Surprisingly, the sample is still not dry until Day 25 where the ink dries clear and broken. Again, because the pandemic impeded daily tracking of the sample, the sample was stored under vacuum for 83 days which then showed a drastic result where the film turned to reddish brown particulates which shrunk in size compared to the former film as shown on Day 25. It was clear that a continuous and conductive film could not be produced, however this color change did indicate that Au NPs were develop albeit isolated from one another as Na-CMC was utilized more as a stabilizer rather than a reducing agent.[9] It is believed here that the introduction of sodium carboxymethyl groups tended to replace the necessary hydroxyl groups therefore decreasing its ability to behave as a reducing agent for the Au MSD ink. For both these case, neither cellulose derivatives could not achieve conductive films however did show moderate success with the development of Au NPs after long exposure periods.

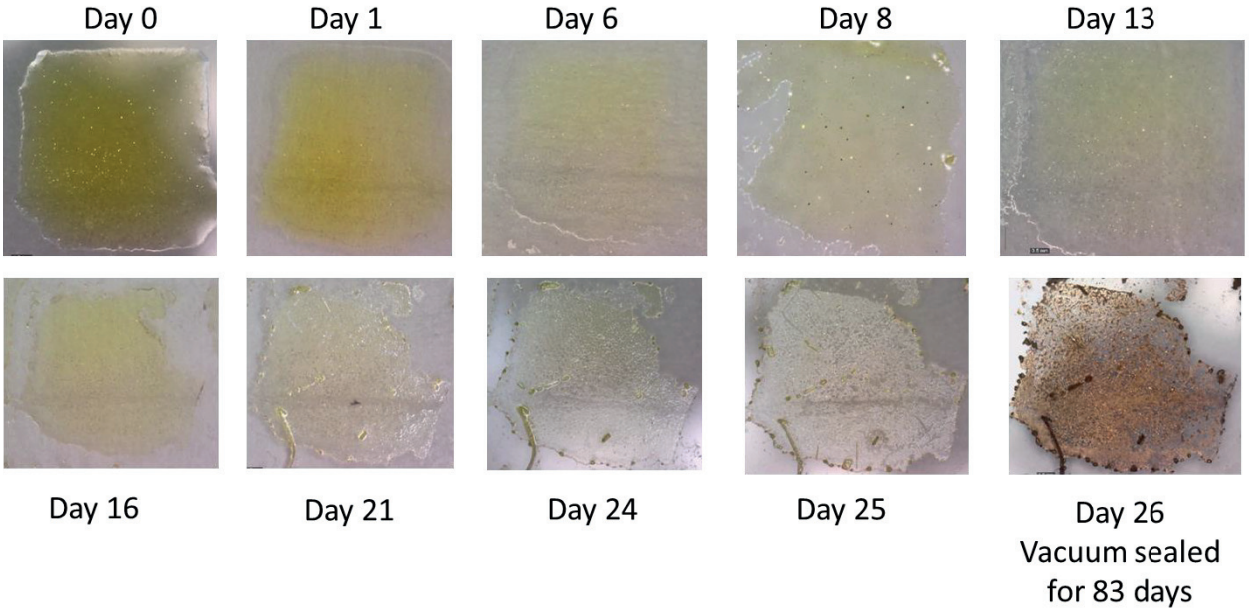

Figure 7.7. $HAuCl_4$ ink square was deposited and tracked for Au NP growth and taken at a 55x magnification with an optical microscope

7.1.4 | OSTEMER

Additionally, an off-stoichiometry thiolene polymer (known as OSTEmer for short) was investigated for its likeness to PDMS. This UV curable polymer is often used to fabricate microfluidic chips, known for its thiol groups which may have the potential to reduce metal ionic inks to elemental metal film. Brust et al. amongst many others first reported the use of organic thiols as a capping agent that have been successfully shown to produce a wide range of nanoparticle shapes.[6] However a characteristic of this substrate is that once exposed to air, is quick to oxidation within 15 – 20 minutes. This makes this substrate not ideal when working with inkjet printing, especially with large structures as the reduction mechanism may occur within days. Moreover, another habitual problem was defining a planar substrate so that it would not affect the spreading of the ink. Therefore 3 different strategies were used to create the flattest possible substrate including standard drop casting, spin coating, and casting into 3D printed mold. Of all the deposition techniques, drop casting (Figure 7.8a) proved to be the poorest as the substrate was clearly uneven to the eye thus resulting in disconnected films and isolated droplets on the substrate surface regardless of any surface treatment used. After heat treatment at 80°C for 30 minutes, no apparent change was however the 3 days afterwards, the deposited layer darkened to a dark brown color however no further change was noted after this. The change in color did indicate that a reaction with the thiol groups did occur however this did not lead to any Au NP reduction, much less a film. At this point, it was supposed that perhaps not enough of the Au

MSD was deposited to drive any reaction, therefore, a spin coated substrate was tested. The spin coated substrate also lacked flatness but did allow for a larger film layer to develop but not to the point of an actual square pattern. This instead resulted in a misshapen square pattern as seen in Figure 7.8b. A more immediate reaction was seen within the first day after sintering at 80°C for 30 minutes where specific outlined and darkened circular areas appeared. Additionally, the dried Au MSD ink displayed a darkened yellow color that proceeded to darken and fade to black color, usually an intermediate color or growth state before appearing as Au film. The development of the film was tracked for over 14 days where the film appeared to reach its development potential by Day 9. However unlike the drop casted sample, specs of Au appeared across the film surface although faintly visible after Day 1, which continued to grow exponentially until Day 9. The majority of the growth appeared towards the top left hand side of the substrate but was found to be significantly less on the darker regions however no predictable growth was found. These specs are presumed to be isolated Au NP clusters which did not see further growth past 14 days. This minor growth indicated that indeed Au NP growth was possible but perhaps required more ink layers in order to create a continuous Au layer. Lastly, OSTE mixture was cured into a mold thus resulting in acceptable flatness where both line test and square patterns as shown in Figure 7.8c below. In fact, the line pattern itself showed the best result forming gold lines directly following oven sintering. Unfortunately, due to the miniscule size of the line pattern, none of the formed lines appeared to be conductive. Regardless of these results, the line pattern provided additional information regarding the optimal DS for printed patterns between 20 – 25 μm which were then utilized to develop squares displaying varying degrees of success. The developed squares exhibited similar results to those found with the spin coated films, however because the full deposited ink amount was available on the substrate, a greater amount of Au NP growth appeared but at an accelerated rate directly following oven exposure. This means that even after 14 days Au NP growth was consistent with what was seen directly after sintering. Once again, a continuous film could not be formed however larger groups did appear to agglomerate together but never formed a layer as the NPs were observed to be separate from one another. However, one change that did appear was that the initially brown areas eventually turned to a black color by Day 9 and remained in that state past 14 days. Interestingly, a DS of 25 μm seemed to produce a greater rate of Au NPs compared to those squares deposited with a DS of 20 μm. However, with more layers, the nucleation of Au NPs was not enhanced as expected. After extensive testing, it was deemed that the development of a conductive layer was not possible using OSTE as only isolated Au NPs appeared, like the behavior exhibited with cellulose fibers as the NP have a tendency to grow but not agglomerate into a film.

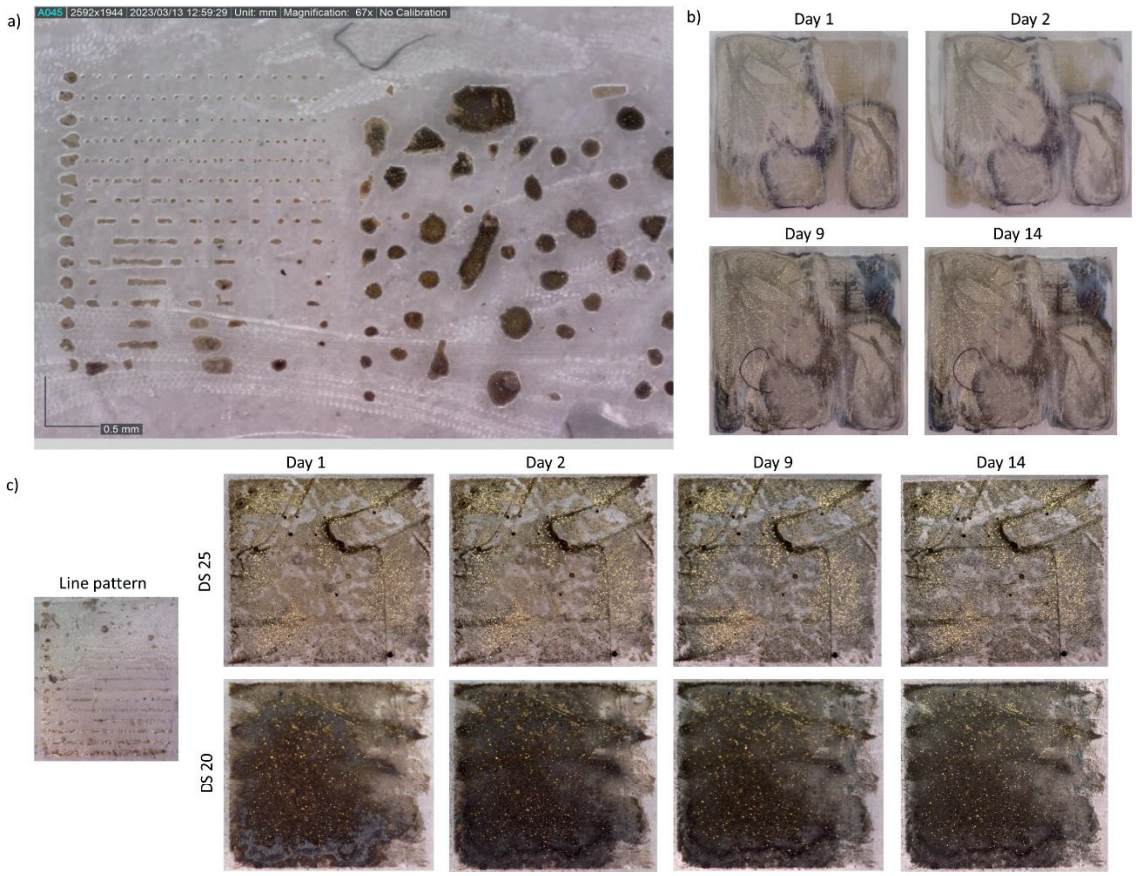

Figure 7.8.Au MSD ink on OSTEMER substrates developed using a) drop casting, b) spin coating, and c) mold

7.1.5 | CARRAGEENAN

Carrageenan is a linear sulfated polysaccharide derived from red seaweed that has found applications in batteries[10], memory devices[11], and various biomedical applications such as drug delivery[12]. The dried substrate was provided for by a IMB-CNM member developed from I-carrageenan which saw a large number of pits throughout the surface giving it an initially high roughness. This formulation resulted in porous membranes of 90% for 4 wt% and 95% for 1 wt%.[5] As carrageenan was only meant to act as the substrate in this case, this roughness was not ideal however it was previously shown that the $HAuCl_4$ ink was quite forgiving to extreme geometries. The printed line pattern could not be visualized as the small amount of ink was immediately absorbed with such a rough surface therefore squares were printed with a range of DS from 15 to 25 µm based off previous experience. As per usual, the sample was heat treated at 80°C for 1 hr and track up to 5 days until a film was formed as shown in Figure 7.9a below. Overall darkening of the film was seen after heat treatment where the squares appeared to be black in color signaling an intermediate growth state to which by day 5 finally grew into a

conductive film copper in color. Those films deposited with a DS of 15 and 20 µm displayed a high sheet resistance at 412.7 and 236.8 Ω respectively while those with DS of 25 µm was underdeveloped and non-conductive (Figure 7.9b). The porous nature of the substrate appears to impede not only the growth but also the resulting sheet resistance as more of the ink is needed to completely fill the pores while once converted continue to see a porous film structure that impedes direct electrical conduction. This signals the potential of carrageenan amongst others that can be identified as a reducing substrate, however due to the poor sheet resistance values, could not be used for developing electronic components.

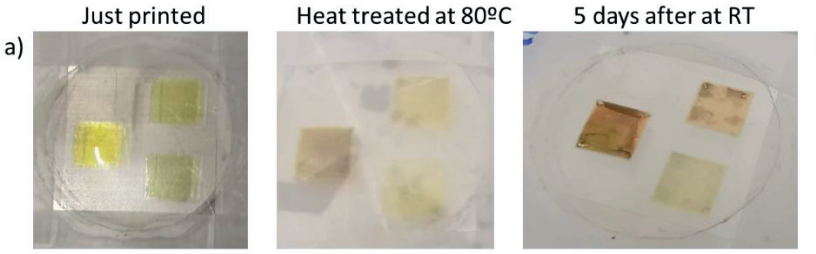

Samples with 2 layers deposition	Sheet resistance (Ω/□)
DS 15 µm	412.7
DS 20 µm	236.8
DS 25 µm	Underdeveloped

Figure 7.9. Au film growth on carrageenan a) at different growth stages and b) their respective sheet resistance values

7.2 | FILM GROWTH MECHANISM ON PVA

An extensive discussion regarding the development of Au NPs on PVA as the reducing substrate will be described below in the following section. Unlike the previously discussed substrates, the development of a Au film was possible and repeatable however its growth occurred in different stages which will be explored in depth. Au films behave similarly to SiO_2 grown or deposited films where the color of the film indicates the approximate thickness when reflected white light is incident to the Au film.[13] Throughout each notable growth stage, the film never appeared transparent unlike plasma sintered samples. Au film thicknesses and its respective colors were experimentally reported by Rouard et al. as shown below in Table 7.1.[13,14] The colors reported here similar to the ones reported where ruddy-purple and indigo can be easily mistaken for a black color although purple was also reported during my experiments. However, no blue color was reported with our films which is not in full agreement with the data. The film growth itself followed similar states going from a purple to green to brown to gold color under ambient conditions. This was later confirmed by Audrey Jaffer who utilized a simulation program called FreeSnell to predict the optical properties of thin film coatings.[14] Color charts for SiO_2 are widely available however this is not the case for metal films such as Ag and Au where are hard to come-by or are non-existent. His work was self-published online providing the missing link between my results and Table 7.1. Figure 7.10 composed by Jaffer reported a wide gamut of colors including the typically brown-black film color seen directly

before a gold film color when using oven sintering to accelerate the process.[14] The x-axis indicated here corresponds to the Au film thickness from 0.6 to 1.0 nm while the y-axis relates more to the ratio or concentration of metal NPs to the substrate from a range of 0.55 to 1.0 as represented in Figure 7.10a. According to this chart, if the deposited films are first heat treated to accelerate the reaction, it follows the scheme of Row I or J where the film appears as a brown-black color that once exposed to light turns to a shiny Au color. However, thin film growth at ambient temperatures allows one to see an even larger gamut of colors. As the $HAuCl_4$ ink is high concentrated within a small area, the wide range of colors of the film predicted here in Row B for example begin at the middle of the chart at 8.9 to 11 on the y-axis. As the NP begin to grow both in number and size, the film color is seen a green color. Due to the unpredictable growth of the film, no direct path can be followed in this case as an increase in the number of Au NPs would simultaneously increase the film thickness at the same time. Additional test trials regarding the difference in growth between 1 and 3 layers was explored as seen in Figure 7.11. Here, 3 squares for each printed layer were imaged daily for up to 30 days displaying the strong dependence on the number of layers needed to create a continuous Au film. For 1 deposited layer (Figure 7.11a), little Au NP growth was seen although it did sparingly appear to develop following the direction of the printed lines by Day 8. These NPs rapidly appeared and did not follow the previously described growth states. Specific areas to the right side of the sample as well as the left side edge eventually grew darker stopping at a dark brown color typically indicative of the growth step prior to Au film development. This color change appears because of the lack of NPs exposed on the surface due to lack of $HAuCl_4$ deposited on the surface. In contrast, 3 deposited layers sees a continuous film with a gold like sheen by Day 11 in Figure 7.11b. Similarly to 1 layer, the appearance of Au NPs was seen within just 5 days specifically at the bottom right hand corner of the sample while the rest of the sample appeared as yellow from the initial ink color. Once again, NP growth appeared as lines due to the printing process. By Day 8, an overall darkening of the substrate appeared along with exponentially more Au NPs growth almost creating a continuous film. As the observation period itself was interrupted due to COVID-19 restrictions up until Day 29, the sample was then stored under vacuum for 83 days which resulted in a devolution of sorts for both 1 and 3 layer samples. That is the previously developed NPs and films were removed almost reversing the conversion process. Both films appeared less developed than what was previously depicted on Day 11 for 3 layers. 1 layer also saw the same effect however placing the film under vacuum also propelled further development of the area areas of the film. This is because it is believed that Au NPs in this area were beneath the PVA surface obscuring the prominent Au color and preventing any sintering from occurring between the particles therefore presenting a brown colored film.

Table 7.1. Effect of Au film thickness on color. This figure was adapted from Rouard et al.[13,14]

Color	Thickness (nm)
Ruddy purple	1.5
Indigo	2.0
Blue	2.7
Green	3.2
Yellow green	4.0
Golden yellow	> 4.0

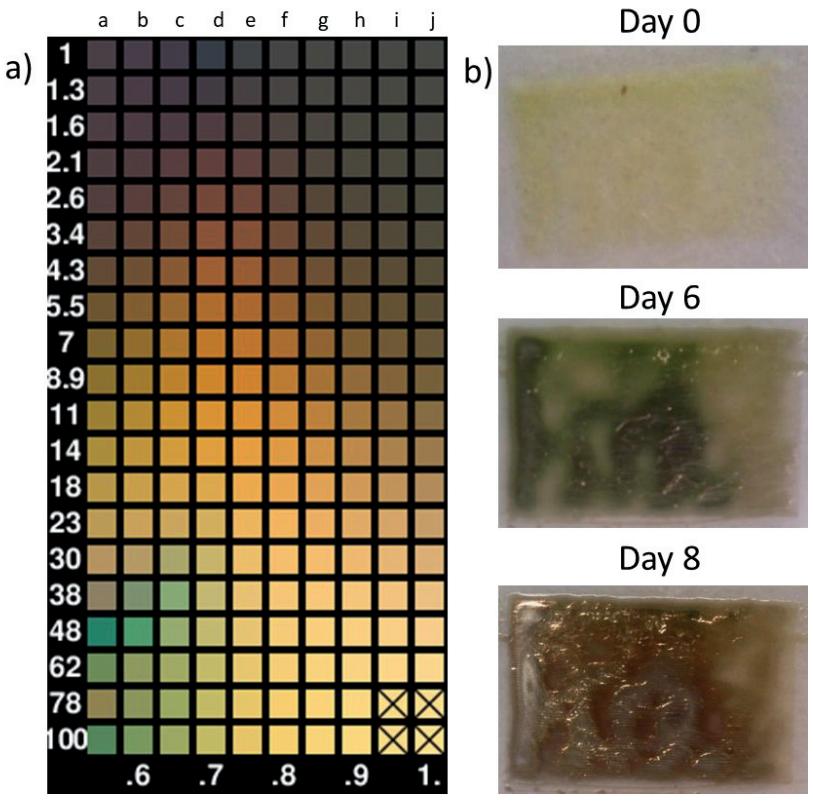

Figure 7.10. a) Au film color chart simulation conducted by Aubrey Jaffer using FreeSnell to predict the color of Au film where the x-axis represents the thickness in nm and y-axis is labeled 1-100 nm/q (the ratio of metal NP to substrate ~ 0.55 to 1.0)[14] b) Au film growth recorded by day at RT for 1 layer

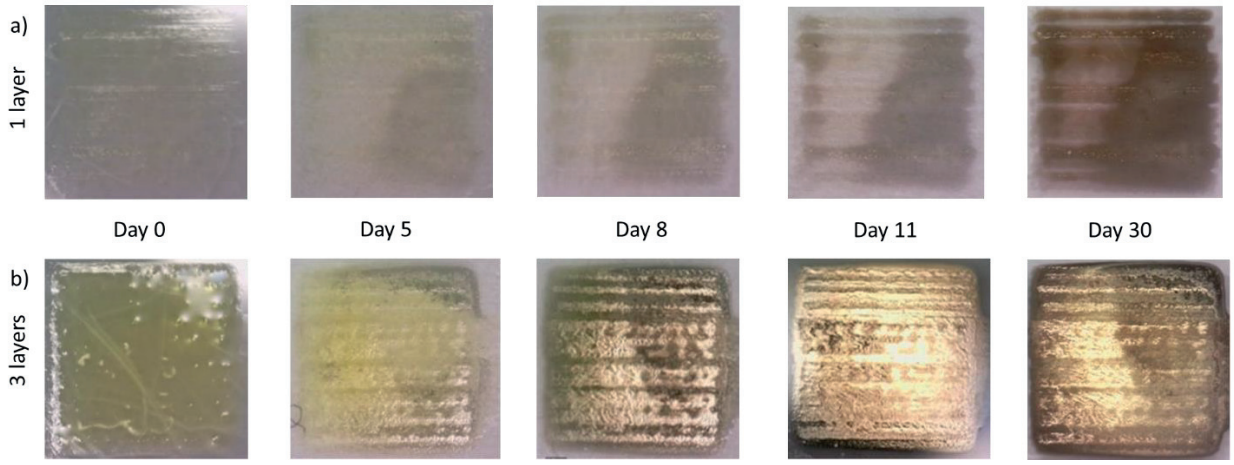

Figure 7.11. Day-to-day tracked Au film growth on PVA displaying a) 1 layer and b) 3 layers of $HAuCl_4$ ink deposition.

Although the film color itself gave a good indication that a Au film was formed, surface analysis was conducted via SEM/EDX to retrieve both topographical (Figure 7.12) as well as quantitative chemical analysis (Figure 7.13) information to be retrieved from the Au thin film. In a singular sample, different growth areas can be seen as the sample exhibited different colors ranging from a brown to characteristic gold. The center image in Figure 7.12 provides an overview of the sample highlighting underdeveloped areas as shown as different shades of grey. Further analysis was performed within these areas starting with the lightest, also noted as the 1st area here, where the film color exhibited externally is a gold sheen. The reason for this is because a uniform and continuous NP film was established even displaying sintering between NPs. Some cracks were found between the NPs as expected however as compared to the stacked films from deposited NP inks, this film is ideal. Mounds or bumps appeared across the surface that are in fact are clusters of Au NPs 100s nm in size that are formed and then expelled from the PVA substrate and settle to create tightly packed Au NP films with 60 – 70 nm thickness. This process occurs until the Au metal salt precursor is completely spent. Although this homogenous growth was shown on most of the substrate, other regions showed underdevelopment in areas noted as the 2nd and 3rd. The brown area (noted as the 2nd area) displayed disproportionate growth where NP growth occurs in a flower-like pattern where smaller NPs do appear to agglomerate and sinter together. It is believed that in this area, there was either due to an insufficient amount of $HAuCl_4$ ink deposited or lower PVA thickness (thus insufficient reducing ability) to achieve a Au gold film. On the other hand, the 3rd area is a transitional growth area where most likely a Au film will be achieved with a longer growth time. Here, homogeneous nucleation is displayed where the average NP sizes is 146.0 ± 17.4 nm. As the NPs start to agglomerate, they exhibit a polygon shape that will eventually lead to a continuous film as shown in the top images.

Homogenous nucleation and growth appear to be the governing reaction and is essential for the development of a Au film.

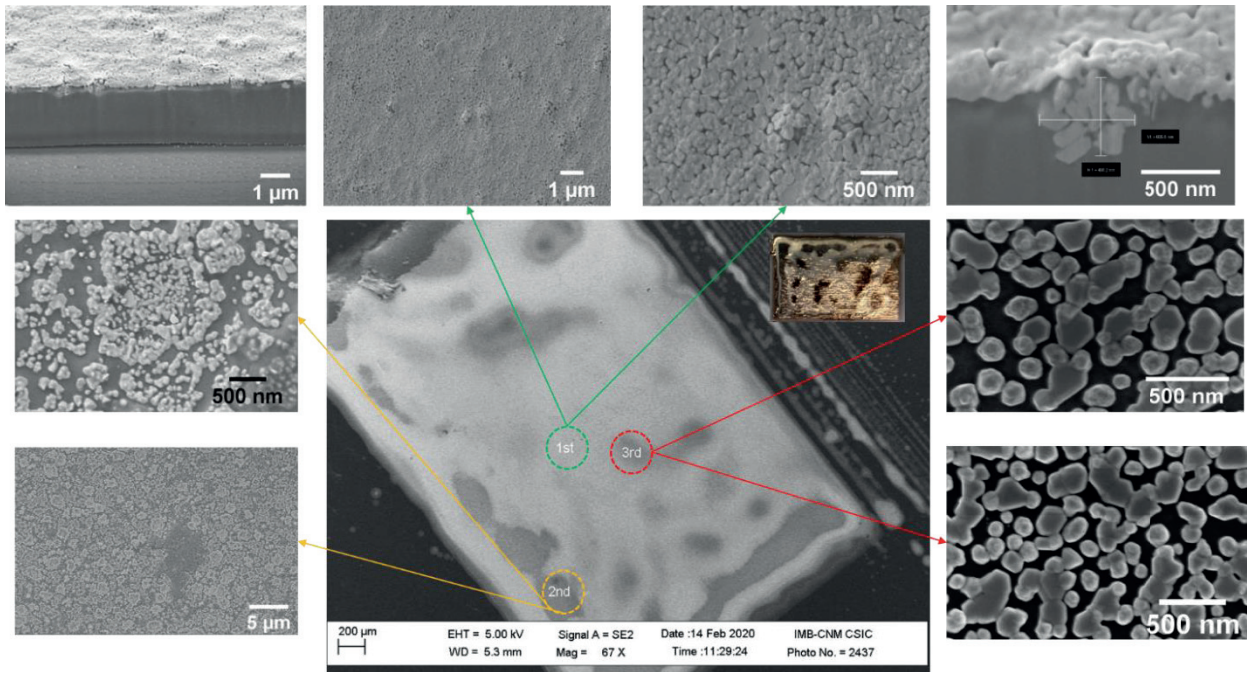

Figure 7.12. SEM analysis of Au film formation in progress displaying different areas

These particular areas were further investigated in terms of their chemical composition displaying that although Au was detected as the main element, remnants of Cl remained as shown in Figure 7.13. The percentage changed matched according to the development of the NPs thus affecting the color of the film. As expected, fully converted films (1st area) contained the highest amount of Au at 88.8% while Cl was found to be at 3.5%. All other elements including O and C are expected are they cannot be fully removed during analysis due to previous sample handling. The 3rd area showed the next best value at 80.5% Au with 5.4% Cl remaining. This is in good agreement as this area was in the process of development and expected to reach similar values as shown in the 1st area. However, this was in complete contrast to the 2nd area, which showed a significantly lower Au content and higher Cl content at 69.7% and 11.6% respectively. The higher Cl content is expected here as the Au NP development was occurring slowly and/or is incomplete and has not been effectively used to create a uniform film as found in the 1st area. All results found here verify that Au NP film growth was possible using a PVA substrate however, due to multiple growth areas, needed to be optimized to guarantee a uniform film as the results reported here took place on the very first developed samples.

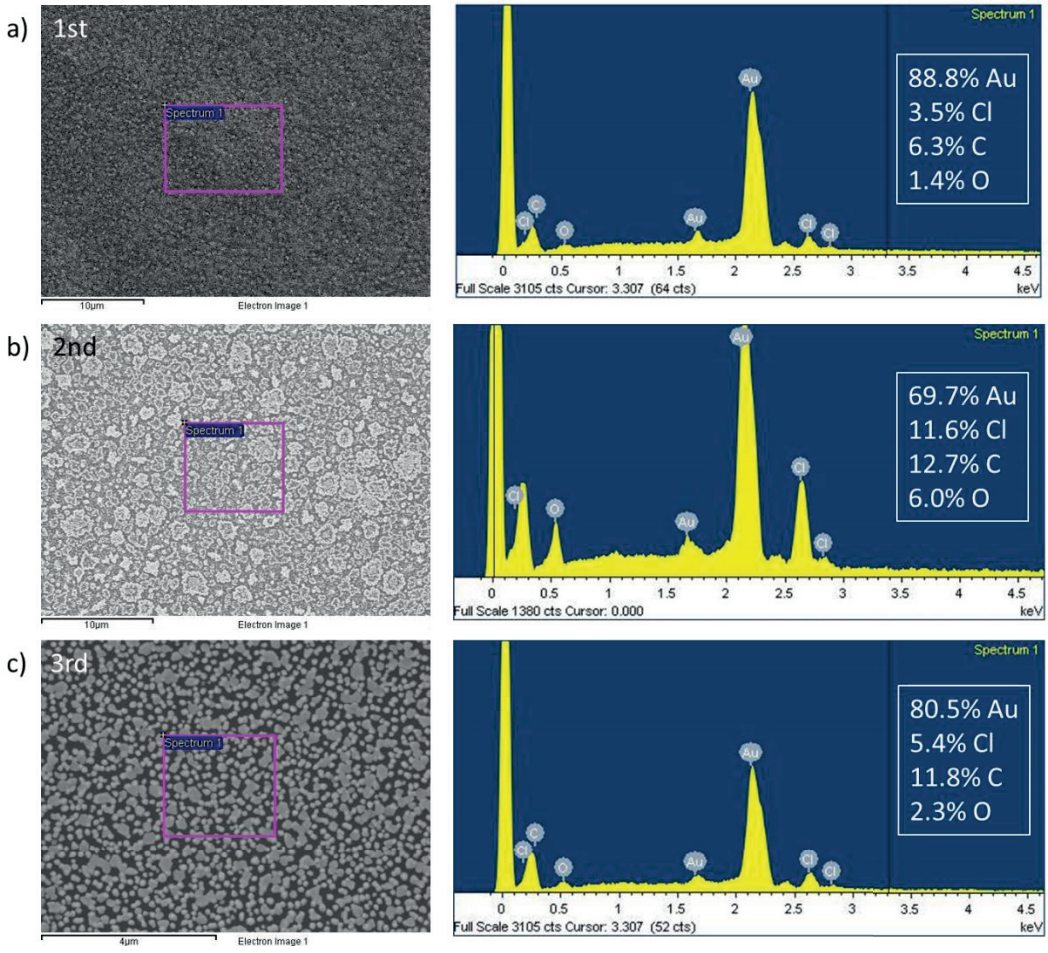

Figure 7.13. SEM-EDX results for multiple areas a) complete, b) incomplete, and c) partial Au film formation.

7.2.1 | GROWTH OPTIMIZATION

One of the basic printing parameters in order to optimize the printing of any new ink is by identifying the optimal number of layers needed to provide the highest conductivity possible on the PVA substrate. For this test, 1 – 4 layers was printed and developed as shown in Figure 7.14. Different sintering times were applied to see what effect it may have on the Au NP growth, as depicted in Figure 7.14a, which tracked Au film development when exposed to 15 minutes and 30 minutes of oven sintering and 15 minutes after being exposed to ambient conditions in a laboratory setting. For rapid Au NP film formation, 15 minutes was insufficient however double this time, at 30 minutes, saw expediated Au film growth with a golden color where films with 1, 3, and 4 layers appeared to be underdeveloped ink at the centers of each square pattern. Fifteen minutes after sintering treatment under ambient conditions outside of the oven, the underdevelopment centers of 3 and 4 layers appeared with a gold sheen however 1 printed layer

was ineffective in developing a full Au film. Full results of each layer can be seen in Figure 7.14b with a detailed view of each individual square at 50x magnification. As previously seen, 1 layer appears to be almost completely transparent although some Au film formation does appear to the right of the sample. Those squares printed with 2 layers appeared to be ideal under these sintering conditions with varying degrees of success for 3 and 4 layers. Beyond 2 layers, the pattern shape began to be bloated and misshapen as the ink exhibits the Marangoni effect.[15] The darken brown layers indicate underdeveloped regions similar to those seen in Figure 7.11 above. The structures were later tested showing a large difference in their respective sheet resistance as shown below in Figure 7.14c. Although 2 layers of deposited Au ink contained the ideal ratio for creating uniform films, its respective sheet resistance was found to be at the highest at 148.8 ± 9.4 Ω/□. With the addition of more layers, the sheet resistance decreased down to 20.9 ± 1.7 Ω/□. However, both the bloating and the underdevelopment of 3 and 4 deposited layers made it impractical to use for further printing, therefore 2 deposited layers was found to be the best results although displayed a higher resistance.

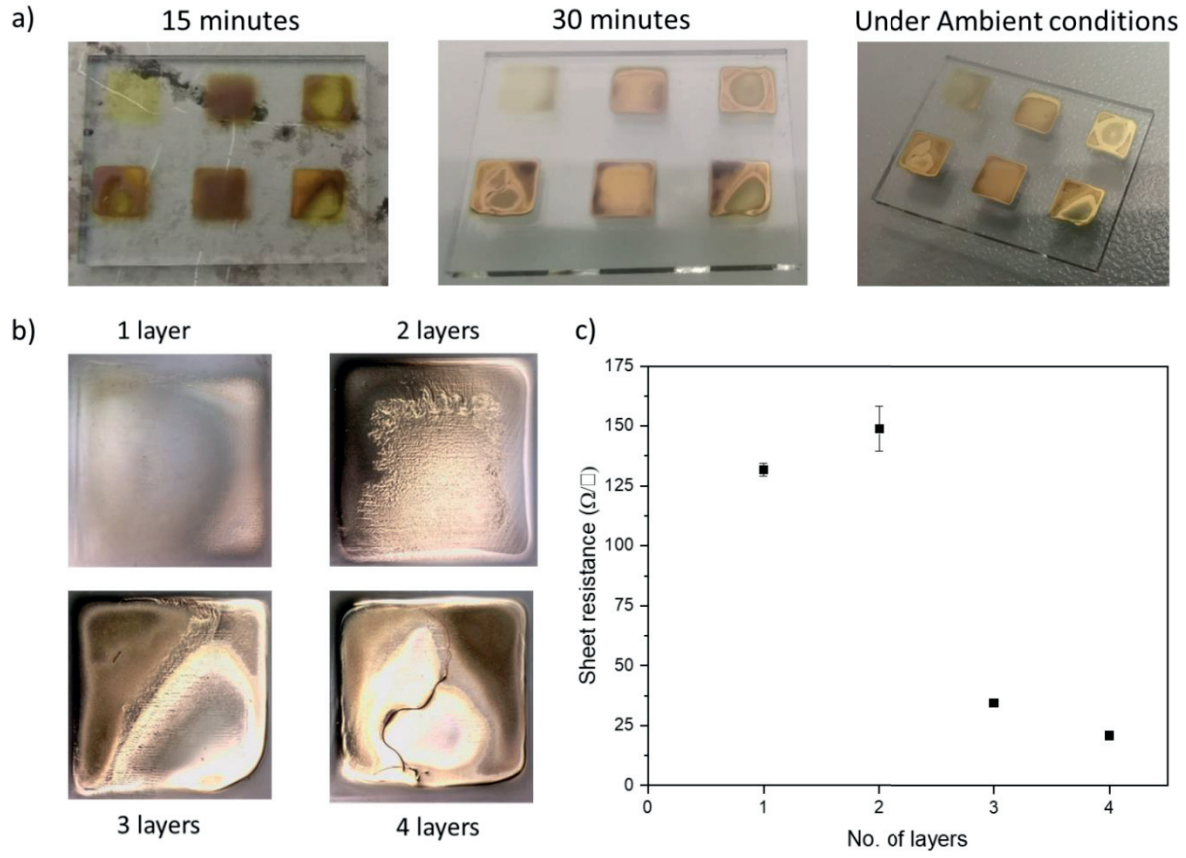

Figure 7.14. Au film formation dependency on number of layers a) progressive appearance of the films every 15 minutes, b) developed Au NP films with 1 – 4 layers, and c) sheet resistance vs no. of layers graph

7.2.1.1 | *EFFECT OF SUBSTRATE THICKNESS AND PVA CONCENTRATION*

Although not initially thought of as an influential factor, it was soon discovered that the substrate thickness had a critical effect on the Au film growth as shown in Figure 7.15. It was determined that substrate thickness between 3 – 6 μm was necessary for uniform Au thin film growth of the deposited area. This means that PVA thickness must be precisely controlled directly following the spin coating of the substrate. This required either 1 or 2 layers of PVA in which the thickness was measured using confocal microscopy. Significantly thicker PVA films (> 6 μm) often drop casted directly onto a PDMS substrate did not result in a Au film but instead resulted in completely yellow films after sintering. Even after multiple days of observation, the film would never change from this opaque mustard color as no Au NP formation was achieved. On the other hand, for films less than 3 μm, heat treated films maintained a brown color signaling partial NP development as previously shown. The brown color is a result of evenly distributed and separated NP nucleation across the surface that was formed due to the lack of reducing agent or in this case, PVA, where the film remained at this state and could not proceed. This behavior was mostly seen with the first deposited samples as well as those with more complex patterns that cover a wide area which emphasized this behavior. Therefore, to ensure that a fully converted Au layer resulted, the substrate was required to be at least 3 – 6 μm in thickness.

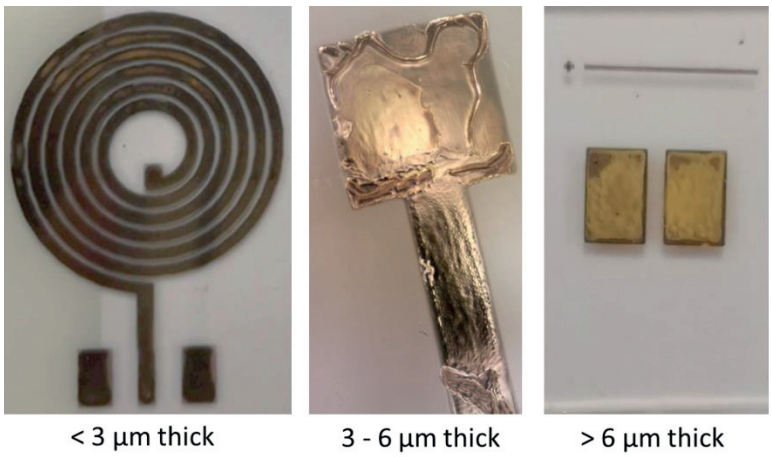

Figure 7.15. Effect that substrate thickness on the resulting film for < 3 μm, 3 - 6, and > 6 μm thick

In addition to substrate thickness, higher PVA concentrations of 8 wt% and 10 wt% were tested. Unfortunately, PVA solutions at 10 wt% and beyond could not be spin coated as the solution itself was extremely viscous and rapidly solidified and therefore was unusable as a substrate as it was impossible to fabricate. This was not the same case with 8 wt% PVA as a

substrate could be spin coated onto a glass slide and was expected to produce Au films at an accelerate rate as compared to those produced with 4 wt% as more hydroxyl groups would be available for reduction. Therefore, 1 – 4 layers of the $HAuCl_4$ ink was printed onto the substrate surface and tracked up to approximately 30 days as shown in Figure 7.16 below. Severely patchy growth was noted here compared to films deposited onto 4 wt% PVA where individual Au NPs first began to appear by Day 6 in 1 and 2 layers. As previously seen, 3 and 4 deposited layers showed bloating outside the printed square pattern and dried slowly in comparison to 1 and 2 layers. The wet films appeared to completely dry by Day 15 for 1 and 2 layers, both of which saw more individual gold colored NP growth however black regions in the interior for 2 layers also appeared. This similar behavior appeared for 3 and 4 layers of which did not appear to dry until Day 22. Over a long period of time, these dark areas eventually became lighter displaying a light brown color from further Au NP growth by Day 28. No further growth was seen for 1 deposited layer from Day 22 to 28 resulting in a fragmented Au film that was ultimately non-conductive. For 2 – 4 layers, growth continued to progress creating a continuous Au film albeit with some dark regions with delayed Au NP growth. The samples were no longer tracked after 30 days of observation. When compared directly to Au films grown on 4 wt% PVA, Au NP growth on 8 wt% PVA was significantly slower growth. Continuous and conductive gold-like films developed within 11 days, far quicker than what was shown below. This delay in growth may specifically be due to the increase in substrate thickness resulting from the higher viscosity of the PVA solution although the thickness itself was not measured. Regardless of this fact, due to both the delayed growth and spotty growth overall, 8 wt% substrate was deemed not optimal for Au film growth as compared to 4 wt%. Although films lower than 4 wt% were not tested, it is believed that a similar issue would arise in terms of both the substrate thickness which would be thinner than desired in addition to the diminished reductive ability due to less available hydroxyl groups from diluted PVA. Therefore it is predicted to be even less likely that a conductive film would be developed without any golden sheen as seen previously.

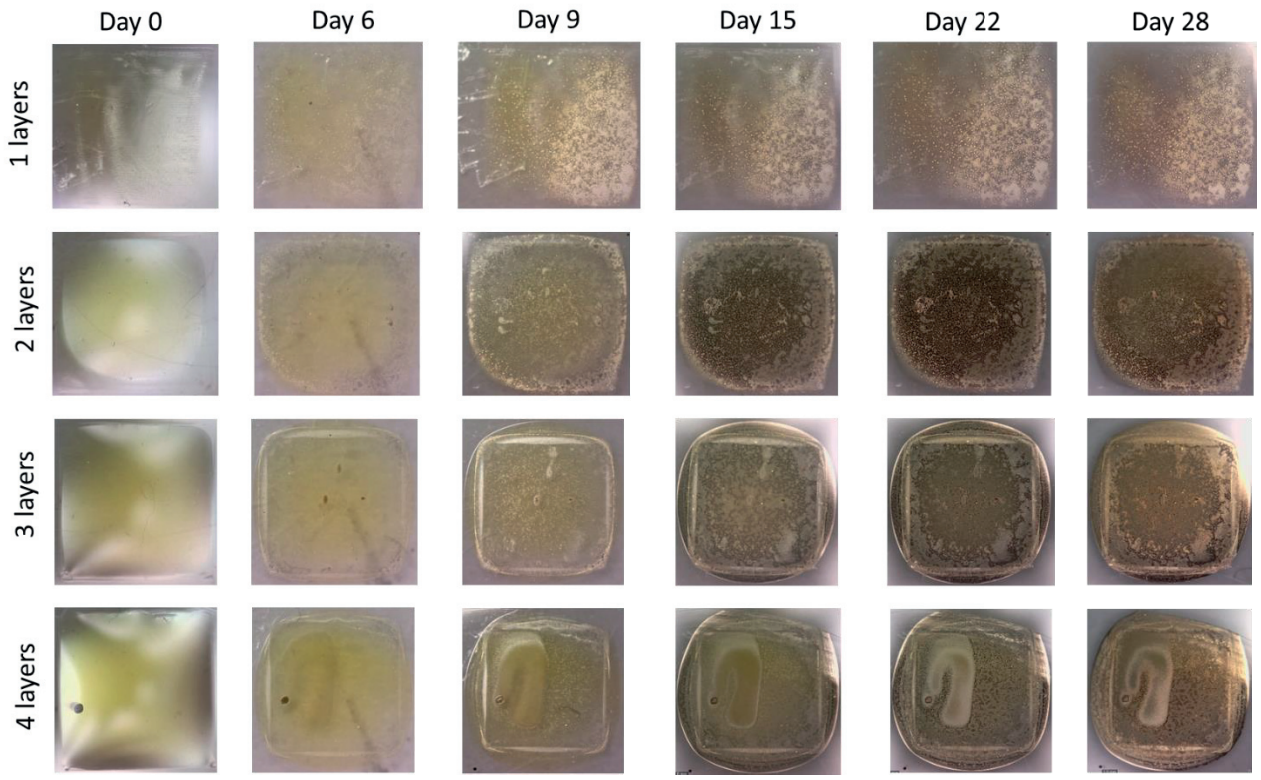

Figure 7.16. Au film development on 8 wt% PVA tracked up to 28 days

7.2.1.2 | *EFFECT OF OXYGEN AND LIGHT*

Although it was not apparently clear when this reaction was first discovered, an investigation regarding oxygen control of the sample was conducted by placing the sample in direct and continuous contact with oxygen flow under a concentrated and covered area with parafilm and observed for 30 days with an optical microscope as displayed in Figure 7.17. Results here showed a similar growth trajectory as previously discussed as the film transitioned from a transparent yellow (Day 0) to green (Day 4) to tan (Day 5) or brown (Day 7) color and eventually to a gold color. Heterogenous growth also appeared in these samples as noted by the tan and brown colored areas resulting in a mix of gold and copper-colored films by Day 30. Rapid NP growth appeared by Day 8 but did not see many changes until Day 30 where the characteristic shiny gold color was noticeable. Regions at the top of sample already showed Au film growth by Day 5 however other areas were much slower in comparison. Because slower growth was reported as a completely reduced film was not seen until Day 30, the continuous introduction of oxygen did not serve to accelerate the film growth but instead impeded it perhaps due to decreased temperatures.

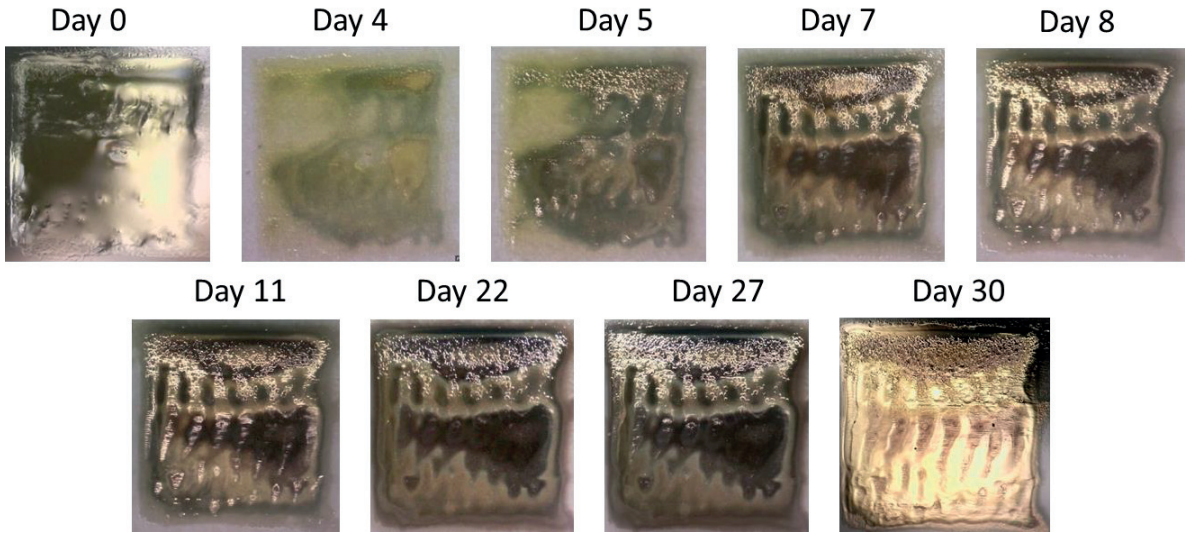

Figure 7.17. Effect of constant oxygen flow on Au film formation on 4 wt% PVA substrate for 2 deposited layers and tracked up to 30 days

However, one aspect not taken into account to explain the slower growth seen in Figure 7.17 above was the effect of light on the film growth. In the previous study, the sample was covered with parafilm partially obscuring any incoming light which may influence the Au film growth. However, the sample was periodically exposed to direct light during imaging sessions which facilitated Au growth. This hypothesis was also supported by previous samples placed into the oven (devoid of any light) for rapid sintering which often presented a brown color film that once exposed to a light source initiated the gold like appearance. It is the interaction that Au NPs have with light that dictates both their appearance in solution and as a film across a wide spectrum of colors. For example, 30 nm diameter NP dispersion displays a red color as they tend to absorb light in the blue-green region (450 nm) while reflecting red light (700nm).[16] As the diameter of the NP increases, the opposite behavior is seen where red light is absorbed while more blue light is reflected exhibiting a purple colored solutions. This characteristic is known as plasmonic resonance. Keeping this behavior in mind, NPs are known to absorb a wide range of wavelengths at least from 450 – 700 nm which indeed cover the range seen from direct sunlight as well as fluorescent light bulbs as shown in Figure 7.18 below. Samples were often left overnight for long periods of time or after quick oven sintering under standard laboratory conditions containing both fluorescent lighting and direct sunlight, both of which may contribute directly to its growth.

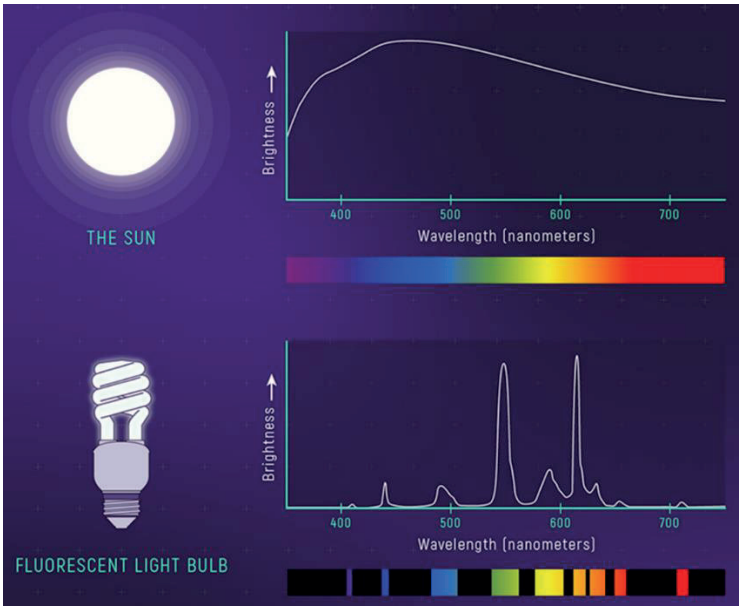

Figure 7.18. Wavelength range for sunlight vs. a fluorescent light bulb. This figure was acquired from the Webb Telescope webpage.[17]

Previous research has demonstrated the use of light to induce Au NP synthesis in solution required both the metal salt and a reducing agent. Multiple papers have reported the use of UV light ranging from wavelengths between 254 to 300 nm that rapidly produced Au NPs at RT. Courrol et al. tested a wide range of amino acids for their reducing ability aided by illumination from a white light xenon lamp displaying a range of wavelengths from ultraviolet to infrared. Exposure to the light provided both photon energy and elevated temperatures facilitating Au NP growth due to loss of electrons leading to the reduction of metal species.[18] Ranjana et al. was able to induce Au NP synthesis using silk fibroin as a reducing agent when exposed to UV-B light with a narrower wavelengths between 280-315nm while Dong et al. reported that synthesis using a singular wavelength of 300 nm within 30 minutes.[19,20] Gomes et al. conducted a test comparing UV light synthesis (wavelength of 254 nm) against ambient light which was determined to be 6 times faster within 10 minutes vs. 60 minutes respectively.[21] This proves that light plays a crucial role in Au NP synthesis under a variety of conditions in solution and for metal film synthesis.

7.3 | REDUCTION MECHANISM BY PVA

An in-depth study conducted in 1984 by Fedorova et al. claims light induced reduction of Au metal salt via a photochemical reaction led to the development of elemental Au film. Here, the Cl ions play a pivotal role in driving the reaction forward via a chain mechanism following a 4 stage process.[22] Stage 1 notes a photochemical reaction (Equation 7.1) whereby the

introduction of the ink to PVA serves to further increase its photosensitivity (UV excitation) by at least an order of magnitude greater whereby

$$[AuCl_4]^- + h\nu \rightarrow [AuCl_2]^- + 2Cl^\bullet \tag{7.1}$$

occurs at low temperatures (77K to 300K) directly from the 220 – 400 nm range and indirectly from 350 – 470 nm.[22] This range coincides with incandescent (280 or 375 nm), white LED, and sunlight which may provide some contribution to this reaction.[23] By Stage 2, decomposition is initiated through thermal activation above 220K where the chloride radical begins to interact with both PVA and $[AuCl_4]^-$as shown in Equation 7.2 below:

$$[AuCl_4]^- + Cl^\bullet \longrightarrow [AuCl_2]^- + Cl^\bullet + Cl_2 \tag{7.2}$$

It is at this stage where the $[AuCl_4]^-$ decomposition further devolves into a chain process interacting with PVA following Equations 7.3 and 7.4 below:

$$(-CH_2 - CHOH) + Cl^\bullet \rightarrow (-CH_2 - CHOH)^\bullet + HCl \tag{7.3}$$

$$(-CH_2 - CHOH)^\bullet + Cl_2 \rightarrow (-CH_2 - CHOH)Cl + Cl^\bullet \tag{7.4}$$

Equation 7.3 shows that PVA molecules orient the $[AuCl_4]^-$ ions (incorporated into PVA matrix) to interact with the chlorine radical and complex ion. The reaction provided in Equation 7.4 provides constant supply of chlorine radical generation to Equation 7.3 as well as molecular chlorine decomposition. Equations 7.2 – 7.4 are mainly responsible for the decomposition of the $[AuCl_4]^-$ ion however there are also minor reaction that only become important at higher temperatures which was not the case for this reduction system and therefore will not be discussed in this section. The 3rd Stage is comprised of photolysis which sees the bulk formation of decomposition products changes that appear according to Equation 7.5 below:

$$3AuCl_2^- \rightarrow 2Au + [AuCl_4]^- + 2Cl^- \tag{7.5}$$

Note that $[AuCl_4]^-$ ion always remains present which predicts that contamination may always be an issue when developing samples. This was found to be the case as discussed later on under Section 7.5. By Stage 4, formation of Au NPs appears as a result. However, one element not taken into account was the introduction of EG which is known to be a reducing agent. It is predicted that the EG further reduces the activation energy needed to initiate the reaction between the PVA and $HAuCl_4$ components.

Physically, what is believed to be occurring is represented below in Figure 7.19 below where Figure 7.19a shows the formulated $HAuCl_4$ ink deposited onto the PVA surface which due to its water solubility (Figure 7.19b) incorporates together where the Au seeds from the Au metal salt precursor increase in size (Figure 7.19c) and start to migrate to the PVA surface as the ink dries. Au NP growth occurs under multiple regimes as shown in Figure 7.19g where solution reduction generates both homogenous and heterogenous nucleation following the reduction of the Au ion. Figure 7.19d and 7.19h depict randomly dispersed NPs under the PVA surface that once pushed to the surface remain isolated from one another (Figure 7.19e) giving a brown film appearance. The remaining Cl ions serve to remove the PVA (Figure 7.19i) destabilizing the Au NP surface thus allowing sintering to occur between the particles ultimately creating a conductive Au film as shown in Figure 7.19f.

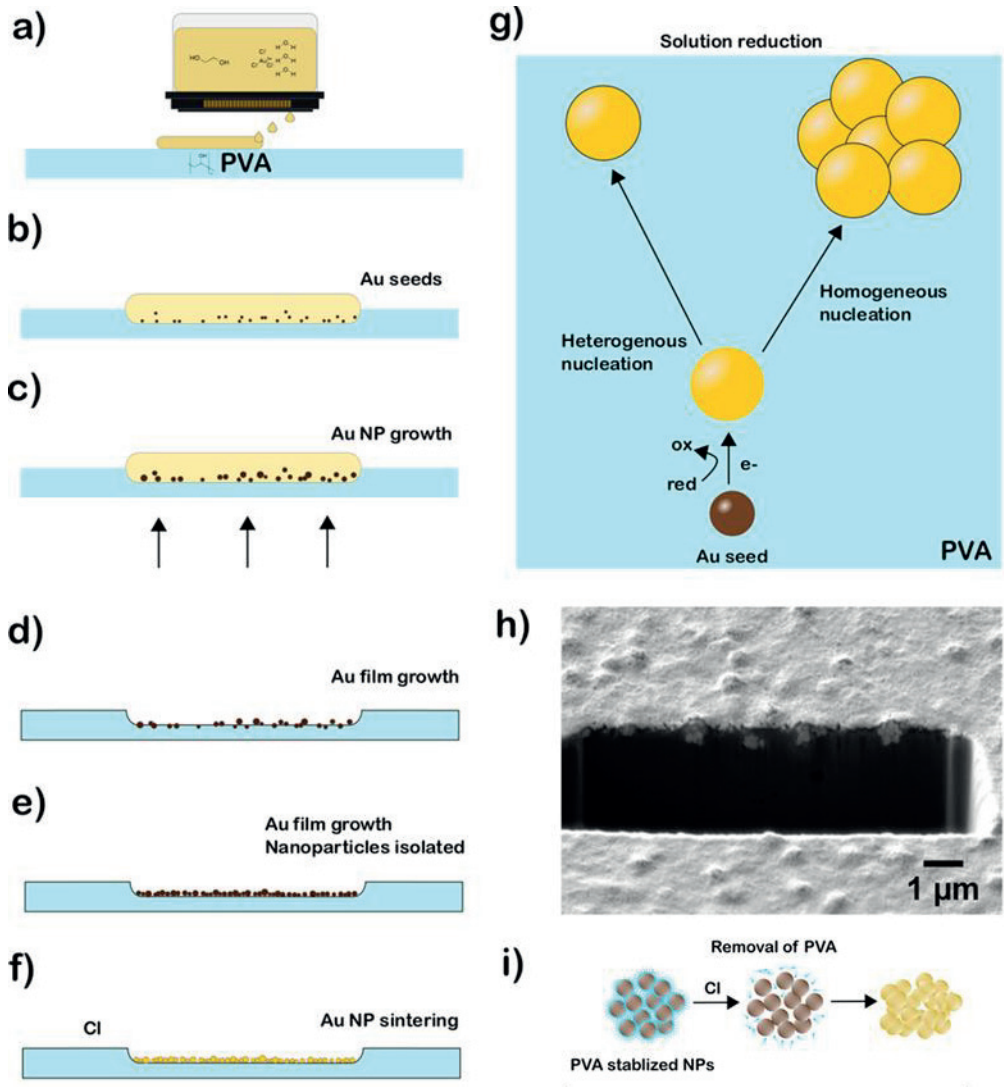

Figure 7.19. Au ink reduction and film formation where a) - f) displays a step by step process where a) as the ink is deposited and b) absorbed into the PVA substrate, c) nanoparticles start to form from Au seeds. When the nanoparticles are fully formed, d - e) they are pushed to the PVA surface however remain non-conductive as they are surrounded by PVA. Sintering then occurs during the drying portion where f) the Cl ions serve to detach the PVA from the nanoparticle surface thus allowing the nanoparticles to sinter together creating a highly conductive and shiny Au film. Different solution reduction mechanisms represented in g) stem from the Au seed displaying heterogenous and homogenous nucleation and growth. Under SEM observation, h) Au NP growth forms in the PVA substrate and is gradually pushed towards the surface creating mounds. The film itself then becomes conductive when i) the remaining Cl ions destabilize the PVA coated NPs leaving solely Au NPs.

7.3.1 | MATERIALS AND INK FORMULATION PROCEDURE

The majority of the inks discussed here were previously reported in Chapter 6 Section 6.2 on Metal salt decomposition ink formulation with the exception of the palladium MSD ink. Here, the ink was contained palladium (II) chloride ($PdCl_2$, ≥99.9%) salt from Sigma Aldrich (Merck). The Pd ink formulation was comprised of 1 mL of 0.5M $PdCl_2$ (1 mL of DI H_2O + 0.09g of $PdCl_2$) + 1 mL (33% EG + 67% DI water). The solution was stirred at 200 rpm for 2 hrs until ingredients were combined and transferred to a 10 pL printhead to be used directly.

7.3.2 | LIMITATIONS

One of the limiting factors of this technique is the ion reducing potential of the metals in each prospective ink. Although this technique has consistently been shown to reduce $HAuCl_4$ ink, this was not the case for others such as $AgNO_3$, H_2PtCl_6, $PdCl_2$, $CuSO_4$ inks using PVA as a reducing substrate. Figure 7.20 below details the Ag film growth when following the deposition of the $AgNO_3$ which was then left at RT to sinter. In general, growth appeared to be more uniform for 4 layers as opposed to 1 – 3 layers as they each maintained an undeveloped center for the duration of testing. After just 1 day, PVA appeared to be reacting to the ink at the very edges of the square patterns which are known to have smallest ink thickness. Day 2 showed even more growth as the ink started to dry whereby crystal formation started to appear (a characteristic of the $AgNO_3$ ink as first reported in Chapter 6). The appearance of both a grey and brown color indicated an intermediate stage of formation. Eventually the brown film dominated over the grey. However following this last imaging session, the pandemic started and affected the experiment meaning that the sample was stored under vacuum for 83 days while it was still growing. Upon return, a silver like color surrounded the edges of the square with a rainbow interior indicated as Day 5. This color change may indicate different Ag thin film thickness which can display a wide range of colors.[14] Fifteen days afterwards, this silver ring turned into a gold color signifying oxidation although there was no further change seen in the interior of the square. Day 30 showed a bit more development but also some darkening in the center parts of the square. Imaging of the films was tracked up to 48 days where growth appeared to stop entirely and instead was found to be oxidized and non-conductive. One of the reasons for this is the fact that Ag can be easily oxidized in air over time which is needed for both the growth and development of the film at RT. It is believed that a Ag film did manifest over the non-observational period during the pandemic however once the sample was exposed to air, the oxidation process then began to take over. Therefore, this same technique is not applicable to $AgNO_3$ inks. However, if previously known, light synthesis or photonic sintering could have been applied as compatible processes to develop Ag NP films which should further explored in the future.

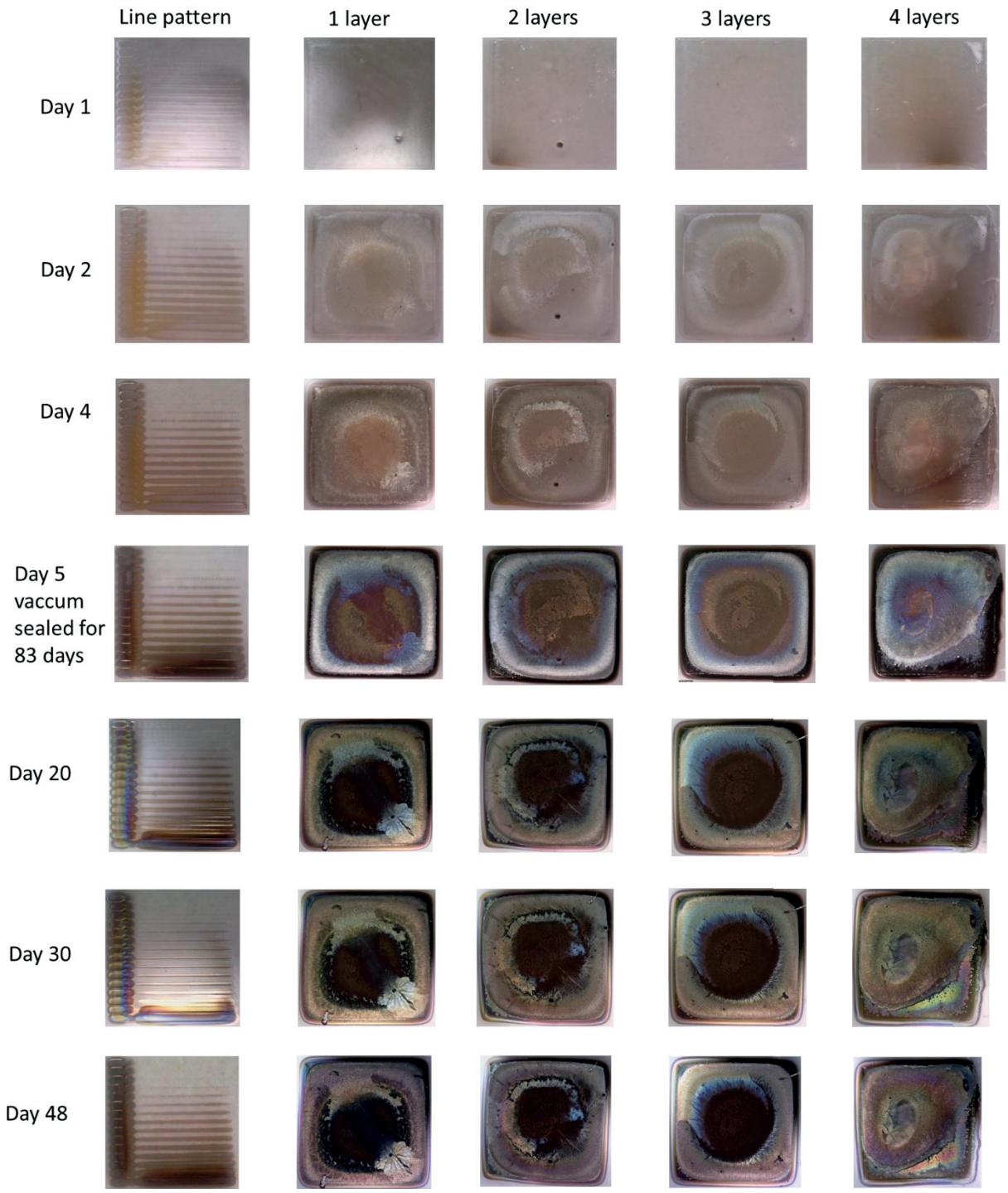

Figure 7.20. Stages of Ag film growth on PVA

A very similar result was seen with the deposition of a Pd MSD ink in which both modes of film growth were tested. The $PdCl_2$ metal salt precursor ink resulted in partially dissolved brown

colored liquid even after 2 hrs of stirring and needed to be filtered before use to avoid any nozzle clogging. The printed line pattern as shown in Figure 7.21a below showed that no well-defined lines were seen for any DS but regardless, squares were deposited based on past experiences with similar inks which was shown in Figure 7.21b. Similarly to the line pattern printing, neither of the DS was ideal for making patterns as they ranged from being undefined and bloated to displaying holes throughout the films. In the end, a DS of 35 μm was chosen as the pattern was acceptably defined where multiple layers were printed until a uniform film was produced. Accelerated film growth using thermal treatment gives a general idea whether or not a conductive film could be obtained through the self-sintering or RT approach. Figure 7.22 shows a wide range of results after the PVA substrate was subjected to sintering and evaluated every 15 minutes. Following 15 minutes of sintering, only 3 layers of the deposited Pd ink began to react already showing a metallic film on the top lefthand corner of the square. Two deposited layers exhibited faint growth on the same area. An increase in film growth was seen after 75 minutes of sintering for all layers around the same areas. However, all edges of 4 layer sample appeared to have been reduced. An indicator that the metallic film would be produced is the darker color most likely signaling nanoparticle growth under the PVA surface. Altogether these films were treated with 210 minutes of thermal sintering at 80°C, far longer than desired. It's for this reason that it was no surprise that under ambient conditions, the Pd film did not grow in the absence of thermal treatment. Figure 7.23 shows overall darkening for 2 – 3 layers signaling that the initial conversion process was occurring. Complete drying of the film occurred by Day 4 whereby cracks in the film started to appear. However not much change was seen after this point which was tracked for a total of 48 days. Although many parts of the substrate appeared to be reducing, the only sample that produced a silver-like film was with 4 layers of deposition also found at the top left corner. This behavior was seen throughout all deposited samples which indicates that there is an accumulation of the ink in that region which allows the reduction to occur at a faster rate than the other areas due to the Marangoni flow. For this reason, the film itself is highly non-uniform and deem to be unsuccessful under these conditions. This result was unexpected as its respective reduction potential was +0.92 V suggesting that metals with much higher potentials would be more successful while those lower or neutral would be unlikely to produce a conductive film.

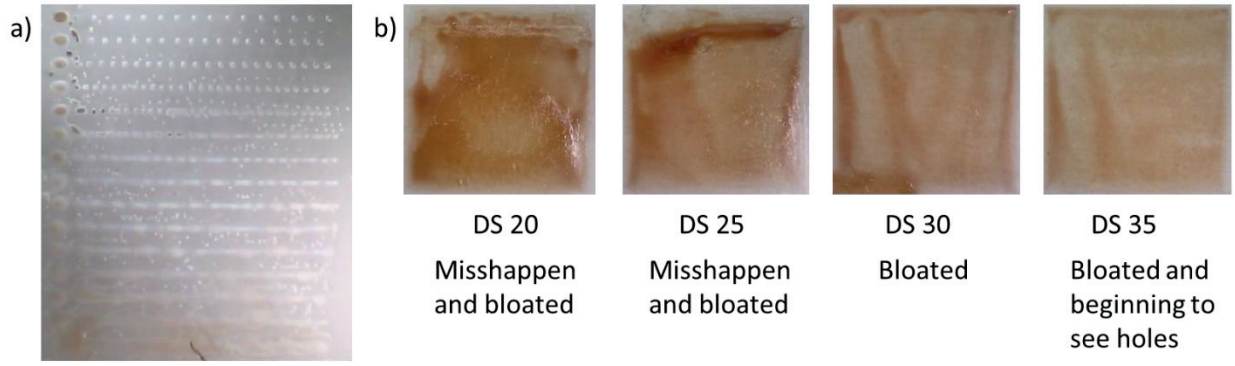

Figure 7.21. Preliminary printing trials of $PdCl_2$ ink where a) line pattern and b) printed squares with DS ranging from 20 - 35 µm

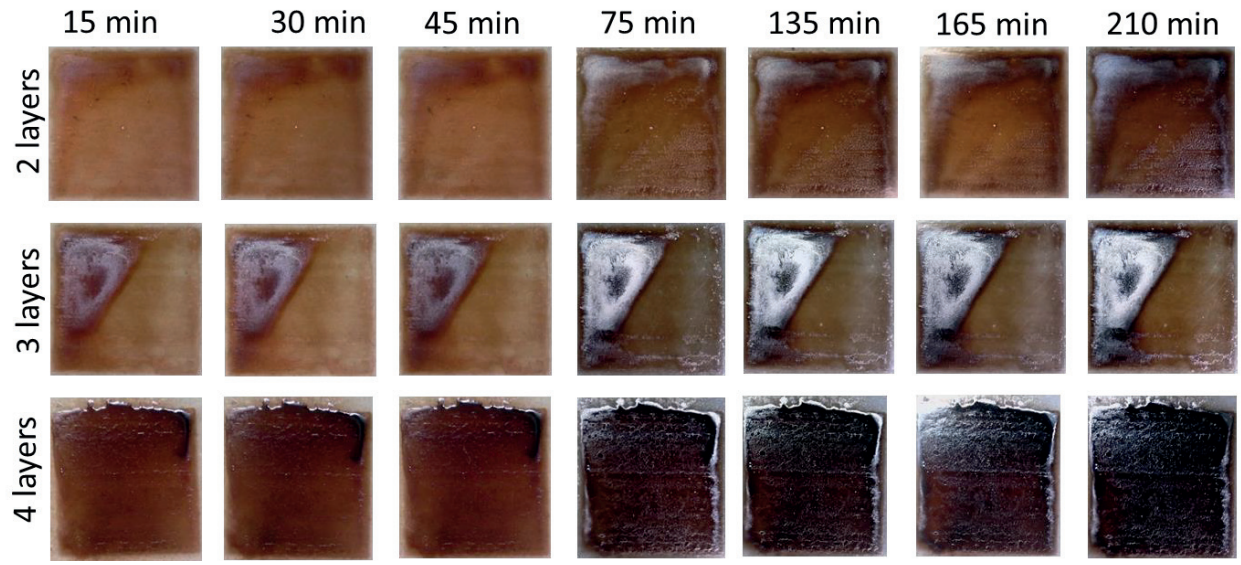

Figure 7.22. Heat treated $PdCl_2$ ink squares for 2 - 4 layers

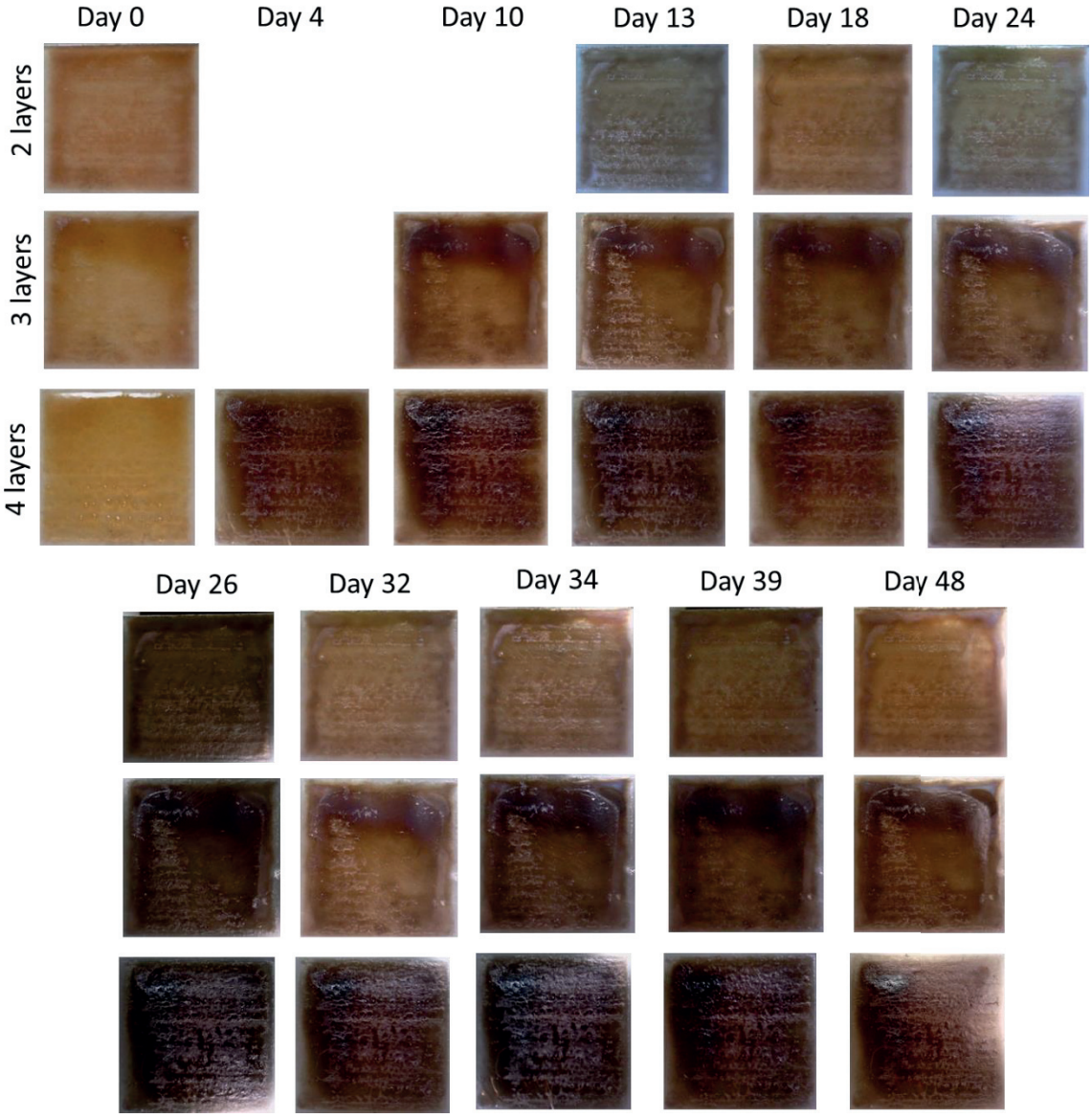

Figure 7.23. Self sintered PdCl2 ink on PVA for 2 - 4 layers

PVA reduction of Pt film was conducted using two strategies as these shown with the $PdCl_2$ ink, that is monitoring by 1) self-sintering under ambient conditions or by 2) heat treat limited at 80°C and then left to develop at RT. Film growth under solely ambient conditions was tracked for approximately 100 days as seen in Figure 7.24. By day 5, milky white areas were seen indicating that the film was completely dried where 3 layer films spread outside of the initially defined patterns signaling that this amount of layers was inappropriate for define shapes. Although not much change was seen with 1 ink layer, the center portion of the 3 layer sample darkened to a dark yellow color by Day 7. These films only continued to slowly darken however

there was no further growth involved nor appearance of a silver color. From Day 56, the film remained the same and was tracked up until Day 103. Also by this time, the 1 layer squares see some slight development of a brown layer, however this was very faint as all printed squares continued to remain transparent. The second strategy was conducted with accelerated heat treatment at an interval of 30 minutes and imaged according to any changes seen as shown in Figure 7.25. After 60 minutes of heat treatment, 1 film layer only showed a mild reaction with PVA while 2 and 3 layers displayed varying levels of dark brown color as expected of which 3 layers displayed the quickest reaction showing the opaquest layer. Unfortunately, past this stage, there was no further change in appearance of the film even with 270 minutes of heat treatment. 2 layers eventually reached a similar development point at 120 minutes which remained the same after an additional 150 minutes was applied while 1 layer displayed both a darkening of the layer but was more concentrated to the right corner edge of the square which only began to slowly spread to the left side of the sample with additional sintering time a less ink was deposited in that area and therefore needed a longer sintering time. The edges themselves were slower to convert than the interior, however this color was not maintained as the next day as a medium brown color appeared in their place which continued to become more transparent with time. A plausible explanation for this phenomenon is the possible development of HCl (1 part of Aqua regia) which can act as an etchant further impeding the Pt film growth. For this reason alone, it was once again confirmed that a Pt film could not be developed using PVA as a substrate.

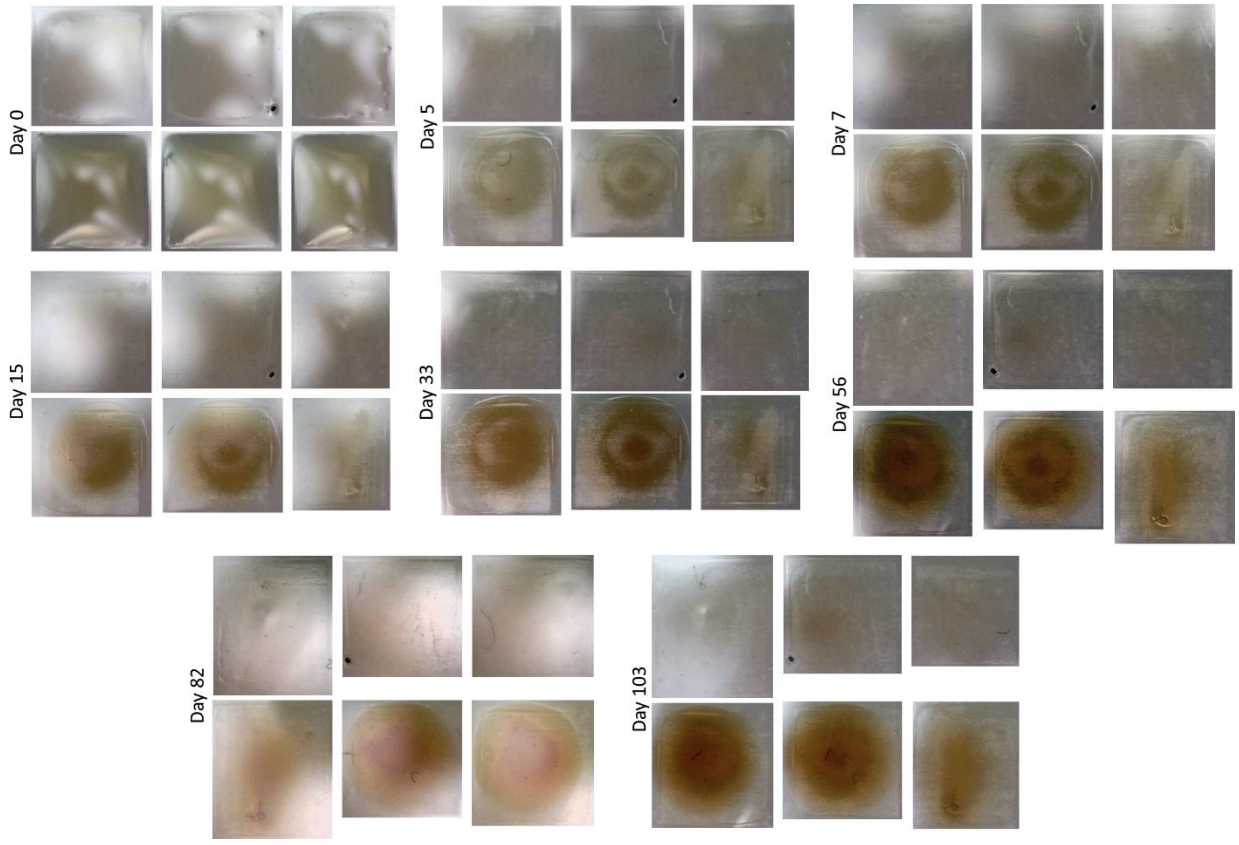

Figure 7.24. RT sintering of Pt ink on PVA for 1 and 2 layers

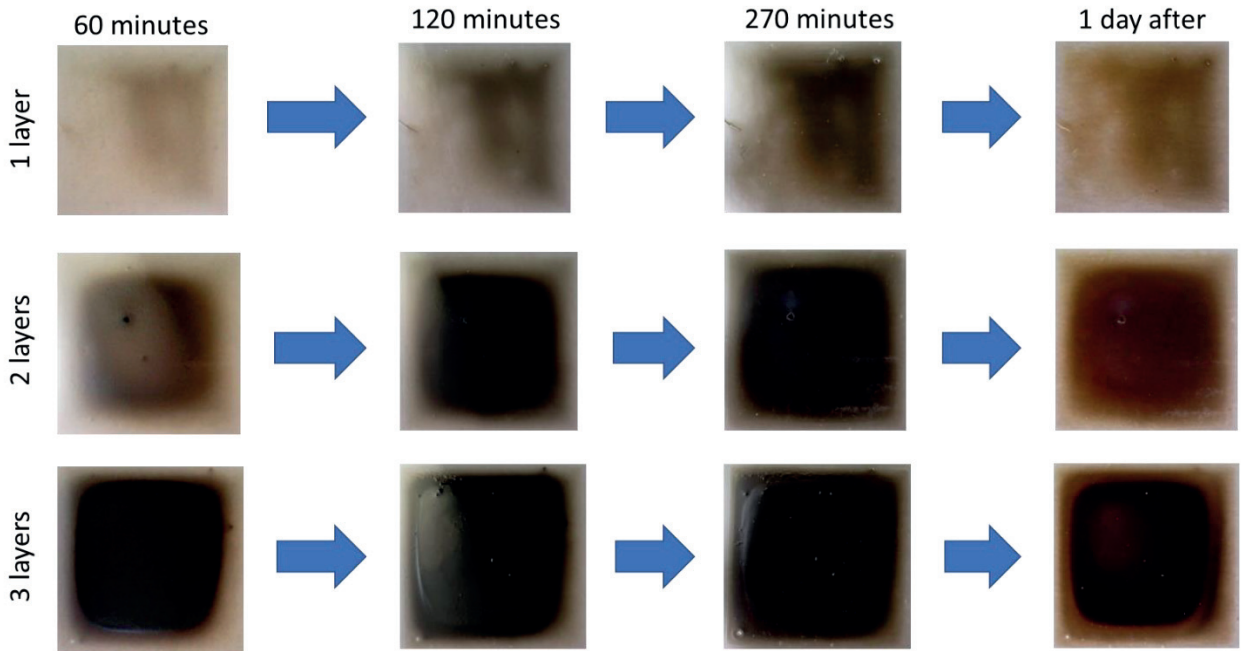

Figure 7.25. Results of thermal sintered Pt ink on PVA substrate for multiple layers

The same $CuSO_4$ ink previously reported in Chapter 6 was also deposited on PVA substrate starting with the line pattern as shown in Figure 7.26a. Although the line pattern itself was not optimal for this substrate, the only line formed during the printing was with a DS of 5 µm. This parameter was then used for further printing where 1 and 2 layers was deposited as shown in Figure 7.26b which was tracked and imaged for 100 days. When first printed, the squares were initially well defined however the pattern then shifted to a point where there was a large accumulation of ink more at the middle than at the sides which is typical for MSD inks due to the Marangoni effect. Within 3 days, both layers were dry and showed crystal formation as typically seen with MSD ink displaying neutral ion reduction potential of +0.34V. The interior of the squares appeared to be milky white in reaction to PVA however never formed a continuous nor metallic film. By Day 20, the ink appeared to spread beyond its initial shape but settled by Day 93. Once again, due to the rapid oxidation of this ink, no conductive film was ever formed always remaining transparent.

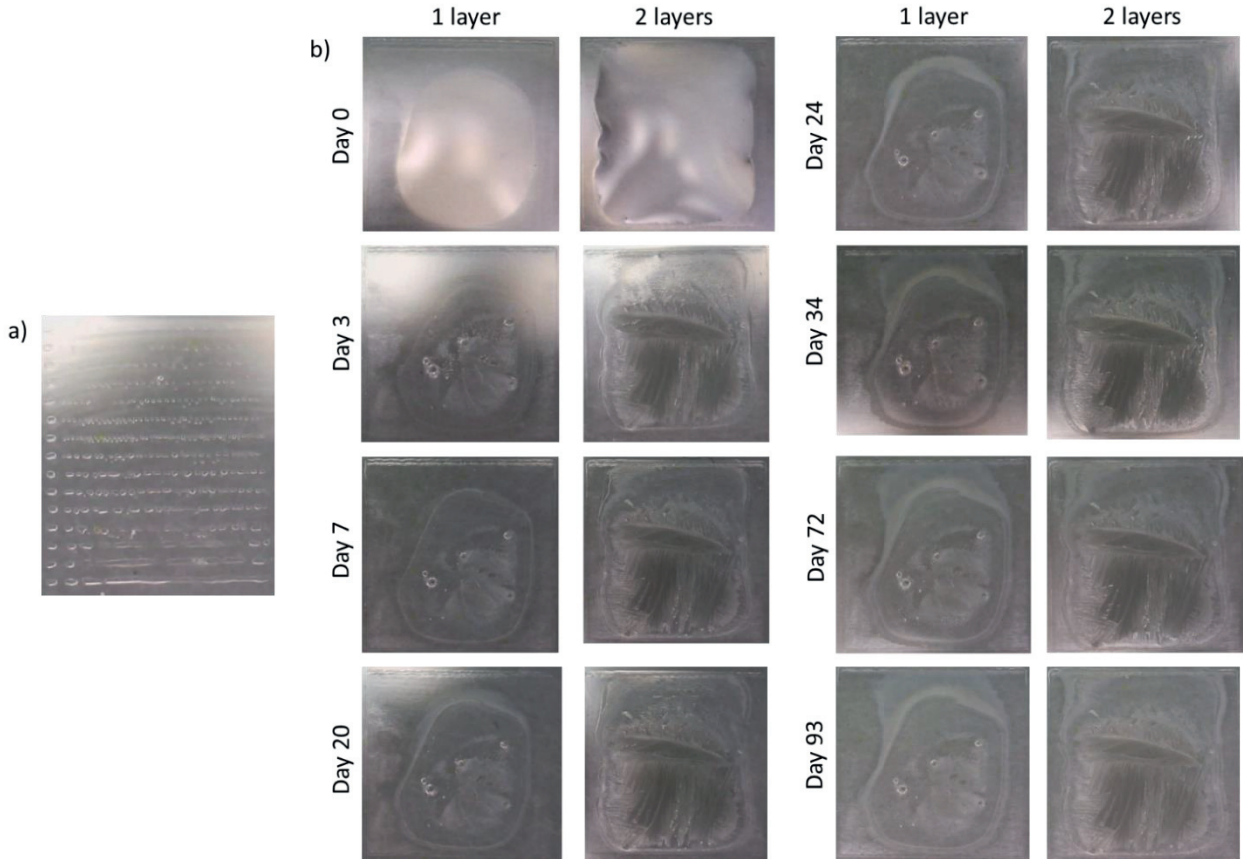

Figure 7.26. $CuSO_4$ ink as deposited on PVA substrate with a) line pattern and b) 1 and 2 deposited layers over 100 days of sintering

A similar result was seen with $SnCl_2$ ink where very little growth was displayed before Day 34 as shown in Figure 7.27a below. As the ink was also initially clear, it was very difficult to note any progress before this time period. Slightly more or wider spread of this milky colored film was seen on Day 47 and 55 but did not show any further progress at the end of 100 days of monitoring. Figure 7.27b reconfirmed the results seen on those left at RT where within 15 minutes heat treatment, a milky white circle appeared as shown below, however and additional 60 minutes saw no further changes. An additional 100 days of tracking was also done after the heat treatment to see if any further development would occur which was not the case. Although no crystallization here appeared, a similar milky outline was developed which indicates some interaction between the salt-based ink and PVA most likely due to the drying and crystallization process. Altogether, the $SnCl_2$ ink also could not be converted with the reduction power of PVA due to a combination of factors including its respective reduction potential at -0.14V.

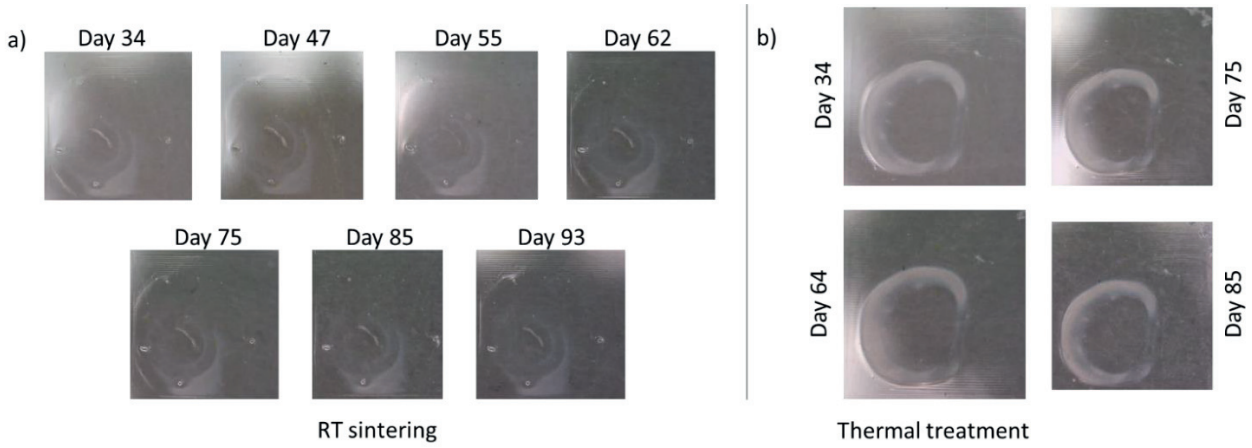

Figure 7.27. $SnCl_2$ ink printed onto PVA and treated at a) RT and tracked up to 100 days and b) saw 80°C heat treatment for 1h and tracked up to 100 days

7.4 | MATERIALS AND ELECTRICAL CHARACTERIZATION

Once the Au film formation was completely optimized, other aspects such as its compositional purity, film thickness, surface roughness, adhesion to PVA, and electrical properties were explored. XRD analysis results can be found below in Figure 7.28 where the deposited Au film was determined to be polycrystalline in nature with peaks at 38.2º, 44.4º, 64.6º, 77.5º corresponding to (111), (200), (220), and (311) reflections respectively. The red dotted lines represent the JCPDS reference card no. 00-004-0784 for synthetic gold matching almost identically with no contamination from any Cl related peaks. These results were agreement to those found in the SEM-EDX with a high Au content however the remnants of chlorine left in the sample can be explained by the analysis volume that can reach up to 3 μm past the Au thin film into the substrate itself.[24]

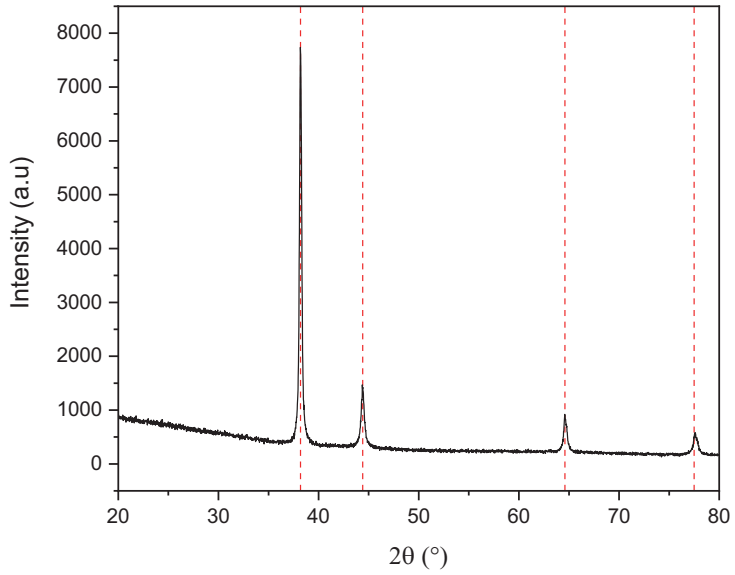

Figure 7.28. XRD analysis for Au film growth on PVA at RT

Both the film thickness and surface roughness were explored by both profilometry and confocal microscopy respectively as shown in Figure 7.29. The use of profilometry (Figure 7.29a) gave a general idea of the surface rastering across the sample (Figure 7.29b) for 1.3 mm showing that there was extreme variation of Au film thickness ranging from approximately 0 to 3.5 µm from the edge towards the middle of the sample. This variation was expected especially when looking at the substrate surface. For this particular measurement, the average thickness was determined to be 1.6 µm. This measurement was then taken to calculate the resulting conductivity for a Au film which saw values up to 1.09 x 10^6 S/m. However, because profilometry results captured with the stylus tip was not able to capture radius larger than 2 mm in length, accurate characterization of the roughness at the microscale level was limited. Therefore, the sample was then further tested with confocal microscopy to obtain a global view. For this, optical confocal microscopy (Figure 7.29c and 7.29d) determined the RMS surface roughness for 1 layer to be 44.4 nm for a scan field of 250 x 200 µm area as analyzed with a 50x objective while 2 layers reported a slighter higher surface roughness value at 56.6 µm for a smaller scan field of 84.9 x 63.6 µm area using a 20x objective. This means that the roughness increases for every deposited layer however it is expected that the surface roughness found with commercial Au NP inks on PET substrates is higher as the NPs are not stacked in this case. Additionally, Au film thickness for 2 layers was obtained from the same measurement and determined to be 268.8 nm. This measurement was in agreement with the average Au NP size determined by SEM analysis which was almost 2 times less than this value. The spikes or peaks encountered during measurement are due to the remnants of salt crystals left on the film surface

(Figure 7.29e) thus contributing to a higher roughness. Unfortunately, due to the water solubility of PVA, the salt could not be removed and remained on the surface without any effect on its respective conductivity.

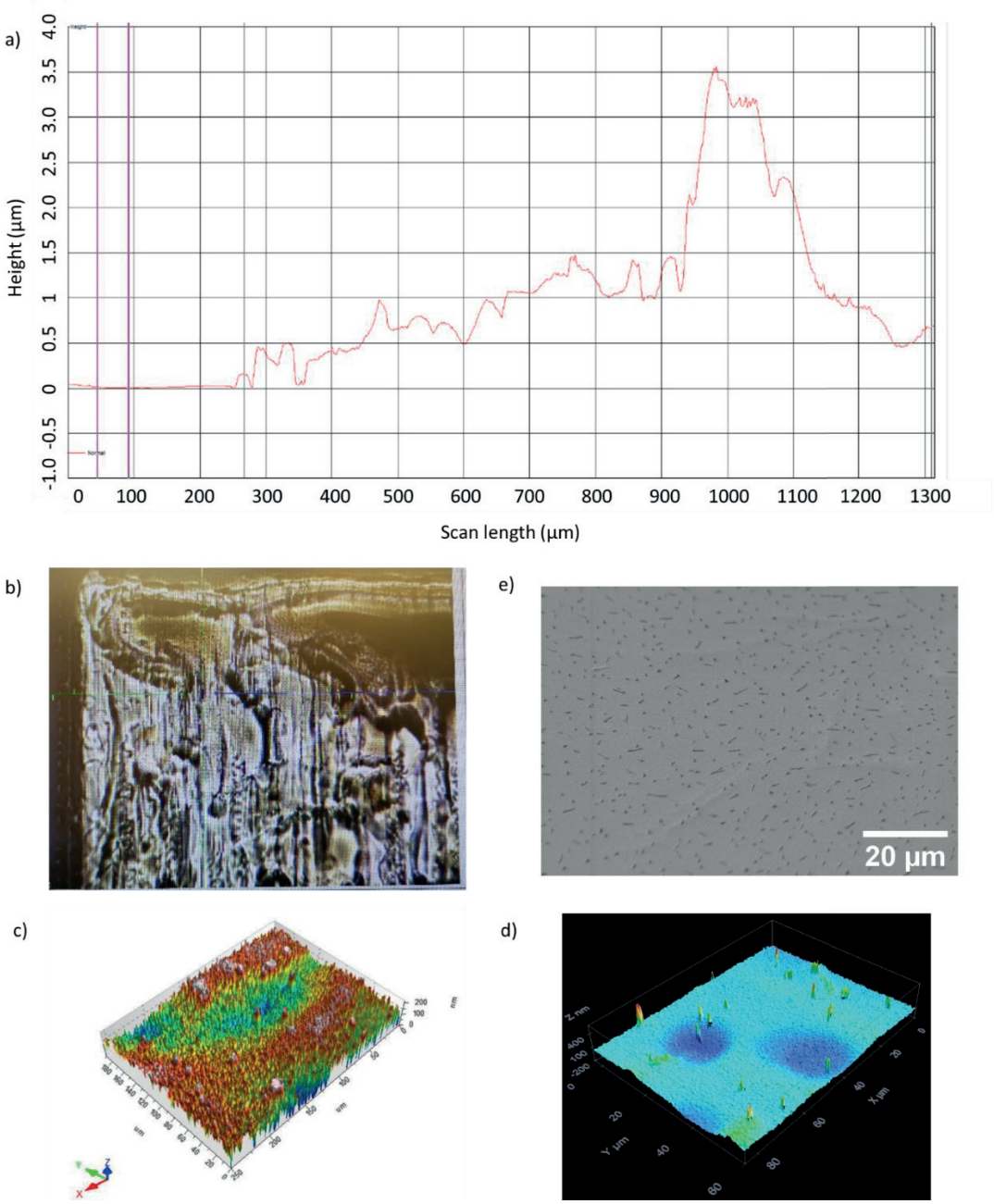

Figure 7.29. Au film thickness and surface roughness measurements conducted by a) profilometry for a 1.3 mm scanning length and surface analysis techniques b) Dimatix fiducial camera and confocal microscopy imaging for c) 1 layer and d) 2 layers, and e) SEM micrograph at 10,000x

One of the key issues plaguing metal thin films deposited onto plastic substrates is poor adhesion. Often times this requires an additional adhesion layer added such as Cr, Ni, of Ti.[15] However, this was not the case for Au films developed on PVA as the film growth process naturally provided excellent adhesive properties which never saw delamination from the film unless placed under prolonged periods under vacuum. Adhesion was assessed using the ASTM D3359 standard by Tape Test Method B.[25] Here a lattice pattern created with a total of 6 parallel cuts (3 vertically and 3 horizontally) were made with a razor blade from the film down to the substrate creating areas of approximately 1 x 1 mm^2 to be removed by a pressure-sensitive tape. Less than initially specified cuts were made as 1) the entire film area was only ~16 mm^2 and 2) film thickness < 50 μm must be cut 1 mm apart. Next, a pressure sensitive translucent tape (3M Scotch Tape No. 811) was placed over the film and attached securely. The tape was then removed swiftly after 120s of application at a 180° angle. Once removed, adhesion was evaluated by comparing against illustrations found in the standard. This test was performed on films that were developed from 2 and 3 printing layers as those with 1 never fully develop. Test results are tabulated below in Figure 7.30a where 2 layers exhibited a 5B Classification as 0% of the cross-cut area was removed while 3 layers was deemed 4B Classification where <5% of the area was removed. The precise areas where the film was removed was noted by the red arrows in Figure 7.30b. Although both films saw good adhesion, 2 layers saw slightly superior adhesion and optimal growth over 3 layers.

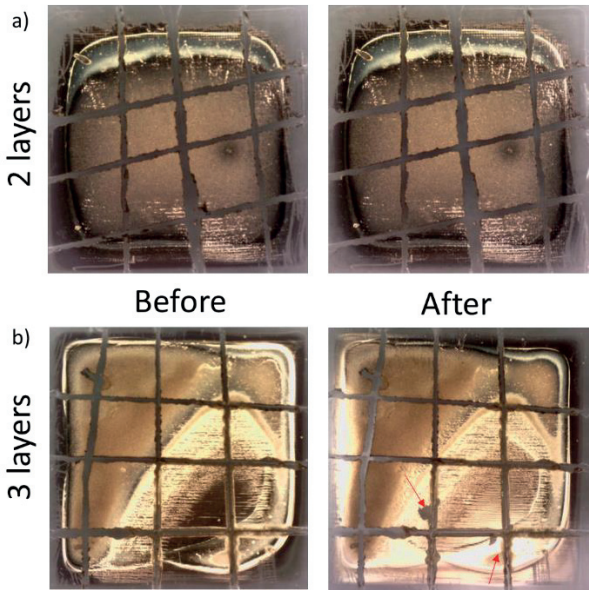

Figure 7.30. Adhesion Test result for a) 2 layers and b) 3 layers before and after removal

Previously, only square patterns were printed mainly to conduct electrical measurements however building more complex structure and patterns requires further optimization of multiple

factors including the line width, length, and spacing of the deposited film on the resulting electrical resistance. Therefore, a study was conducted on the minimum and thus optimal line width and length that can be printed and developed using this technique. Figure 7.31a shows a variety of line lengths (1 – 10 mm) and width (300 – 1000 µm) printed with 2 layers and converted per usual following rapid sintering in an oven at 80°C for 30 minutes. All patterns were printed without incidence and well defined following the heat treatment. As all films appeared to be well developed, its conductivity was tested by resistance measurements and tabulated in Figure 7.31b. As indicated from previous results, the line thickness or width increases proportionally to its resistance seeing difference between the thicknesses up to 91.6%. Similarly, the resistance increases as the line length increases. For example, for 1000 µm thickness, the resistance increases from 0.7Ω to 13.3Ω between 1 mm and 10mm, a 94.7% increase which must be considered when designing structures. Although some outliers were seen with some of the measurements, those with 900 and 1000 µm thickness showed the lowest resistance values across all printed lengths, therefore these thicknesses were favored over others to reduce any parasitic resistance that may arise during testing.

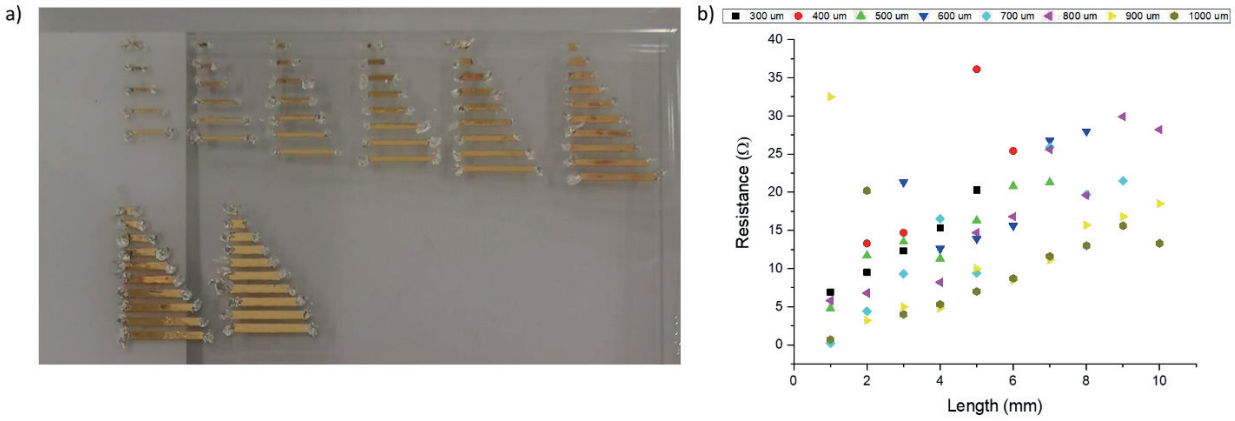

Figure 7.31. Au film development based on a) line length and width and b) their effect on its determining resistance

Lastly, line spacing as shown in Figure 7.32 was also tested for line widths 200 – 500 µm with line spacing between 100 – 550 µm depending on the initial line width. Initially line widths of 200 and 250 µm (Figure 7.32a and 7.32b) were considered which ultimately found to be non-conductive. Unlike NP inks, the addition of multiple layers did not serve to increase the overall conductivity as there is a limitation where the film can both be developed and conductive which is not always apparent just by color. That is a golden color is not always an indicator of a conductive film as it was shown that nanoparticles can agglomerate below the PVA surface as previously shown in Figure 7.19h. This behavior was certainly indictive of those with line pattern widths containing 250 µm and lower which presented a gold color but showed no

conductivity even at different line widths. All lines printed with 100 μm were not shown here as the lines were combined and presented no spacing. As first suspected, both the actual line width and line spacing were larger than initially printed by the ink as the ink tends to spread increasing the line thickness therefore affecting the actual line spacing. The actual line thickness for a 200 μm and 250 μm line were found to be 315.4 μm and 362 μm respectively, meaning there was an 57.7% and 44.8% increase over their original expected values. This increase must be taken into account especially when building patterns as the actual line spacing is at minimum 35.4% larger than expected and as high as 82.3%. As the line spacing increases, the change in the actual line spacing decreases meaning there is a higher probability that the printed lines will not be touching. As a general rule, the line spacing must be at least 50 μm larger than the line width itself to avoid any short circuits as a result. This rule was true only for larger line widths (> 300 μm) as shown in Figure 7.32 but may not always be necessary. For an expected line width of 300 μm, a minimum line spacing of 450 μm was needed as ink spreading for smaller line width is more severe meaning more spacing is needed to compensate as found in Figure 7.32c. Figure 7.32d highlighted that for a line width of 400 μm, at least 400 μm spacing was necessary (compared to the actual distance of 132.3 μm) showing a 67% difference in expect spacing. Those lines with a 500 μm line width required a minimum of 400 μm spacing as spreading was less of an issue for these films as shown in Figure 7.32e. Additionally, if smaller line spacings are needed, a 1 pL or 2.5 pL Samba printhead may be used in this case but for the purposes of this study was not investigated.

a)

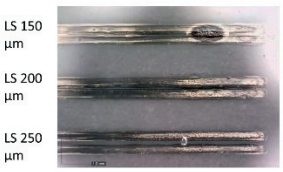

LW 200 = 315.4 µm

Expected line spacing (µm)	Actual line spacing (µm)	Distinct?
100	----	No
150	49	Some areas no
200	74.5	Yes
250	147	Yes

b)

LW 250 = 362 µm

Expected line spacing (µm)	Actual line spacing (µm)	Distinct?
100	----	No
150	50.8	Yes
200	110	Yes
250	132.8	Yes

c)

Expected line spacing (µm)	Actual line spacing (µm)	Distinct?
250	----	No
300	----	No
350	----	No
400	70.7	Yes, barely
450	182.0	Yes
500	248.7	Yes
550	333.0	Yes

d)

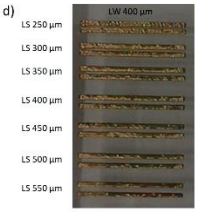

Expected line spacing (µm)	Actual line spacing (µm)	Distinct?
250	----	No
300	----	No
350	----	No
400	132.3	Yes
450	164.7	Yes
500	249.7	Yes
550	355.3	Yes

e)

Expected line spacing (µm)	Actual line spacing (µm)	Distinct?
250	----	No
300	----	No
350	----	No
400	134.0	Yes
450	219.7	Yes
500	221.3	Yes
550	355	Yes

Figure 7.32. Line spacing study ranging from line widths of a) 200 µm, b) 250 µm, c) 300 µm, d) 400 µm, and e) 500 µm

7.5 | POTENTIAL APPLICATIONS

Because excellent conductivity was displayed with such films, a wide range of prospective applications were considered including electrodes, strain gauge sensors, antennas, and transistors, each with their own specific requirements. The next section will review the thought and design process as well as the results for each of these applications. Here, multiple designs were fabricated and tested but unfortunately were unable to be fully optimization due to the lack of time. Therefore, future improvements will also be addressed at the end of each subsection.

7.5.1 | ELECTRODE STRAIN CHARACTERIZATION

Initially, strain sensors were deposited on a bilayer of PVA/PET substrates that were used for mechanical stability as precise control of the PVA substrate thickness was necessary to reproducibly develop Au films. A myriad of samples were developed including those with 1 and 2 printed layers, both of which developed equally following oven sintering as seen in Figure 7.33a below. The electrodes were built similarly to dog bone specimens, first presented in Chapter 6, where the square pads on each side are 4 x 4 mm with a gauge length of 11.4 mm and width of 1.5 mm. All 2 printed layer electrodes exhibited excellent definition and uniform Au film growth as evidenced by Figure 7.33b focusing on the electrode pad and necking area,

however this was not always the case for 1 printed layer as it consistently showed uneven growth. Regardless, both types of samples were tested under a wide range of tensile strains using a customized piece of 5 mm thick acrylic sheets that could fix the bent substrate over a defined radius facilitating consistent and reliable electrical characterization as seen in Figure 7.33c. This was important as extreme bending radii of < 1 mm were used and not achievable without the use of an external device. The bilayered PVA/PET substrate saw a thickness of 129 μm, a property that was taken into account when calculating the applied strain. Here, testing was conducted at 0%, 0.13%, 0.65%, and 1.3% tensile strain derived from bending radii of 0 mm, 50 mm, 10 mm, and 5 mm respectively as shown in Figure 7.33d below. The average resistance for 1 and 2 layer is 48.8 ± 12.7 μm and 17.6 ± 2.9 μm respectively where unfortunately, 75% of the samples containing just 1 layer broke after being subjected to a tensile strain of 1%. Partial reason for this may be due to the ultrathin and underdeveloped Au films that once the connections between NPs were severed could not be recuperated. As a consequence, testing continued onto all samples with 2 layers which were able to handle testing with and without the underlying PET substrate. As expected, the change in resistance steadily increased with increasing strain seeing a peak value at ~ 0.04. However, at 1.3% strain, the error in the measurement was equal to the change in resistance value showing high inaccuracy beyond strains of 0.65%. This behavior more or less mimicked those seen by semiconductor strain gauges where the strain regime was limited to < 0.6%.[26] Greater values of strain could not be tested using this substrate because the bending radius was physically unachievable, the strain sensor was removed from the PET substrate and tested solely on the PVA foil. As the substrate was only 4 μm in thickness, a wider range of strains were able to be tested starting at 0%, 0.1%, 0.5%, 1%, and 3.2% corresponding to a bending radius of 0 mm, 0.4 mm, 0.2 mm, and 0.06 mm respectively. Initially, the change in resistance grew exponentially between 0% and 0.1% strain seeing a change of 0.06. It is believed here that crack formation grew directly affecting its conductivity however with greater applied strain, began to stabilize showing the highest value at 0.13. This showed that the change in resistance was not found to be linear but displayed more of a monotonic growth where eventually a plateau in the strain value was reached. The change in resistance between 1% and 3.2% was minimal signifying that it would be difficult to differentiate any strains beyond 1% making the sensor less reliable at higher strains. A quicker plateau in terms of average strain measurements was seen here mostly due to the smaller substrate thickness, a behavior that was in agreement with a model previously reported by Yang et al.[26]

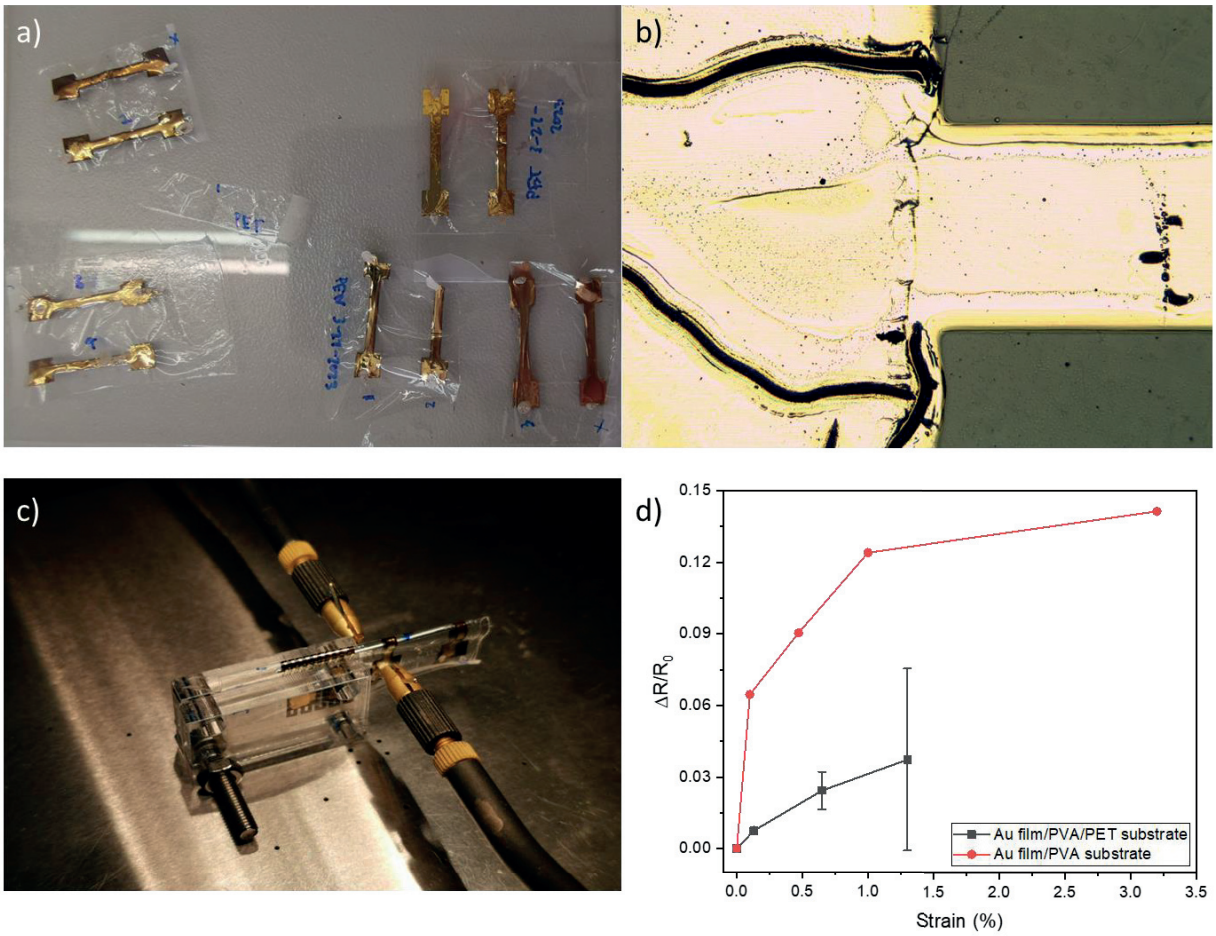

Figure 7.33. Printed and reduced electrodes a) fabricated on PVA substrate, b) optical image taken at 20x magnification of the electrode pad, c) tensile strain test setup, and d) electrode tensile strain testing comparing Au film on PVA/PET vs Au film on PVA directly

Although initially planned, stretchability was not executed here as it was discovered that the stretchability of PVA was extremely poor even at miniscule thicknesses and would completely tear instead of stretch. In the future, stretchability can be better tested using a combination of this ink coupled with plasma sintering onto well-known bendable substrates such as Thermoplastic Polyurethane (TPU).

7.5.2 | DEVELOPMENT AND CHARACTERIZATION OF A STRAIN GAUGE SENSOR

Multiple designs were considered from the standard linear strain gauge design to the more complicated serpentine gauges optimized for stretchability. Due to the excessive length of the

latter and the known dimensional length limitations, this was eventually eliminated from testing. Therefore 2 linear strain gauges with differing dimensions were printed, reduced, and tested as shown below in Figure 7.34. The first design consisted of 3 turns (Figure 7.34a and 7.34c) with an active grid length (gauge length) and width of 13.5 and 6.8 mm respectively. The wire length or line thickness here was defined as 500 µm and was attached to 3 x 3 mm solder pads. Additionally, a 5-turn design (Figure 7.34b and 7.34d) was also fabricated with the same line thickness however the active grid area was slightly bigger at 13.5 x 8.0 mm for the length and width respectively. Here the solder pads were larger in size (4 x 4 mm) to accommodate for large wire attachments. Figure 7.34e emphasized the well-developed end loops of the 5-turn (T5) strain sensor where the line separation was sufficient to prevent any cross connections between the wires verifying the optimal strain sensor design for this ink and substrate.

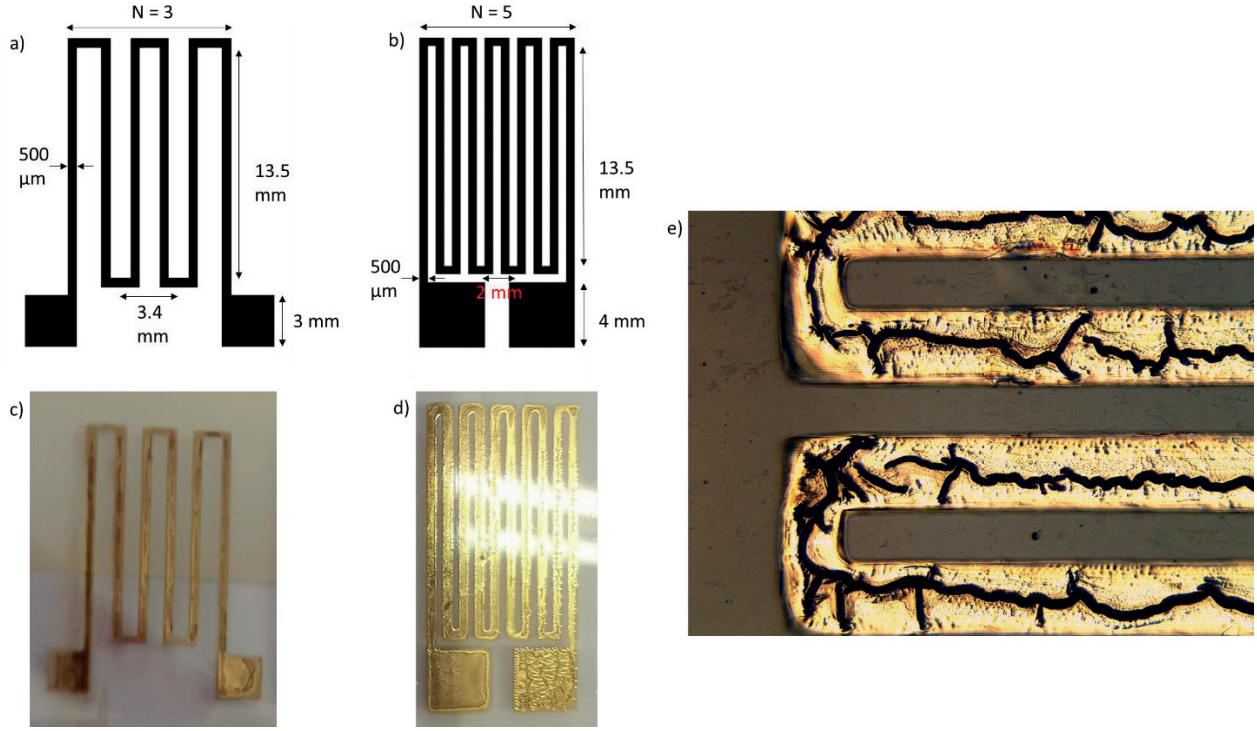

Figure 7.34. Au NP film strain gauge a) design for 3 turn sensor and dimensions, b) design for 5 turn sensor, photographs of c) the printed 3 turn sensor and d) 5 turn sensor, e) enhanced view of the curvature at 50x magnification

Similarly to the Au electrodes, the T5 strain sensor was subjected to strain testing dependent on their respective film thickness. As the strain sensors were also initially deposited onto mechanically stable PET substrate, bend testing was conducted at 0%, 0.13%, 0.65%, and 1.3% tensile strain as shown in Figure 7.35a below. Similar to those results found with the electrodes tested in the previous section, an increase in the change of resistance was found after being

subjected to greater amounts of strain. A 70% increase in the change in resistance was seen between the 0.13% and 0.65% strain indicating standard crack formation from this point. However, past a strain of 0.65%, the resistance dropped back down to those found during the initial stages of testing at 0.1% strain. This once again indicates the variability of this sensor as previously noted at 0.6% strain. A common factor used to determine the sensitivity of a strain gauge is characterized by the gauge factor (GF) as defined in Equation 7.6 below:

$$GF = \frac{\Delta R}{R_0} \times \frac{1}{\varepsilon} \tag{7.6}$$

where ΔR is resistance change under the applied strain, R_0 is the resistance at 0% strain, and ε is the applied strain. The same data logged in Figure 7.35a was used to calculate their respective GF which was found to be severely different especially when taking substrate thickness into consideration. For reference, a linear metal based strain gauge sees a GF around 2 however those produced with NP inks based on different printing methods can see up to 100 or more, reaching those made with semiconductor materials.[27,28] A GF of 1.73 at a 0.1% strain was achieved on the PVA/PET substrate which grew as high as 65 at a 0.1% strain when tested only the PVA substrate. When tested beyond this value, the GF saw a dramatic decrease symbolizing that the use of such strain sensors was not permittable above this strain. In fact, similar strain sensors published in literature were mostly tested using microstrains which was not done here.[27,29] However the difference found between the GFs when just removing the PVA-based strain sensor from the PET substrate meant that the sensor itself was highly substrate dependent as previously reported. In general, the high sensitivity achieved here is due to the exponential dependency of the tunnel resistance on the Au NP interspacing.[27] However other factors must be taken into account including the substrate thickness as well as the stiffness of the substrate material which is represented by its Young's Modulus (E_s) of which were experimentally found to be 2.55 – 2.79 GPa[30] and 707.9 MPa[31] for PET and PVA respectively. Finite elemental modelling (FEM) was conducted by Yang et al. which looked specifically into these variables albeit independently which could not be directly done in our case as their respective material properties could not be separated from one another. When the substrate thickness increased from 20 to 200 μm, the calculated GF increased by 12% when considering constant length and E_s. Similarly, simulations run for a constant length and substrate thickness saw that those substrates containing a greater E_s also saw orders of magnitude difference in GF. Unfortunately, these results did not correspond with what was reported in literature meaning that redesign and testing is still needed to fully understand and characterize the behavior seen here.

Although already indicated by the behavior seen previously, cyclical tensile testing was enforced on a T5 strain sensor on a PVA substrate for 370 cycles as shown in Figure 7.35b. Here, testing was conducted at neutral and bent states respectively using 1% tensile strain which creates a noisy profile. Within the first 10 cycles (inset), large variations were seen ranging from 0 – 0.06, similar to those first seen between 0 and 0.1% strain, however still maintained its initial resistance throughout. Unfortunately, with further testing, the change in resistance began to increase linearly by cycle 50 and never recovered. It is supposed that the extreme bending exhibited here caused large cracks to form that with further testing continued to worsen showing a maximum of 0.13. We would like to remind the reader that the extreme cyclical bend testing seen here is significantly beyond any typical strain sensor applications and normal body curvatures, the finger being amongst the smallest of the body parts which reaches an average of 20.3 ± 2.4 mm[32] or only 0.01% tensile strain for a 4 μm thick PVA substrate. Therefore, these results were considered good in terms of stability. Lastly, the strain sensor exhibited good adhesion due to the thin PVA foil with a 4 μm thickness without the need for any gel or external adhesive. This sensor was tested on multiple areas but excelled mostly at surfaces with extreme geometries such as the finger (Figure 7.35c) so much so that the PVA foil mimicked the texture of the human skin thus displaying its potential to be used as a wearable device.

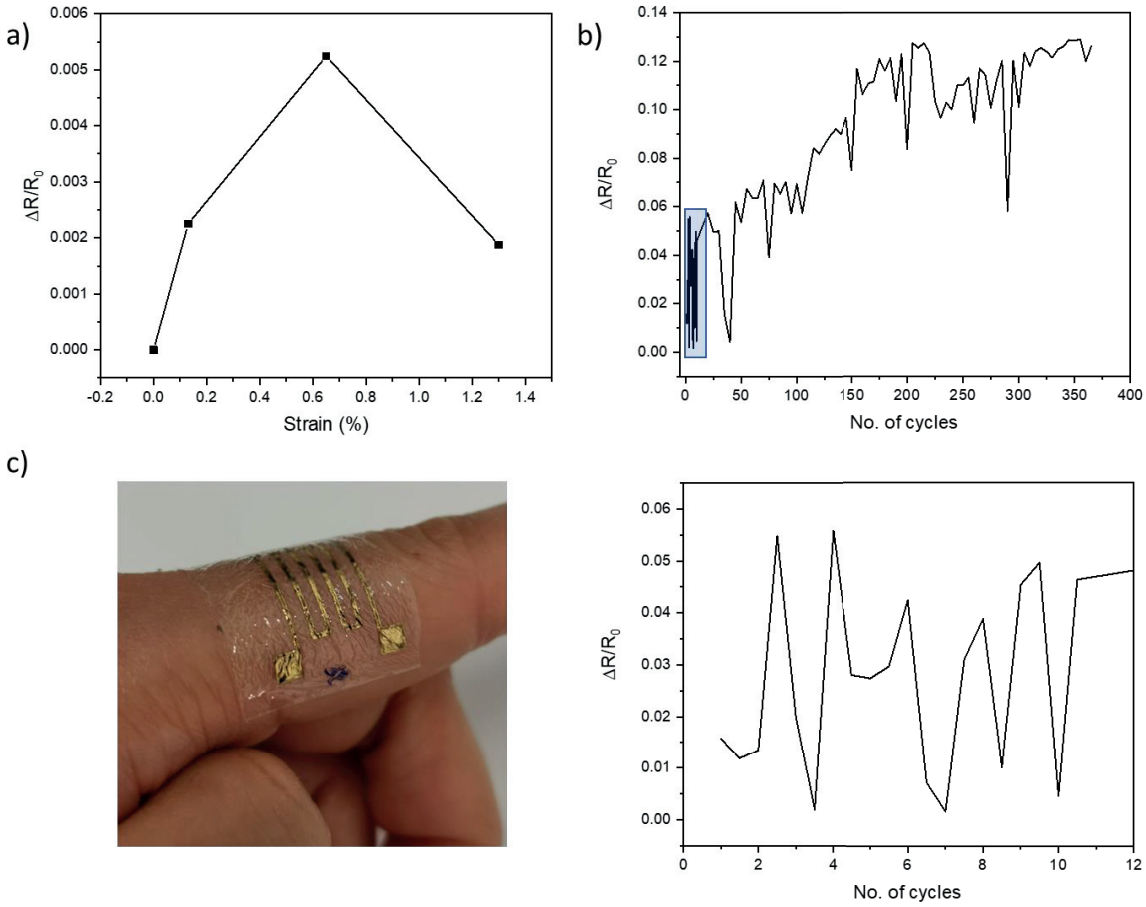

Figure 7.35. Strain gauge testing on a) Au films printed on PET and PVA substrates with respect to change in resistance, b) cyclical tensile strain testing at 1% strain up to 370 cycles, and c) sensor on a finger

Both sensors with different number of turns displayed similar resistances averaging 280.3 ± 11.2 Ω. T5 sensor was tested for its response to touch to determine its viability as a tactile sensor. Here, the strain sensor initially began with a resistance of 288.08 Ω and concluded with a slightly higher resistance of 288.17 Ω after being subjected to different types of touch including light, medium, and heavy using the index finger (Figure 7.36a). The heavier and thus more compressed the sensor became, the greater the corresponding peak. Unfortunately, testing was not conducted with weights meaning that proper calibration was not done. After some resting time, the same sensor returned to its initial resistance and was therefore investigated in terms of its recovery time corresponding to different types of touch in Figure 7.36b. The lightest touch exhibited a small spike however required a recovery time of 7.4s while the next lightest requires more than double that time at approximately 16s. A similar behavior was exhibited with the medium and heavy touches at 42.3 s and 91.6 s respectively, more than twice as much time. In general, this

meant that the heavier and longer the touching period, the longer the recovery time was needed. The excessively long recovery time signified that this particular design was not optimal for real life continuous monitoring however did show a linear response as expected. Similar tests were accomplished with the 3-turn (T3) strain sensor which appeared to have greater sensitivity in terms of touch and faster response time. Here initially, the sensor reported a resistance of 270 Ω and ended almost 5 times higher at ~ 1 kΩ with a single touch (Figure 7.36c). Recovery time occurred in < 1 s, almost in complete contrast to the T5 sensor. Therefore, the T3 strain gauge design overall was superior in all aspects and thus was used for further testing for wearable applications.

Another potential application for such sensors is as an optical sensor that measures intensity change or light beam reflectance that is converted into a change in electrical signal. Although not fully studied for its viability due to lack of time, each fabricated strain gauge responded to variations in light. The results can be found below in Figure 7.36d where solely a hand was used to cover the sensor from ambient light used in the laboratory. Each spike seen here represents the exponential increase seen when creating a shadow on the sensor however once removed, the resistance can be recovered to a point after a long recovery time (> 25 s). Next, an even greater peak was created by placing a hand directly above the sensor seeing the same behavior as previously noted followed by the same movement again for a 3rd peak. It was clear that the recovery time here was particularly slow but after a resting time of 10 minutes before the next test, the original resistance value fully recovered. Initially, as Au NPs are known to have plasmonic resonance and have been used in a wide range of optical applications, it was first thought that this sensor could potentially be used for a similar purpose. However, these results could not be reproduced signifying that the sensor itself was not reacting to light nor indicated proximity. In fact, what was really occurring here was the response to temperature or heat caused by the proximately of the hand to the sensor thus causing the spike. Therefore, temperature compensation for these strain sensors must first be accomplished in order to obtain an accurate reading, as they are considered thermal error in the output. Here, the liner expansion coefficient of the material must be taken into account as a change in temperature itself or thermal effects can elongate or contract the sensor thus inducing thermal strain.[33] There are different ways to compensate for this temperature variation which can be done either physically with a temperature compensated strain gauge or Wheatstone bridge or theoretically through calculation of the thermal expansion coefficient for the sensor which should be minimized as much as possible ~ 10^{-6} strain/°C meeting manufacturing standards.[33] In this case, temperature compensation methods are necessary however due to lack of time during experimentation, no compensation could be accomplished showing that the results reported here include thermal variation effects.

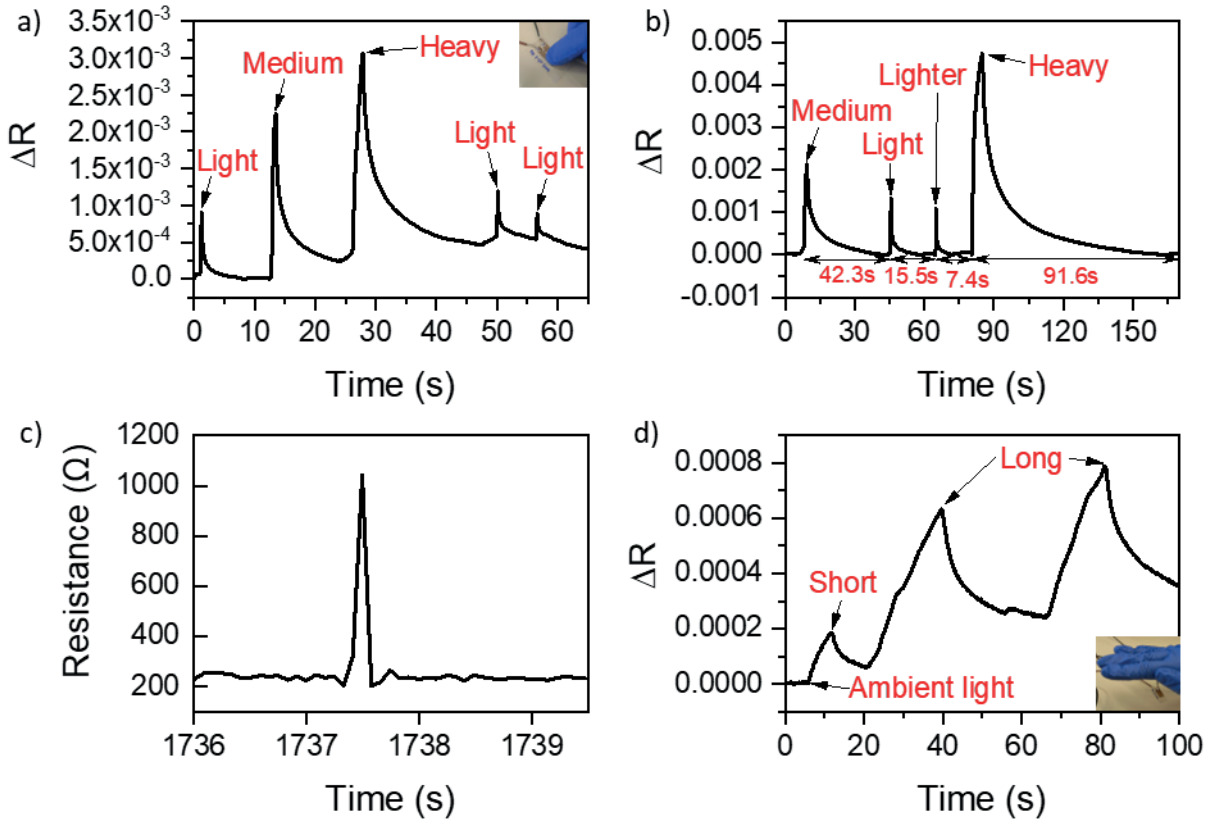

Figure 7.36. Strain gauge as a tactile sensor a) response of 5 turn (T5) sensor showing sensitivity to different types of touch and b) touch recovery test, c) response of a 3 turn (T3) sensor to light touch, and d) optical response of a 5 turn (T5) sensor

7.5.2.1 | *DISSOLUTION TESTING*

Instantaneously dissolution of the PVA substrate occurred within seconds as shown below in Figure 7.37a due to its known sensitivity to water. Fewer than a couple of droplets of water are enough to destroy the sensor with which the Au film can easily still be handled following its dissolution. After 5 days in water, the developed Au film tracks remain however without the PVA substrate backing it lost its original coil shape in the process as shown in Figure 7.37b. Surprisingly, the tracks as well as the contact pads remain connected together which then can easily be recycled. However, the water itself became contaminated with non-sintered Au NPs as some NPs immobilized in PVA film were released. Such testing truly revealed that all devices made using this technique could be easily degraded simply with water and recycled for reuse if desired. Additionally, if the release of the Au foil was better controlled, there is a potential for water assisted transfer printing onto any target substrate.

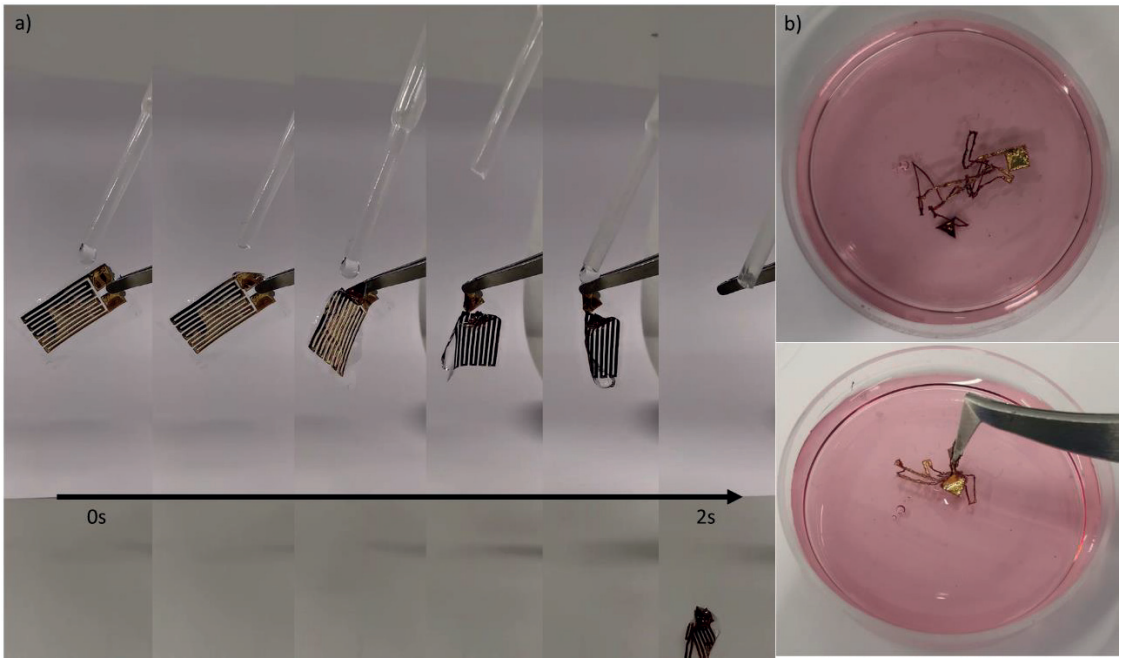

Figure 7.37. Dissolution test of strain sensors by a) water droplets within 2 seconds and b) by immersion in water after 5 days

7.5.3 | DEVELOPMENT OF AN ANTENNA

Amongst other applications, printed radio frequency identification (RFID) tags have also been demonstrated. Although, this specifically pertains to high frequency (HF) antennas[34,35], HF RFID tags must operate with induction and thus, require a highly conductive coil (quality (Q) factor > 40) to achieve the best range. Unfortunately, the limiting factor here is often the high resistivity of printed conductive inks. In fact, several printing techniques were employed to reduce this effect as reported by Pudas exhibiting varied results.[36] Of these, the highest reported Q factor has been demonstrated by Mujal et al. using inkjet printing.[37] Even though inkjet printed shows less than ideal results, this can be offset by the significantly lower manufacturing costs. Thus, the goal of this work was to study the potential of inkjet printing to fabricate HF RFID antennas, specifically exploiting the highly conductive Au NP films produced from Au MSD inks.

Multiple designs were considered from a basic L-shaped design (2.4 GHz Industrial Scientific Medical ISM band) to a typical coil design (13.56 MHz) shown in Figure 7.38 below. In particular, the complex coil design was first considered where Figures 7.38a and 7.38b displayed antennas with a symmetrical spiral design containing 6 and 3 turns with a line separation (turn spacing) of 500 and 2800 μm and wire thickness of 600 and 4000 μm respectively. The 6-turn (referred to as C6) has an inner and outer diameter of approximately 23

mm and 7 mm respectively while the 3-turn (referred to as C3) is 46.6 mm and 19.8 mm for the inner and outer diameter respectively. Additionally, Figure 7.38c depicted an L-shaped design antenna with an approximate length of 19 mm containing a 1000 µm thickness was explored as shown in Figure 7.38c. All antennas were successfully printed and converted as displayed in Figures 7.38d - 7.38f below.

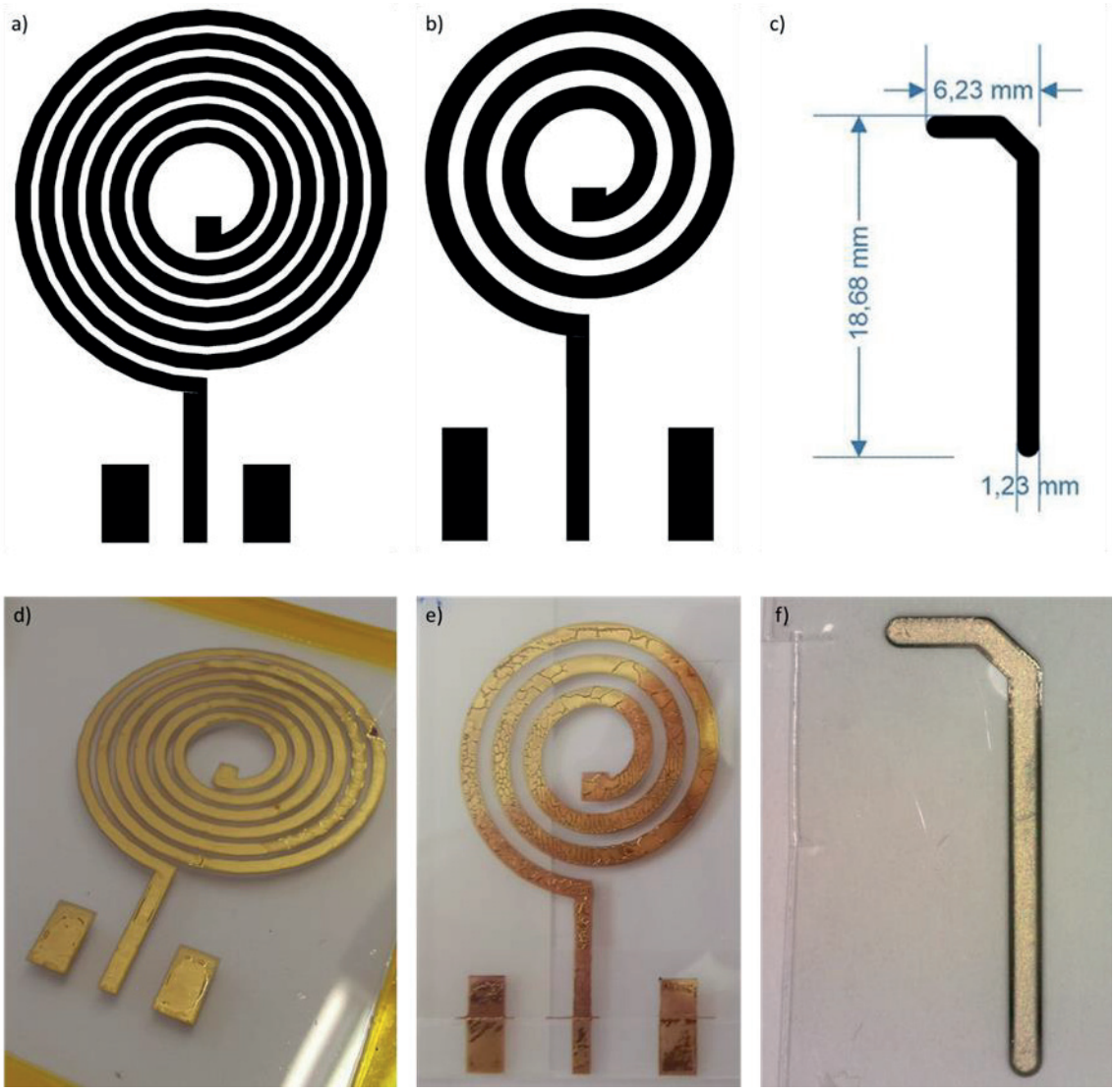

Figure 7.38. Antenna designs with different shapes with a) 6 turns and b) 3 turns, and c) L-shape. Actual printed and reduced antennas onto PVA substrates with d) 6 turns, e) 3 turns, and f) L-shape.

At first, C6 antennas were printed and converted with some success as shown below in Figure 7.39a. Although both antennas here were produced under the same deposition and sintering conditions, it was believed that the printing of the first pattern was inconsistent leading to connected parts between the coils and underdevelopment in some regions along the coil as the

ink to substrate ratio was imprecise however the second pattern was converted as expected. Although the second coil appeared to be ideal in appearance as well as in its electrical resistance, a second sintering performed at 80°C for 3 hours used to adhere a wire connecting the inner and external pads entirely changed the antenna morphology and properties to the point where the once Au film areas appeared brown in color and was no longer conductive (Figure 7.39b). This became a reoccurring issue that is due to the incomplete conversion process just below the Au film. If left for a longer period, the initial wire thickness would spread past the boundaries and eventually connect to the neighboring wire as highlighted in Figure 7.39c. This continuous growth was never considered before as it was believed that the Au film growth was assumed to be the peak of the process. Unfortunately, due to the length of the C6 antenna, the large resistance prevented antenna functionality from acquiring a good quality factor (Q). Therefore, the functionality of the antenna, resulting in a resistor-like behavior. Therefore, the antenna was too highly resistive to function. This meant that the coil design needed to be adapted to the limitations of the ink by reducing the number of turns to 3 with a line separation of 2800 µm. This larger separation between lines was done to prevent any crossover or connection between adjacent lines. Unfortunately, the same issue reported previously occurred rendering the pattern non-conductive. Therefore, more testing must be done to optimize the entire fabrication process to avoid any effects from delayed conversion by either depositing ink with less layers and adjust for the imminent growth following a second sintering step.

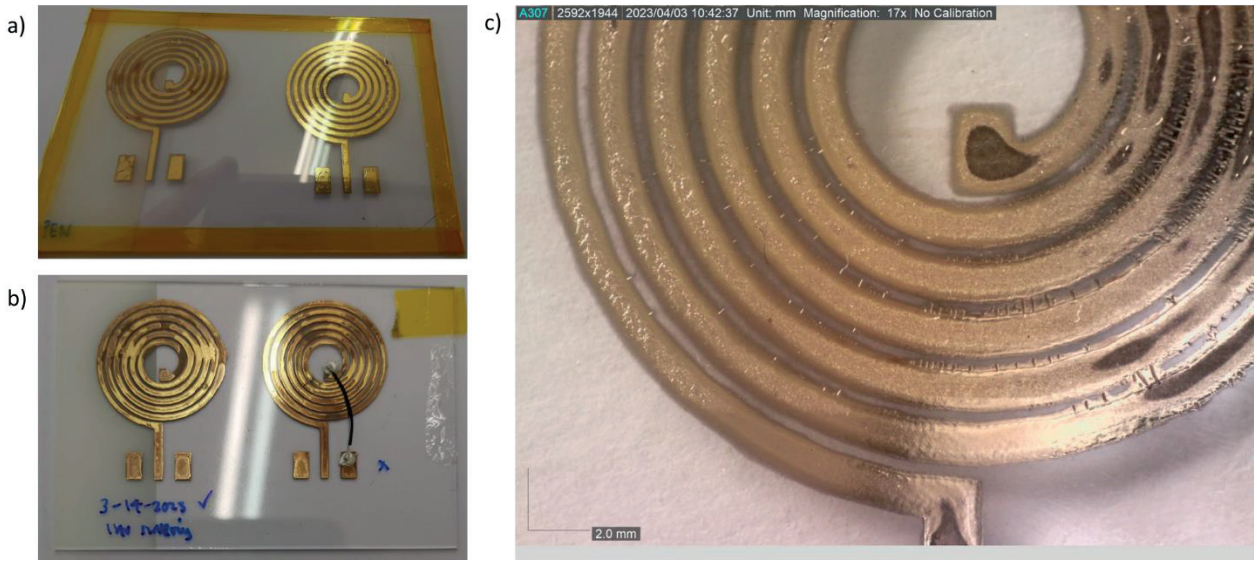

Figure 7.39. Printed and converted 6 turn antennas a) after oven sintering b) following additional sintering to adhere a wire to the pattern via silver epoxy, and c) disappearance of line separation between the coils

A typical measure of the antenna performance is represented through the Q factor. This a parameter indicates the quality of an inductor through how many times the current can pass through the circuit before the energy is radiated.[38] Coils easily pass direct current but act as a

resistor to alternating current. This behavior is called inductive reactance. The higher the frequency of the alternating current, the higher the inductive reactance. However, although the coil is a conductor, the wire winding has certain resistance components ®. The ratio between the resistance components and the frequency-dependent inductance ($R/2\pi fL$) is called the loss factor, and its inverse number is the Q value as shown below in Equation 7.7 where L is the inductance. Because f is the frequency of the current flowing through the coil, the Q value will differ according to the frequency. In simple terms, a higher Q value means lower losses and better suitability for use as a high frequency inductor.

$$Q = 2\pi fL/R \tag{7.7}$$

Taking into account the inductance of the C6 antenna (L = 1.701 μH), the measured resistance (R = 165.16 Ω) and the frequency (13.56 MHz), the resulting Q factor is 0.87. By comparison, an industrial HF antenna integrated in NFC systems usually has a Q factor higher than 40. They are fabricated with laminated copper with a thickness of 18 or 25 um on top of fiberglass-reinforced epoxy-laminated sheet (FR4) substrates. Because the conductivity of printed conductive inks is lower than copper, the quality factor obtained was too low for its suitability.

Therefore, a simpler L-shaped antenna for 2.4 GHz ISM RF systems was also considered as previously shown in Figure 7.38f. These antennas were experimentally compared to a commercial UHF system for their respective operation ranges. RF characterization test bench was used consisting of two Nordic Bluetooth Low energy (BLE5) Development Kits (nFR52 DK) to measure the (Received Signal Strength Indicator) RSSI signal. RSSI was measured by using the integrated PC antenna on the Design Kit and replacing the same by our printed antennas. The RSSI is a measurement of the power present in a received radio signal. In an IEEE 802.11 system, RSSI is the relative received signal strength in a wireless environment, in arbitrary units. Therefore, it is an indication of the power level being received by the receiving radio after the antenna and possible cable loss. Therefore, the greater the RSSI value, the stronger the signal.

The results obtained from the RSSI level as a function of distance are shown in Figure 7.40. It is observed that the signal levels are very similar for a PCB and a flexible substrate using our Au MSD ink, obtaining signal levels between -34 dBm and -84.7 dBm in average up to a distance approximately 20m. These levels can be considered acceptable and guarantee the transmission of the data sent by the BLE transmitter. When an RSSI value is represented in a negative form, the closer the value is to 0, the stronger the received signal has been. Table 7.2 displays the measurements from 3 different antennas tested here. Thus, we can conclude that the use of our metal salt-based inks on PVA substrate has been successful with measured values close to the ones obtained in commercial PCB (laminated copper with 35um thickness) in FR$ substrates.

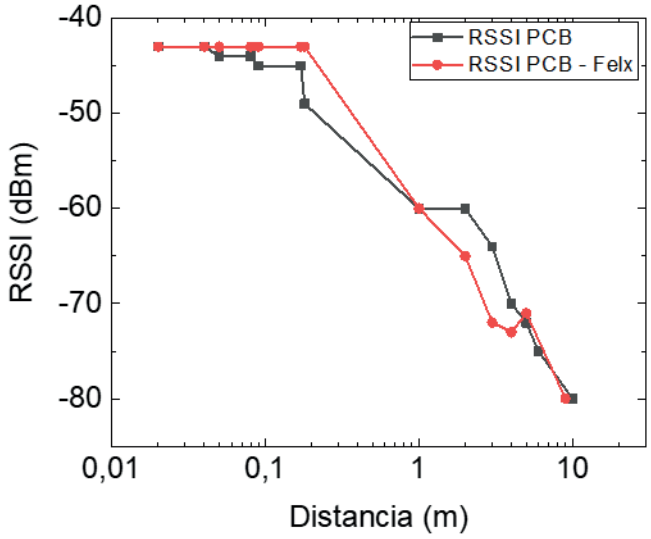

Figure 7.40. Summary of RSSI values vs distance for 3 samples

Table 7.2. Summary of RSSI values vs distance for 3 samples

	RSSI (dBm)							
Distance (m)	Au	Au	Au	Au (average)	Cu	Cu	Cu	Cu (average)
0	-32	-32	-32	-32.0	-24	-23	-27	-24.7
5	-74	-76	-75	-75.0	-74	-73	-72	-73.0
7	-80	-84	-81	-81.7	-83	-81	-80	-81.3
12	-94	-98	-98	-96.7	-96	-88	-91	-91.7
16	-96	-92	-90	-92.7	-93	-95	-98	-95.3
20	-94	-95	-95	-94.7	-95	-99	-97	-97.0
24	disconnected	disconnected	disconnected	disconnected	disconnected	disconnected	disconnected	disconnected

7.5.4 | DEVELOPMENT OF A ROOM TEMPERATURE PROCESSED TRANSISTOR

Different transistor architectures were considered ranging from the conventional bottom contact bottom gate (BCBG) to in plane interdigitated electrolyte-based transistors where the self-sintering Au films would be used as the source, drain, and gate electrodes as shown in Figure 7.41 below. Although Au is not known to be biodegradable, organic thin film transistors (OTFTs) require rigid electrical resistance tolerances that operationally stable nanoparticles can provide.[39] Additionally, Au itself provides a work function value close to the ionization energy of the majority of p-type organic semiconductors as it is critical for good charge carrier injection. As PVA can serve as both the dielectric and substrate layer, the only other layer that required development was the organic semiconductor (OSC) layer which will be discussed later in this section. Figures 7.41b and 7.41c highlight the structure for the electrolyte gated transistor (EGT) and electrolytic gated organic field effect transistor (EGOFET) respectively, both considered for

their potential to reduce the operational voltage compared to standard organic transistors. For the EGT, this requires the development of a ionic PVA gel where the mobile ions under an electric field develop electric double layers (EDLs) at the PVA/gate and PVA/OSC interfaces thus polarizing and inducing a conductive channel in the OSC. This process has effectively shown to increase the capacitance 2 to 3 orders higher as compared to conventional dielectrics.[40]

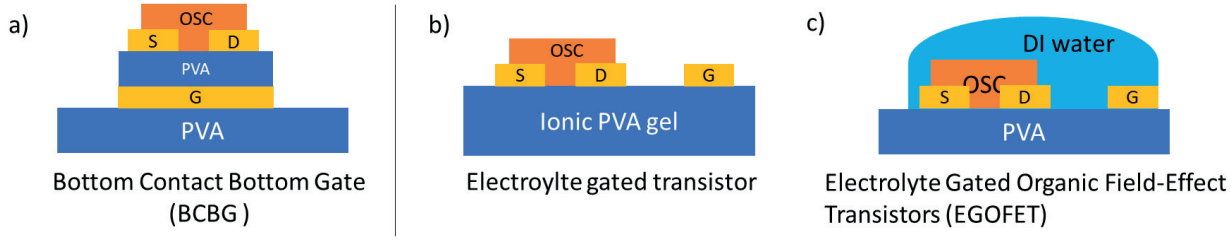

Figure 7.41. Transistor architectures including a) Bottom Contact Bottom Gate (BCBG), b) Electrolyte gated transistors (EGTs), and c) Electrolyte Gated Organic Field Effect Transistors (EGOFET)

A previously optimized transistor design was used as the inspiration for the in-plane transistor and adapted to the limitations of Au thin film development on PVA, meaning that is all line width must be at minimum 900 µm in thickness. Figure 7.42a below shows the exact dimensions of the in-plane transistor where the gate pads were between 4 – 5 mm^2 squares and line spacing between the fingers (as known as the channel length) were a minimum of 500 µm for a line width of 900 or 1000 µm. Thus, the W/L ratio here is determined to be 14. Additionally, the area of the gate was calculated to be 4.05 mm^2.For the BGBC transistor, the same line thickness and spacing were maintained whereas the contact pads maintained a 9 mm^2 area as shown in Figure 7.42b. Source and drain electrodes were deposited following the spin coating of the dielectric area which were 3 mm in width and 4.6 mm in height. Here, the channel width and length are 4.6 mm and 0.7 mm respectively presenting a W/L ratio of 6.6.

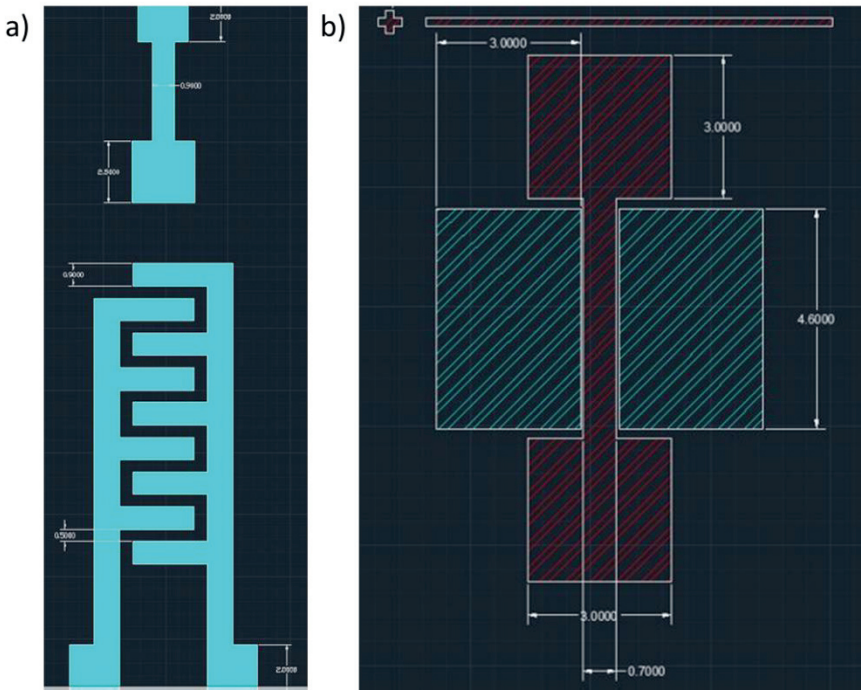

Figure 7.42. Transistor patterns including dimensions for a) in plane transistor and b) BCBG transistor

7.5.4.1 | *MATERIALS AND METHODS*

The procedure discussed here only refers to the conventional BCBG and in plane transistor mentioned in Figure 7.42 above. Both the fabrication of PVA coated glass substrates as well as the $HAuCl_4$ ink formation were first reported previously in Chapter 4 Section 4.2 and Chapter 6 Section 6.2 respectively which remained the same. Printing parameters using the Fujifilm Dimatix Materials Printer DMP-2831 printer were continuously adapted to the state of the ink, however the 2 factors that did remain the same were the DS of 20 μm and 2 printed layers for any design. Once the patterns were printed onto the 8 wt% PVA substrates, they were subjected to thermal sintering in an oven at 80°C for 30 – 60 minutes. 4 wt% PVA solution was used as the dielectric insulating layer varying between 1 – 3 coatings to determine the optimal thickness need to act as a dielectric layer. Each deposited layer was followed by a drying step using a hot plate at 60°C for 15 minutes to which more layers were added if needed. Tape was lightly placed on half of the contact pads to ensure that the area was still accessible for subsequent testing without covering the entire area with the final semiconductor layer.

Different semiconductors were considered including 1,4,8,11-tetramethyl-6,13-triethylsilylethynyl (TMTES) pentacene semiconductor solid which was acquired from Ossila Ltd. and High Purity Semiconducting Nanotubes IsoSol-S100/sc-SWCNT ink which was purchased from Raymor Nanotech and used as is without further manipulation. The following chemicals were added to achieve various semiconductor concentrated solutions: Anhydrous

chlorobenzene (CB, 99.8%) and polystyrene beads (average MW 280,000 by GPC) obtained from Sigma-Aldrich. From this, two types of TMTES-pentacene inks were prepared with and without polystyrene (PS). PS is added in order to provides greater uniformity and surface coverage of the developed film.[41] Different ratios between the TMTES pentacene and PS were prepared including 1:1, 2:1, and 4:1 ratios. Both the 2 wt% semiconductor and 2 wt% PS solutions were prepared separately and adapted to the ratio needed. Taking the 1:1 ratio as an example, 120 μL of the TMTES-pentacene and 120 μL of the PS were precisely calculated and prepared based on the weighed sample. For 4.6 mg TMTES-pentacene sample, 204 μL of CB was added. The solution was then stirred for 1 hr at 105°C until the TMTES-pentacene was completely dissolved. Similarly, a PS crystal has various weights that first must be weighed and back calculated in order to correctly prepare the solution. In this case, because the crystal weighed 20.3 mg, 898 μL of CB was needed to dissolve it. This mixture was stirred on a hot plate for 1.5 hrs at 105°C until the crystal was completely dissolved. An equal amount of the TMTES:CB solution (204 μL) and PS:CB (204 μL) solutions were combine together at 105°C for 1 hr. Prior to any deposition, the solution must be heated at 105°C to prevent any further crystal formation. This recipe was taken from the Marta Mas group at Institute of Materials Science of Barcelona (ICMAB).[42–44]

Directly following the semiconductor solution preparation, all ratios (1:1, 2:1, 4:1) were deposited using different deposition such as drop casting, spin coating, and a meniscus technique to determine which technique provided the best film. Drop casting was done using a 40 μL droplet of each prepared dispersion directly into the middle of a 4 wt% PVA substrate and allowed to dry overnight. Additionally, these same solutions were spin coated at 4000 rpm or 6000 rpm for 1 minute in order to ensure the coverage over the entire substrate and flash heated on a hot plate at 105°C. This meniscus technique was used to develop directional thin film semiconductor layers at 2 speeds (1 or 10 mm/s). Only a small amount is needed (30 μL droplet) to create films over large areas which were tested with and without the electrodes present. The formed film was then characterized using a polarized optical microscope (POM).

7.5.4.2 | *DEVELOPMENT OF THE DIELECTRIC PVA LAYER*

As previously stated, PVA was utilized as a substrate, reducing agent, and as a dielectric layer to build a BCBG transistor. Because PVA was a necessary tool to develop all electrodes at RT, this restricted the viable transistor architectures compatible with this type of growth. This means that the substrate must be placed at the bottom of the stack in order to fabricate the electrodes which is more optimal for an in-plane geometry. It was reported that PVA films observe dielectric constants between 5 – 8 at frequencies between 10-10^6 Hz.[45,46] However, the disadvantage in using a low cross-linking density material like PVA is that it requires a thick film of > 1 μm to ensure low leakage currents.[47] This was not a problem for the transistors

developed here as a PVA film thickness of at least 3 µm is needed to properly develop all electrodes. The gate electrode presenting with the I shape was first printed with 2 layers and converted without any issues (Figure 7.43a). Although each of the electrodes were printed under the same conditions, variability in terms of resistance was seen across the 4 samples from as little as 9.0 – 79.0 Ω as shown in Table 7.3. This behavior can be explained by the uncontrolled ink to substrate ratio where the higher resistance signified slower Au film development as here less Au NPs nucleated and sintered. A second layer of 4 wt% PVA was spin coated above which was primarily used as the dielectric layer in addition to serving as the reducing layer to develop both the source and drain electrodes. However, a tertiary effect was that it further reduced the previously deposited gate electrode whose values stabilized up to 25 days. Resistance decreased in excessive of 52% which was the case for Electrode 3 from 53.1 Ω to 25.5 Ω. For some electrodes, this reduction was immediate while others needed 20 days to fully stabilize. However, unfortunately, the development of the second PVA layer was poor and unpredictable as spin coating onto a non-planar layer proved difficult to create a consistent layer, that is a 3 – 6 µm PVA layer was not achievable. For this reason, the source and drain electrodes were slow to develop but did approach a Au like color however these areas remained completely non-conductive. On the other hand, the in-plane transistor (Figure 7.43b) saw decent conversion where the electrode printed with 900 µm line width saw a stable electrical resistance at 75 Ω while increasing the line width to 1000 µm saw 3 times less at 25 Ω. Because of the inconsistent development for the stacked transistor, the development of in-plane transistor was pursued more intensely and was further utilized as no issues in terms of electrical measurements nor inconsistencies were found.

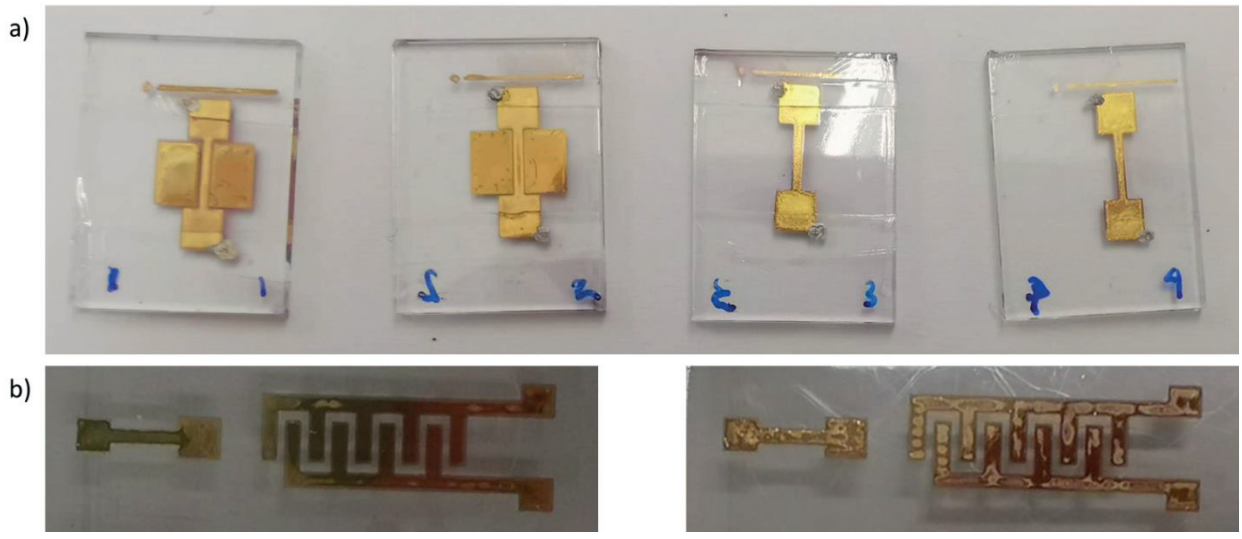

Figure 7.43. Printed Electrodes for a) BCBG transistor labelled according to the number of deposited layers and b) in-plane transistor with interdigitated source and drain electrodes

Table 7.3. Resistance measurements before and after spin coating a 2nd PVA layer to develop the BCBG transistor

Time period	Electrode #1	Electrode #2	Electrode #3	Electrode #4
Before spin coating	79.0 Ω	24.3 Ω	53.1 Ω	9.0 Ω
5 days after	76.3 Ω	19.7 Ω	25.9 Ω	8.5 Ω
7 days after	----	----	25.7Ω	8.3 Ω
12 days after	69.0 Ω	18.6 Ω	----	----
20 days after	----	----	25.5 Ω	7.0 Ω
25 days after	52.0 Ω	18.7 Ω	----	----

7.5.4.3 | *DEPOSITION OF SEMICONDUCTOR INK AND LAYER FORMATION*

A study was solely conducted on the optimal deposition of the organic semiconductor layer onto the PVA film layer using different deposition methods. Semiconductors in liquid phase are often prepared with organic solvents harsh chemicals which may directly affect the compatibility with the substrate. Due to its hydrophilic nature, PVA can potentially react to any number of reagents. For example, H_2O could not be used in this case as PVA can quickly dissolve in its presence in addition to the restriction of the organic semiconductor which must be dissolved in an organic solvent. Three semiconductors and their solvents we considered as follows: 1,4,8,11-tetramethyl-6,13-triethylsilylethynyl (TMTES) pentacene in anhydrous chlorobenzene (CB), single-walled carbon nanotubes (SWCNT) in toluene, and ZnO ink in isopropanol.

Because PVA is not a typically used polymer substrate, information regarding its chemical compatibility could not be easily found. Prior to the deposition of semiconductor inks, the chemical compatibility testing following the ASTM standard D543 on the Standard Practices for Evaluating the Resistance of Plastics to Chemical Reagents was performed.[48] For this testing, 2 inch (50.8 mm) PVA disks with 0.125 in or 3.175 mm thickness were immersed in the reagent (40 mL/in^2) for up to 24 hrs with occasional stirring. Following testing, the substrate was removed and placed to dry overnight in a fume hood. Before and after submersion, measurements of the center thickness as well as x – and y – diameters were measured with calipers. Incompatibility was both visually and quantifiably measured where the development of any swelling, decomposition, discoloration, cracking, or development of texture signaled poor compatibility. Additionally, if ±5% change in mass or diameter was detected, the solvent incompatible with the substrate. It was found that following testing, toluene did not affect the gloss or color of the film however it was found to be more severely warped most likely due to

the swelling seen. CB also caused the substrate to be slightly warped and brittle making it less flexible however its overall gloss was maintained as seen in Figure 7.44. However, reactivity to isopropanol was immediate where the edges of the PVA film were attacked, detached from the main body, and swelled and became cloudy (discolored). This is mostly likely due to the polarity of isopropanol as a solvent compared to CB and toluene. It was apparent from this testing that isopropanol was completely incompatible meaning that the ZnO ink could no longer be used for further testing. In terms of thickness and diameter measurements, none exceeded the 5% threshold as stated in Table 7.4. However visual testing was the decisive factor where both CB and toluene were acceptable for further testing.

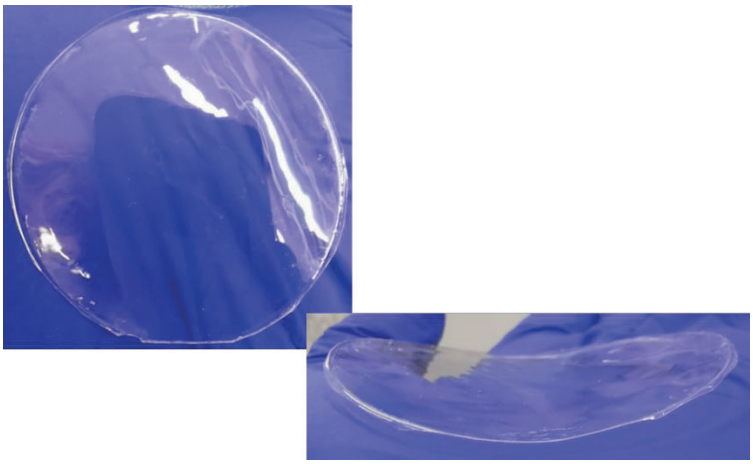

Figure 7.44. Visual inspection of the PVA substrate following immersion in CB

Table 7.4. Chemical compatibility results

Solvent	Mass (%)	Center (%)	Diameter (x, %)	Diameter (y, %)	Compatible?
Chlorobenzene	0.0187434	-0.19607843	-0.0152236	-0.001051265	Yes
Isopropanol	0,002309469	-0,42105263	-0,00195398	-0,022393247	No
Toulene	0,008107717	-0,70307692	0,00710725	0,004369242	Yes

Three ways to develop a thin film semiconductor layer were investigated and characterized to determine which provided the most uniform crystalline layer which included drop casting, spin coating, and meniscus technique with the help of Dra. Carme Martinez Domingo, co-supervisor of this work/thesis.

Figures 7.45a – 7.45b depict drop casting of 40 µL drops of the TMTES-pentacene and TMTES pentacene-PS (1:1 ratio) served as preliminary testing of the behavior of the inks on the PVA surface. The plain TMTES-pentacene film presented a mixture of large grains as well as

crystal formation leaving a non-continuous film. TMTES-pentacene:PS (1:1) solution showed a similar behavior where the edges of the drop contained larger grains while the interior exhibited smaller grains. These smaller grains contained 3D star-shaped crystals that were stacked and overlapping and somewhat directional oriented diagonally. However, it did not fully cover the substrate showing that drop casting is not an appropriate method of creating semiconductor film layers. The drop casted film by the 2:1 ratio showed similar behavior where the grain appeared as a star shape and multifaceted as seen in Figure 7.45c. Additionally, there were a mixture of grain sizes that ultimately resulted in a discontinuous film. In contrast, Figure 7.45d depicts 4:1 ratio drop casted films which appeared to have good coverage creating a continuous layer. Large crystals appear while smaller grains appear in the background to fill any gaps. On average, drop casting allowed for larger grains to be developed which increased in size when a greater amount of TMTES-pentacene was used looking at the grain size tabulated in Table 7.5. If drop casting must be used to create a semiconducting layer, the most optimal ink for this technique is a TMTES-pentacene:PS ratio of 4:1 showing an average grain size of 216.6±91.3 μm.

It was assumed that spin coating would provide significantly better coverage due to the even distribution of the solution across the surface. This certainly was the case for TMTES-pentacene where the film saw uniform formation of star-like grains distributed across the surface. Unfortunately, Figure 7.45e showed that these grains were separated not forming a continuous film. Figure 7.45f found that the film deposited from the 1:1 ratio solution saw smaller grains than its drop casted equivalent. In fact, around points of contamination, the grains were found to be larger and highly concentrated. Each individual grain presented an intersecting line in the middle showing much higher amount of grain boundaries than the drop casted film. Altogether, the film was comprised of small grains showing a polycrystalline behavior. The 2:1 ratio mixture showed larger grains intermixed with smaller grains shown in Figure 7.45g. In fact, there was a high ratio of smaller grains to large grains. Specifically, the larger grains presented with intersecting lines dividing the grains which tends to follow the direction of the grains with some salt crystals contaminated the surface. Figure 7.45h displayed that a similar behavior was seen with 4:1 ratio solution where the random angle grain boundaries note that indeed a polycrystalline semiconductor film was formed. Although all spin coated films presented a percolation of tiny single crystals, the grains were randomly oriented which may present a problem during testing. Comparatively, the average grain size of the spin coated films were 25.0 ± 6.1 μm or less however the overall coverage of the film increased significantly. Similarly, if spin coating was to be used as the main technique, the 4:1 ratio is the optimal formulation. It must be noted that different spin coating speeds were used, mainly 4000 and 6000 rpm which in the end did not result in any apparent differences.

Lastly, all TMTES-pentacene formulations with PS were subjected to meniscus technique testing due to their respective successful development using spin coating. This use of this

technique resulted in highly directional and elongated fine needle grains. The direction follows exactly the shearing direction of the meniscus technique blade meaning that the grains could be manually placed at the desired direction. At higher speeds, smaller grain sizes exhibited more of a plate-like behavior whereas the increased TMTES-pentacene concentration increased grain size. At the 1:1 ratio and 1 mm/s speed (Figure 7.45i) presented well aligned and directional needle-like microstructure, however at 10 mm/s exhibited different crystalline areas like the elongated grains with larger grain sizes as large as 15.5 μm (Figure 7.45l). It is believed at this point, crystal growth mode changes from a 1D to a 2D microstructures, specifically those films made at higher speeds of 10 mm/s. Figures 7.45j and 7.45m present the 2:1 ratio inks deposited at 1 mm/s and 10 mm/s respectively showing greatly different films. Elongated and well aligned grains were found however there were some holes found, similarly to the microstructure found with 1:1 ratio at the 1 mm/s speed. There was significantly higher grain boundary density due to the finer grain sizes (0.5 μm) as compared to the 1:1 ratio (4.8 μm). At 10 mm/s, the film was mostly composed of plates with smaller grain sizes (8.4 μm) than those seen at the 1:1 ratio. However, the film itself was filled entirely with these flake-like grains. Further increasing the TMTES pentacene ratio up to 4:1 ratio saw an even greater number of holes that developed in the film with an average grain size of 0.3 μm as seen in Figure 7.45k. Although the grains remained well aligned and directional, it was ultimately found that the film was non-continuous in nature. Figure 7.45n displayed that the resulting film deposited at 10 mm/s contained an even smaller plate-like morphology with a grain size average of 2.2 μm. Generally, the grain size decreases as the TMTES-pentacene concentration increases, most likely due to the solvent evaporation. In all, the optimal deposition parameters and ink formulation for the meniscus technique were 1 mm/s and 1:1 ratio. However, none of the reported films above exhibited 2D structures spherulite behavior as previously reported which was fully attributed to the amorphous PVA substrate below.[42,49,50]

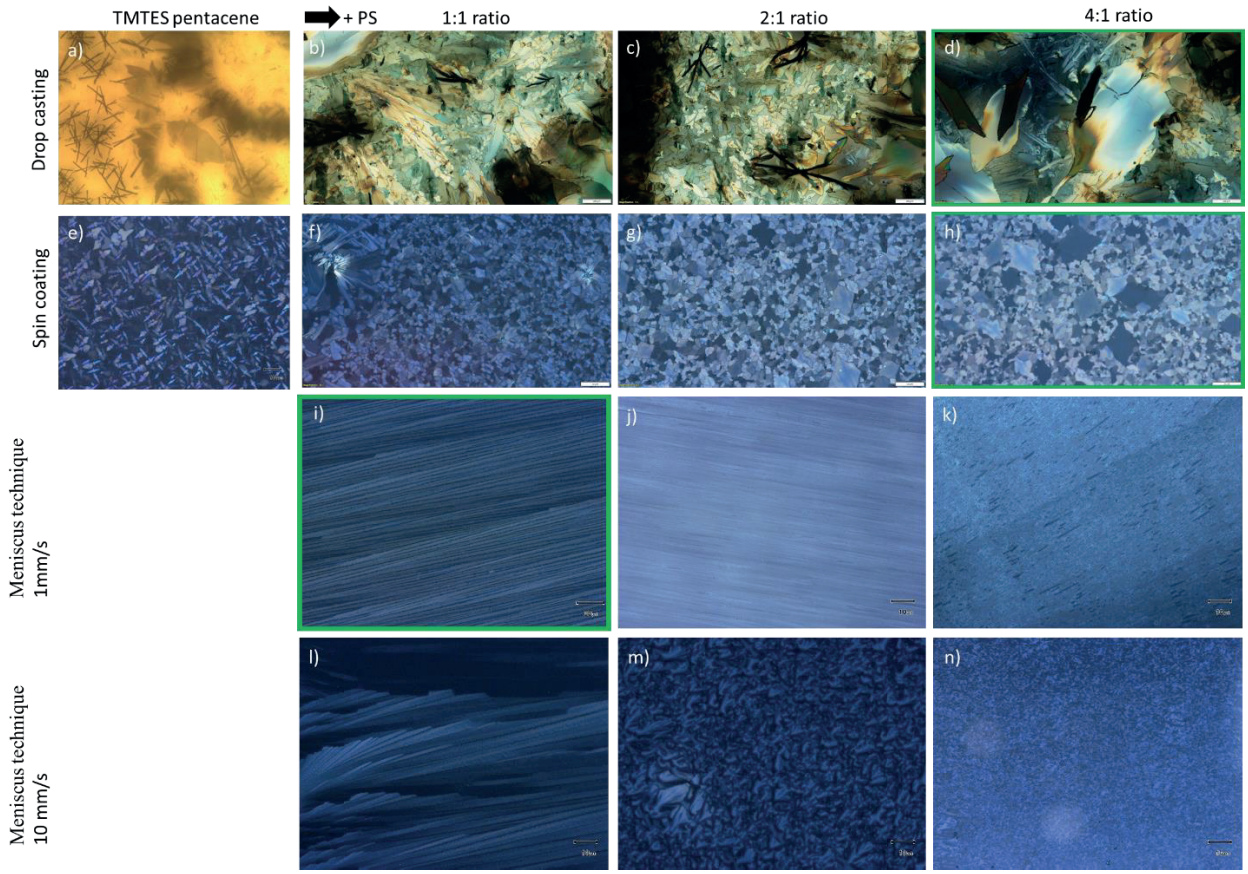

Figure 7.45. TMTES pentacene(:PS) films organized according to ratio and deposition technique. This data was acquired by Dra. Carme Martinez Domingo. All photographs were taken at 20x magnification.

Table 7.5. Effect of deposition method on TMTES-pentacene semiconductor layer

Deposition method	OSC:PS (1:1 ratio)	OSC:PS (2:1 ratio)	OSC:PS (4:1 ratio)
Drop casting	68.8±5.7 µm	85.0±10.7 µm	216.6±91.3 µm
Spin coating	19.6±0.6 µm	18.7±2.3 µm	25.0±6.1 µm
Meniscus Technique (1 mm/s)	4.8 µm	0.5 µm	0.3 µm
Meniscus Technique (10 mm/s)	3.2 – 15.5 µm	8.4 µm	2.2 µm

These exact parameters were then used to deposit the semiconductor layer in the development of an in-plane transistor following the design of Figure 7.42a. Results from the deposition were seen in Figure 7.46a below where the transistor with 900 µm line width only saw half of the source and drain interdigitated electrodes covered while the gate electrode was partially removed due to the strong adhesion of the tape. In effect, the large gaps in the film were found to be divergent, almost perpendicular to the electrodes. However, this was not the case for the 1000 µm wide transistor as the continuous film showed directional lamellar grains as shown in Figure 7.46b. Gaps in the film also appeared simply due to the roughness of the Au film surface due to uneven growth. Unfortunately, the majority of the gate was removed meaning that it could not be used during testing.

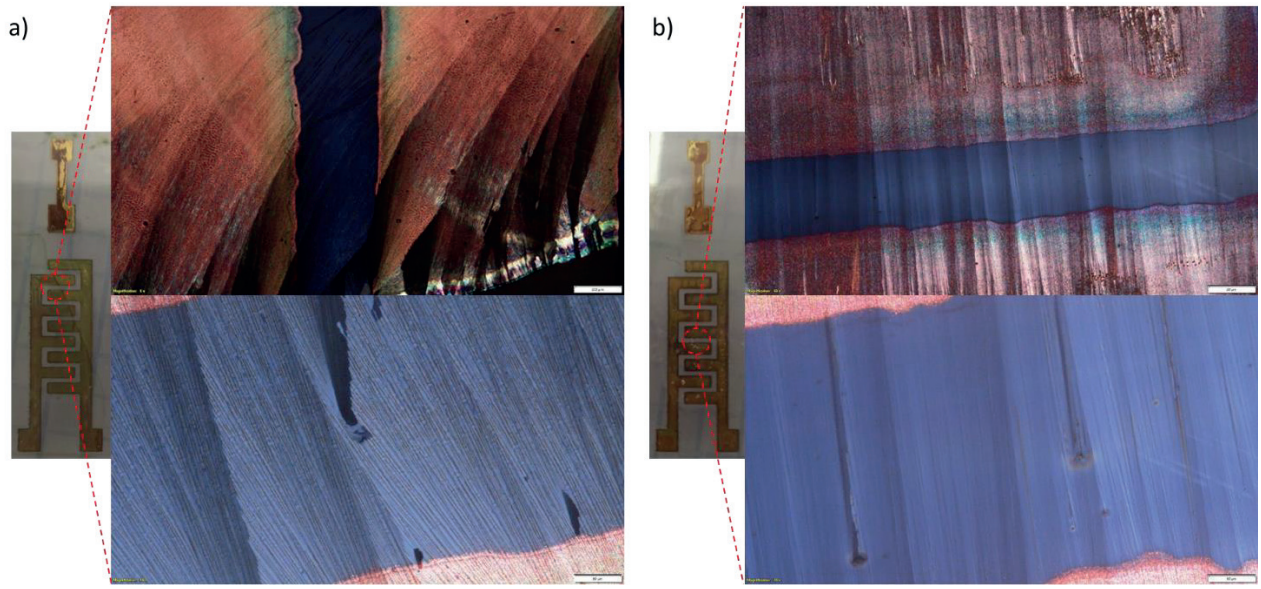

Figure 7.46. TMTES-pentacene film development by a meniscus technique for different sizes a) 900 µm width and b) 1000 µm width transistors. This data was acquired by Dra. Carme Martinez Domingo.

7.5.4.4 | *ELECTRICAL CHARACTERIZATION OF THE EGOFET TRANSISTORS*

First it must be noted that all electrical characterization testing here was done with the help of Dra. Carme Martinez Domingo. Low operational voltages (< 1V) are expected here as the electrolyte develops high electrical capacitance between the electrolyte/OSC and the electrolyte/gate. This then generates 2 electric double layers (EDLs): one at the interface between the gate and electrode and the other between the OSC and electrolyte when applying source-gate voltage (V_{sg}).[43,51] Fully completed p-type organic transistors were then subjected to current-voltage (IV) testing at gate voltages (V_g) between 0 to -500 mV measuring both its output and transfer characteristics as seen in Figure 7.47 below. Unfortunately, the Au gate was accidentally removed from the 900 µm line width thick therefore, a Pt needle served as the top gate while DI water was used as the electrolyte. It must be noted that this arrangement was not ideal as the PVA substrate below is known to be reactive to water however as this test was achieved quickly, thus any effect was negligible. The output curves as shown in Figure 7.47a displays linear regime across all tested drain voltage (V_d) never reaching saturation. This means that ohmic contact between the semiconductor layer and the source and drain electrodes was established.[52] Although the output curves do not behave ideally, modulation of the OSC is reached through the V_g. Figure 7.47b indicates hole transportation occurs by the increase in drain current (I_d) with decreasing gate voltage (V_g). From the transfer curves, electrical parameters such as the threshold voltage (V_{th}) and on current (I_{on}) and off current (I_{off}) current values can be determined

from Figure 7.47c. V_{th} was calculated to be 1.0V at a V_d = -500 mV however this value could not be determined for – 200 mV. Additionally, the I_{on} and I_{off} were found to be 3.56 x 10^{-5} A and 2.38 x 10^{-5} A respectively displaying a ratio of 1.49. The abnormally high I_{off} indicates that the OSC is being doped as a positive voltage must be applied in order to turn off the channel. This is also further verified by the fact that at a current appears between the source and drain at V_g = 0V. Unusually, the transfer curves only saw saturation occuring at 500 mV meaning that a high turn on voltage was seen which was contradictory to the desired characteristics for an EGOFET.

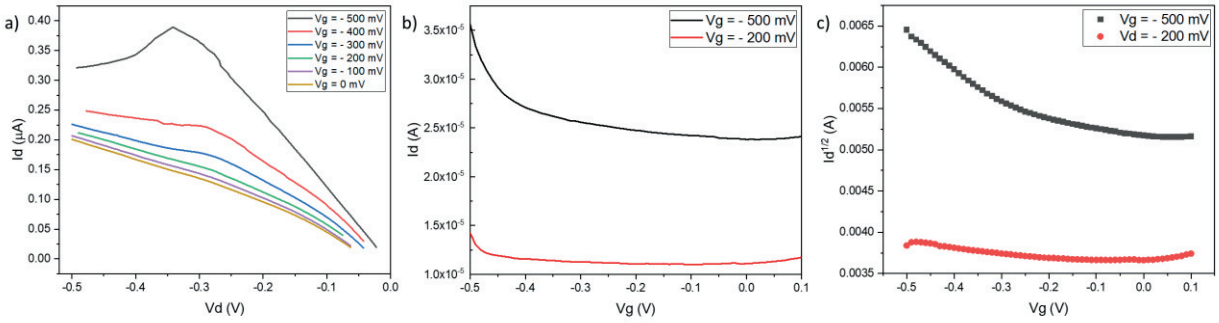

Figure 7.47. Transistor characteristics a) output (I_d v. V_d), and b) – c) transfer curves ((I_d and $Id^{1/2}$ vs V_g) under with PBS as the electrolyte using a Pt needle as a gate

As the characteristics of the transistor were found to be non-ideal, further refinement is needed to understand and optimize the behavior found here. Because PVA itself is hydrophilic, it is important to know its effect on the transistor response, something that should be investigated in the future. Eventually, it was discovered that the physical dimensions of gate electrode were far too small for this design and would need to be redesigned to achieve electrode polarization thus explaining the low I_{on}/I_{off} ratios. This can be done by encircling the transistor or by substantially increasing the gate electrode, parameters that will need to be defined and further tested. Lastly, another issue that may have occurred is related to the formulation of the OSC:PS layer which did not ensure good operation. It was expected that phase separation developed stacking the OSC layer above the PS layer and PVA substrate. This strategy is often used to neutralize any traps at the interface where the OSC is not in direct contact with the PVA thus preventing channel formation in that area. However, it was not fully verified that phase separation properly occurred as doping of the OSC was seen. However, these results do show promise for the development of low temperature processed transistors although further testing must be conducted in the future.

7.6 | DEVELOPMENT OF AN IONIC PVA GEL

As Au film formation was dependent on the reducing mechanism present by the PVA substrate, curiosity arose whether an ion gel could be developed using PVA as the base to develop electrolyte gated transistors (EGT). Inspiration for this idea arose from a published journal article, written by Jaehoon Jeong, a former PhD student at Institute of Nanotechnology at Karlsruhe Institute of Technology (KIT-INT) where I did my research stay, that successfully reported PVA-based ion gel. This was the basis for my stay meaning that all work was performed under the supervision of Ben Breitung at KIT-INT.

An ion gel is a combination of polymer matrix that can hold ionic species contained in liquid, like a liquid electrolyte, containing both cations and anions which are used as a dielectric for electrolyte gated transistors. Figure 7.48 below gives a general overview of this process where the first step in creating these gels is to crosslink a polymer which in our case, PVA was chosen due to its biodegradability as well as its relatively high glass transition temperature. Here we will focus more on the chemical crosslinking of PVA and will consider a few crosslinking agents which will be discussed later on. Secondly, a biodegradable and biocompatible ionic liquid was chosen as typical ionic liquids often contain sulfuric or fluoride ions which interact negatively with metal salt-based inks. Once correctly synthesized, they were combined to create ion gels and characterized.

However, it was unknown whether changing the basic chemistry of the substrate would have a great effect on the development of the Au film as it was shown previously that a reduced number of hydroxyl groups affects the film development and overall presented higher sheet resistance values. This is highly dependent on the number of hydroxyl groups available for its reduction as controlled by the crosslinking process. Considering this, the desired requirements for the ionic PVA gel for this application is that it must 1) be able to reduce the Au MSD ink to elemental Au and create a conductive film and 2) retain good capacitance and high ionic conductivity.

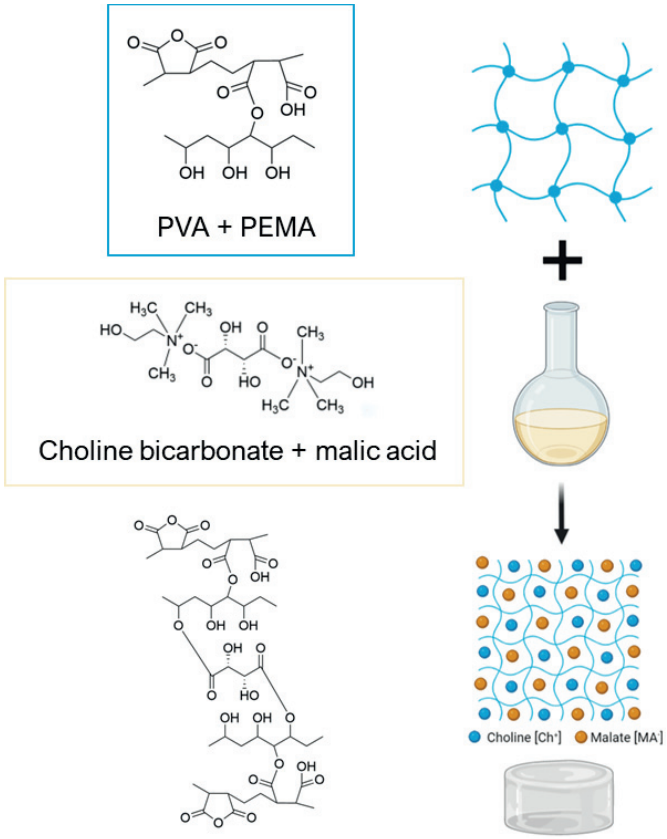

Figure 7.48. A representation of the chemical structures of a) the polymeric gel, b) ChMA ionic liquid, and c) the Ionic PVA gel structure and its respective ion organization in the polymer matrix.

7.6.1 | MATERIALS AND METHODS

Poly(vinyl alcohol) PVA powder (MW 31,000 – 50,000, 98 – 99% hydrolyzed) was purchased from Sigma Aldrich. The next following reagents were brought or provided for by KIT-INT in a visiting scientist research stay agreement under the guidance of Ben Breitung. All products were obtained from Sigma-Aldrich Chemie GmbH including suberic acid (98%), terephthalic acid (98%), poly(ethylene-alt-maleic anhydride (PEMA powder with average Mw 100,000 – 500,000), dimethyl sulfoxide (DMSO) Grade ReagentPlus®, ≥99.5%, choline bicarbonate (~80% in H_2O), and DL-Malic acid (99 – 100.5% alkalimetric) in the preparation of a ion PVA gel. Additionally, methanol (MeOH zur Analyse EMSURE® ACS,ISO,Reag. Ph Eur) was obtained from VWR International GmbH.

Any testing related to ion gel was performed at KIT-INT. Surface morphology of the films was imaged using HIROX High resolution 3D digital microscopy (for profile and surface roughness measurements) and SEM-FIB Dual Beam Zeiss Auriga 60 to look more deeply into

the thin film microstructure. BRUKER D8 XRD with LynxEye Detector (Cu Kα) was used to determine the chemical composition of the films. Verification for ion gel synthesis was done through the use of the Nicolet iS50 FTIR spectrometer and Bruker Nuclear Magnetic Resonance (NMR 500) Instrument.

7.6.1.1 | *CROSSLINKING PVA*

All crosslinking experiments discussed here were first reported by Sonker et al.[53] and Jeong et al.[54] and adapted according to the results. 5 wt% PVA stock solution was made with 0.5 g of PVA in 10 mL of DMSO and stirred at 100°C until completely dissolved. Different concentrations were investigated including 25% (2g) and 40% (1.25 g) of the corresponding acid (suberic acid or terephthalic) was then added. In order to facilitate dissolution, both solutions are placed in an ultrasonic bath at 60°C to dissolve for 4hrs. Once dissolved, the solution was drop casted into plastic petri dishes to dry overnight on a hot plate at 60°C.

Fresh batches were created prior to drop casting or spin coating first with the dissolution of PVA and PEMA respectively with DMSO. Different weight ratio between two components were explored from 70:30, 80:20, and 90:10. In the case of the 80:20 ratio, 1.6 g of PVA was dissolved in 1 mL of DMSO while 0.4g of PEMA was dissolved in 1 mL of DMSO simultaneously for 2 hrs at 60°C on a hot plate. Once both solutions were cooled to room temperature, they were combined and saw gelatinization within 5 minutes. For spin coated samples, the combined solution was directly applied to a small Ossila glass substrate and coated with Laurell Spin-coater Series 650 model WS-650-23B provided by KIT-INT at 500 rpm for 30 seconds. The films were then left overnight to solidify at RT. Thicker samples required larger amount of the PVA:PEMA solution to be made, drop casted, and dried overnight accordingly. Initially the gel saw a transparent orange color which then lost its color over time.

7.6.1.2 | *BIODEGRADABLE IONIC LIQUID PREPARATION*

Following the procedure outlined by Wu et al.[55], 2 M Malic acid (6.7045g malic acid in 25 mL of MeOH, stirred at 250 rpm at RT) was slowly combined with 125 mL of choline bicarbonate (as is) and stirred at RT at 700 rpm for 4 hrs until CO_2 generation ceased. This solution was placed into a 500 mL round bottom flask so that both the methanol as well as the remaining water was removed using rotary evaporation. Both the vapor pressure and temperature were adjusted according to the solvent removal which was conducted for a total of 2 days until a highly viscous solution was achieved. To ensure complete water evaporation, the liquid was placed in the vacuum oven at 80°C for 24 hrs. Following its synthesis, the ionic liquid (IL) was stored at RT until needed.

To create the PVA based ion gel, aliquots of 83, 166, or 249 μL of IL were added to the PVA:PEMA mixture. Following both the development of the PVA:PEMA gel as well as the ion gel, $HAuCl_4$ ink was printed on the newly fabricated substrate using both the Dimatix Material Printer model no. DMP-2831 and DMP-2850 as provided for by KIT-INT. Two different printers were used as DMP-2831 contained only 10 pL printheads while the DMP-2850 could handle both 1 and 2 pL printheads. Following the printing procedure, sintering treatment was maintained at 80°C for 1 hr in a ceramic oven.

7.6.2 | CROSSLINKING OF PVA AND CHARACTERIZATION

Crosslinking is a process in which esterification occurs between carboxyl groups of acids and hydroxyl groups of PVA. This process is typically performed with dialdehydes, carboxylic acids, and boric acid.[53] Three crosslinkers: suberic acid, terephthalic acid, and PEMA were chosen specifically for their interaction with PVA, that is they each tend to leave a large number of unreacted hydroxyl groups on the surface, allowing for only partial crosslinking of PVA as shown in Figure 7.49. This characteristic is important and advantageous as this will facilitate the reduction of the Au MSD inks while maintaining degradability.

Sonker et al. was the first to investigate the use of suberic and terephthalic acids as PVA crosslinkers. It was reported that increasing the suberic acid concentration as well as the crosslinking time reduces the number of hydroxyl groups therefore a lower concentration with a short crosslinking time was used. 25% and 40% concentrations for both acids were explored. After several attempts, both suberic and terephthalic acid were unable to form a gel as compared to the self-assembled PVA-PEMA gel. Initially, PVA-suberic acid started to crystalize but never hardened to form a film while terephthalic acid was found to be insoluble in a variety of solvents (isopropanol, methanol, ethylene glycol, DMSO) and itself is known to have poor solubility in DMSO (26 g/100 mL DMSO). Therefore, both acids were eliminated as a gel could not be achieved.

Of the chosen crosslinkers, only PEMA formed a usable and stable gel. Before further testing, the optimal weight ratio must first be defined as it is imperative to maintain as many hydroxyl groups as possible. For this, 4 different ratios were explored where 60:40, 70:30, 80:20, and 90:10 varies with respect to PVA. Previous investigation first reported by Jeong et al. stated that the amount of PVA dictates the gelation therefore at higher concentrations of PVA, rapid gelation occurs within minutes while maintaining a greater number of hydroxyl groups.[56] It was found that ratios 80:20 and 90:10 saw immediate gelation which was both unusable for both spin coating and even drop casting deposition. At a ratio of 60:40, it was reported that only 79 mol% of hydroxyl groups remained on the surface which can impede the Au film growth altogether.

Therefore, a good balance between these two factors were reached at a 70:30 ratio which continued to be used throughout further testing.

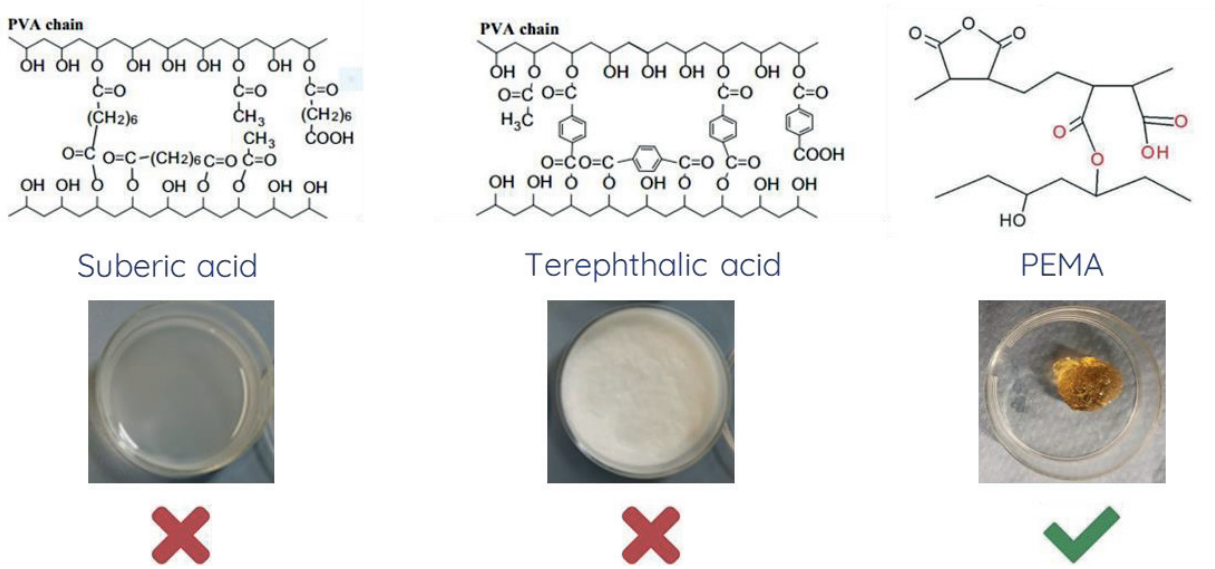

Figure 7.49. Chemical synthesis of crosslinked PVA structures based on crosslinking agent: a) suberic acid [53], b) terephthalic acid [53], and c) PEMA[57]

FTIR analysis was performed on both PVA and PEMA solutions as well as the PVA:PEMA gel as seen in Figure 7.50a. PEMA + DMSO spectra displayed peaks at 1777 cm^{-1} and 1846 cm^{-1} correspond to characteristic symmetric and asymmetric C=O groups attributed to cyclic anhydride. Analysis of the gels revealed partial crosslinking between the PVA and PEMA as the characteristic peak at 1846 cm^{-1} was missing from the gel. However, this is not an issue as this means that more hydroxyl groups were available on the surface for Au film formation. Due to the delayed gelation, a thin film could be spin coated on a small glass carrier where it was further analyzed using the HIROX High resolution 3D digital microscopy model no. HRX-01 as provided for by KIT-INT to obtain information regarding the surface morphology. It was found that the spin coated surfaces showed a surface roughness of 0.385 μm (Figure 7.50b) were non-uniform varying between 0 and 800 nm as seen in Figure 7.50c. This may be due to the high viscosity of the PVA-PEMA gel which is known to rapidly gelatinize. This process has yet to be fully optimize due to the short length of the research stay.

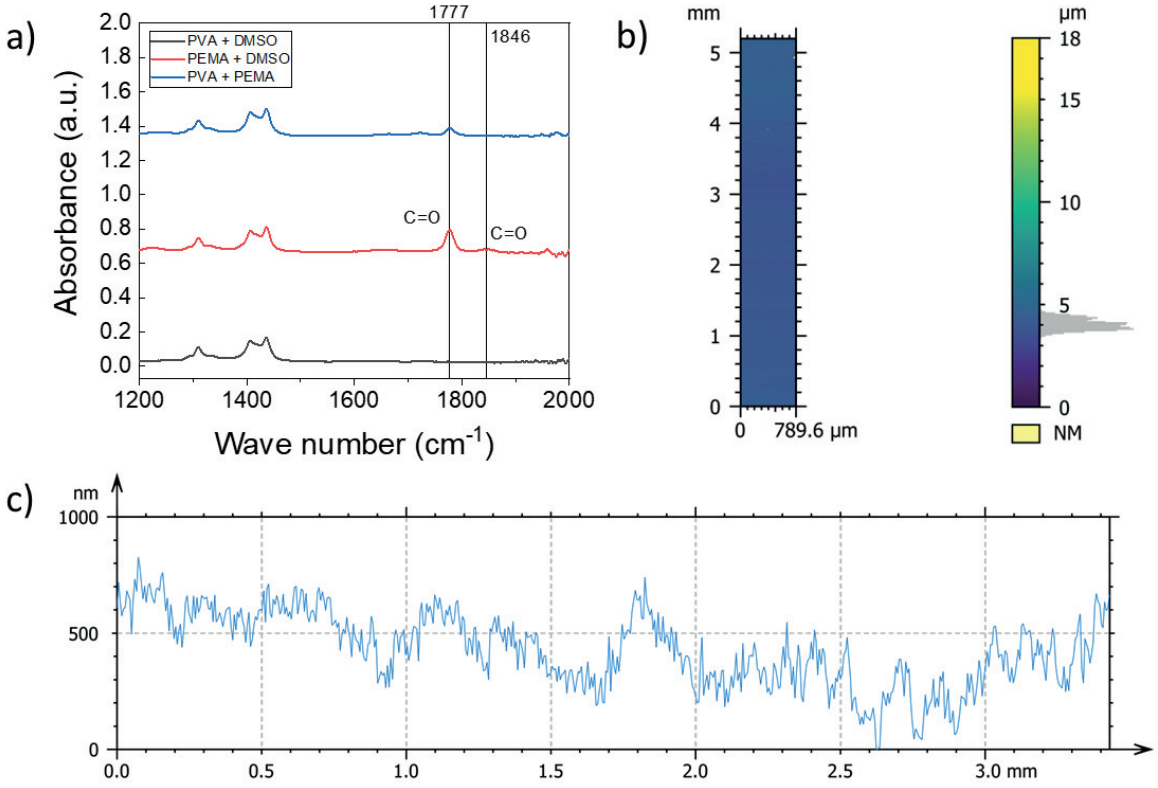

Figure 7.50. Characterization of PVA:PEMA gel by a) FTIR analysis of all chemical components and by digital optical imaging regarding b) the surface roughness, and c) profile of the substrate surface

7.6.3 | AU THIN FILM CHARACTERIZATION

However, the most important test was whether or not it was possible to growth a Au film even with the diminished reducing capacity of the PVA-PEMA substrate. Two types of printheads (2.5 pL and 10 pL) to investigate any printing differences that may arise from depositing different volumes of inks to create Au films. A wide range of films were developed with vastly different morphologies which can be seen in Figure 7.51 below. Surprisingly, these films were transparent in nature and unlike the growth on plain PVA, developed equally even from the smallest dots in the line pattern to squares with multiple layers as shown on Figure 7.51a. Films deposited with both printheads developed at a similar rate which is vastly different than those deposited on PVA as Au thin film growth which is highly dependent on the substrate thickness and ink volume deposited. Small ink volumes were deposited using the 2.5 pL printhead (Figure 7.51b) generally creating films with a characteristic gold border while the interior was not uniformly converted and showed a brown color. Additionally, due to uneven distribution of the PVA:PEMA gel, the resulting film was affected displaying a ripple-like

behavior highlighting its conformal growth on any surface. As more layers were added, the PVA:PEMA substrate began to eaten away causing folds as seen in Figure 7.51b. However even with standard heat treatment, gold film formation occurred at a delay of 8 days which means that the addition of PEMA had only a slight reduction of the hydroxyl group which did not affect too severely the Au film growth.

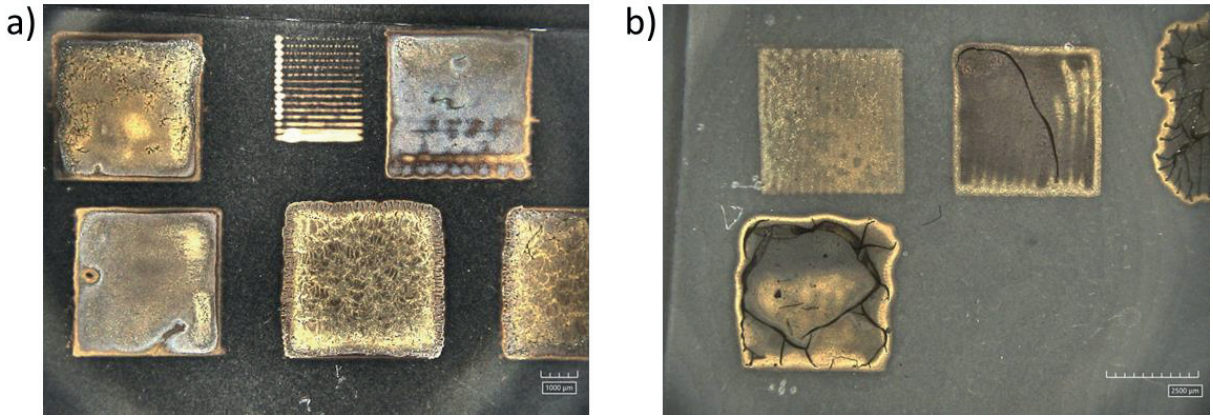

Figure 7.51. Variety of printed squares with different drop spacings using a) 10 pL and b) 2.5 pL printheads

Further examination of particular films is shown in Figure 7.52a and 7.52d highlights two films printed with a 10 pL printhead with 1 and 2 layers respectively showing vastly different growth formation. Characteristic Au color was seen only at the edges of the square in Figure 7.52a while the center showed non-uniform Au film growth. This behavior is expected due to the Marangoni effect of the ink. One printed layer showed good uniformity (Figure 7.52b) with low surface roughness of 0.3879 µm as the deposited ink volume did not completely etch through the film displaying a thickness ~ 1 µm as displayed in Figure 7.52c. In contrast, there was uniform Au film growth as seen in Figure 7.52d almost resembling the crosslinking behavior of PVA. It is believed that at this point, the double layer of ink begins etching through the PVA:PEMA substrate to the glass periodically (Figure 7.52e and 7.52f) that it creates a high surface roughness of 2.382 µm. Figure 7.52g documented the ripple-like Au film as printed by the 2.5 pL printhead for 1 layer with a drop spacing of 15 µm. Interestingly, this effect was not found in during both the surface morphology and profile measurements. Instead, a uniform and continuous film were seen with a surface roughness of 1.320 µm (Figure 7.52h) and film thickness of 0.332 µm (Figure 7.52i). With respect to its electrical characteristics, it was found that this film saw good conductivity of 6.92 x 10^4 S/m. This value is approximately 2 orders of magnitude lower than those seen on plain PVA (1.09 x 10^6 $S \cdot m^{-1}$) however for the development of an electrode, this value is acceptable.

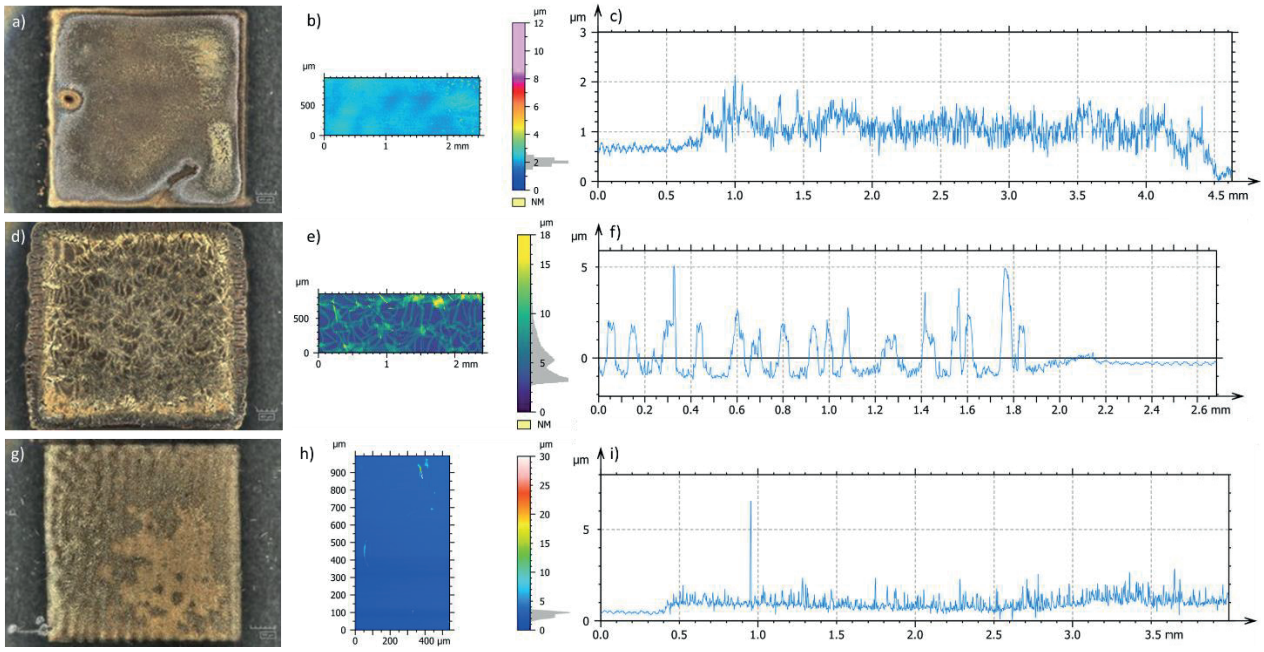

Figure 7.52. Reduced Au film formed on PVA:PEMA substrate a) Photograph of 1 printed layer and DS of 25 µm and its b) surface morphology and c) profile measurement. d) Photograph of 2 printed layers and DS of 25 µm using a 10 pL printhead and its e) surface morphology and f) profile measurement. g) Photograph of 1 printed layer and DS of 15 µm using a 2.5 pL printhead and its h) surface morphology and i) profile measurement

Based on both the appearance of the film as well as their respective sheet resistances, DS of 30 µm was the best printing parameter to create conductive Au films as determined from Figure 7.53a. The lowest DS of 10 µm presented the highest sheet resistance of 122.7 Ω which was expected due to underdevelopment of the film. An additional factor that was not considered previous was also due to the purity of the reduced Au film. Figure 7.53b displays the XRD spectra of the analyzed film where a broad peak at 19° can be attributed to amorphous PVA while the remaining peaks at 38.2°, 44.4°, and 64.6° were positively identified as polycrystalline Au.

The curious growth as displayed in Figure 7.52d was further investigated using the Zeiss Auriga 60 Scanning Electron Microscope (SEM) as provided for in collaboration with KIT-INT. Figure 7.53c showed that different areas of the sample showed selective film growth where Au line threads were surrounded by isolated Au NPs. Other areas were comprised of sintered Au nanoparticles as shown in Figure 7.53d whose formation was first reported by Leung et al.[15] through plasma reduction of the same ink however this film was inconsistent in terms of thin film growth. To a degree, all deposited and reduced square samples saw this selective film growth but those samples containing too much liquid such as squares printed with a DS of 5 µm, 2 layers of DS of 10 µm, and 2 layers of DS of 25 µm consistently reported the same thread-like

effect. Although the spin coated PVA:PEMA substrate was not directly imaged using SEM, Jeong et al. reported a rough surface morphology of the gel that contained stacked and bundled agglomerates creating large pores in the gel which are suitable to contain an ion liquid.[54] These pores appeared to be several micrometers in diameter, consistent with the structures formed on Figure 7.52d. Similar structures have been reported in literature on a wide range of hydrogels including crosslinked PVA with glutaraldehyde[58] as well as a wide variety of cellulose based hydrogels[59] resulting in highly porous films. Although it was already previously reported that the PVA:PEMA gel saw non-uniform deposition by spin coating, its physical structure can also be inconsistent as one area may contain a higher and larger number of pores versus another area. This is because incomplete crosslinking was a desired property to stimulate Au film growth therefore causing different types of film morphologies to manifest on a single substrate as seen on Figure 7.51. This means that the PVA:PEMA gel structure itself heavily influences the Au film formation becoming porous as a result and must be accounted for in the development of electrodes. Again this highlights the conformity of the $HAuCl_4$ ink which has the ability to conform to any surface which was first reported by Leung et al.[15] but now also shows the ability to attach to 3D surfaces and still initiate Au film growth. However, the reader must keep in mind that optimization specifically on this substrate was not the main goal for this experiment but was used just as verification that even with fewer hydroxyl groups that Au thin film could still be formed.

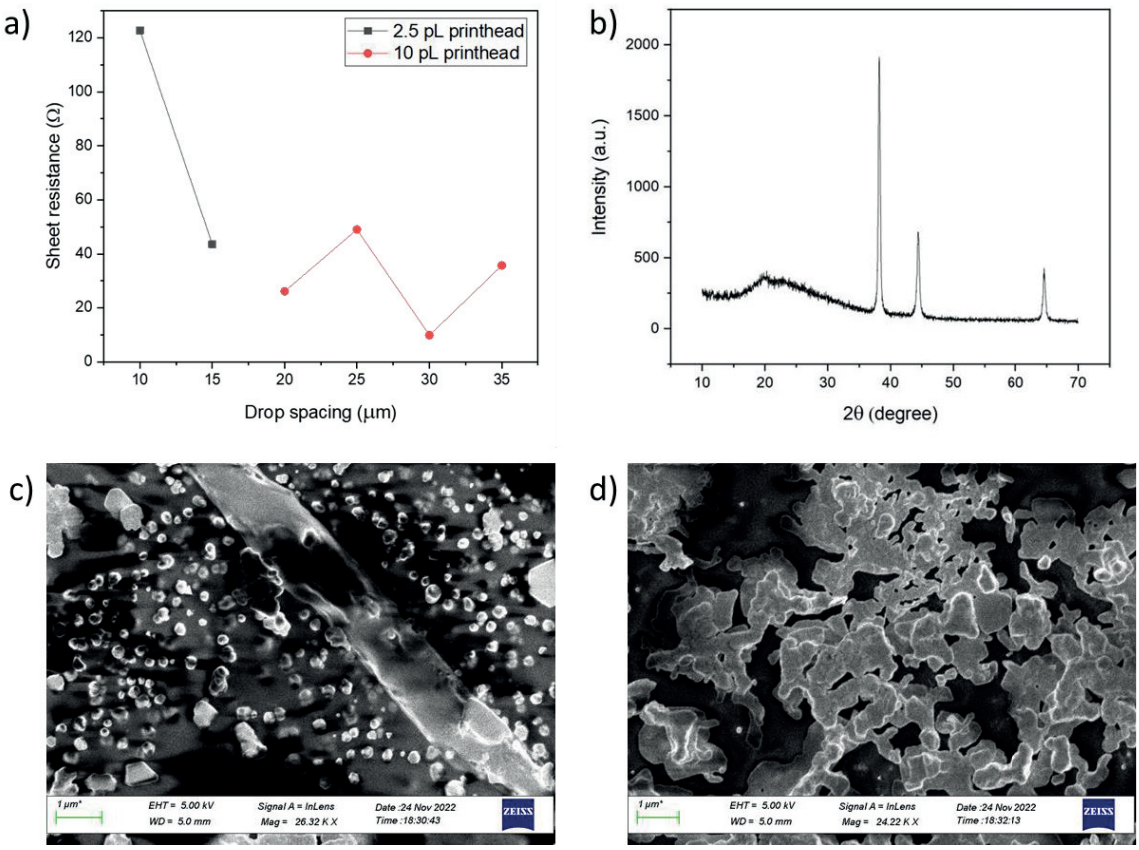

Figure 7.53. Printing parameters and film characterization of Au film on PVA:PEMA substrate where a) Sheet resistance values with respect to DS comparing the deposition of 2.5 pL and 10 pL printheads, b) corresponding XRD spectra, c) and d) SEM micrographs of selective Au film growth

7.6.4 | BIODEGRADABLE IONIC LIQUID

Although a larger variety of ionic liquids (IL) are commercially available, they not known to be biodegradable and can prove harmful in terms of interaction with the Au MSD ink. A minor test was performed with carrageenan infused with 1-Ethyl-3-methyl-imidazolium-thiocyanate (EMIM-SCN) as provided for as a sample from David Batet. If the reader previously recalls, direct printing onto carrageenan resulted in a conductive layer however when in contact with an ionic liquid, it instantly turned to a blood wine color as shown in Figure 7.54. However following heat treatment at the standard 80°C, the ink returns to an orange color which did not change afterwards. What is believed to be occurring here is a ligand substitution process through direct ligand exchange as shown in Equation 7.8 below:

$$[AuCl_4]^- + SCN^- \rightarrow [AuCl_3(SCN)]^- + Cl^- \quad (7.8)$$

following the reduction of the Au (III) species to Au (I) thiocyanate species.[60] Although this reaction is a stepwise process, ligand substitution occur much faster than the reduction, especially at higher Au concentrations.[60,61] From this mini-test, it was apparent that any IL containing SCN was incompatible with Au MSD ink and could not be used as an ionic liquid in this case. This example highlights the importance of the chemical composition of the IL, especially its interaction with the metallic cation.

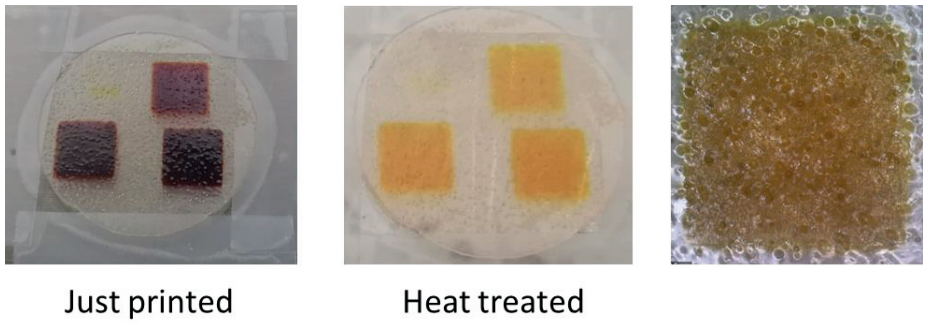

Figure 7.54. Reaction of Au MSD ink on Carrageenan + IL for a) just printed films, b) heat treated films at 80°C for 1 hr, and c) optical microscope view of the heat treated film

For this reason, a biodegradable and biocompatible ionic liquid was first introduced by Wu et al. containing choline and malic acid, both of which were typically used as food additives.[55] Jo et al. developed the same choline based ionic liquid and applied it to levan polysaccharide substrate to develop fully biodegradable transistors. This ionic liquid contains cations from choline and malate anions that observed a large specific capacitance of 40 μF cm^{-2} at 10 Hz.[62] Chemical synthesis reaction between choline bicarbonate and malic acid stated in Figure 7.48 found that when combined, start to outgas carbon dioxide and form water as a result which was then removed through rotary evaporation where in the end, obtained a purified and highly viscous ionic liquid with a transparent yellow color. The exact reaction is stated below in Equation 7.9:

$$[Ch]^+HCO_3^- + [MA]^-[H]^+ \rightarrow [Ch]^+[MA]^-H_2O + CO_2 \quad (7.9)$$

which means further testing is needed to verify its correct synthesis using ^{1}H-NMR as shown in Figure 7.55. Two different samples were analyzed from the same batch but was

dissolved in different dissolvents which gave different results mainly revealing that only choline bicarbonate was present. It is known that choline is physically a bigger ion than the malate ion which can easily overpower any reading and be seen as the dominant chemical. Figure 7.55a presented the IL dissolved in deuterium oxide (D_2O) while Figure 7.55b presented the IL in DMSO which was found to be insoluble. Those signals at δ 3.12 (d, 3H, CH_3), δ 3.84 (m, 2H, CH_2), and δ 3.43 (m, 2H, CH_2) were identified as corresponding to 6 methyl groups, 4 methylene groups, and choline-based fragments respectively while those relating to malic acid were found at δ 2.30 (dd, 3H, CH_3) related to a methylene group. Of these, the most important signal should appear at δ 2.43 which was nowhere to be found questioning its correct synthesis. An extremely small amount of malic acid detected of < 1% showing that the ionic liquid may have not been synthesized correctly, removed during the evaporation step, or expired. These samples were tested almost 1 month after its synthesis which can justify its absence.

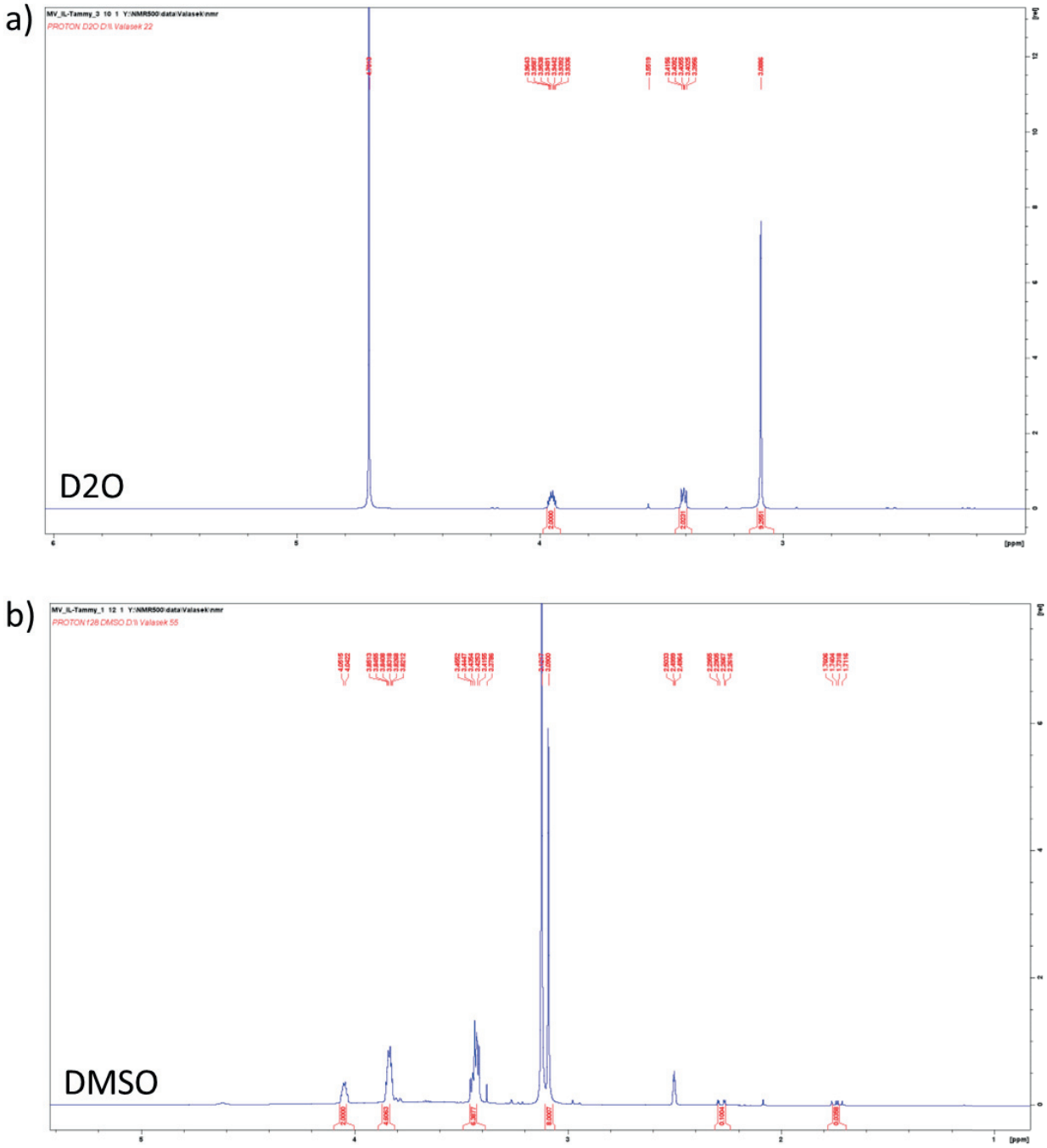

Figure 7.55. H-NMR spectra in dissolved a) D_20 and b) DMSO

Immediately after the biodegradable ionic liquid was achieved, it was then combined with the crosslinked PVA to create the ion gel. Similar to the crosslinking process between PVA and PEMA, esterification of hydroxyl groups in PVA backbone chain and carboxyl groups of malate

ions in ionic liquid should be observed quickly forming this gel noted by the peak found at 1715 cm^{-1} however unfortunately no specific ester bond was found between PVA and the ionic liquid showing that maybe the complete formation of the gel maybe lacking as shown in Figure 7.56a. This could potentially be the result of an incomplete synthesis of the IL which detected little malic acid meaning any bonding with malate ions are miniscule to none. Different aliquots amounts (41, 83, 166, 249 µL) were added to the PVA:PEMA mixture during its formation and reported in Figure 7.56b. Although not shown here, the ion gel doped with 249 µL instantaneously formed a gel meaning a thin film could not be developed and was therefore not included in this testing. Fourier-transform infrared spectroscopy (FTIR) was used to further characterize the liquid, as seen in Figure 7.56b, which should see absorption bands for -OH and C=O groups at 3261 and 1584 cm^{-1} respectively but in this case we see them a bit shifted. In fact, there was no distinguishable difference between the addition of the 83µL and 166 µL of IL perhaps indicating a saturation point of the crosslinked PVA gel was reached.

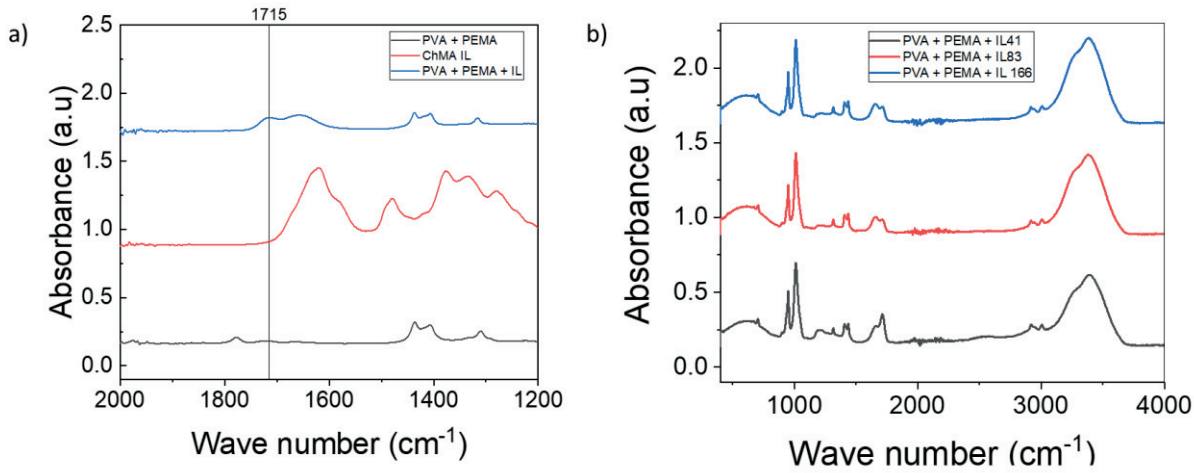

Figure 7.56. FTIR analysis a) Spectra from the PVA + PEMA, IL, and a combination of both respectively and b) spectra of various PVA + PEMA + IL concentrations

7.6.5 | ION GEL CHARACTERIZATION

Electrochemical Impedance Spectroscopy (EIS) measurements were performed with customized Swagelok cell assembly (Figure 7.57a, b, and c) where the ion gel was uniformly compressed with a spring to determine the exact thickness of the gel during measurement which is important for the correct characterization of the ion gel. Alternatively, preliminary testing was performed using a coin cell testing board in order to quickly determine if the ion gel was working properly as shown in Figure 7.57d.

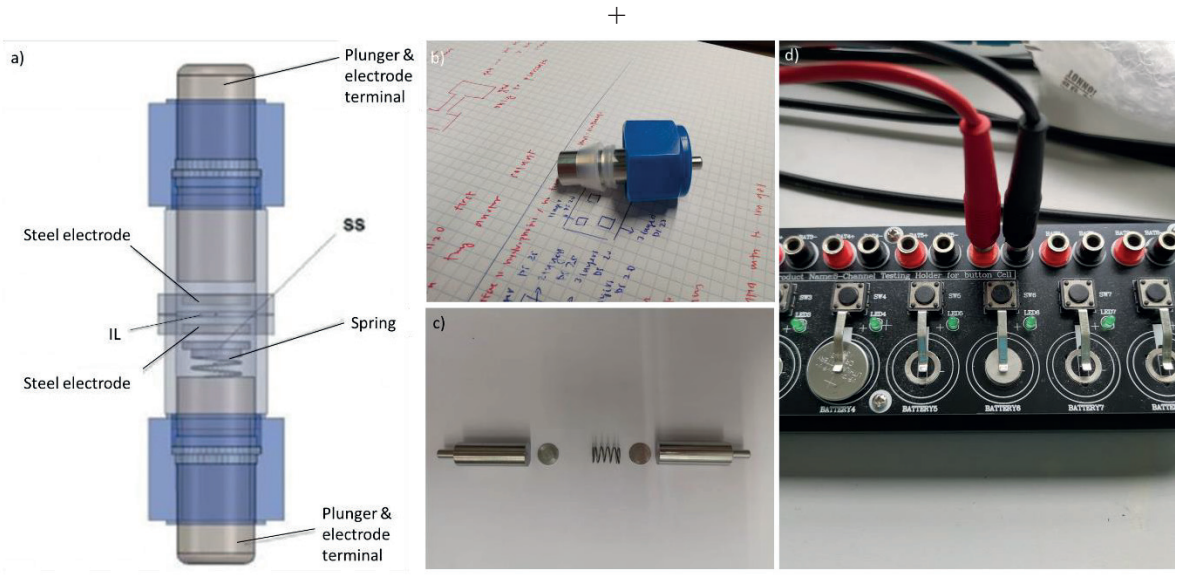

Figure 7.57. Swagelok cell assembly a) schematic representation of the cell adapted from Safa et al.[63], b) Swagelok fittings and ferrules, c) custom made components of the plunger, spring, and steel brushed electrodes, d) coin cell testing board

Figure 7.58a depicts a 12 mm diameter cut PVA based ion gel that could easily be handled and placed into the Swagelok cell assembly to determine its thickness depicting an average of 73.3 µm. Often the thickness of the samples varied due to the non-planar surface of the gel during the setting period seeing up to 1.00 mm in thickness. Different ion gels were tested but not reported here as they were found to be either completely non-functional or only showed mass transfer phenomenon which was seen with all samples containing no or 83 µL of the biodegradable IL. This is most likely due to an insufficient IL concentration which therefore was doubled to 166 µL resulting in the plots displayed in Figure 7.58 below. From the Nyquist graph as shown in Figure 7.58b, the PVA-PEMA gel shows no response as the gel acts purely as a dielectric. However, when the biodegradable IL is included, a semicircle behavior noting charge transfer phenomenon is seen where the electrolyte resistance is found to be >250 kΩ when tested at 5mV. Such a large resistance value already suggests that the ionic conductivity will be significantly lower than desired. Bode plot displays frequency dependency on both the phase angle and the log($|Z|$) values as shown in Figure 7.58c. Here, an electric double layer (EDL) effect indicating capacitive behavior is seen at the lower frequencies until 100 Hz which verifies that the ion gel is functioning but far from ideal. Although a plateau was not necessarily achieved, there is a clear distinction seen at a frequency of 100 Hz where the EDL polarization layer turns from capacitive to a resistive behavior, most likely due to electrode polarization. At this frequency, a phase angle of -18° was reported whereas a saturated phase angle appears between -10° and -20°, far from an ideal capacitive response of -90°.[54] From the perspective of

the phase angle, a resistive behavior at higher frequencies (>10^4 Hz) is seen while at lower frequencies (<10^4 Hz) the ion gel behaves as a non-ideal capacitor. Based on these results, the capacitance can no longer be calculated through the standard equation and instead is adapted for higher frequency ranges where the resistive behavior dominates thus providing a more conservative value of 0.16 μF/cm^2. This effective capacitance (C_{eff}) was calculated using Equation 7.9 below.

$$C_{eff} = \frac{-Z_{im}}{2\pi A f |Z|^2} \tag{7.9}$$

A frequency of 1585 Hz was taken from the plateau-like region revealing an ionic con conductivity of 0.28 μS·cm^{-1} which were quite poor however expected when considering the electrolyte resistance value previously reported. For comparison, high ionic conductivity for an IL is between 10^{-4} to 10^{-2} S·cm^{-1} where generally the ionic conductivity increases as the viscosity decreases.[64] Figure 7.58d displayed the frequency dependency of both ionic conductivity and effective capacitance showing unusual behavior. Ionic conductivity never stabilizes and in fact increases at higher frequencies. The plot for C_{eff} sees a similar behavior where the capacitance value increases from 0.16 μF/cm^2 at 100 Hz to a maximum of 3.5 μF/cm^2 at 100 kHz. This value confirms that an EDL and a bulk capacitor are formed at the interface between the electrode and ion gel with increasing IL concentration.[62] Regardless, neither of these values reach those previously reported by Jo et al. for the same IL at ≈40 μF/cm^2.[62] One of the main causes for drastic difference may be the poor ionic liquid quality itself which was not tested directly following its synthesis nor stored under the appropriate conditions.

The corresponding equivalent circuit obtained from the Nyquist plot is found below in Figure 7.58e which first consists of R_u or an uncompensated resistance accounting for the ohmic resistance between the reference and working electrode, as well as that of the working electrode and connection cables can ultimately be neglected.[65] R_u is then placed in series with 2 components, the electrolyte or bulk resistance (R_b) which is in parallel with the bulk capacitance (C_b). This capacitance arises from dipolar relaxation of the ion gel molecules.[64,66] Finally, a constant phase element (CPE) was place in series to compensate for the non-ideal capacitive behavior (C_{dl}). From this, a well fitted model was found for all plots including both the Nyquist and Bode plots as seen below in Figure 7.58f and 7.58g respectively.

.

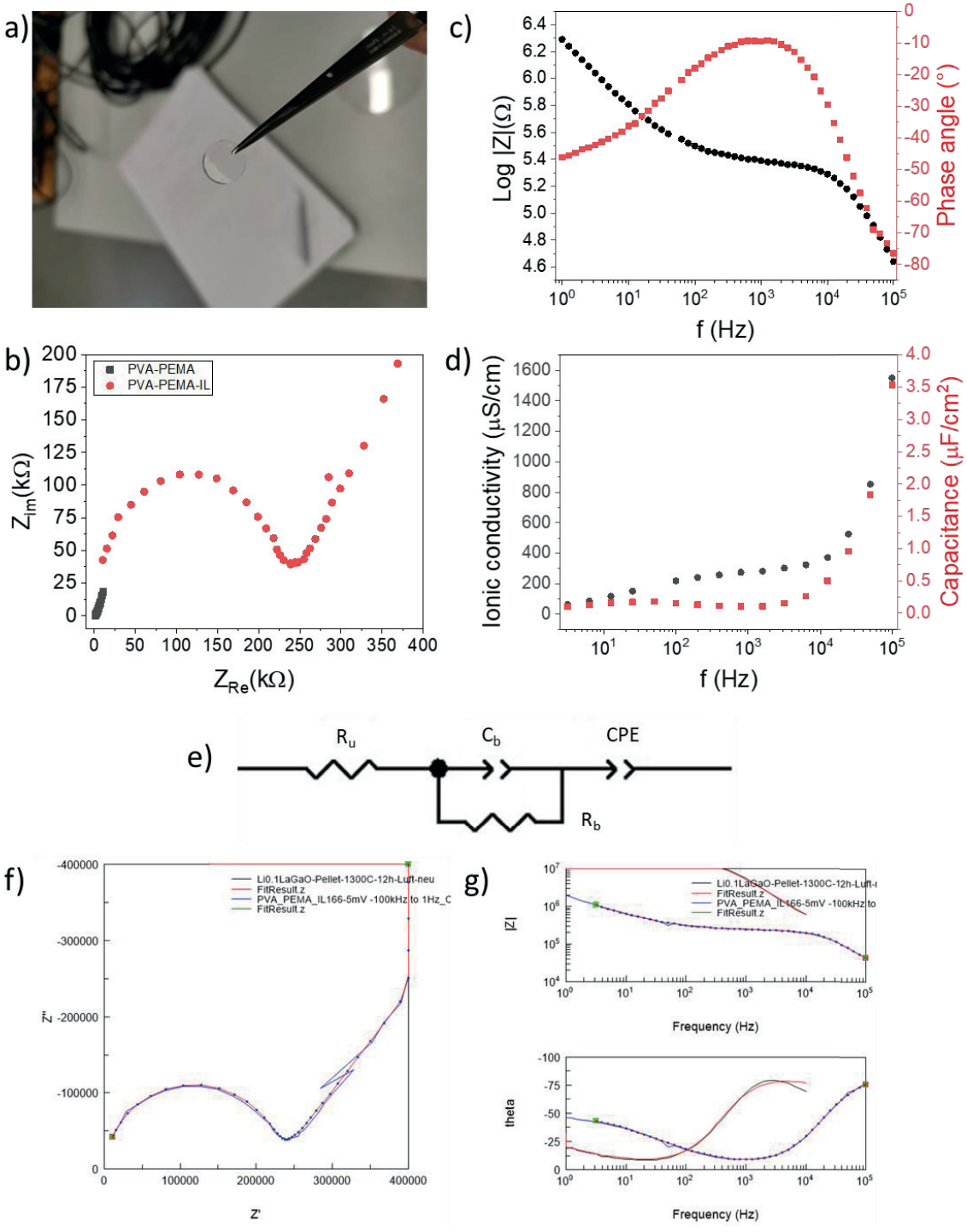

Figure 7.58. Comparative EIS measurements of PVA+PEMA gel and ionic PVA gel containing 166 µL of biodegradable IL a) photograph of the ion gel before testing, b) Nyquist plot, c) Bode plot, and d) ionic conductivity and capacitance vs. frequency plot, e) equivalent circuit

Unfortunately, complete optimization of the ion gel was not achieved due to a limited experimental period of less than 3 months. Although not directly applicable, Hasan et al. indicated that the maximum capacity for EMIM-SCN liquid held in a polymer matrix is 20%, however in terms of optimized ionic conductivity and capacitance, the IL concentration should never reach past 9%.[59] In our case, the highest IL to PVA ratio achievable before rapid solidification stands at 8.3% IL concentration signaling that perhaps the maximum capacity was already reached when adding 50% more than this value causing instant solidification. Additionally, the small gel thickness which will hold considerably less IL may also play a role in the low ionic conductivity found here. For example, a similar gel with 900 μm thickness containing EMIM-SCN exhibits an significantly higher ionic conductivity as high as 3.7 mS/cm.[54] This was experimentally verified by Lee et al. who found that the resistance proportionally increased with an increase in film thickness, thus having an effect on the conductivity.[64] Additionally the capacitance is also dependent on the gel thickness therefore explaining the lower than expected capacitance value.[62] One way to verify the highest ionic conductivity achievable is by directly measuring the IL using a conductometer, an instrument of which unfortunately was not available at KIT-INT If the conductivity is already low in its bulk form, then the previously obtained measurements are valid. Lastly, it was also proposed that it was perhaps the use of a lower molecular weight PVA polymer (31 – 50k) that triggers quick gelation, therefore, PVA with higher molecular weight (146k -186k) was tested which unfortunately did not reduce the gelation time. The issue of solidification of the gel itself can be mitigated if the process itself is takes place in a glove box where the humidity is well controlled removing any reaction with the moisture sensitive PEMA. It is clear that at least, the biodegradable liquid should be resynthesized and characterized appropriately before implementation into the PVA-PEMA gel. Once these steps are achieved, only then can EIS measurements take place to ensure the functionality of the ion gel as a whole.

7.6.5.1 | *REACTION TO $HAUCL_4$ INK*

Once a spin coated layer of 40% PVA:60% PEMA:IL was achieved, its reaction to the Au MSD ink was studied to determine whether or not a conductive Au NP film could be formed. As per usual, directly following printing, the printed squares were subjected to heat treatment at 80°C for 1 hr, the results of which can be seen below in Figure 7.59. A mixture of films was formed from a purple to gold-like colored film at least noting some formation of Au NPs. Two different substrates were subjected to testing containing different concentrations of IL. A line pattern was first printed to give an approximate idea of the ideal DS which was found to be 25 μm. Unlike previous printings, the PVA:PEMA surface was determined to be less hydrophilic than PVA making it difficult to form a continuous film. The substrate containing <166 μL of IL (Figure 7.59a) displayed a greater proclivity to generate gold color films compared to the substrate containing > 166 μL of IL (Figure 7.59b). The resulting Au film formation closely

resembled those found on the PVA:PEMA gel exhibiting the misshapen deposited squares as well as the ripple-like behavior first reported in Figure 7.52d. Different DS (20 or 25 μm) and layers (1 – 3 layers) were deposited to gauge the optimal Au film growth parameters which was clearly demonstrated with 2 layers using a DS of 20 μm. This standard was then implemented onto the substrate containing a higher concentration of IL (> 166 μL of IL), however resulted in a completely unified film that mostly exhibited a purple color with minimal Au NP growth. Each substrate and their individual squares were imaged 4 days after sintering as shown in Figures 7.59c and 7.59d. Similarly, they highlighting the porous structure of the crosslinked PVA substrate as previously reported indicating selective growth in these particular areas. The image taken in Figure 7.59d does not properly reflect the real state of the film as it appears as gold which can be deceiving but in fact remains as a purple color to the naked eye. Both substrates were tracked over a 4-month period but did not show any further growth past its initial sintering stage. Equally, none of the developed films displayed conductivity despite their color as no continuous film was developed instead displaying dispersed Au NP throughout the substrate surface similar to those found in Figure 7.53c.

The use of a biodegradable IL was not only proposed due to the negative reaction of Au MSD inks to standard ILs but also for its known biodegradability and its chemical structure that contained at least 4 additional hydroxyl groups for a ChMA molecule. It was first supposed that the introduction of hydroxyl groups would further help to initiate the Au reduction process which does occur but only under specific conditions. In the literature, malic acid has been previously shown to be used as a capping agent for the green synthesis of Ag NPs[67] while, although not 100% applicable, choline chloride was reported to act as a ligand perhaps forming $Au(Ch)Cl_3^-$ species.[68,69] In the case of the former, the use of malic acid would hinder the formation of a conductive film and would first need to be removed while the latter issue mentioned here mimics that found when using SCN^- underlining a fundamental problem when combining metal salt inks with ILs. This was most apparent through the appearance of the purple film especially when subjected to a greater IL concentration in which the reaction between the Au MSD ink and the IL dominated thus forming these species. Conversely, the substrate containing a lower IL concentration reacted first to the PVA:PEMA substrate alone before the IL thus allowing for significantly more Au NP formation. It is clear from this short study that the reaction between the Au metal salt and the biodegradable IL is still not well understood and must be further elaborated on in the future.

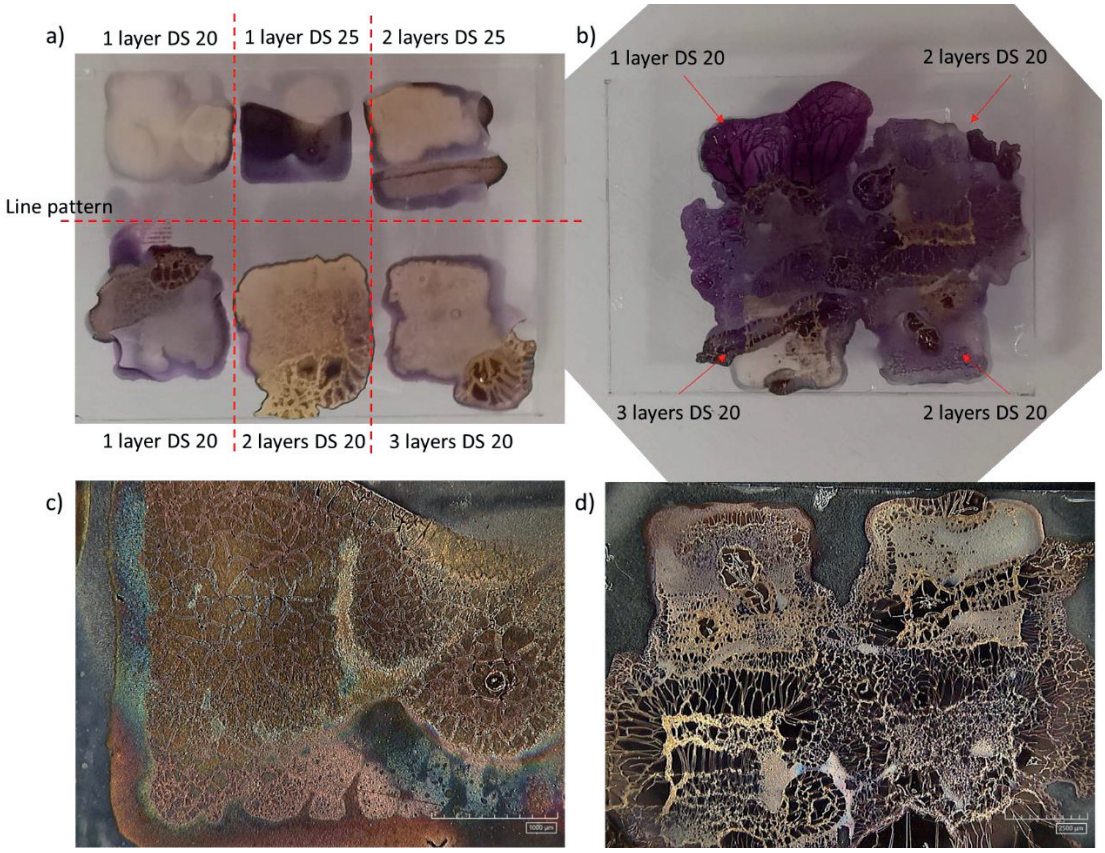

Figure 7.59. Development of Au NP film on PVA:PEMA:IL substrate containing ~ 166 µL a) with less IL and b) more IL, c) 50x magnification of Square no. 2, and d) 20x magnification of all squares

7.7 | CONCLUSIONS

The effectiveness of hydroxyl containing substrates and their potential to develop reduced metal films was studied here. Such substrates included well known green polysaccharide substrates such as PVA and cellulose derivatives to the less familiar natural polymers such as carrageenan and silk fibroin. Of the substrates investigated, PVA displayed superior results amongst all others which did see similar Au NP development but never to the extent of a continuous film. The growth itself can occur under ambient conditions within 11 days and more rapidly under low temperature heat treatment at 80°C within 30 minutes. Optimization factors such as PVA foil thickness had a direct effect on the Au film formation, maintaining that PVA thickness must be precisely controlled between 3 – 6 µm. Microstructural analysis of such films using SEM revealed the film growth process of Au NPs initiating first in the PVA substrate that then broached the surface creating a continuous and conductive film at RT. Similarly, EDX showed that such films were mainly composed of Au (≈ 90%) with minimal Cl and while XRD provided proof that polycrystalline Au was formed.

More complex designs were printed and tested including electrodes, strain sensors, antennas, and transistors. Design limitations with regards to conductivity were considered which affected each design in different ways where a simplified design was necessary to avoid any shortcuts between neighboring areas which were found to be optimal for electrode and strain sensors. The films themselves showed excellent resistance to high tensile strains (<3.2%) as well as good cyclical stability. In addition, the conductive Au film was determined to be sufficient to develop a HF RFID antenna. On the other hand, this did not affect the development of transistors where multiple designs were considered but eventually established with an in-plane interdigitated transistor design where all electrodes were developed in Au and the semiconductor layer was deposited using a meniscus technique to produce directionally aligned TMTES-pentacene films. Overall, the transistors showed poor electrical response to different electrolytes attributed to the doping of the organic semiconductor. Work surrounding the development of electrolyte gated transistors (EGT) is an ongoing process where the PVA based ion gel itself still must first be fully optimized as the resulting ionic conductivity and capacitance were significantly lower than expected at 0.28 μS/cm and 0.16 μF/cm^2 respectively. However, the ion gel does show signs that Au NP formation is still possible under these conditions partially fulfilling its desired requirements. All work presented here in currently in the process of being comprised into a second journal article addressing solely the development of reduced Au films at RT and its potential applications.

7.8 | REFERENCES

1. Mallakpour S, Behranvand V, Tabesh F. Natural polymer–based organic–inorganic hybrid nanosorbents. *Nat Polym Green Adsorbents Water Treat*. January 2021:159-193. doi:10.1016/B978-0-12-820541-9.00005-3
2. Aravamudhan A, Ramos DM, Nada AA, Kumbar SG. Natural Polymers: Polysaccharides and Their Derivatives for Biomedical Applications. *Nat Synth Biomed Polym*. January 2014:67-89. doi:10.1016/B978-0-12-396983-5.00004-1
3. Duan H, Wang D, Li Y. Green chemistry for nanoparticle synthesis. *Chem Soc Rev*. 2015;44(16):5778-5792. doi:10.1039/c4cs00363b
4. Díaz-Cruz C, Alonso Nuñez G, Espinoza-Gómez H, Flores-López LZ. Effect of molecular weight of PEG or PVA as reducing-stabilizing agent in the green synthesis of silver-nanoparticles. *Eur Polym J*. 2016;83:265-277. doi:10.1016/J.EURPOLYMJ.2016.08.025
5. Serra JP, Fidalgo-Marijuan A, Teixeira J, et al. Sustainable Lithium-Ion Battery Separator Membranes Based on Carrageenan Biopolymer. *Adv Sustain Syst*. 2022;6(12):2200279. doi:https://doi.org/10.1002/adsu.202200279
6. Palui G, Ray S, Banerjee A. Synthesis of multiple shaped gold nanoparticles using wet chemical method by different dendritic peptides at room temperature. *J Mater Chem*. 2009;19(21):3457-3468. doi:10.1039/B818594H
7. Wu X, Lu C, Zhou Z, Yuan G, Xiong R, Zhang X. Green synthesis and formation mechanism of cellulose nanocrystal-supported gold nanoparticles with enhanced catalytic performance. *Environ Sci Nano*. 2014;1(1):71-79. doi:10.1039/C3EN00066D
8. Ogundare SA, van Zyl WE. Nanocrystalline cellulose as reducing- and stabilizing agent in the synthesis of silver nanoparticles: Application as a surface-enhanced Raman scattering (SERS) substrate. *Surfaces and Interfaces*. 2018;13:1-10. doi:10.1016/J.SURFIN.2018.06.004
9. He F, Zhao D, Liu J, Roberts CB. Stabilization of Fe−Pd Nanoparticles with Sodium Carboxymethyl

Cellulose for Enhanced Transport and Dechlorination of Trichloroethylene in Soil and Groundwater. *Ind Eng Chem Res*. 2006;46(1):29-34. doi:10.1021/IE0610896

10. Huang Y, Liu J, Zhang J, et al. Flexible quasi-solid-state zinc ion batteries enabled by highly conductive carrageenan bio-polymer electrolyte. *RSC Adv*. 2019;9(29):16313-16319. doi:10.1039/C9RA01120J
11. Chang Y-C, Lin C-H. Degradable Carrageenan as a Substrate and Resistive Material for Flexible Applications. *ACS Omega*. 2023;8(13):12387-12392. doi:10.1021/acsomega.3c00165
12. Li L, Ni R, Shao Y, Mao S. Carrageenan and its applications in drug delivery. *Carbohydr Polym*. 2014;103(1):1-11. doi:10.1016/J.CARBPOL.2013.12.008
13. Optical Properties of Thin Solid Films - O. S. Heavens - Google Books. https://books.google.be/books?id=gRsZytsSnkQC&pg=PA169&lpg=PA169&dq=ruddy-purple+15A+gold+films&source=bl&ots=fkriJbCyR8&sig=ACfU3U0FvSk1Cbz3Yd2Oh2o7vFirsVNYMg&hl=en&sa=X&ved=2ahUKEwi38peh8cCAAxURyaQKHVBeBYwQ6AF6BAgJEAM#v=onepage&q=ruddy-purple 15A gold films&f=false. Accessed August 3, 2023.
14. FreeSnell: Granular Metal Films. https://people.csail.mit.edu/jaffer/FreeSnell/granular.html. Accessed August 3, 2023.
15. Leung TSW, Ramon E, Martínez-Domingo C. Low-Temperature Plasma Sintering of Inkjet-Printed Metal Salt Decomposition Inks on Flexible Substrates. *Adv Eng Mater*. 2022;2200834. doi:10.1002/adem.202200834
16. Gold Nanoparticles: Properties and Applications. https://www.sigmaaldrich.com/BE/en/technical-documents/technical-article/materials-science-and-engineering/biosensors-and-imaging/gold-nanoparticles. Accessed August 4, 2023.
17. Spectrum of a Fluorescent Light Bulb vs. Spectrum of the Sun. https://webbtelescope.org/contents/media/images/01F8G7TT6ZPK2APENNVVEZ5DY8. Accessed August 3, 2023.
18. Courrol LC, Matos RA de, Courrol LC, Matos RA de. Synthesis of Gold Nanoparticles Using Amino Acids by Light Irradiation. *Catal Appl Nano-Gold Catal*. August 2016. doi:10.5772/63729
19. Ranjana R, Parushuram N, Harisha KS, Asha S, Sangappa Y. Silk fibroin a bio-template for synthesis of different shaped gold nanoparticles: Characterization and ammonia detection application. *Mater Today Proc*. 2020;27:434-439. doi:10.1016/J.MATPR.2019.11.259
20. Dong S, Tang C, Zhou H, Zhao H. Photochemical synthesis of gold nanoparticles by the sunlight radiation using a seeding approach. *Gold Bull*. 2004;37(3-4):187-195. doi:10.1007/BF03215212/METRICS
21. Gomes DSB, Paterno LG, Santos ABS, et al. UV-Accelerated Synthesis of Gold Nanoparticle–Pluronic Nanocomposites for X-ray Computed Tomography Contrast Enhancement. *Polymers (Basel)*. 2023;15(9):2163. doi:10.3390/POLYM15092163/S1
22. Fedorova AP, Kartuzhanski AL, Peshchevitski BJ, Plachenov BT. A chain mechanism of radiolysis and photolysis in H[AuCl4]-polyvinyl alcohol system. *Radiat Phys Chem*. 1985;26(3):273-276. doi:10.1016/0146-5724(85)90064-0
23. Spring, Kenneth R., Davidson MW. Sources of Visible Light - Introduction | Olympus LS. https://www.olympus-lifescience.com/en/microscope-resource/primer/lightandcolor/lightsourcesintro/. Accessed June 4, 2023.
24. Energy Dispersive X-ray Spectroscopy Services | EAG Laboratories. https://www.eag.com/techniques/spectroscopy/energy-dispersive-x-ray-spectroscopy-eds/. Accessed August 7, 2023.
25. Yu JJW, Jung J, Choi Y, et al. ASTM D3359: Measuring Adhesion by Tape Test. *Am Soc Test Mater*. 1997;7(1):36-43. http://metalroofpaint.ca/documents/ASTM TAPE ADHESION TEST.pdf%5Cnhttp://dx.doi.org/10.1039/c5py01483b.
26. Yang S, Lu N. Gauge Factor and Stretchability of Silicon-on-Polymer Strain Gauges. *Sensors (Basel)*. 2013;13(7):8577. doi:10.3390/S130708577
27. Farcau C, Sangeetha NM, Moreira H, et al. High-Sensitivity Strain Gauge Based on a Single Wire of Gold Nanoparticles Fabricated by Stop-and-Go Convective Self-Assembly. *ACS Nano*. 2011;5(9):7137-7143. doi:10.1021/nn201833y
28. Herrmann J, Müller KH, Reda T, et al. Nanoparticle films as sensitive strain gauges. *Appl Phys Lett*.

2007;91(18):89-92. doi:10.1063/1.2805026
29. Wennersten K. Additive Manufacturing of Strain Gauges A Study of the Feasibility of Printing Strain Gauges Using Inkjet Printing. 2022.
30. Bin Y, Oishi K, Yoshida K, Matsuo M. Mechanical Properties of Poly(ethylene terephthalate) Estimated in Terms of Orientation Distribution of Crystallites and Amorphous Chain Segments under Simultaneous Biaxially Stretching. *Polym J 2004 3611*. 2004;36(11):888-898. doi:10.1295/polymj.36.888
31. Jain N, Singh VK, Chauhan S. A review on mechanical and water absorption properties of polyvinyl alcohol based composites/films. *J Mech Behav Mater*. 2017;26(5-6):213-222. doi:10.1515/JMBM-2017-0027/MACHINEREADABLECITATION/RIS
32. Johnson PW, Blackstone JM. Children and gender—differences in exposure and how anthropometric differences can be incorporated into the design of computer input devices. *SJWEH Suppl*. 2007;(3):26-32. https://www.sjweh.fi/show_abstract.php?abstract_id=1179.
33. Jin Z, Li Y, Fan D, Tu C, Wang X, Dang S. Calibration Experiment and Temperature Compensation Method for the Thermal Output of Electrical Resistance Strain Gauges in Health Monitoring of Structures. *Symmetry 2023, Vol 15, Page 1066*. 2023;15(5):1066. doi:10.3390/SYM15051066
34. Yang L, Rida A, Vyas R, Tentzeris MM. RFID tag and RF structures on a paper substrate using inkjet-printing technology. *IEEE Trans Microw Theory Tech*. 2007;55(12):2894-2901. doi:10.1109/TMTT.2007.909886
35. Kaija K, Virtanen J, Ukkonen L, Sydänheimo L, Virtanen J, Joutsenoja T. Characterization of inkjet printed UHF RFID antennas. 2010:222-225. https://researchportal.tuni.fi/fi/publications/characterization-of-inkjet-printed-uhf-rfid-antennas. Accessed September 19, 2023.
36. Pudas M, Halonen N, Granat P, Vähäkangas J. Gravure printing of conductive particulate polymer inks on flexible substrates. *Prog Org Coatings*. 2005;54(4):310-316. doi:10.1016/j.porgcoat.2005.07.008
37. Mujal J, Ramon E, Diaz E, et al. Inkjet printed antennas for NFC systems. *2010 IEEE Int Conf Electron Circuits, Syst ICECS 2010 - Proc*. 2010:1220-1223. doi:10.1109/ICECS.2010.5724738
38. What Is the Quality Factor (Q Factor) of Antennas? - TurboFuture. https://turbofuture.com/industrial/The-Q-Factor-of-Antennas-What-is-Q-Factor-What-Affects-It-and-How-Do-You-Calculate-It. Accessed September 19, 2023.
39. Tan HW, An J, Chua CK, Tran T. Metallic Nanoparticle Inks for 3D Printing of Electronics. *Adv Electron Mater*. 2019;5(5). doi:10.1002/aelm.201800831
40. Narasimhan V, Park SY. An Ion Gel as a Low-Cost, Spin-Coatable, High-Capacitance Dielectric for Electrowetting-on-Dielectric (EWOD). *Langmuir*. 2015;31(30):8512-8518. doi:10.1021/ACS.LANGMUIR.5B01745/ASSET/IMAGES/MEDIUM/LA-2015-01745B_0008.GIF
41. Abdullah I, Lan H, Morrison J, Alharbi A, Macdonald JE, Yeates SG. The synergistic role of azeotropic solvent mixtures and atactic polystyrene on the morphology, crystallization and field effect mobility of thin film 6,13-bis(triisopropylsilylethynyl)-pentacene based semiconductors. *J Mater Sci Mater Electron*. 2018;29(12):9804-9813. doi:10.1007/s10854-018-9020-5
42. Tamayo A, Fratelli I, Ciavatti A, et al. X-ray Detectors With Ultrahigh Sensitivity Employing High Performance Transistors Based on a Fully Organic Small Molecule Semiconductor/Polymer Blend Active Layer. *Adv Electron Mater*. 2022;8(10):2200293. doi:https://doi.org/10.1002/aelm.202200293
43. Zhang Q, Tamayo A, Leonardi F, Mas-Torrent M. Interplay between Electrolyte-Gated Organic Field-Effect Transistors and Surfactants: A Surface Aggregation Tool and Protecting Semiconducting Layer. *ACS Appl Mater Interfaces*. 2021;13(26):30902-30909. doi:10.1021/acsami.1c05938
44. Del Pozo FG, Fabiano S, Pfattner R, et al. Single Crystal-Like Performance in Solution-Coated Thin-Film Organic Field-Effect Transistors. *Adv Funct Mater*. 2016;26(14):2379-2386. doi:10.1002/ADFM.201502274
45. Abdelhamid HN. Dielectric, Thermal, and Electrical Conductivity Properties of Biodegradable Polymer Nanocomposites. *Res Sq*. 2022. doi:10.21203/RS.3.RS-2003331/V1
46. Canimkurbey B, Çakirlar Ç, Piravadili Mucur S, Yasin M, Berber S. Influence of Al2O3 nanoparticles incorporation on the dielectric properties of solution processed PVA films for organic field effect transistor applications. *J Mater Sci Mater Electron*. 2019;30(20):18384-18390. doi:10.1007/S10854-019-02192-1/FIGURES/7

47. Wang B, Huang W, Chi L, Al-Hashimi M, Marks TJ, Facchetti A. High- k Gate Dielectrics for Emerging Flexible and Stretchable Electronics. *Chem Rev*. 2018;118(11):5690-5754. doi:10.1021/acs.chemrev.8b00045
48. D543 Standard Practices for Evaluating the Resistance of Plastics to Chemical Reagents. https://www.astm.org/d0543-21.html. Accessed August 22, 2023.
49. Lee JH, Seo Y, Park YD, et al. Effect of Crystallization Modes in TIPS-pentacene/Insulating Polymer Blends on the Gas Sensing Properties of Organic Field-Effect Transistors. *Sci Rep*. 2019;9(1):1-10. doi:10.1038/s41598-018-36652-1
50. Meneau AYB, Olivier Y, Backlund T, et al. Temperature Dependence of Charge Localization in High-Mobility, Solution-Crystallized Small Molecule Semiconductors Studied by Charge Modulation Spectroscopy. *Adv Funct Mater*. 2016;26(14):2326-2333. doi:https://doi.org/10.1002/adfm.201502502
51. Larsson O, Said E, Berggren M, Crispin X. Insulator polarization mechanisms in polyelectrolyte-gated organic field-effect transistors. *Adv Funct Mater*. 2009;19(20):3334-3341. doi:10.1002/adfm.200900588
52. Kim H, Auyeung RCY, Lee SH, Huston AL, Piqué A. Laser-printed interdigitated Ag electrodes for organic thin film transistors. *J Phys D Appl Phys*. 2010;43(8). doi:10.1088/0022-3727/43/8/085101
53. Sonker AK, Rathore K, Nagarale RK, Verma V. Crosslinking of Polyvinyl Alcohol (PVA) and Effect of Crosslinker Shape (Aliphatic and Aromatic) Thereof. *J Polym Environ 2017 265*. 2017;26(5):1782-1794. doi:10.1007/S10924-017-1077-3
54. Jeong J, Marques GC, Feng X, et al. Ink-Jet Printable, Self-Assembled, and Chemically Crosslinked Ion-Gel as Electrolyte for Thin Film, Printable Transistors. *Adv Mater Interfaces*. 2019;6(21). doi:10.1002/admi.201901074
55. Wu X, Chen Z, Li Y, et al. Improving dermal delivery of hydrophilic macromolecules by biocompatible ionic liquid based on choline and malic acid. *Int J Pharm*. 2019;558:380-387. doi:10.1016/J.IJPHARM.2019.01.021
56. Jeong J. The Study of Chemically Cross-Linked Ion Gels for Electronic Devices. 2020.
57. Jeong J, Singaraju SA, Aghassi-Hagmann J, Hahn H, Breitung B. Adhesive Ion-Gel as Gate Insulator of Electrolyte-Gated Transistors. *ChemElectroChem*. 2020:2735-2739. doi:10.1002/celc.202000305
58. Rudra R, Kumar V, Kundu PP. Acid catalysed cross-linking of poly vinyl alcohol (PVA) by glutaraldehyde: effect of crosslink density on the characteristics of PVA membranes used in single chambered microbial fuel cells. *RSC Adv*. 2015;5(101):83436-83447. doi:10.1039/C5RA16068E
59. Hasan AMA, Abdel-Raouf ME-S. *Cellulose-Based Superabsorbent Hydrogels*.; 2019. doi:10.1007/978-3-319-77830-3_11
60. Elding LI, Gröning A-B, Gröning Ö. Kinetics and mechanism of the reaction between tetrachloro- and tetrabromo-aurate(III) and thiocyanate. *J Chem Soc{,} Dalt Trans*. 1981;(5):1093-1100. doi:10.1039/DT9810001093
61. Durović M, Puchta R, Bugarčić ŽD, Van Eldik R. Studies on the reactions of [AuCl4]- with different nucleophiles in aqueous solution. *Dalt Trans*. 2014;43(23):8620-8632. doi:10.1039/c4dt00247d
62. Jo YJ, Kim H, Ok J, et al. Biocompatible and Biodegradable Organic Transistors Using a Solid-State Electrolyte Incorporated with Choline-Based Ionic Liquid and Polysaccharide. *Adv Funct Mater*. 2020;1909707:1-12. doi:10.1002/adfm.201909707
63. Safa MN. Poly (Ionic Liquid) Based Electrolyte for Lithium Battery Application. *FIU Electron Theses Diss*. May 2018. doi:10.25148/etd.FIDC006891
64. Lee KH, Zhang S, Lodge TP, Frisbie CD. Electrical impedance of spin-coatable ion gel films. *J Phys Chem B*. 2011;115(13):3315-3321. doi:10.1021/JP110166U/ASSET/IMAGES/MEDIUM/JP-2010-10166U_0008.GIF
65. Lazanas AC, Prodromidis MI. Electrochemical Impedance Spectroscopy─A Tutorial. *ACS Meas Sci Au*. 2022. doi:10.1021/acsmeasuresciau.2c00070
66. Dasgupta S, Stoesser G, Schweikert N, et al. Printed and electrochemically gated, high-mobility, inorganic oxide nanoparticle FETs and their suitability for high-frequency applications. *Adv Funct Mater*. 2012;22(23):4909-4919. doi:10.1002/adfm.201200951
67. Umadevi M, Bindhu MR, Sathe V. A Novel Synthesis of Malic Acid Capped Silver Nanoparticles using Solanum lycopersicums Fruit Extract. *J Mater Sci Technol*. 2013;29(4):317-322.

doi:10.1016/J.JMST.2013.02.002
68. Datta S, Mahin J, Liberti E, Manasi I, Edler KJ, Torrente-Murciano L. Role of the Deep Eutectic Solvent Reline in the Synthesis of Gold Nanoparticles. *ACS Sustain Chem Eng*. 2022. doi:10.1021/ACSSUSCHEMENG.2C07337
69. De Vreese P, Brooks NR, Van Hecke K, et al. Speciation of copper(II) complexes in an ionic liquid based on choline chloride and in choline chloride/water mixtures. *Inorg Chem*. 2012;51(9):4972-4981. doi:10.1021/IC202341M/SUPPL_FILE/IC202341M_SI_003.CIF

8

Conclusions and Future Work

This final chapter serves to summarize and reiterate the major achievements reported in this dissertation to the originally outlined objectives set in Chapter 1. If certain goals were not fully addressed, suggestions to resolve each issue will be addressed below in future work section.

The sheer quantity of accumulated disposable electronic waste is unsustainable and has already shown to be detrimental to the environment. One strategy to combat this is by directly utilizing biodegradable materials in common electrical components and devices. This idea inspired the development of transient and biodegradable electronics that, unfortunately, still mostly rely on conventional microfabrication techniques that contribute to waste and hazardous material generation. Therefore, the adoption of environmentally friendly manufacturing processes is impertinent to establishing a more sustainable system. Inkjet printing can meet these requirements as it is known as a low impact, low cost, and minimal waste technique that serves to replace conventional techniques. Its versatility allows for the deposition of a myriad of ink materials to be deposited directly on any chosen substrate independent of temperature, rigidity, and composition. Thus, materials selection and characterization were conducted to determine the most compatible biodegradable substrates for the printing process. Next, novel functional and biodegradable metal inks were formulated according to the recommended jetting standards and treated using low temperature sintering techniques such as plasma, chemical, or photonic sintering. This was necessary due to both the temperature sensitivity of biodegradable substrates and the excessive sintering temperatures of the respective inks. Both printing and sintering parameters were optimized according to their resulting electrical properties. Additionally, thin film characterization was performed to determine their respective morphology and chemical

composition. Once achieved, different electrical components were fabricated and tested for their viability.

In this work, novel biodegradable materials were incorporated to replace the substrate, conductive metal films, and dielectrics layers in order to demonstrate a fully printable and biodegradable transistor amongst other electrical components. In order to achieve these goals, a layer-by-layer approach was conducted from the bottom up starting with the substrate.

Substrate

The substrate can be easily replaced with biodegradable alternatives all of which must meet basic requirements based on their respective glass transition and melting temperatures, surface roughness and surface tension, as well as dissolvability. Here a total of 7 substrates were tested and characterized ultimately resulting in the qualification of silk fibroin under all conditions achieving the lowest possible surface roughness at 0.2 nm and highest glass transition temperature at 180°C amongst the tested substrates as shown in Figure 8.1 below. This was followed closely by CNF and PVA both of which were acceptable if alternative sintering techniques were applied.

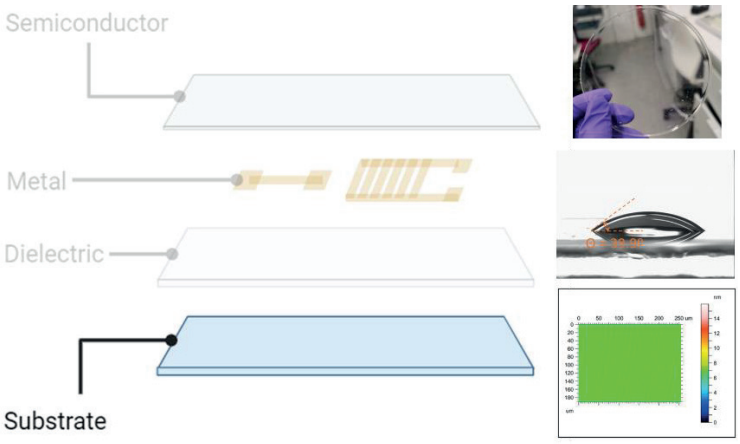

Figure 8.1. Fabricated silk substrate and its respective materials properties

Conductive metal thin film layers

Different types of inks were developed in order to create conductive metallic layers stemming from metal salt-based decomposition (MSD) inks to biodegradable Zn nanoparticle inks. Au and Pt metal thin films could be easily developed using plasma sintering on a large

range of flexible substrates as demonstrated on polymers, papers, and textile seeing conductivities as high as 3 x 10^5 S·m^{-1} for Au and 4 x 10^4 S·m^{-1} for Pt achieved at low sintering temperatures. The conformal coverage of such inks compensates for the rugosity of non-planar substrates making this ink inclusive for any surface while maintaining good film conductivity as seen in Figure 8.2 below.

In the case of room temperature chemical-light sintering, Au MSD ink responded most strongly to PVA as a reducing substrate seeing excellent conductivities up to 1 x 10^6 S·m^{-1}. Such values have not even been reported with commercially available Au NP inks exemplifying the superiority in using such inks. A thorough investigation of the both the reducing and growth mechanisms was defined in addition to thin film analysis as displayed in Figure 8.3. This validated the elemental purity of the formed polycrystalline Au film exhibiting a uniform, conformal, and densely packed appearance. This technique has not yet been reported in literature which due to its facile Au film development is an invaluable discovery for the printed electronics community.

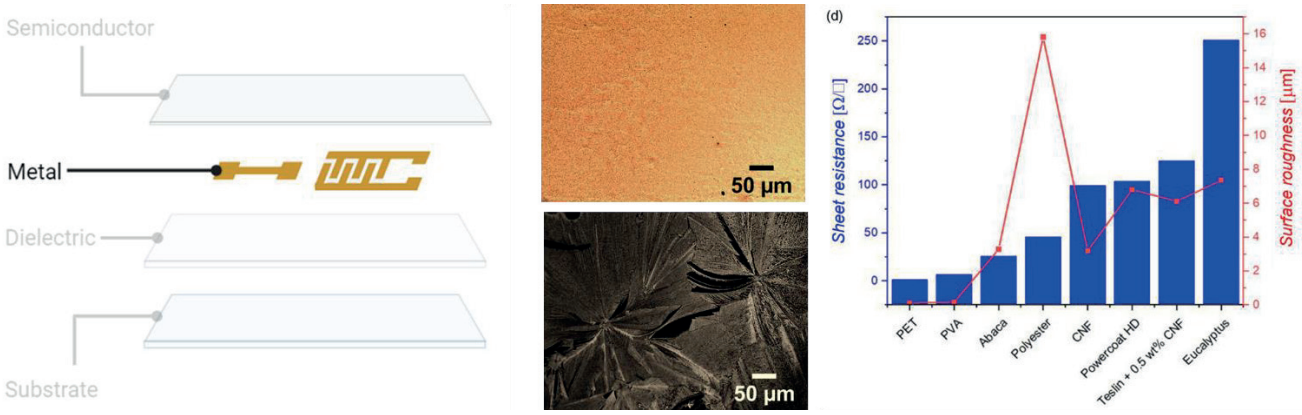

Figure 8.2. Plasma treated Au and Pt metal films and their respective sheet resistance values on non-conventional substrates

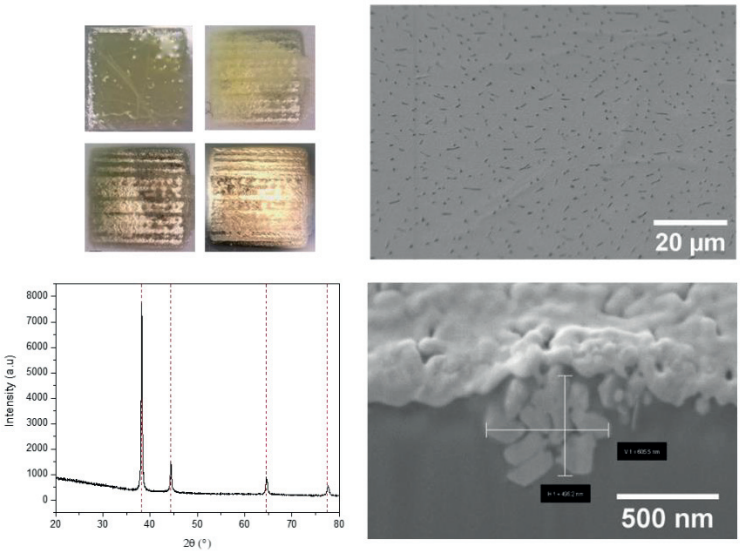

Figure 8.3. The development of self-sintering Au films and its materials properties

Additionally, biodegradable Zn and Mo metal inks were formulated after rigorous stability testing and adapted to inkjet printing to create deposited films. Because biodegradable metals are known to oxidize rapidly and require excessive sintering temperatures, photonic curing was implemented. This technique indeed served to remove the oxide from Zn NPs thus developing films with moderate conductivity despite their oxidative states up to 8.1 x 10^3 $S \cdot m^{-1}$ for Zn, similar to values reported in literature. Figure 8.4 below provides important highlights and characterization for photonically sintered Zn films.

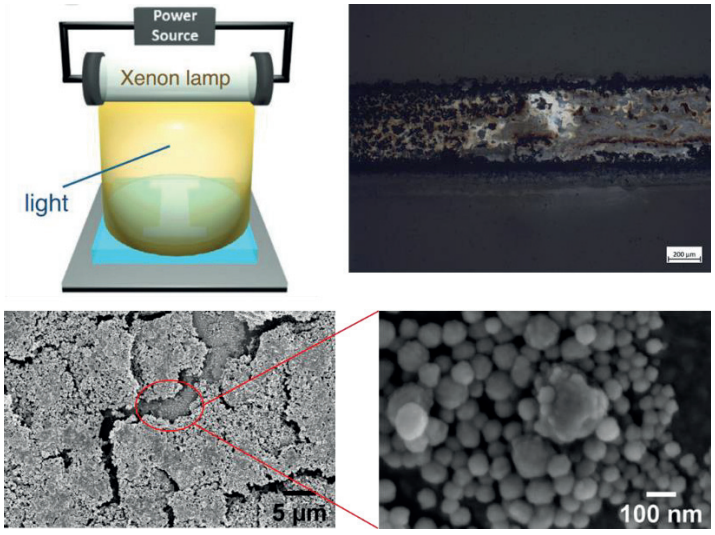

Figure 8.4. Schematic of a photonic curer[1] and Zn sintered films and its morphology

Dielectric layer

Although PVA itself can be considered an insulator layer, a facile approach for the development of a PVA based ion gel was pursued. Even with the decline in hydroxyl groups, the PVA-PEMA gel combination was found to successfully reduce the deposited Au MSD ink and form a conductive Au film layer. Additionally, a biodegradable choline-malate ionic liquid was synthesized and combined with the PVA-PEMA polymer matrix to form an ion gel that displayed ionic conductivity and capacitance as highlighted in Figure 8.5 below. Biodegradability was also achieved with this combination displaying its viability to be used as a dielectric ion gel layer.

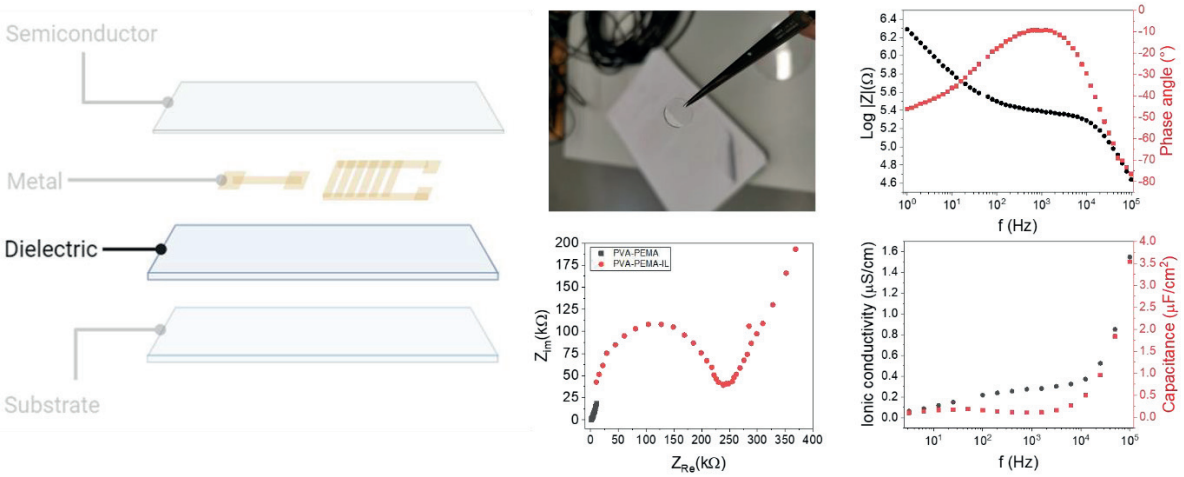

Figure 8.5. PVA-PEMA dielectric ion gel and its properties

Semiconductor layer

Due to the limited number of biodegradable semiconductors in existence, this layer was instead deposited using TMTES-Pentacene, a p-type small-molecule semiconductor, derived from the well-known TIPS-pentacene, with significantly higher mobilities. Chemical compatibility testing confirmed that chlorobenzene did not affect the substrate and therefore was used to further testing. Here, different deposition methods were explored and resulted in polycrystalline films with elongated and highly directional fine needle grains as a result of the meniscus technique. When placed directly above the interdigitated source and drain electrodes, the film remained similar in morphology as seen in Figure 8.6 below.

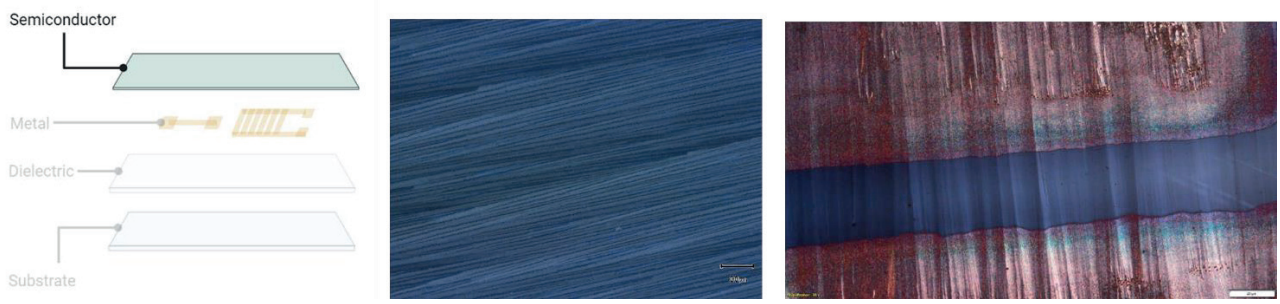

Figure 8.6. TMTES Pentacene semiconductor layer deposited by a meniscus technique on PVA and Au gate electrode

Applications

The example shown above correlate specifically to building an EGOFET with in-plane Au source and drain interdigitated electrodes as shown in Figure 8.7 below. Here, PVA was used as both the substrate and dielectric layer. Although modulation has been observed, the doping effects on the semiconductor negatively affected the transistor performance thus, its electrical characteristics must be improved.

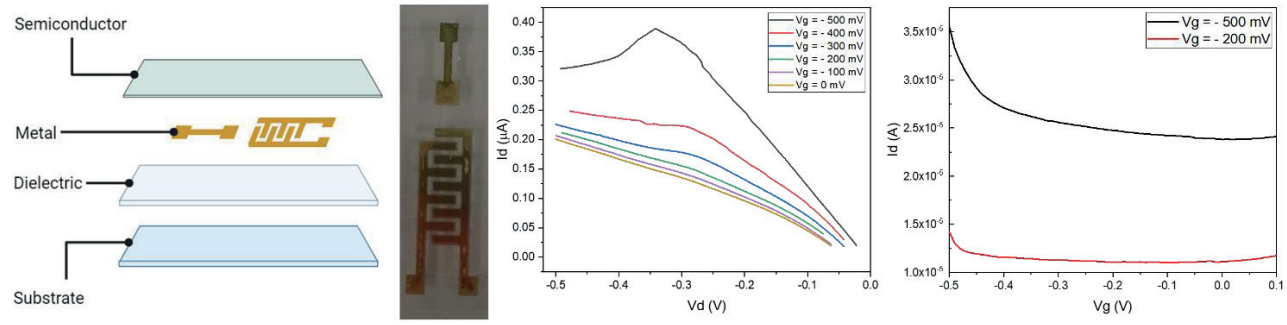

Figure 8.7. Inkjet printed EGOFET and its respective electrical performance

Other structures such as electrodes, LED circuits, and strain gauges were developed to evaluate the functionality and bending strain of the Au films deposited on both polyester textile and PVA substrates. Due to the substrate backing of the film, extreme bending strains beyond 2% strain were tested showing overall excellent resistance to bending, durability, and long-term stability. In fact, this ability was advantageous for strain gauges as it displayed a gauge factor of 2, equal to commercially sold sensors showing sensitivity to both touch and heat. Additionally, its biodegradability was confirmed by exposing the sensor to water which immediately dissolved leaving behind only the Au conductive tracks for facile recycling. Additionally, fully printed glucose biosensors were printed with the Au MSD inks as both the counter and working

electrodes showed response to different glucose concentrations. The incorporation of these inks in respect to commercially available Au NP inks significantly reduces the cost per sensor. Lastly, a 2.4 GHz L-shaped antenna successfully generated a signal with an amplitude between -32.0 and -84.7 dBm up to 20 m distance. All devices and their respective response are shown below in Figure 8.8.

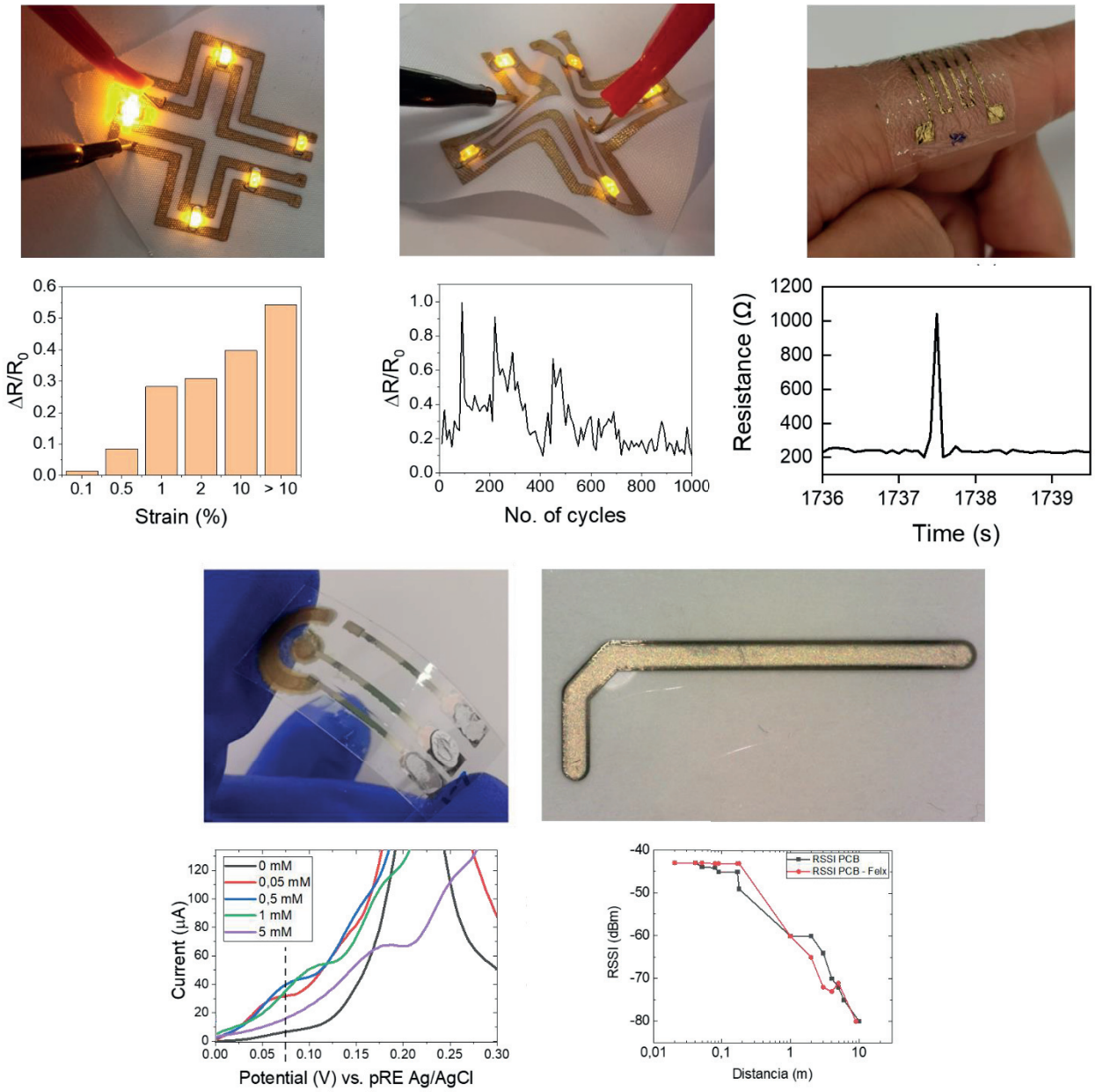

Figure 8.8. Images and testing of LED circuit, strain sensor, and biosensor

8.1 | FUTURE WORK

The main work of this thesis concentrated on the ink and thin film development of metal ink films using inkjet printing as a deposition technique as well as their corresponding thin film characterization. As this has already been thoroughly investigated, future work should be focused on using these developed Au films from plasma or chemical-light sintering into appropriate applications. In the case of the former, is the development of a functional and reliable glucose biosensor using solely MSD inks. For the latter, the strain sensor has yet to be fully exploited, especially for its known plasmon resonance.

Work concerning the development of Zn and Mo inks is also currently ongoing and should be further elaborated on by focusing heavily on the reduction of the oxide layer surrounding the nanoparticle. This can be done through multiple routes by controlling oxidation at its source, that is during the chemical synthesis step. If this is still not achievable, the oxide layer can be removed after ink deposition using an acid etchant which can be achieved at room temperature. A tertiary solution is directly using laser sintering or a combination of different sintering techniques to effectively increase its respective conductivity. Lastly, if the conductivity itself cannot reach acceptable levels, the nanoparticles themselves can be combined with carbon derivatives to enhance its electrical properties.

Lastly, one of most notorious and most difficult layers to achieve biodegradability is with the semiconductor layer itself. Only a handful of semiconducting materials are known to be biodegradable which often contains poor mobility compared to standard semiconductors thus limiting their application into real world devices. This issue must first be addressed and researched to be implanted in everyday electronics.

Annex A: List of Publications and Conferences

A brief summary of publications and conferences are present below in consideration. A comprehensive review of the PhD candidates qualifications and publications can be found in Annex B: Scientific Curriculum Vitae.

Articles

Paper I (accepted and published)

Leung TSW, Ramon E, Martínez-Domingo C. *Low-Temperature Plasma Sintering of Inkjet-Printed Metal Salt Decomposition Inks on Flexible Substrates*. Adv Eng Mater. 2022;2200834. doi:10.1002/adem.202200834 (IF = 4.122 @2021, Q1)

Paper II (To be submitted in 2024) – with the tentative title: Room Temperature Sintering of Conductive Inks on Biodegradable Substrates

Conferences

Participant at "Large-area, Organic & Printed Electronics Convention (LOPEC)", Munich, Germany 2019.

Oral Presentation at "Innovations in Large Area Electronics (INNOLAE) Conference", Cambridge, United Kingdom, 2023.

Annex B: Curriculum Vitae

Tammy Leung

16th May 1987, Los Angeles

Email: tammy.sw.leung@gmail.com

Former Position: PhD Student at the Institute of Microelectronics of Barcelona (IMB-CNM)

Education:

UNIVERSITAT AUTONÒMA DE BARCELONA
PhD student in Electrical Engineering, 2019 - 2023
- Doctoral thesis provisionally titled "Development of functional inks and printed devices for transient and eco-friendly electronics" with predicted submission at the end of September 2023. This thesis relies heavily on the use of temperature independent methods such as inkjet printing and alternative sintering techniques and to produce low cost, flexible, and transient devices ranging from basic electrodes to more complicated structures such as transistors.

SAN JOSE STATE UNIVERSITY
Masters in Materials Engineering, 2010 - 2012
- Masters Project on the Deposition and Characterization of Crystalline Si Thin Films
- Specialization in microelectronics and semiconductors

UNIVERSITY OF CALIFORNIA DAVIS
Bachelors in Material Science and Engineering, 2005 - 2009
- Senior Design Project on Pb-Free Process Development in collaboration with Agilent Technologies
- Member, Materials Research Society

Research Experience:

PHD CANDIDATE | IMB-CNM (CSIC) | Mar 2019 - current
- Development of functional and biodegradable inks
- Inkjet printing of electronic components and sensors onto biodegradable substrates
- Perform electrical characterization of fabricated devices
- Incorporate biodegradable materials for the development of transient electronics

RESEARCHER | Catalonia Institute for Energy Research | Mar 2017 - Nov 2017
- Utilized both PLD and ALD techniques to deposit and characterize ZrO2 and Al2O3 thin films using XRD, confocal microscopy, ellipsometry, and SEM
- Consulted on microfabrication processes of a MEMS based fuel cell in collaboration with UAB
- Built, designed, and printed a mini-reactor aided by Solidworks and a 3D SLA ceramic printer

PHD CANDIDATE | Institute of Bioengineering of Catalonia | Dec 2016 - Dec 2017
- Exploited electrochemical and electrodeposition techniques (amperometry, cyclic voltammetry) to test biosensors and deposit various thin films
- Performed chemical synthesis and materials characterization of nanomaterials
- Experimented with new ink formulations using reduced graphene oxide and copper nanowires for inkjet printing
- Designed and created project related 3D printed structures using AutoCAD &SLA 3D printer

STUDENT ASSOCIATE | SRI International | Apr 2011 - Dec 2011
- Designed and fabricated PN junctions from Si films using a variety of microfabrication techniques
- Developed and implemented a novel CVD-reactor technique to create epitaxial, polycrystalline, and doped Si thin films
- Prepared and performed chemical synthesis for various experimental demands and determined optimal deposition conditions using DOE

RESEARCH EXPERIENCE FOR UNDERGRADUATES INTERN | University of Illinois, Urbana-Champaign | Jun 2009 - Aug 2009
- Executed a wide range of microfabrication techniques including photolithography, wet chemistry (etching, RCA Clean), dry etching (RIE, Plasma etch), and deposition(CVD, PVD)
- Implemented a transfer printing technique using a PDMS stamp to create flexible electronics
- Tested resulting diodes with a solar simulator to test performance under illumination

SENIOR DESIGN RESEARCH PROJECT | University of California, Davis | Sept 2008 - Jun 2009
- Identified and analyzed intermetallic compounds using EDS/EDX and OM techniques
- Participated in a collaborative research with Agilent Technologies on the integration of Pb-free solders into Ecal module
- Established the durability of 3 solders through wettability, shear lap strength, thermal cycling, leak testing, and drop testing

Work Experience:

3D REMOTE SUPPORT ENGINEER | HP/Sellbytel | Jun 2018 - Mar 2019
- Provide proactive support to European and American clients in terms of hardware, software, and all around print quality issues with manufactured parts
- Alignment of field service engineers and part deliveries with customers for onsite installs through

various communication channels
- Establish, develop, and maintain ongoing relationships with high profile customers
- Responsible for the setup and maintenance of the 3D laboratory and provide hands-on troubleshooting and repair when necessary

FREELANCE EDITOR
CACTUS Communications | Jan 2018 - Jun 2018
- Correct and modify grammar and formatting of scientific articles until acceptance
- Provide English grammatical tips to the writer based on their writing style
- Grade each writing assignment to a strict rubric

Teaching Experience:

LABORATORY INSTRUCTOR | San Jose State University | Aug 2010 - May 2011
- Prepared, taught, and supervised 2 sections of an introductory material science course
- Advised, assisted, and trained 35 undergraduate students in scientific writing, instrument setup, and operation
- Assessed student comprehension/knowledge of the material through grading quizzes, worksheets, and lab reports

Scientific Publications:

- Leung TSW, Ramon E, Martínez-Domingo C. Low-Temperature Plasma Sintering of Inkjet-Printed Metal Salt Decomposition Inks on Flexible Substrates. Adv Eng Mater. 2022;2200834. https://doi:10.1002/adem.202200834

- Romeo, A., Moya, A., Leung, T. S., Gabriel, G., Villa, R., & Sánchez, S. (2018). Inkjet printed flexible non-enzymatic glucose sensor for tear fluid analysis. Applied Materials Today, 10, 133–141. https://doi.org/10.1016/j.apmt.2017.12.016

- Romeo, A., Leung, T. S., & Sánchez, S. (2016). Smart biosensors for multiplexed and fully integrated point-of-care diagnostics. Lab Chip, 16(11), 1957–1961. https://doi.org/10.1039/C6LC90046A

- Perez-Mariano, J., Leung, T., Moro, L., Gleixner, S., Lau, K., Chavez, B., Sanjurjo, A. (2011). Progress on crystalline silicon thin film solar cells by FBR-CVD: Effect of substrates and reactor design. 2011 37th IEEE Photovoltaic Specialists Conference, 003068–003072. https://doi.org/10.1109/PVSC.2011.6186592

Invited Talks and Conferences:

- **Leung, T**., Ramon, E., Martinez Domingo, C. Novel Metal Salt Decomposition inks for low temperature conductive film development on flexible substrates. Oral Presentation at Innovations in Large-Area Electronics Conference (innoLAE) 2023, 22nd – 23rd February 2023, Cambridge, UK.

- Attended Large-area, Organic & Printed Electronics Convention (LOPEC) Congress 2019, 19th-21th March 2019, Munich, Germany

- Alayo, N., **Leung, T**., Garbayo, I., Chiabrera, F., Morata, A., Tarancón, A. (2017). Micro Solid Oxide Fuel Cells, towards a new generation of miniaturized portable power generator. Poster Presented at the 2017 International Conference on Micro and Nano Engineering, Braga, PT.

- Assisted at the 2010 Materials Research Society (MRS) Spring Meeting, 5th – 9th April, San Francisco, USA.

- Powers, M., Shackelford, J., Fong, D., Kwan, Z.G., **Leung, T**., Mak, K.Y., Pedron, E. (2010). Pb-Free Process Development for Microcircuit Package Assemblies – A University/Industry Design Project Collaboration. Paper presented at the 2010 TMS Annual Meeting and Exhibition, Seattle, WA, USA

Guest scientist stay

- Short term stay at the Institute of Nanotechnology, Karlsruher Institute of Technology (KIT) from 1st September 2022 to 30th November 2022 in Germany

- Contracted stay at the Max Planck Institute for Solid State Research, Stuttgart from December 2016 to December 2017 in Germany.

Skills

3D Printing Techniques: Inkjet Printing, Stereolithographic Printing (SLA), MultiJet Fusion (MJF), SLS

Materials characterization techniques: Scanning electron microscopy (SEM), XRD, CV profiling, Confocal microscopy

Thin film deposition: CVD, Electrodeposition, PLD, ALD, Sputtering

Microfabrication Techniques: Spin coating, Plasma and Photonic Sintering, Photolithography, Plasma Etch, Wet Etch,

Metrology and Test Instruments: Potentiostat, Impedance Spectroscopy, Reflectometry, Ellipsometry, Profilometry, 4 point probe, Instron Tensile Tester, Impact tester, Hardness tester

Software: AutoCAD, Solidworks, Origin, Rhinoceros, Autolab, Microsoft Office, ChemOffice, Inkscape

Languages: English – Native, Catalan – A2 level, French – A2 level

List of Abbreviations

$AgNO_3$	Silver nitrate
Au	Gold
AFM	Atomic Force Microscope
CNF	Nanofibril Cellulose
DI	Deionized water
DMSO	Dimethyl sulfoxide
DS	Drop spacing
DSC	Differential Scanning Calometry
$HAuCl_4$	Gold (III) chloride hydrate
H_2PtCl_6	Chloroplatinic acid
IPA	Isopropanol
MOD	Metal Organic decomposition
MSD	Metal salt decomposition
NP/s	Nanoparticle/nanoparticles
PEN	Polyethylene naphthalate
PDMS	Polydimethylsiloxane
PET	Polyethylene terephthalate
PVA	Polyvinyl alcohol
PVP	Polyvinylpyrrolidone

RMS	Root Mean Squared
SEM	Scanning Electron Microscope
UV	Ultra-violet
XPS	X-ray photoelectron spectroscopy
XRD	X-ray Diffraction Analysis

List of Figures

List of Tables